Studying Phase Transitions and Co-crystallisation in Pharmaceutical Materials

Alexander E. Clout

A thesis submitted for the degree of Doctor of Philosophy

UCL

Declaration

I Alexander Edward Clout confirm that the work presented in this thesis is my own. Where information has been derived from other sources, I confirm that this has been indicated in the thesis.

Acknowledgments

Firstly I would like to express my gratitude to my academic supervisors Gareth Williams, Simon Gaisford and Christoph Salzmann for their guidance during my PhD at the SoP and CIB and for their doors always being open. I would also like to acknowledge UCL for giving me the opportunity and means to carry out this research by providing the funding of an Impact Studentship.

Special thanks go to Asma Buanz, Jacob Shepard, Martin Vickers and Yue Wu for their guidance and helpful discussions, without whom I would never have been able to collect or analyse the data in this thesis.

I would like to express my profound gratitude to my family who have given me their unwavering support throughout this long and difficult process, both emotionally and financially.

Finally I would like to thank all the members of the CGS research group and the SG research group for helpful discussions and particularly the residents of Research Space 308 from when I started until now for the friends I have made and the fun times we've had. You know who you are, and if you don't it's not you.

Abstract

For a drug to be effective it must be in solution so that it can be absorbed by the body at the site of action. Therefore, it must be soluble in an aqueous environment. For practical reasons many drugs are formulated in the solid state; an understanding of how the drug transitions from solid to solution is hence critical. The two key factors to be considered are the drug's solubility and dissolution rate.

In this work a novel method for the analysis of phase transitions in pharmaceutical materials was developed by combining high energy synchrotron X-ray diffraction with differential scanning calorimetry (DSC-XRD). This was used to collect *in situ* structural and calorimetric data on temperature driven phase transitions. Initial work was carried out to prove the utility of the technique by examining two enantiotropically polymorphic systems, and subsequently it was used to examine phase transitions in materials exhibiting multiple polymorphs. Building on this, the effect of sugar based excipients on the crystallisation behaviour of paracetamol glasses upon heating was examined, with particular emphasis on the stabilisation of metastable polymorphs II and III.

DSC-XRD was further employed in the production of new co-crystals between isonicotinamide and three antioxidant compounds. The ability of four different techniques (solvent evaporation, thermal inkjet printing, heating, and milling) to prepare these co-crystals was investigated in detail.

Finally, physical vapour deposition, a novel technique in the field of pharmaceuticals, was investigated for the preparation of amorphous materials, with particular emphasis on drugs considered to be poor glass formers.

DSC-XRD has been demonstrated to be an incredibly powerful tool for the analysis of phase transitions and co-crystallisation in pharmaceutical materials, and physical vapour deposition has been shown to have great potential for preparing amorphous drugs from poor glass formers.

Table of Contents

Impact Statement

For a drug to be effective it must be absorbed by the body at the site of action. In order for this to happen the drug must be in solution and so, regardless of the pathway it is to take, it must be soluble, to some extent, in an aqueous environment. One of the most significant barriers to the success of new chemical entities is their solubility, with up to 70 % of candidates being reported as having poor aqueous solubility in the past decade.

The formulation of drugs in the amorphous or metastable forms and co-crystallisation all have the potential to overcome this problem. However, current methods of vitrification are incapable of producing amorphous matrices of adequate stability and methods of screening possible co-crystals are slow and expensive. Methods of stabilising metastable polymorphs using molecular additives are well known, but detailed knowledge of the mechanism and rate of conversion between the polymorphs of drugs is lacking. More significantly, knowledge of the interactions occurring between additives and active pharmaceutical ingredients, and consequently which additives to use for any given scenario, is lacking.

The research contained within this thesis goes some way to addressing the problems outlined above and in particular presents a novel and powerful technique for the simultaneous structural and thermal analysis of phase transitions in pharmaceutical materials. It further reports a number of new co-crystals with potential pharmaceutical applications.

Finally, a novel deposition technique for the preparation of amorphous materials is presented. The method’s ability to produce amorphous materials where this cannot be achieved using traditional methods may make this new approach an invaluable tool for future pharmaceutical research. Armed with these tools, future researchers will be able to design more intelligent medicines.

List of Abbreviations

API	Active Pharmaceutical Ingredient
ASW	Amorphous Solid Water
BZA	Benzoic acid
CBZ	Carbamazepine
CSD	Cambridge Structural Database
C_p	Heat capacity
DHC	Dihydrocarbamazepine
DHPAA	3,4-dihydroxyphenylacetic acid
DSC	Differential Scanning Calorimetry
DVS	Dynamic Vapour Sorption
FTIR	Fourier Transform Infrared Spectroscopy
GF	Griseofulvin
HPAA	4-hydroxyphenylacetic acid
HPMC	Hydroxypropyl methylcellulose
IGC	Inverse Gas Chromatography
IMC	Indomethacin
INCT	Isonicotinamide
JEEP	Joint Engineering Environmental and Processing Beamline
KWW	Kohlrausch-Williams-Watts
LOD	Limit of Detection
MDSC	Modulated Temperature Differential Scanning Calorimetry
NCT	Nicotinamide
NIR	Near-Infrared Spectroscopy
NMR	Nuclear Magnet Resonance Spectroscopy
PCM	Paracetamol
PVD	Physical Vapour Deposition

PXRD	Powder X-ray Diffraction
PID	Proportional Integral Derivative
QCM	Quartz Crystal Microbalance
SAC	Saccharin
SSA	Salicylsalicylic acid
TGA	Thermogravimetric Analysis
T_f	Fictive temperature
T_g	Glass transition temperature
T_K	Kauzmann temperature
T_m	Melting temperature
UCL	University College London
VNA	Vector Network Analyser

1 Introduction

1.1 Solubility and Dissolution

For a drug to be effective it must be absorbed by the body at the site of action. In order for this to happen the drug must be in solution and so, regardless of the pathway it is to take, it must be soluble, to some extent, in an aqueous environment.[1] However, for practical reasons such as stability, ease of manufacture, transportation and administration, many drugs are formulated in the solid state; an understanding of how the drug transitions from solid to solution is therefore critical.[2] The two key factors to be considered are the solubility: the extent to which a solute (*i.e.* a drug) will disperse as molecules throughout the solvent, and dissolution: the process by which the molecules of the solid transfer into solution.[1] The rate at which dissolution occurs is particularly important as fast dissolution is often linked to high bioavailability. As dissolution is defined by a rate it is a kinetic process, whereas solubility, an equilibrium state, is thermodynamic.[3]

One of the most significant barriers to the success of new chemical entities is their solubility, with up to 70% of candidates being reported as having poor aqueous solubility in the past decade.[4–6] The solubility of a substance is directly related to its physical form. Materials may exist as solids, liquids and gases and the form they take is dependent on the conditions (pressure and temperature) of the environment that surrounds them. Unlike liquids and gases solids are rigid forms of matter, and their shape is independent of the container in which they are held. A crystal's external shape is known as the habit and is determined by the underlying structure.[7] Molecular crystalline solids consist of a repeating array of molecules termed the crystal lattice. The smallest unit of the lattice is known as the unit cell and may consist of one or more molecules. The molecules in a molecular crystal are held together to form the lattice by intermolecular bonds: hydrogen bonds (H-bonds), and van der Waals forces. The energy required to break these bonds and separate the molecules, for example during dissolution, is called the lattice enthalpy. Different crystal structures are held together by a different combination of intermolecular bonds and so have a unique lattice enthalpy.[8] Materials may exist in a number of crystal forms, which are summarised in Figure 1-1 and Table 1-1.

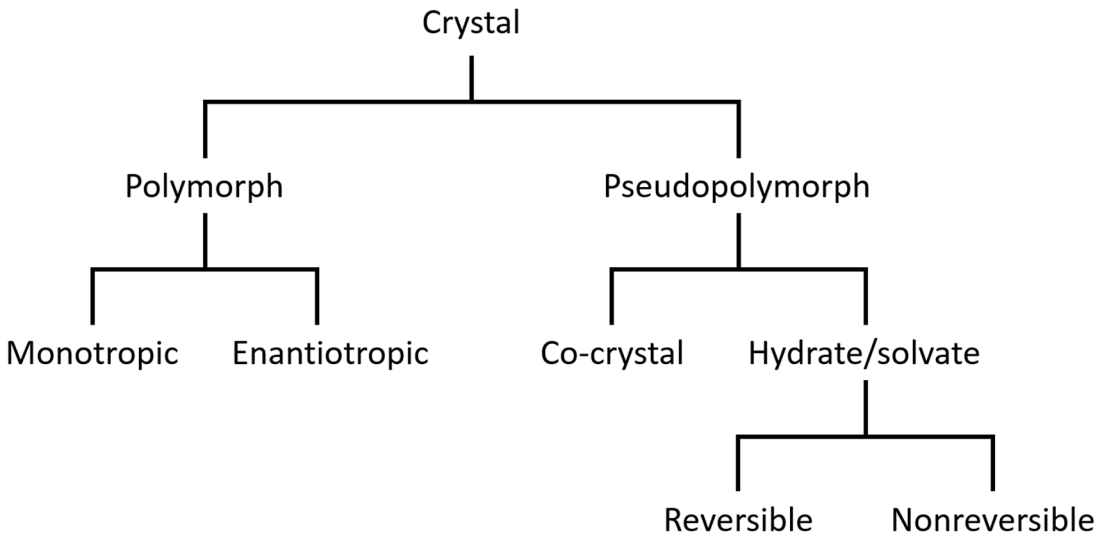

Figure 1-1. Overview of crystalline forms. Reproduced with permission from ref [9].

Table 1-1. Summary of the crystalline forms and their definitions.

Crystal Form	Definition
Polymorph	Any one of the individual crystalline forms of a single substance.
Monotropic	Polymorphic system in which the order of stability is independent of the pressure and temperature. Phase transitions observed upon heating are irreversible.
Enantiotropic	Polymorphic system in which the order of stability changes at a critical temperature. Transitions between enantiotropic polymorphs are reversible.
Pseudopolymorph	Different crystal structures arising from the addition of one or more chemical entities to the unit cell.
Co-crystal	Solid that is a crystalline single phase material composed of two or more different molecular and/or ionic compounds, generally in a stoichiometric ratio which is neither a solvate nor a simple salt.[10]
Hydrate/solvate	Solid that is a crystalline single phase material in which the unit cell comprises a drug and water or another solvent in a stoichiometric ratio.
• *Reversible*	A hydrate/solvate in which dehydration/desolvation results in a stable dehydrate/desolvate that may be rehydrated/resolvated to give the original hydrate/solvate.
• *Nonreversible*	A hydrate/solvate that when dehydrated/desolvated becomes unstable and converts to an anhydrous form. Addition of further solvent will not result in formation the original hydrate/solvate.

In ambient conditions the majority of drugs exist as crystalline solids[11] in their most stable state. This is ideal for long term storage but their high stability presents a problem for solubility and dissolution. There has been a great deal of research into ways of improving the apparent solubility and dissolution rate of poorly soluble active pharmaceutical ingredients (APIs) in an attempt to improve their bioavailability.[4–6] These include; particle size reduction, modification of the crystal habit, polymorph formation, amorphous phase preparation, co-crystallisation, solid dispersion and chemical modification among others,

and there are a number of review papers in the literature which discuss them in detail.[12–14]

1.2 Characterisation

1.1.1. X-ray diffraction

Full characterisation of the crystalline solid state (and to a lesser extent the amorphous) requires determination of the positions of the atoms and molecules, in the unit cell, and its dimensions. Single crystal X-ray diffraction is the only tool capable of collecting this information. However, often single crystals are not easily obtainable, but powders consisting of many small crystallites (too small for single crystal diffraction) are, and limited information on the structure of a material can be collected by powder X-ray diffraction (PXRD). The technique relies on the repeating nature of the crystal lattice to build an image of the internal structure of the crystal.[9,15]

When X-rays are focused onto a substance they are scattered by electrons within that material, and the pattern of the diffracted light can be collected using an X-ray detector. If the subject is crystalline then the ordered arrangement of atoms, and so electrons, results in a diffraction pattern of regularly spaced spots. The intensity and position of these spots can be used to calculate the positions of the atoms in the crystal lattice.[8]

The crystal lattice can be described by sets of parallel planes that extend infinitely throughout the lattice (Figure 1-2 (a)). The relationship between the distance separating adjacent planes and the angle at which X-rays must hit the crystal for constructive interference (intense reflections resulting from X-rays diffracting in phase) is known as Bragg's Law:

$$n\lambda = 2dsin\theta \qquad (1)$$

Where λ is the wavelength of the incident beam, d is the interplanar spacing, and θ is the incident angle (Figure 1-2 (b)) of the beam. For constructive interference to occur n must be an integer (*i.e.* the difference in path length between planes must equal an integer number of wavelengths so that the diffracted waves remain in phase).[8]

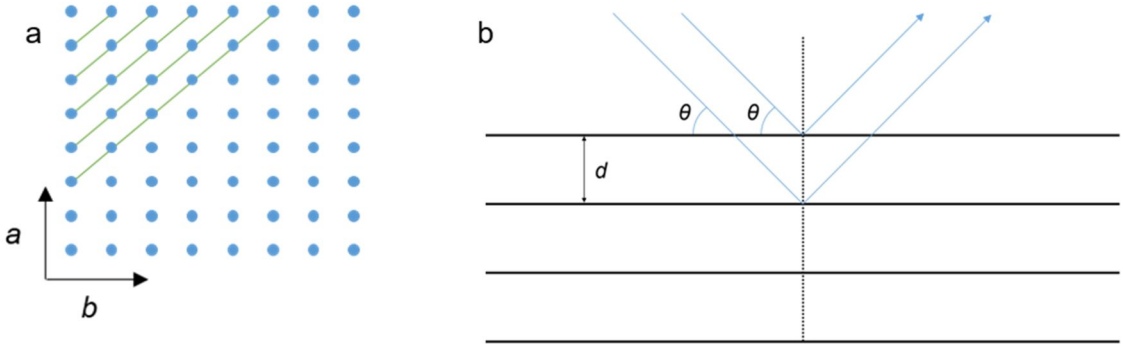

Figure 1-2. A schematic representation of (a) planes in a crystal lattice, and (b) X-rays diffracting constructively off of lattice planes in a crystal.

From the diffraction pattern collected it is a simple process to calculate the *d*-spacing of the lattice planes using the Bragg equation (1), and this information can be used to find the unit cell parameters and crystal system/structure. Electron rich atoms scatter X-rays more strongly than lighter atoms and so the intensity of the reflections can be used to calculate the position of the atoms. This is not a simple process.[8]

As previously mentioned often single crystal XRD is not possible and so PXRD must be employed. Rather than the spots produced by single crystal XRD, as the crystallites in a powder are arranged in all possible orientations in relation to the beam, and so the X-rays diffract in 360° resulting in a pattern of rings. A consequence of this is that all symmetry equivalent reflections have the same *d*-spacing and so individual intensities cannot be measured,[16] making full structure elucidation from powder samples very difficult. However, if structure solution is not an issue then PXRD is a powerful tool for identifying polymorphs, monitoring structural changes within a polymorphic system (see Section 1.1.3) and phase quantification in multiphase materials.

1.1.2. Differential scanning calorimetry

Differential scanning calorimetry (DSC) is used to measure the flow of energy into or out of a material as it undergoes temperature related phase changes such as melting and crystallisation. Each phase change will be either endothermic or exothermic and will have an enthalpy associated with it. The DSC measures this enthalpy and the temperature at which it occurs. However it gives no specific structural information related to these changes, and so often the technique is used in conjunction with PXRD.[8,17]

DSC measures the power required to maintain the sample at a temperature equal to that of an inert reference in accordance with a prescribed temperature programme. The reference is an empty sample pan identical to the one in which the sample is held. Thus,

the difference in power can be ascribed to the sample alone. The theory of DSC will be discussed in more detail in Chapter 2.

1.3 Excipients and metastable polymorphs

1.1.3. Polymorphism

For the majority of drugs, the most stable form under ambient conditions is a crystalline solid.[18] However, a drug can exist in more than one crystalline state.[19] Polymorphism describes the existence of multiple crystal systems defined by different unit cells but having the same molecular composition (Figure 1-3).[20] With monotropic materials, the polymorph with the highest melting point is considered to be the stable polymorph at all temperatures, and all others are metastable. Enantiotropic materials exhibit polymorphs with a different order of stability either side of a critical temperature.[9]

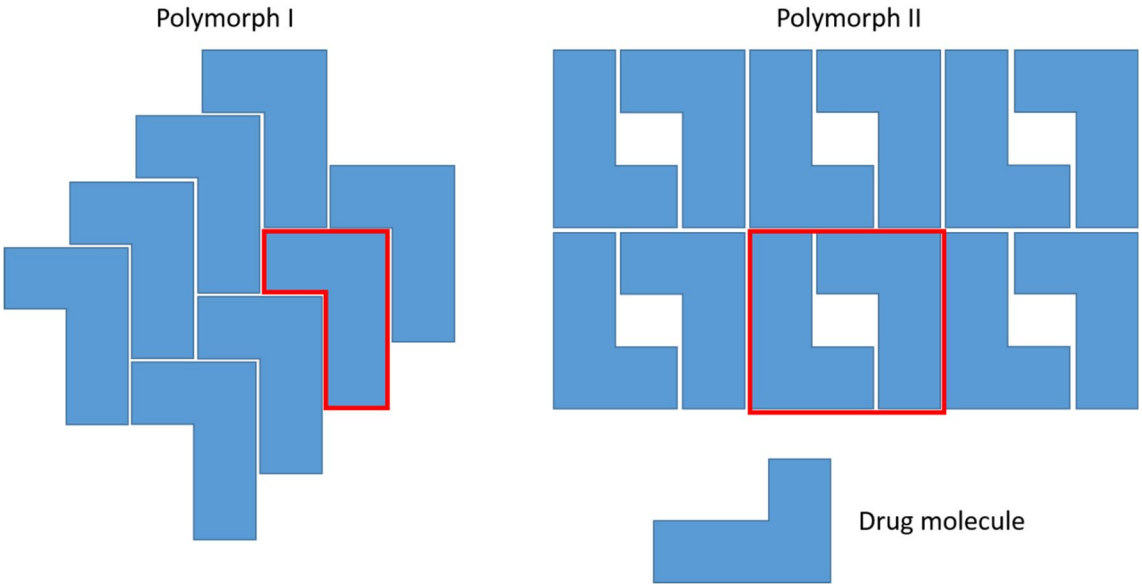

Figure 1-3. A schematic representation of two polymorphs of the same drug. The unit cell in each case is marked by a red outline.

Each polymorph of a material possesses different physicochemical properties such as density,[9,21,22] solubility,[12,21,22] dissolution rate,[12,22] flow properties,[15,22] compressibility, and crystal habit.[15] By definition, metastable forms are less stable than the stable form and so will have a higher dissolution rate and solubility, and, often a higher bioavailability. However, as the stable polymorph is the only form that is in thermodynamic equilibrium all metastable forms will eventually convert to it over time.[18] That being said, kinetic stability is often very high and polymorphs considered to be metastable can take years to convert to the thermodynamically stable form.[23] This causes an obvious problem for pharmaceutical scientists as with this conversion comes an accompanying drop in

solubility and/or dissolution rate, as well as changes to many other physicochemical properties. Therefore, in cases where the stable form of a drug has poor bioavailability and conversion from the metastable form to the stable form occurs rapidly at ambient temperatures,[9,18] it is desirable to find some method of stabilising the metastable form of choice.

1.1.4. Polymorph control

Methods of polymorph control currently employed include: introduction of additives (e.g. seeding, templating, polymorph growth inhibition), solvent modification, physical confinement of crystals during growth, and the use of radiation to stimulate nucleation.[22]

1.1.4.1. Seeding

As the name suggests, seeding involves growing the desired bulk crystalline product from a seed-crystal of the same polymorph added to a supersaturated solution. The obvious disadvantage of this method is the necessity for the presence of the initial seed-crystal. It is also important to know the width of the metastable zone (Figure 1-4) as seeding is most likely to be successful under these conditions. If a solution is cooled or the solvent allowed to evaporate so that eventually it becomes supersaturated nucleation will not occur immediately. Rather, there is a point to which the solution must cool or concentrate past the line of solubility before spontaneous nucleation will occur. The line of solubility and the nucleation border form the limits of the metastable zone. It is important to note that the border of nucleation is not a clearly defined line and should be determined by performing controlled crystallisations[24,25] If seeding is attempted in too dilute a solution then the seed-crystal will dissolve. Conversely, if the seed is added to a supersaturated solution in which nucleation has already begun then growth from the seed may be negated.[22] Quench cooling (see Section 1.1.9.1) is a typical method of obtaining seed-crystals, because nucleation from the quenched material should begin with the least stable polymorph and progress through the other polymorphs *via* minimal changes in free energy (Ostwald's rule of stages).[25,26] In theory, this allows access to, and isolation of, all metastable polymorphs of a material. However, in practice this is not always the case, for instance in the case of concomitant polymorphism: the phenomenon of a particular set of crystallisation conditions yielding more than one polymorph.[27] Seed-crystals of paracetamol (PCM) form II have been grown by this method and used to seed its growth from ethanolic solution.[28]

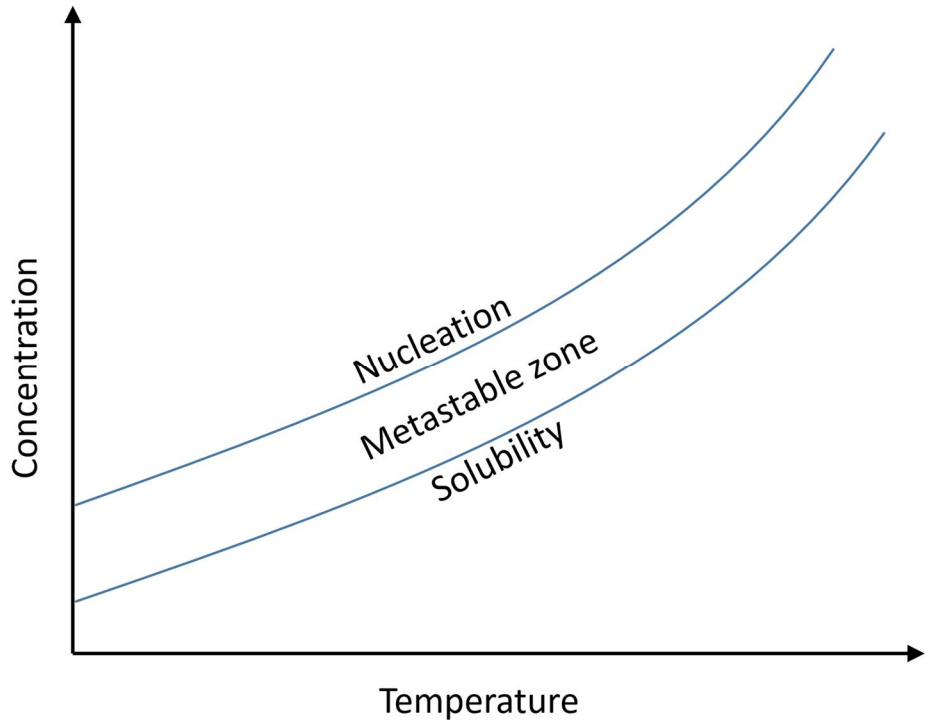

Figure 1-4. A graphical representation of the metastable zone for crystallisation from solution.

1.1.4.2. Growth inhibition

By inclusion of soluble additives to a crystallisation solution it is possible to inhibit the growth of some polymorphic forms whilst permitting the evolution of others (Figure 1-5).[29] The additive must be able to mimic motifs (characteristic intermolecular bonding patterns) of the target higher stability polymorph on one side, allowing it to attach, and be sufficiently different from it on the other side that no more drug molecules can attach.[27] In so doing it must inhibit, at the very least, the stable polymorph's fastest growing face. This results in relative stabilisation of the metastable form.[22,30] Molecular modelling is of particular use in this field of polymorph control, and has been utilised to design experiments which successfully inhibited the growth of the stable *β* phase of *L*-glutamic acid and in so doing stabilized the *α* form.[31]

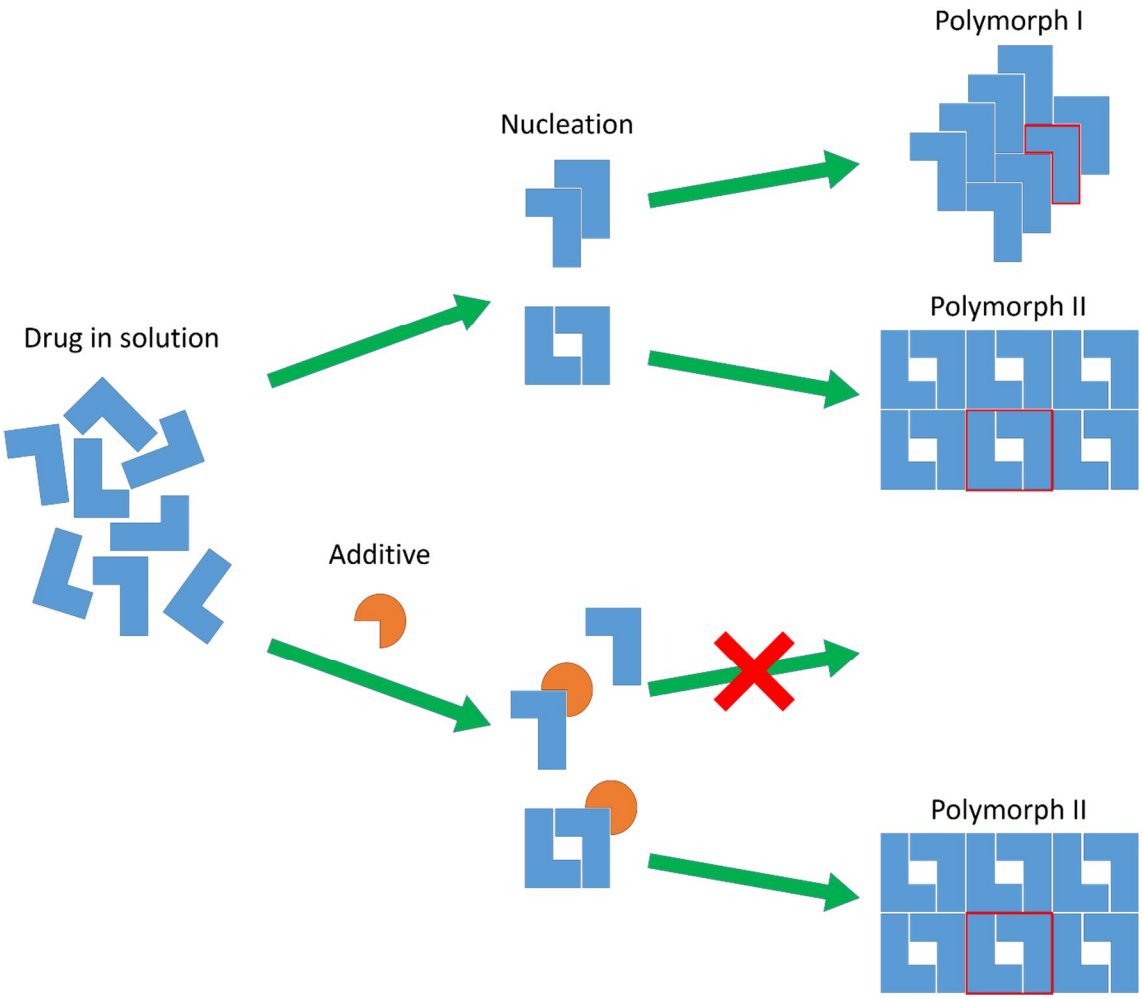

Figure 1-5. A schematic representation showing the selective inhibition of polymorph growth in solution.

1.1.4.3. Templating

Templating relies on heterogeneous nucleation[27] from the surface of a substrate. The substrate is chosen so that it has either a similar lattice to the desired polymorph, or a morphology that directs molecular ordering of the subject material to that of the desired polymorph.[32] Prior to crystal growth in solution the molecules must form an aggregate, which must eventually form a nucleus with the structure of the ultimate crystal. This process is enthalpically unfavourable due to the energy associated with the phase boundary between the nucleus and the solution.[33] The presence of the template serves to lower the free energy barrier to nucleation, and consequently the process is more favourable than homogeneous (spontaneous) nucleation.[32–34] A number of examples of pharmaceutical polymorphs that have been templated can be seen in Table 1-2.

Table 1-2. Examples of polymorph templating in pharmaceutical materials.

Material	Form	Template	Crystallisation method	Ref.
1,3-bis(*m*-nitrophenyl) urea	*α*	Gold-thio self-assembled monolayers (SAMs) 4-mercaptobiphenyl	Growth on template from saturated solution	35
	β	4'-iodo-4mercaptobiphenyl		
	γ	4'-bromo-4mercaptobiphenyl		
5-methyl-2-[(2-nitrophenyl)amino]-3-thiophenecarbonitrile	YN	Pimelic acid	Physical vapour deposition	36
Carbamazepine	II	Cyano silanised glass	Solution cooling	37
	IV	Hydroxypropyl cellulose Poly(4-methylpentene) Poly(*α*-methylstyrene) Poly(*p*-phenylene ether-sulfone)	Solvent evaporation	38
	V	Dihydrocarbamazepine II	Physical vapour deposition	39,40
Cyheptamide	III	Dihydrocarbamazepine II	Physical vapour deposition	36
Entacapone	A	Gold-entacapone SAM Gold SAM	Precipitation from solution Solution cooling	41
L-glutamic acid	*α*	Phenylalanine SAMs	Solution cooling	42
Glycine	*α*	Water soluble hydrophobic *α*-amino acids	Crystallisation at the air-solution interface	43
Indomethacin	*α*	Polymerised 2-(dimethylamino) ethyl acrylate and *tert*-butyl acrylate	Reheating of the quenched glass	44
Mefenamic acid	I	2-((4-vinylphenyl)amino)benzoic acid* co-polymerised with divinylbenzene	Solution cooling	45
Tolbutamide	II	Methyl SAMs Trifluoromethyl SAMs	Solution cooling	46
	IV	Phenyl SAMs		

*tailor-made additive

1.1.4.3.1. Metastable paracetamol

Paracetamol is well known to exhibit three polymorphic forms, named I,[47] II,[48] and III[49] (Figure 1-6). Form II is of particular importance due to its superior compression properties[50] (important for making tablets) compared to those of form I, resulting from its layered structure. However, form II is difficult to prepare in large quantities[51] as polymorph I is the thermodynamically stable structure.[52] Form III is the least stable of the three, and its instability is evidenced by the fact it was known to exist for 27 years prior to the elucidation of its crystal structure in 2009.[49]

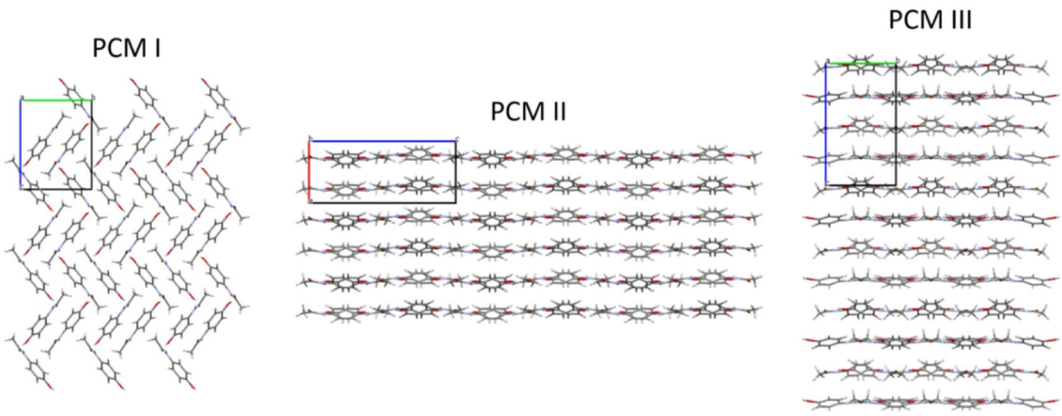

Figure 1-6. Graphical representations of the herringbone structure of PCM form I and the layered structures of forms II and III.

Lang *et al.*[38] templated the growth of pure PCM form II from solution using a number of different polymers. Prior to their work, pure form II had only been grown from solution once[48] (although it had been isolated by crystallisation from the melt)[53] and all subsequent efforts resulted in a mixture of form II and the more thermodynamically stable form I. Lang's work appears to be the first example of such heteronucleation of crystal growth. The method is referred to as polymer templating; it is particularly useful as it requires no prior knowledge of the lattice or surface chemistry of the polymorph[38] and can produce single crystals.[22,38] The process works in the same way as templating, with the generality of the method resulting from the use of a library of polymers with diverse functional groups and spacing of the groups, from which polymorphs are grown. Characterisation of the products informs which polymorph is templated by each polymer.[38]

In 1994 Femi-Oyewo and Spring[54] grew PCM crystals from aqueous solutions containing various concentrations of the additives agar, gelatin, polyvinylpyrrolidone (PVP), and hydroxypropylmethyl cellulose (HPMC). They observed significant modification to the PCM crystal habit for each of the excipients, with PVP and HPMC suppressing crystal growth somewhat and resulting in low yields of microcrystalline material. Kachrimanis and Malamataris[55] also showed that crystallisation of PCM in the presence of polymers resulted in alteration of the crystal shape and in some cases an improved yield. No mention was made of the polymorphic form grown in either of these studies, although all crystals grown in the presence of a polymer additive showed improved compressibility over those grown without. This appears to suggest the presence of at least some form II. A study by Garekani *et al.*[56] in 2000 on the effect of crystallising PCM with PVP at different molecular weights showed good agreement with these results. These authors too make no mention of the polymorph grown but present DSC and powder X-ray

diffraction data that is consistent with data recorded for crystals grown without polymer additives, suggesting polymorph I. Furthermore, all DSC traces are described as showing a sharp melting point at *ca.* 171 °C with a flat baseline, confirming the presence of polymorph I.

The three studies discussed in the previous paragraph all involved crystallisation of PCM from solution. In 1997 Di Martino et al.[53] attempted to develop a thermal method for the preparation of larger quantities of PCM forms II and III than had previously been reported. Initial experiments were carried out and analysed *in situ* prior to scaling up the synthesis in a glass flask and using an oven as the heat source. *In situ* experiments showed form II to be prepared by crystallisation from a PCM glass prepared by slowly cooling the melt (whereas fast quenching resulted in recrystallisation to form I). The slowly cooled material was shown to either melt or covert to form I upon heating, depending upon the ramp rate. Preparation of polymorph II was successfully scaled up. However, the bulk always converted to form I upon heating. Form III was prepared by melting crystals of form I between a microscope slide and cover slip using a hot stage. The melt was then held isothermally at 54 °C for 90 minutes, in which time the material crystallised to form III. Crystallisation below 50 °C was found to be very slow and above 56 °C nearly impossible, with 54 °C being the optimum temperature. Form III was stable between the slide and cover slip for several months, but removal of either slide resulted in conversion to form II. This crystallisation to polymorph III was reproduced by DSC in a closed pan but by no other method, leading the authors to postulate the necessity of closed conditions for its preparation.

In 2002 Giordano et al.[52] examined the effect of recrystallising PCM from the melt in the presence of polymeric excipients (microcrystalline cellulose, HPMC, and cross-linked PVP). They melted and cooled binary mixtures ranging from 50 % w/w to 90 % w/w drug and found that both form II and form III could be reproducibly crystallised (although phase purity was not assessed, and in most cases mixtures were prepared). The degree of crystallinity of the product was influenced by the polymer, the composition of the mixture, and the thermal history. Microcrystalline cellulose was found to be particularly effective at stabilising form II.

Further work by Rossi *et al.*[51] showed that PCM forms II and III can be prepared from binary mixtures of form I with 10 % w/w HPMC using thermal methods. Following an identical melting step at 180 °C both samples were reheated, each to a specific temperature, and held isothermally for 2 minutes to allow crystallisation. Material prepared by DSC resulted in form II or form III depending upon the hold temperature.

Upon reheating form II showed no phase changes except for its melt at 158 °C. Form III prepared by DSC was shown to convert to form II when reheated following a melt at *ca.* 139 °C, whereas the same polymorph prepared in larger quantities using a Köfler hot stage bypassed the conversion to form II and instead converted directly to form I. Analyses were carried out separately using DSC, powder X-ray diffraction (PXRD) and micro-Fourier transform infrared spectroscopy (MFTIR) and the transitions observed in the sample of form III prepared by DSC were not reproducible by other methods.

Burley and co-workers[26] investigated the method of Di Martino *et al.*[53] for preparing PCM form III between a microscope slide and cover slip, and discovered that holding the material at 54 °C following the melt was not necessary. Gently warming the glass was sufficient for crystallisation (Figure 1-7). Further heating caused the transformation to form II above 120 °C, and this subsequently melted at 159 °C. Furthermore, the authors prepared form III in a NMR rotor by melting form I at 190 °C and cooling to form a glass which they then warmed to 50 °C, demonstrating that confinement between glass slides is not essential. This constituted the preparation of a relatively large amount of pure paracetamol form III, however neither it nor form II could be removed from the rotors without dissolution.

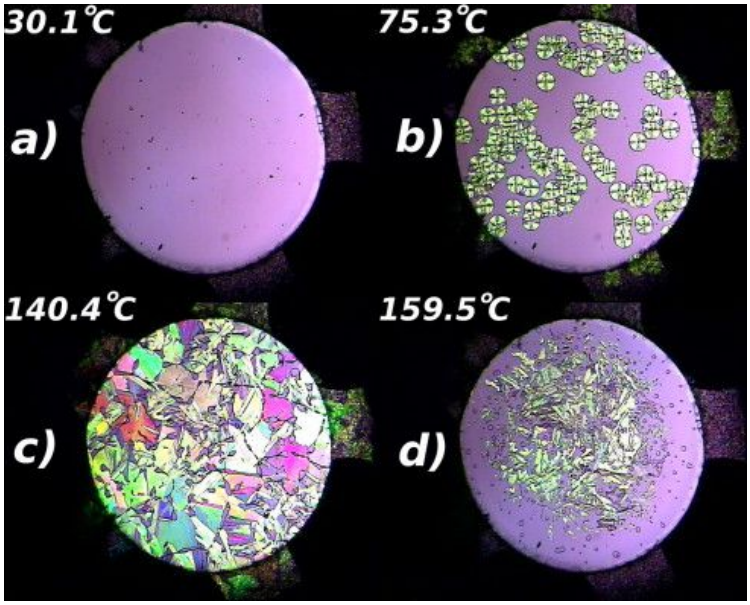

Figure 1-7. Hot stage microscopy images recorded whilst heating a PCM glass formed by cooling the melt. (a) the glass, (b) PCM form III, (c) PCM form II, and (d) PCM form II melting. Reproduced with permission.[26]

Gaisford *et al.*[57] prepared PCM form III by annealing a PCM glass at 113 °C for 2 minutes and used rapid-heating DSC to supress the solid-solid III→II transition. In so doing they observed the melt of form III at 143 °C. However, they argue that due to differences in the enthalpies of crystallisation and fusion relating to polymorph II it was not possible to

crystallise pure polymorph III from the melt and propose that prior evidence in the literature of its isolation is inconclusive. In DSC experiments, the data show an exotherm following the melt of form III that is ascribed to the crystallisation of form II. This is followed by form II melting. In all cases the enthalpy of crystallisation of form II is lower in magnitude than its enthalpy of fusion. Thus, as the enthalpy of fusion for any polymorph is equal and opposite to its enthalpy of crystallisation, form II must always have been present. Gaisford and co-workers support this theory by annealing the quenched samples at lower temperatures, so favouring the crystallisation of form III, which results in a slight increase in the magnitude of the form II crystallisation exotherm prior to its melt, but it never equals the enthalpy of the melt. In the same work, this team assessed the effect of HPMC on the thermal recrystallisation behaviour of PCM from the glass (Figure 1-8) and show that it favours the formation of form III. The authors suggest that it does this by restricting molecular movements: since the movements required to crystallise to polymorph III are smaller than those needed to generate polymorph II, the former is favoured. Furthermore, they demonstrate that a higher molecular weight (hence viscosity) HPMC results in stronger stabilising effects on form III. Increasing the proportion of HPMC in the mixture was found to stabilise the amorphous phase, and at a mass ratio of 1:1 the PCM remains amorphous when heated well past the melting temperature of the stable polymorph.

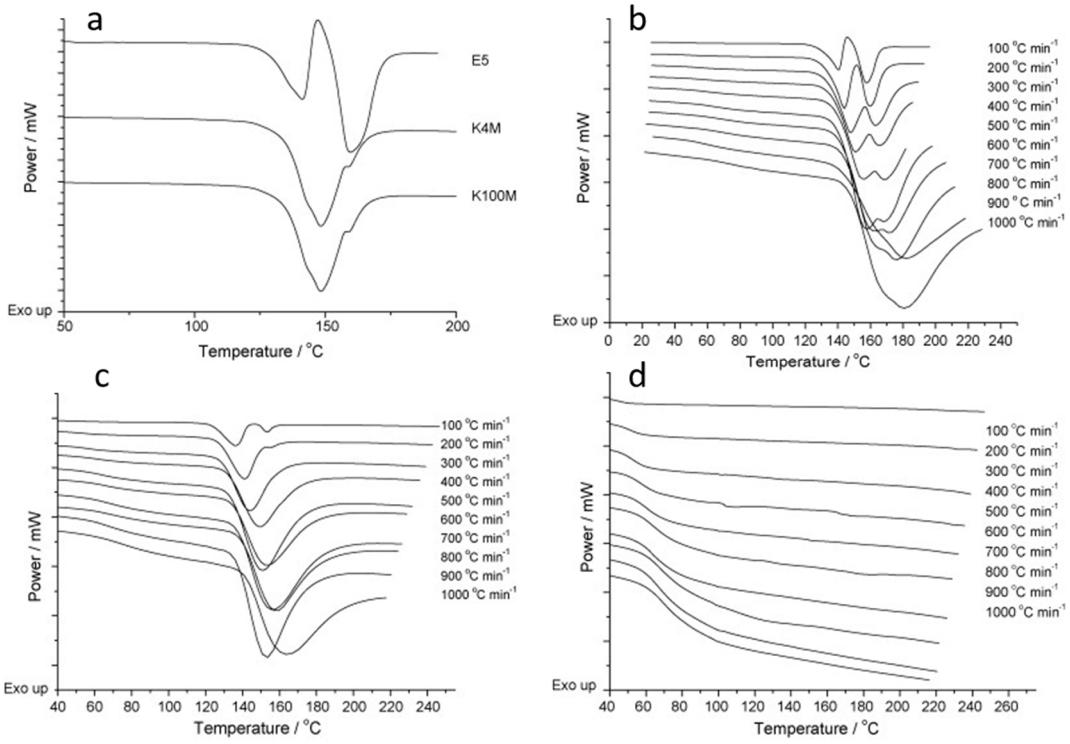

Figure 1-8. DSC data for mixtures of PCM and HPMC following crystallisation from the glass at 113 °C. (a) 9:1 PCM:HPMC grades E5, K4M, and K100M heated at 200 °C min^{-1}. (b) 9:1 PCM:HPMC E5 at heating rates up to 1000 °C min^{-1}. (c) 7:3 PCM:HPMC E5 at heating rates up to 1000 °C min^{-1}. (d) 5:5 PCM:HPMC E5 at heating rates up to 1000 °C min^{-1}. Reproduced with permission.[57]

1.4 Co-crystallisation

Co-crystallisation is another method by which the chemical and/or physical properties of a molecule can be tuned without making or breaking any covalent bonds.[58] It can be used to improve a material's solubility and/or rate of dissolution and, as a consequence of the substance existing in a crystalline form, co-crystals are likely to be more stable, reproducible and easier to purify than high energy solids such as glasses and therefore more desirable.[58,59] Examples of co-crystals that have been developed with APIs and the properties that have been improved include: carbamazepine (CBZ) and nicotinamide (NCT) to improve the physical stability of CBZ;[60] CBZ and saccharin (SAC) to improve both the dissolution rate and the oral bioavailability of CBZ;[61] indomethacin (IMC) and SAC to increase the physical stability and dissolution rate of the drug.[62] Saccharin is a sweetener, providing the additional benefit of taste masking, a useful property considering the common problem of bitterness in pharmaceuticals.

A recent perspective,[10] prior to which there was little consensus, has attempted to clarify the definition of co-crystals, concluding that "co-crystals are solids that are crystalline single phase materials composed of two or more different molecular and/or ionic compounds, generally in a stoichiometric ratio, which are neither solvates nor simple

salts." It is important to ensure that a suitable non-toxic, pharmaceutically acceptable[59,63] co-former is used that will not interact covalently with the drug and alter its chemical structure.[58] A graphical representation of a co-crystal can be seen in Figure 1-9.

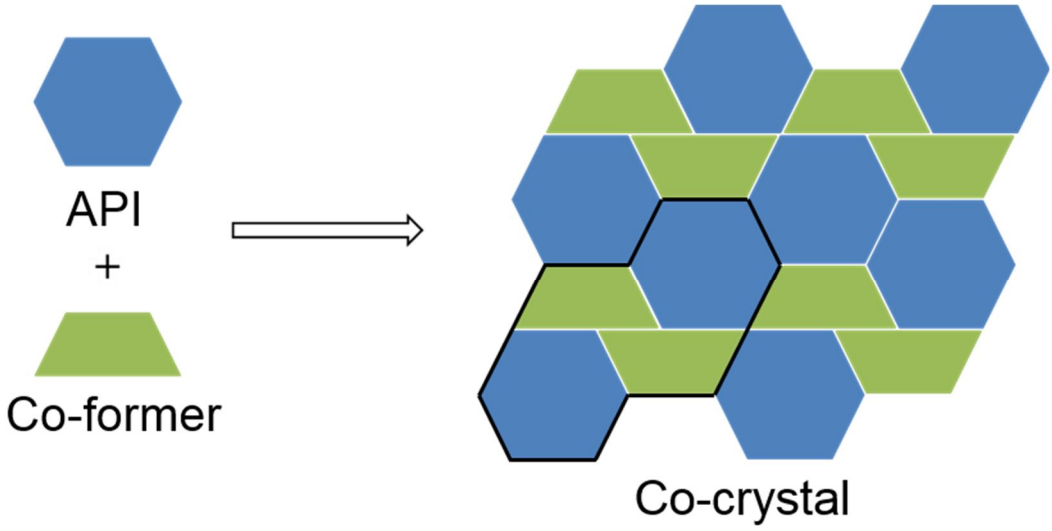

Figure 1-9. A schematic of the composition of a co-crystal [adapted from Schultheiss and Newmann, 2009[64]].

Co-crystals rely on non-covalent intermolecular interactions (usually hydrogen bonds) to make associations between the molecules of the different compounds involved, with the necessity that the interactions between drug and co-former must be more favourable than those between two molecules of the same species.[65] Co-crystals can be designed by selecting molecules[59] where hydrogen bonds can form between specific functional groups. These interactions have been termed supramolecular synthons (Figure 1-10) and are defined as "structural units within supermolecules which can be formed and/or assembled by known conceivable synthetic operations involving intermolecular interaction".[66] Pharmaceuticals are ideally suited to this type of interaction as they very frequently contain external hydrogen bonding moieties.[67]

Crystal engineering is a term which refers to using these synthons for the design and manipulation of molecular solids with the aim of tailoring the entity's physical and/or chemical properties, often to improve solubility and dissolution.[68] Synthons (Figure 1-10) may comprise either homosynthons (both functional groups are the same, e.g. carboxylic acid to carboxylic acid) or heterosynthons (two different functional groups, e.g. carboxylic acid to amide).[59,68] It is the competitive nature of the attraction between these functional groups that allows for the formation of different supramolecular synthons and ultimately the formation of co-crystals.[59]

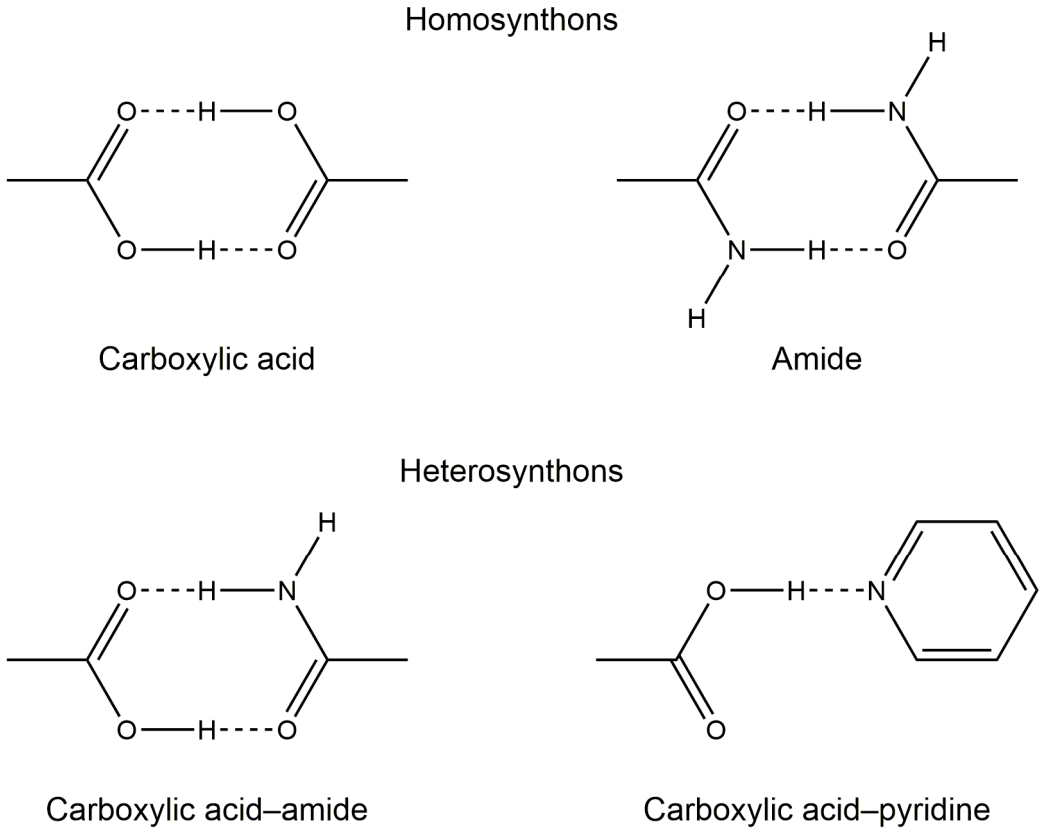

Figure 1-10. Examples of supramolecular homosynthons and heterosynthons.

A number of methods are currently employed in the screening/discovery of co-crystals, including; solution crystallisation[59,62,68,69] crystallisation from the melt,[68,70] and grinding.[69] Microfluidic and supercritical fluid tecnologies[59] are also known to aid the formation of co-crystals but are less common. Failure to form a co-crystal *via* one route does not preclude its production by another, and so it is often necessary to carry out comprehensive screening employing multiple techniques to obtain the material of interest.[59,71,72] Thus, it is desirable for these techniques to be fast, inexpensive and environmentally friendly.

1.1.5. Solution methods

Solution crystallisation is of great importance as it is currently the most common method for producing co-crystals of sufficient quality for single crystal XRD.[69] The technique can be divided into four categories depending on the treatment of the solution.

1.1.5.1. Evaporation

Evaporation from solution is the most common[72–79] method of co-crystallisation. It requires the API and co-former to be dissolved in a stoichiometric solution, the solvent from which is then allowed to evaporate. The solution becomes saturated with respect

to the co-crystal and further evaporation results in its precipitation. A disadvantage of this method is that both components need to have similar solubility in a particular solvent, and it is possible that they may crystallise individually.[72] A recent novel approach to evaporation crystallisation has seen the employment of thermal inkjet printing for the preparation of pharmaceutical co-crystals. The rapid evaporation of solvent associated with the technique promotes the growth of metastable polymorphs. Recent work by Buanz and Gaisford[80] has isolated the highly metastable *β* polymorph of glycine using inkjet printing of aqueous solutions in small volumes (< 0.1 *μ*L). The authors ascribe their results to the confinement of the solution in small drops on a scale at which the *β* form is thermodynamically stable. Upon printing larger drops (> 0.1 *μ*L) a mixture of forms *α* and *β* grew. The growth of the *β* form in this instance was thought to be due to the rapid evaporation of water resulting from the small volume of the droplet. The method also offers a much more rapid option for screening than traditional methods of solvent evaporation.[81]

1.1.5.2. Reaction crystallisation

Similarly to solvent evaporation, reaction crystallisation involves dissolving the co-crystal components in a stoichiometric ratio. However, here there is no need for evaporation of the solvent. Instead, a saturated or near saturated solution of one component is prepared and the second solid component is added until the solution becomes saturated with respect to the co-crystal; subsequently, co-crystallisation proceeds. This method has the advantage of being applicable to materials with different solubility in the chosen solvent.[69,72,82]

1.1.5.3. Cooling crystallisation

The third method of solution crystallisation, known as cooling crystallisation, involves mixing the solid co-crystal components and solvent in a vessel and heating the mixture to ensure all solutes have dissolved. Co-crystallisation occurs as the solution is cooled and becomes supersaturated with respect to the co-crystal.[69,72]

1.1.5.4. Ultrasound assisted solution co-crystallisation

Ultrasound assisted solution co-crystallisation is another method by which materials of differing solubility in the solvent can be co-crystallised. It is similar to cooling crystallisation but, following dissolution of the components and during cooling, the solution it is subjected to high intensity ultrasound. The ultrasonic waves lower the

supersaturation level at which primary nucleation (nucleation without pre-existing crystals)[83] can occur.[84]

1.1.6. Melt methods

1.1.6.1. Mixed fusion

Mixed fusion (Figure 1-11) uses hot stage microscopy to examine phase behaviour between two components, and hence has been used as a strategy for co-crystal screening.[70] Initially the higher melting component is melted before allowing it to cool and solidify, following which the second component is melted and brought into contact with it. This results in the solubilisation of the first material, and upon cooling and re-crystallisation of the mixture a zone of mixing can be examined. Each side of this zone lie regions of pure crystalline material of each of the components, and across it is a concentration gradient, similar to a binary phase diagram. Observing the material under polarised light microscopy whilst heating reveals phase changes, in particular eutectic melting points (the occurrence of a singular melting point for a mixture, provided the components are present in the correct stoichiometric ratio), relating to co-crystals. It therefore allows for the identification of the number of phases present and their melting points. A disadvantage of this method is the necessity for both components to be stable in the liquid phase.[70,85]

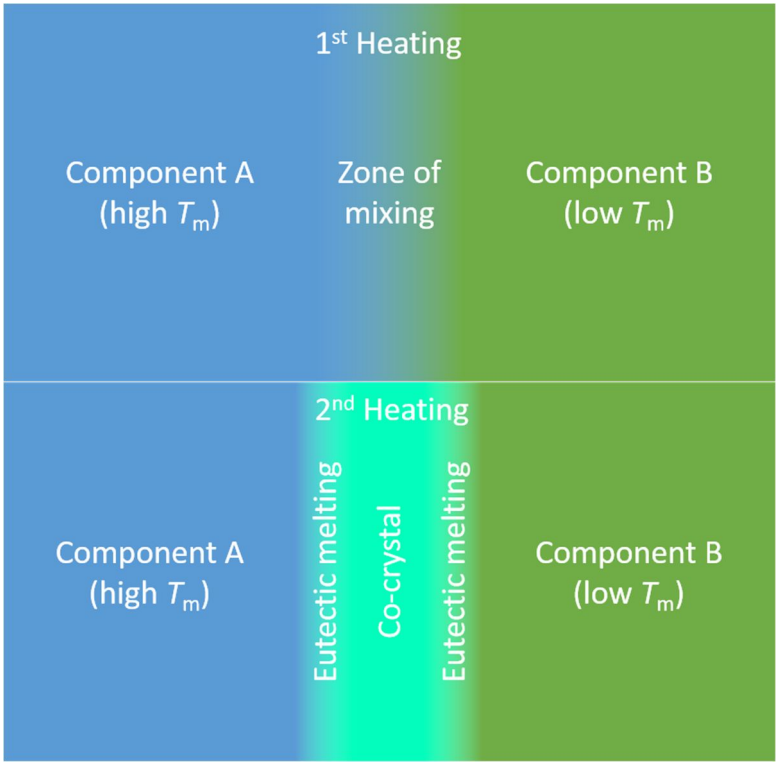

Figure 1-11. A schematic representation of the process of mixed fusion.

1.1.6.2. Co-melting

Co-melting bypasses the problem of stability in the liquid phase, as the process does not require either of the pure components to be melted prior to mixing. Instead it takes advantage of the eutectic melt of a system, which effectively lowers the temperature at which the components melt. The main benefit of co-melting is that it is a rapid method that does not require organic solvents and is therefore cheap and environmentally sound.[86] A thorough investigation of the mechanism by which co-crystallisation occurs when a mixture is heated is yet to be carried out, although interesting work has been done based on binary phase diagrams.[86,87] Fucke *et al.*[88] showed that although piroxicam could not be co-crystallised by the mixed fusion method due to its poor melt stability, heating a physical mixture of it and a co-former on a microscope slide sufficiently lowered the melting point, in most cases, to produce co-crystals. Lu *et al.*[89] demonstrated the utility of the method for rapid co-crystal screening in a study in which they heated 20 binary systems using a DSC and found that 16 formed co-crystals, nine of which were previously unreported. A more recent study using the same methods, but with the mixtures being ground together prior to heating, has shown similar results.[86] Others have also produced co-crystals by this method,[71,90,91] with one group concluding screening *via* DSC to be the most efficient method at early stages of research, stating that it makes it possible to screen out systems in which co-crystal formation is most unlikely.[92]

1.1.7. Mechanochemical methods

The term mechanochemical co-crystallisation encompasses three techniques by which the raw materials are ground together to form co-crystals:[93,94] neat grinding,[95,96] liquid assisted grinding,[88,97] and the relatively novel technique of polymer assisted grinding.[93,94] These have advantages over the traditional technique of solvent evaporation in that they are faster, cheaper, and “greener” as either no or very little solvent is required.[98] Mechanochemical routes also avoid the possibility of unwanted solvate formation.[93] Another benefit of the technique is that it can be used to co-crystallise heat-sensitive materials that cannot be submitted to mixed fusion or, to a lesser extent, co-melting. Its limitations lie in the fact that it produces very small crystals or fine powders, from which structure solution, although possible,[99,100] is more difficult than from larger single crystals.[101]

1.1.7.1. Neat grinding

Neat grinding is the simplest of the three mechanochemical co-crystallisation techniques[102] and involves grinding the two solid raw materials together, either in a pestle and mortar or using a mill, in the correct stoichiometric ratio for co-crystals to form.[69,71] It has been used to study co-crystal polymorphism and variations in co-crystal stoichiometry.[103] Possibly the earliest example was reported in 1893 for the synthesis of the quinhydrone co-crystal consisting of equimolar amounts of *p*-benzoquinone and hydroquinone.[104] Etter *et al.*[105] stated that the driving force is the formation of stronger hydrogen bonds in the co-crystal than in the crystals of the two components. Caira *et al.*[106] demonstrated that the method is able to produce co-crystals identical to those produced by solution methods, crystallising sulfadimidine with several aromatic carboxylic acids. First order kinetics were observed, suggesting the reaction proceeded *via* a random nucleation mechanism.

Jayasankar *et al.*[107] found that the co-crystallisation of an equimolar mixture of carbamazepine and saccharin by neat grinding occurred *via* an amorphous intermediate. Samples ground both at ambient temperature or under liquid nitrogen resulted in partial vitrification, with the greatest disruption being observed in the cryogenically milled sample. The material milled at ambient temperature partially co-crystallised during grinding. Upon storage, co-crystallisation from the glass occurred for both and the rate of crystallisation was found to increase with relative humidity, due to the plasticising effect of water. The lack of co-crystallisation during cryogenic milling was attributed to the material being at least 200 °C below the T_g of both of the components and the blend. A study of an equimolar mixture of carbamazepine and indomethacin found similar results, with the additional finding that grinding amorphous starter materials produced the same co-crystal as grinding them in crystal form. However, simply mixing the components in either form (crystalline or amorphous) did not cause any co-crystallisation after storage under the same conditions.[95]

Friščić *et al.*[104] published a review in 2009 and stated that, provided that the components are low volatility and are held together by strong intermolecular interactions (hydrogen bonds), criteria that many pharmaceutical compounds meet, an amorphous intermediate is the most likely mechanism of co-crystallisation. These authors also discussed the effect of grinding time on co-crystal/glass formation, concluding that there must be an optimum time during which co-crystal formation is not overwhelmed by glass formation. Grinding for longer causes the ratio of glass to co-crystal to increase.

1.1.7.2. Liquid assisted grinding (LAG)

The LAG methodology (otherwise known as solvent-drop grinding) is similar to neat grinding but with the addition of a catalytic amount of solvent to assist the co-crystallisation process. The mechanism by which the liquid influences the mechanochemical process is unknown. However, it has been shown that the addition of a small amount of liquid to the grinding vessel can accelerate co-crystallisation and enable the formation of co-crystals that cannot be formed by neat grinding.[108] There appears to be no correlation between reactant solubility in the liquid and reaction efficiency. Instead the volume of liquid added appears to be the key parameter, with an increase in volume resulting in an increase in rate of crystallisation.[97] Recently Tan *et al.*[108] proposed an explanation for the independence of reaction rate and solubility, suggesting that due to its small volume the liquid is in a state of constant saturation with the reactants, thus negating any effects resulting from differences in solubility. Furthermore, Tan suggested that the liquid facilitates a mobile layer on the surface of the solid components which results in co-crystallisation irrespective of the solubility of either material.

1.1.7.3. Polymer assisted grinding (POLAG)

POLAG utilizes the process of LAG but substitutes the solvent/liquid with a small amount of polymer, in either the liquid or solid phase. Hasa *et al.*[93] showed that POLAG with solid or liquid polyethylene glycol (PEG) catalyses and assists co-crystal nucleation, demonstrating the formation of caffeine and citric acid co-crystals that could not be formed by neat grinding. They utilised PEG with six different molecular weights, three of which were liquid and three crystalline solids. The authors proposed no explanation for the role of the polymer, except that it may be similar or different to that of the liquid in LAG. Further work by Hasa *et al.*[94] has demonstrated the ability to control the polymorphic form of the product by varying the polymer chain length. Lengthening the polymer chain, and in so doing reducing the microenvironment polarity, favoured the formation of the more stable polymorph of the caffeine–glutaric acid co-crystal (CAF-GA). Hasa suggests the reason for this lies in the crystal structure of the two known polymorphs (Figure 1-1), citing the explanation of Trask and co-workers[109] that form I consists of sheets stacked along the *b* axis to form what may be described as non-polar cleavage planes, whereas form II sheets are stacked in a staggered arrangement. The latter lack non-polar cleavage planes. Trask suggests that these cleavage planes are stabilised by non-polar solvents and showed that CAF-GA form I could be prepared selectively by LAG using a non-polar solvent, while form II could be prepared using a

polar solvent. A significant and notable advantage of POLAG over LAG is the elimination of the possibility of the formation of undesired solvates.

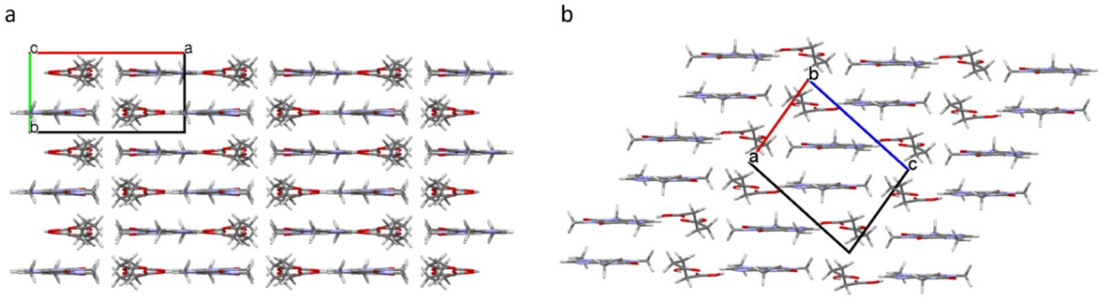

Figure 1-12. The crystal structures of (a) polymorph I, and (b) polymorph II of the CAF-GA co-crystal.

1.5 The Amorphous Form

Often, the rate of dissolution is the rate determining step in the absorption process, and so increasing the rate of dissolution will increase the bioavailability of the drug. For crystalline solids to dissolve the solute-solvent system must overcome the lattice energy of the crystal and replace solute-solute interactions with solute-solvent interactions.[2] Amorphous materials have the structure of a liquid, and so no crystal lattice, but the viscosity of a solid. More explicitly, they are high energy solids without the molecular ordering of a crystal but with randomly oriented molecules. If the material has no crystal lattice, there is no lattice energy to overcome and therefore the drug will likely have a higher thermodynamic solubility and a higher rate of dissolution.[110] Unfortunately, due to the high energy nature of amorphous materials, they are thermodynamically unstable and with time will relax, with the molecules reorienting towards the crystalline configuration. Eventually they will crystallise and lose the aforementioned beneficial properties.[2]

Amorphous solids have no long range (crystalline) order and little short range order. They can be formed either by rapid cooling of the melt or a solution of the drug, in which the molecules are not allowed sufficient time to reorient to the crystalline from the disordered fluid state, or by disruption of the structure of a crystalline solid (by milling or grinding for example). Molecules in a fully amorphous material will be arranged completely randomly with no long or short range order. In practice, this is very difficult to achieve and each different method employed will impart a different degree of amorphous character on the sample. It is considered that any amorphous material is likely to consist of a number of regions, each with a different degree of short range order.[2]

As mentioned above, amorphous materials are high energy, and as such are thermodynamically unstable.[111] The molecules are not held securely in a crystal lattice with the energy evenly spread throughout the structure and unlike a crystal, which may only exhibit molecular vibration, the molecules can also undergo rotational and translational movement. This will, over time, result in relaxation to a more stable amorphous state prior to recrystallisation of the substance,[2] and is the principal reason the amorphous form is not more widely used in medication.[110] The challenge is to develop a method of inducing amorphous character onto drugs whilst also imparting a level of stability.

Amorphous materials, also referred to as glasses, undergo a step change in their physical properties and heat capacity at a temperature specific to the compound, known as the glass transition temperature (T_g). They are formed as a result of cooling a supercooled liquid below this temperature at a rate sufficiently fast to avoid crystallisation. Above the T_g but below the melting point (T_m) amorphous materials are said to be rubbery, whereas below the T_g they are more brittle and are termed glassy. These two states are directly related to the molecular mobility within the sample.[18] Molecular rotations in a liquid above the T_m will occur extremely rapidly, on the picosecond or nanosecond scale. As the sample is cooled these molecular rotations become slower and the viscosity increases until the temperature drops below the T_g and the time scale for these rotations moves to minutes or hours.[112] At this point the viscosity is similar to that of the crystalline form of the same material.

A liquid that is cooled below its melting point but above the T_g is considered to be in structural equilibrium with respect to enthalpy/volume. In this state, any change in temperature is followed by a corresponding rearrangement of the molecules to maintain the structural equilibrium. If this linear behaviour were to continue as the temperature decreased, eventually the enthalpy or volume of this supercooled liquid would become smaller than that of the stable crystal. The theoretical temperature at which this would occur is named the Kauzmann temperature (T_K) (Figure 1-13). However, this cannot happen as the stable crystalline form is usually the form of a material with lowest enthalpy and volume (with water being an exception).[2] Instead, as the temperature drops below the T_g the molecular movements become too slow for them to reorient into an equilibrium state before the temperature drops further. At this point the system deviates from equilibrium (Figure 1-13) and becomes a glass.[112] As the molecules are randomly oriented throughout the glass there are regions of differing energies: thus, whereas in a crystal the energy around each molecule is balanced and equal, in an amorphous

material the energy around each molecule is unbalanced, which causes their physical instability.

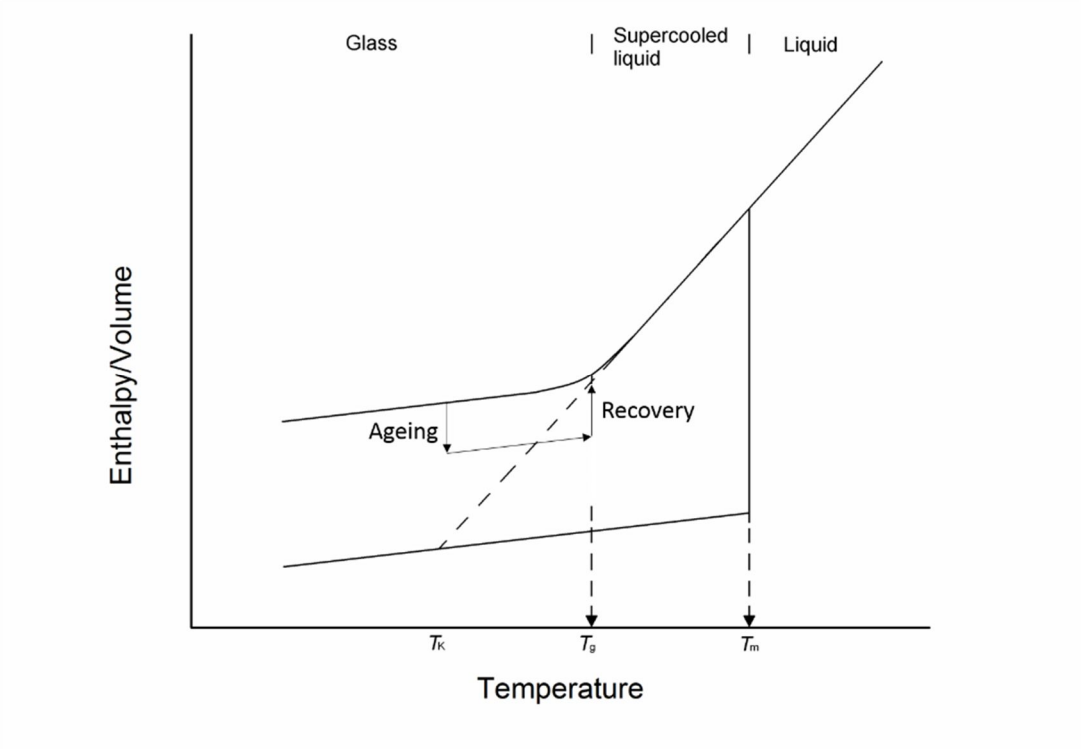

Figure 1-13. A schematic representation of the cooling of a liquid to form a glass, displaying the melting point, glass transition temperature, Kauzmann temperature, and the ageing and recovery processes.

1.1.8. Annealing and Relaxation

As previously stated, due to their lack of crystal lattice, glasses are fundamentally unstable materials and will undergo molecular movements and revert to crystallinity over time. Annealing is the process of holding a glass isothermally for a period of time. During annealing the material will undergo structural rearrangement towards a more stable state. The line extrapolated from the supercooled liquid line in Figure 1-13 represents the equilibrium glassy state. If the supercooled liquid continued to be cooled slowly enough that the material remained in equilibrium, providing that it avoided crystallisation, then this is the line it would follow. When annealing, the structure of a glass will alter so that the enthalpy or volume will approach this state: this process is termed relaxation and is represented by the ageing process in Figure 1-13. Relaxation will eventually end in crystallisation and loss of the enhanced solubility of the amorphous state.[2] There are two types of relaxation that can occur in an amorphous matrix, structural α-relaxation and Johari-Goldstein β-relaxation (Figure 1-14). Structural relaxation is slower but more significant for pharmaceuticals and involves movements or rotation of entire

molecules.[2,112] The faster *β*-relaxation processes can be attributed to intramolecular motions, such as rotation of a group around a bond within a molecule.[2,112] Both processes contribute to the overall relaxation of the glass.

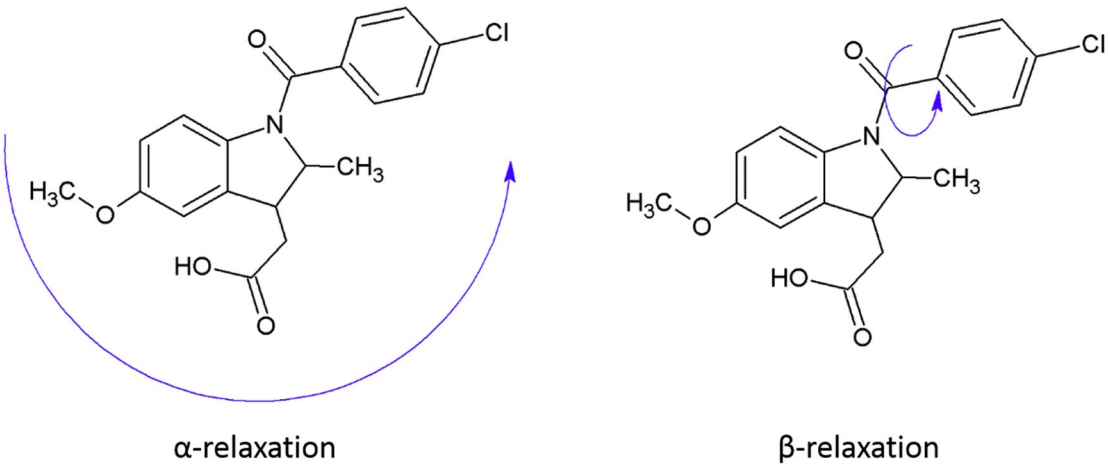

Figure 1-14. A diagram to show structural *α*-relaxation and Johari-Goldstein *β*-relaxation.

When an aged amorphous material is heated, at the glass transition there will be enough energy input that the molecules will respond to any change in temperature with movement. As when cooling they become “frozen”, when heated they become free to move again and will tend towards the equilibrium state. The energy associated with this process is known as the enthalpy of recovery and is depicted in Figure 1-13. It is considered to be equal and opposite to the enthalpy of relaxation, and can be measured using modulated temperature differential scanning calorimetry (MDSC).[2]

1.1.9. Vitrification of Pharmaceuticals

There are a number of methods currently employed to vitrify pharmaceuticals, and they fall into two mechanistic categories. The most effective with respect to disruption of crystallinity involves converting the crystalline raw material to a thermodynamically unstable, non-crystalline, intermediate (generally a melt or solution). The amorphous product is prepared by quenching the melt, or by rapid precipitation from solution (e.g. spray drying, freeze drying, quench cooling).[113] This mechanism often results in almost entirely amorphous matrices. The second mechanism employs the direct solid-state conversion of the crystalline material to a glass (e.g. compaction or milling). These methods usually result in partially amorphous products.[2]

1.1.9.1. Transformation *via* a Non-Crystalline Intermediate

Quench cooling is the simplest method for vitrifying drugs and involves melting the crystalline form and rapidly cooling it to below the T_g. Providing that the material does not degrade upon melting and the cooling process occurs faster than the molecules in the sample can rearrange into an ordered crystalline structure, a glass is formed. Glasses formed by quench cooling are considered to be completely amorphous, having no long range order.[2] A drawback of this method is the tendency for quench cooled glasses to form cracks upon cooling; these can then act as nucleation sites for subsequent crystallisation. However, this can often be avoided by adjusting the rate at which the melt is quenched.[114]

The spray-drying process (Figure 1-15) involves pumping a solution or suspension of the material through an atomiser using heated air at a high pressure. The droplets produced are subsequently dried by evaporation in a vortex of air. If successful, the result of this rapid precipitation from solution is spherical amorphous particles.[2] This technique may be used to vitrify the drug alone or in combination with a polymer, and can result in a fully or partially amorphous matrix, depending on the compound and experimental parameters. A significant drawback to this method is the temperature at which materials are processed. Often the temperature required to evaporate the solvent exceeds the T_g of the drug. As a consequence, upon exiting the spray-drying chamber the particles may be in the rubbery state, allowing sufficient molecular mobility for crystallisation to occur before they cool below the T_g.[113]

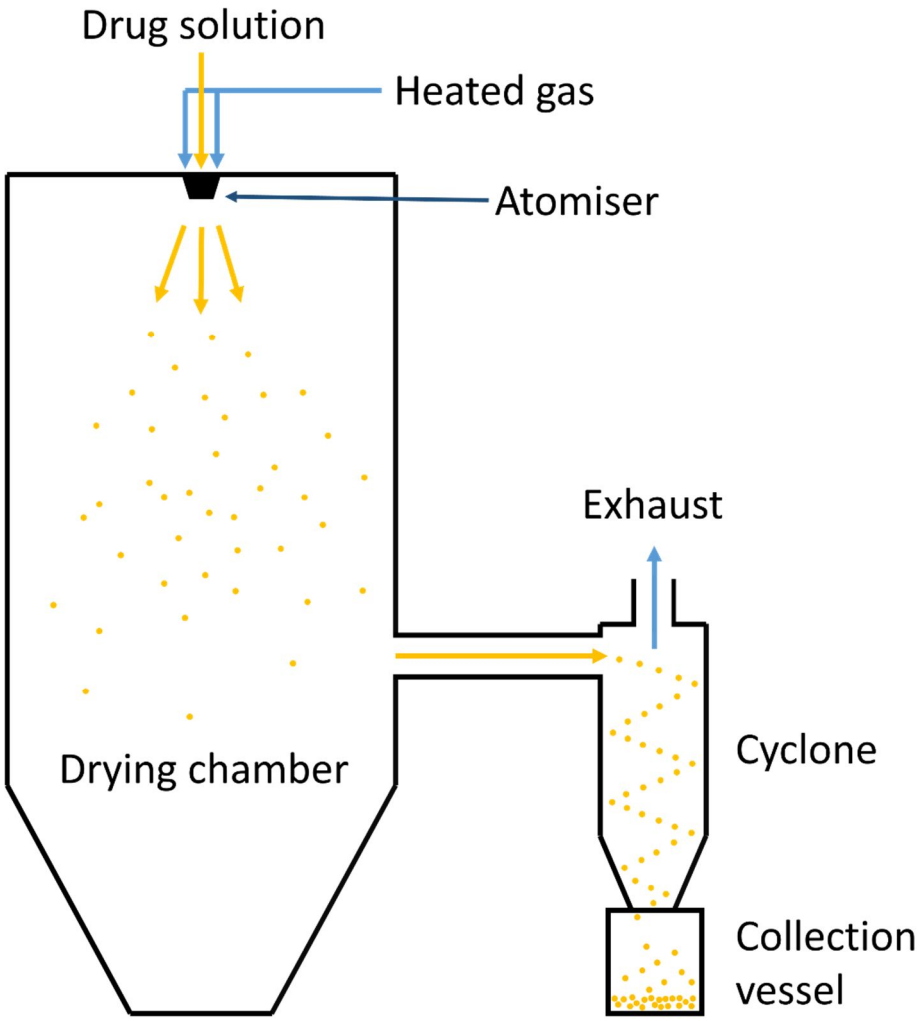

Figure 1-15. A schematic of the spray drying process.

Freeze-drying may be used to vitrify materials that are heat-sensitive and so unable to be converted to glasses by quench cooling or, to a lesser extent, spray drying. The compound must first be in aqueous solution or suspension at ambient temperature and pressure (Figure 1-16, point 1), which is then frozen (point 2). After freezing, the pressure of the system is reduced to below 610 Pa (point 3), the triple point of water. The temperature is then increased (point 4) and, provided the pressure remains below 610 Pa, the water will sublime. If the solute avoids crystallisation upon freezing then an amorphous product will remain after the completion of sublimation.[2,18] Upon freezing, the water forms a matrix of ice crystals, between which are regions of drug. Consequently, when dried the remaining material occupies the same volume as the initial solution/suspension, and so is very low density and porous with a high surface area. Freeze-dried materials therefore often have very rapid dissolution rates.[2] Other advantages of the technique stem from its gentle nature; the low temperature inhibits

decomposition, and due to the vacuum conditions oxidation is minimised. Its main drawbacks are the long timescale required for the drying process and the expense.[18]

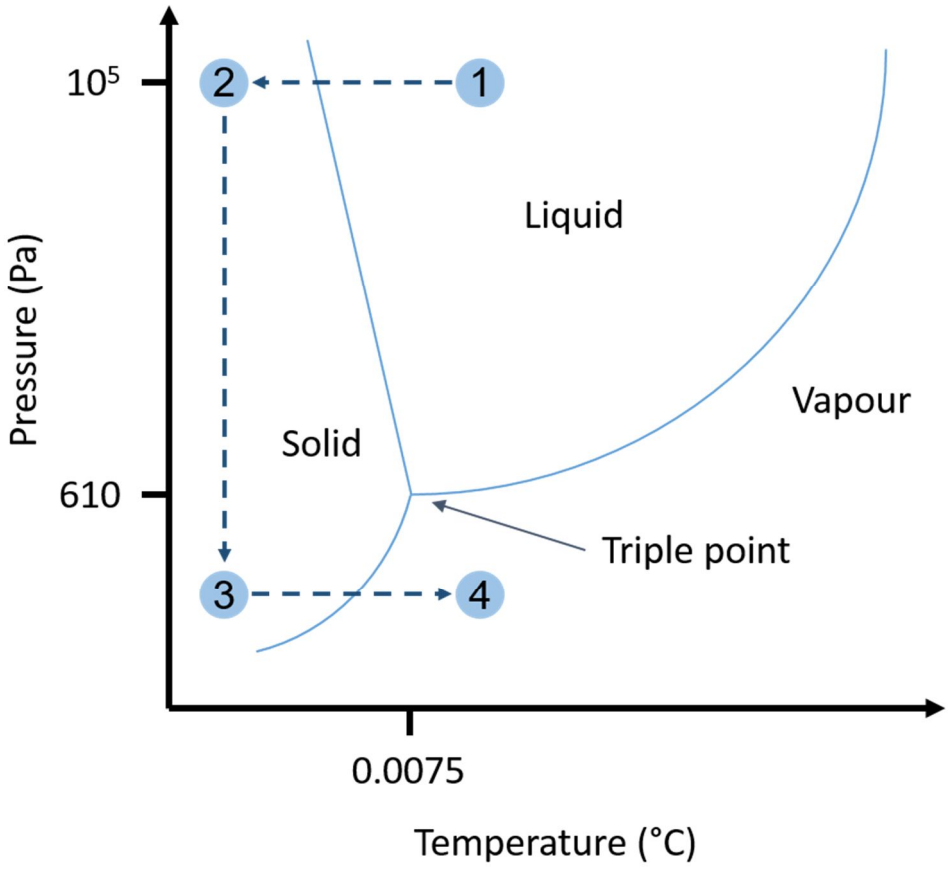

Figure 1-16. A schematic phase diagram of water with the stages of freeze drying superimposed.

1.1.9.2. Amorphous solid dispersions

Amorphous solid dispersions (ASDs), also termed glass solutions, consist of molecules of an API dispersed amongst molecules of an amorphous excipient (usually a polymer). The result is a single phase amorphous system with the drug dissolved or suspended in a pharmaceutically acceptable excipient.[115] The role of the excipient is to stabilise the otherwise unstable glass form of the drug (see Section 1.5) whilst retaining its increased dissolution rate and solubility relative to the crystalline form(s).[115]

The method involves vitrifying a solution or mixture of the API and carrier *via* a non-crystalline intermediate (commonly by spray drying or hot melt extrusion). If spray drying is employed then a solution of the drug and carrier in a common solvent or mixture of solvents is dried as described in Section 1.1.9.1. Hot melt extrusion applies the theory of

quench cooling to produce an ASD, and thus requires no solvent. The materials are simply mixed before being fed into a heated barrel with a rotating screw which further mixes them in the liquid state. The melt is then fed through a die and forms strands, films, pellets or tablets. The heat applied at the screw, shear forces, and rate of cooling all have an effect on the final structure of the ASD.[115] The stabilising action of the polymer gives ASDs the advantage over glasses formed from the pure drug. However, the addition of a polymer has the effect of reducing the total w/w drug content in the dosage form and brings added manufacturing costs and considerations, such as; polymer solubility in water (important for the end product) and organic solvent (if spray drying), or thermal stability and melt viscosity if extrusion is to be employed.

1.1.9.3. Transformation *via* solid-state mechanical disruption

Milling uses mechanical stress to induce transformation of the crystalline material to a glass, and is more commonly regarded as a particle size reduction process.[2,113,116] The technique can be divided into three categories relating to the method by which energy is applied to the material: ball mills, shear action mills, and shock action mills.[113] During ball-milling the powder is placed in a jar with ceramic balls typically ten times the sample mass. The jar is then either rotated or shaken at high speeds, subjecting the material to both shear and tensile stresses.[2,113] Shear action mills grind the material by way of rotating crushing elements[113] and shock action (air-jet) mills use air pressure to collide two streams of particles, with the impaction causing a reduction in particle size. All three methods apply force to the particle surface and act to reduce their size in the first instance. Eventually the force applied will no longer cause a reduction in size but will instead begin to disrupt the crystal structure at the surface. The resulting material will be only partially amorphous (1-5 %), but as the glass sits at the surface of the particles it has the potential to dominate the powder properties.[2] Vitrification by milling is temperature dependent and must be carried out at a temperature sufficiently low (in relation to the T_g of the material being processed) that recrystallisation does not occur during or soon after processing. However, the use of low temperatures has the advantage of avoiding degradation of the sample, and the lack of solvent reduces costs and has positive ecological consequences.[113] As milling involves disruption of the crystalline state it is often difficult to distinguish whether a truly amorphous material or a highly defective crystalline state has been formed. This is not always simple, as has been described in a recent review by Descamps and Willart.[117]

1.1.9.4. Physical vapour deposition

Physical vapour deposition (PVD), a method little explored in the context of pharmaceuticals,[12–14,111] is a process in which a crystalline solid sample is placed in a vacuum and heated so that it vaporises. A substrate is placed above the sample and the vapour deposits onto the substrate. Varying the temperature at which the sample is heated affects the rate at which it vaporises, and so the rate of deposition onto the substrate. It is also possible to vary the substrate temperature. The combination of the two variables affects the physical properties of the resulting deposited film.[118–120]

The ability of PVD to vitrify organic materials has long been known but, until recently, it was considered only to result in high energy, thermodynamically unstable products.[112,121–124] The last decade has seen this theory challenged and it is now known that PVD can produce glasses with stabilities far in excess of those formed by quench cooling of the liquid, so long as the rate of deposition and the temperature of the substrate are appropriate.[118–120,125–129] A more detailed explanation of the theory is given in Chapter 5.

In 2007 Swallen *et al.*[129] used PVD to create high density glasses with high thermodynamic and kinetic stability using low deposition rates and substrate temperatures near 0.85 T_g. It was proposed that this could be beneficial for amorphous pharmaceuticals. This substrate temperature was again reported to produce the most stable glasses in a paper examining the effect of substrate temperature on the stability of amorphous indomethacin (IMC) prepared by PVD. It was also stated that glasses produced at 0.6 T_g were unstable.[119] Following this, in 2008, Kearns *et al.*[127] studied the effect of varying the deposition rate on the stability of IMC glasses and found a slower deposition rate to give a more stable product.

In 2009 Dawson *et al.*[118,130] published data on IMC and showed that stable glasses prepared by PVD at 0.84 T_g and a deposition rate of 0.2 nm s^{-1} absorb fivefold less water than those prepared by quench cooling (a property attributed to higher stability), but that diffusion in the stable glass occurred 5-10 times faster than the quenched material. They also prepared glasses by PVD that had similar stabilities to quench cooled melts and absorbed similar amounts of water.[130] X-ray diffraction (XRD) was utilised to characterise the local structure of PVD IMC glasses and compare it to that of quench cooled samples. The deposited samples had an undefined different packing arrangement, characterised by a broad high intensity peak at low angles, to that of the quench cooled glass and supercooled liquid, which were the same. Over long annealing times (in excess of 8

hours) the molecules in the PVD material reoriented to give the same WAXS pattern as that of the quenched glass. It was suggested that this was a result of an underlying first order liquid-liquid phase transition.[118]

More recently, glasses were deposited at 0.99 T_g and 0.85 T_g by Sepúlveda *et al*. in an effort to examine the mechanism of molecular diffusion. The results support the theory mentioned above that very stable glasses are produced at 0.85 T_g, and that low stability glasses are produced at 0.99 T_g; the former and latter were referred to as stable and ordinary glasses respectively. Differences in the mechanism by which the two amorphous forms transformed into the supercooled liquid when heated were described. Ordinary glasses follow Fickian diffusion in which molecules throughout the matrix begin to diffuse and this continues at a rate inversely proportional to the fraction of equilibrium supercooled liquid present until the entire material has transformed. In contrast, in stable glasses the molecules are so efficiently packed that they are effectively trapped, and only those at the free surface have sufficient mobility to move. This mobility moves into the sample at a constant velocity as a growth front. The supercooled liquids resulting from both glasses have the same translational mobility. This is in contrast to previously reported data, and is attributed to lower levels of impurities in the samples prepared in Sepúlveda's study.[128]

Work in the last few years has shown that stable glasses prepared by PVD have anisotropic structures, owing to the time allowed for molecular configuration sampling at the free layer. These structures allow for stronger intermolecular interactions than a more disordered matrix, whilst still lacking the lattice enthalpy of a crystal.[131,132] A study in 2017 by Laventure *et al.*[133] looked at the influence of H-bonding on the stability of glasses of triazine derivatives (Figure 1-17) prepared by PVD. They found that, although all three compounds studied exhibited properties commonly associated with highly stable vapour deposited glasses (e.g. high density and anisotropic molecular packing), the derivative containing a functional group with greater propensity for H-bonding was only slightly more stable than the corresponding quench-cooled glass. In contrast, the other two compounds formed glasses with relatively high kinetic stability.

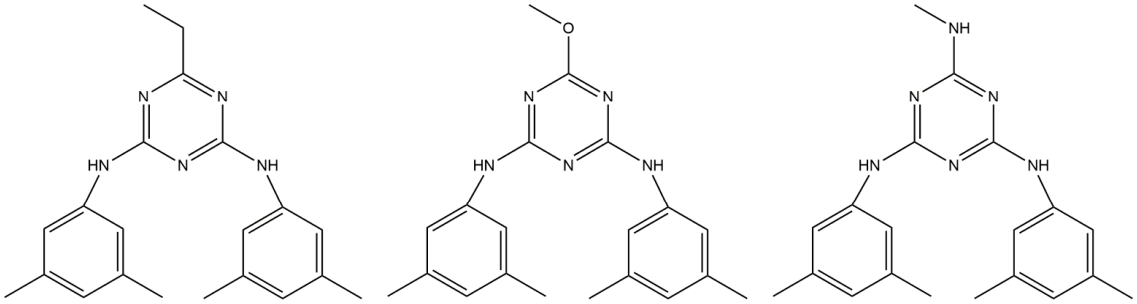

Figure 1-17. Structures of the three triazine derivatives examined by Laventure and co-workers.[133]

So far much of the literature has concentrated on making stable glasses from molecules that readily form glasses: in particular, IMC (a very good glass former) has been used as a model drug. The mechanism by which the molecules diffuse within the matrix when annealed and upon heating has been the subject of much work, but so far there is little information on stable glasses prepared from drugs known to be poor glass formers and which either cannot be vitrified by any other method, or that revert to crystallinity very quickly after vitrification.

1.6 Conclusion and Aims

Solubility and dissolution are major barriers to the successful development of new solid state medicines. The formulation of drugs in the amorphous or metastable forms and co-crystallisation all have the potential to overcome this problem. However, current methods of vitrification are incapable of producing amorphous matrices of adequate stability and methods of screening possible co-crystals are slow and expensive. Methods of stabilising metastable polymorphs using molecular additives are well known, but detailed knowledge of concurrent calorimetric and structural changes at transitions between the polymorphs of drugs is lacking. More significantly, knowledge of the interactions occurring between additives and APIs, and consequently which additives to use, is lacking. This thesis will present a rapid method for the screening of co-crystals, and additives for stabilising metastable polymorphs, and a second technique for preparing amorphous materials from poor glass formers.

Chapter 2 of this thesis describes the development of the novel hyphenated technique of simultaneous synchrotron X-ray diffraction and differential scanning calorimetry (DSC-XRD). It goes on to demonstrate the utility of the method and its advantages over using the two methods separately for studying phase transitions in pharmaceutical materials, using two compounds that display enantiotropic polymorphism.

Chapter 3 is concerned with the use of DSC-XRD to study polymorphic phase transitions in three pharmaceutically relevant compounds, and in particular the stabilisation of the polymorphs of paracetamol through the addition of saccharides; as, although the use of additives to stabilise the metastable form is well known (as described in Section 1.1.4.3.1), a detailed understanding of how they function is lacking. Calorimetric and structural data have not previously been collected simultaneously on the same sample and differences in sample mass and volume between analytical techniques used have led to discrepancies in the observation of phase transitions. The work described in this chapter aims to provide additional understanding of these processes.

Chapter 4 explores the formation of co-crystals by four different routes: evaporation, thermal inkjet printing, co-melting, and milling. Particular attention is paid to the application of DSC-XRD for the simultaneous formation and analysis of four co-crystals, three of which are novel. This method has the potential to be an incredibly useful technique for the screening of new co-crystal forming systems. Combining the technique of co-melting in a DSC with high energy synchrotron XRD will enable, for the first time, structural analysis of the reactants and co-crystal products as a function of temperature as they co-crystallise upon heating. The data will give an insight into the mechanism by which theses co-crystals form and the phase transitions that occur.

PVD has the potential to produce highly stable glasses (see Section 1.1.9.4) but is yet to be tested on a drug known to be a poor glass former. Chapter 5 outlines the development of a vacuum chamber, previously used for depositing films of amorphous solid water, for the purpose of depositing films of amorphous pharmaceuticals. It further demonstrates the ability of the apparatus to vitrify a number of pharmaceutical materials, two of which show little evidence in the literature of previous glass formation.

2. Simultaneous synchrotron X-ray powder diffraction – differential scanning calorimetry for the *in situ* investigation of phase transitions in pharmaceuticals

2.1. Introduction

Differential scanning calorimetry (DSC) is an extremely widely used tool for studying temperature-driven phase changes in solid materials.[134] Its utility stems from the fact that nearly all phase changes are accompanied by a change in heat content and so it can be applied to virtually any sample. Heat flux DSC measures the difference in temperature of a sample compared to that of an inert reference as they are simultaneously subjected to an identical heating programme within a furnace (Figure 2-1). Transitions in the sample will be either endothermic (e.g. melting) or exothermic (e.g. crystallisation). Endothermic samples will heat more slowly and exothermic more quickly than the reference. If we consider a sample heated at a linear rate (e.g. 10 °C min^{-1}), as it experiences a transition its temperature will deviate from linear behaviour for a time (Figure 2-2). This deviation is used to calculate the difference in power required to maintain the sample at the reference temperature and subsequently the enthalpy associated with the transition.

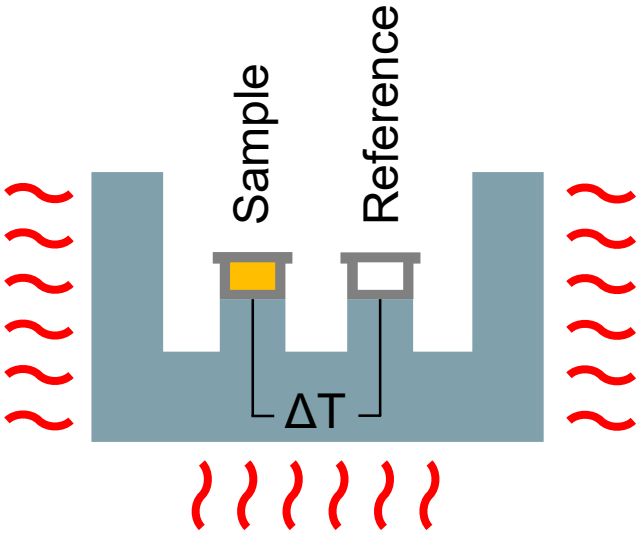

Figure 2-1. A schematic illustration of a heat flux DSC.

Heat transfer, however, is a ubiquitous parameter that does not provide molecular or structural insight into the source from which it originated. Further, other events such as

decomposition, sintering, separation, foaming and bubbling, and creep of melts may give rise to heat changes that are not actually a result of phase transitions in the sample. Thus, while DSC analysis in isolation can be extremely informative, absolute assignment of the changes in physical form which occur with each phase transition is impossible without ancillary data.

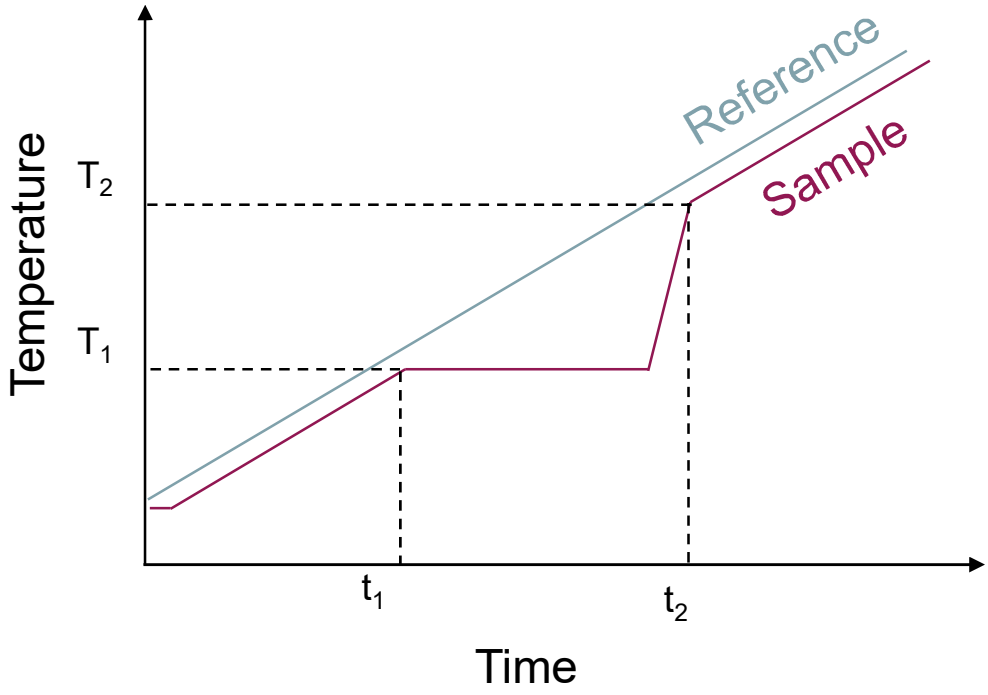

Figure 2-2. A schematic showing the effect of an endothermic transition on the temperature of a sample compared to that of the reference as they are heated in a heat flux DSC.

Two common experimental approaches to interpret thermal data and to identify and assign phase changes are to change the DSC operating conditions or to analyse the sample with thermogravimetric analysis (TGA). Changing the DSC heating rate determines whether phase transitions are thermodynamic (*e.g.* melting) or kinetic (*e.g.* recrystallization) in nature, because thermodynamic transitions do not show a dependence on heating rate while kinetic transitions do. TGA allows determination of whether the sample loses volatile components or degrades with temperature. However, while both approaches aid interpretation, neither affirms what actual structural changes in phase have occurred.

It is of course possible to take sample material directly from the DSC and analyse it with another technique, but this approach can only be used to identify the material at the measurement temperature and the assumption must be made that the sample does not change between removal from the DSC and subsequent analysis (potentially an issue

for metastable or intermediate phases). The best option therefore is *in situ* analysis of the sample while it is being heated in the DSC itself, by linking a second instrument to the calorimeter (so called hyphenated techniques).[135] Such an approach ensures that the temperature of the sample is known and controlled throughout the measurement and, if the secondary method of analysis is sufficiently rapid, information on physical form can be collected in real time for all the phases the material may progress through. The additional analysis should ideally be non-invasive, so as not to affect the temperature of the sample or to introduce further erroneous heats, and hence spectroscopic probes are often used. For instance, DSC has been hyphenated with Fourier-Transform infra-red (FTIR),[136] near infra-red (NIR)[137] and Raman[81,138–141] spectrometers, and light microscopy (to make simple optical observations).[142]

While these approaches have proved extremely powerful, the 'gold-standard' analytical tool for the characterisation of physical form remains X-ray diffraction (XRD). XRD analysis can provide absolute determination of the position of atoms and molecules within unit cells, and laboratory variable-temperature XRD has led to useful insights in the changes occurring to the structure of a sample upon heating.[143,144] Unfortunately, standard equipment is not able to deliver the high heating rates and short data collection times used in DSC, and thus its application to *in situ* DSC analysis is limited. However, the data collection time can be reduced significantly if a synchrotron X-ray (SX) source is used.

Synchrotrons generate X-rays of a much shorter wavelength and higher energy than sealed glass X-ray tubes (the most common laboratory X-ray source for powder diffraction). Generation of X-rays in a synchrotron begins with an electron gun, which produces a beam of electrons that is then accelerated by a linear particle accelerator (also known as a linac) (Figure 2-3). Following this the electrons pass into a booster ring, which further accelerates them before feeding a larger storage ring. As the beam passes around the ring it is accelerated to nearly the speed of light and its path directed by bending magnets. This change in direction causes the particles to emit an intense beam of radiation over a wide range of frequencies. This radiation can then be intensified and monochromated to a specific wavelength for powder diffraction studies. A typical laboratory diffractometer will utilise a copper X-ray source, which produces X-rays with a wavelength of *ca.* 1.5 Å (8 keV), whereas the I12: Joint Engineering, Environmental and Processing (JEEP) beamline at Diamond Light Source (Didcot, UK) produces X-rays in the range 50-150 keV.[16]

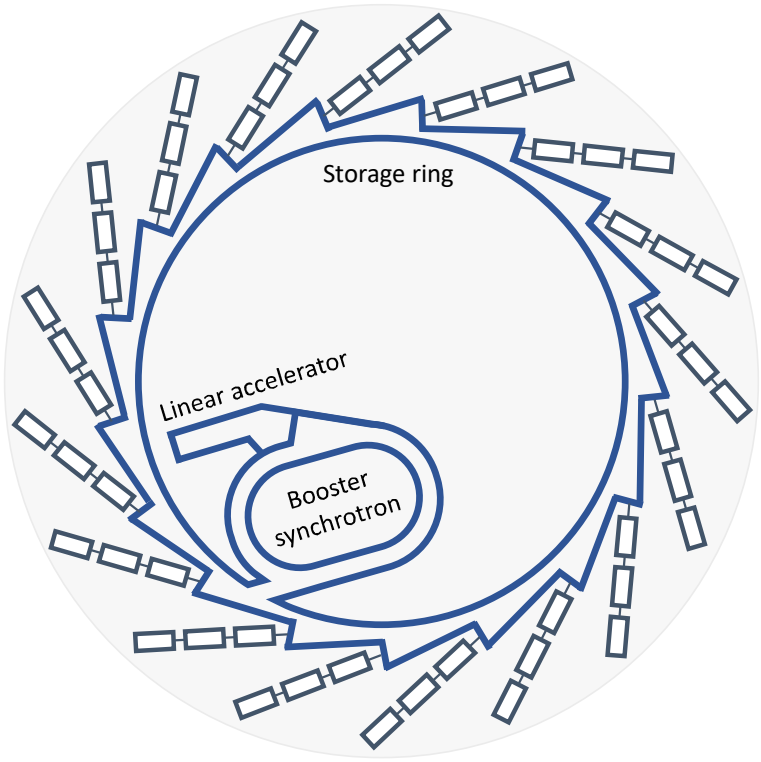

Figure 2-3. A schematic showing a synchrotron and its main particle accelerating components.

Researchers have for around 20 years employed SX to explore the mechanisms and kinetics of solid-state reactions, initially using powerful white beams of X-rays to penetrate bulky reaction vessels.[145] This energy-dispersive technique suffered from poor spatial resolution, making high-quality structural information difficult to obtain. Recent developments in both synchrotron and detector technologies allow the combination of high-energy monochromatic X-rays and exquisitely sensitive detectors to obtain high-resolution diffraction patterns in as little as 1 s or less.[146] Hence, it is now feasible to obtain high-quality data suitable for structural (Rietveld) refinement from the direct hyphenation of SX and DSC.

Researchers have combined calorimetric analysis with diffraction techniques for over three decades. The earliest example, from Russell and Koberstein,[147] describes the melting and crystallisation of polyethylene using DSC and small angle X-ray scattering (SAXS). This was achieved by modifying a Mettler FP84 combined hot stage microscope/DSC so that it could be mounted in the beamline of a synchrotron. Modification required removal of all glass windows in the instrument and mounting of the sample pan vertically by altering its base so that it could be held by a press fit in the hole through which the incident beam passed. The data collected gave valuable insight into the melting and crystallisation behaviour of the sample upon heating and cooling, respectively. Several other groups have used a similar set up for both SAXS and wide angle X-ray scattering (WAXS), employing the FP84[148–153] or FP82[154] mounted vertically

and modifying the sample pan so that the horizontal beam will pass through the material. Although effective these studies have all involved significant effort to modify and mount the DSC.

Other groups have carried out similar experiments with a Linkam TMH600 hot stage or DSC600 mounted vertically in the beam. Ryan *et al.*[155] modified sample pans, fitting them with mica windows and gluing them, once loaded, to a thermocouple to examine the crystallinity and lamellar thickness of polyethylene. Bras and co-workers[156] have also reported the utility of this set up for materials characterisation. Gilbert *et al.*[157] studied the influence of quenching on the phase separation of unstable *n*-alkane blends with DSC-wide-angle X-ray scattering. This geometry required replacement of glass windows in the beamline with other materials and also some mechanical method of supporting the pan in position.

Yoshida *et al.*[158] modified a different model of DSC (a Seiko DSC 200). Again the heat sink and sample and reference pans were mounted at 90° to the standard laboratory configuration with holes added to the instrument and sample pan to allow passage of the beam. Sample pans consisted of four pieces for solids and additional silver or Teflon ring spacers were incorporated for liquid samples. The groups of Keller *et al.*[159] and Brubach *et al.*[160] utilised the alternative design of a Microcalix version 2.0 microcalorimeter to study the potential of the combined techniques and explore transitions in glyceryl behenate, respectively. The Microcalix is a microcalorimeter that employs a glass capillary as a sample holder rather than a sample pan.

All of these studies, with the exception of the two involving the Microcalix, have involved complex modifications of either the DSC pans, the DSC itself or both, to permit transmission of the synchrotron X-ray beam. These include adding mica windows to the pans, mounting the cell vertically and holding the pan in position on the thermocouple via a mechanical method such as a press fit, rubber O-rings or a spring. These modifications have the potential to alter the pathways of heat-transfer from the sample to the DSC, and so affect the DSC data. The same can also be said for the capillaries of the Microcalix. The apparatus required is also complex and the experiment difficult to implement in comparison to a simple lab DSC.

Although these effects might be small, in this work efforts were made to determine whether it would be possible to construct an experiment to use unmodified DSC pans in a synchrotron source, and so minimise errors in DSC measurement and maximise the ease by which lab DSC protocols can be translated into DSC-XRD. The DSC 2010 series of heat-flux DSC instruments (TA Instruments LLC, USA) have the advantage that the

element used to heat the sample and reference pans is coiled around the cell (Figure 2-4). The heat generated is transferred to the DSC head via a metal shield (ca. 5 mm thickness). Ordinarily this shield would be impenetrable to a synchrotron X-ray beam, but it is possible to drill holes through it to allow the beam to pass unhindered. It is also advisable to carefully separate the coils of the element and to apply heat sink paste to allow space for the beam to pass and to insulate against short circuiting of the instrument, respectively. Correct placing of the holes means that the sample pan can be located in the direct path of the synchrotron X-ray beam, with the reference pan to one side. Further, the pans themselves are located on pedestals (which contain the thermocouples), which means that the diffracted X-ray beam can exit the instrument without contacting any part of it (Figure 2-4 and Figure 2-5). The pans are made of thin aluminium, through which the synchrotron beam can pass. Although X-rays are scattered by aluminium, this gives only a few Bragg reflections which can easily be modelled or excluded from analysis. With this arrangement, DSC data and diffraction patterns can be collected simultaneously on a single sample, using a standard laboratory calorimeter.

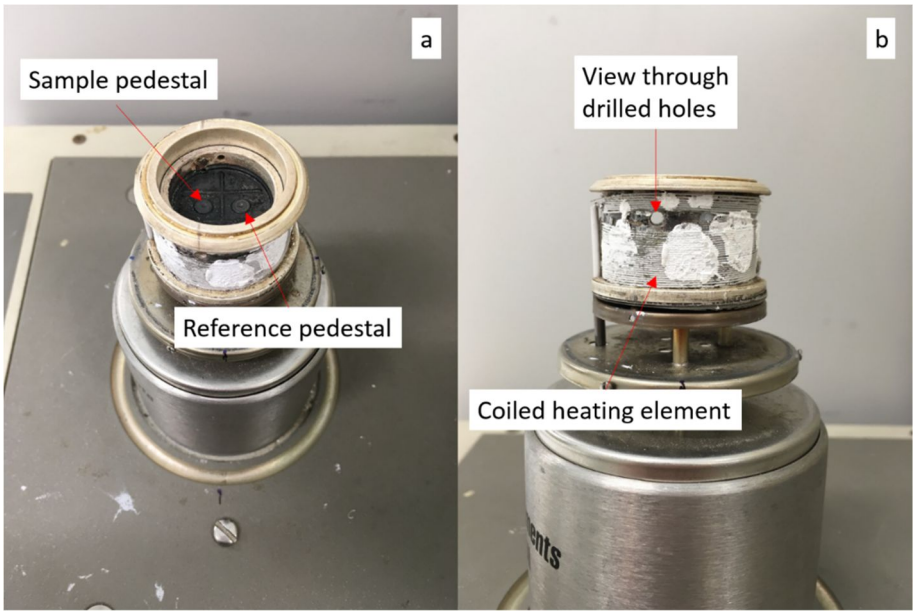

Figure 2-4. Photographs of the DSC 2010 furnace showing the (a) sample pedestal and reference pedestal, each of which contains a thermocouple, and (b) the path of the X-ray beam through the holes drilled in the cell.

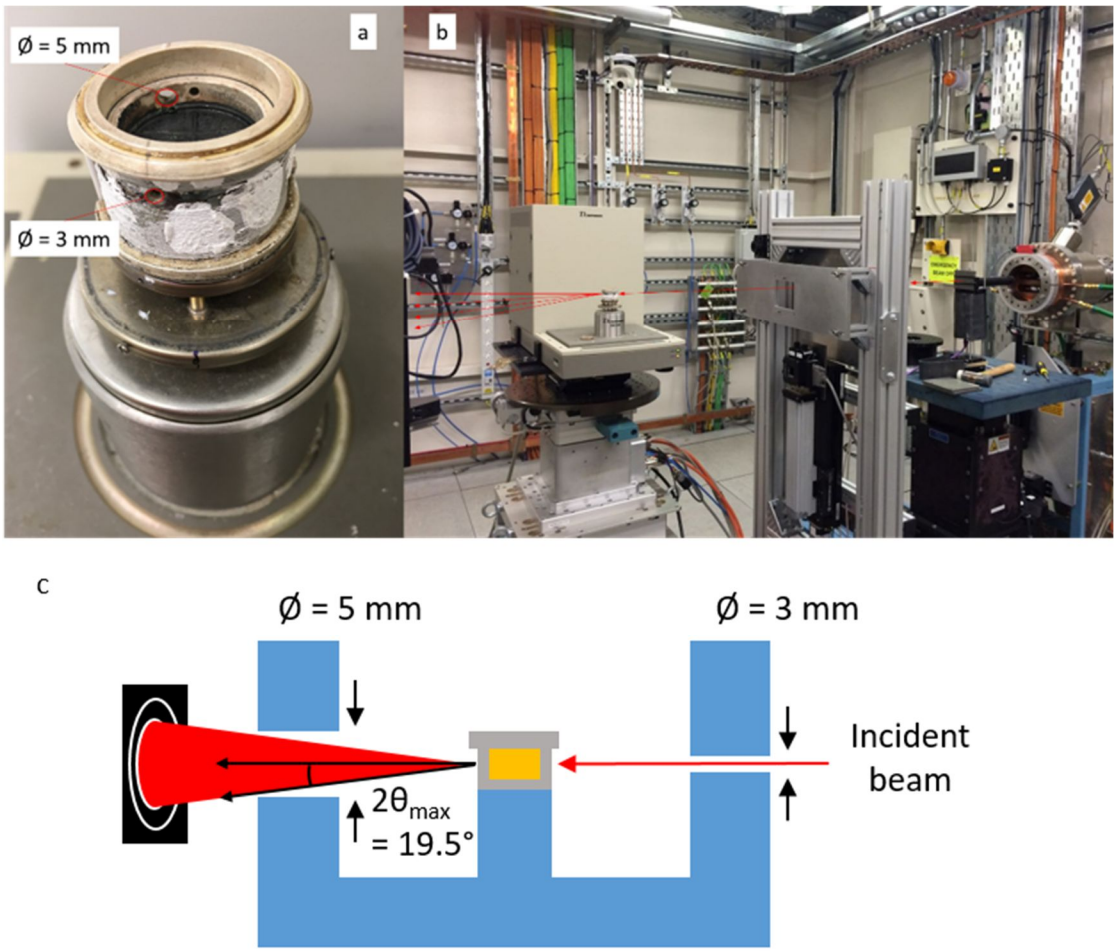

Figure 2-5. Photographs of (a) the modified DSC 2010 head and hole diameters and (b) the DSC positioned on Beamline I12 at the Diamond Light Source and (c) a schematic showing the maximum attainable 2θ with the experimental geometry. The red lines describe the path of the X-ray beam.

This chapter details the modifications to the DSC required to allow the use of unmodified pans and applies the method to the analysis of two model compounds, both of which have enantiotropically-related polymorphs: glutaric acid and sulfathiazole.

2.2. Materials and methods

Sulfathiazole (99 %) and glutaric acid (99 %) were purchased from Alfa Aesar, UK. Sulfathiazole was used as received. Due to its large particle size, glutaric acid was gently ground in a pestle and mortar before loading into the sample pan.

Simultaneous differential scanning calorimetry and synchrotron X-ray powder diffraction (DSC-XRD) experiments were carried out on the Joint Engineering Environmental and Processing beamline I12 (JEEP) at the Diamond Light Source.[161] The beamline produces a continuous spectrum of X-rays in the energy range 50-150 keV, which for these experiments was monochromated to 53.16 keV (λ = 0.233 Å). The diameter of the beam was 0.5 mm. A Thales Pixium RF4343 detector was positioned 1.9 m behind the sample.

Detector calibration was performed using cerium dioxide. Diffraction patterns were recorded every few seconds (data were collected for 2 s with a pause between collections).

DSC measurements were performed with a TA 2010 instrument (TA Instruments LLC). The DSC furnace was modified by drilling a hole either side of the sample holder to allow unhindered passage of the X-ray beam through the sample. Prior to drilling, the heating coils were carefully separated such that they were placed either side of the holes. Heat sink paste was applied post-drilling to insulate against short circuiting of the instrument. The entry hole was 3 mm in diameter and the exit hole 5 mm (to account for diffraction of the X-ray beam), as shown in Figure 2-5(a). Calibration was performed with a certified indium standard according to the manufacturer's instructions. Samples (*ca*. 30 mg) of glutaric acid or sulfathiazole were held in Tzero aluminium pans and heated at 10 °C min^{-1} from 30 °C to 180 °C and 220 °C respectively. It was found that the X-ray beam was sufficiently intense to pass through the thin aluminium pans, and so no modification of the pans was necessary. DSC data were recorded with the TA Advantage software package, analysed with TA Universal Analysis, and plotted with Origin 9.1.

XRD data were analysed as follows. The large grain size of the samples resulted in unrepresentative spots of high intensity in the 2D Pixium data, and thus the DAWN Science Workbench was first used to mask these regions of the 2D data. The same software was used to convert the 2D data into 1D diffraction patterns.[162] Contour plots of the raw XRD data were then plotted using bespoke software routines. Selected patterns were first analysed by Dr. Tim Prior (University of Hull) using the Rietveld method implemented within GSAS,[163] in order to obtain realistic values for the unit cell parameters at elevated temperatures. Backgrounds were fitted using a 6-term shifted Chebyshev polynomial of the first kind. Lattice parameters and a single Gaussian peak shape parameter were refined. In cases where more than one phase was present, the peak shapes for each phase were constrained to be the same. Where more than one phase was present, the phase fraction was refined. The models used came from the CCDC (details are given below). The atom positions were not refined. Atom displacement parameters, U_{iso} were set to be 0.15 $Å^2$ in each phase.

The TOPAS-Academic suite of programs[164] was further employed to perform batch refinements of all datasets collected, using the same procedures as in GSAS. No zero point was refined as entire diffraction patterns were collected using a 2D area detector.

2.3. Results and discussion

2.3.1. Apparatus

Before analysing any samples it was necessary to assess the effect of drilling holes in the DSC furnace. Calibration was carried out with a certified reference sample of indium and a clear single melt was observed with onset and enthalpy values within the manufacturer's specified tolerances. Temperature versus time data for the modified DSC 2010 were recorded and compared with the same heating profile on an unmodified DSC, and can be seen in Figure 2-6. It is clear from the linear nature of the heating rate and its similarity to that of the unmodified DSC that the ability of the DSC 2010 to control temperature and heat was not compromised by the addition of the holes.

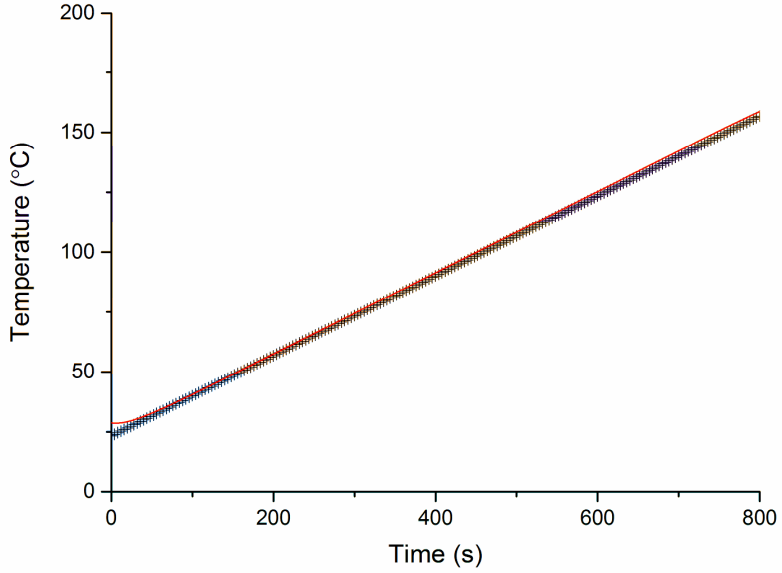

Figure 2-6. Measured temperature versus time data for the modified DSC 2010 (red line) and an unmodified Q20 DSC (black crosses).

2.3.2. Sulfathiazole

The polymorphism of sulfathiazole has been the subject of extensive research by both the crystallographic and pharmaceutical communities since it was first reported in 1941,[165] and it has been known to exist in at least five crystal forms since 1999.[166,167] As a result of the high number of studies and the authors' lack of attempts to reconcile their work with previous publications[27] there is inconsistency in the identification of polymorphs and their nomenclature. Fortunately a recent investigation[168] has attempted to reconcile this by listing the

works and relating the identities of the polymorphs reported in each to those of the Cambridge Structural Database (CSD). All references to polymorphs in this work utilise the same nomenclature as the CSD.

To aid interpretation of the data, the XRD patterns were first converted to contour plots; these show peak intensities as a colour-scale as a function of temperature and permit easy visualisation of changes in crystalline form. DSC-XRD data for sulfathiazole are given in Figure 2-7. The DSC data show two clear endotherms with onsets at 154 °C and 202 °C. The former corresponds to a stark change in the diffraction pattern, while the latter is coincident with the complete disappearance of all diffracted intensity and agrees well with the reported melting point of sulfathiazole form I at 201 °C.[169] It is important to note that there are no unexpected events in the DSC data, and that the observed transitions all occur at the expected temperatures based on the literature. We have calculated the X-ray absorption cross-section of the samples, and even on the most pessimistic assumptions find heating from the X-ray beam to be <0.1 °C min^{-1}. Hence, while a small amount of local heating of the sample by the beam may occur, the DSC is able to effectively compensate for this and the heating profile is unaffected by the exposure to X-rays.

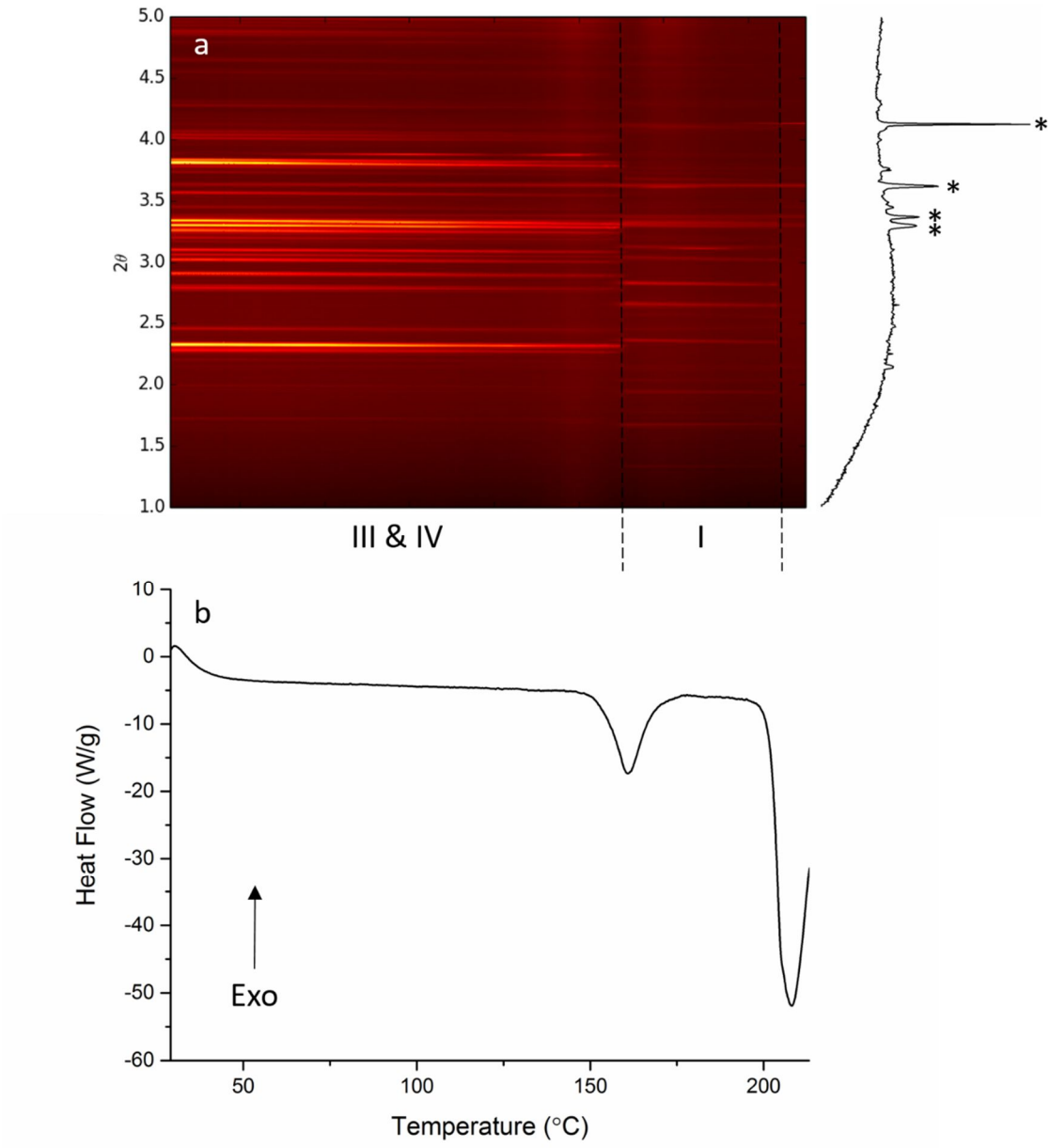

Figure 2-7. DSC-XRD data for sulfathiazole. (a) A contour plot of the diffraction data and (b) the corresponding DSC trace. The 1D diffraction pattern is an example of those collected at temperatures above the melt and reflections marked * are a result of the experimental set up.

The changes in the diffraction pattern are complete at the apex of the first endotherm in the DSC trace, indicating the phase transition is complete here and the return of the heat flow to baseline can be attributed to the instrument and not the sample. Form III is reported to be the most stable form of sulfathiazole between 10 °C and 100 °C[169] and the temperature of the first endotherm corresponds well to literature values for a solid-solid phase transition from form III to I, reported to occur between 150°C and 170°C.[170]

To verify the assignment of the phases present in each segment of the contour plot, selected patterns at 29°C and 161°C were analysed using the Rietveld method. A relatively poor fit was obtained at 29°C when considering only form III in the

model (Figure 2-8), and a more detailed analysis revealed that in fact the material present at this temperature was a mixture of forms III (67.6 %) and IV (32.4 %) (

Figure 2-9). This was somewhat unexpected as form III is reported to be the most stable polymorph at room temperature,[169] although the stability difference between form III and IV is relatively small.[169] As expected, form I was not observed to be present at this temperature. In contrast, after the transformation endotherm the diffraction pattern can be successfully fitted using the known structure for form I. Selected final fits and unit cell data are presented in Figure 2-10, Figure 2-11 and Table 2-3. It should be noted that the imperfect final fit of the patterns can be attributed to the presence of some larger crystallites in the samples, which resulted in spots of intense diffraction rather than the smooth rings expected of a finely ground powder.

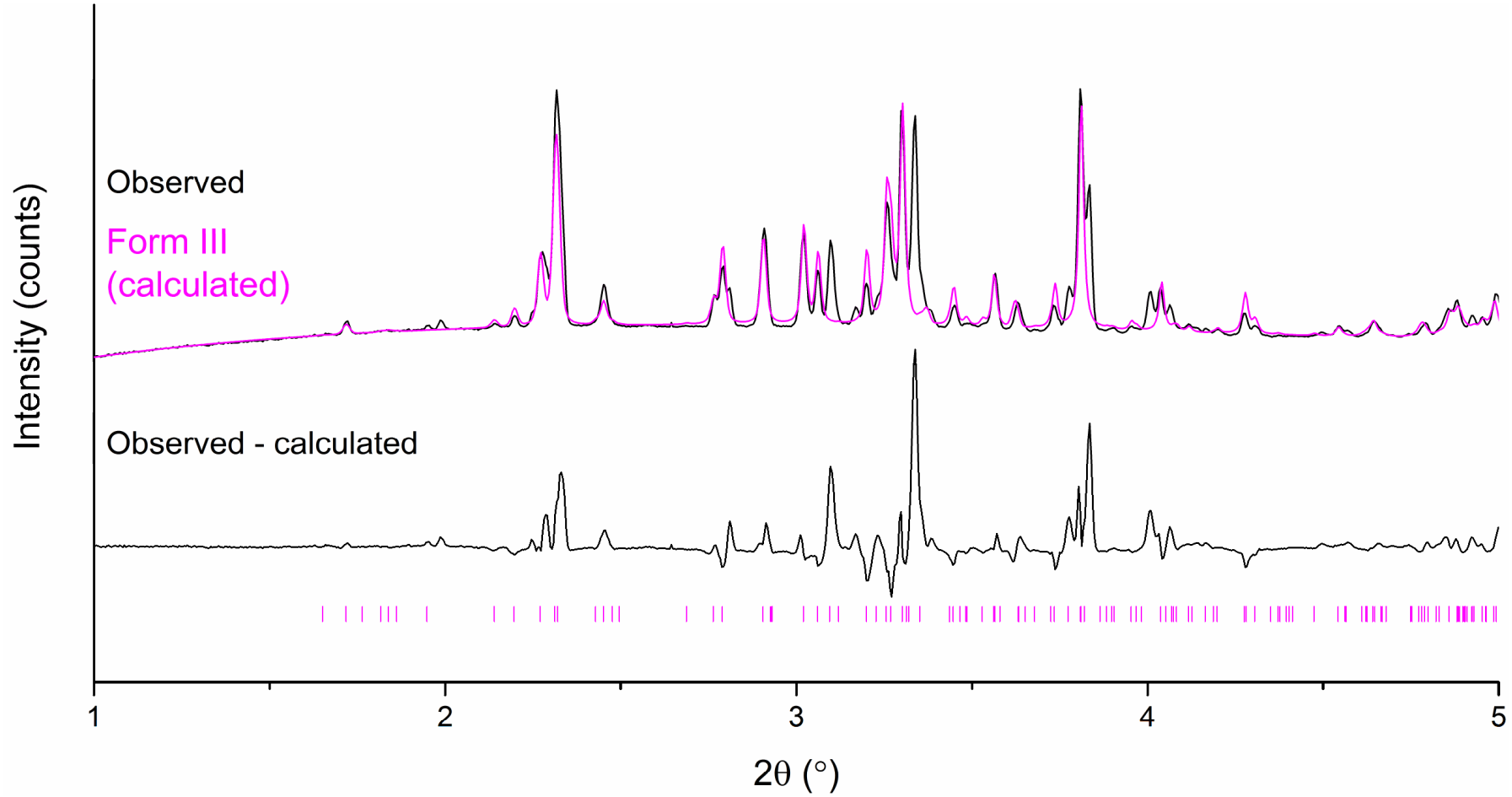

Figure 2-8. TOPAS Rietveld fit of sulfathiazole form III (pink) to the observed pattern (top black) at 29°C. Tick marks show the expected positions for form III, and the difference between the calculated and observed diffraction profiles is shown as the lower line.

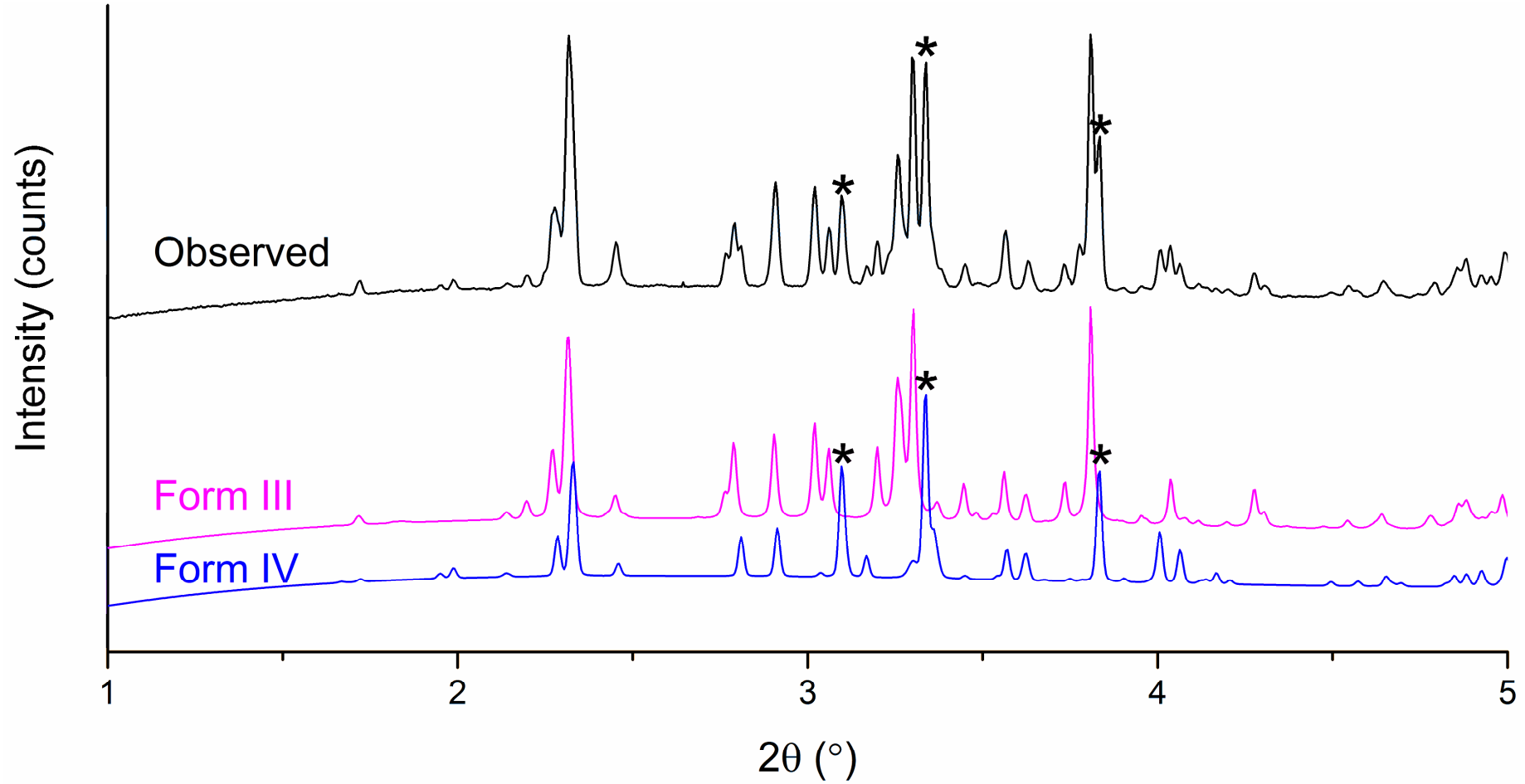

Figure 2-9. Initial observed pattern for sulfathiazole at 29 °C and the corresponding contributions of sulfathiazole polymorphs III and IV. Distinct reflections in the observed pattern that can only be matched with the inclusion of form IV are marked *.

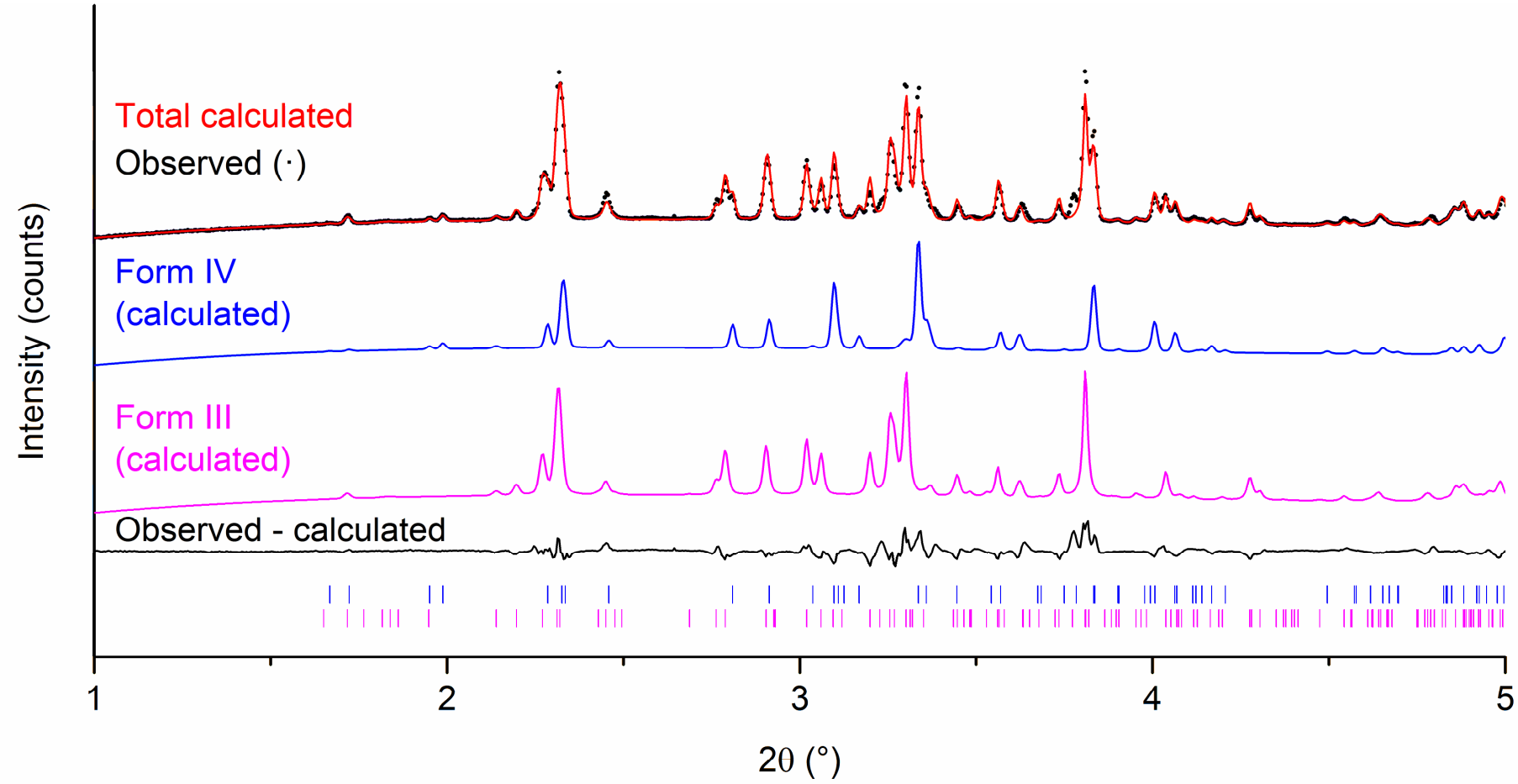

Figure 2-10. Powder X-ray diffraction patterns for sulfathiazole at 29°C and 161°C. The tick marks show the positions of allowed reflections from the polymorphs labelled in the corresponding colour.

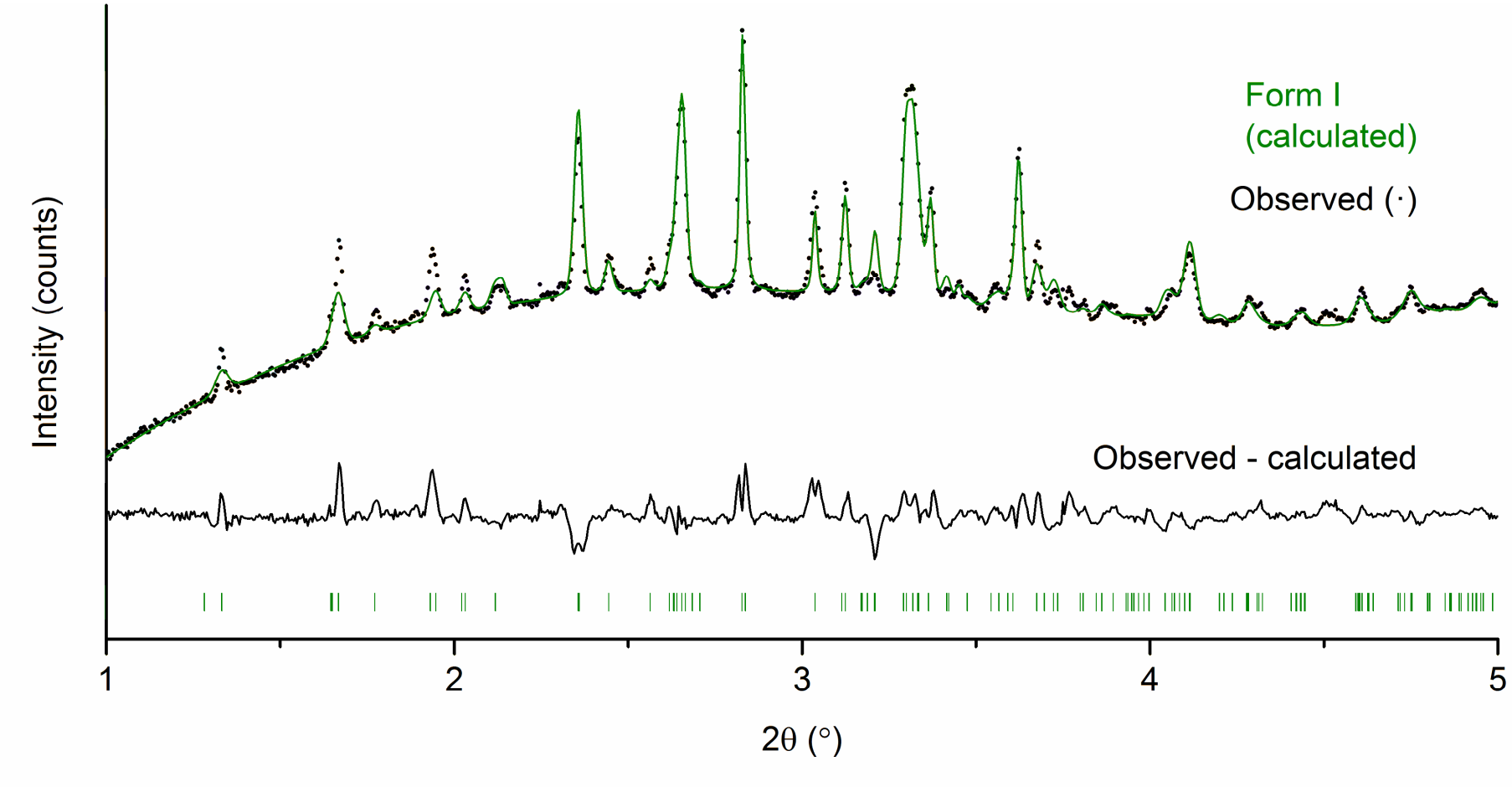

Figure 2-11. Powder X-ray diffraction patterns for sulfathiazole at 161°C. The tick marks show the positions of allowed reflections.

Table 2-3. Refinement parameters for sulfathiazole. The starting models were taken from the CSD (form III: SUTHAZ02; form IV: SUTHAZ04; form I: SUTHAZ43).

Property	Form III	Form IV	Form I
T / °C	29		161
Space group	$P2_1/c$	$P\ 1\ 1\ 2_1/n$	$P2_1/c$
a / Å	17.564(1)	10.864(1)	10.574(1)
b / Å	8.560(1)	11.441(2)	13.715(2)
c / Å	15.572(2)	8.543(2)	16.893(3)
α / °	90	90	90
β / °	112.932(9)	90	108.596(19)
γ / °	90	91.852(12)	90
Cell volume / Å^3	2156.1(4)	1061.2(3)	2321.8(7)
R_{wp}	0.0561		0.0242
$R_{wp\text{-}bkd}$	0.1907		0.2632
Phase fraction*	67.6 %	32.4 %	100 %

*Due to the graininess of the sample, representative errors cannot be calculated. However, the author conservatively estimates the error to be in the region of 5 %. Phase fractions for the initial mixture of sulfathiazole are reported as individually refined patterns in Figure 2-9.The quality of the data collected permitted batch refinement of the lattice constants and scale factor for each form present against all the patterns, giving fits with weighted profiles (R_{wp}) in the range 0.0242 to 0.0561. The unit cell parameters could be extracted from these and plotted as a function of temperature (Figure 2-12, Figure 2-13 and Figure 2-14). As expected, increasing the temperature of the sample causes expansion of the unit cell in all three dimensions for all three polymorphs present, with the exception of the *c* axis of form I which exhibited little change. This appears to be the first time that the structures of purely organic species have been refined using data collected on JEEP and also the first example of refinement using data collected during a live DSC run.

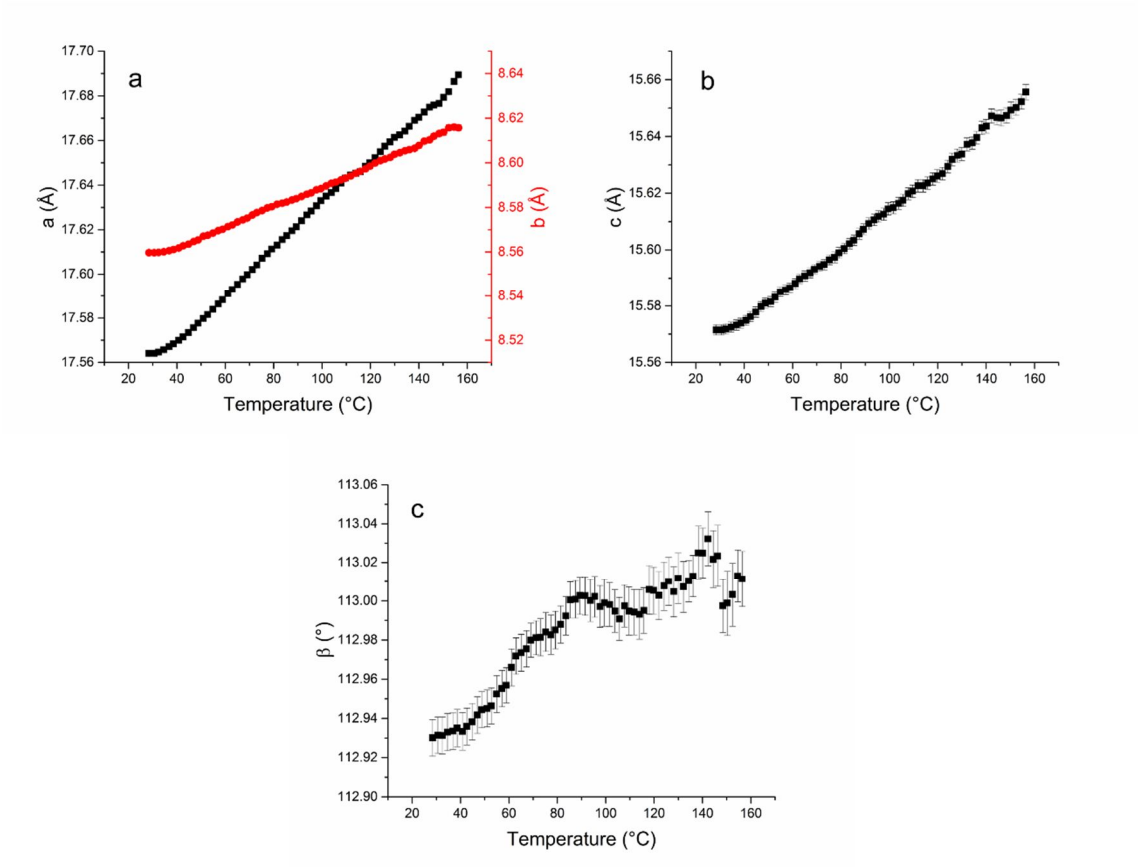

Figure 2-12. Lattice constants as a function of temperature for sulfathiazole polymorph III: (a) the *a* (black squares) and *b* (red circles) parameters; (b) the *c* parameter; (c) the *β* angle.

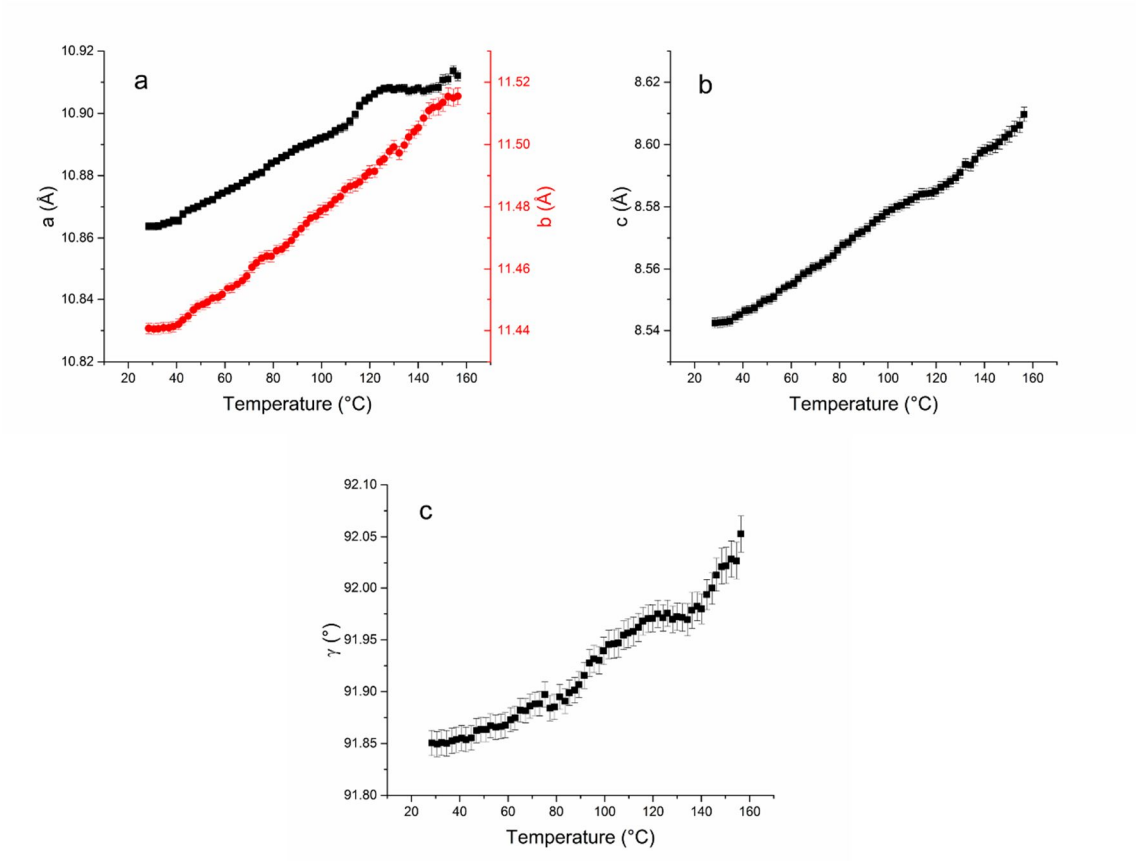

Figure 2-13. Lattice constants as a function of temperature for sulfathiazole polymorph IV: (a) the *a* (black squares) and *b* (red circles) parameters; (b) the *c* parameter; (c) the *γ* angle.

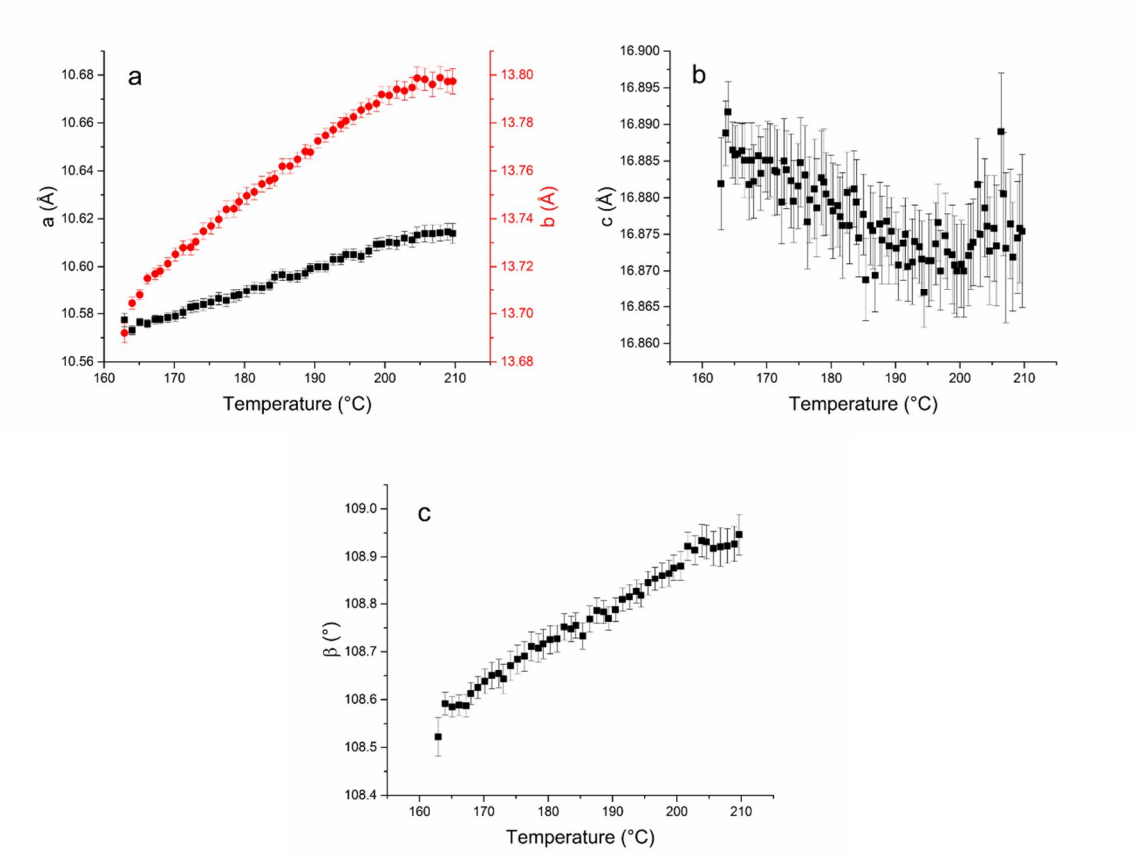

Figure 2-14. Lattice constants as a function of temperature for sulfathiazole polymorph I: (a) the *a* (black squares) and *b* (red circles) parameters; (b) the *c* parameter; (c) the *β* angle.

In the past it has sometimes been assumed in the literature that when phase transitions between forms are observed in DSC experiments, there is a melt of one form followed by recrystallization of a new form.[171,172] The constant presence of reflections in the XRD contour plot indicates that there is no wholesale melt here, however: if the entire sample melted we would expect to see a diffraction pattern devoid of reflections. This suggests that the transition between the crystalline forms of sulfathiazole occurs via a direct solid-solid pathway, rather than by melt-recrystallisation. That said, these measurements are bulk averaged over many particles and microscopic transient melting on a per particle basis cannot be ruled out.

In order to gain a more quantitative understanding of the transformation, the individual contributions of each polymorph to the overall pattern at each temperature were integrated and the results normalised to obtain a phase fraction. The results are given in Figure 2-15. Below 155 °C the relative contributions of the three polymorphs are constant, with 67.6% form III and 32.4% form IV present and form I absent. Subsequently, the amount of form I begins to increase, whilst those of III/IV diminish simultaneously until 166 °C when the conversion is complete. If the phase fractions of form III and IV are summed, a plot of their combined phase fraction vs. temperature

crosses that of form I around 0.5 indicating a solid-solid phase transition (Figure 2-16). It is of particular interest that the transition to form I occurs simultaneously for both forms III and IV.

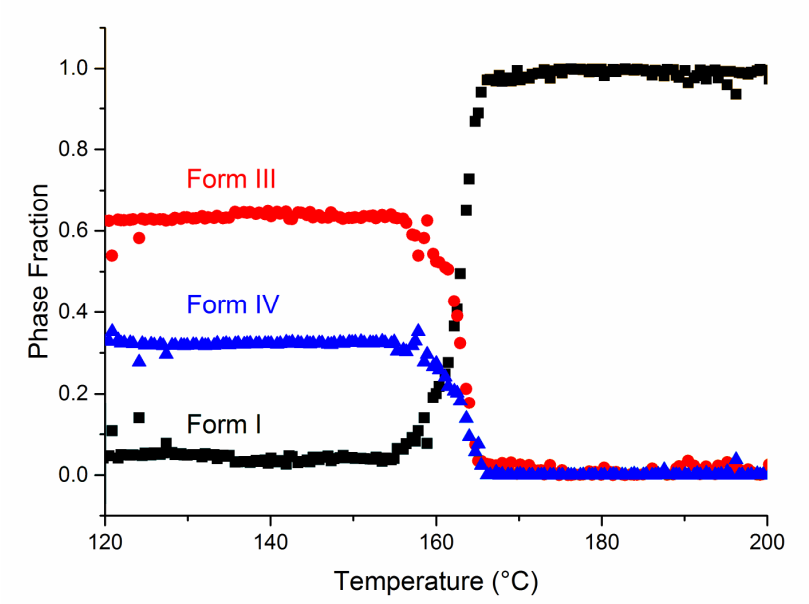

Figure 2-15. Plot of phase fraction vs temperature for the heat- induced transformation of sulfathiazole from a mixture of forms III and IV to form I.

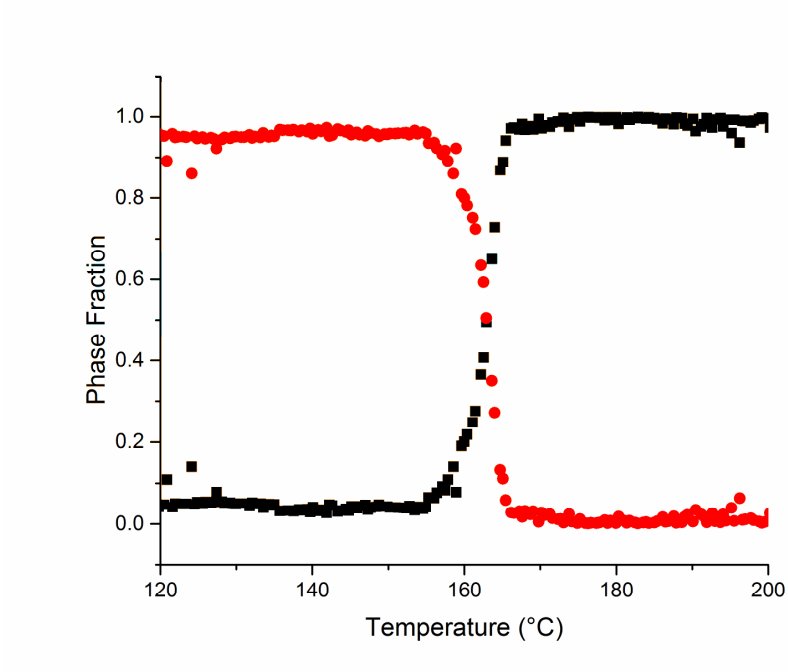

Figure 2-16. Sum of phase fractions of sulfathiazole forms III and IV (red circles), and the phase fraction of form I (black squares) as a function of temperature.

The transformations of forms III and IV to form I are known to occur in the temperature range 150-170°C.[170] Form III is reported to undergo conversion via either a melt[140] or a solid-solid pathway[173] depending on the purity of the sample, and form IV has been

shown to undergo a solid-solid transformation.[170] The data collected here show that when a mixture of forms III and IV are heated both undergo a solid-solid transformation to form I simultaneously. The differences in the structure of these forms[170] are very small, and evidently not sufficient to make the transition from one to the other energetically more favourable than their conversion to the high temperature polymorph. It is unlikely to be coincidental that the conversion happened at the same temperature for both.

For many years the separate existence of sulfathiazole polymorphs III and IV was a source of confusion in the scientific community. In 1971 Mesley[174] discussed the existence of two low temperature forms, designated IIA and IIB, referred to here (and in the CSD) as form III and form IV, respectively, pointing out that the mixture of the two was commonly mistaken for a distinct form and that all commercial samples tested were in fact a mixture of these two polymorphs. The author also highlighted the similarities between the two forms in relation to their hydrogen bonding, as observed by infrared spectroscopy, and concluded that the similarity in the enthalpy of transition from each metastable species to form I indicates they must have very similar structures.

More recently, structural analysis of the different polymorphs of sulfathiazole has shown that, in forms II, III and IV, the molecules exist as dimers[175,176] linked by hydrogen bonding. The dimers are orientated in the same conformation in all three species, but it is the position of these dimers relative to each other that defines the crystal structure of each polymorph. Blagden *et al*[175] described the relationship of pairs of dimers as being enantiomeric and labelled them L and R. In all three structures these pairs link to form a chain of a repeating combination of four molecules. This single monolayer is then hydrogen bonded to another parallel monolayer of the same construction. Within the crystal structures of forms II, III and IV there are two arrangements of the monolayers. One having dimers of the same “enantiomer” adjacent (e.g. LLLL) and the other alternating (e.g. LRLR). Gelbrich *et al*[176] described the two arrangements as A-type (adjacent) and B-type (alternating) bilayers. Polymorph II consists solely of layers connected by the A mode and polymorph IV only the B mode. The bilayers in polymorph III alternate (e.g. ABAB).

The unit cells used for Rietveld refinements for forms III and IV were taken directly from the CSD and are given in Table 2-4.

Table 2-4. Unit cells used for Rietveld refinements. Data from Dr Tim Prior (University of Hull).

Form III (from CSD) $P2_1/c$ T = 295 K		Form IV (from CSD) $P112_1/n$ T = 295 K	
a/ Å	17.570(9)	a/ Å	10.867(3)
b/ Å	8.574(4)	b/ Å	11.456(3)
c/ Å	15.583(8)	c/ Å	8.543(2)
α/ °	90	*α*/ °	90
β/ °	112.93(1)	*β*/ °	90
γ/ °	90	*γ*/ °	91.87(2)
cell volume/ Å^3	2162.01	cell volume/ Å^3	1062.97
Z	8	Z	4

The cell for form IV can be reset in the standard form of $P2_1/n$ as described in Table 2-5.

Table 2-5. Unit cells given in standard settings. Data from Dr Tim Prior (University of Hull).

Form III (from CSD) $P2_1/c$ T = 295 K		Form IV (from CSD) $P2_1/n$ T = 295 K	
a/ Å	17.570(9)	a/ Å	10.867(3)
b/ Å	8.574(4)	b/ Å	8.543(2)
c/ Å	15.583(8)	c/ Å	11.456(3)
α/ °	90	*α*/ °	90
β/ °	112.93(1)	*β*/ °	91.87(2)
γ/ °	90	*γ*/ °	90
cell volume/ Å^3	2162.01	cell volume/ Å^3	1062.97
Z	8	Z	4

Form IV can be reset into $P2_1/c$ for comparison with Form III, as detailed in Table 2-6.

Table 2-6. Unit cells quoted in P21/c. Data from Dr Tim Prior (University of Hull).

Form III (from CSD) $P2_1/c$ T = 295 K		Form IV (from CSD $P2_1/c$ T = 295 K	
a/ Å	17.570(9)	a/ Å	10.867
b/ Å	8.574(4)	b/ Å	8.543
c/ Å	15.583(8)	c/ Å	15.5308
α/ °	90	*α*/ °	90
β/ °	112.93(1)	*β*/ °	132.503
γ/ °	90	*γ*/ °	90
cell volume/ Å^3	2162.01	cell volume/ Å^3	1062.97
Z	8	Z	4

The relationship between these two cells is not a trivial doubling of one of the axes, for example. In the revised set of cells the b and c parameters are similar, which reflects some similarity in the packing, but crucially ***a*** and β are very different.

The structures (i.e. the arrangement of molecules) of these two forms are very similar despite the different unit cells (see Figure 2-17, which relates to the settings in Table 2-6).

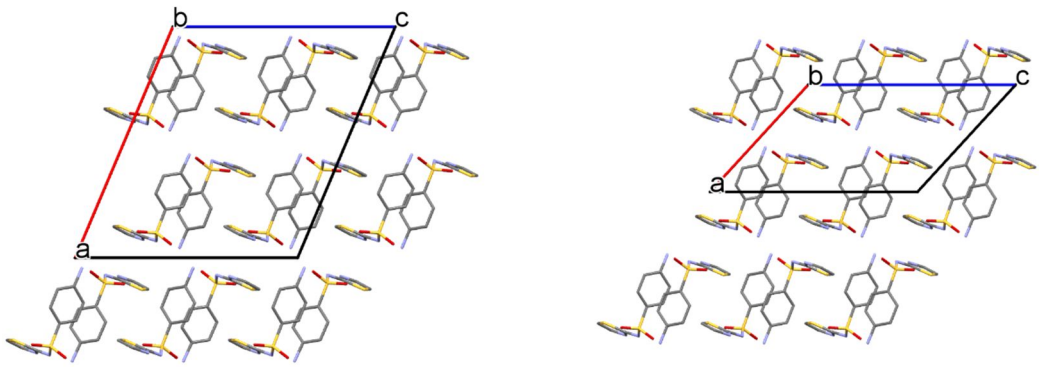

(a) **(b)**

Figure 2-17. Views down the b axis in sulfathiazole (a) form III, and (b) form IV (set in $P2_1/c$).

The structure of form III has two independent sulfathiazole molecules in the asymmetric unit. Form IV has a single sulfathiazole molecule in the asymmetric unit. A phase change between the forms (III ⇨ IV) would render the two molecules equivalent and then be associated with a change of unit cell. It is notable that in both forms (Table 2-6) there are hydrogen-bonded layers that run parallel to the (10-2) plane. Adjacent layers are related by inversion centres and stacked in an ABAB fashion along the crystallographic *b* direction. In practical terms these two forms are very similar, and thus it is unsurprising that they co-exist at low temperatures and simultaneously transform to form I as the temperature is raised.

The unit cell of form I is not related to that of form III or IV, and the structure is different. Form I contains a 3-D hydrogen bonded network that is sustained by a variety of classical hydrogen bonding interactions, notably a centrosymmetric $R_2^2(8)$ embrace (shown in Figure 2-18), not present in form III or IV.

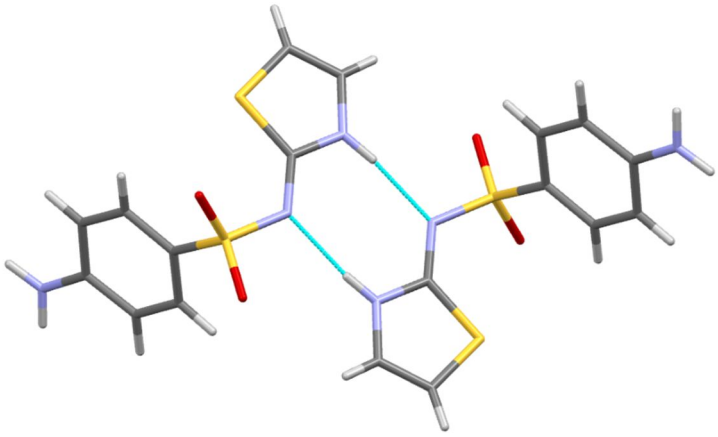

Figure 2-18. The centrosymmetric $R_2^2(8)$ motif of form I sulfathiazole.

If these structural similarities are taken into account it is unsurprising that the existence of forms III and IV was a source of consternation for some time.

2.3.3. Glutaric acid

Figure 2-19 shows the contour plot for glutaric acid (GA) and the corresponding thermal trace recorded by the DSC. It is immediately apparent from the contour plot in Figure 2-19(a) that GA exists in two distinct crystalline phases, with an abrupt change in the diffraction pattern at 72 °C. There is then a complete loss of diffracted intensity at *ca*. 100 °C. The DSC data in Figure 2-19(b) contain two clear endotherms, one with an onset at 72 °C and one at 98 °C. The latter occurs at the same temperature as the loss of diffracted intensity in XRD, and corresponds to the known melting point of the α form of GA.[177]

The former corresponds to the abrupt changes in diffraction pattern seen at *ca.* 72 °C, and thus can be ascribed to the previously reported transition between the β (low temperature) and α (high temperature) forms of GA. As for sulfathiazole, the changes in the XRD contour plot are complete at the apex of the first endotherm, and the return to baseline is attributable to the instrument rather than the sample.

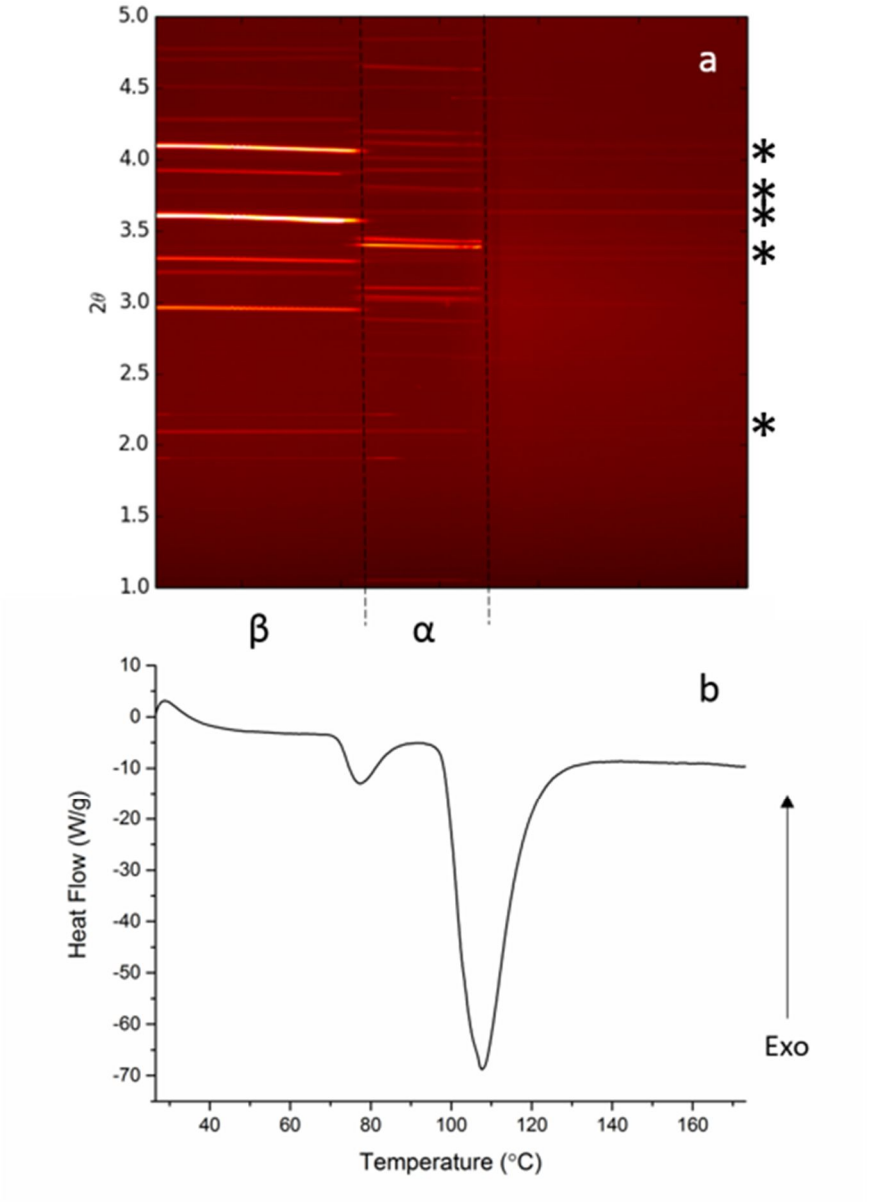

Figure 2-19. DSC-XRD data for glutaric acid. (a) Contour plot of the diffraction data and (b) the corresponding DSC thermogram. Reflections marked * are a result of the experimental set up.

As for sulfathiazole, Rietveld refinements were undertaken on selected patterns. The results are depicted in Figure 2-20 and Figure 2-21 with refinement parameters in Table 2-7. The lower temperature pattern can be successfully fitted using an expanded version of the known structure for *β*-GA (recorded at –153°C),[178] and that at 94°C similarly with the *α*-form. The fit parameters are all acceptable, and it is clear that a single phase exists at both temperatures.

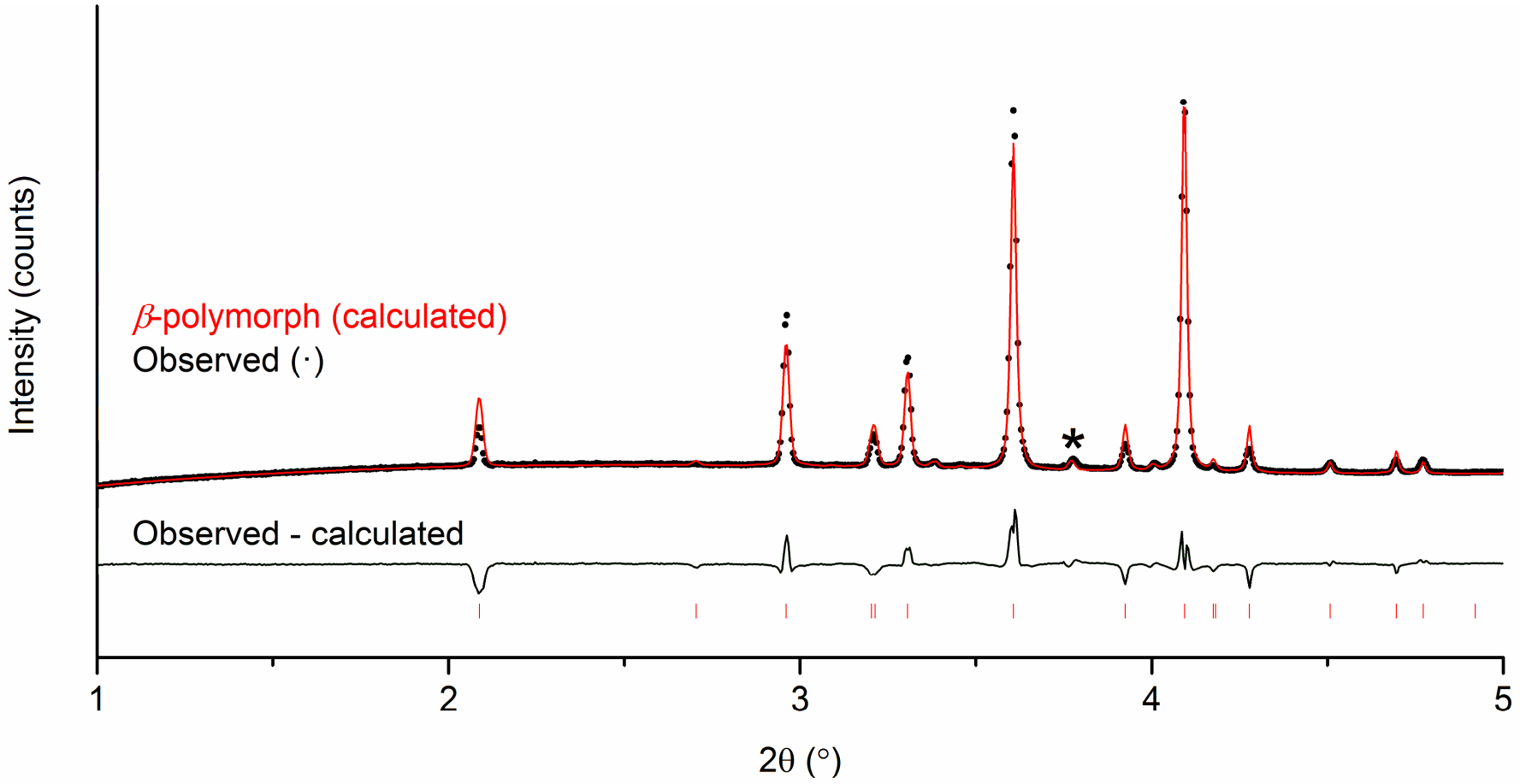

Figure 2-20. Powder X-ray diffraction patterns for GA at 27°C. The tick marks show the positions of allowed reflections from *β*-GA. [The * shows a reflection from the presence of a persistent impurity].

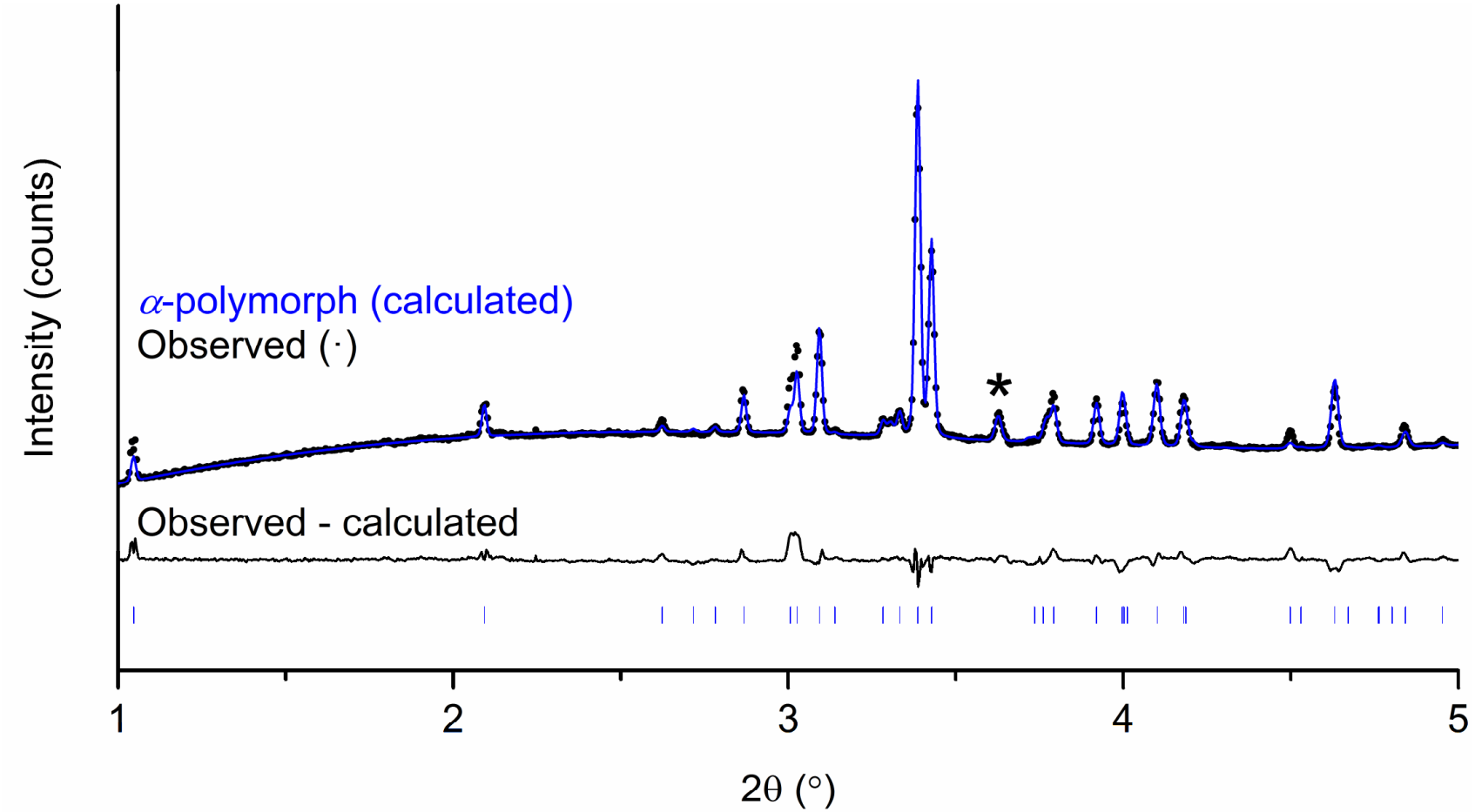

Figure 2-21. Powder X-ray diffraction pattern for GA at 94˚C. The tick marks show the positions of allowed reflections from *α*-GA. [The * shows a reflection from the presence of a persistent impurity].

Table 2-7. Refinement parameters for glutaric acid. The starting models for both α and β forms were taken from the CSD (IDs: GLURAC06 and GLURAC12 respectively).

Property	*β*-glutaric acid	*α*-glutaric acid
T / °C	27	94
Space group	*C*2/*c*	*C*2/*c*
a / Å	12.902(1)	25.577(3)
b / Å	4.826(0)	5.015(0)
c / Å	9.960(1)	10.200(2)
α / °	90	90
β / °	96.838(8)	92.531(10)
γ / °	90	90
Cell volume / Å^3	615.7(1)	1307.2(3)
R_{wp}	0.0623	0.0267
$R_{wp\text{-}bkd}$	0.2310	0.1929

As for sulfathiazole, batch refinements were carried out on the entire data set. Rietveld refinements yielded R_{wp} values ranging from 0.0238 to 0.0623. Due to the smaller, side-centred, unit cells, and the presence of just two polymorphs, there were fewer instances of overlapping reflections than for sulfathiazole and so, in addition to Rietveld, it was possible to carry out batch Pawley refinements (resultant R_{wp} between 0.0120 and 0.0197). Both sets of refinements show that upon heating, rather than the unit cell expanding in three dimensions as might be expected, it expands in the *b* and *c* axes and *a* and *β* contract. This is true for both the *β* and *α* forms of GA (Figure 2-22 and Figure 2-23).

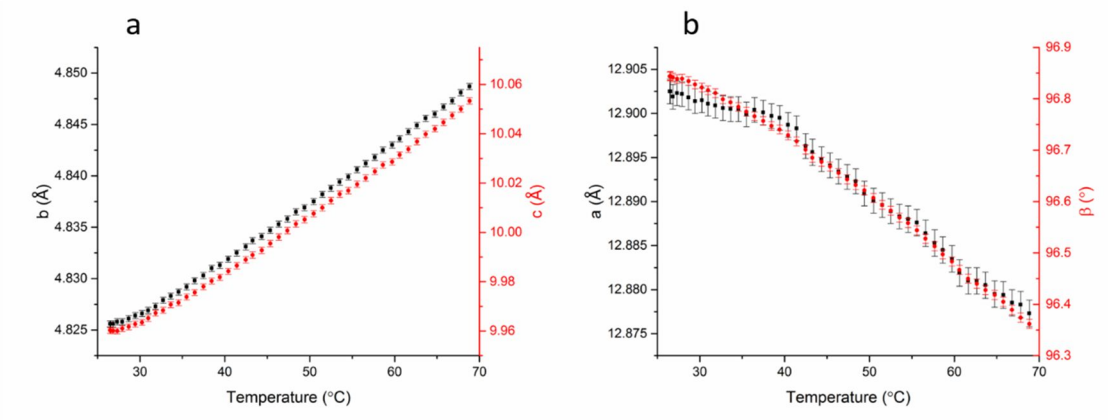

Figure 2-22. Lattice constants as a function of temperature for *β*-GA: (a) the *b* (black squares) and *c* (red circles) parameters; (b) the *a* (black squares) parameter and *β* (red circles) angle.

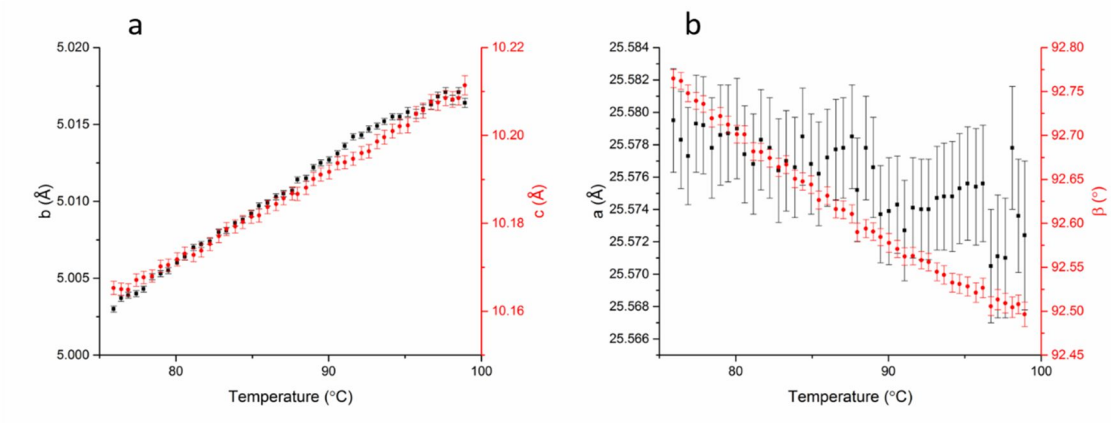

Figure 2-23. Lattice constants as a function of temperature for *α*-GA: (a) the *b* (black squares) and *c* (red circles) parameters; (b) the *a* (black squares) parameter and *β* (red circles) angle.

As for sulfathiazole, the contribution of each polymorph was obtained via Rietveld refinement and the phase fraction calculated. A plot of phase fraction *vs.* temperature is given in Figure 2-24. As with sulfathiazole, the curves for the two forms cross at *ca.* 0.5, indicating that conversion between them occurs via a solid-solid transition with no observable melt or intermediate phase.

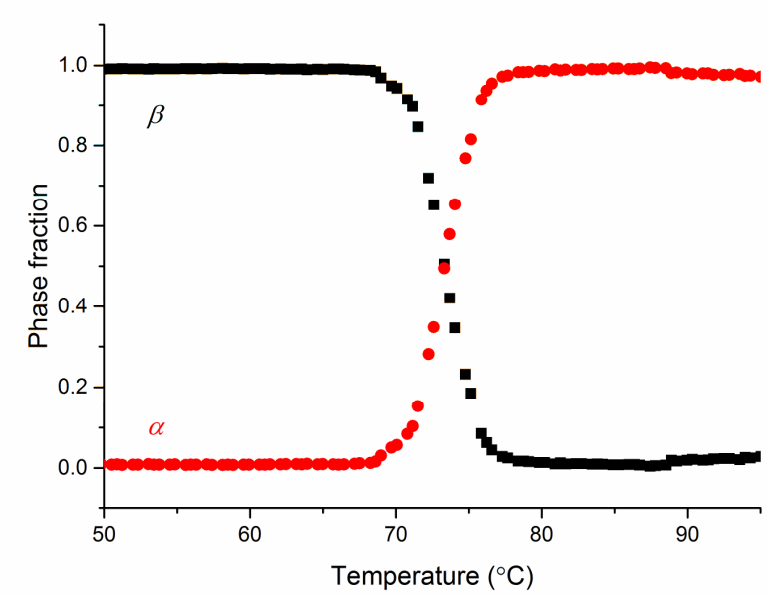

Figure 2-24. Plot of phase fraction vs temperature for the heat induced transformation of GA from the *β* phase to the *α* phase.

These observations are in agreement with the literature. Jorunn and Samuelsen[179] used Raman spectroscopy to study the effect of temperature on the crystal structure of the *β* polymorph and Espeau *et al.*[177] investigated the effects of an increase in pressure on the nature of the phase transition. Both report a solid-solid transformation from *β* to *α*.

2.4. Conclusions

It has been shown that hyphenated DSC-synchrotron XRD experiments can easily be performed by making only a simple modification to a laboratory DSC instrument. Using a high-intensity synchrotron X-ray source (Beamline I12, Diamond Light Source) it is possible to collect diffraction patterns on a sample mounted in a conventional DSC pan in a few seconds, permitting a single sample to be effectively interrogated both in terms of its thermal and structural features. The potency of the approach is demonstrated through a study of two systems displaying enantiotropic polymorphism. Of particular interest is the potential of the technique to provide information on otherwise hidden phases, as exhibited in the data recorded for sulfathiazole. Direct solid-solid phase transitions are observed, with no wholesale melting of the sample. That said, care should be taken not to discount the possibility of microscopic transient melting on a per particle basis. The XRD data obtained here are of sufficient quality to permit Rietveld refinements to be performed and, in favourable instances, Pawley refinements. Batch refinements were undertaken allowing a rapid (< 30 min) analysis of the hundreds of patterns comprising each dataset. This provided a detailed description of structural changes as a function of temperature. DSC-XRD thus comprises a simple and powerful analytical tool with much promise in pharmaceutical science and materials chemistry.

3. Phase transitions in 10,11-dihydrocarbamazpine, carbamazepine and paracetamol

3.1. Introduction

Solid crystalline materials may exist in many different physical forms, each of which will have different physicochemical properties such as: solubility, dissolution rate, stability, hygroscopicity, strength, flowability and compressability.[9] All of these properties will have a significant effect on the utility of the compound as a pharmaceutical material. It is therefore essential that as much as possible is known about the physical form of an active ingredient and how it will behave under different conditions before it can be used as a medicine. Accessing and stabilising metastable polymorphic forms of active pharmaceutical ingredients remains a major challenge in pharmaceutical product innovation.[22,180] Systemic approaches to understanding polymorphic diversity in organic solids remain elusive.

Carbamazepine (CBZ) (Figure 3-1) is an anticonvulsant commonly used to treat epilepsy and trigeminal neuralgia.[181] There has been much research into CBZ, reaching as far back as its first use as an anticonvulsant in the 1960s.[181] It has extremely poor solubility in water[182] and is therefore an ideal candidate for screening for metastable polymorphs. To date there have been five polymorphs reported,[39,183–186] and their structures have been characterised with enough rigour to be published in the CSD. The most stable form at room temperature is form III,[186] and that at high temperatures is form I.[185] The majority of the known polymorphs of CBZ (modifications I–IV) pack as dimers with the two molecules connected *anti* to each other by H-bonds between the oxygen and nitrogen atoms of the carbamoyl group.[39,185,187] The differences in structure stem mainly from the way in which these dimers are packed relative to each other. The most recently discovered form (V) is the only known polymorph of CBZ to pack catemerically, without forming dimers; its discovery was achieved by templating crystal growth on the surface of a crystal of 10,11-dihydrocarbamazepine (DHC) (Figure 3-1) form II, an analogue of CBZ chosen due to its unit cell's similarity to the previously predicted but unobserved structure of CBZ V.[39] The difference between the two molecules is the presence or absence of a double bond directly opposite the nitrogen of the azepine ring (Figure 3-1).

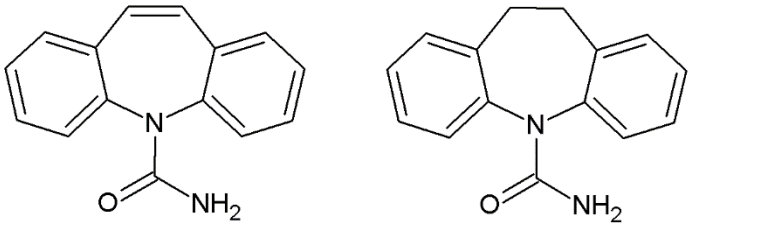

Carbamazepine 10,11-dihydrocarbamazepine

Figure 3-1. Chemical structures of carbamazepine and 10,11-dihydrocarbamazepine.

As previously stated, structurally CBZ forms I–IV have strong similarities, with all four consisting of almost identical dimers with the molecules in an almost identical conformation, which is unusual for polymorphic materials.[185] Calorimetrically it has been shown that upon heating at 20 °C min^{-1} form II undergoes a solid–solid phase transition to form I between 140 °C and 160 °C and form III undergoes a melt–recrystallisation to form I in the range 168–175 °C. At the same heating rate form IV melts at 188 °C and partially converts to form I, but slower heating results in a more complete conversion. In all four cases form I was shown to melt at 192–194 °C.[185] It is clear from these results that form I is the stable form at high temperatures.

10,11-dihydrocarbamazepine (Figure 3-1) has four known polymorphs[188–191], three of which display a catemeric H-bonded motif similar to that of CBZ V. In contrast, the most recently discovered form (IV) displays a dimer motif in the same form as the one seen in CBZ forms I–IV. There has been little research into DHC and a literature search revealed no results relating to phase transitions between polymorphs or describing the behaviour of any of its forms upon heating. Here both topics will be discussed.

Paracetamol (PCM) exists in three polymorphic forms; a stable phase (I) and two metastable phases (II, III). Form I packs with a herringbone motif, while forms II and III display layered structures.[47,49,192] The structure of form I results in poor compactibility, leading to poor tablet quality.[192] However, difficulties in producing suitable quantities of either form II or III have limited research into their physical properties. While form III has been reported as highly unstable in air, even being referred to as ‘elusive’,[49] recent reports indicate that surfaces such as glass[53] and silica[193] can promote its growth, and careful control of heating and cooling rates during melt crystallisation have also been demonstrated to lead to form III.[26,194] Additionally, inclusion of hydroxypropyl methylcellulose (HPMC) into the paracetamol melts can alter the kinetics of the crystallisation of the two metastable phases.[51,57]

The addition of molecular additives to alter the kinetics of the crystallisation process to obtain metastable polymorphs has been a frequent topic of study.[27,29] The inhibition of

the formation of a stable phase through preferential interactions between the additive and the surface available functional groups of the crystal may lead to slowing of crystal growth,[30,195–198] while preferential interaction of the additive with an unstable phase may lead to stabilisation of this phase or alter the balance of the kinetic growth rates of the two phases.[198] Design or selection of a suitable additive may then be used to control the crystallisation processes and tailor the creation of a desired polymorph.

Here we report studies into the polymorphism of DHC, CBZ and PCM, and pay particular attention to phase transitions between polymorphs and the effect of temperature on the unit cell. There is also discussion of work with PCM that indicates a promising role for the 'excipient' matrix to direct and stabilise metastable forms and the importance of *in situ* characterisation of polymorphism for formulation design.

3.2. Materials and Methods

3.2.1. Materials

Carbamazepine (98 %) forms II and IV were supplied in a personal communication by Dr. Vijay Srirambhatla, paracetamol (USP) and trehalose (TRH, USP) were purchased from Sigma-Aldrich, UK and used as received. Lactose (LCT) was procured from Acros Organics, BE and used as received. Hydroxypropyl methylcellulose K100M (HPMC, METHOCEL) was obtained from Colorcon, UK and used as received. 10,11-dihydrocarbamazepine (99 %) was purchased from Alfa Aesar, UK and used as received.

3.2.2. Methods

3.2.2.1. DSC-XRD

To obtain glasses of PCM, paracetamol and each of the three excipients HPMC, TRH and LCT (PCM: 90 % w/w) were mixed in a glass sample tube using a vortex mixer. Each of the four samples were then weighed into a Tzero aluminium DSC pan without a lid. The samples were heated from ambient temperature to 180 °C at 10 °C min^{-1} and held for 2 minutes to melt the mixture, before removing from the DSC and air cooling to ambient temperature to generate an amorphous phase. Finally, the product was reheated to 180 °C at 10 °C min^{-1}.

DSC Measurements were performed with either a TA 2010 instrument (TA Instruments LLC) modified as described in Chapter 2 or with a Q20 instrument, modified by drilling a hole either side of the sample holder (Figure 3-2), as with the 2010. Calibration was

performed with a certified indium standard according to the manufacturer's instructions. Attempts to vitrify selected samples were made by melting in the DSC and immediately quenching the melt by removing the pan from the furnace and placing it on the bench. Samples of all materials (5.1–26.9 mg) were held in Tzero aluminium pans and heated at 10 °C min^{-1} from ambient to slightly above the melting point of the most stable polymorph.

Figure 3-2. Photograph of modified Q20 DSC cell, showing holes drilled either side of the sample pedestal to allow passage of the beam.

3.2.2.2. Data analysis

The DAWN Science Workbench was first used to convert the 2D data into 1D diffraction patterns.[162] Contour plots of the raw XRD data were then plotted using OriginPro 2016. Selected patterns were analysed using the Rietveld method implemented within the TOPAS-Academic suite of programmes,[164] in order to obtain realistic values for the unit cell parameters at elevated temperatures. Backgrounds were fitted using a shifted Chebyshev polynomial of the first kind with between 6 and 15 terms. Lattice parameters and peak shape parameters were refined. In cases where more than one phase was present, the peak shapes for each phase were constrained to be the same and the phase fraction was refined. The models used came from the CCDC (details are given below). The atom positions were not refined. Atom displacement parameters, U_{iso} were set to be 0.15 $Å^2$ in each phase. Once starting parameters were obtained batch refinements were performed on all datasets collected. No zero point was refined as entire diffraction patterns were collected using a 2D area detector.

3.3. Results and Discussion

3.3.1. 10,11-dihydrocarbamazepine

Combined DSC-XRD data for a sample of DHC can be seen in Figure 3-3.

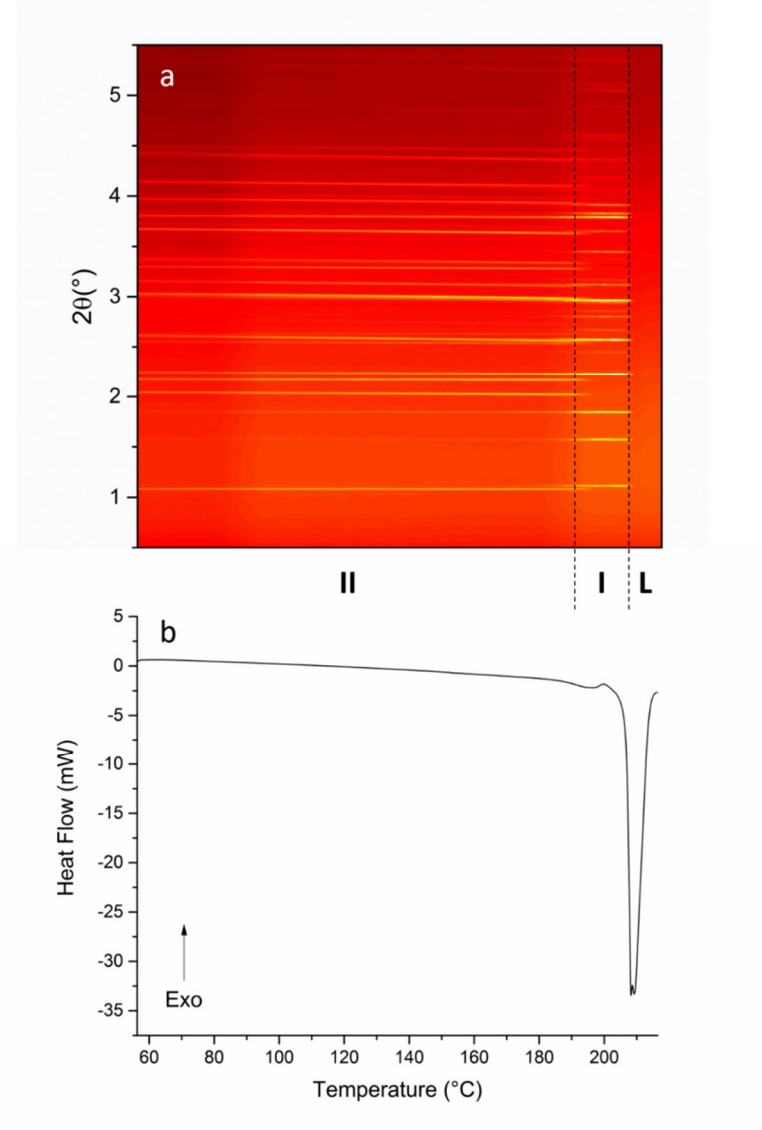

Figure 3-3. DSC-XRD data for 10,11-dihydrocarbamazepine. (a) A contour plot of the diffraction data showing the phases present; DHC II (II), DHC I (I), and liquid DHC (L). (b) The corresponding DSC thermogram

The contour plot of XRD data clearly shows three distinct phases. Two of these phases are represented by horizontal lines indicating the occurrence of Bragg reflections and the third is conspicuous by its lack of reflections. The DSC thermogram shows no events until the sample reached *ca.* 190 °C where there is a small endotherm. At the same temperature there is also a change in the positions of Bragg reflections in the XRD data. Following this, at *ca.* 207 °C, there is a much larger endothermic event coinciding with the total loss of Bragg reflections in the contour plot..

3.3.1.1. Polymorph II

Rietveld refinement of a number of DHC crystal structures from the CSD against the pattern recorded for the initial starting material at 56.3 °C (Figure 3-4, Table 3-1) confirms that it was mostly polymorph II with a very small amount of polymorph I present. The refinements fit with a R_{wp} of 0.0349, and all subsequent refinements were carried out using the starting models VACTAU01 (form I) and VACTAU02 (form II) from the CSD. From 56 °C to 190 °C there are no events in the DSC thermogram, and so there are no phase transitions occurring. However, there are subtle changes in the diffraction data. Some, but not all, of the reflections relating to form II gradually shift to lower 2θ angles. This is a consequence of the expansion of the unit cell as it is heated. In fact, the *b* dimension expands significantly more than either the *a* or *c* dimensions. As was the case in Chapter 2, the quality of the data permitted batch Rietveld refinement against all patterns, with R_{wp} values ranging from 0.0271 to 0.0449.

s

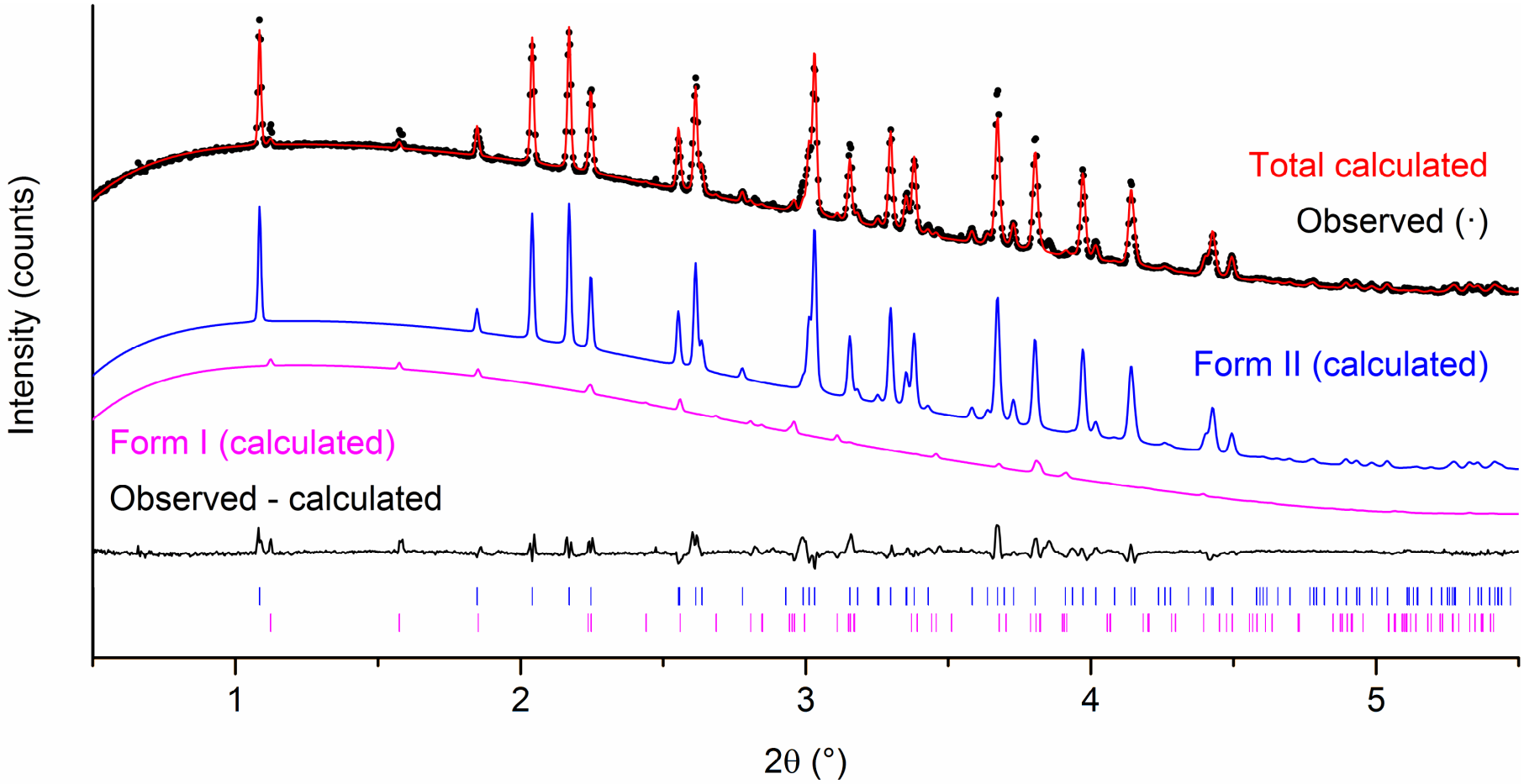

Figure 3-4. Rietveld refinement data for 10,11-dihydrocarbamazepine at 56 °C. Tick marks show the positions of allowed reflections of 10,11-dihydrocarbamazepine form II (upper) and form I (lower).

Table 3-1. Refinement parameters for 10,11-dihydrocarbamazepine at 56.3 °C and 202.5 °C. The starting models were taken from the CSD (form I: VACTAU01; form II: VACTAU02).

Property	Form II	Form I
T / °C	56.3	202.5
Space group	*Pbca*	$P2_1/c$
a / Å	9.0412(9)	5.5573(2)
b / Å	10.5748(8)	9.1969(6)
c / Å	24.914(2)	24.433(1)
α / °	90	90
β / °	–	96.505(4)
γ / °	90	90
Cell volume / Å^3	2382.0(5)	1240.7(1)
R_{wp}	0.0349	0.0440
$R_{wp\text{-}bkd}$	0.1487	0.1944
Phase fraction*	94.7 %	99.0 %

*Due to the graininess of the sample, representative errors cannot be calculated. However, the author conservatively estimates the error to be in the region of 5 %.

Unit cell expansion and intermolecular bonding

Figure 3-5 shows plots of the lattice constants as a function of temperature. Each of the three plots has been fitted with a linear trend line and the slopes calculated to allow comparison of the expansion of the cell in each direction. The growth in *b* is larger per degree increase in temperature than that in *a* and *c* by factors of 9 and 4 respectively. This is a consequence of the alignment of the molecules relative to each other in the crystal and so the distances between them; this affects both the length and strength of the intermolecular bonds. The dominant intermolecular force in the structure of polymorph II is hydrogen bonding between one hydrogen from N2 and the oxygen of an adjacent molecule[189] (O1) (Figure 3-6 and Figure 3-7). This is in fact the only hydrogen bonding throughout the lattice and is relatively weak for an H-bond with an H···O distance of 2.206 Å.[189,199] That being said, it is the strongest interaction holding the crystal together. The N2 of the second molecule forms a similar bond with the O1 of a third adjacent molecule and so strings of molecules are formed in one direction. This corresponds exactly to the lattice constant *a*.

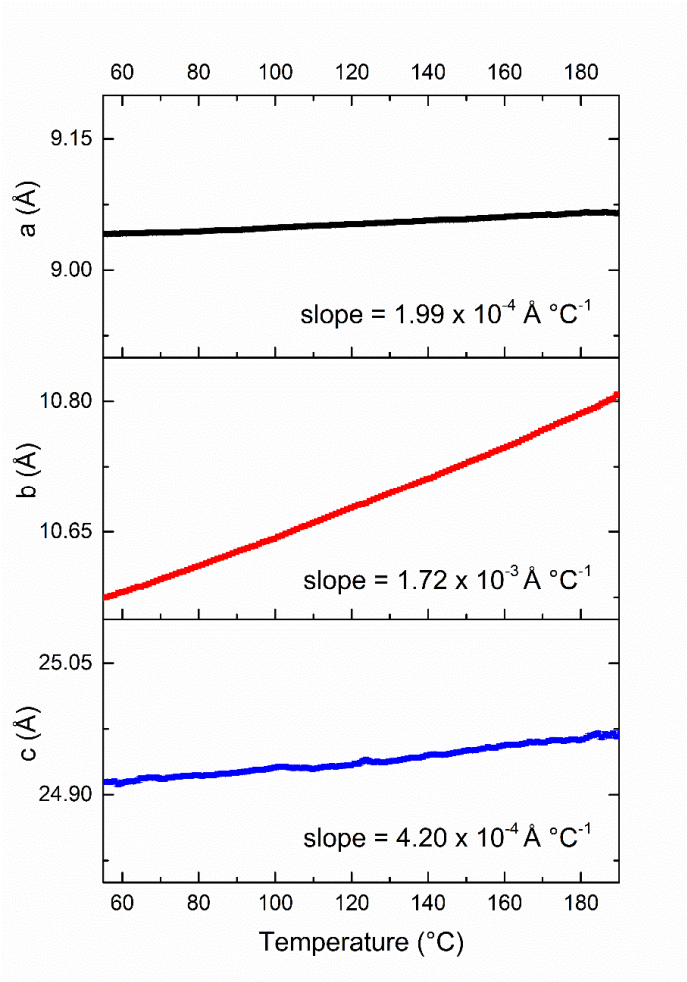

Figure 3-5. Lattice constants as a function of temperature for 10,11-dihydrocarbamazepine polymorph II. Each of the three x-axes are depicted on the same scale to allow for easy comparison.

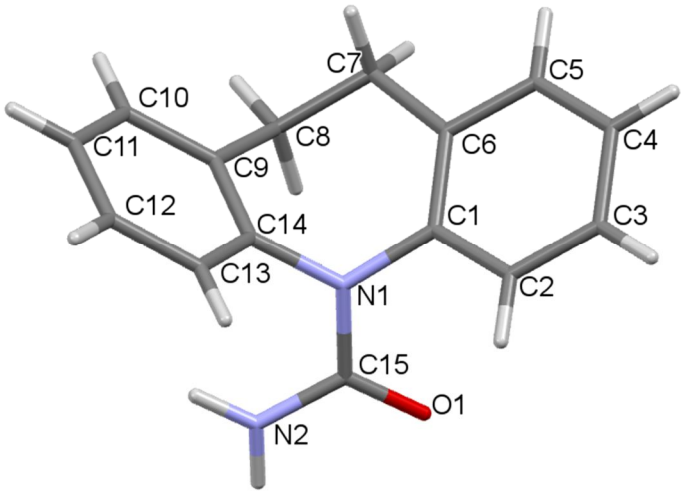

Figure 3-6. Molecular structure of 10,11-dihydrocarbamazepine with atoms numbered for ease of identification [Image produced using Mercury 3.8].

The second hydrogen of the NH_2 group interacts with the benzene ring centroid of the adjacent molecule (Figure 3-7). This enables interaction between the proton and the *π*-electrons, which appears to stabilise the one dimensional chains.[189] In fact, when viewed in the *ac* plane it is clear that these two interactions stabilise the crystal in both the *a* and *c* directions.

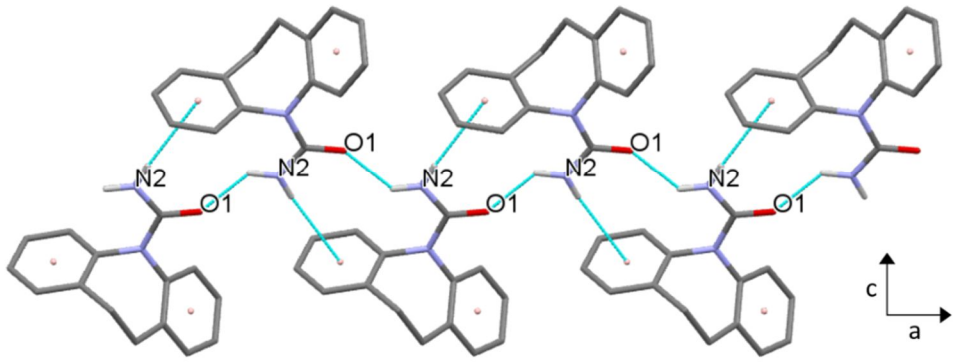

Figure 3-7. Intermolecular bonding in 10,11-dihydrocarbamazepine II in the *ac* plane of the unit cell, showing N—H···O hydrogen bonds and N—H···*π* interactions. All C bound H have been omitted for clarity.

When viewed in the *bc* plane (Figure 3-8) it can be seen that the chains are arranged in pseudo-sheets with the orientation of the carbamoyl group alternating with each new layer. Bonding in the *b* direction is much weaker than in any other direction as there are no H-bonds to speak of and there can only be interactions between *π* electrons of the aromatic rings. Harrison *et al.*[189] have suggested that these interactions must be relatively weak as the shortest centroid···centroid separation between adjacent molecules is 4.82 Å. Bonding in the *c* axis is a little more interesting. As previously stated, the N—H···O H-bonds between the carbamoyl groups and the supporting N—H···*π* interactions form chains in the *a* dimension and offer some support in *c*. Nevertheless, between the chains in this direction there are no hydrogen bonds and interactions are similar to those in the *b* axis, but slightly weaker, with the shortest C···C separation being 4.077 Å. This intermolecular bonding structure fits well with the unit cell expansion pattern observed.

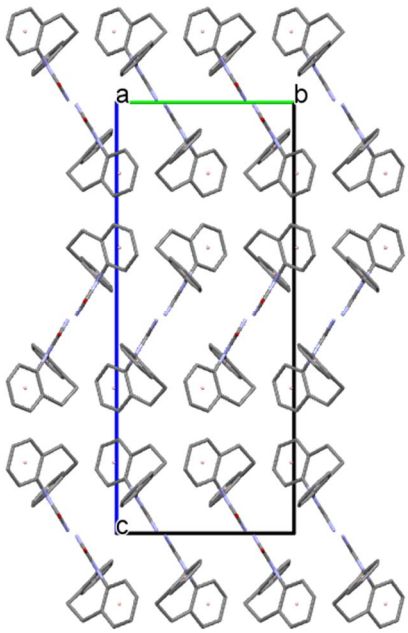

Figure 3-8. 10,11-dihydrocarbamazepine II viewed in the BC plane of the unit cell. All H have been omitted for clarity.

At 190 °C the form II reflections fade away and new ones grow in at different angles; a small endotherm also appears in the thermogram. These two events indicate a phase transition. Rietveld refinement of the diffraction pattern recorded at 202.5 °C (Figure 3-9) shows that the second phase is DHC I. Thus, the phase transition occurring is form II converting to form I. It is notable that, as was seen in Chapter 2, the presence of crystalline material in the beam was constant. The results of integration of the calculated patterns for the two forms as a function of temperature can be seen in Figure 3-10. It is clear that the initial sample consisted almost entirely of form II. As the temperature rises the content of form II appears to increase, whilst the amount of form I remains relatively constant. One explanation for the apparent growth of form II may be that there was some amorphous material present in the initial sample and that the energy supplied upon heating allowed sufficient molecular mobility for crystallisation. However, glassy DHC would produce a broad shallow “hump” rather than sharp peaks in a diffraction pattern. Further inspection of the initial pattern (Figure 3-4) reveals no indication of the presence of amorphous material. There is a visible curve to the background but this persists throughout all of the data collected on all of the samples during this beamtime. More significantly, there are no exothermic events in the DSC trace and crystallisation is an exothermic process. Therefore there must be another explanation for the increase in form II. It may be a consequence of the expansion of crystals in the sample resulting in more material being lifted from the bulk into the passing beam.

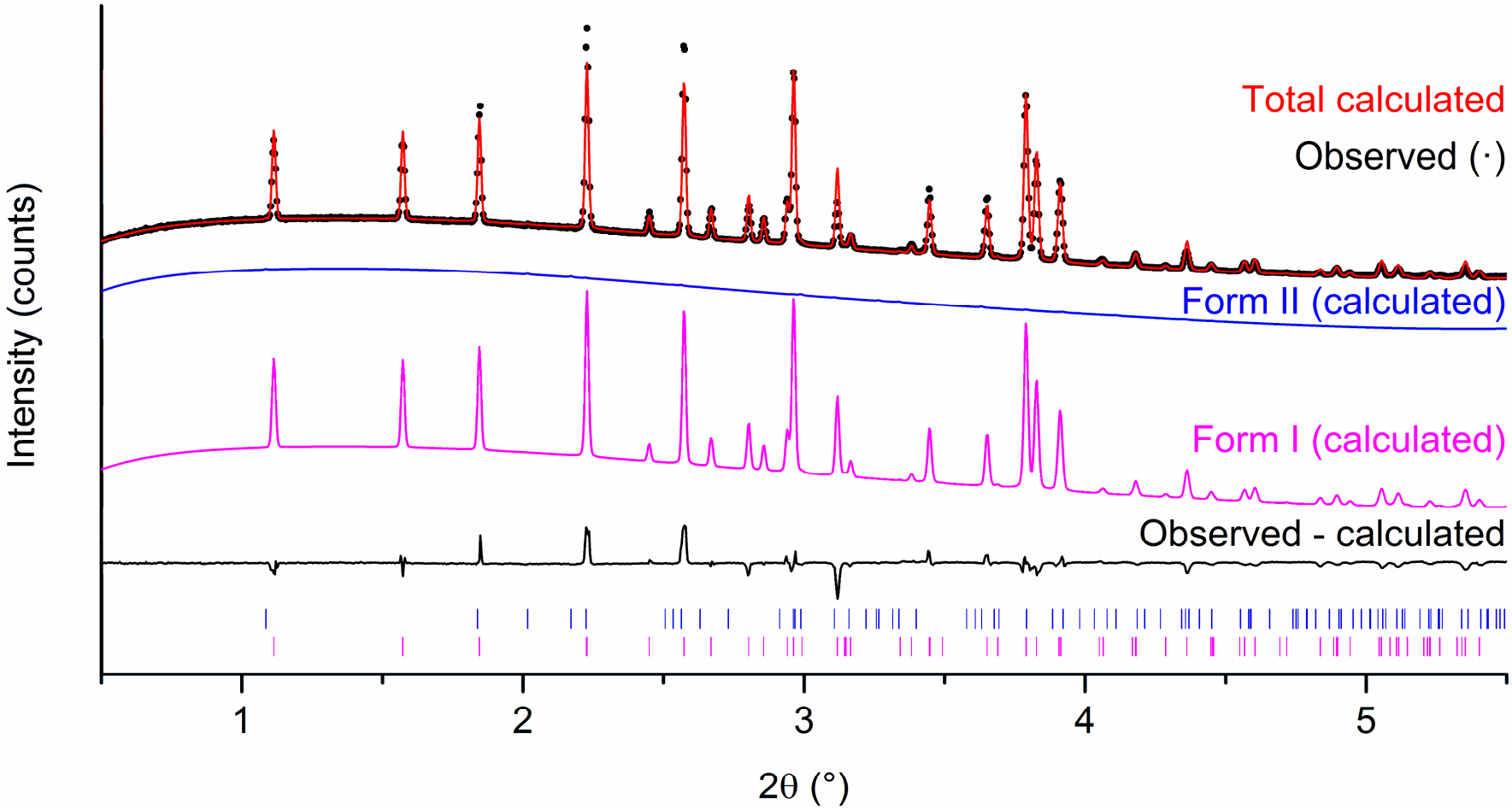

Figure 3-9. Rietveld refinement data for a diffraction pattern recorded for DHC at 202.5 °C. The structure fits the data with a R_{wp} of 0.0440. Tick marks show the positions of allowed reflections of DHC form II (upper) and form I (lower).

3.3.1.2. II→I phase transition

At *ca.*150 °C the amount of form I in the beam begins to increase, whilst the growth of form II slows. Following this, at 175 °C, the amount of form II in the beam begins to decrease and the rate of growth of form I rises sharply. The growth and decay of these two crystal structures continues more or less linearly until the sample reaches 200 °C and there is no more form I present. The small endotherm in the calorimetric data covers the same temperature range and the combination of these results indicates the occurrence of a phase transition from form II to form I. As was explained in Chapter 2, the crossing of the two curves at around half the maximum quantity of either of the two species indicates the transition does not occur via a complete melt of the sample. Instead it is likely a solid-solid transition or possibly the result of many smaller melt-recrystallisation events on a particle by particle basis. The absence of an exotherm in the thermogram and the presence of the endotherm suggests the latter. Analysis of the gradient of the two curves has shown the decline of form II content to be -0.78 $°C^{-1}$ and the growth of I to be 0.81 $°C^{-1}$ between 191 °C and 196 °C (the most linear part of the curves). The similarity between these two numbers indicates that the conversion was a one step or continuous process and agrees with these hypotheses.

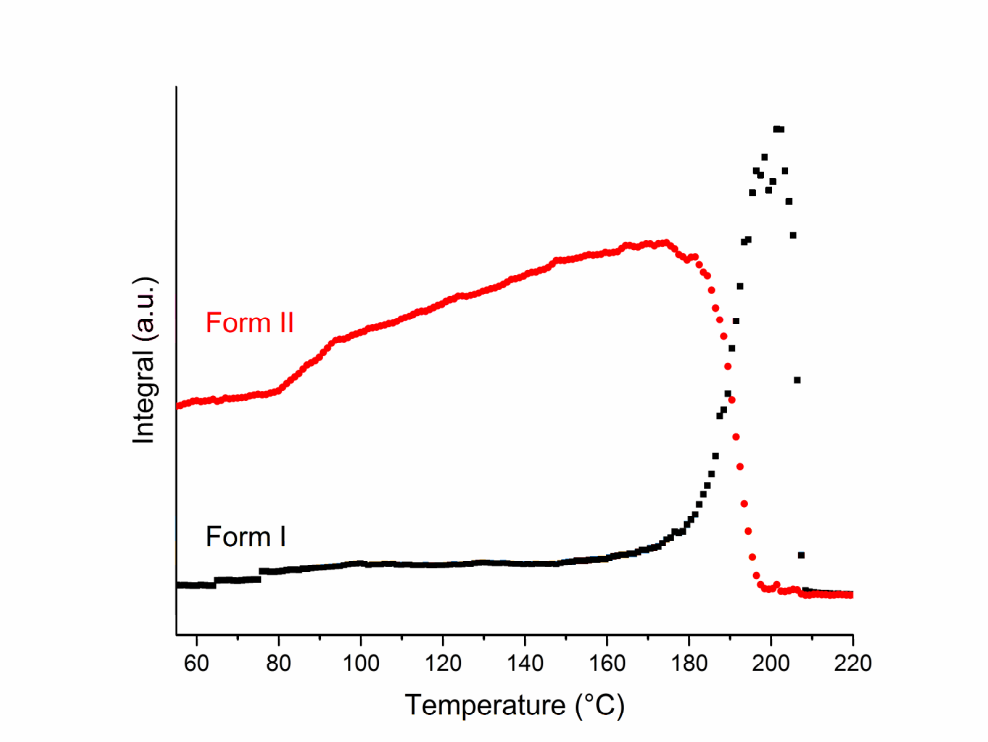

Figure 3-10. Plot of integrated total diffracted intensity for calculated patterns of 10,11-dihydrocarbamazepine form I and form II as a function of temperature.

3.3.1.3. Polymorph I

Following the II→I conversion, crystalline material is only present in the beam over a temperature range of around 10 °C before total loss of reflections is observed in the XRD data and the integrated data. The large endotherm in the DSC trace at 207 °C confirms that the sample has melted.[200] Although polymorph I was not present for long, it has been possible to extract the lattice constants from the refinements and plot them as a function of temperature (Figure 3-11). There are fewer data points than those obtained for form II but it is still possible to see a trend in the expansion of the unit cell.

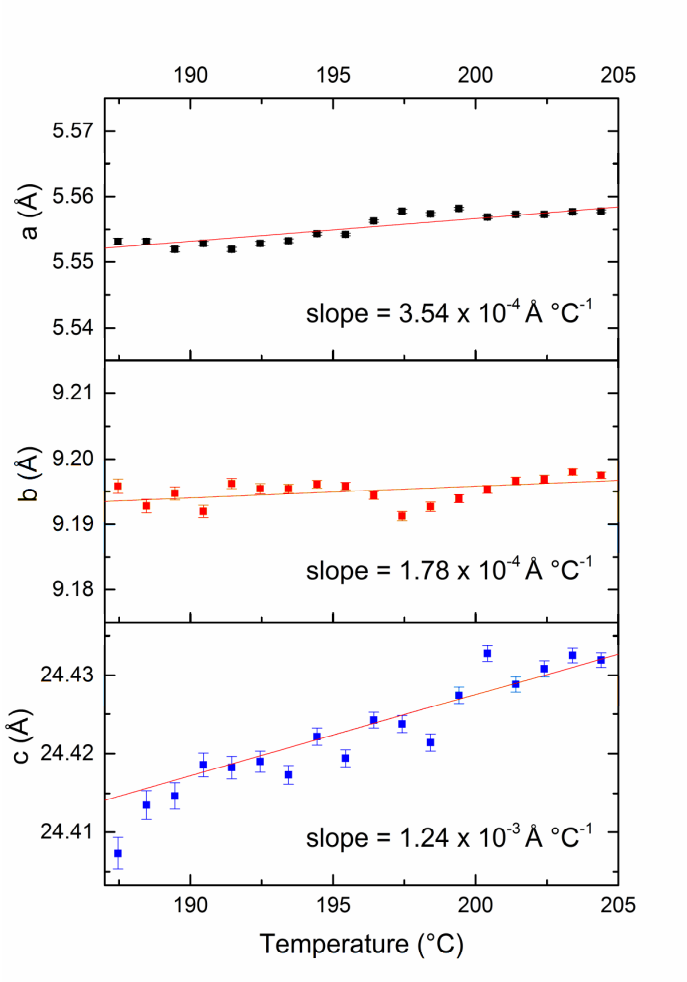

Figure 3-11. Lattice constants as a function of temperature for 10,11-dihydrocarbamazepine polymorph I. Each of the three x-axes are depicted on the same scale to allow for easy comparison.

3.3.1.4. Unit cell expansion and intermolecular bonding

As with form II the unit cell expands in three dimensions as the temperature increases but at different rates in the order *c* > *a* > *b*. Growth in *c* per degree temperature rise is greater than that in *a* and *b* by factors of 3.5 and 7 respectively. The reasons for this are

similar to those for form II. Table 3-1 lists the unit cell data for the two forms calculated from refinements of patterns recorded at two different temperatures when each polymorph was the only species present. Form I exhibits the same molecular chains held together by weak hydrogen bonding between N2 and the O1 of the adjacent molecule[188,189] and stabilised by N—H···π interactions between N2 of the second molecule and a benzene centroid of the first, but instead of the *a* direction, they propagate along *b* (Figure 3-12).

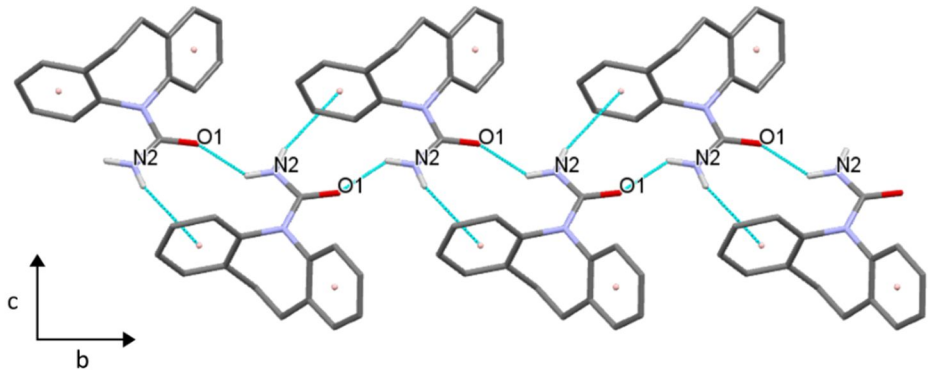

Figure 3-12. Intermolecular bonding in 10,11-dihydrocarbamazepine I in the *bc* plane of the unit cell. Showing N—H···O hydrogen bonds and N—H···π interactions. All C bound H have been omitted for clarity.

When viewed in the *ac* plane (Figure 3-13) the difference between the two structures is clear. In both, the chains are arranged in pseudo sheets, but where in form II, the orientation of the carbamoyl groupings alternates with each layer (Figure 3-8), form I presents them in the same orientation. In both forms the layers are positioned so that the ring structures of each molecule are adjacent to ring structures in another molecule, allowing for $\pi\cdots\pi$ interactions.

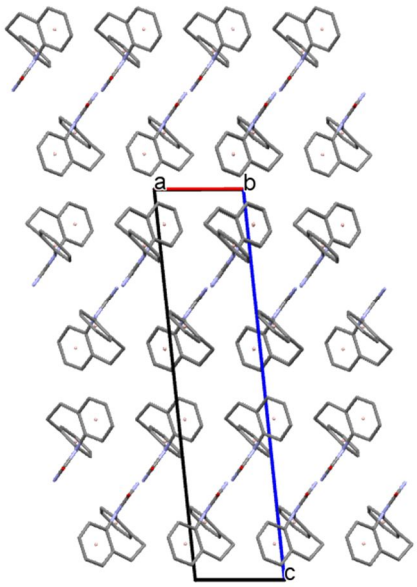

Figure 3-13. 10,11-dihydrocarbamazepine I viewed in the *ac* plane of the unit cell. All H have been omitted for clarity.

It is interesting that the order of growth in the unit cell parameters as a function of temperature is different for the two forms. For both, the smallest expansion is observed in the same direction as the propagation of the chains (form II – *a*, form I – *b*). This is to be expected as this is the direction in which the strongest intermolecular interactions are observed. However, the greatest growth and so the weakest interactions are seen in different relative directions. Form II expands most in *b* (equivalent to *a* in form I), effectively increasing the area of the pseudo sheets, whereas form I expands most in *c* (equivalent to *c* in form II), increasing the space between the pseudo sheets. Both of these dimensions are dominated by $\pi\cdots\pi$ interactions, which are weaker than H-bonds.[201,202]

3.3.2. Carbamazepine

3.3.2.1. Carbamazepine IV

There has been some confusion over the nomenclature of CBZ polymorphs in the literature, so this work uses the numbering of the CSD (Table 3-2).

Table 3-2. Unit cell information and CSD identifiers for VBZ forms I-IV.

Property	Form I	Form II	Form III	Form IV
CSD identifier	CBMZPN11[185]	CBMZPN03[184]	CBMZPN01[183]	CBMZPN12[186]
T / °C	-115	10-30	10-30	-115
Space group	*P*-1	*R*-3	$P2_1/c$	*C*2/*c*
a / Å	5.1705(6)	35.454(3)	7.529(1)	26.609(4)
b / Å	20.574(2)	35.454(3)	11.148(2)	6.9269(10)
c / Å	22.245(2)	5.253(1)	15.470(2)	13.957(2)
α / °	84.124(4)	90	90	90
β / °	88.008(4)	90	116.17(1)	109.702(2)
γ / °	85.187(4)	120	90	90
R-Factor	0.0506	0.069	0.035	0.0357

DSC-XRD data for a sample of anhydrous CBZ can be seen in Figure 3-14. The diffraction data are similar to those of DHC, with the occurrence of one crystalline to crystalline and one crystalline to liquid transition. Data collection began at 52 °C and no major structural changes occurred until 182 °C, at which point there is a change in the 2*θ* positions of the Bragg reflections. The second crystalline phase is present until the sample reaches *ca.* 192 °C and all reflections disappear. The DSC trace shows a small endotherm-exotherm event coinciding with the crystalline–crystalline transition. Immediately following this and superimposed upon it there is a much larger endotherm, resulting from melting of the material, evident from the total loss of diffracted intensity at the same temperature. The proximity of these events indicates that, at a heating rate of 10 °C min^{-1}, the two transitions occur at very similar temperatures. Unfortunately, a consequence of the overlapping thermal events is that there can be no accurate quantification of the associated enthalpies. It may however be possible to separate the events and carry out quantitative analysis using a slower ramp rate. This will be discussed later in this section.

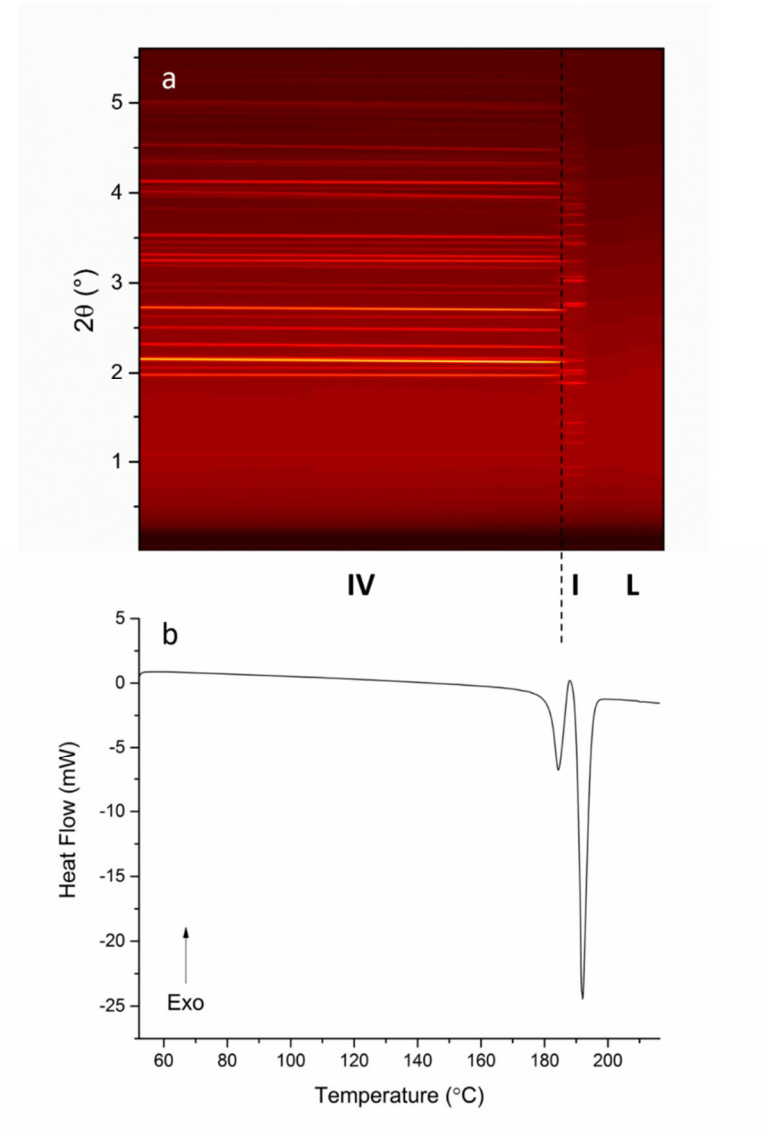

Figure 3-14. DSC-XRD data for carbamazepine. (a) A contour plot of the diffraction data and (b) the corresponding DSC thermogram.

As with previously discussed samples, batch Rietveld refinement was carried out on all patterns recorded and selected patterns were examined individually. Initially, selected patterns were analysed to establish which of the five reported forms of CBZ[39,184–186,203] were present throughout the experiment. These analyses found evidence of forms I and IV but no other species. All further refinements were carried out using starting models from the CSD (form I: CBMZPN13, form IV: CBMZPN12). Unit cell data are presented inTable 3-3. Refinement of the initial pattern recorded at 52 °C and a pattern recorded at 189 °C can be seen in Figures 3-15. Evidently, the initial sample was entirely form IV, and the structural refinements fit with a R_{wp} of 0.0441.

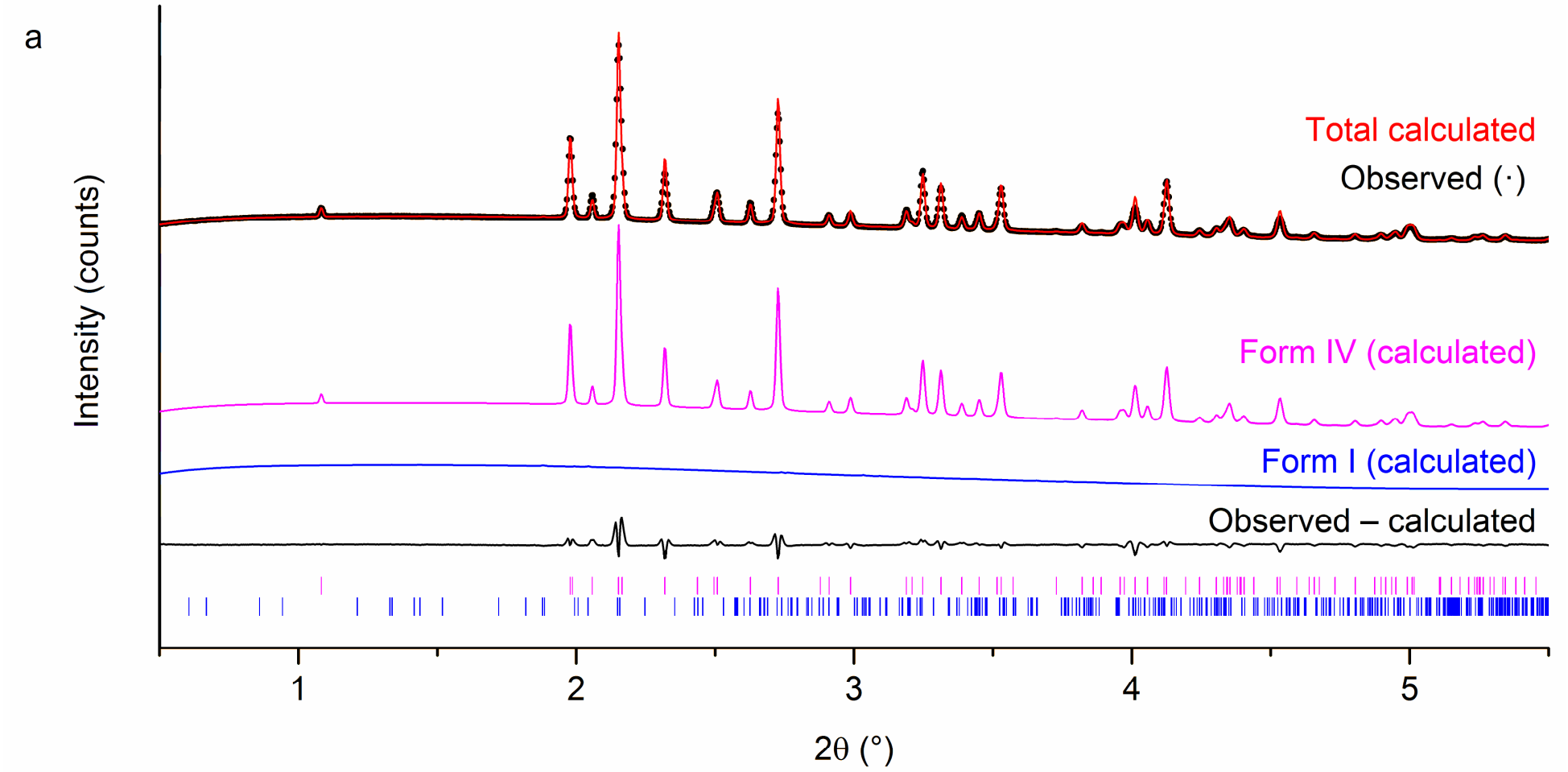
a
Intensity (counts)
Total calculated
Observed (·)
Form IV (calculated)
Form I (calculated)
Observed – calculated
1
2
3
4
5
2θ (°)

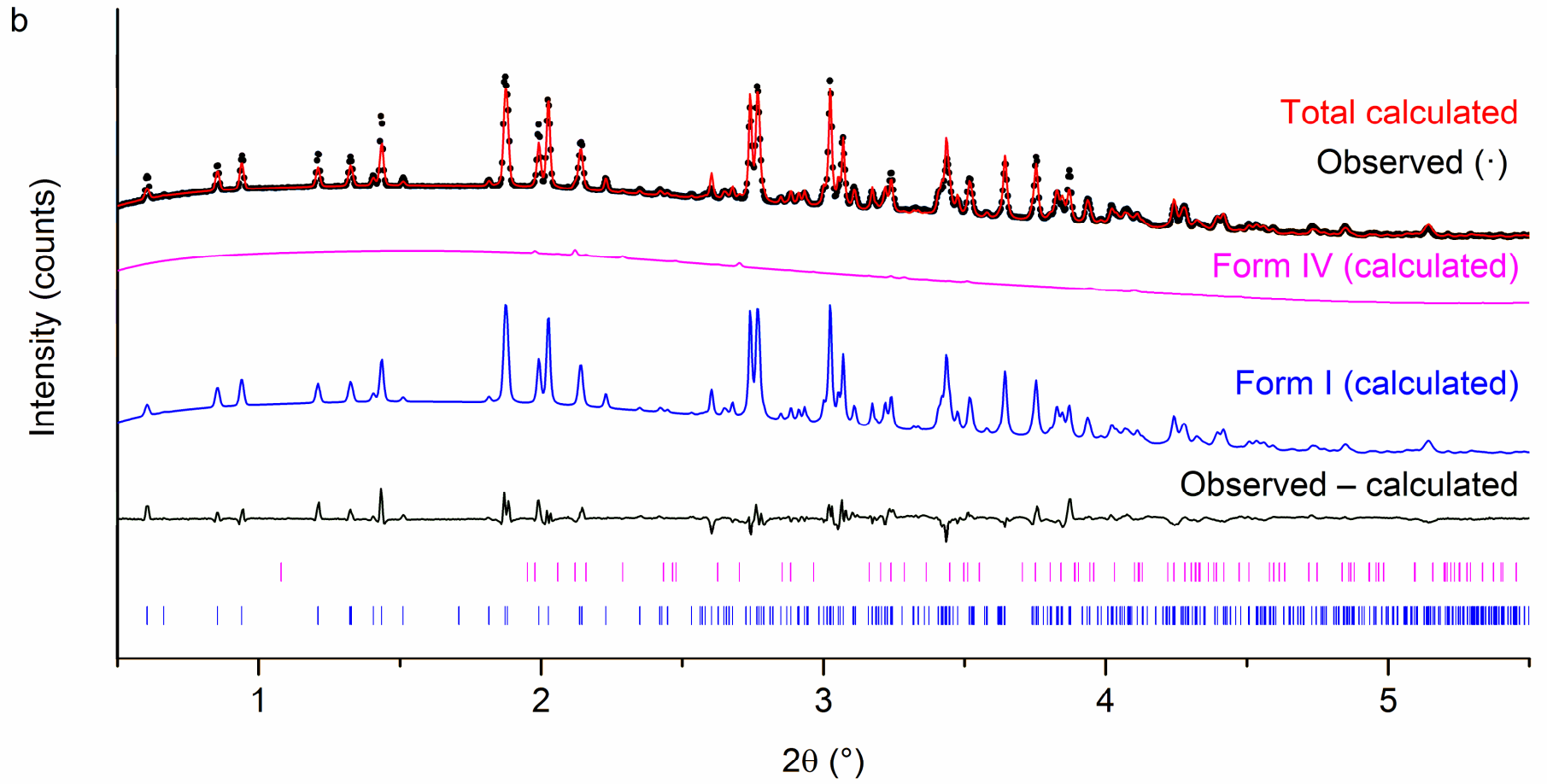

Figures 3-15 (a-b). Rietveld refinement data for diffraction patterns recorded at (a) 52 °C and (b) 189 °C when heating a crystalline sample of carbamazepine from 52 °C to 217 °C in a DSC. Tick marks show the positions of allowed reflections of carbamazepine form IV (upper) and form I (lower).

Table 3-3. Refinement parameters for carbamazepine. The starting models were taken from the CSD (form IV: CBMZPN12; form I: CBMZPN11).

Property	Form IV	Form I
T / °C	52.2	188.5
Space group	*C*2/*c*	*P*21/*c*
a / Å	26.517(1)	5.3585(3)
b / Å	7.076(0)	20.522(1)
c / Å	13.949(1)	22.472(2)
α / °	90	84.318(6)
β / °	109.578(5)	87.363(6)
γ / °	90	85.540(5)
Cell volume / Å^3	2465.9(2)	2449.8(3)
R_{wp}	0.0441	0.0401
$R_{wp\text{-}bkd}$	0.1671	0.2071
Phase fraction*	98.8 %	98.4 %

*Due to the graininess of the sample, representative errors cannot be calculated. However, the author conservatively estimates the error to be in the region of 5 %.

3.3.2.1.1. Polymorph IV unit cell expansion and intermolecular bonding

Although CBZ is analogous to DHC with some of its polymorphs having similar structures to those of DHC already discussed, the structure of form IV (Table 3-2) is not one of these and so will be discussed independently. Unsurprisingly, plotting the lattice parameters as a function of temperature (Figure 3-16) has revealed that the unit cell of form IV expands upon heating, with expansion in *b* being around twice that of *a* and *c*. As has been discussed for other materials, the relative magnitude of growth for each of the three cell lengths can be linked to the intermolecular bonding in the crystal. It has previously been shown that CBZ IV packs as dimers, held by two H-bonds (1.86 Å) through the carboxamide group with the two molecules *anti* to each other[186] (Figure 3-17).

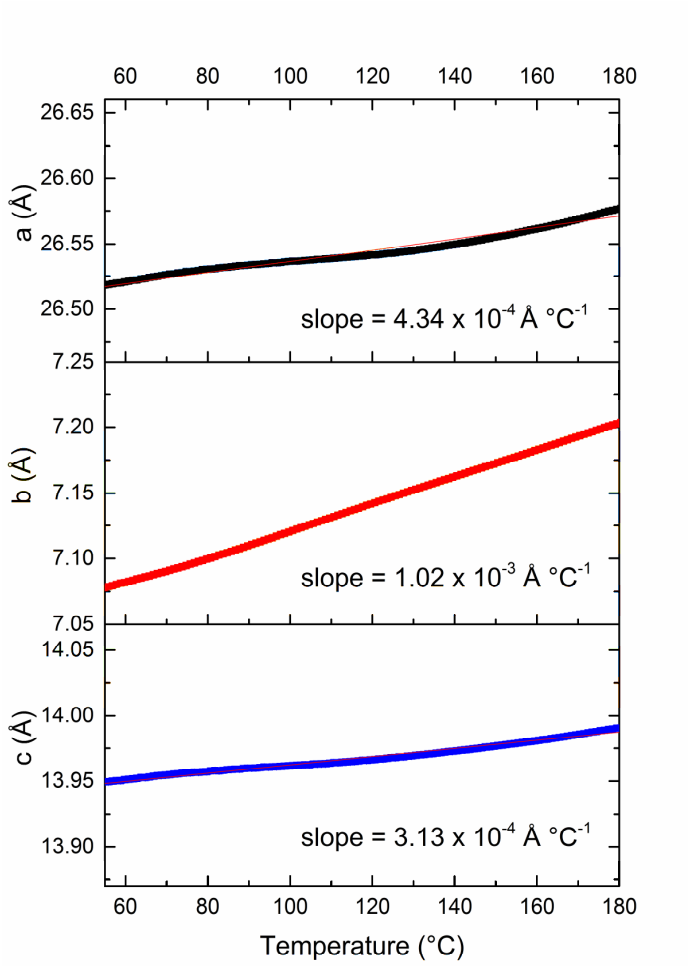

Figure 3-16. Lattice constants as a function of temperature for carbamazepine IV. Each of the three x-axes are depicted on the same scale to allow for easy comparison.

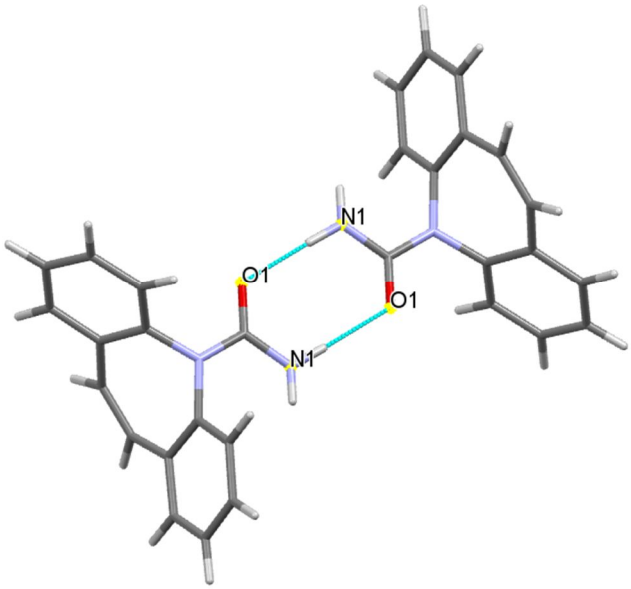

Figure 3-17. Graphical representation of a CBZ IV dimer, showing hydrogen bonding.

The oxygen also takes part in another interaction (2.28 Å) with a hydrogen on the seven membered ring of an adjacent molecule, and so chains of molecules are formed, which propagate along *c* (Figure 3-18). These chains are held together along *a* and *b* by centroid-centroid interactions at a distance of 3.809 Å. The bonding pattern in *a* alternates between the two H-bonds forming the dimers and centroid–centroid interactions linking each dimer with the next (Figure 3-19).

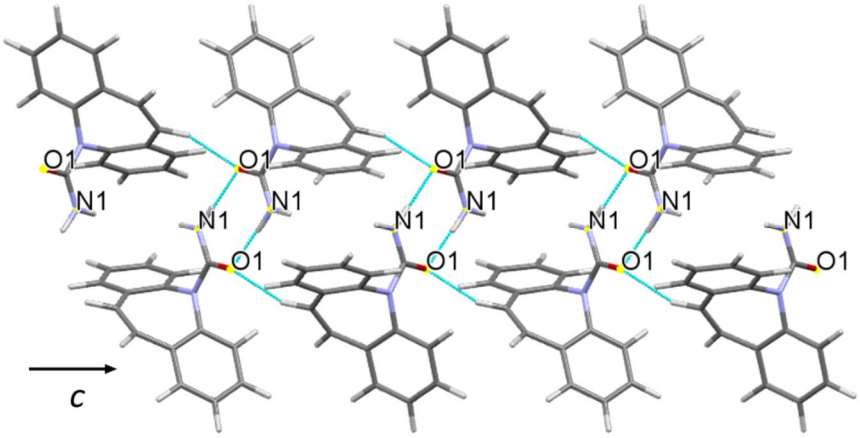

Figure 3-18. Intermolecular bonding in CBZ IV along the *c* axis of the unit cell, showing N—H···O H-bonds within dimers and C—H···O interactions between dimers.

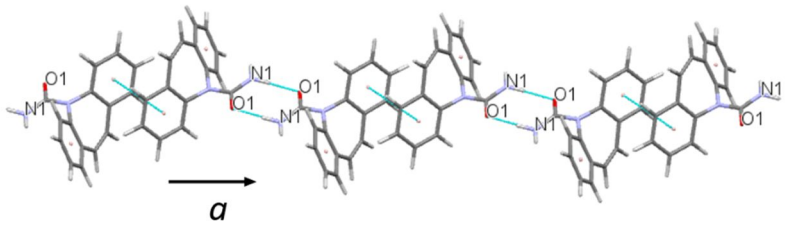

Figure 3-19. Intermolecular bonding in CBZ IV along the *a* axis of the unit cell, showing N—H···O H-bonds within dimers and centroid···centroid interactions between dimers.

Figure 3-20 shows the three types of intermolecular bonds present throughout the crystal. It is immediately apparent that, with regard to the *b* axis, the H-bonds exist as individual units and offer very little support in this dimension. As a result, bonding in this direction is dominated by benzene ring interactions, which do form very clear chains, but the interactions in these chains are much weaker than in the other two dimensions. This becomes clear when comparing the distances between the interacting species (N—H···O, 1.86 Å, C—H···O, 2.28 Å; centroid···centroid, 3.809 Å).

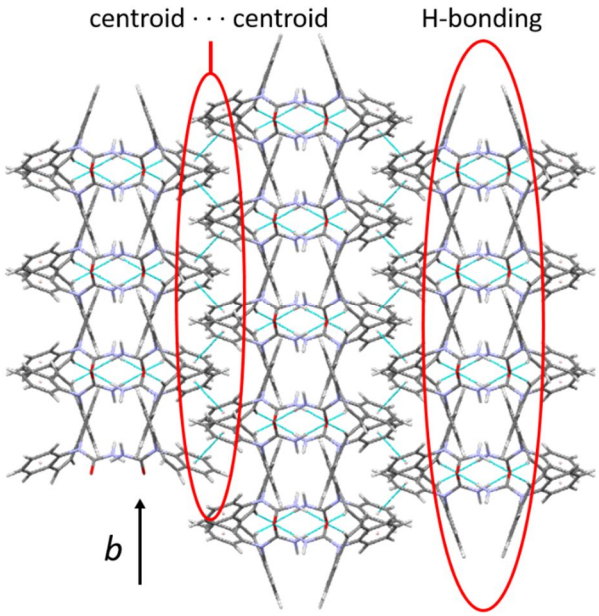

Figure 3-20. Intermolecular bonding in CBZ IV along the *b* axis of the unit cell with *c* perpendicular to the page, showing N—H···O H-bonds within dimers and C—H···O H-bonds and centroid···centroid interactions between dimers.

Clearly the domination of H-bonding in *c* makes the interactions in this direction stronger than *a*, which has a combination of both H-bonds and *π*···*π* interactions, and *a* in turn has stronger intermolecular interactions than *b*, which exhibits almost entirely *π* interactions. It comes as no surprise then that expansion in the *a* axis then is slightly larger (x 1.39) per °C than that in the *c* axis and that in *b* is larger than *a* and *c*, by factors of 2.35 and 3.26 respectively.

3.3.2.1.2. IV→I phase transition

Subsequent to this expansion of the unit cell the data show a small endotherm–exotherm and a sharp change in profile of the diffraction patterns. Together these events strongly suggest the occurrence of a solid–solid phase transition. Rietveld refinement of the pattern recorded after the profile change and the peak of the exotherm (188 °C), at 189 °C, (Figures 3-15(b)) identifies the second phase is CBZ polymorph I with a trace of IV remaining. Plotting the integrated total diffracted intensity for each pattern as a function of temperature (Figure 3-21) reveals that the lack of form I below 170 °C is constant and the amount of form IV seems to grow as the temperature increases. This may be due to crystal growth within the pan or possibly thermal expansion resulting in more material being lifted into the beam as it heats. This peaks at 152 °C, at which point it begins to decrease before leading to a very sharp drop which flattens out at 192 °C. This signifies the total loss of all form IV crystal content in the sample. At 172 °C form I begins to grow;

this is around the same point at which the decrease in form IV accelerates. The two changes considered together suggest that form IV converts to form I upon heating.

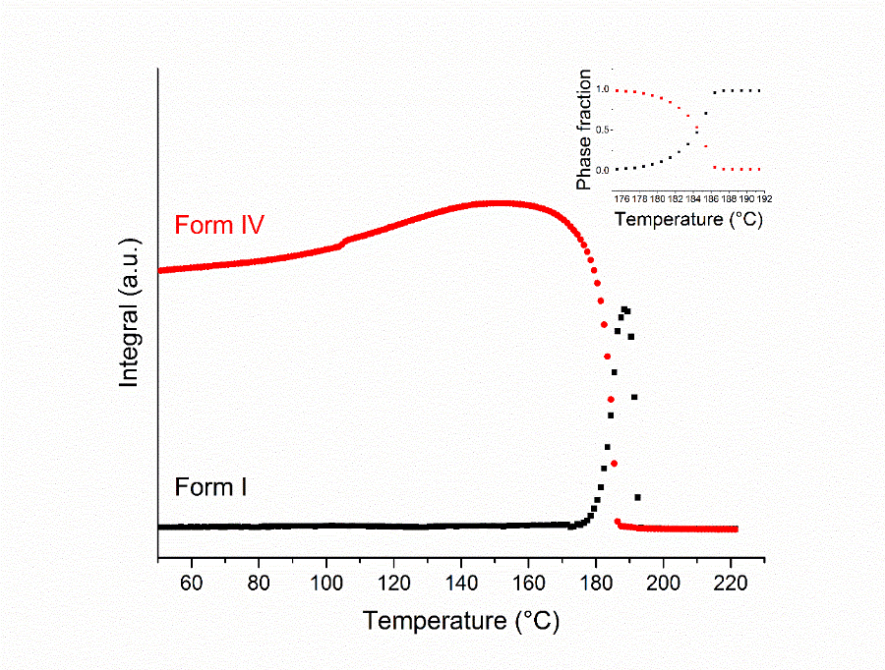

Figure 3-21. Plot of integrated total diffracted intensity for calculated patterns of CBZ I and IV as a function of temperature, with inset plot of phase fraction as a function of temperature.

As with previous samples, the integrated data were converted to phase fractions and plotted as a function of time (Figure 3-21 (inset)). The curves cross at 0.5 and so the transition occurred without any wholesale melt. With difficulty, as the curves are not completely straight at any point, a linear fit of the integrated data has been carried out around the intersection. It appears that the decline of form IV (-5.100 $°C^{-1}$) occurs at a slightly faster rate than the evolution of form I (3.567 $°C^{-1}$). This is unsurprising as melting is a thermodynamic event and occurs very quickly, since the molecules are not required to rearrange into any particular position relative to their neighbours. In contrast, crystallisation is a kinetic event and requires the molecules to reorient into an ordered structure, which takes time. The presence of the endotherm–exotherm in the DSC trace (Figure 3-14) offers strong support to the theory of co-crystallisation *via* a melt as melting is endothermic and crystallisation is exothermic.

The initial small endotherm has an onset of 180 °C and represents the melting of form IV. Unfortunately the onset of the subsequent exotherm is hidden due to the events overlapping but its presence signifies crystallisation of the melted portions of the material to form I. The reason for the overlap is that the temperature at which the material

crystallises to I is reached by the instrument before all of form IV has melted. As has been stated previously, were the experiment to be carried out at a different heating rate the two might be separated. A slower rate would allow more time for the melt to complete before the onset of crystallisation, which could separate the two events. For these reasons a sample of the same material was analysed by DSC-XRD at a ramp rate of 2 °C min^{-1} (the results can be seen in Appendix 1) but even at this low rate the events were found to be overlapping. It appears that the transformation of CBZ IV to CBZ I must occur by a melt–recrystallisation mechanism at these heating rates. The possibility of a separate melt and recrystallisation occurring at a lower heating rate cannot be ruled out.

Following the conversion it can be seen that the maximum form I content barely reaches 70 % of the maximum form IV content prior to the conversion (Figure 3-21). This, however is not due to loss of material, but rather incomplete recrystallisation to form I. It is another consequence of the heating rate. At 10 °C min^{-1} the DSC reached the melting temperature of form I[204] (represented by the large endotherm, onset 191 °C in Figure 3-14(b)) before the material had all been able to crystallise, and so that which had already crystallised melted and any liquid remained in that state. When repeated at 2 °C min^{-1} the crystallisation was allowed ample time to complete and the total content of form I after the conversion had completed was similar to that of form IV. This agrees with work by Grzesiak *et al*.[185]

3.3.2.2. Carbamazepine II

DSC-XRD data for a sample of carbamazepine form II are given in Figure 3-22. The DSC data show a small exotherm-endotherm with an onset at 126 °C, and then a large endotherm with two peaks and an onset at 190 °C. The former corresponds to a complete change in the diffraction pattern, while the latter is concurrent with the complete loss of all Bragg reflections and is in agreement with the reported melting point of CBZ form I.[204,205] The reason for the double peak is unclear, however it may be explained by the large sample size (12.1 mg). In all DSC-XRD experiments it was necessary to use a sample size significantly larger than the 5 mg recommended for DSC by TA Instruments to ensure that there was always sample in the X-ray beam.

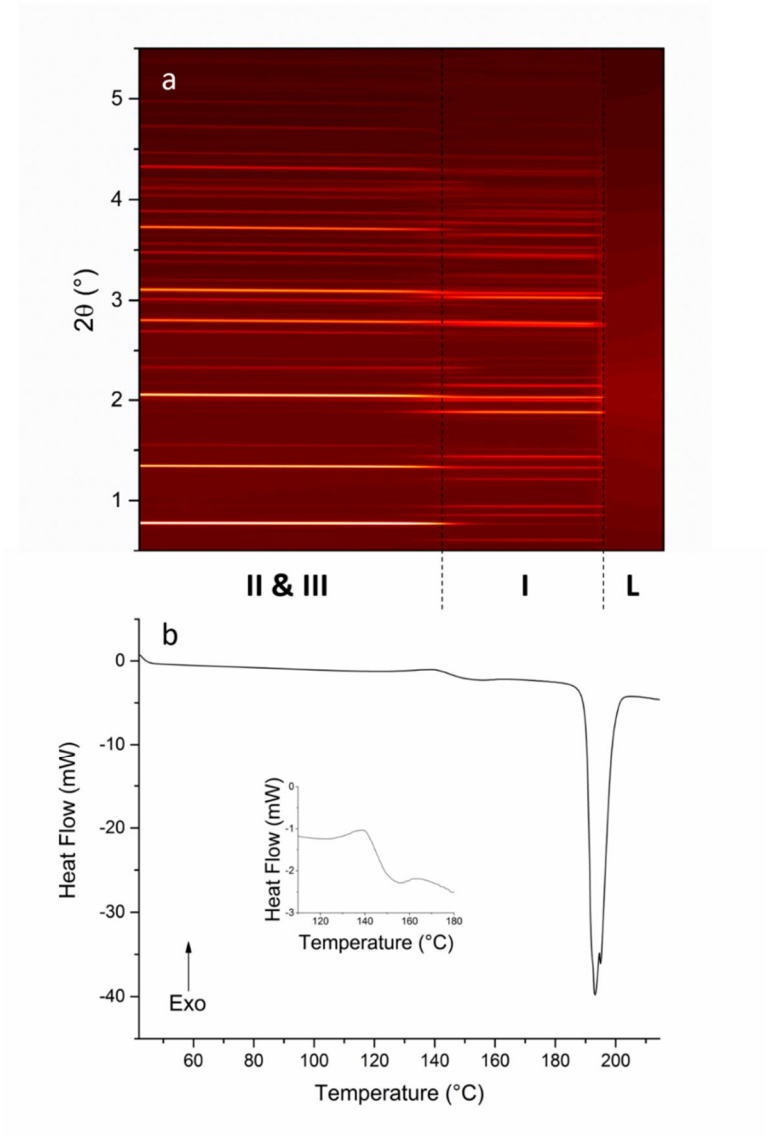

Figure 3-22. DSC-XRD data for a sample of carbamazepine (procured as form II) heated from 42 °C to 215 °C at 10 °C min^{-1}. The inset in (b) shows magnified view of DSC events between 110 °C and 180 °C. Dashed lines indicate the position of phase transitions visible to both DSC and XRD.

It is interesting that the initial change in diffraction pattern is accompanied by an exotherm-endotherm in the DSC trace, as this suggests crystallisation followed by melting. Following the transition there is clearly a crystalline material present, but a portion of the material appears to be melting while some crystallises. This might indicate that the initial sample may have been a mixture of polymorphs rather than pure form II as expected. Furthermore, form II is reported to undergo exothermic conversion to form I between 140 °C and 160 °C at a heating rate of 20 °C min^{-1}.[185] The onset of the exotherm in this experiment occurs at 119 °C, which can be accounted for by the slower heating rate (10 °C min^{-1}) but the endotherm cannot be attributed to the same conversion. Unfortunately the onset occurs whilst the preceding exotherm is ongoing and so cannot be accurately determined, but it must begin above 119 °C. Additionally, due to the small

enthalpy of the endotherm it is unclear whether the signal subsequently returns to baseline or if there is another exotherm prior to the melt.

3.3.2.2.1. Phase identification

Phase identification was carried out on patterns collected at 42 °C and 178 °C using the Rietveld method. Similarly to sulfathiazole (Chapter 2) a relatively poor fit was obtained at 42 °C when considering only form II in the model, leading to a more detailed analysis in which the structures of all five reported polymorphs were introduced. The conclusion of these refinements was that the initial sample was in fact a mixture of forms I (3.5 %), II (87.8 %) and III (8.7 %) (Figures 3-23(a)). All further refinements were carried out using starting models from the CSD (summarised in Table 3-2). Upon closer inspection of the pattern recorded at 42 °C (Figures 3-23(a)) it appears that all form I content was attributable to a shift in the background curve and that there were no specific reflections assigned to that structure; as a result, we believe the detection of form I was an artefact and it was excluded from refinements at low temperature. Refinement of the higher temperature pattern (Figures 3-23(b)) revealed that following the phase transition almost all of the material had converted to form I (96 %) with a very small quantity of form II (2 %) and III (2 %) remaining. However, as with form I in the low temperature pattern, there were no characteristic reflections of form III remaining in the observed data at 178 °C and the 2 % can again be accounted for by a slight discrepancy in the background curve. Final unit cell data for the patterns discussed are presented in Table 3-4. It should be noted that the high R_{wp} values are a direct result of including aluminium in the refinements. As the sample pan was a single piece of aluminium both the peak shape and intensity were poor and as such were difficult to fit.

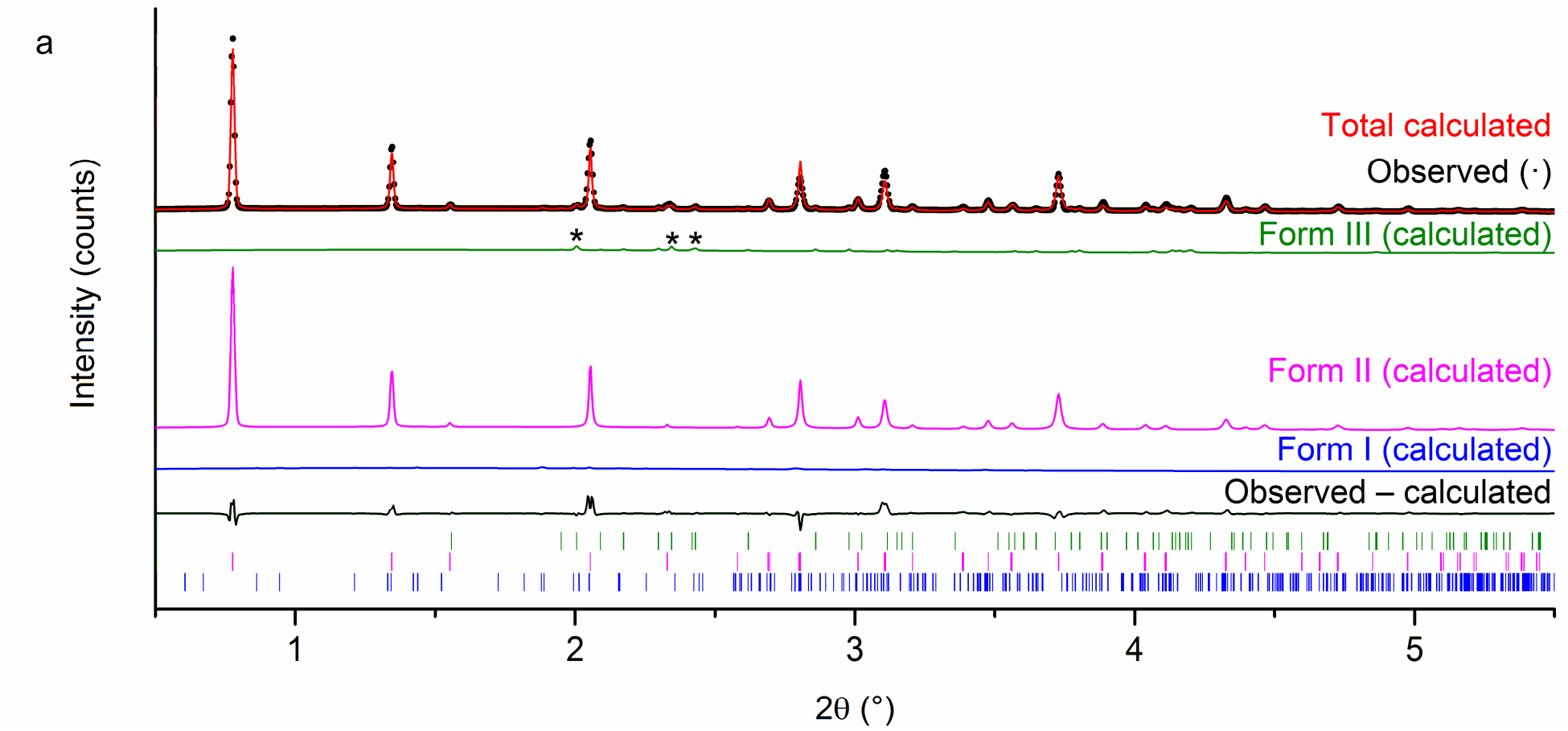
a
Intensity (counts)
Total calculated
Observed (·)
Form III (calculated)
*
* *
Form II (calculated)
Form I (calculated)
Observed – calculated
1
2
3
4
5
2θ (°)

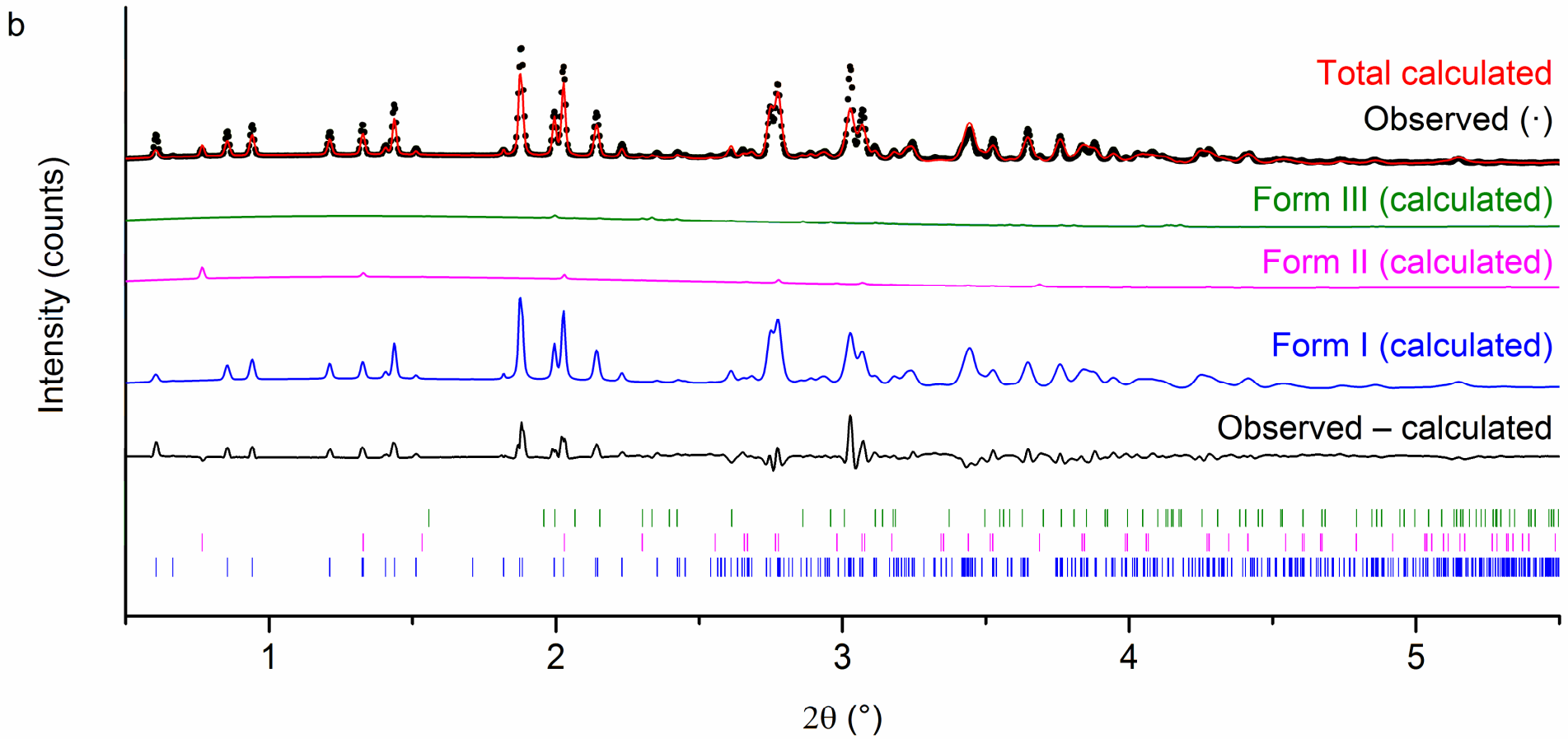

Figures 3-23 (a-b). Powder X-ray diffraction patterns for carbamazepine at (a) 42 °C and (b) 178 °C, including calculated patterns for the contribution of each polymorph. The tick marks show the positions of allowed reflections from carbamazepine form I, form II and form III and the asterisks denote characteristic reflections of form III.

Table 3-4. Refinement parameters for carbamazepine II. The starting models were taken from the CSD (form I: CBMZPN13; form II: CBMZPN03; form III: CBMZPN26).

Property	Form II	Form III	Form I	Form II
T / °C	42		178	
Space group	*R*-3	$P2_1/n$	*P*-1	*R*-3
a / Å	34.830(1)	7.515(3)	5.3435(8)	35.25(4)
b / Å	-	11.128(4)	20.510(3)	-
c / Å	5.3209(4)	13.883(9)	22.440(3)	5.372(12)
α / °	90	90	84.272(13)	90
β / °	90	92.85(4)	87.440(18)	90
γ / °	120	90	85.476(16)	120
Cell volume / Å^3				
R_{wp}	0.1301		0.1337	
$R_{wp\text{-}bkd}$	0.2324		0.2438	
Phase fraction	91.0 %	9.0 %	98.0 %	2.0 %

3.3.2.2.2. Unit cell expansion and intermolecular bonding

Batch refinements were carried out and fits were obtained with R_{wp} values between 0.0944 and 0.1401. Figure 3-24, Figure 3-25 and Figure 3-26 show plots of lattice constants as a function of temperature for the three forms of CBZ present. As with all previous materials, increasing the temperature of the sample causes expansion of the unit cell in all three dimensions for all three polymorphs. In all three structures the molecules pack as very similar dimers to those already discussed for CBZ IV (Figure 3-17), held by intermolecular H-bonds between the carboxamide groups. Polymorph II expands over 5 times more per °C in the *a* and *b* dimensions than it does in the *c* dimension. The dimers in the structure arrange to form pseudo-layers in the ab plane.[184] These layers stack with translational symmetry that runs parallel to the *c* axis. It is clear from these data that the sum of the intermolecular bonding in the *c* axis is much stronger than in the other dimensions resulting in the broadening of the layers as the sample is heated, whilst the chains of stacked dimers increase in length more slowly.

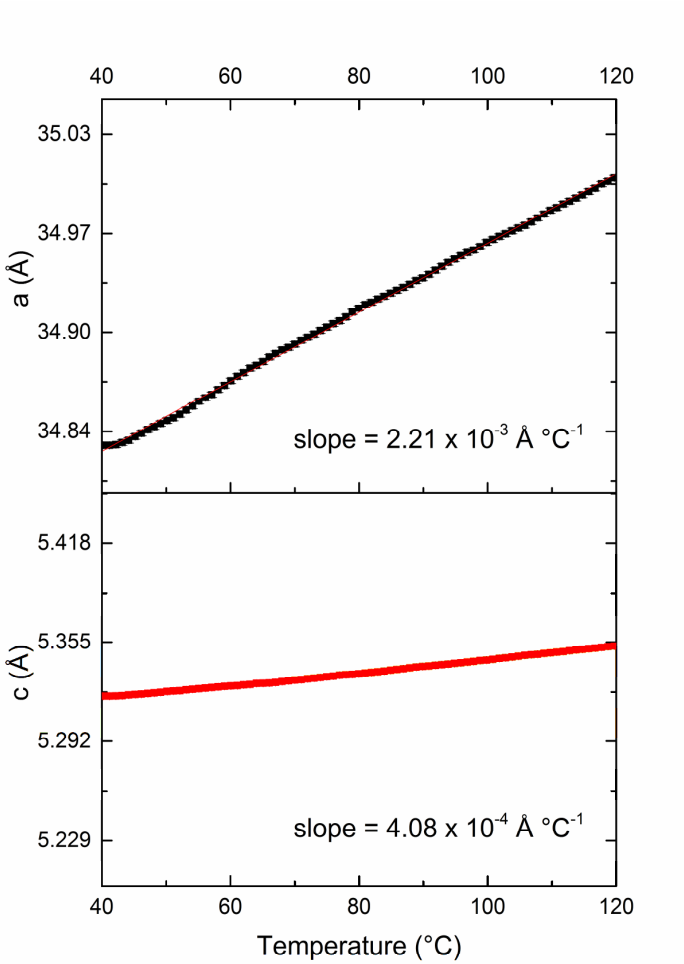

Figure 3-24. Lattice constants as a function of temperature for carbamazepine form II. Each of the three x-axes are depicted on the same scale for ease of comparison.

Expansion differences between the three lattice constants of form III are far less pronounced than those of form II. The intermolecular bonding in this structure consists of the H-bonds forming dimers, two centroid···centroid interactions of slightly different lengths, two C—H···O interactions, a N—H···π contact and a C—H···π interaction.[206] This combination of intermolecular bonding is complex and has clearly led to more evenly spread bond strengths throughout the structure, hence the more uniform expansion of the unit cell upon heating.

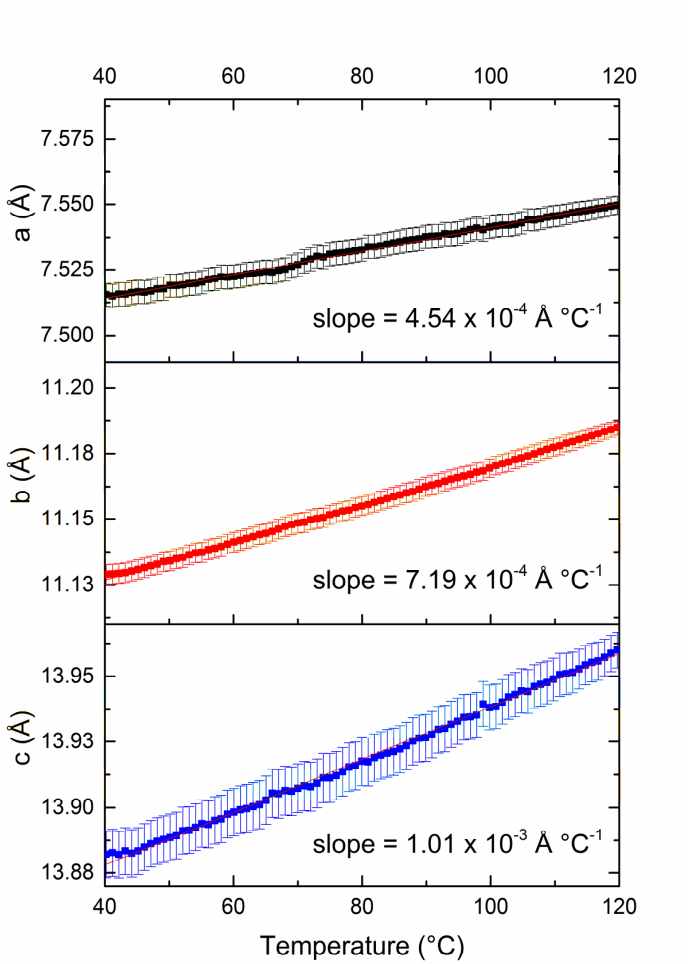

Figure 3-25. Lattice constants as a function of temperature for carbamazepine form III. Each of the three x-axes are depicted on the same scale for ease of comparison.

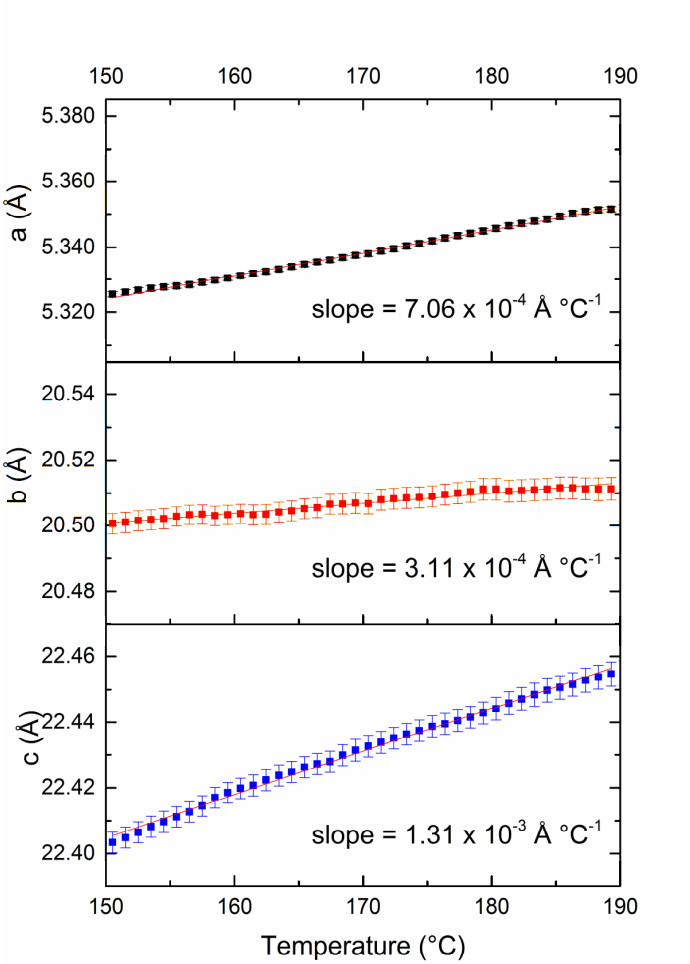

Figure 3-26. Lattice constants as a function of temperature for carbamazepine form I. Each of the three x-axes are depicted on the same scale for ease of comparison.

Intermolecular bonding in polymorph I is also complex and has many similarities with form III. In both forms the oxygen is involved in dimer formation as well as interactions with the same vinylic carbons of adjacent molecules. A more detailed description is given by Grzesiak and co-workers.[185] Using this description it was possible to examine the packing of the crystal using Mercury 3.8. Initially it appeared that the interactions in the *b* and *c* axes were similar and the difference in rates of growth upon heating was a source of consternation. However, when only the H-bonds which form the dimers are considered (Figure 3-27), it can be seen that three of the four pairs of bonds are orientated so that they offer support along *b* and only one of the pairs offers support to *c*. As these are the dominant intermolecular interactions in the crystal this explains the much larger degree of growth in *c*.

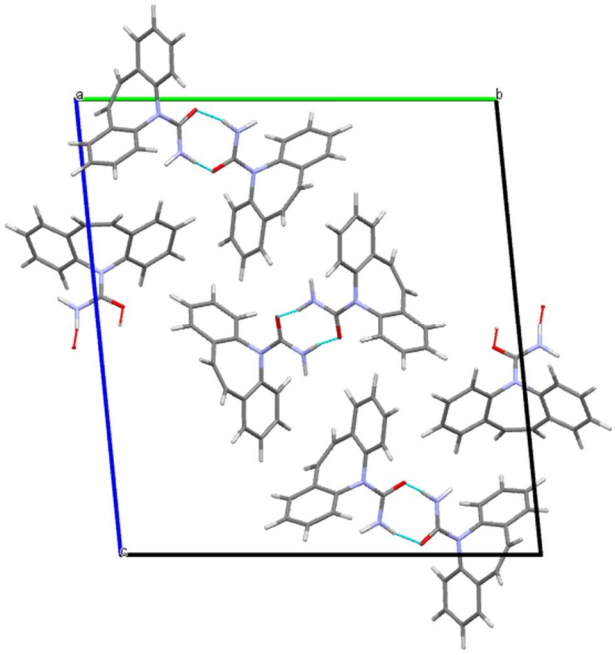

Figure 3-27. Graphic representation of the unit cell of CBZ I, showing H-bonds.

3.3.2.2.3. Phase transitions

As can be seen from the contour plot (Figure 3-22), the presence of solid crystalline material in the path of the beam was constant from 42 °C to 196 °C. However, as the initial sample was a mixture of two polymorphs it cannot be determined from this plot alone whether either of the components melted at any point. Figure 3-28 shows the amount of each polymorph present in the sample as a function of temperature. Below 100 °C the relative contributions of the three polymorphs is constant, with no form I, a little form III and the sample consisting mainly of form II. As with DHC and CBZ IV the total content of form II appears to increase with the temperature until it reaches 100 °C, at which point the first phase transition begins. This increase is probably a result of thermal expansion. Form I begins to grow in at around the same temperature and the gradients of both curves become much steeper at 120 °C, which coincides with the onset of the exotherm in the DSC trace (119 °C) and suggests crystallisation from II to I. A linear fit was carried out at the straightest section of the curves around the point at which they cross (132-144 °C) and the rate of decay of form II (-3.794 $°C^{-1}$) and the rate of growth of form I (3.164 $°C^{-1}$) are similar, with form I growing a little more slowly, as is to be expected when comparing crystallisation (kinetic) to melting (thermodynamic). During this time form III appears to grow at an increasing rate until its content peaks at around 140 °C and immediately begins to decay. It is difficult to say whether form II melts or converts directly to form I, however, the presence of the endotherm in the DSC data

suggests a melt. A plot of the sum of the calculated contributions of forms I and II shows a dip in the crystalline content in the beam between 120 °C and 160 °C, during the phase transition and prior to the waning of form III. This supports the hypothesis that there is some melting of form II involved in the transformation, but disagrees with the literature which describes a solid–solid transition, based on a combination of thermomicroscopy and DSC carried out on separate samples.[185] However, presumably there must be a point during the transition at which the structure of the material sits somewhere between those of the two crystals and is disordered, unless the conversion is simultaneous and instantaneous for all molecules in the crystal lattice; this may be what causes the drop in overall crystalline content at *ca.* 140 °C, and may not strictly be described as a melt.

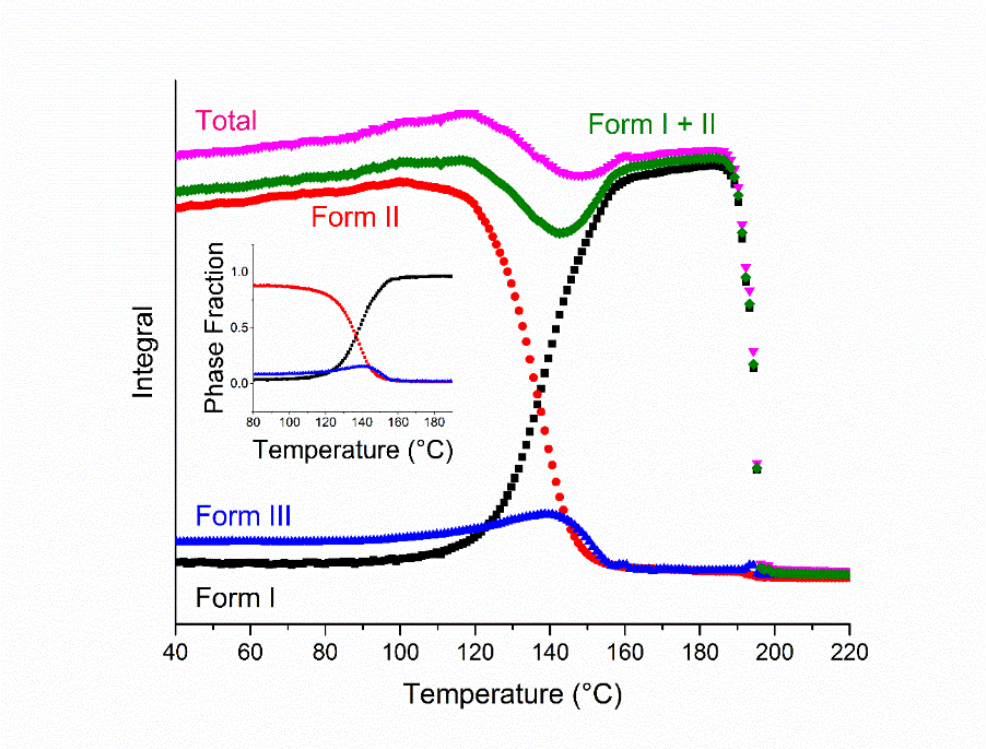

Figure 3-28. Plot of integrated total diffracted intensity for calculated patterns of CBZ I, II, III, their sum and CBZ I + II as a function of temperature, with an inset plot of phase fraction as a function of temperature.

Plotting the sum of the content of the three polymorphs as a function of temperature (Figure 3-28) it can be seen that the total crystalline content is lower following the phase transition. A thorough investigation of the thermal relationship between forms I and III was carried out by Behme and Brooke[207] who concluded that the heating rate has a strong effect on the behaviour of form III. At 2 °C min^{-1} there is sufficient time allowed for the full conversion to form I, *via* a sublimation–condensation mechanism between 150 and 170 °C, with no apparent melting. However, once increased to 10 °C min^{-1} they state that “the endotherm recorded in the range 165–175 °C reflects several thermal events”,

representing the combination of some conversion to form I via sublimation and some melting. At all rates studied in the range 2–40 °C min^{-1} the endotherm was followed by an exotherm resulting from the crystallisation of form I from the melt. This melt–recrystallisation pathway is well documented in the literature.[185,204,205,207–209] It is likely that the drop in overall diffracted intensity is a result of some form III subliming and moving out of the incident beam whilst in the gas phase and condensing in another area of the sample or being lost from the pan, which was left open for these experiments. Hence, it seems that there are two distinct phase transitions occurring simultaneously by three mechanisms. Form II is undergoing melt–recrystallisation to form I on a microscopic particle by particle basis and form III is undergoing part sublimation–recrystallisation and part melt–recrystallisation to form I.

The conversion data presented here are consistent with the literature, except that the conversion of III occurs at a lower temperature than expected. This may be due to the presence of form II destabilising it. Due to the overlapping events in the thermogram and the open pan it is impossible to quantify either the enthalpy of conversion of form III→I or the enthalpy of conversion of II→I. Consequently, the amount of form III lost by sublimation cannot be determined *via* enthalpic calculations. However, the diffraction data were used to calculate a rough fraction of III lost by calculating the difference between the maximum total crystal content prior to the phase transition and the equivalent immediately following. This was compared to the maximum area under the curve for form III and the resulting figure suggests that only 30 % recrystallised to form I following the melt and 70 % was lost from the beam. This may be partially prevented in future work by using hermetically sealed DSC pans; however, this would not prevent recrystallisation from the vapour phase in areas of the sample not interrogated by the incident beam.

3.3.3. Paracetamol

Melt synthesis of air-stable PCM form III utilises the sugar-based excipients lactose monohydrate and HPMC. Crystallisation from II to I from the melt utilises trehalose, another sugar based excipient. The crystallisation process has been followed with time-resolved X-ray diffraction-DSC experiments. Critically, computational modelling of the interfacial interactions at the predicted major faces of the respective paracetamol crystals and the excipient indicate significant drivers to the stabilisation of form III through hydrogen bonding.

Telford *et al.*[210] used computational modelling to examine interactions between lactose monohydrate and PCM forms I and III (Figure 3-29), through the minimisation of the intermolecular interactions between crystal surfaces of the differing paracetamol polymorphs and a lactose molecule. The dominant crystal faces for each phase, as indicated by several morphology prediction methods, were investigated.

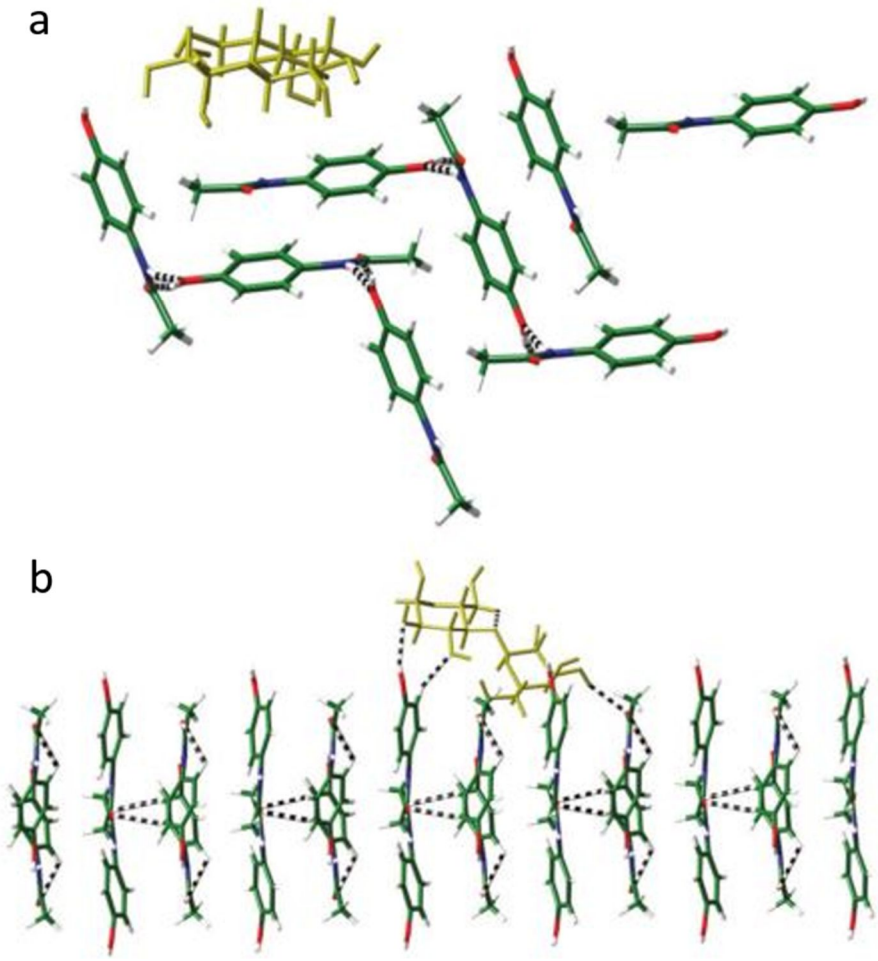

Figure 3-29. Computational model of the interactions between the lactose molecule (yellow) and the dominant crystal faces of PCM (a) form I and (b) form III.

For a single lactose molecule, significantly stronger interactions were indicated with the surfaces of form III compared to form I. As can be seen in Figure 3-29, the match between hydrogen bonding groups is greater for form III than form I. It appears that the repeat of the location of the OH groups on this surface matches the lactose molecule ensuring a number of hydrogen bonds can be formed between the two systems. This matching of system size and orientation of hydrogen bonding functional groups may be the source of the stabilisation of form III and points to an active role for the excipient in stabilising the metastable form. Here the effect of sugar based excipients on the stabilisation of metastable polymorphs of PCM will be examined by *in situ* DSC-XRD.

3.3.3.1. Pure paracetamol

Figure 3-30 displays a contour plot of PXRD data above a DSC trace for a sample of melt quenched paracetamol. In contrast to the data sets depicted thus far, the x-axis represents time and the temperature data are linked to the lower right hand y-axis. Paracetamol is known to have three crystalline polymorphs.[57,211] Research by Rossi *et al* in 2003 showed that if an amorphous sample of paracetamol is heated to 113 °C in a DSC and cooled spontaneously to ambient temperature it crystallises to form III.[51] Further research has shown that form III will crystallise from the amorphous phase without the need for an isothermal step at 113 °C.[26] Therefore, in an attempt to observe the most phase transitions possible for paracetamol, rather than simply heating, the decision was taken to heat an amorphous sample at 10 °C min^{-1} from ambient temperature to 200 °C with a 5 minute isothermal interval at 113 °C. It was hoped that the interval would ensure evolution of form III would complete before any further transitions began.

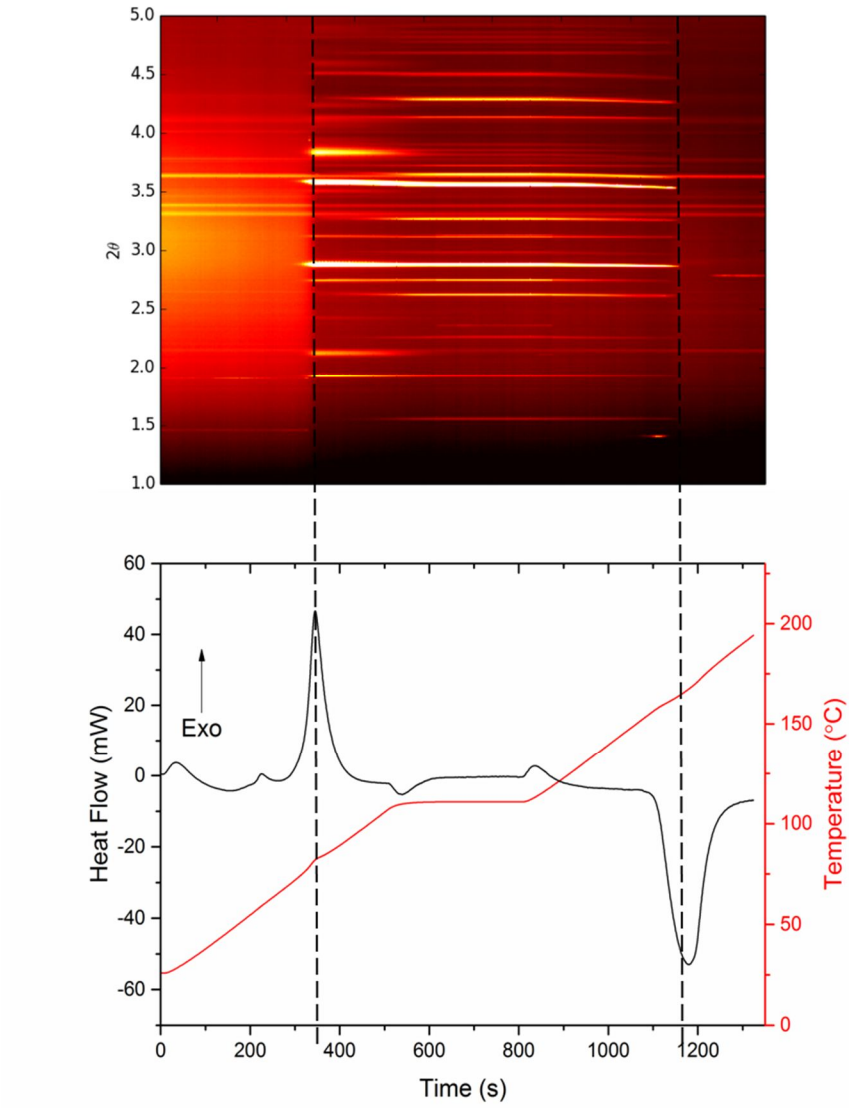

Figure 3-30. DSC-XRD data for paracetamol. The x-axis shows time, as the temperature profile was not linear. Dashed lines indicate positions of phase transitions visible to both DSC and XRD.

Initially the X-ray data show only those reflections that may be attributed to the experimental apparatus and a "halo" (Figure 3-31) characteristic of amorphous material.[2] The glass transition (T_g) temperature of paracetamol occurs at 23 °C,[212,213] however the apparatus used for this experiment did not include a cooler for the DSC and so it was not possible to cool below ambient temperature. The lowest temperature recorded for this sample was 26 °C, making it impossible to observe the T_g. Notwithstanding, synchrotron XRD has been shown to have a limit of detection (LOD) of crystalline content in an amorphous material of 0.2% w/w.[214] This is sufficient to say that, although no T_g could be observed, the sample was successfully vitrified.

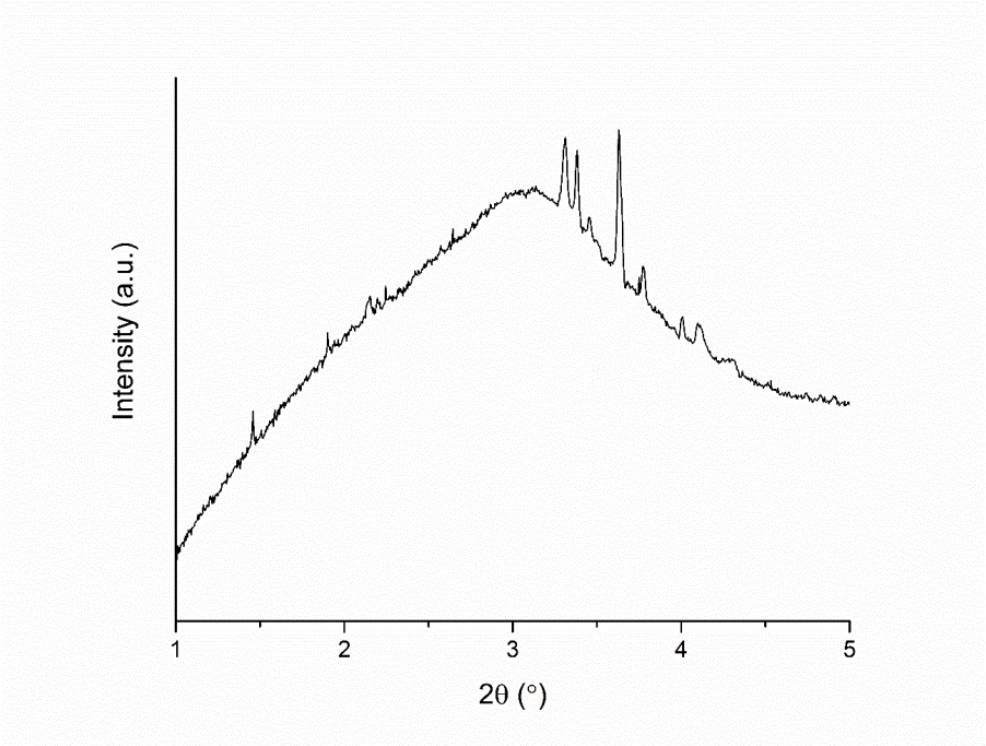

Figure 3-31. Diffraction pattern for glassy paracetamol at 26 °C. All reflections are attributable to the experimental set up. The background “halo” is characteristic of amorphous material.

Upon heating, the first change in the sample is indicated by a small exotherm in the DSC trace with an onset of around 56 °C. This event does not have any accompanying change in structure visible in the X-ray data. The second exotherm (onset 75 °C, *ca.* 350 s) is clearly caused by the crystallisation of the amorphous material as, at this time point, there is a dramatic change in the contour plot and a number of Bragg reflections grow in very quickly. Subsequently there appear to be two small events in the DSC trace, the first endothermic and the second exothermic, at around 500 s and 800 s. However, if the temperature data are considered, it can be seen that these events correspond directly to the beginning and end of the isothermal portion of the heating profile, respectively, and are in fact artefacts of the instrument.

It should be noted that, although the instrument was programmed to hold the temperature at 113 °C it only achieved 111 °C. This is likely due to the holes being drilled in the head and the fact that heat shielding could not be used as it would have diffracted too much of the incident beam intensity before reaching the sample. This is unlikely to have had an effect on the results as the crystallisation was complete before the sample reached this temperature, as can be seen in the X-ray data. From this point and until the material melts, changes in the diffraction pattern do not appear in the DSC data. The reflections that appear at 75 °C reach a maximum intensity very quickly, and this then begins to decrease more slowly. Another set of reflections begin to grow in at the same time, but

much more slowly than the first, and reach a maximum at 111 °C (*ca.* 740 s) before fading and then disappearing altogether. This disappearance is coincident with the final event in the DSC thermogram, a large endotherm (onset 158 °C, *ca.* 1100 s).

It was thought that the first exothermic event (56 °C) may be due to the presence of a contaminant or impurity in the sample, but this would need to be non-crystalline before and after the exotherm as there are no Bragg reflections relating to the event. In an attempt to identify the cause of the exotherm the experiment was repeated by quench cooling paracetamol in an unmodified Q20 DSC a number of times then following the same heating regime as previously described (Figure 3-32). The event was not reproducible. In all collected data no events were observed prior to that at 75 °C, the same temperature as the second exotherm in Figure 3-30. For this reason it is taken to be an artefact, probably related to the modifications to the cell.

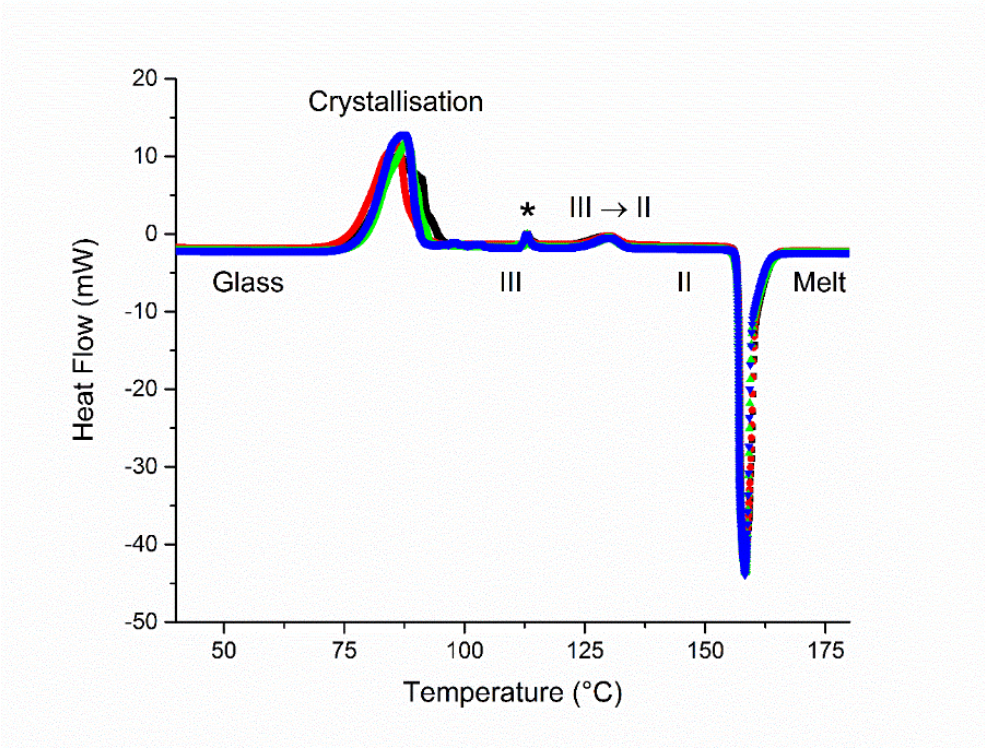

Figure 3-32. DSC data for paracetamol quenched *in situ* and reheated at 10 °C min^{-1} with an isothermal period at 113 °C. [Different colours represent different samples. Peak marked * denotes signal resulting from the hold].

3.3.3.1.1. Polymorph III

Rietveld refinement of the pattern recorded at 82.3 °C (just prior to the apex of the second exotherm in Figure 3-30) can be seen in Figure 3-33. As can be seen from the calculated patterns the initial exotherm can be attributed to the crystallisation of the sample from amorphous to paracetamol form III.[26] The angles of reflection all match the expected

positions and this is the behaviour expected of amorphous paracetamol.[26,57] Again, as the experimental set up did not allow for spinning of the sample and as the sample itself was not a powder but began as a single piece of amorphous material, the intensity ratios of the reflections are not a perfect representation of the structure of form III. There are however, no characteristic reflections of any other polymorphs of PCM present in the recorded pattern. The Rietveld refinements fit with a R_{wp} of 0.0801.

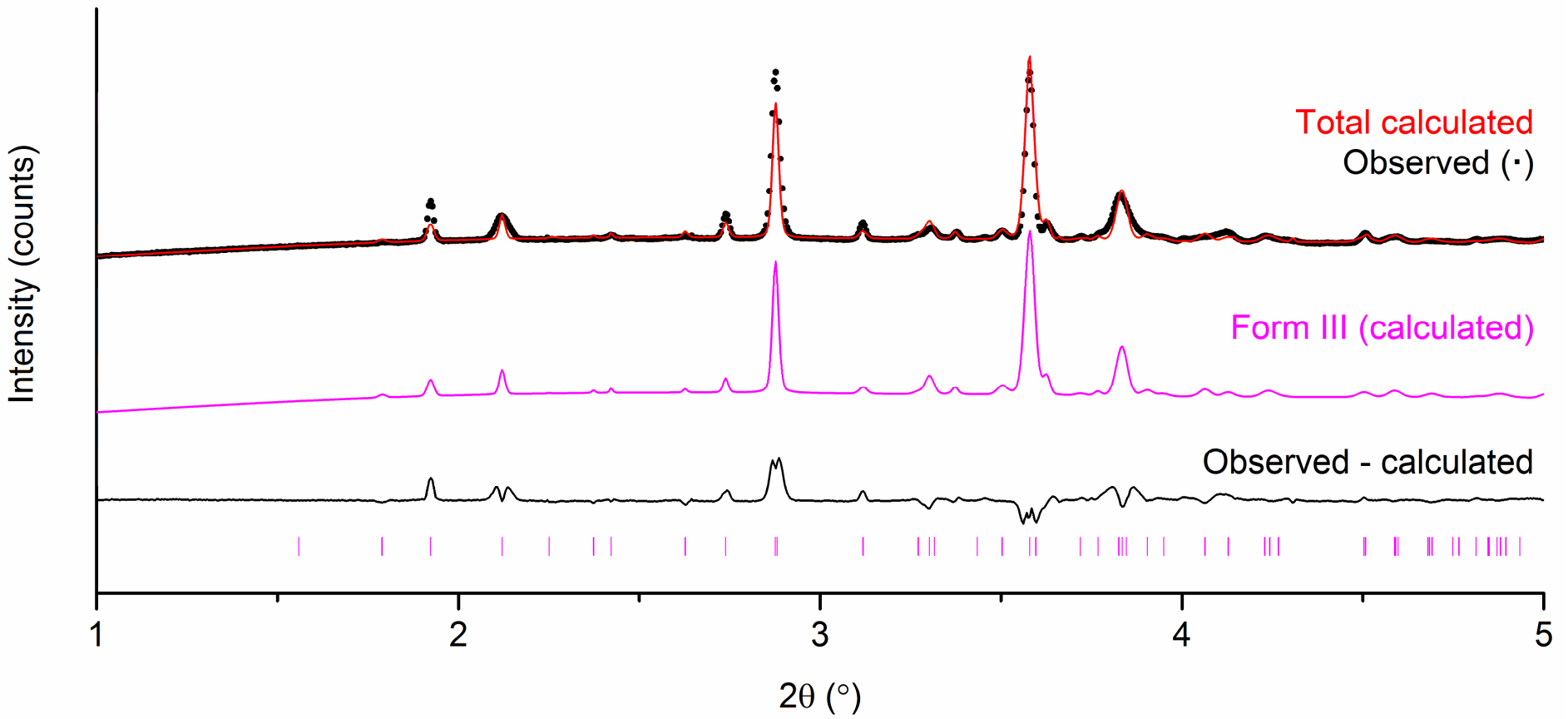

Figure 3-33. Rietveld refinement data for a diffraction pattern recorded at 82.3 °C when heating an amorphous sample of paracetamol. Tick marks show the positions of allowed reflections of paracetamol form III.

3.3.3.1.2. Phase transitions

It has previously been stated that, following the initial crystallisation to form III paracetamol is stable until a solid–solid phase transition, which occurs at *ca.* 125 °C (when heating at 10 °C min^{-1}) and is characterised by a small exotherm of −1.0 kJ mol^{-1}.[26] This was not the case during this experiment. Rietveld refinement of a pattern recorded within the isothermal period at 111 °C (Figure 3-34) clearly shows the presence of both form II and form III at this temperature in approximately equal measure. Clearly the content of form II is growing in relation to form III. Unfortunately the calorimetric data do not contain any useful information relating to this, due to the isothermal portion of the heating programme, but refinement of a further pattern at 143.1 °C (Figure 3-35) shows the transformation of the material to form II is complete.

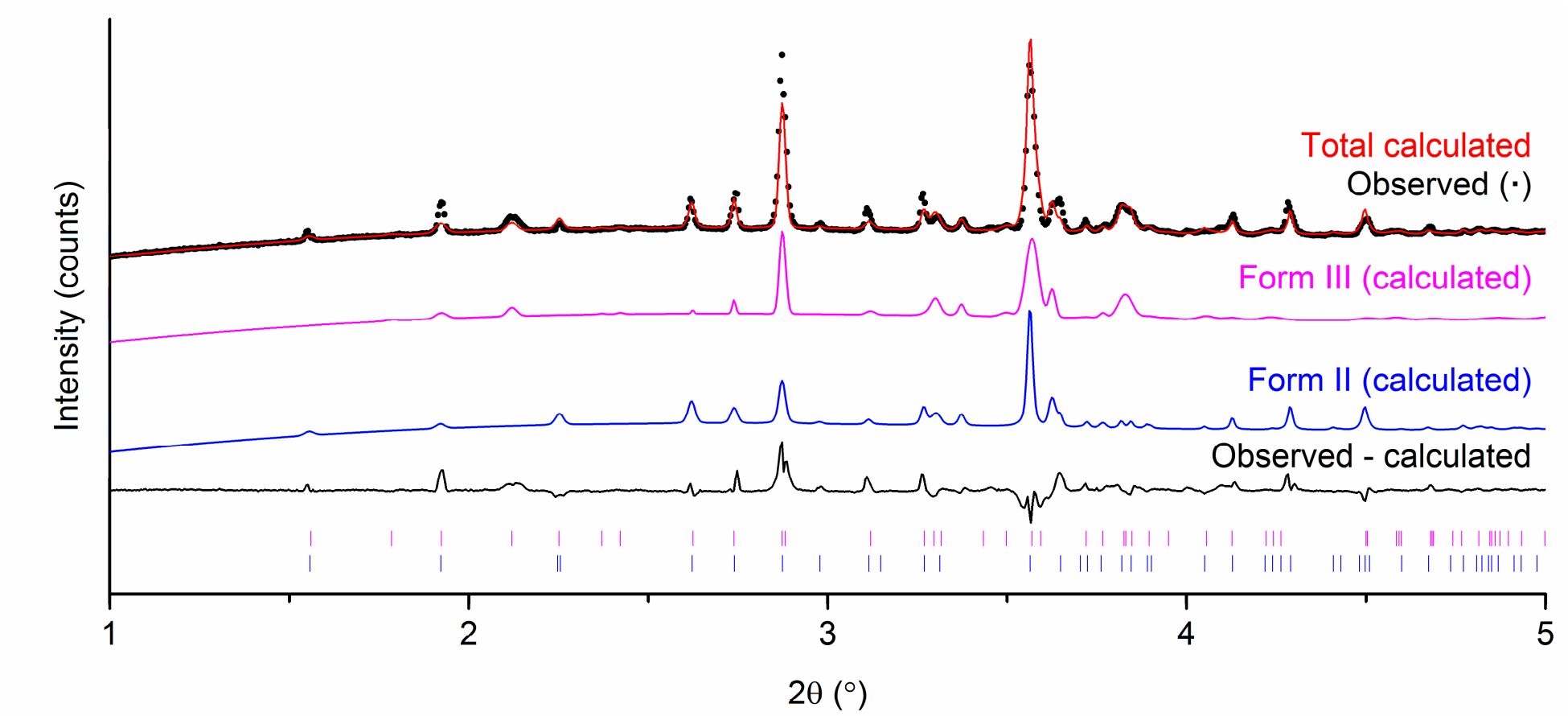

Figure 3-34. Rietveld refinement data for a diffraction pattern recorded at 111 °C when heating an amorphous sample of paracetamol from 26 °C. Tick marks show the positions of allowed reflections of paracetamol form II (upper) and form III (lower).

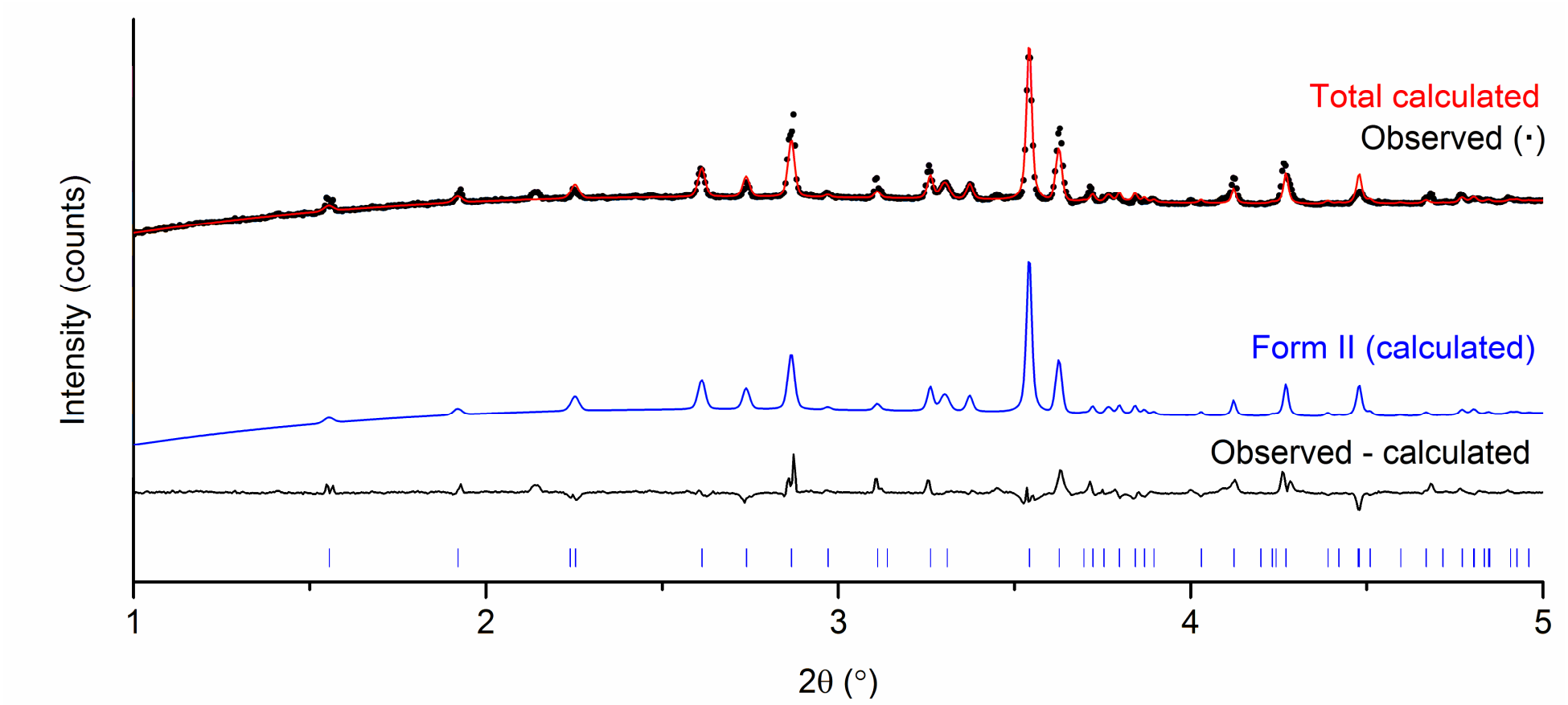

Figure 3-35. Rietveld refinement data for a diffraction pattern recorded at 143.1 °C when heating an amorphous sample of paracetamol from 26 °C. Tick marks show the positions of allowed reflections of paracetamol form II (upper). Asterisks denote reflections caused by the experimental set up.

Batch refinements were carried out on the data as described in Chapter 2; the results can be seen in Figure 3-36. It is clear that form III begins to grow in from the amorphous phase after 285 s (70 °C) and rapidly reaches its maximum content after 347 s (82 °C), which agrees closely with the second exothermic peak in the DSC trace and the literature.[26] Following this the form III intensity begins to decline immediately until its contribution to the diffraction pattern is negligible. It appears that form II also grows in at around the same temperature. This agrees with the conclusions drawn by Gaisford *et al.*[57] that both forms II and III grow in from the amorphous form as pure paracetamol is heated, and Burley *et al.*[26] who observed that there is a temperature range within which the two forms co-exist. Although both groups suggest the growth of III presupposes that of II, the data here suggest both metastable polymorphs begin to crystallise from the amorphous form at the same temperature. However, form III grows in more rapidly than form II, and at its maximum form III represents *ca.* 96 % of the content of the sample.

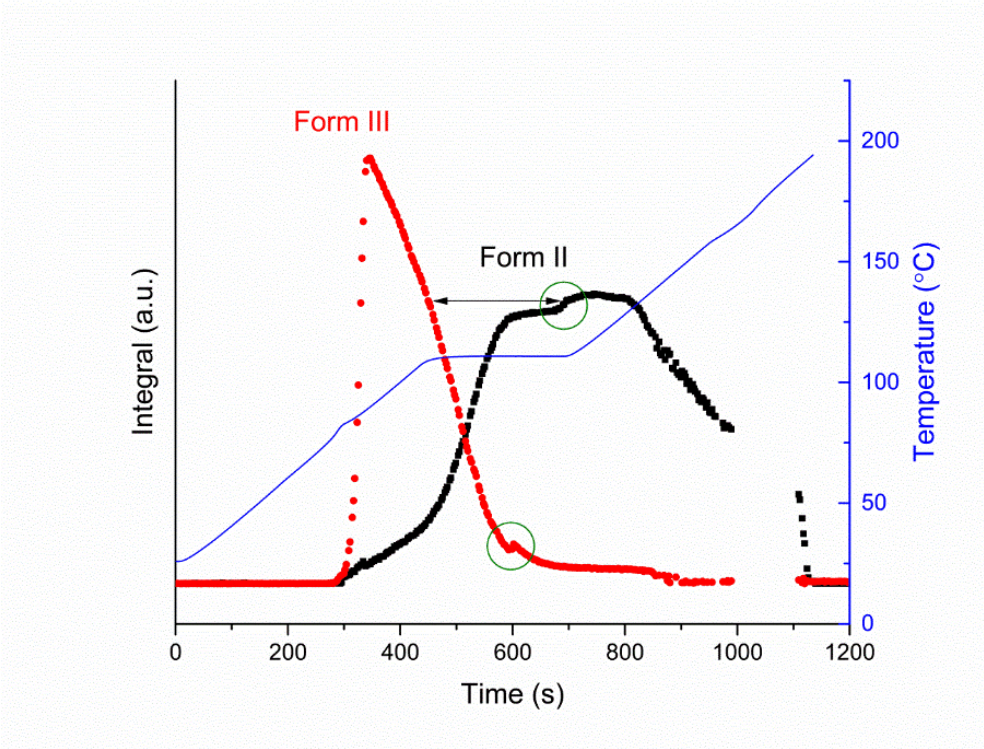

Figure 3-36. Plot of integrated total diffracted intensity for calculated patterns of paracetamol form II and form III versus time. The solid blue line represents the temperature of the sample. The arrow highlights the point at which the rate of decay of form III increases, which matches the maximum intensity of form II. [Green circles indicate artefacts from the refinements caused by a slight change in the background. Data points between 855 s and 1109 s have been removed as the data could not be fitted in this range].

It appears that form II develops in two stages as the profile of the curve between 350 s (83 °C) and 600 s (111 °C) can be split into two gradients. From 350 s to 450 s the rate of growth is far slower than that after 450 s. Presumably the initial growth can be

attributed to crystallisation from the amorphous material and the second stage is a result of the conversion from form III. There is a slight increase in the rate of decay of form III coincident with this increase in rate of formation of form II. Approximations of the rate of conversion for each form have been carried out using OriginPro 9.1; these indicate that the average rate of growth of form II between 460 s and 550 s was around 9 $°C^{-1}$ and the corresponding decay of form III was 10.5 $°C^{-1}$. The similarity between these two figures appears to support the theory of a III→II conversion. The initial decay of form III is much faster than the growth of form II and is therefore unlikely to be attributable to a conversion between the two. It begins at 340 s and increases at 445 s when the proposed conversion to form II begins. It is interesting to note that the quantity of form III at 445 s is very similar to that of the maximum quantity of form II after the transition is complete. This suggests that the portion of the material decaying during the initial part of the transition does not recrystallise to form II, or in fact any other form (as no other Bragg reflections are observed). It must therefore be melting.

Unlike melting, which is a thermodynamic event and requires only thermal energy, crystallisation is a kinetic event and so it requires time as well as energy for the molecules present to rearrange themselves into the correct relative orientation so that intermolecular bonds can develop and form the crystal lattice.[9] The rate of crystallisation of polymorph II from the glass is slower than that for its conversion from polymorph III. The molecules in an amorphous material have no long range order and are effectively randomly orientated, similar to the structure of a liquid. There is essentially no regular arrangement and so it will take a relatively long time and large amount of energy for the molecules to move into the exact positions required to form the crystal lattice. In contrast, the molecules in a crystal are arranged uniformly in a repeating array. The structures of forms II and III of paracetamol are closely related[49] as can be seen by the similarity in their diffraction patterns (Figure 3-37). Therefore, the molecules are required to make much smaller positional adjustments to transform between the two crystalline polymorphs than to convert from the amorphous to form II. For this reason the second stage of growth of form II is much faster than the first.

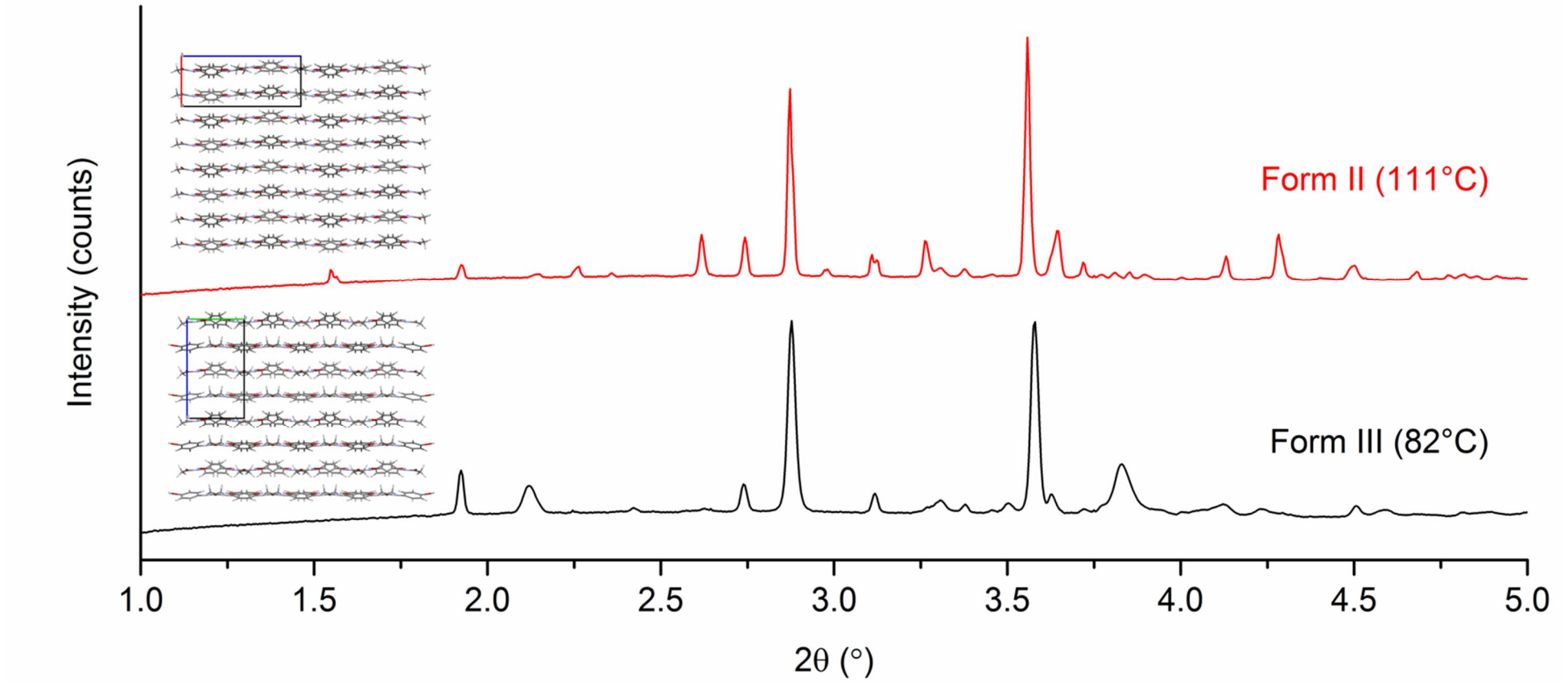

Figure 3-37. Diffraction patterns for paracetamol recorded at 82 °C and during the isothermal step at 111 °C. Insets present the structures of the two polymorphs showing the similar stacked layers. The patterns are clearly very similar, particularly with reference to the main reflections.

Unfortunately, as both II and III begin to evolve from the glass at the same temperature there is no way of separating the relative energies from the exotherm in the DSC trace. However, as the diffraction data show, the growth of form III begins at 285 s (70 °C) and completes at 347 s (82 °C). This time/temperature range corresponds directly to the position of the crystallisation exotherm in the thermogram. Since, at the apex of the thermogram, the diffracted intensity is 96 % form III it is reasonable to assume that the enthalpy of the exotherm is almost entirely due to this form.

The growth profile of form II is not typical of the behaviour of amorphous paracetamol, as shown by Burley *et al.*[26] and further supporting DSC studies (Figure 3-32). This suggests there may have been some seed crystals of form II in the glassy material. Although the diffraction data show that the sample was amorphous the presence of a small amount of crystalline material cannot be ruled out. The X-ray beam passed through a maximum cross sectional area of the sample of 0.5 mm x 0.5 mm. Any crystals outside of this would not have been detected.

3.3.3.2. Paracetamol and HPMC

Combined DSC and diffraction data for a melt-quenched mixture of PCM with 10 % w/w HPMC K100M can be seen in Figure 3-38. As was seen with pure paracetamol the quenched sample was completely amorphous with no Bragg reflections occurring in the X-ray data. The sample remained this way until 90.9 °C, at which point there is a large endotherm (peaking at 100 °C) coinciding with the appearance of Bragg reflections in the diffraction pattern. This indicates that the sample has undergone a phase transition from the glass to PCM III, which was confirmed by Rietveld refinement (Figure 3-39).

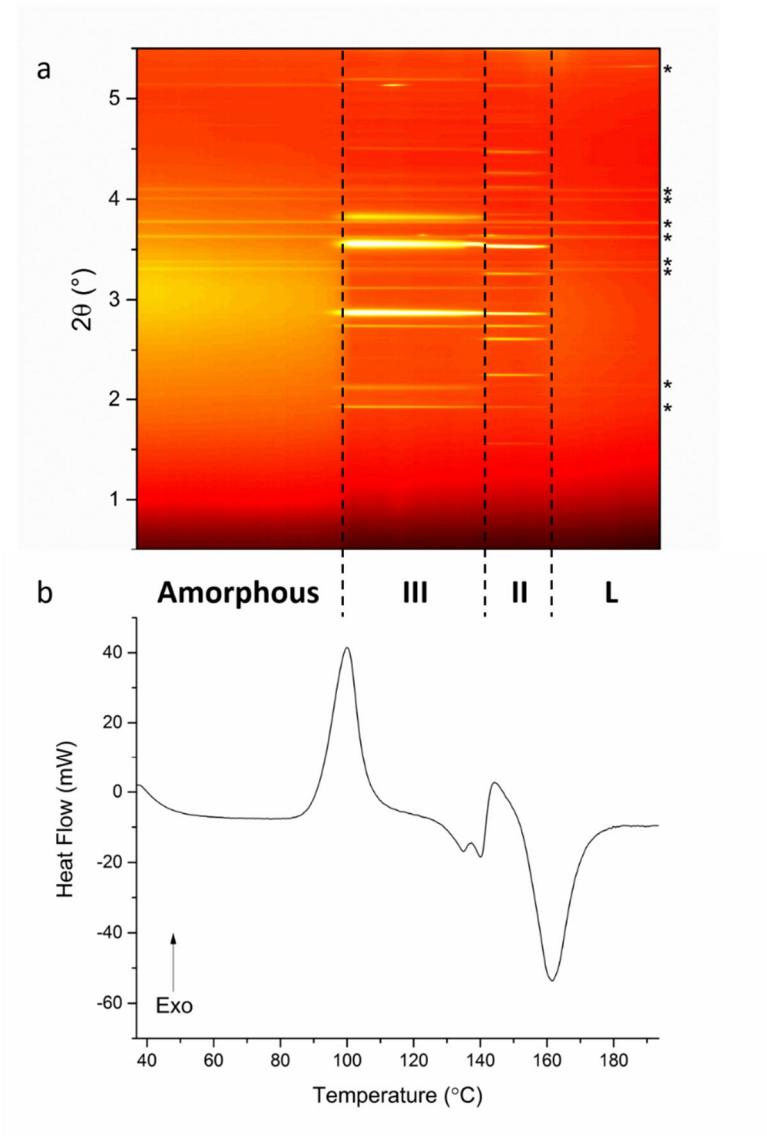

Figure 3-38. DSC-XRD data for a quench cooled sample of paracetamol and 10 % w/w HPMC K100M heated from ambient to 194 °C at 10 °C min^{-1}. Reflections in the liquid phase marked * are a result of the experimental set up.

Immediately following the phase transition the tail of the exotherm leads into an endotherm in the DSC trace, which peaks at 135 °C. This coincides with a sharpening of the reflections in the diffraction data and results from the growth of crystals of form III in the sample. It seems from both datasets that this growth occurs very quickly, immediately before a phase transition from form III to form II, represented by an endo-exo event in the thermogram and the loss of all reflections relating to form III in the diffraction pattern (Figure 3-40). The final exotherm is inseparable from the subsequent large endotherm which peaks at 161.7 °C and is caused by the melting of form II,[26,49,53,57,192,210,211] and coincides with the loss of all sample related reflections in the X-ray patterns.

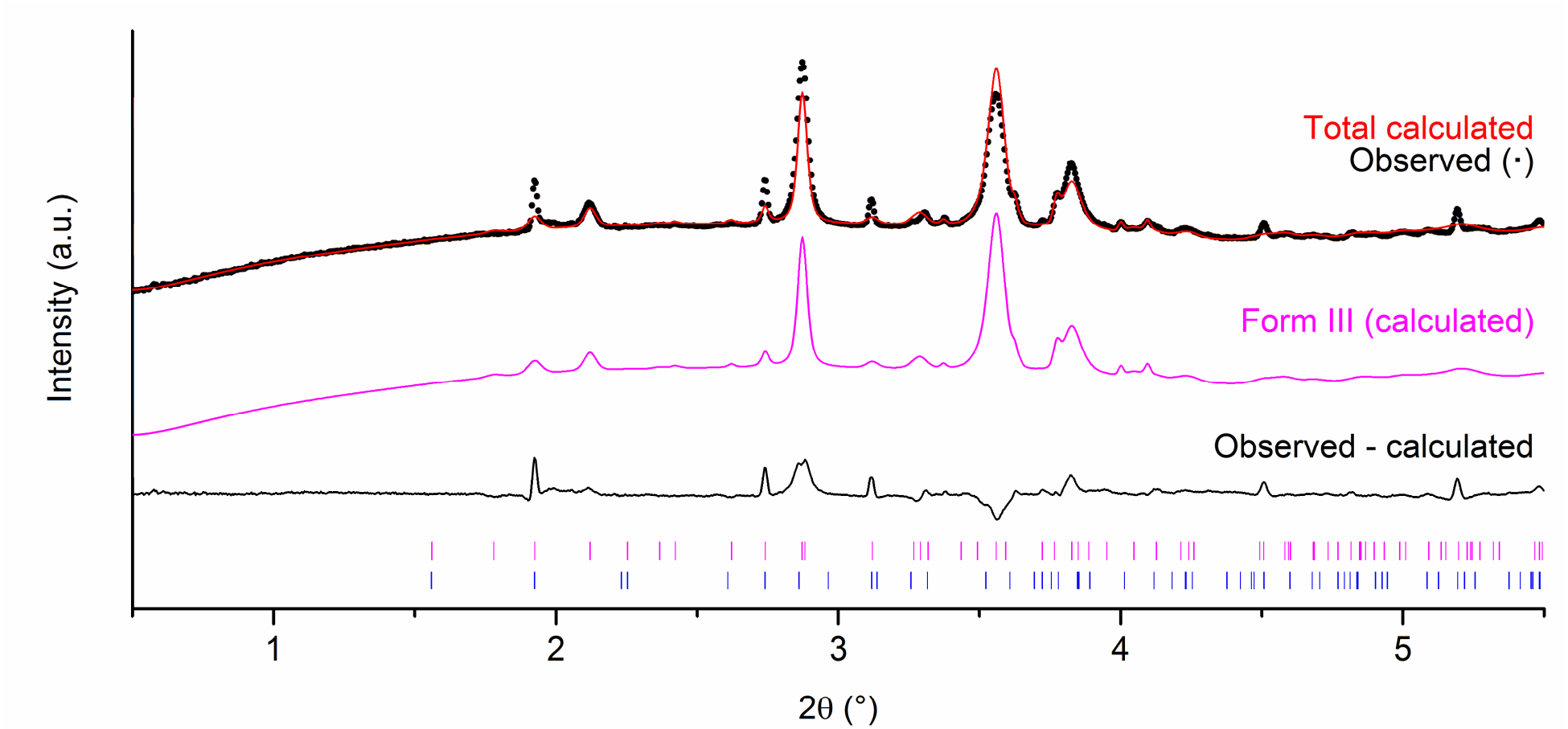

Figure 3-39. PXRD pattern for a quench cooled sample of a mixture of paracetamol with 10 % w/w HPMC K100M recorded at 102.3 °C. Reflections marked * are a result of the experimental set up.

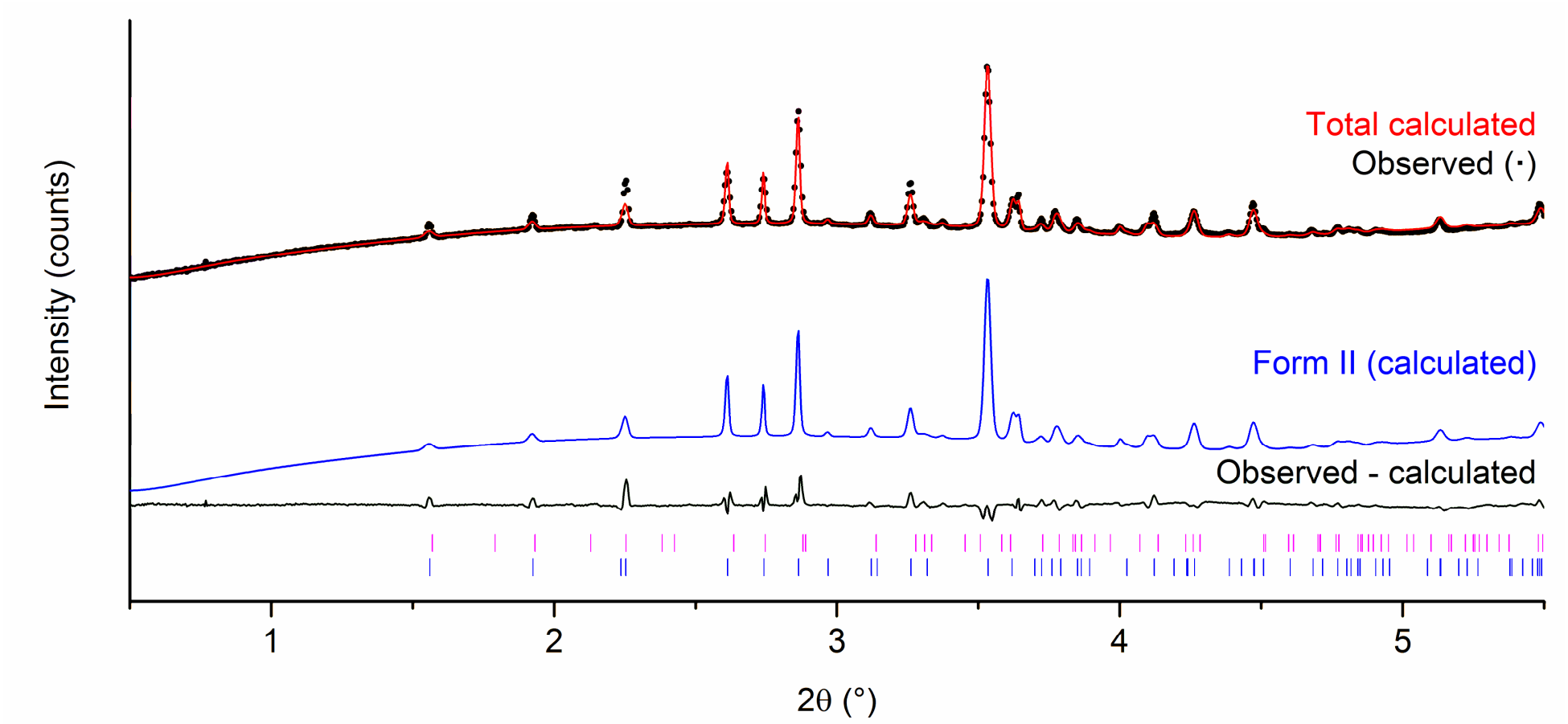

Figure 3-40. PXRD pattern for a quench cooled sample of a mixture of paracetamol with HPMC K100M (10 % w/w) recorded at 143.0 °C. Reflections marked * are a result of the experimental set up.

3.3.3.2.1. Unit cell expansion of polymorph III

Unit cell growth for polymorph III can be seen in Figure 3-41. As expected from the structure of the crystal, which consists of stacked hydrogen bonded two dimensional layers in the *ab* plane,[49] the unit cell exhibits no growth in the *b* dimension upon heating and little in *a* (6.39 x 10^{-4} Å $°C^{-1}$). Whereas, in the *c* direction there is 1.10 x 10^{-3} Å $°C^{-1}$ expansion over the temperature range 100–120 °C. The same is seen in polymorph II (Figure 3-42), where the 2D layers sit in the *bc* plane and the unit cell expands by 1.04 x 10^{-3} Å $°C^{-1}$ along *a* but very little along the other two axes. These values are similar to those seen in many of the other materials discussed in this chapter and reflect the difference in intermolecular bonding patterns along each axis of the crystal.

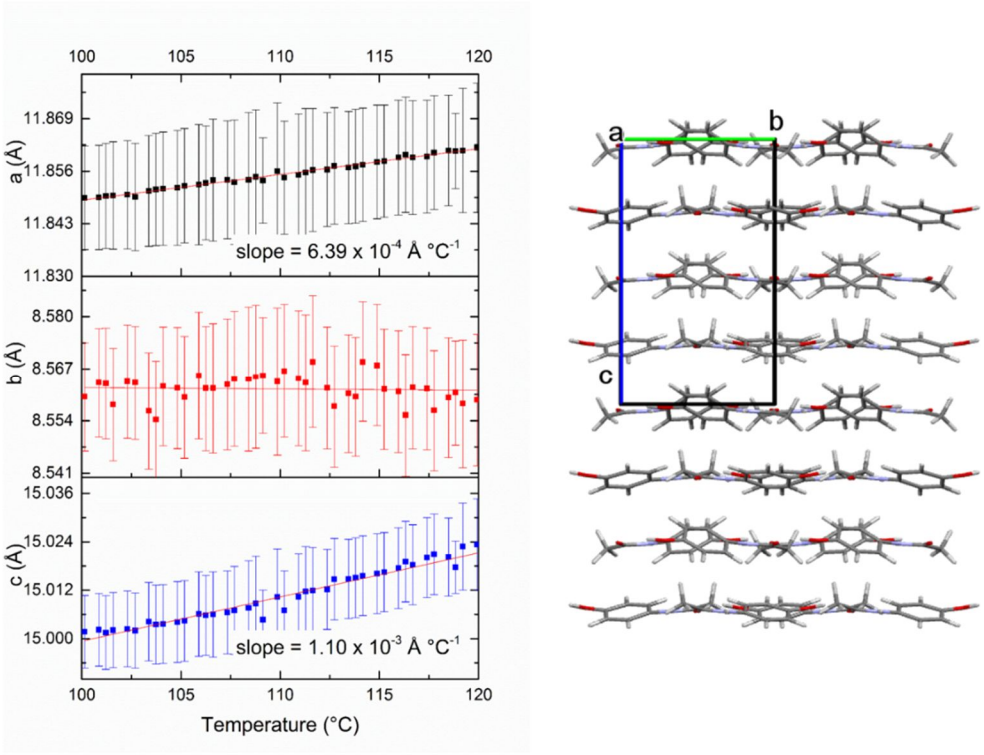

Figure 3-41. Plot of lattice constants as a function of temperature for a sample of paracetamol III with 10 % w/w HPMC K100M and the structure of PCM III viewed down the *a* axis.

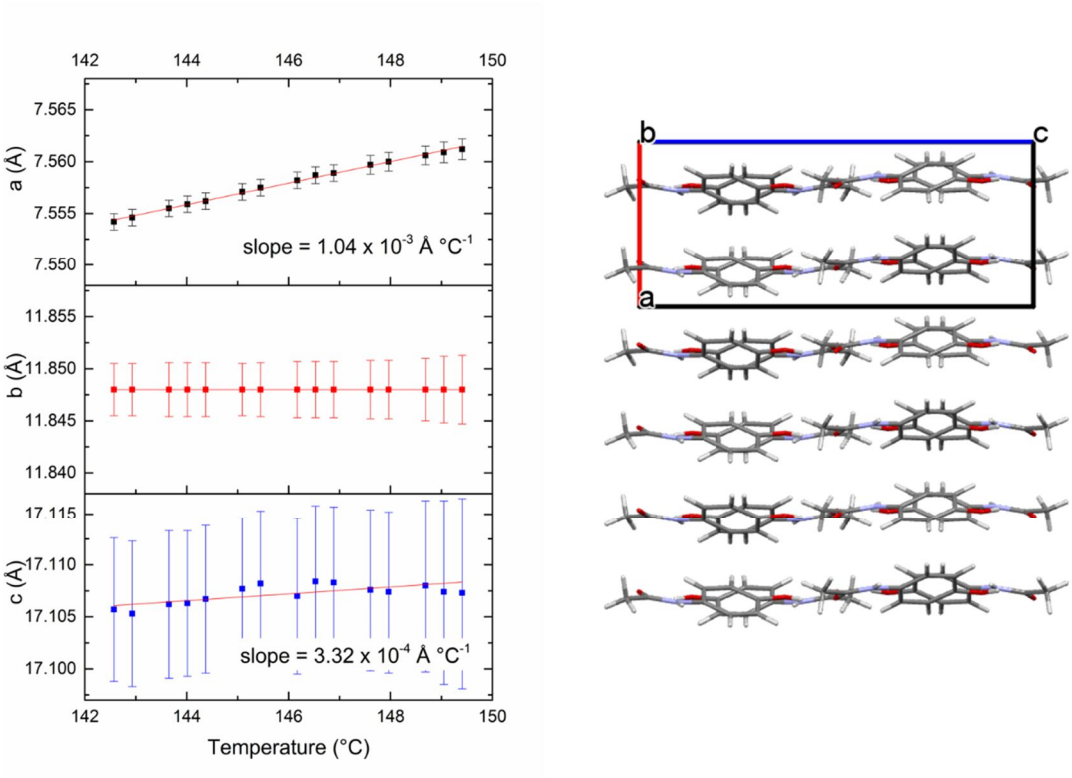

Figure 3-42. Plot of lattice constants as a function of temperature for a sample of paracetamol II with 10 % w/w HPMC K100M and the structure of PCM II viewed down the *b* axis.

3.3.3.2.2. Phase transitions

Plotting the integrated refinement data as a function of temperature (Figure 3-43) reveals that the sample remained amorphous until *ca.* 90 °C, at which point form III grew very rapidly to a maximum content at *ca.* 100 °C. Unlike the sample of paracetamol alone, in which form II grew in at *ca.* 70 °C, here it did not form until *ca.* 135 °C and appears to be the result of a conversion from form III, with none growing from the glass. These data suggest that the addition of HPMC to PCM is able to promote the growth of form III from the glass whilst suppressing the growth of form II.

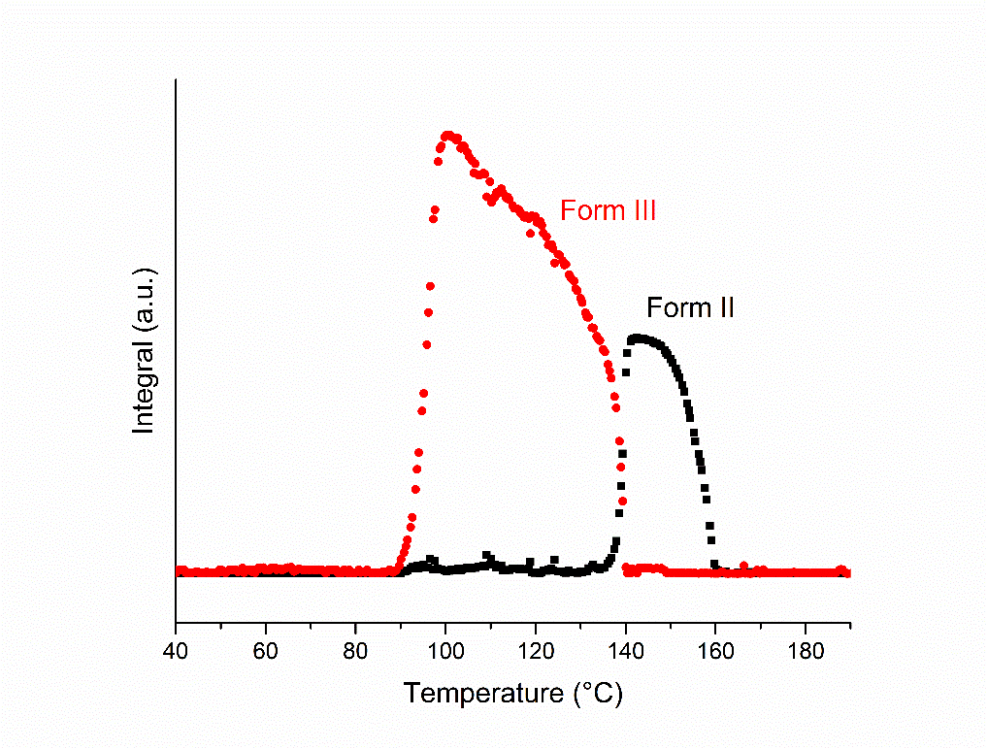

Figure 3-43. Plot of integrated total diffracted intensity for calculated patterns of paracetamol form II and form III as a function of temperature.

Giordano *et al.*[52] reported that upon heating a sample of PCM with 10 % HPMC K4M, at 93 °C it crystallised from the glass into a mixture of forms II and III. Following this at 139 °C form III underwent a melt-recrystallisation to form II (as opposed to the solid-solid conversion reported in the literature)[26,52,57,215] and finally form II melted at 156 °C. The DSC data presented by those authors is similar to that shown in Figure 3-38. Giordano suggested that both forms II and III crystallise from the glass, but offered no explanation of the assumption that form II is present. This work has shown this not to be the case and that amorphous paracetamol with 10 % HPMC K100M crystallises to pure form III at 90.9 °C. Giordano also neglected to discuss the cause of the first endotherm in the DSC trace (herein observed at 135 °C) and appear to have ascribed it to the III→II conversion, as have Rossi *et al.*[51] Here it has been shown to be a consequence of molecular rearrangements within the bulk form III present in the sample. The data are in agreement with the work of Gaisford *et al.*[57] who have shown that the addition of HPMC to PCM favours the formation of form III and acts to prevent the crystallisation of form II.

3.3.3.3. Paracetamol and Lactose

The aim of this experiment was to vitrify a sample of paracetamol and lactose by quench cooling the melt in the DSC pan and then subject the glass to a linear heating programme (10 °C min^{-1}) for analysis by DSC-XRD, analogous to the HPMC experiments described

in Section 3.3.3.2. It is immediately apparent when viewing the combined diffraction data (Figure 3-44(a)) that the quenching did not result in an entirely amorphous sample as there are Bragg reflections in the initial pattern. This is an unfortunate consequence of the experimental set up. There was no active cooling element attached to the calorimeter and so quenching could only be carried out by removing the sample from the cell and allowing it to cool to ambient temperature. Faster cooling would have produced a fully amorphous matrix.

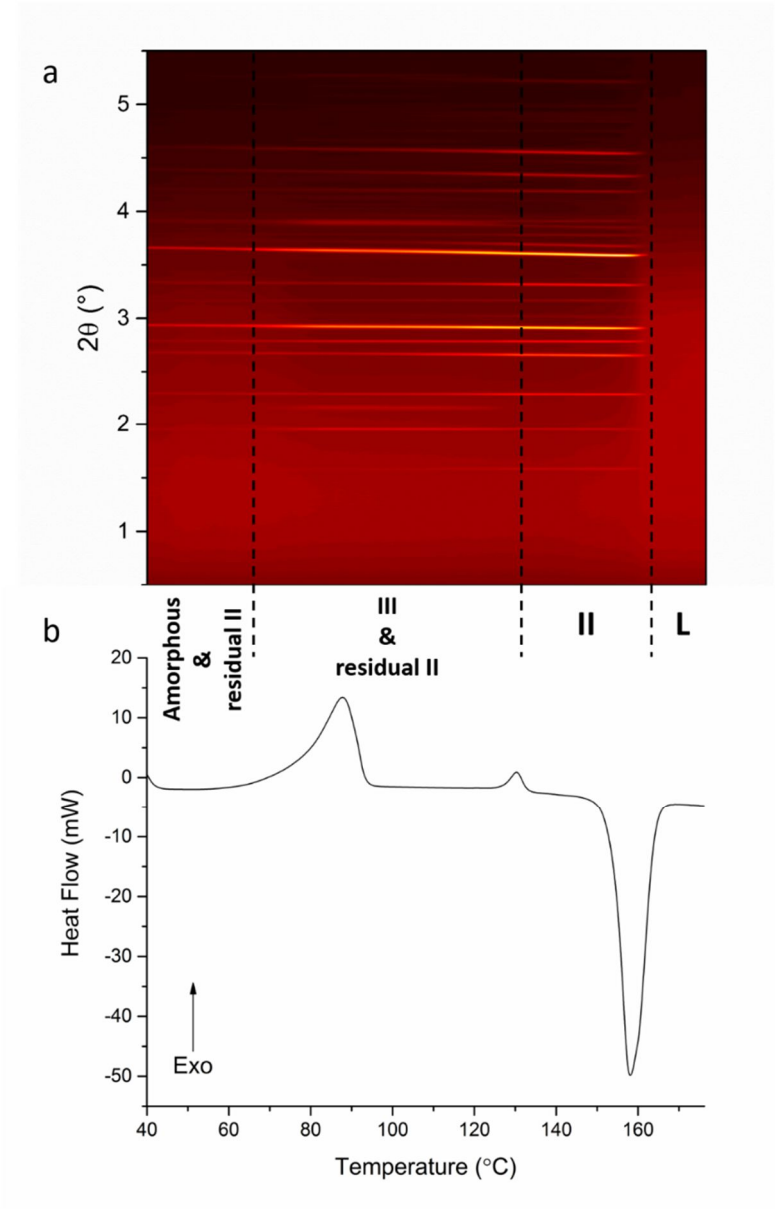

Figure 3-44. DSC-XRD data for a sample of paracetamol with 10 % w/w lactose heated from 40 °C to 176 °C at 10 °C min^{-1}. Dashed lines indicate position of phase transitions visible to both DSC and XRD.

Upon reheating of this sample, the DSC trace (Figure 3-44(b)) shows a broad exotherm with a maximum at *ca.* 85 °C, followed by a second exotherm at 130 °C and an

endotherm at just below 160 °C. The latter corresponds to the melt of form II, and XRD patterns collected above this temperature show no diffraction features. The two exotherms correspond to distinct changes in the XRD patterns. The first exotherm is coincident with the crystallisation of forms II and III from the amorphous material present. The second exotherm corresponds to the conversion of form III present into form II, resulting in pure form II above 130 °C; this persists until the mixture melts at 154.6 °C in agreement with the literature.[49,50,57] A parallel study of the melt synthesis of form III with lactose was undertaken using hyphenated *in situ* Raman-DSC (Figure 3-45), using similar protocols to the DSC-XRD studies.[210] The results obtained upon reheating the quenched melt are in support of the results reported here.

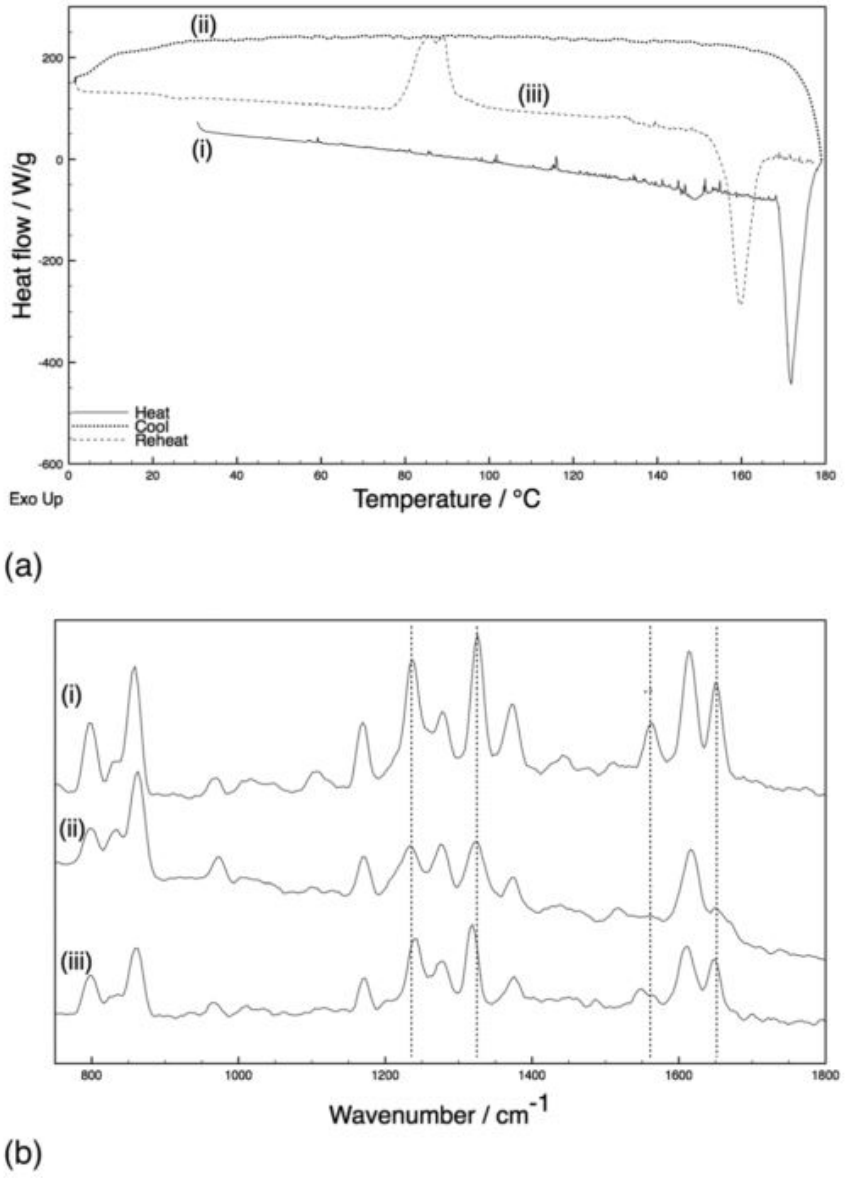

Figure 3-45. (a) DSC thermograms and (b) Raman spectra recorded at (i) 30 °C before heating [PCM I], (ii) 30 °C after quench cooling [amorphous] and (iii) 110 °C [PCM III] after reheating for a 10 % lactose containing sample of paracetamol (annotated with key spectral shifts observed). Reproduced with permission from ref [210].

3.3.3.3.1. Phase identification and transitions

Each pattern was analysed using the Rietveld method (selected datasets are given in Figure 3-46) and the area under the diffraction pattern from each phase was calculated (Figure 3-47). It appears from the pattern recorded at 40 °C that the initial sample following the quench was a mixture of both forms II and III. However, the intensities of all reflections were very low, indicating that the majority of the material was in fact amorphous, and the material was not an ideal powder so the familiar problem of poor intensity ratios was encountered again. Therefore it was concluded that there was no form III present in the initial sample. Had there been any form III it is likely that this would

have seeded the growth of more from the beginning and the integrated data plot would be similar to that of form II, with the quantity of form III increasing from the start of the experiment.

The increasing content of form II in the sample throughout the experiment up to the melting point is clear, as is the fact that form III grows in during the first exotherm and is converted to form II at the second. The formation of form II is a relatively gradual process that is continuous from the beginning of the experiment. This may be why there is no exotherm visible for the formation of II from the amorphous system. In contrast, the formation of III is a very quick process, occurring over a period of 20 °C (2 min) and so there is a large, sharp exotherm. The peak of the first exotherm corresponds to the point at which the growth of form III halts and it is at its maximum content for the experiment.

It is clear that the amount of form III present is largely constant between the two exotherms, despite the fact that form II crystals are also present. The amount of form II present increases throughout the experiment until the second exotherm, presumably a result of seeding of crystallisation from the amorphous material. Thus the lactose additive is able to stabilise form III even in the presence of form II crystals. The absence of form I throughout the experiment indicates the presence of lactose has either a stabilising effect on form III or destabilising effect on form I, in good agreement with the computational work carried out by Telford *et al.* and discussed in Section 3.3.3.

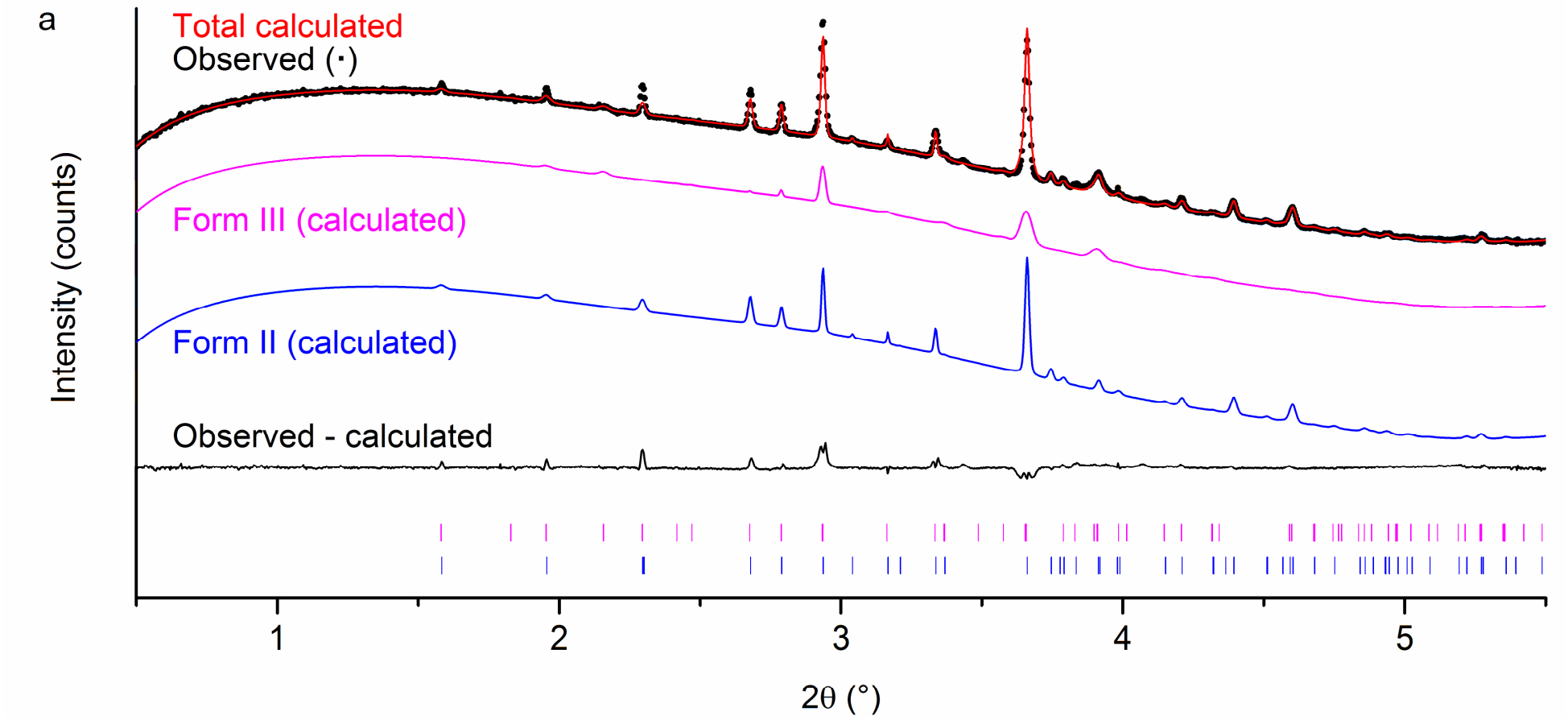
a
Total calculated
Observed (·)
Form III (calculated)
Form II (calculated)
Observed - calculated
Intensity (counts)
1
2
3
4
5
2θ (°)

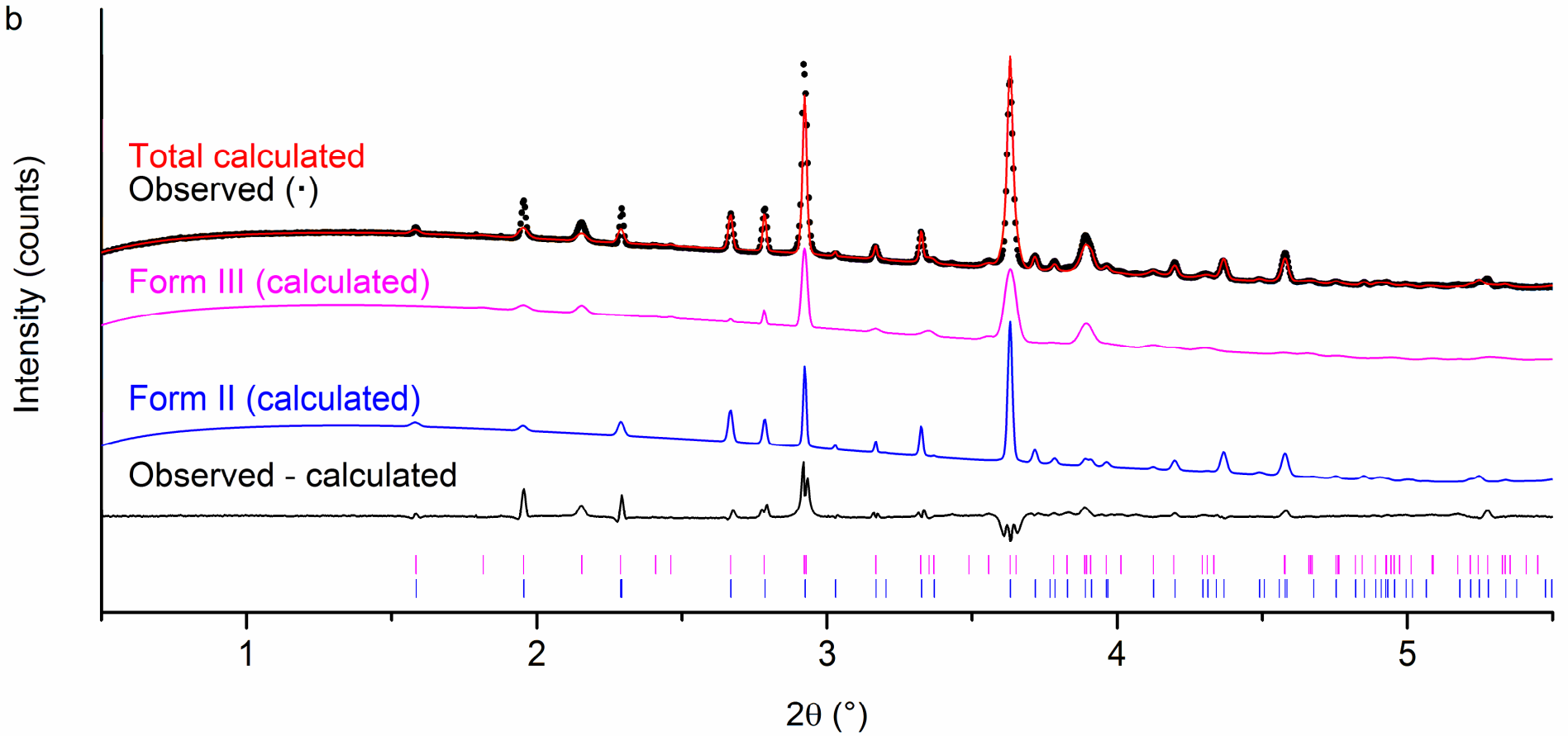
b
Intensity (counts)
Total calculated
Observed (·)
Form III (calculated)
Form II (calculated)
Observed - calculated
1
2
3
4
5
2θ (°)

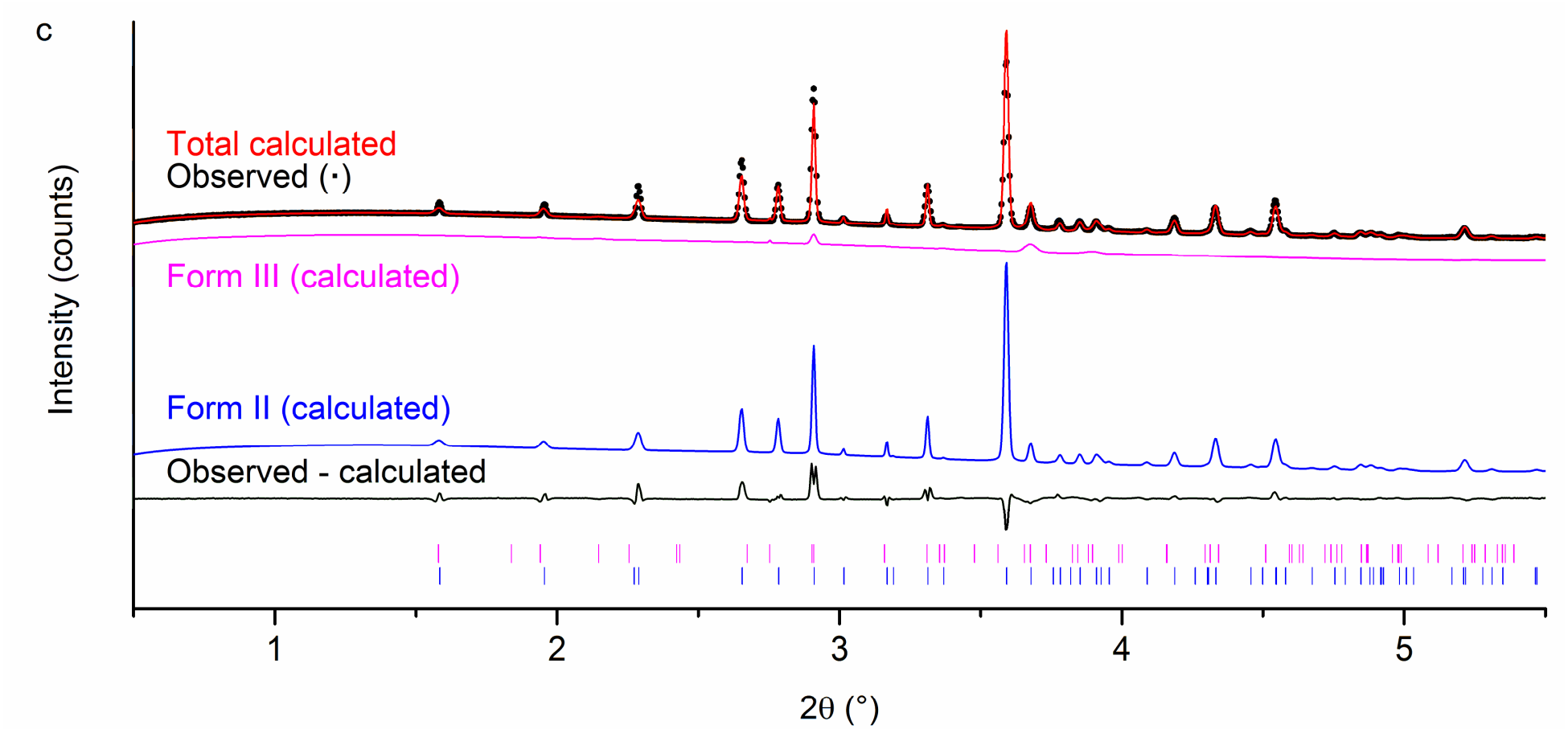

Figure 3-46 (a-c). Powder X-ray diffraction patterns for a mixture of paracetamol and lactose at (a) 40 °C, (b) 94 °C, and (c) 151 °C, including calculated patterns for the contribution of each polymorph present. The tick marks show the positions of allowed reflections from paracetamol forms II (blue) and III (pink).

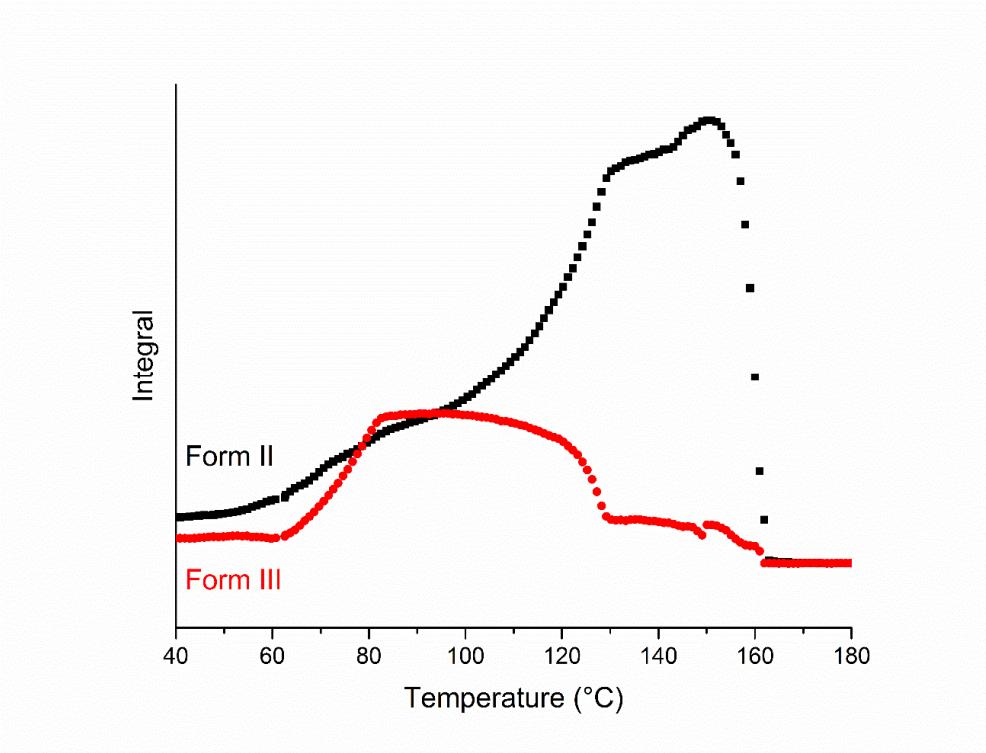

Figure 3-47. Plot of integrated total diffracted intensity for calculated patterns of paracetamol in a binary mixture with lactose as a function of temperature. Form II and form III. The continued presence of form III between 130 °C and 160 °C is a result of the poor intensity ratio of reflections resulting from a grainy sample.

As with previous samples, the lattice constants of the two polymorphs observed were plotted as a function of temperature and can be seen in Figure 3-48 and Figure 3-49. In the temperature range 100–120 °C the order of growth of the unit cell parameters of PCM III and the behaviour of the *a* and *b* constants is the same as that seen in the mixture with HPMC. However, there is a significant difference in the magnitude of growth in *c*, with that in the lactose mixture growing 75 % more per °C than in the HPMC mixture. Suggesting that HPMC may interact more strongly with PCM form III than lactose was predicted to by Telford and co-workers.[210]

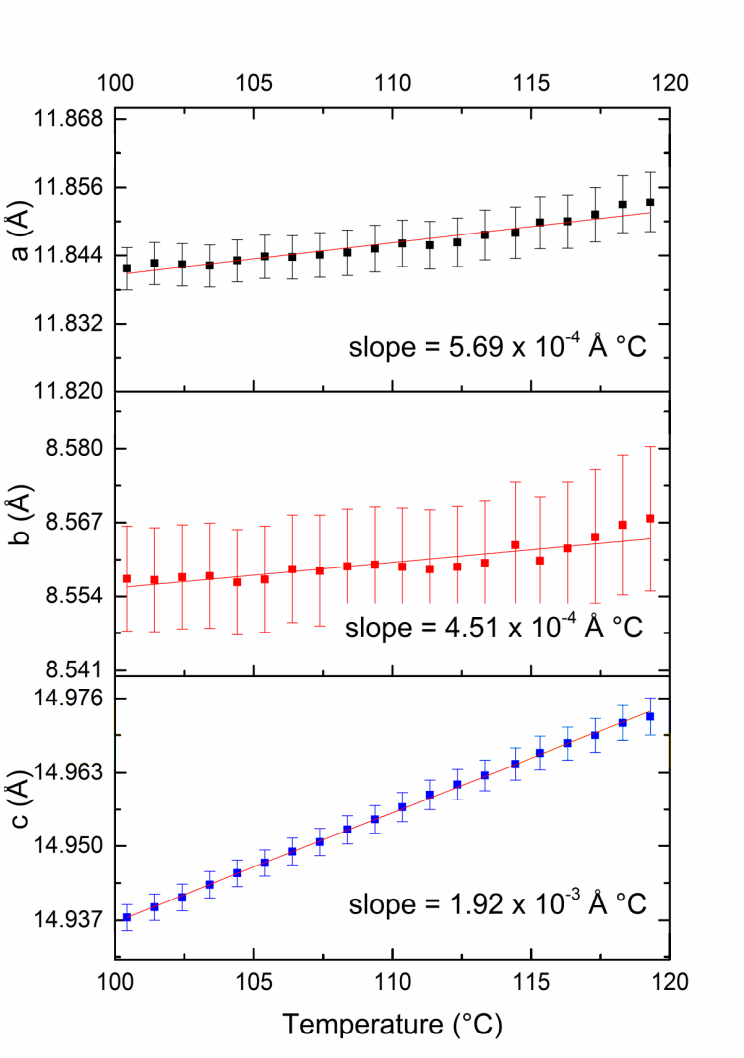

Figure 3-48. Lattice constants as a function of temperature for paracetamol III in a sample of quench cooled paracetamol with 10 % w/w lactose heated from ambient to 176 °C at 10 °C min^{-1}.

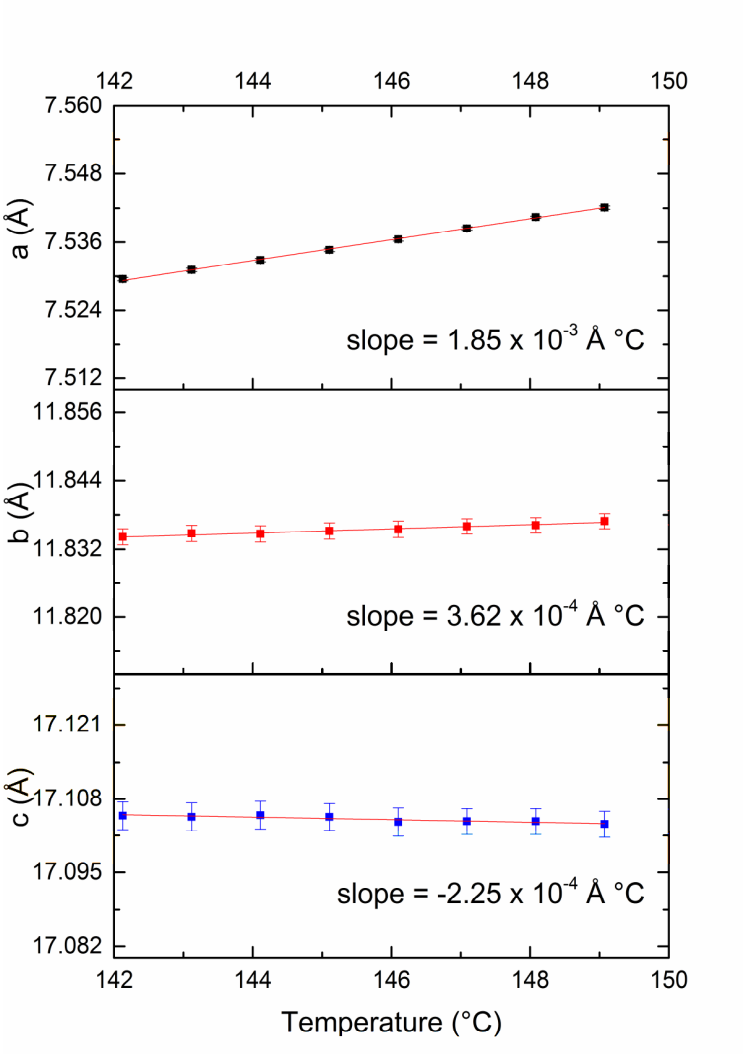

Figure 3-49. Lattice constants as a function of temperature for paracetamol II in a sample of quench cooled paracetamol with 10 % w/w lactose heated from ambient to 176 °C at 10 °C min^{-1}.

The data discussed in this section have been published in the journal *Chemical Communications*.[210]

3.3.3.4. Paracetamol and Trehalose

As with the paracetamol–lactose mixture, the quenching process did not produce a fully amorphous sample here. Upon reheating of this sample, the DSC data (Figure 3-50) shows a broad exotherm with a maximum at *ca.* 79 °C, followed by a second much smaller exotherm at 116 °C, a small endotherm at just below 160 °C and a much larger endotherm at 170°C. The first endotherm corresponds to the melt of form II, the latter corresponds to the melt of form I, and XRD patterns collected above this temperature show no diffraction features relating to the sample. These data are in good agreement with the literature.[53,192] The first exotherm corresponds to an increase in the intensity of

the reflections present, and the second to distinct changes in the XRD patterns. The first exotherm is coincident with the crystallisation of form II from the amorphous material present. The second exotherm corresponds to the conversion of form II present into form I, resulting in almost phase pure form I with some residual form II above 130 °C; this persists until the mixture melts.

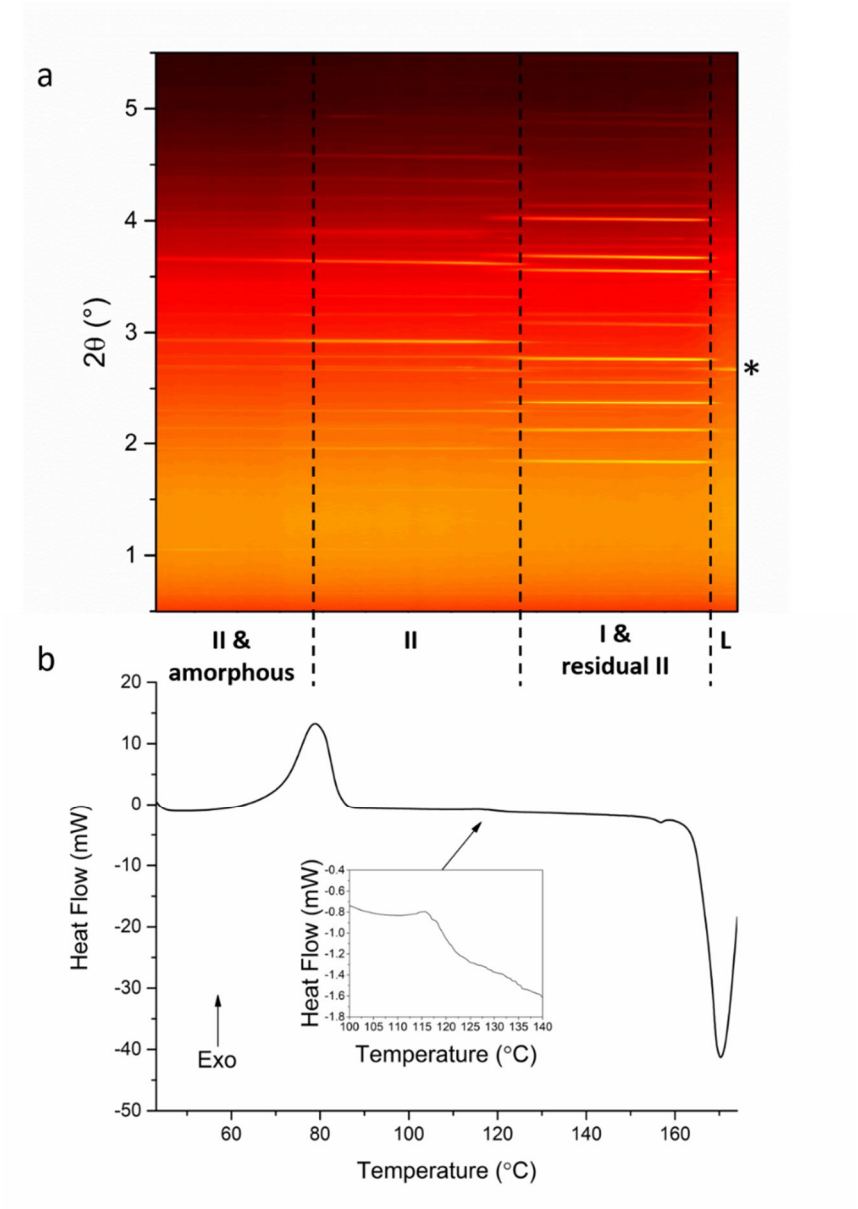

Figure 3-50. DSC-XRD data for a sample of paracetamol and 10 % w/w trehalose heated from 43 °C to 174 °C at 10 °C min^{-1}. Dashed lines indicate the position of phase transitions visible in both DSC and XRD. The reflection marked * in the liquid phase is a result of the experimental set up.

3.3.3.4.1. Phase identification and transitions

Selected Rietveld refinement datasets are presented in Figures 3-51 and phase quantification data are given in Figure 3-52. It is clear from the low relative intensities of

the reflections recorded at 43 °C (Figures 3-51) that the majority of the sample was amorphous. As with previous samples, the lack of active cooling prevented the attainment of an entirely amorphous matrix, and some reflections attributable to paracetamol polymorph II were recorded. There was however no form I present in the quenched sample.

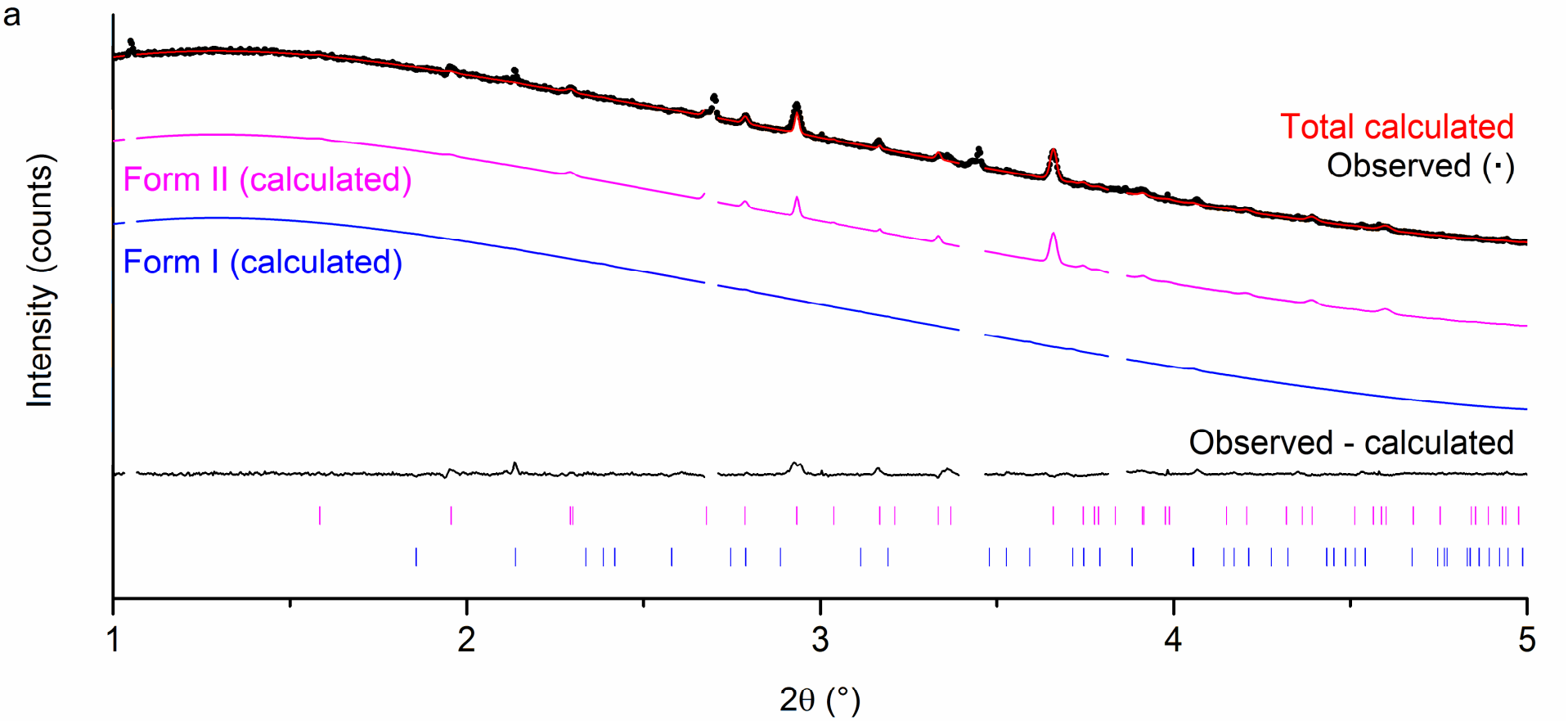
a
Intensity (counts)
Total calculated
Observed (·)
Form II (calculated)
Form I (calculated)
Observed - calculated
1
2
3
4
5
2θ (°)

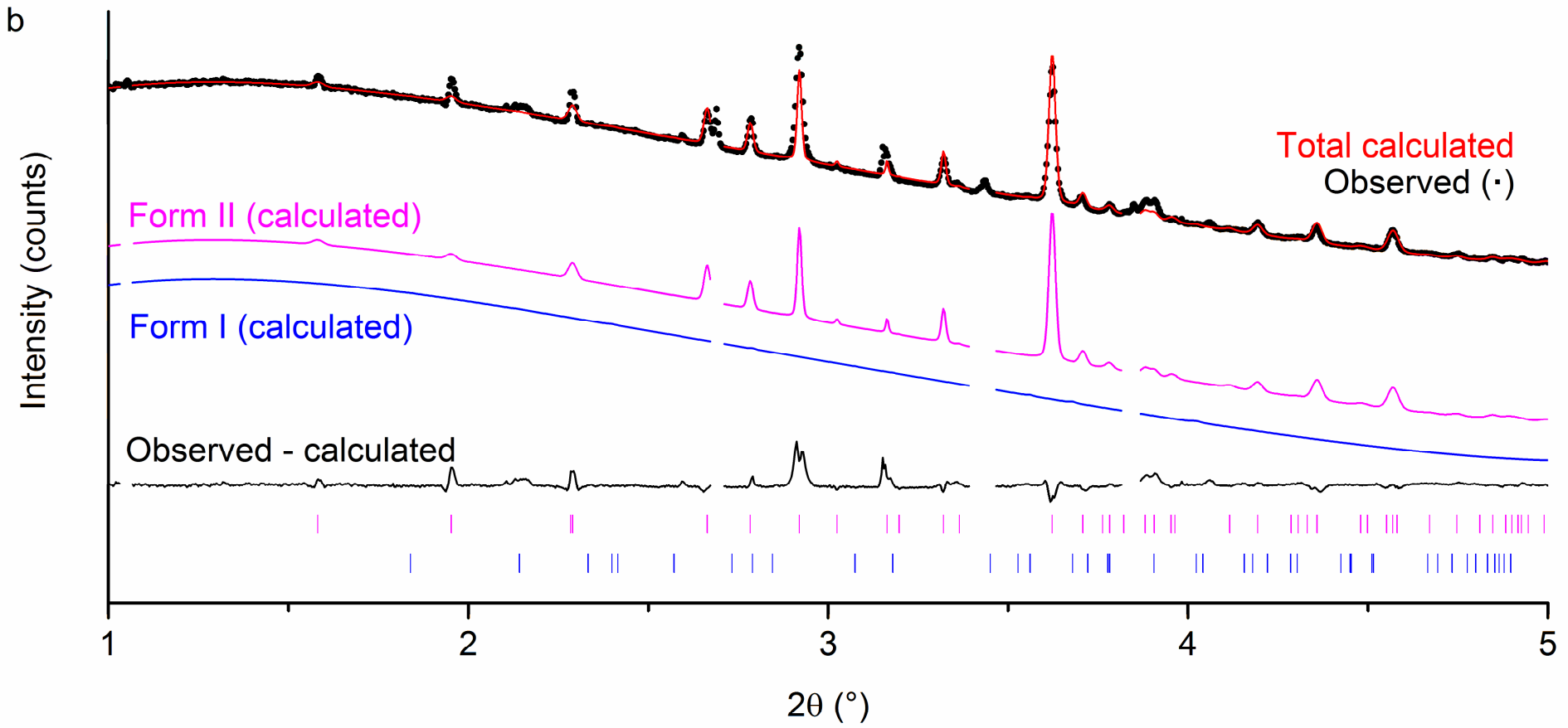
b
Intensity (counts)
Total calculated
Observed (·)
Form II (calculated)
Form I (calculated)
Observed - calculated
1
2
3
4
5
2θ (°)

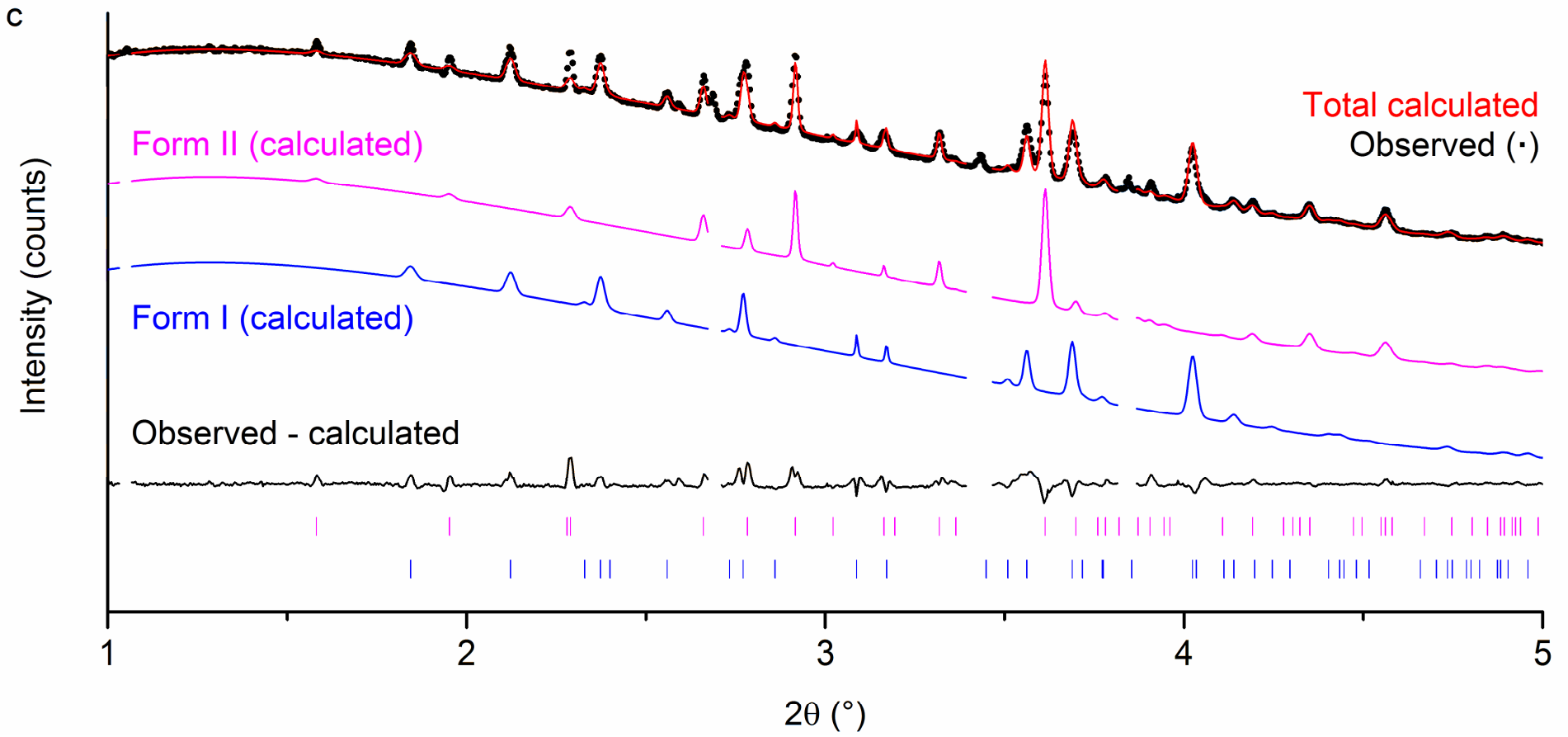
c
Intensity (counts)
Total calculated
Observed (·)
Form II (calculated)
Form I (calculated)
Observed - calculated
1
2
3
4
5
2θ (°)

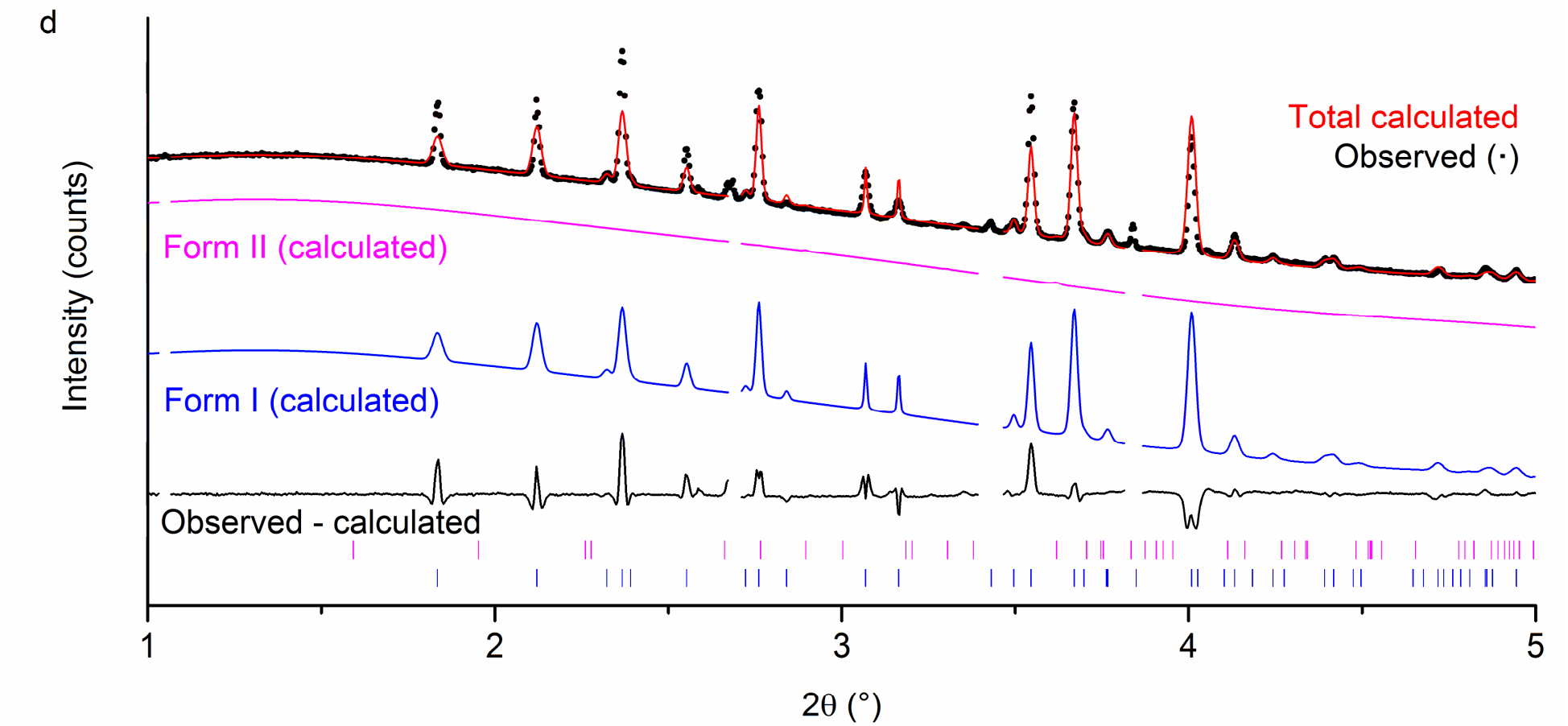

Figures 3-51 (a-d). Powder X-ray diffraction patterns for a mixture of paracetamol and trehalose at (a) 43 °C, (b) 112 °C, (c) 124 °C, and (d) 162 °C including patterns calculated by Rietveld refinement for the contribution of each polymorph present. The tick marks show the positions of allowed reflections from paracetamol forms I (blue) and II (pink). Gaps in the data are regions excluded from the refinements due to reflections arising from the experimental set up.

The absence of form I remains constant below 113 °C, whereas the reflections representing form II grow stronger in intensity as the sample is heated. At 112 °C (Figures 3-51 (b)) the pattern recorded clearly shows that the form II content of the sample has grown significantly whilst there is still no form I present. This is a result of form II growing from the amorphous phase, in all likelihood by seeding from the residual form II present in the sample following quenching of the melt. This growth can be seen clearly in (Figure 3-52).

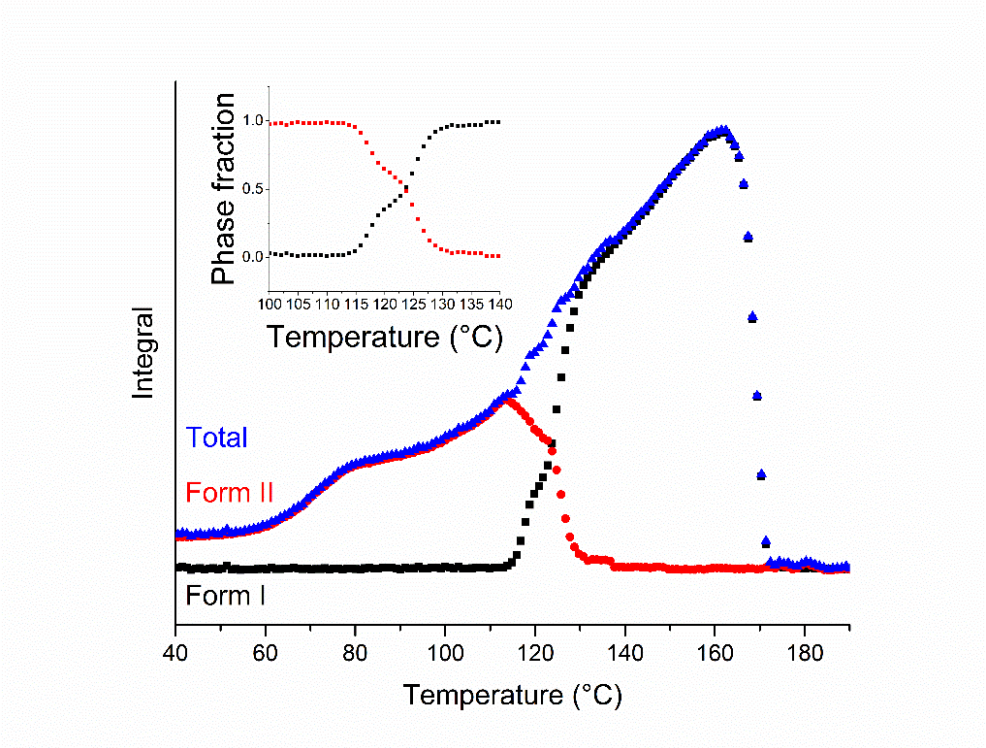

Figure 3-52. Plot of integrated total diffracted intensity for calculated patterns of paracetamol in a binary mixture with trehalose, as a function of temperature. Form I, form II and the sum of forms I and II. The inset shows a plot of phase fraction as a function of temperature. Gaps in the data are regions excluded from the refinements due to reflections resulting from the experimental set up.

The quantity of form II in the sample reaches its maximum at 113 °C and then immediately begins to decline. At the same temperature Bragg reflections from form I begin to grow in, and rapidly increase in intensity. Patterns recorded at the point at which the phase quantity curves intersect (Figures 3-51 (c)) show strong sharp reflections belonging to both polymorphs and the sample at this temperature (*ca.* 124 °C) is effectively a 1:1 ratio of the two forms. It is obvious from the plot of phase fraction as a function of temperature that the sample does not undergo a wholesale melt and that form II is converting to form I between 113 °C and *ca.* 131 °C. Interestingly, the conversion appears to occur as a two-step process. The initial growth of form I is much faster than

the decline in form II, suggesting that it is growing from the residual amorphous material as well as transforming from form II.

At 124 °C (the point of intersection (Figures 3-51 (c))) the rates of growth of I and reduction of II increase significantly. It may be that, at this temperature, the energy in the system is sufficient that the conversion occurs by a different, faster mechanism than below 124 °C. Unfortunately, due to the growth of form I from both amorphous material and conversion from form II it is impossible to separate the contribution of the two phase transformations. The fact that the amount of form I present continues to grow, even after the almost total disappearance of form II, up until its melting temperature proves that some glass remained throughout the experiment. It is interesting that the growth of polymorph I from the glass results in no exothermic events in the DSC thermogram. This may be due to the large temperature range over which the crystallisation occurs. As it is constant and occurs throughout the experiment the exotherm would be too broad to be easily visible by DSC and may in fact be characterised by a change in the baseline of the data. Another interesting feature is the small endotherm in the trace resulting from the melt of form II. The X-ray data suggest that all form II has converted to form I at *ca.* 131 °C, well below the melt at 154 °C. The most likely explanation for this is that some of the sample in the pan remained as form II but none of it was in the beam and so no characteristic Bragg reflections of form II were recorded. This suggests that the sample may not have been homogeneous. Paracetamol has been shown by Nanubolu and Burley[194] to crystallise from the glass to polymorphs I and II *via* surface crystallisation if left uncovered but to form III by crystallisation from the bulk if confined between a glass slide and coverslip. It may be that, in this work, the open pan allowed some surface crystallisation whilst the remainder of the material, which was confined by the pan, crystallised to form III from the bulk.

3.3.3.4.2. Unit cell expansion

It appears from these data that trehalose stabilises form II at the expense of form III. This is also the only sample in which PCM polymorph I was observed, suggesting that trehalose not only stabilises form II at the expense of form III but also that it promotes the conversion of form II to form I. As the conversion occurs at 116 °C it was not possible to plot meaningful data for the lattice constants of form II as a function of temperature over the same range as the mixtures with HPMC and lactose (142–150 °C) for comparison. However, plots over different temperature ranges can be seen in Figure 3-53 and Figure 3-54. Polymorph II follows the same trend seen in the other paracetamol samples, with little growth in the *b* and *c* directions and 1.09 x 10^{-3} Å $°C^{-1}$ in *a*. This is

strikingly similar to the growth in the same direction in the sample mixed with HPMC (1.04×10^{-3} Å $°C^{-1}$), and suggests that these two additives may interact with the drug in a similar way. These findings also support the theory that lactose destabilises form II in the *a* direction, effectively weakening the interactions between the pseudo-sheets so that they undergo greater separation upon heating.

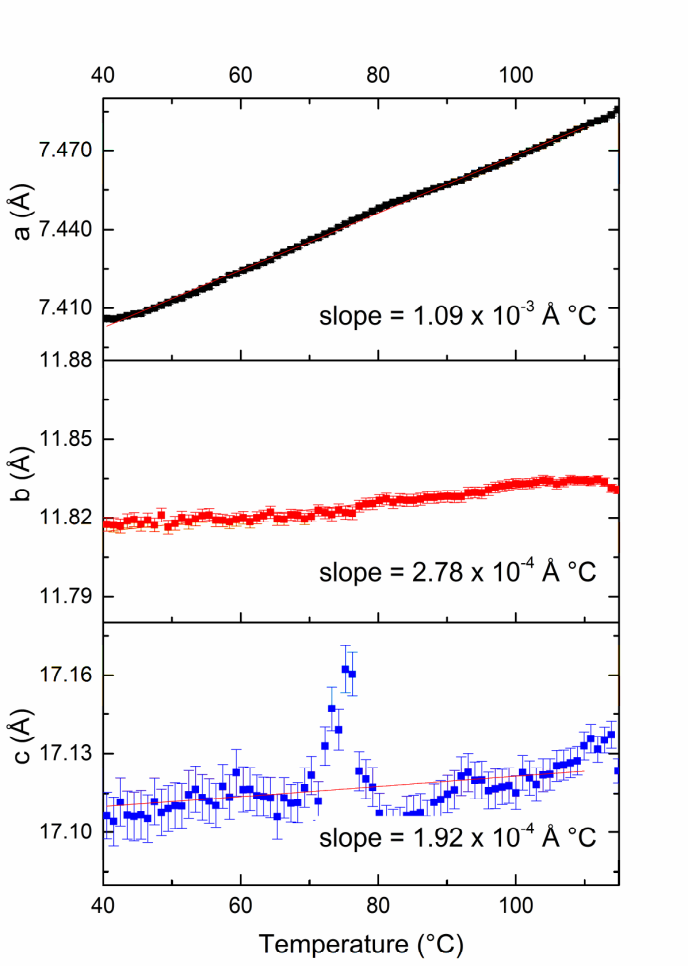

Figure 3-53. Lattice constants as a function of temperature for paracetamol II in a sample of quench cooled paracetamol with 10 % w/w trehalose heated from ambient to 175 °C at 10 °C min^{-1}.

Observation of the growth of the unit cell of form I as it was heated (Figure 3-54) reveal that there is little growth in either *a* or *c*, yet *b* expands significantly at a rate of 1.75×10^{-3} Å $°C^{-1}$. The structure of paracetamol form I has been described as pleated sheets in the *ac* plane, which are stacked along *b* (Figure 3-54).[47] Thus, the heat expansion behaviour observed is a result of the separation of the pleated sheets, which are held together more weakly than the molecules within the sheets. This is much like the behaviour seen here and with both HPMC and lactose for form II, and for form III in the systems with HPMC and lactose.

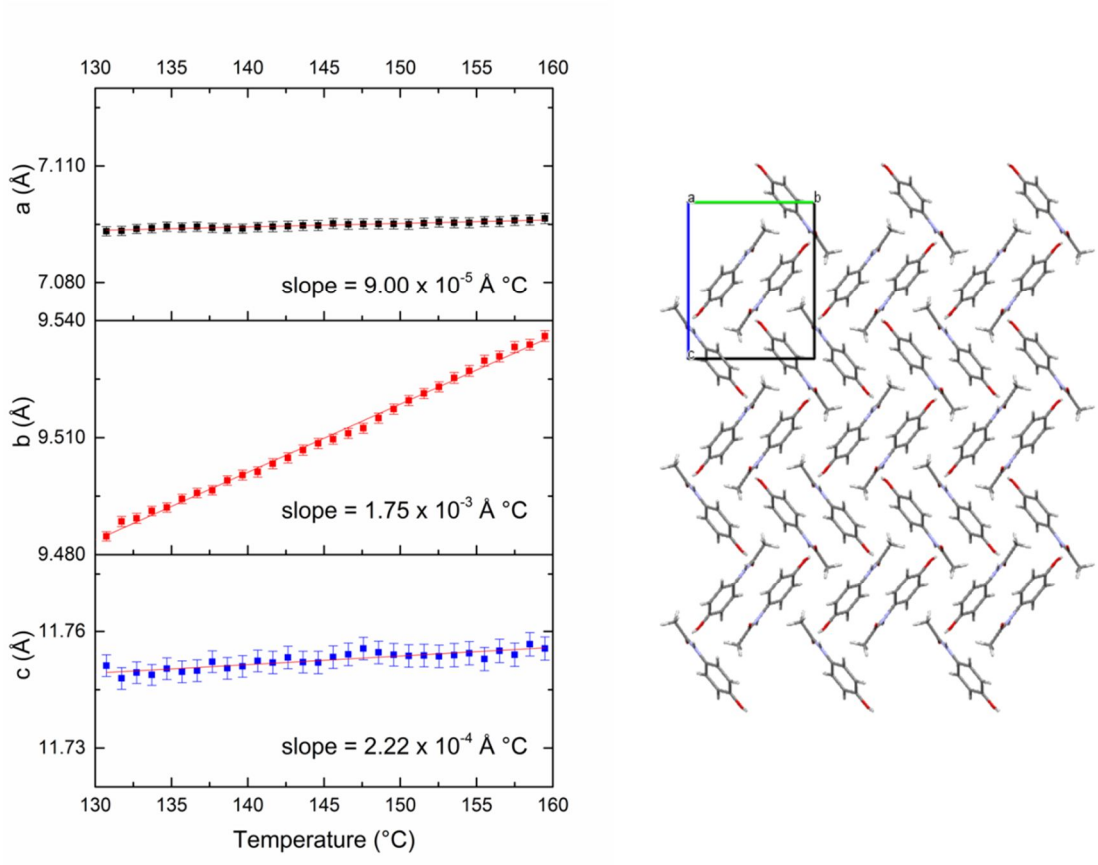

Figure 3-54. Lattice constants as a function of temperature for paracetamol I in a sample of quench cooled paracetamol with 10 % w/w trehalose heated from ambient to 175 °C at 10 °C min^{-1} and a graphical representation of the structure of form I viewed down the *a* axis of the unit cell.

3.4. Conclusions

Heat induced phase transitions in DHC II, CBZ II, CBZ IV and PCM glass were studied by simultaneous DSC-XRD, following which PCM glasses prepared with the addition of 10 % w/w of one of three sugar based excipients (HPMC, lactose and trehalose) were examined. The phase transitions in all the systems investigated have been shown to be more complex than previously reported. The combination of XRD and DSC data initially allows for identification of the phases present at any temperature, including during transformations. Furthermore, batch analysis of the data has revealed that many transitions considered to occur *via* a solid–solid pathway, actually involve what may be considered a transitional melt phase. However, this melt is so quickly followed by recrystallisation to the subsequent crystalline phase that regions of the sample melt and recrystallise before other regions begin to melt. Consequently the presence of crystalline material in the sample is continuous, hence the prior solid–solid assumption.

Batch refinements have also allowed monitoring of the expansion of the unit cell as a function of temperature of many of the polymorphs. It has been shown that these data

can then be used in conjunction with structural information to confer a directional order of stability in relation to the lattice constants. Perhaps predictably the dimensions which contain stronger intermolecular bonding (e.g. H-bonds) have shown smaller growth per °C than those with weaker interactions (e.g. $\pi\cdots\pi$). Additionally, growth in unrelated polymorphs of different molecules is has proven to occur at similar rates.

DHC II was shown to undergo a conversion to form I by what appears to be a localised melt phase. CBZ IV converted to form I at 182 °C, by either a solid–solid pathway or a localised intermediate melt phase. CBZ II was in fact found to contain a small amount of form III. Form II converted to form I at 119 °C by a pathway that appears to have included some melting and form III underwent what appears to be a part melt-recrystallisation and a part sublimation-recrystallisation to form I.

Pure PCM glass crystallises to both form II and form III upon heating, although much more rapidly to form III which then goes on to immediately convert to form II at *ca.* 125 °C. Form II goes on to melt at 158 °C. The addition of HPMC to PCM proved to stabilise form III which crystallised alone from the glass and remained phase pure until *ca.* 135 °C, at which point it converted to form II which melted at *ca.* 160 °C. No form II grew from the glass.

PCM with the addition of lactose was incompletely vitrified and the initial sample contained some residual form II, however even in the presence of this polymorph form III grew in from the amorphous and remained stable until 130 °C, at which point it converted to form II. Thus it seems lactose is able to stabilise form III even in the presence of form II crystals.

As with the sample containing lactose, that mixed with trehalose was not completely vitrified and there remained some form II crystals. Upon heating, at *ca.* 70 °C form II crystallised from the glass and subsequently converted to form I at 116 °C There remained a small amount of form II in the sample, which then melted at 160 °C, followed by form I at 170 °C.

For PCM the introduction of 10 % w/w of different plasticisers to the drug has demonstrated an ability to selectively alter the rate of growth in specific axes as well as selectively stabilising polymorphs. With HPMC and lactose stabilising form III and trehalose stabilising form II and promoting the growth of form I.

4. Novel pharmaceutical co-crystals

4.1. Introduction

Co-crystallisation is a method by which the chemical and/or physical properties of a molecule can be altered without making or breaking any covalent bonds.[58] This can directly affect the physical properties of a compound and may improve its solubility and/or rate of dissolution. As a consequence of the substance existing in a crystalline form, co-crystals are likely to be more stable, reproducible and easier to purify than other solid forms of a drug and therefore more desirable.[58] Aakeröy defined a co-crystal as "a crystalline material that consists of different molecular (and electrically neutral) species held together by non-covalent forces",[216] and Vishweshwar *et al* defined pharmaceutical co-crystals as "co-crystals that are formed between a molecular or ionic API and a co-crystal former that is a solid under ambient conditions,".[67] It is important to ensure that a suitable non-toxic co-former is used that will not interact covalently with the drug, to alter its chemical structure, and that a stoichiometric ratio of all components is used.[58]

Isonicotinamide (INCT, Figure 4-1) has been shown to exhibit anti-inflammatory activity[217] and has been associated with a reduction of Huntington disease related cell toxicity.[218] More commonly it has been used extensively as a pharmaceutical co-crystal co-former to improve the solubility of an active pharmaceutical ingredient (API) without compromising its efficacy or stability,[219–228] and is a component of at least 40 co-crystals reported in the Cambridge Structural Database (CSD).[229,230] The pyridine derivative's utility as a co-crystal co-former stems from its distinct but relatively strong hydrogen bonding moieties (the pyridine nitrogen and the amide) and its ability to form crystals with different components.[231]

Due to the aforementioned properties, INCT was employed in this work with a range of co-formers. Vishweshwar *et al* have reported data for a 1:1 co-crystal[232] between the antimicrobial and antioxidant[233] API 4-hydroxybenzoic acid (HBA, Figure 4-1) and INCT formed by crystallisation from hot methanol. 4-hydroxyphenylacetic acid (HPAA) and 3,4-dihydroxyphenylactic acid (DHPAA, Figure 4-1) are also antioxidants[234] and were chosen for study as they are analogues of HBA and so were presumed to have high potential for co-crystallisation with INCT. L-ascorbic acid (LABA), another antioxidant, is taken as a supplement to aid wound healing[235] and to prevent scurvy[236] and was chosen as it has six hydrogen bonding moieties and so a high potential for co-crystallisation.

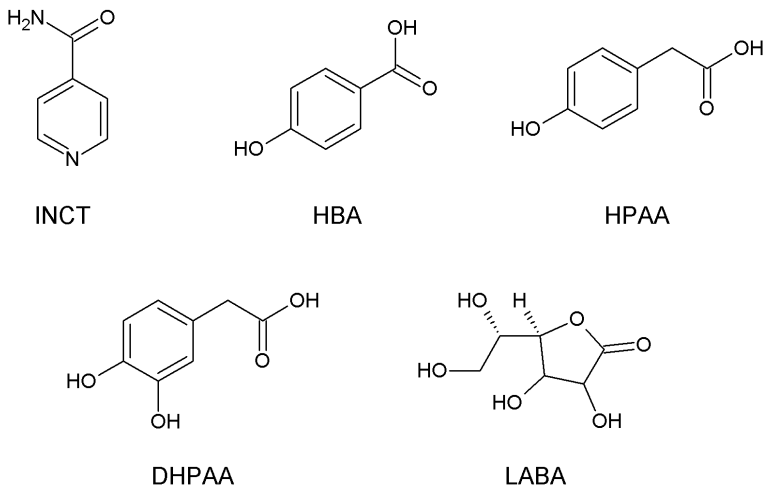

Figure 4-1. Chemical structures of INCT, 4-hydroxybenzoic acid (HBA), 4-hydroxyphenylacetic acid (HPAA), 3,4-dihydroxyphenylacetic acid (DHPAA), and L-ascorbic acid (LABA).

There are a range of routes which have been explored for co-crystal formation, all of which have advantages and disadvantages. Traditionally, solvent evaporation has been the most commonly employed method for the preparation of pharmaceutical co-crystals.[237] However, due to the use of organic solvents it is ecologically unsound. It is also time consuming, with evaporation of the solvent occurring over days and weeks required just to grow a single crystal. Recently, thermal inkjet printing has proven to be a rapid method for the preparation of pharmaceutical co-crystals, with Buanz *et al* suggesting "the technique would appear to offer potential for early phase pharmaceutical co-crystal screening".[81] Inkjet printing takes minutes to produce crystals of sufficient quantity and high enough quality for analysis (albeit inferior to crystals grown by solvent evaporation). However, the materials must first be in solution before they can be printed and so the "green" problem remains.

Grinding or co-grinding of stoichiometric amounts of two dry powdered crystalline materials has been known to produce co-crystals since as early as 1893, although it was unpopular in academic laboratories until the late 2000s.[104] The method has advantages over solvent evaporation and thermal inkjet printing in that it is both fast (over the minutes scale) and clean/green (requires no solvent). However, it produces fine powders and not the single crystals required for full structure elucidation by X-ray diffraction.

In 2013 Yamashita and co-workers examined a number of binary systems for their ability to form co-crystals as a result of heating.[86] Using binary phase diagrams they identified two possible routes to forming a co-crystal which could be characterised by different thermal events, easily investigated via DSC. They state that only a mixture capable of forming a co-crystal will exhibit exothermic events. That is, crystallisation is an exothermic event and so the formation of a co-crystal will result in an exothermic signal

on a DSC thermogram. Two stable crystalline species which cannot form a co-crystal will only melt and give one or two endothermic signals, characteristic of melting (this is not true for metastable species, however). Yamashita *et al.* supported their DSC analysis with X-Ray-DSC and polarisation microscopy and found that all of the seventeen systems reported to be capable of co-crystal formation exhibited an exothermic peak in the DSC data. Interestingly, no exothermic peaks were seen in the three systems in which co-crystals had never before been reported, suggesting this is a good indication of the existence of co-crystals.

This chapter will discuss data collected during attempts to co-crystallise INCT in combination with each of the four antioxidants *via*: solvent evaporation, thermal inkjet printing, ball milling and the simultaneous DSC-XRD technique discussed in Chapter 2.

4.2. Materials and Methods

4.2.1. Materials

4-Hydroxyphenylacetic acid, 3,4-dihydroxyphenylacetic acid, 4-hydroxybenzoic acid, L-ascorbic acid, isonicotinamide and absolute ethanol were obtained from Sigma-Aldrich and used as received. Distilled water was used when water was required.

4.2.2. Fourier transform infrared spectroscopy (FTIR)

FTIR spectroscopy was conducted on a Perkin Elmer Spectrum 100 instrument. All spectra were recorded between 650 and 4000 cm^{-1} with 64 scans at a resolution of 4 cm^{-1}.

4.2.3. Thermogravimetric analysis (TGA)

TGA measurements were performed using a TA Instruments Discovery machine. Samples were loaded into aluminium cups and heated from ambient to 300°C at a 10°C min^{-1} with a nitrogen purge of 25 mL min^{-1}.

4.2.4. Single crystal X-ray diffraction (XRD)

X-ray diffraction experiments were performed by Dr. Gary Parkinson on an Oxford Diffraction, Xcalibur microfocus NovaT X-ray diffractometer, using Cu Kα radiation. Titan CCD image data were processed by CrysalisPro (Agilent Technologies), and the structure was solved by direct methods using ShelXS[238] and refined using SHELXL.[239]

All non-hydrogen atoms were refined by full-matrix, least squares with anisotropic temperature factors, with hydrogen atoms positioned using normal geometry.

4.2.5. Powder X-ray Diffraction (PXRD)

PXRD was carried out at room temperature on a Rigaku Miniflex 600 diffractometer at 40 kV and 15 mA fitted with a CuK*α* source, over the range 3 to 50° with a 0.02° step size and 2° min^{-1} scan rate.

4.2.6. Differential scanning calorimetry (DSC)

DSC measurements were performed on a TA Instruments Q2000 machine. Samples were loaded into Tzero aluminium pans with non-hermetic lids. Calibration was performed with a certified indium standard according to the manufacturer's instructions. Samples were heated to a maximum of 220°C at 10°C min^{-1} with a nitrogen purge of 50mL min^{-1}.

4.2.7. DSC-XRD

DSC-XRD data were collected and analysed using the methods described in Chapter 2.

4.2.8. Single crystal growth *via* solvent evaporation

INCT and each of the co-formers were combined in molar ratios determined by work carried out previously in the group and specified in Table 4-1, and dissolved in ethanol to the highest concentration possible (i.e. ethanol was added whilst stirring until all solids had dissolved). The solutions were transferred to glass vials sealed with Parafilm. The Parafilm was pierced with a needle to allow the solvent to evaporate. Further experiments were performed where in place of the glass vials solutions were transferred to 96-well polymerase chain reaction (PCR) plates, which were covered with Parafilm and pierced in the same manner.

Samples were stored at ambient temperature in a fume cupboard, 9 °C in an incubator, 5 °C in a fridge, or 4 °C in an incubator. Selected single crystals were analysed by XRD.

Table 4-1. Molar ratio in which INCT and co-formers were mixed.

Co-former	Co-former: INCT
HBA	1:1
HPAA	1:2
DHPAA	1:1
LABA	1:1

4.2.9. Thermal inkjet printing

Solutions (3 % w/v in 10 mL of a solvent system comprising EtOH; EtOH:H_2O, 9:1 (v/v); EtOH:H_2O, 7:3 (v/v)) of each of the binary mixtures were loaded into an empty HP 344 Tri-color ink cartridge (foam removed) in an HP Officejet 100 mobile printer. A 10 cm x 10 cm square was printed onto an A4 acetate sheet at 300 dpi (fast draft) with 20 overlays. The printed crystals were removed from the acetate sheet with a spatula and analysed with FTIR, PXRD, TGA and DSC. A more detailed description of the method used can be found in the literature.[240]

4.2.10. Heat induced co-crystallisation

Binary mixtures of INCT and the four co-formers in the ratios described in Table 4-1 were prepared using a vortex mixer. A second set was prepared by grinding each of the components separately in a pestle and mortar for 30 seconds. Both sets were analysed by FTIR, PXRD and TGA prior to heating to rule out any spontaneous interactions or any caused by the mixing process. Samples were heated by DSC using the instrument and parameters described in Section 4.2.4. The experiments were repeated using the DSC-XRD experimental set up described in Chapter 2.

4.2.11. Co-crystallisation by ball milling

As received samples of all raw materials were loaded into the grinding jar of a Retsch MM 200 ball mill and milled at 20 Hz for 15 minutes, INCT and LABA were milled for 1 minute as any longer resulted in vitrification.

4.3. Results and Discussion

4.3.1. Crystallisation from Solution

Attempts were made to grow co-crystals of INCT with the four co-formers by evaporation from solution in ethanol. The aim was not to investigate an exhaustive collection of methods and solvents in an effort to grow single crystals, but rather to produce single

co-crystals using the simplest procedures possible. A prior study has shown INCT and HBA are amenable to co-crystallisation from hot methanol,[232] however there are no reports of co-crystal formation between INCT and any of the other three materials. Although, previous work in the group has produced co-crystals between INCT and DHPAA.

Many attempts were made at growing co-crystals from each of the four systems, initially with limited success due to the rate of solvent evaporation. The best results were obtained by transferring the solutions to 96-well PCR plates and storing at 4 °C. Single crystals of sufficient quality for structure determination were grown between INCT and the remaining three co-formers. Diffraction data for each of the co-crystals grown can be seen in Table 4-2.

Table 4-2. Structural information for co-crystals of INCT with four co-formers (HBA, HPAA, DHPAA, and LABA) and a model from the CSD (VAKTOR).[232] All experimental crystals were grown from ethanolic solutions.

	VAKTOR	INCT-HBA *This work*	INCT-HPAA	INCT-DHPAA*	INCT-LABA**
Crystal system	Monoclinic	Monoclinic	Triclinic	Triclinic	Orthorhombic
INCT:co-former ratio	1:1	1:1	2:1	1:1	1:2
T / °C	-120	-166	-73	-	-168
Space group	$P2_1/c$	$P2_1/c$	P-1	P-1	$P2_12_12_1$
a / Å	6.0729(1)	10.5720(3)	6.7543(6)	5.4891(3)	5.1690(5)
b / Å	9.4013(2)	29.8495(9)	12.3422(14)	9.8742(6)	11.4943(9)
c / Å	22.0762(4)	7.6215(3)	12.6520(12)	13.1825(9)	33.570(2)
α / °	90	90	111.976(10)	71.679(6)	90
β / °	111.185(10)	97.887(3)	96.764(8)	82.455(5)	90
γ / °	90	90	99.604(9)	89.408(4)	90
Cell volume / Å^3	1260.40	2382.36	945.448	672.04	1994.53
Z	4	4	4	2	4
R-Factor	0.0411	0.0422	0.0527	0.0475	0.0620

*INCT–DHPAA crystals were grown by Dongpeng Yan. **Inspection of the structure following refinement indicates that INCT and LABA reacted rather than co-crystallised.

4.3.1.1. INCT-HBA

Of the four systems, only INCT–HBA has previously been shown to form co-crystals. When compared to the literature structure (VAKTOR) it is immediately obvious from the data in Table 4-2 that the crystal grown in the experiments reported here is not the same as that reported by Vishweshwar *et al*[232] and must therefore be another polymorph.

The previously reported co-crystal between INCT and HBA has been described as forming zigzag tapes through phenol···pyridine heterosynthons and acid···amide $R^2_2(8)$[241] bimolecular cyclic hydrogen-bonded motifs, with adjacent tapes being held

together by N–H···O hydrogen bonds from acid to amide and other weak C–H···O interactions (Figure 4-2 (a)).[232] The co-crystal grown here (Figure 4-2 (b)) forms similar tapes *via* phenol···pyridine heterosynthons and acid···amide $R^2_2(8)$ heterosynthons as well as acid···acid and amide···amide $R^2_2(8)$ homosynthons, with adjacent tapes interacting through N–H···O hydrogen bonds from acid to amide. However the interactions in the new co-crystal extend to form pseudo-sheets that stack along the *b* axis rather than just tapes.

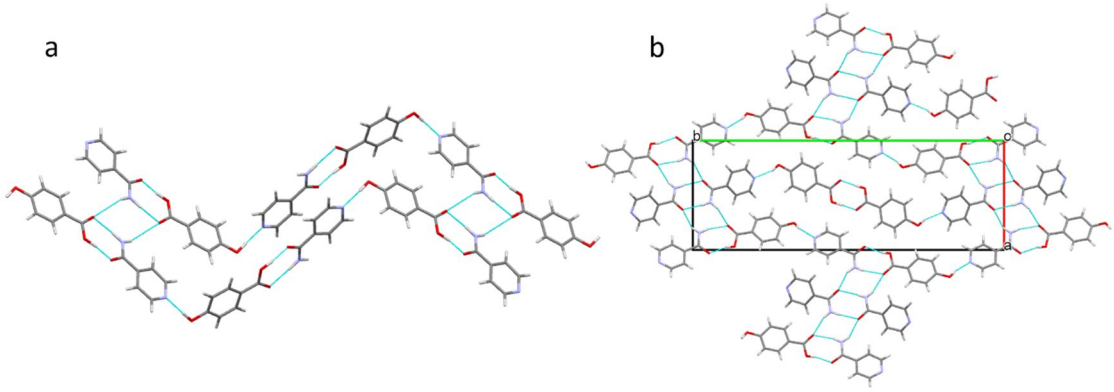

Figure 4-2. Structures of (a) VAKTOR and (b) the INCT-HBA co-crystal grown from solution in this work.

Simulation of interactions in the raw materials and VAKTOR from single crystal data shows that the amide of pure INCT (Figure 4-3 (a)) is involved in two hydrogen bonds, one for each hydrogen, whereas in the co-crystal (Figure 4-3 (b)) one of the hydrogens acts as a donor for two H-bonds and so the amide forms three in total. HBA also experiences a change in H-bonding (Figure 4-3 (c)) with the phenolic hydroxide group reducing its interactions from two to one and the carboxyl hydroxide gaining an H-bond through interactions as both donor and acceptor with two INCT molecules. The carbonyl oxygen also gains an interaction and becomes an acceptor for two INCT molecules at the amide. Also depicted in Figure 4-3 (d) are the two bonding environments in which INCT and HBA sit in the new co-crystal grown in this work, although this crystal was not observed in the printed samples.

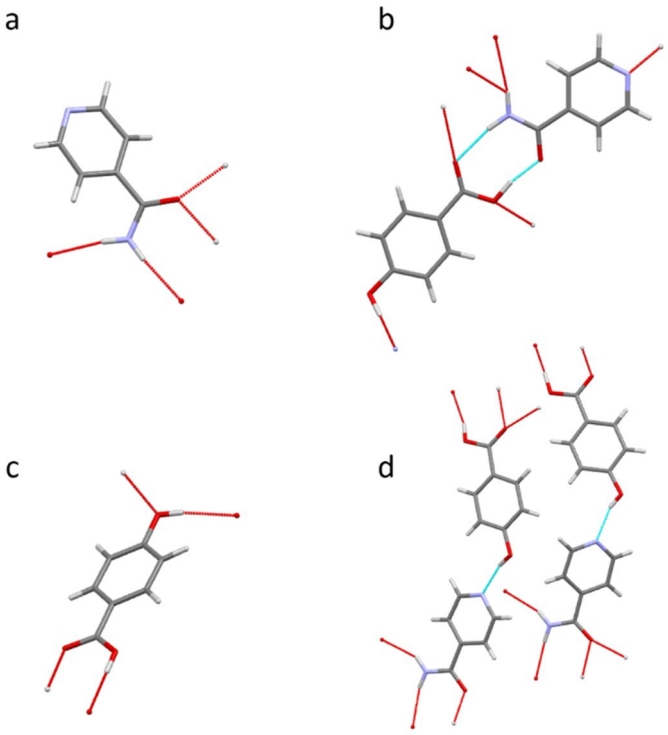

Figure 4-3. Graphical representation of the asymmetric unit of (a) INCT polymorph I (EHOWIH01),[242] (b) the previously reported structure of INCT-HBA (VAKTOR),[232] (c) HBA,[243] and (d) the new INCT-HBA co-crystal grown in this work showing hydrogen bonding.

4.3.1.2. INCT-HPAA

The dominating features of the structure of the INCT-HPAA co-crystal grown from solution can be seen in Figure 4-4. As with the two INCT-HBA co-crystals the molecules are arranged in tapes. The tapes are formed *via* acid···pyridine heterosynthons at either end of the HPAA terminated by amide···amide $R^2_2(8)$ homosynthons and are linked together by N–H···O hydrogen bonds from the amide to the acid group of the HPAA and also between adjacent INCT molecules.

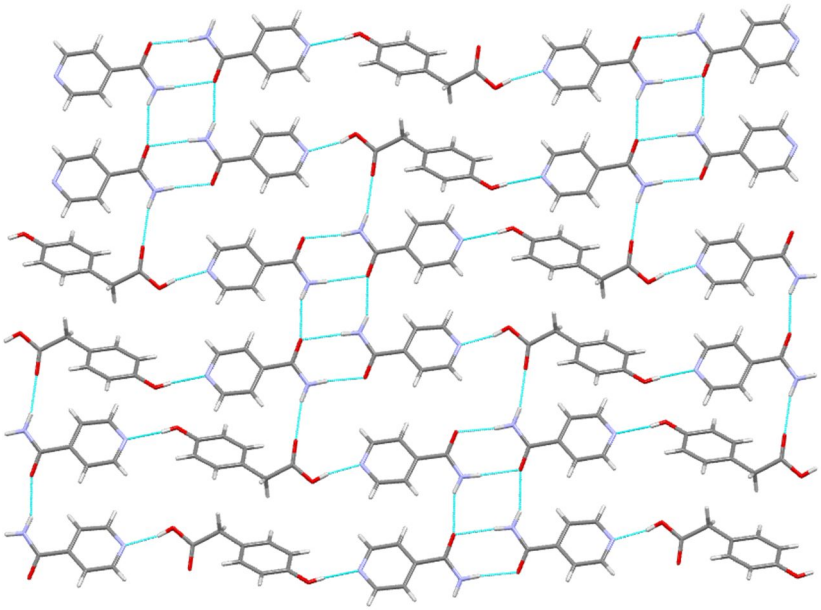

Figure 4-4. Structure of INCT-HPAA co-crystal.

The asymmetric unit of the co-crystal (Figure 4-5 (a)) has two INCT molecules and one HPAA. Each of the two INCT molecules has slightly different H-bonding. One molecule has five associated H-bonds, with four interactions around the amide in a similar pattern to that of the pure INCT crystal (Figure 4-3 (a)), and acts as an acceptor at the cyclic nitrogen to the hydrogen of the phenolic hydroxide of HPAA. The other INCT unit has only three H-bonds at the amide group, with the carbonyl losing one, and an interaction at the cyclic nitrogen with the carboxylic hydroxide.

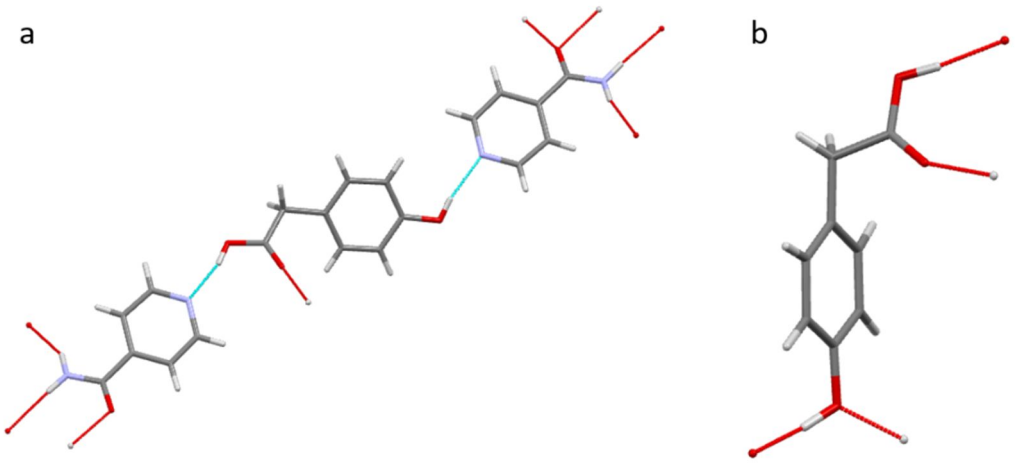

Figure 4-5. Graphical representation of the asymmetric unit of an INCT-HPAA co-crystal grown by evaporation from solution in ethanol, showing hydrogen bonding.

Hydrogen bonding around the HPAA molecule in the co-crystal (Figure 4-5 (b)) is largely similar to that of the pure crystal except for the loss of one bond at the phenolic hydroxide group, where the oxygen no longer acts as an acceptor.

4.3.1.3. INCT-DHPAA

INCT and DHPAA do not form any of the $R^2_2(8)$ observed in the structures of INCT-HBA and INCT-HPAA. Instead they form staggered chains (Figure 4-6 (a)) with alternate INCT and HPAA molecules linked by phenol···acid and phenol···pyridine hydrogen bonds. The chains are cross-linked by N–H···O and O–H···O hydrogen bonds between molecules of alternating species.

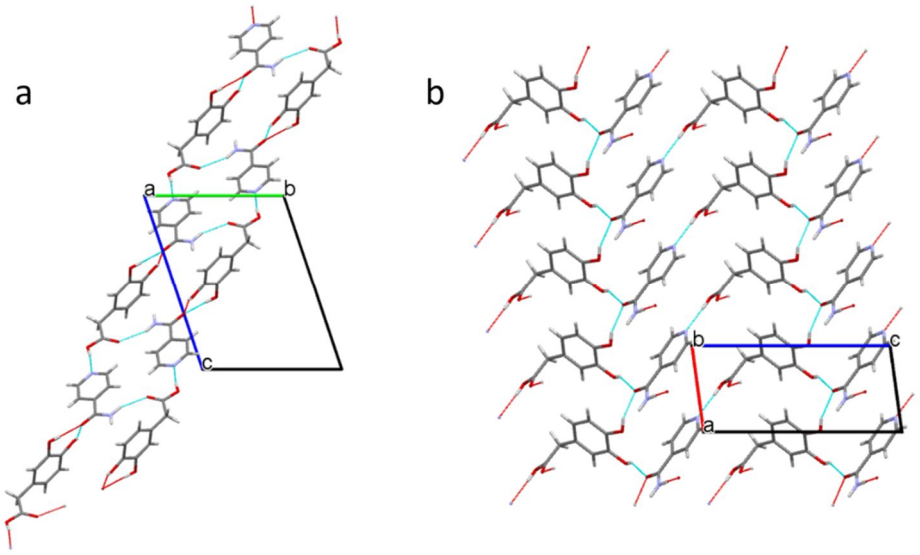

Figure 4-6. Structure and bonding in INCT-DHPAA viewed down (a) the *a* axis and (b) the *b* axis.

In the pure DHPAA crystal[244] each of the hydroxyl groups are involved in two H-bonds (Figure 4-7), with the hydroxyl in the 3 position acting as a hydrogen donor for two bonds and the other two OH groups acting as both donors and acceptors for two molecules. The carbonyl oxygen is also involved in two H-bonds as an acceptor. This pattern of interactions is very different to that observed in the co-crystal (Figure 4-8), where each of the oxygen containing functional groups are involved in only one H-bond. All of the hydroxyls act as hydrogen donors and the carbonyl acts as an acceptor.

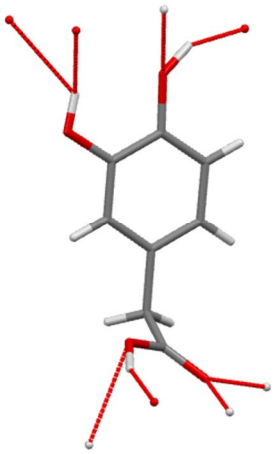

Figure 4-7. Graphical representation of the asymmetric unit of the previously reported structure of DHPAA,[244] showing hydrogen bonding.

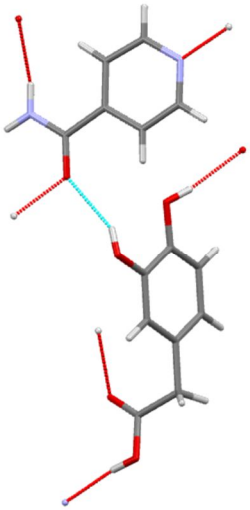

Figure 4-8. Graphical representation of the asymmetric unit of an INCT-DHPAA co-crystal grown by evaporation from solution in ethanol by Dongpeng Yan, showing hydrogen bonding.

Changes in H-bonding around the INCT molecule (see Figure 4-3 for the asymmetric unit of polymorph I and the associated bonding) are fewer than around DHPAA, with only one of the amide hydrogens acting as a donor and the cyclic nitrogen acting as an acceptor for a new H-bond. The carbonyl oxygen acts as an acceptor for two interactions in both the pure INCT I crystal and the INCT-DHPAA co-crystal.

4.3.1.4. INCT-LABA

Structural refinements (Figure 4-9) of the crystal grown from a solution of INCT and LABA revealed the materials had reacted and crystallised, with proton transfer occurring from one of the OH groups on the ring structure of LABA to the nitrogen on the pyridine of

INCT. As the aim was to form co-crystals without reactions the crystal structure will not be discussed further.

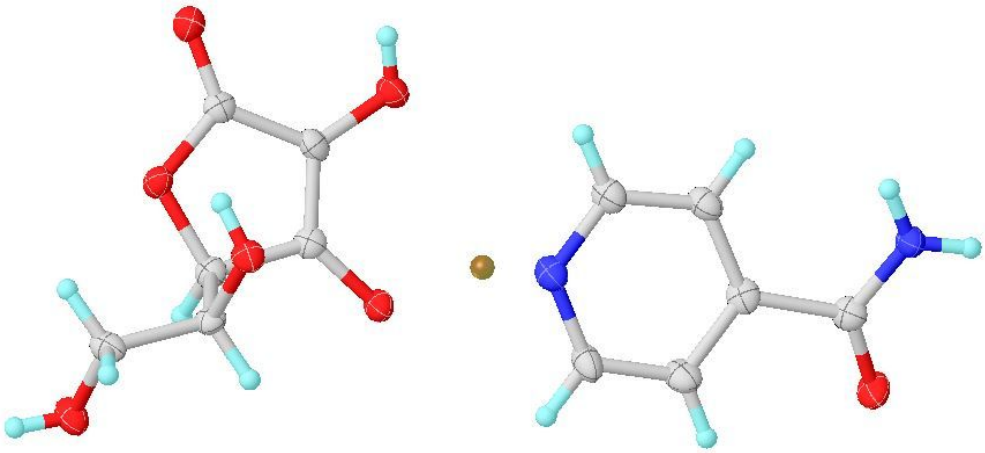

Figure 4-9. A graphical representation of the relationship between the INCT (right) molecule and one of the LABA molecules (left) from the crystal grown between the two. The gold sphere represents a hydrogen that appears to have undergone proton transfer from LABA to INCT.

4.3.2. Thermal inkjet printing

4.3.2.1. INCT-HBA

4.3.2.1.1. PXRD

Crystals were formed when printing three ethanolic solutions of INCT and HBA in equimolar proportions. There are a number of different variables that can be adjusted when using thermal inkjet printing as a technique for printing crystals. Figure 4-10 displays a number of diffraction patterns recorded for crystals collected from acetate sheets following printing from ethanolic solutions of equimolar mixtures of INCT and HBA. Initially it was necessary to establish the best print settings with respect to the number of dots of solution being printed per inch of acetate (dpi). The two standard settings are 300 dpi and 600 dpi and so crystals were printed using each. The peak shape and intensity to noise ratio was similar for both print resolutions, however the higher resolution setting (600 dpi) resulted in a high volume of solution being printed onto the acetate and so the sheets were very wet when ejected from the printer, consequently a smearing of the solution was observed, which may have affected the crystal growth. There was also one extra reflection (2θ = 16.5°) observed in the diffraction pattern recorded using this setting compared to those recorded at 300 dpi. This reflection is not present in either of the starting materials or any of the patterns recorded from crystals

formed using different settings, and is believed to be an unknown impurity. It was therefore decided to continue the experiments using 300 dpi.

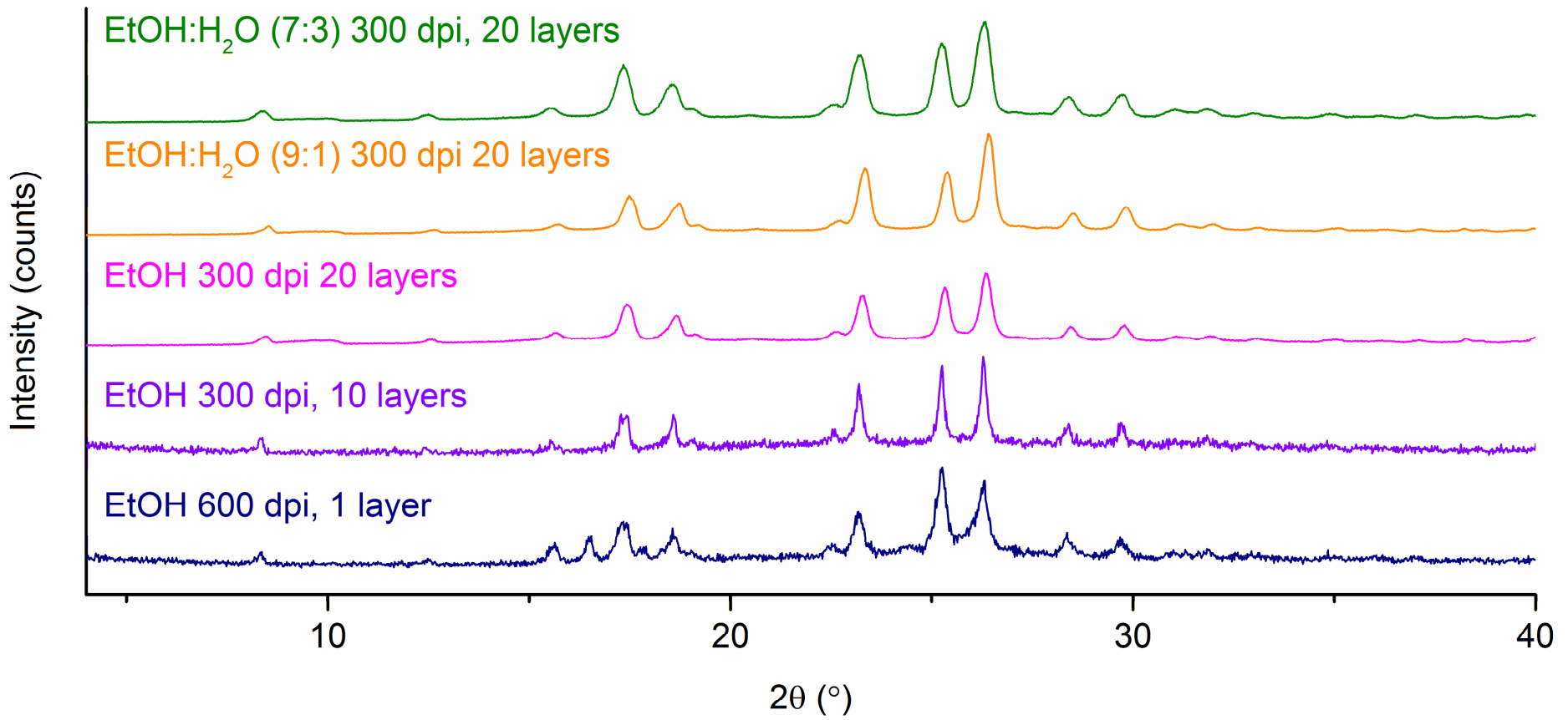

Figure 4-10. Diffraction patterns for crystals printed from equimolar solutions of INCT and HBA in EtOH, and EtOH and water.

The second variable was the rate of evaporation of the solvent. Crystals were printed from solutions of 100 % ethanol or mixtures of ethanol and water in ratios of either 9:1 v/v % or 7:3 v/v % respectively. Water was added to slow the evaporation of the solvent after printing and so slow the rate of crystallisation in an effort to encourage co-crystallisation. The three patterns recorded for 20 layers of crystals printed at 300 dpi (Figure 4-10) are clearly all representative of the same crystal structure and so it was decided to continue the experiments using solutions in ethanol without water. Crystals were printed over 20 layers so that sufficient material could be collected for analysis.

The diffraction patterns recorded for the crystals following printing have some significant differences to those of the raw materials (Figure 4-11). There are unique reflections present in the printed crystals at 13.0°, 16.0°, and 28.8° that are absent in the raw materials. There are also significant absences of raw material reflections in the patterns collected from the printed material, at 21.0°, 24.5°, and 30.9°. When compared to the predicted powder pattern of the structure of the known crystal from the CSD (VAKTOR)[232] and that of the crystal formed by solvent evaporation and discussed in Section 4.3.1 (Figure 4-12) it is clear that the pattern of the printed crystals is similar to the previously reported co-crystal. The data recorded here are of much lower resolution due to the small crystal size and sample size but all of the reflections occur at the correct 2θ angles and the intensity ratios are also very similar to those of the known structure.

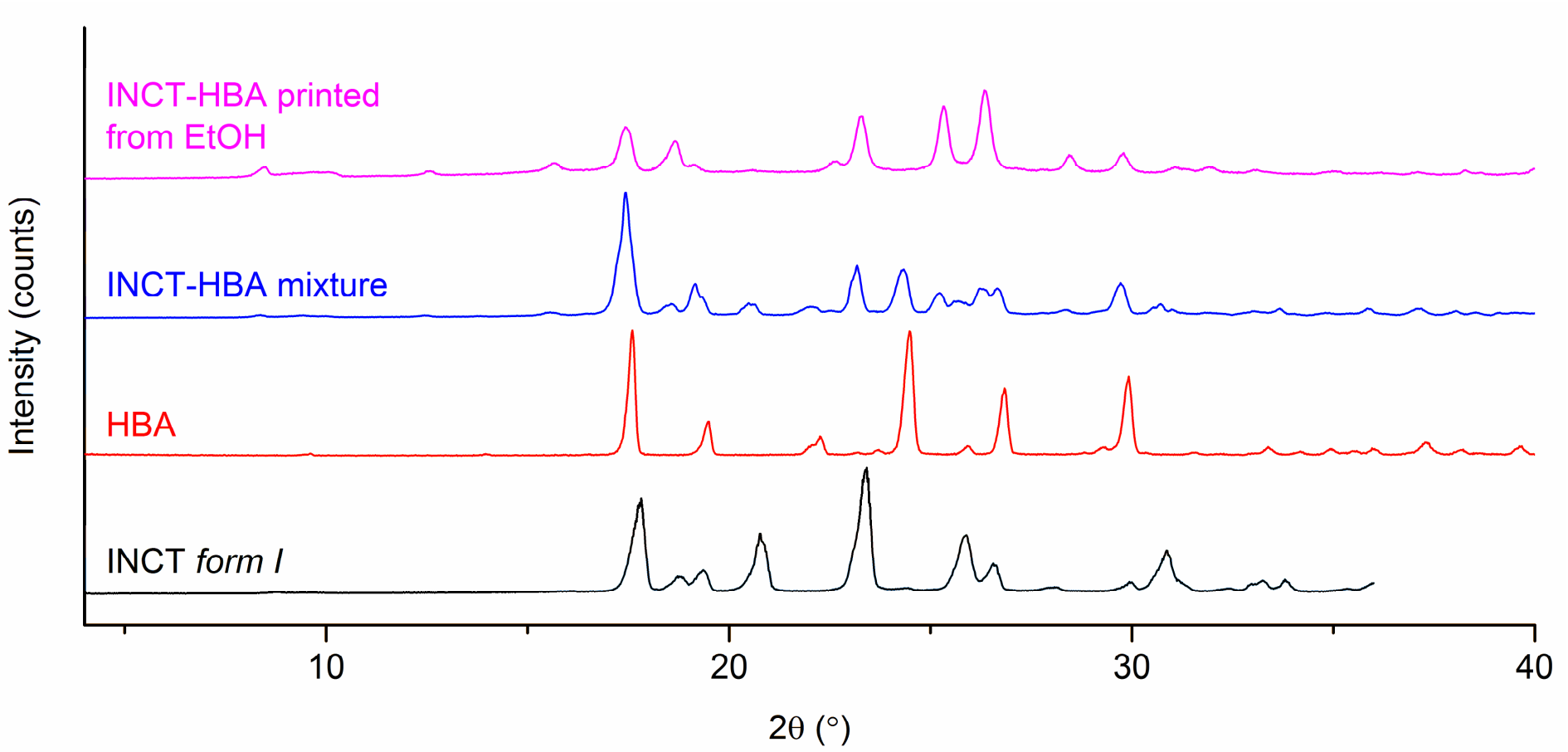

Figure 4-11. Diffraction patterns for INCT I, HBA, a physical mixture of the two and crystals printed from an equimolar ethanolic solution of the two.

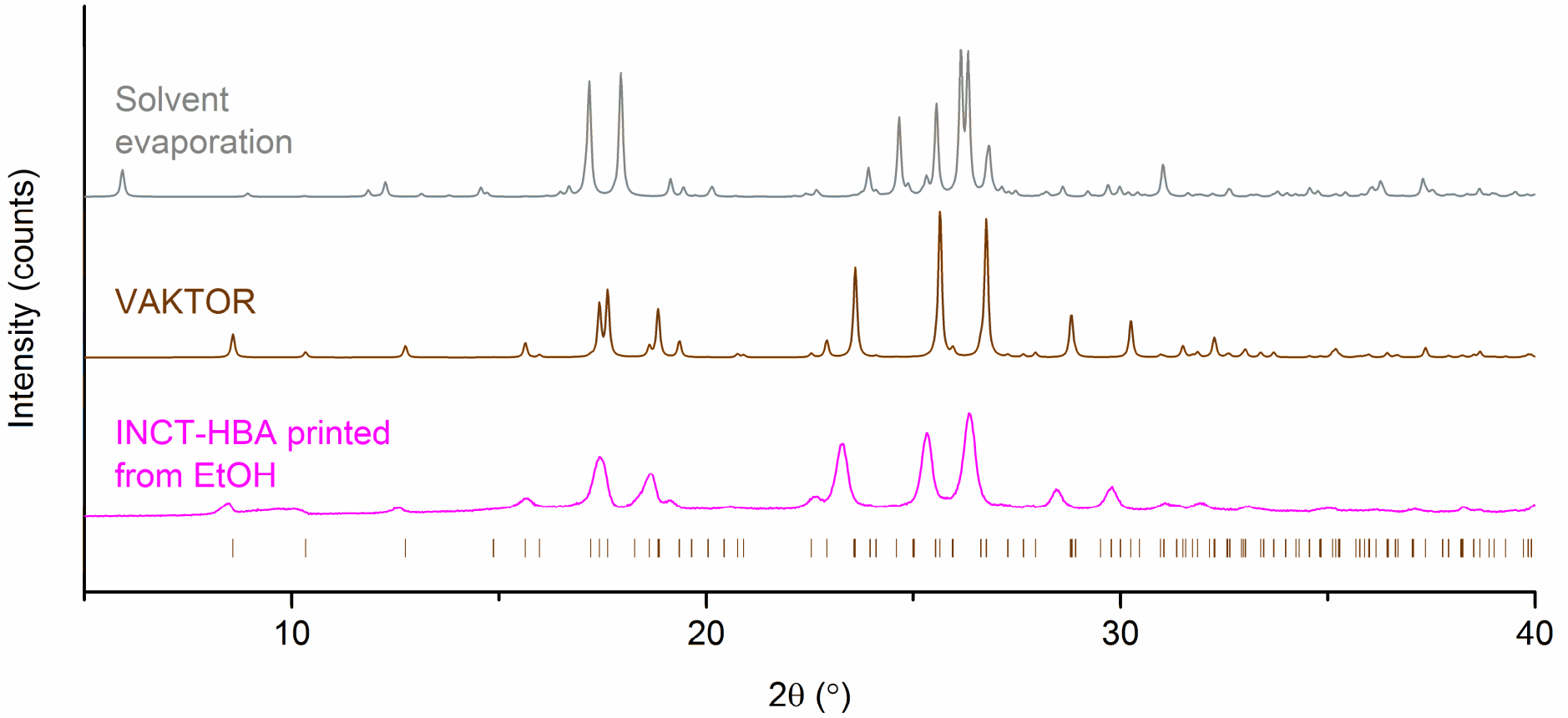

Figure 4-12. Diffraction pattern recorded for crystals of INCT-HBA. Tick marks show the positions of allowed reflections for VAKTOR.

4.3.2.1.2. DSC and TGA

Results of the DSC analyses of these crystals can be seen in Figure 4-13. All three of the thermograms relating to the printed mixtures show a single endotherm with an onset at 181-182 °C followed by a steady drop in heat flow, caused by decomposition of the material at temperatures above 190 °C. The lack of events prior to the endotherm at 181 °C suggests that the crystals are stable at low temperatures. Thermograms for the raw materials exhibit endotherms with onsets at the melting points of each of the two components (157 °C, INCT II; 215 °C, HBA), with an additional small endotherm (onset 115 °C) in the INCT data representing a conversion from polymorph I to polymorph II. It is particularly significant that neither of the endotherms observed in the trace for INCT are seen after printing. Consequently the INCT must be involved in some kind of interaction that prevents these events occurring, *i.e.* formation of a co-crystal. The sharp endotherm at *ca.*181 °C for the products of printing indicates that there is melting occurring. This event occurs at a higher temperature than the reported melting point of form II of INCT[245–247] and is not present in the trace associated with HBA and so suggests the formation of a co-crystal.

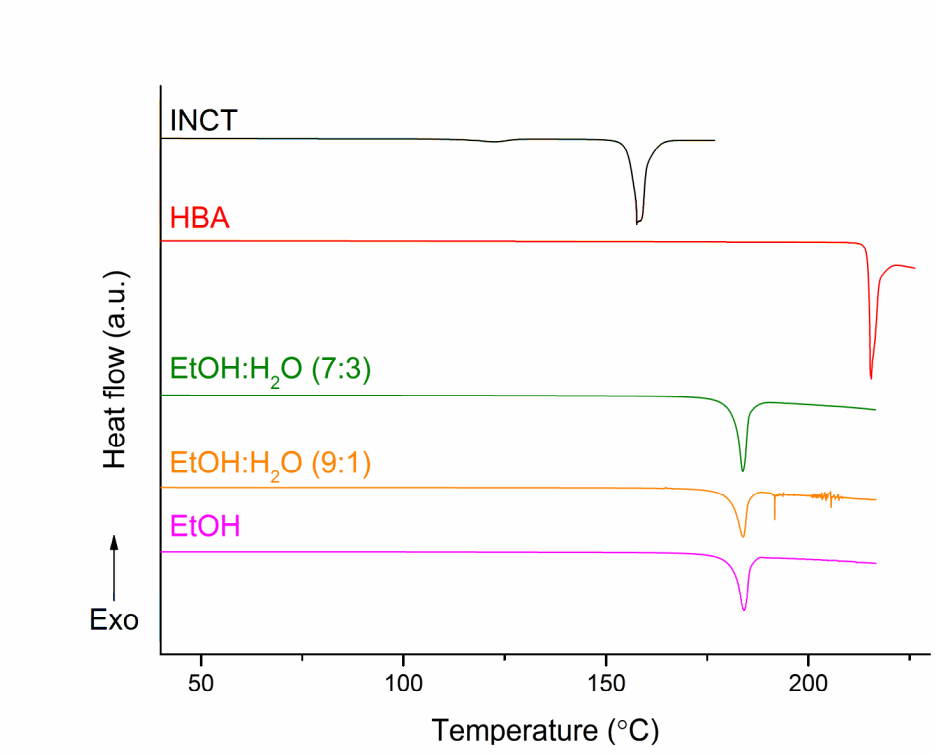

Figure 4-13. DSC thermograms for crystals formed by inkjet printing a solution of INCT and HBA in EtOH, EtOH and H_2O (9:1 v/v), and EtOH and H_2O (7:3 v/v) and the two raw materials; INCT and HBA.

Examination of the TGA data (Figure 4-14) shows that decomposition of the printed crystals begins at a lower temperature than either of the individual components, and also that of a physical mixture of the two. It also levels off at around 20 % mass rather than continuing to decay to 0 %, suggesting that printing has resulted in some kind of interaction.

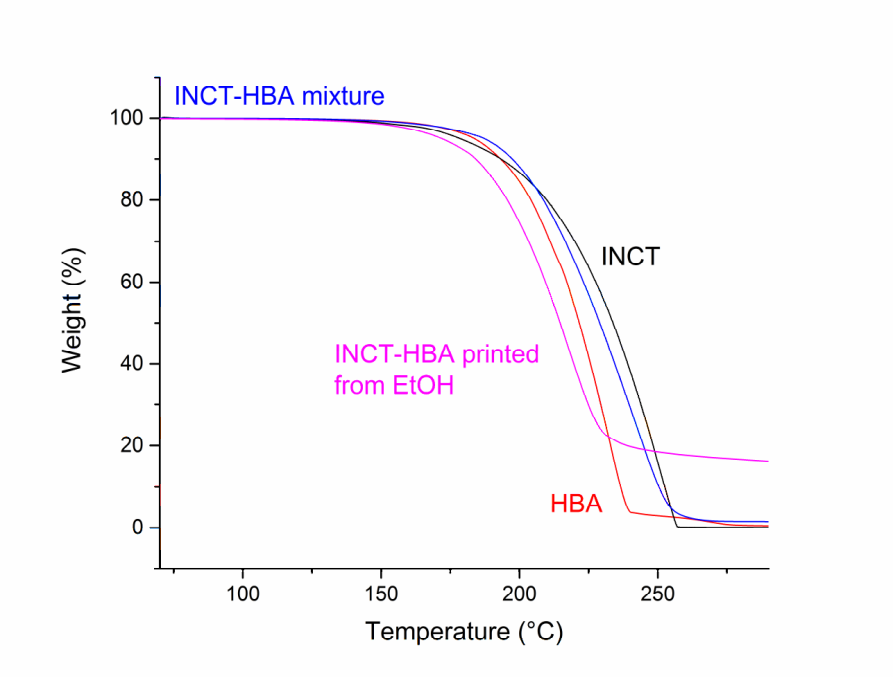

Figure 4-14. TGA traces for INCT, HBA, a mixture of INCT and HBA, and crystals printed from a solution of INCT-HBA in EtOH.

4.3.2.1.3. FTIR spectroscopy

A spectrum was recorded for a physical mixture of the two raw materials (Figure 4-15) and compared to that of the printed crystals to ensure that they were not simply a physical mixture of the two components with no new interactions. The two spectra have significant differences between 3100 cm^{-1} and 3500 cm^{-1}, which suggests that co-crystals have formed. There are no significant differences observed below 1800 cm^{-1}.

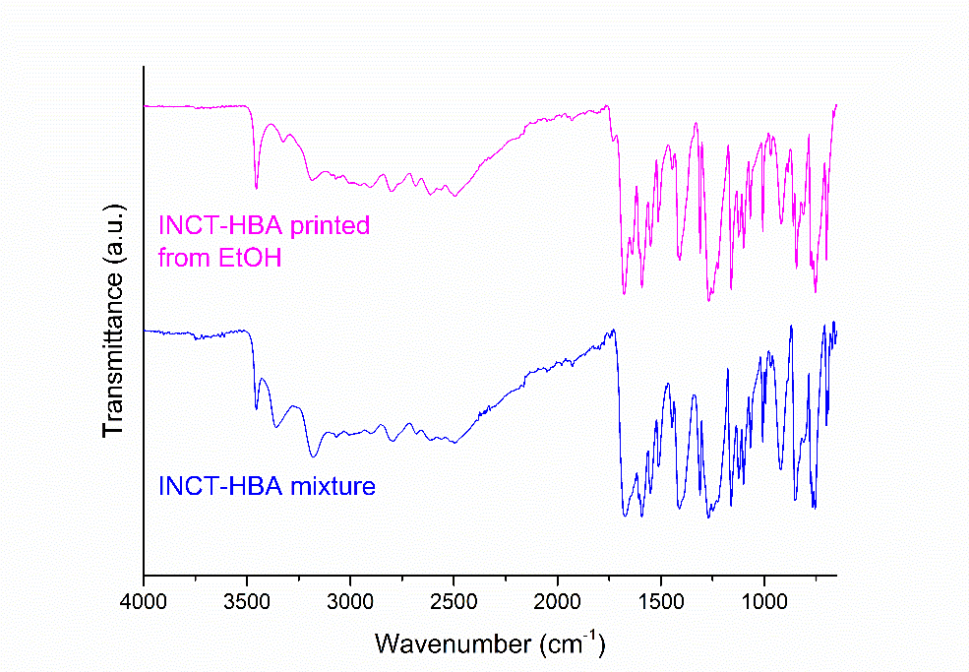

Figure 4-15. FTIR spectra for a physical mixture of INCT and HBA and crystals printed from an equimolar ethanolic solution of INCT and HBA.

FTIR spectra for the raw materials and the printed crystals can be seen in Figure 4-16. The most obvious difference between the spectra is a significant shift of the sharp N—H stretch peak at 3360 cm^{-1} in INCT to 3455 cm^{-1} in the printed crystals, which occurs with a concomitant reduction in intensity of the second N—H stretch in INCT (3180 cm^{-1}) and the broad strong O—H stretch seen at 3360 cm^{-1} in the HBA spectrum. The rest of the spectrum of the printed crystals displays all of the peaks associated with the raw materials, as would be expected, with the exception of the region between 1200 cm^{-1} and 1300 cm^{-1} where there is a slight shift to a lower wavenumber of the band relating to the C—O bond of the carbonyl of HBA.

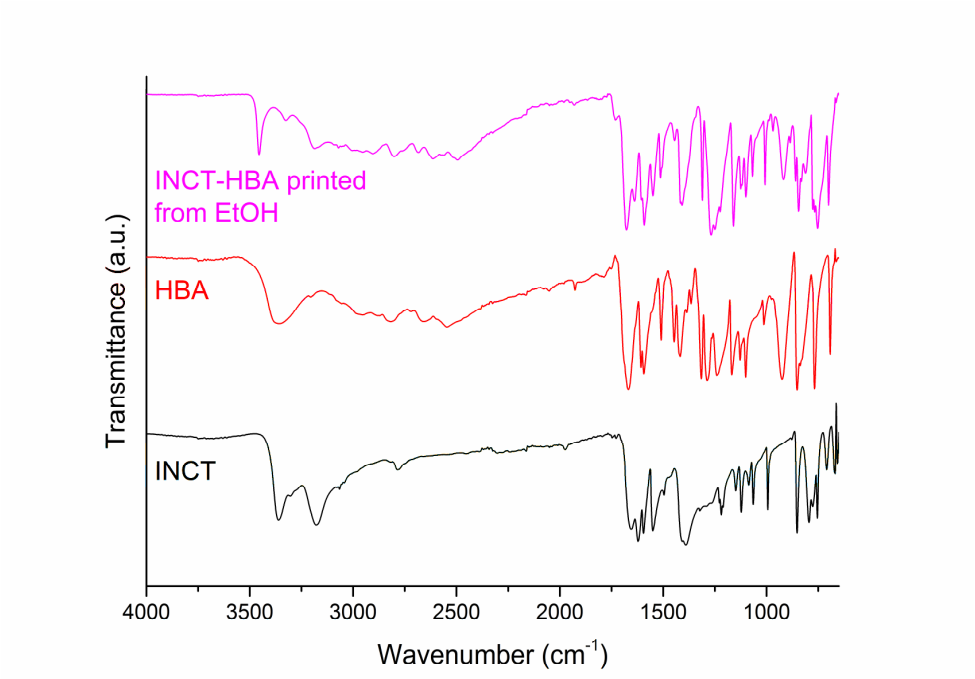

Figure 4-16. FTIR spectra for INCT, HBA and crystals printed from an equimolar ethanolic solution of the two.

All of the shifts described are consistent with a change in hydrogen bonding interactions within the materials and support the formation of a co-crystal. Furthermore, simulation of hydrogen bonding from the single crystal diffraction data (4.3.2.1.1) confirms these changes.

4.3.2.2. INCT-HPAA

4.3.2.2.1. PXRD

Examination of diffraction patterns collected for crystals printed from three solutions of INCT and HPAA (molar ratio: 2:1) in either ethanol or ethanol and water in two different ratios (Figure 4-17) reveals that all three solutions resulted in crystals with the same structure. The Bragg reflections all occur at the same 2θ angles and the intensity ratios are all similar. Unlike INCT-HBA, the addition of water to the solution does appear to have improved the quality of the crystals slightly. The reflections of the pattern for crystals printed from EtOH:H_2O (7:3 v/v) solution are better resolved and they are slightly narrower than those of the other two solutions. Also, the intensity to noise ratio is higher, as can be seen when looking at the lower intensity reflections at 7.5°, 14° and 17°.

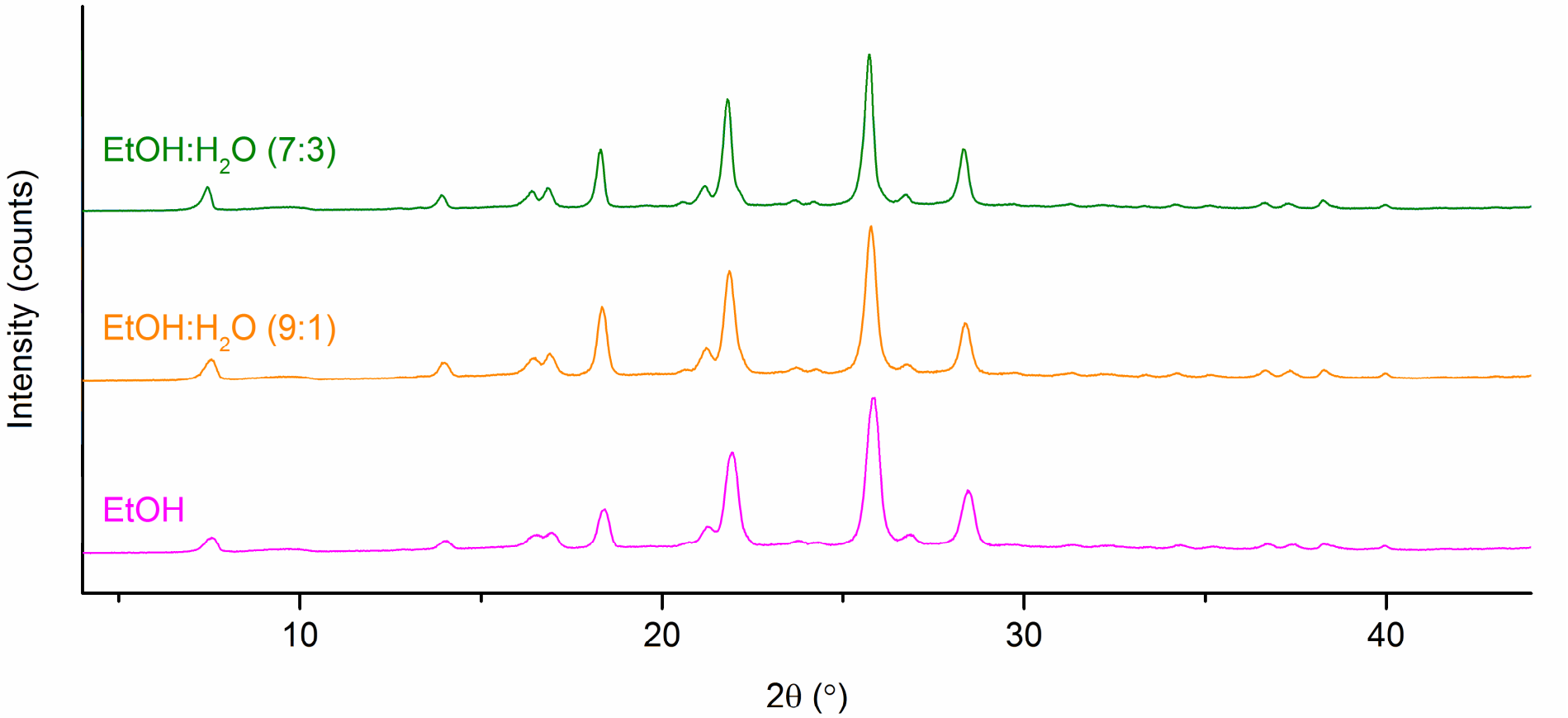

Figure 4-17. Powder diffraction patterns for crystals printed from ethanolic solutions of INCT and HPAA in a molar ratio of 2:1 respectively.

Powder diffraction patterns were recorded for both INCT and HPAA as well as for a physical mixture of the two in molar ratio of 2:1. When compared to the pattern recorded for the printed crystals (Figure 4-18) the positions of reflections and their intensities are very different. Had there been no interactions and had the two components recrystallized from solution into separate crystal entities then the pattern collected should consist of Bragg reflections with 2θ angles matching the patterns of the raw materials and with similar intensity ratios. This however is not the case. Particularly obvious is the absence of reflections from INCT I in the data for the printed crystals at 23.4°, and 30.9° and 11.3°, and at 30.3° from HPAA. There are also characteristic reflections of the printed crystals at 7.6°, 14.0°, 16.8°, and 21.9° which do not appear in the raw materials.

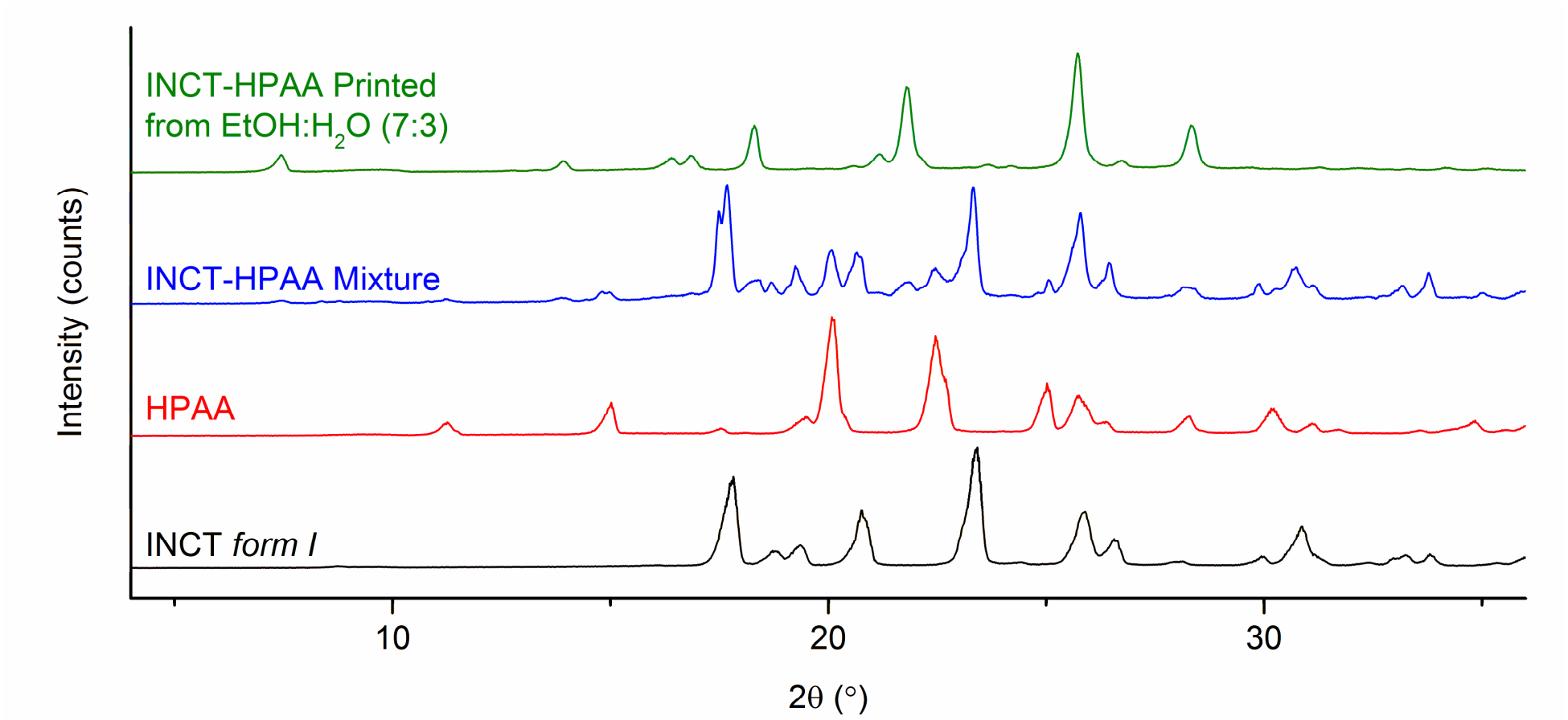

Figure 4-18. Diffraction patterns for INCT, HPAA, a 2:1 molar ratio physical mixture of the two, and crystals printed from a 2:1 molar ratio solution of INCT and HPAA in EtOH:H_2O (7:3 v/v).

It is possible that the two materials may have crystallised separately into different polymorphs from those recorded prior to dissolution. For this reason the printed crystal pattern was compared to powder patterns (Appendix 2) of the known polymorphs of the two components. These patterns were predicted from structures collected from the CSD (INCT: EHOWIH01-05; HPAA: QAPBAL) and none were a good match.

Finally, the printed crystal pattern was compared to the powder pattern predicted from the refined structure of the single crystal grown by solvent evaporation and discussed in Section 4.3.1 (Figure 4-19). The quality of the collected pattern was not such that refinements could be carried out, due to the small size of the crystals produced by inkjet printing. However, the pattern of the printed crystals agrees well with the predicted pattern. The profiles of the patterns are very similar, albeit with much lower resolution for the printed crystals, and the ratios of intensities are also very similar for both. Diffraction for the printed crystals occurs at slightly lower angles than for the single crystal data. This is simply a result of the temperature difference between the measurements. Data for the printed crystals were collected at ambient temperature (*ca.* 25 °C), whereas the single crystal data were collected at -73 °C. At higher temperatures the unit cell of the crystal would be larger, resulting in larger d-spacings and so lower angles of diffraction. Had more crystals been printed or longer collection times been used then it may have been possible to resolve more of the peaks to increase confidence in the similarity of the patterns. Nevertheless, the data quality is sufficient to suggest that the two materials have the same structure, especially considering the differences when compared to powder patterns for all of the known polymorphs of the two contributing materials.

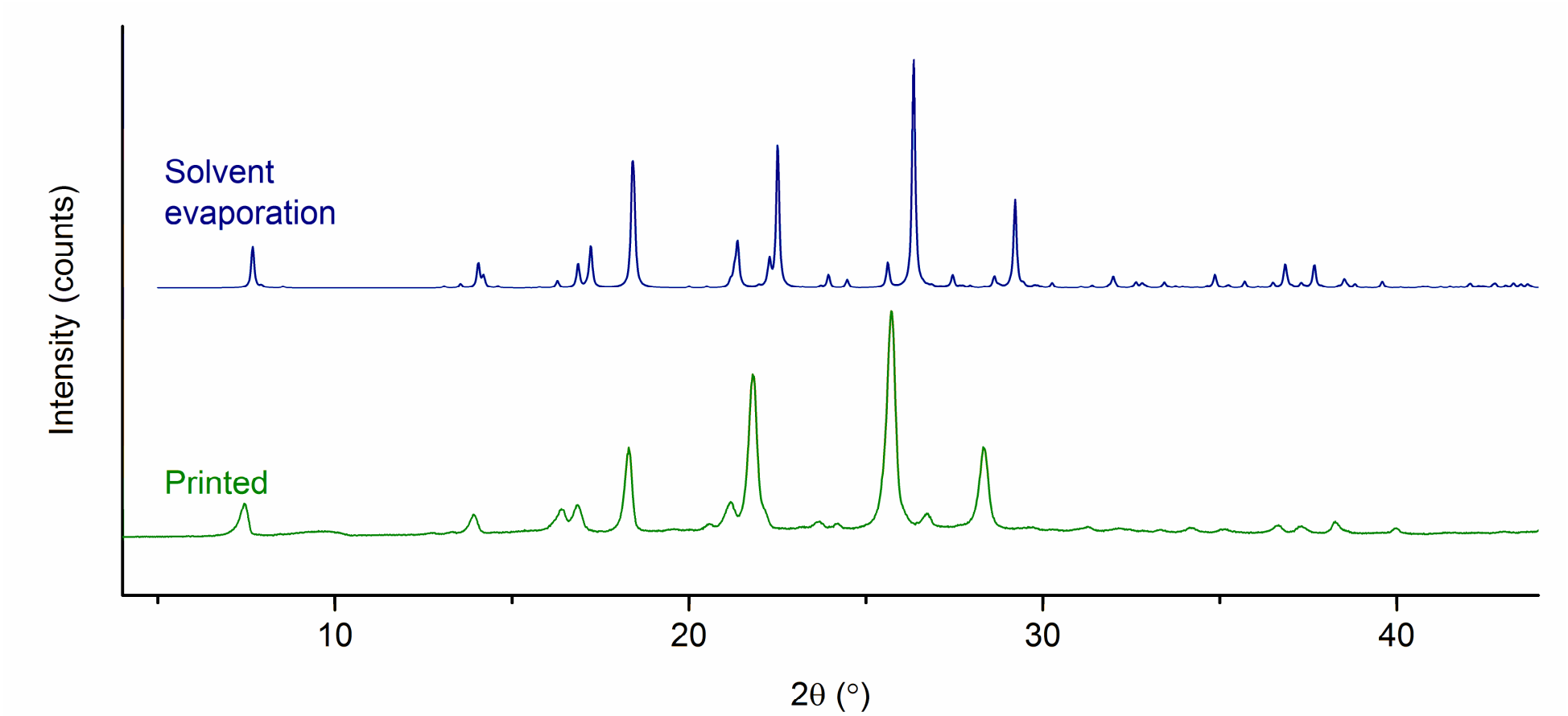

Figure 4-19. Powder diffraction pattern for crystals printed from a solution of INCT:HPAA (2:1 molar ratio) in EtOH:H_2O (7:3) and a predicted powder pattern for crystals grown from a similar solution by solvent evaporation.

4.3.2.2.2. DSC and TGA

As with the crystals printed from INCT and HBA the DSC traces (Figure 4-20) for crystals printed from solutions of INCT and HPAA in ethanol and ethanol/water have a different profile to those of the raw materials. All three of the printed crystal thermograms have only one endothermic event with an onset at 125-126 °C and an enthalpy of *ca.* 150 J g^{-1}. It is likely that this event is the melting of the co-crystal formed between the two components. The highest temperature melting endotherms for INCT and HPAA have onsets at 157 °C and 150 °C and have associated enthalpies of fusion of 184 J g^{-1} and 194 J g^{-1} respectively. These temperatures and enthalpies are much higher than those observed for the printed crystals. It is unlikely that the combination of INCT and HPAA would have had such a destabilising effect on each other that they would both melt simultaneously more than 24 °C below their reported melting points.

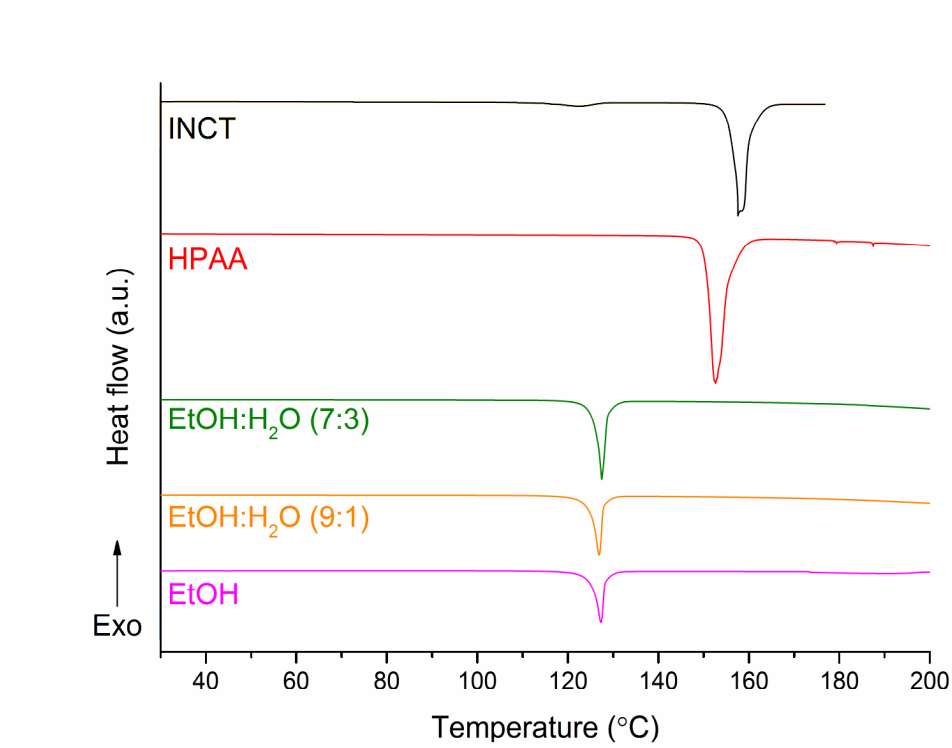

Figure 4-20. DSC thermograms for crystals formed by inkjet printing a solution of INCT and HPAA in EtOH, EtOH and H_2O (9:1), and EtOH and H_2O (7:3) and the two raw materials; INCT and HPAA.

INCT has another endotherm with an onset at 115 °C with an enthalpy of 13 J g^{-1}. However, this occurs around 10 °C lower than the event in the traces of the proposed co-crystals and the enthalpy is lower by a factor of more than 11. These data strongly suggest the occurrence of intermolecular interactions between molecules of the two components, particularly the presence of a single endotherm in the DSC trace of the

printed crystals. TGA data show that the printed crystals begin to lose mass at temperatures 25-30 °C below that recorded for either of the crystalline components individually or in a physical mixture at the same ratio used for printing and solvent evaporation (Figure 4-21). This offers support to the summation that a co-crystal has been formed by inkjet printing, although sample size may be a factor as the printed crystal mass was much less than that of either of the raw materials.

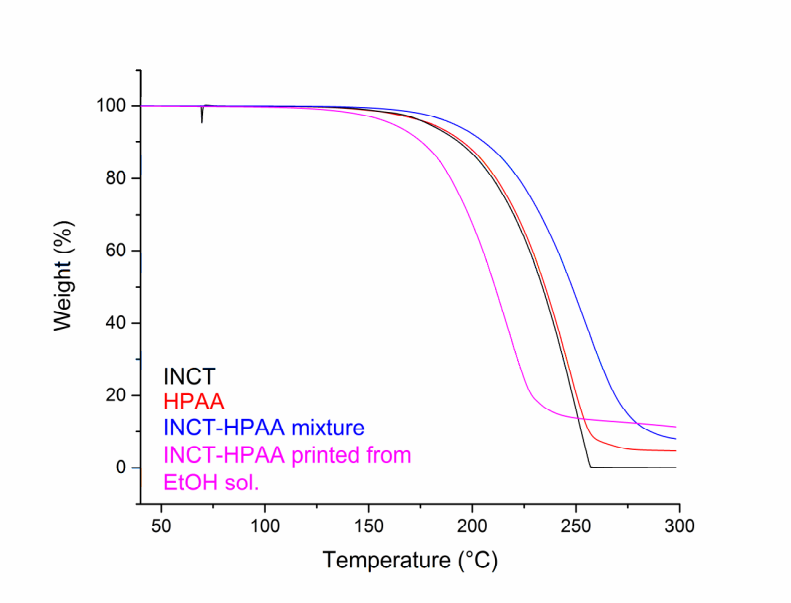

Figure 4-21. TGA data for INCT, HPAA, a physical mixture of the two and crystals printed from an ethanolic solution of the two.

4.3.2.2.3. FTIR spectroscopy

The IR spectrum for a physical mixture of INCT and HPAA in a 2:1 molar ratio is compared to the spectrum for the printed crystals in Figure 4-22. There are clear differences, suggesting that the printed crystals are not simply a mixture of the two materials but that there are intermolecular interactions between the two different molecules.

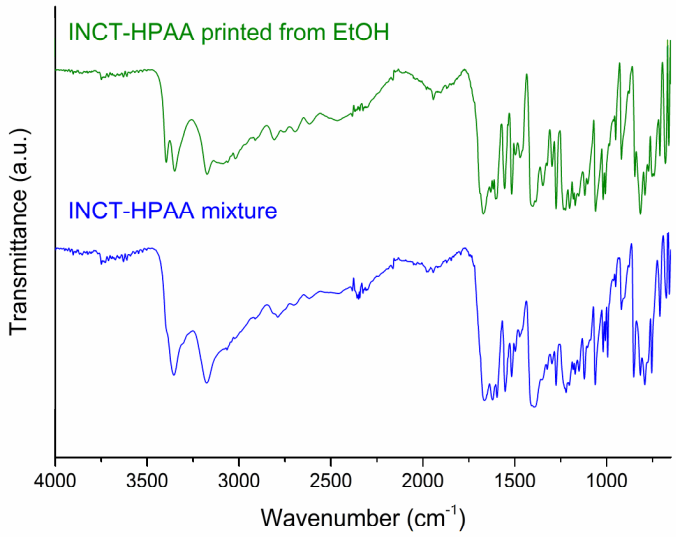

Figure 4-22. FTIR spectra for a physical mixture of INCT and HPAA and crystals printed from a 2:1 molar ratio EtOH:H_2O (7:3 v/v) solution of INCT and HPAA.

Comparison of the FTIR spectra of the printed crystals and raw materials (Figure 4-23) reveals that there have been some band shifts. INCT has two strong bands at 3355 cm^{-1} and 3175 cm^{-1} characteristic of stretching of N—H bonds in a primary amide. HPAA has a strong band at 3245 cm^{-1} resulting from the stretching of the O—H bond of the alcohol in the O1 position (Figure 4-24) and a much broader medium intensity band peaking at 2990 cm^{-1} relating to the stretching of the carboxylic acid O—H bond. The N—H bands of the INCT have not shifted, but the bands relating to the O—H bonds in HPAA have moved to higher wavenumbers by 150 cm^{-1} and 110 cm^{-1} respectively.

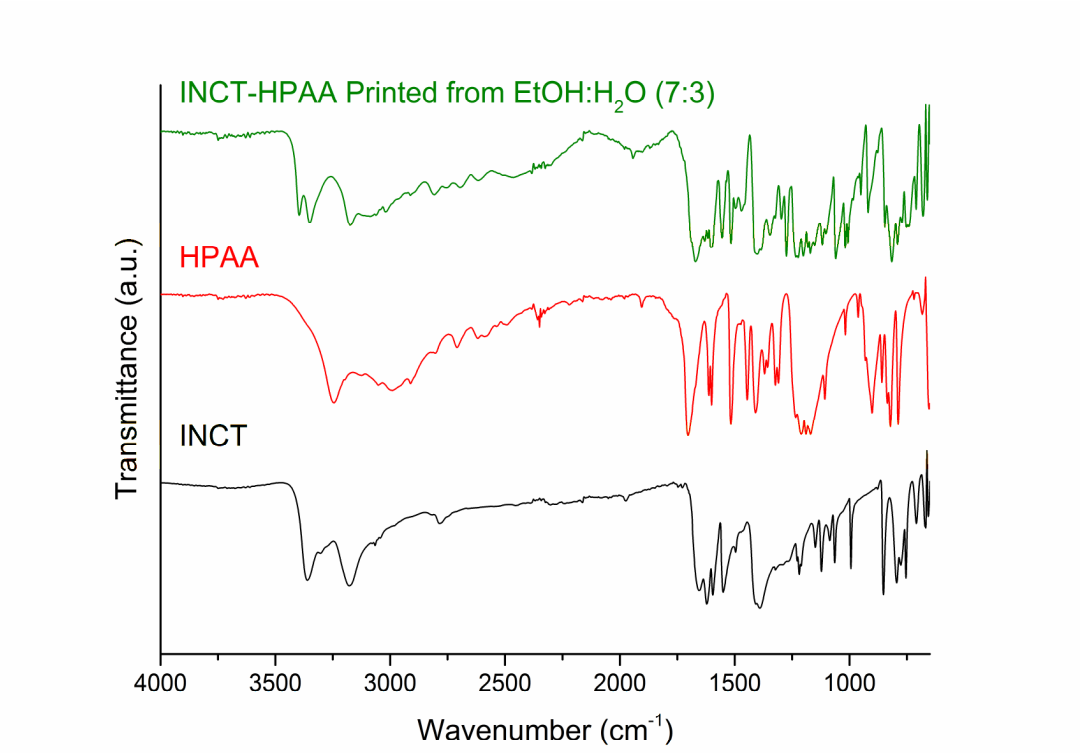

Figure 4-23. FTIR spectra for INCT, HPAA and crystals printed from a 2:1 molar ratio solution of the two in EtOH:H_2O (7:3).

Changes at lower wavenumbers are more complex, with the most significant being the shift of the sharp medium intensity band at 1445 cm^{-1} in the spectrum for HPAA to a higher wavenumber and the presence of a new sharp absorbance in the crystals at 1275 cm^{-1} (relating to the C—O bond of the carbonyl group of HPAA). Due to the complexity of the region below 1800 cm^{-1} it is difficult to identify this band in the spectra of the raw materials. There is also a smaller shift to a higher wavenumber of the strong sharp band at 1655 cm^{-1} for INCT and to a lower wavenumber for that at 1705 cm^{-1} for HPAA, both are associated with the C=O double bond. From these observations it appears that the carboxyl group of HPAA has undergone significant changes in relation to the intermolecular bonding, a finding consistent with the formation of a co-crystal.

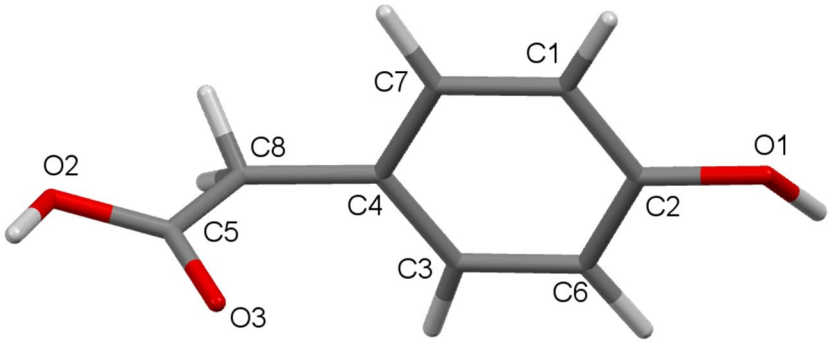

Figure 4-24. The HPAA molecule.

Simulation of the hydrogen bonding confirms the changes seen in the FTIR data. Bonding at the amide is very similar in both the co-crystal and pure INCT and so the lack of shift of the associated bands in the IR spectra is unsurprising. The loss of a bond at the carbonyl in half of the INCT molecules explains the small shift in the band at 1655 cm^{-1}.

The largest of the shifts observed in the IR data may be explained by the change in bonding around the phenolic hydroxide group discussed in Section 4.3.2.2.1. The shift in the band at 1705 cm^{-1} relating to the C=O bond is probably a result of the change in donor identity. In the pure HPAA crystal the bond donor is the hydrogen from the phenolic hydroxide group, whereas in the co-crystal it is a hydrogen from the amide of INCT.

4.3.2.3. INCT-DHPAA

4.3.2.3.1. PXRD

Equimolar solutions of INCT and DHPAA in either ethanol or ethanol and water all produced powders suitable for analysis. Comparison of the three diffraction patterns (Figure 4-25) confirms that all three solutions produced crystals with the same structure. Those printed from ethanol appeared to be very low density and had a very “fluffy” appearance when removed from the acetate sheet onto which they were printed. This resulted in them being very difficult to handle and also meant that forming a flat bed of crystals in the PXRD sample holder was not possible. The material appears to have poor crystallinity, evident from the low intensity to noise ratio of the reflections and the poor resolution and peak shape. Conversely, the patterns recorded for crystals grown in mixtures of ethanol and water are much better. The reflections are well resolved, with

narrow peak shapes and higher intensity to noise ratios. These crystals appeared to have a much higher density when removed from the acetate sheet and were generally much easier to handle. The superior quality of these crystals may be due to the slower growth caused by the addition of water to the solutions, which reduces the rate of solvent evaporation after printing. The quality of the crystals printed from both solutions with water was very similar, but the resolution of the reflections in the pattern for the 9:1 (EtOH:H_2O) solution is higher and so all further analysis will be discussed in relation to these crystals.

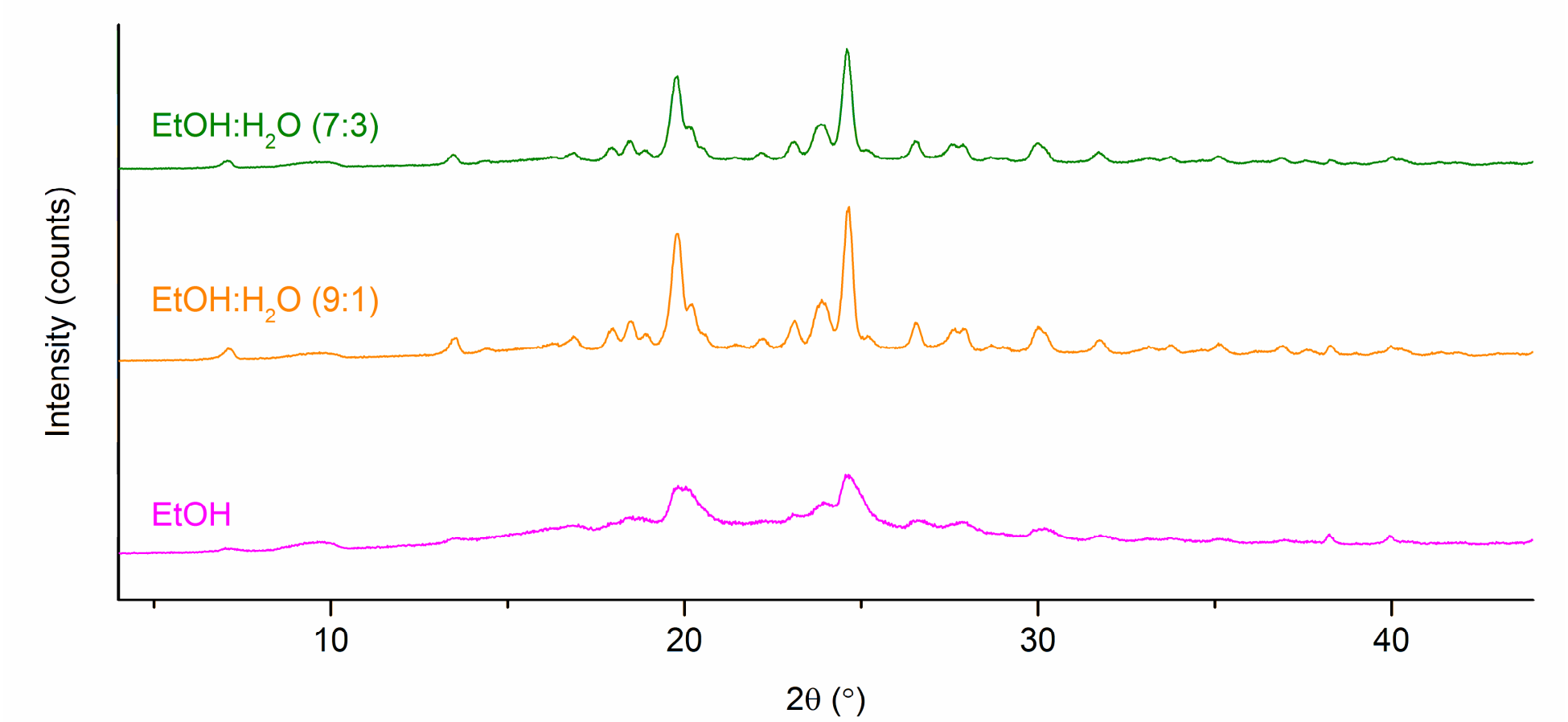

Figure 4-25. Diffraction patterns for crystals printed from equimolar solutions of INCT and DHPAA in EtOH, EtOH with 10 % v/v water and EtOH with 30 % v/v water.

Comparison of patterns recorded for the printed crystals, the raw materials separately and a physical mixture of the two can be seen in. The pattern for the printed crystals is clearly very different to those of the raw materials. The reflections of the printed crystals at 7.1°, 16.9°, and 23.9° do not appear with either of the raw materials, and the reflection at 24.6° in the printed crystals' pattern has a much higher relative intensity than any in the other patterns at the same angle. Additionally, there are reflections in the data for the raw materials that are absent in the printed crystals (at 10.9°, 20.9°, 25.8°, 26.1°, and 30.8°). The differences in diffraction patterns are indicative of different crystal structures, and strongly suggest the formation of a co-crystal.

DHPAA has only one known polymorph but INCT has five and to ensure that it had not simply crystallised into a different polymorph from that recorded prior to dissolution the printed crystal pattern was compared to powder patterns of the known polymorphs (Appendix 3). These patterns were predicted from structures collected from the CSD (EHOWIH01-05) and none were a good match.

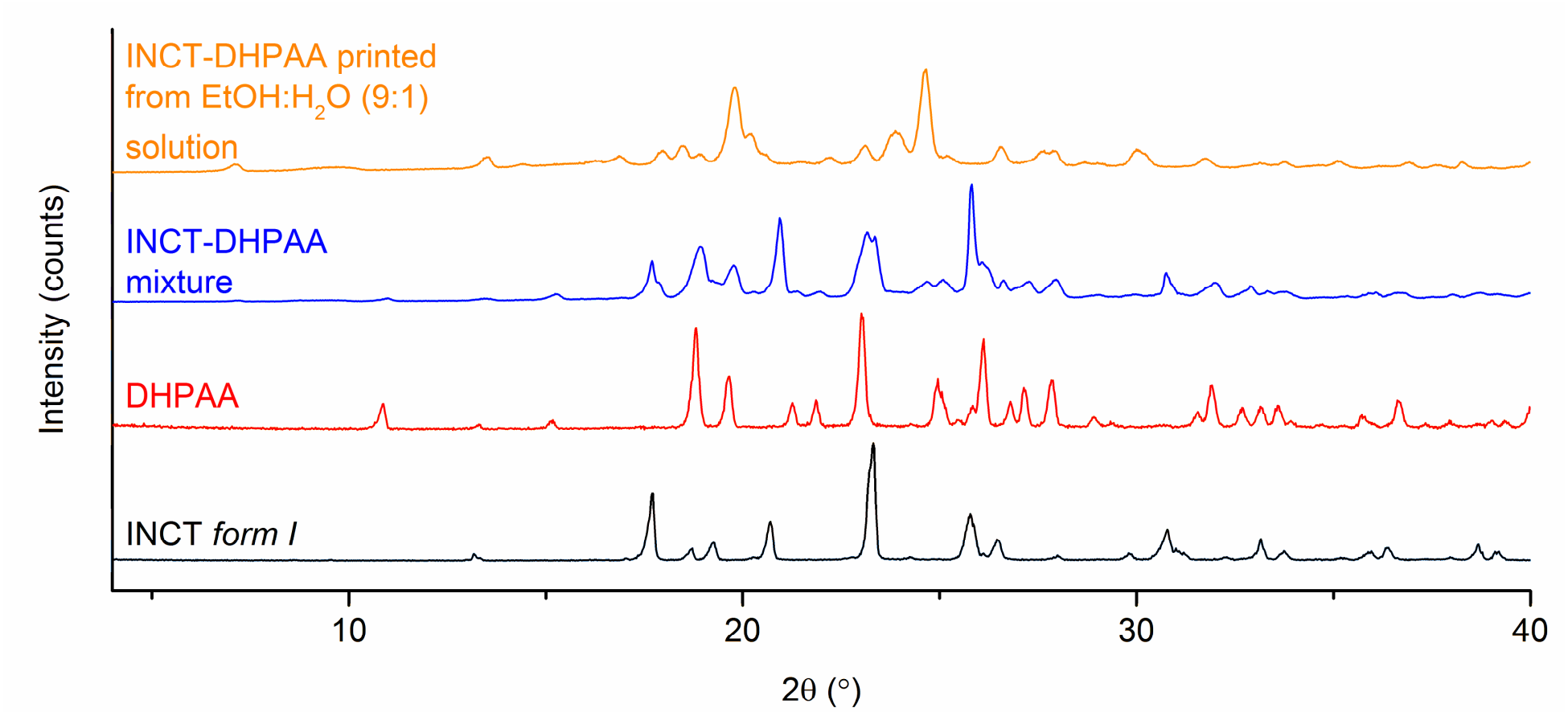

Figure 4-26. Diffraction patterns for INCT, DHPAA, a physical mixture of the two and crystals printed from an equimolar solution of the two in ethanol and water (9:1).

Refinement of the structure of a single co-crystal of INCT-DHPAA grown previously in the group[248] was used to create a predicted powder pattern, which is compared to the pattern recorded for the printed crystals in Figure 4-27. Despite the lower resolution of the pattern for the printed crystals it can be seen that Bragg reflections occur at very similar angles for both, and the intensity ratios are also strikingly similar. It appears from these data that the printed crystals have the same structure as that grown slowly by solvent evaporation.

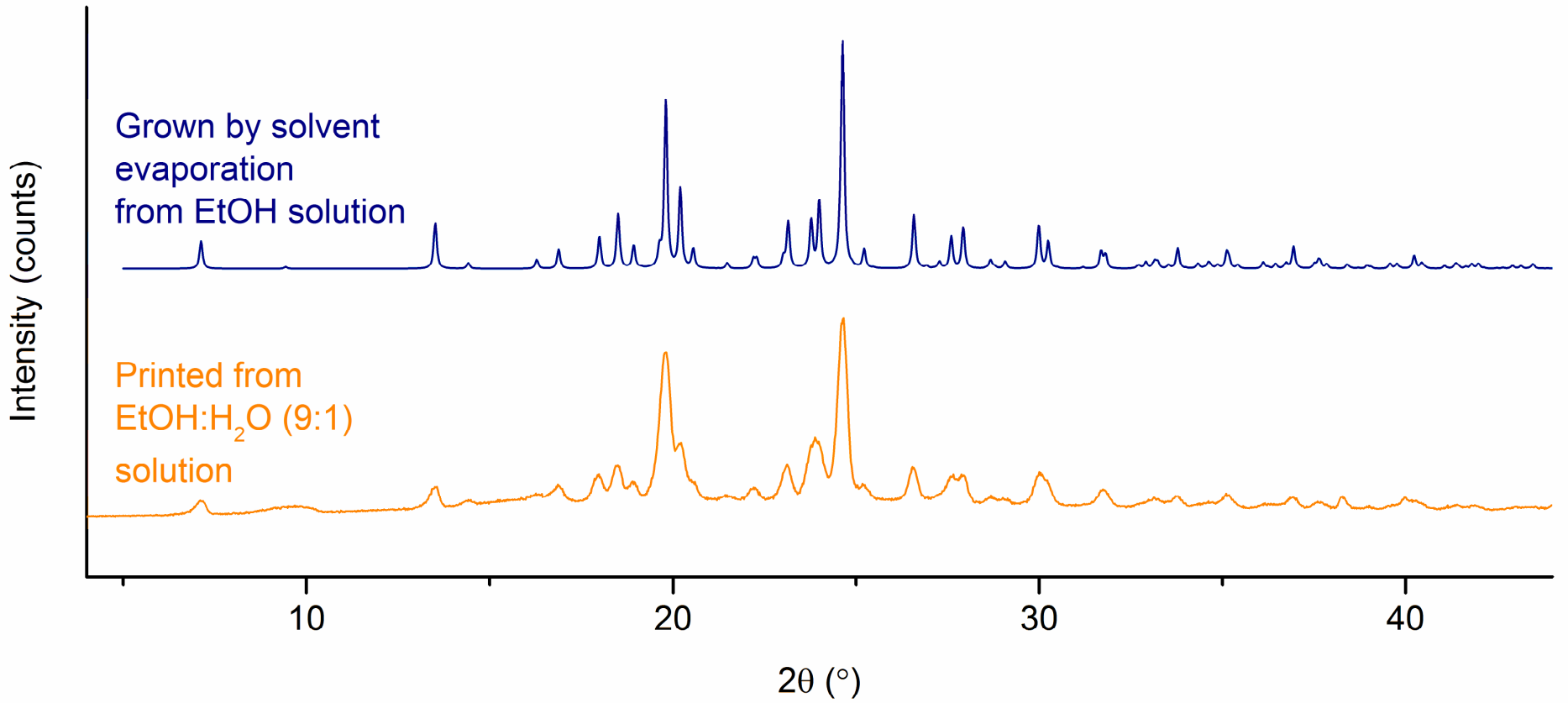

Figure 4-27. Powder diffraction pattern for crystals printed from an equimolar solution of INCT:DHPAA in EtOH:H_2O (9:1 v/v) and a predicted powder pattern for crystals grown by solvent evaporation from an equimolar ethanolic solution by Dongpeng Yan.

4.3.2.3.2. DSC and TGA

DSC thermograms recorded for crystals printed from solutions of INCT and DHPAA can be seen in Figure 4-28. The thermograms for samples of crystals printed EtOH and 9:1 v/v EtOH/water display endothermic events, with onsets at 118.8 °C and 118.6 °C, peaks at 122.3 °C and 122.2 °C, and enthalpies of 95.4 J g^{-1} and 112.0 J g^{-1} respectively. The crystals printed from the EtOH:H_2O 7:3 solution have an endotherm in a similar position, with a peak at 120.9 °C, and also a smaller endotherm just prior to this with an onset of *ca.* 99.6 °C (Figure 4-28, inset). This may indicate the occurrence of a phase transition immediately prior to the second endotherm. The lower temperature event appears as a shoulder to the second much larger event, and as a result it is not possible to accurately analyse the onset or enthalpies of either of the endotherms in this trace. The larger of the two events is probably the same as is observed in the thermograms of the crystals printed from the other two solutions, albeit occurring at a slightly lower temperature. This earlier onset may be a result of destabilisation caused by the prior event.

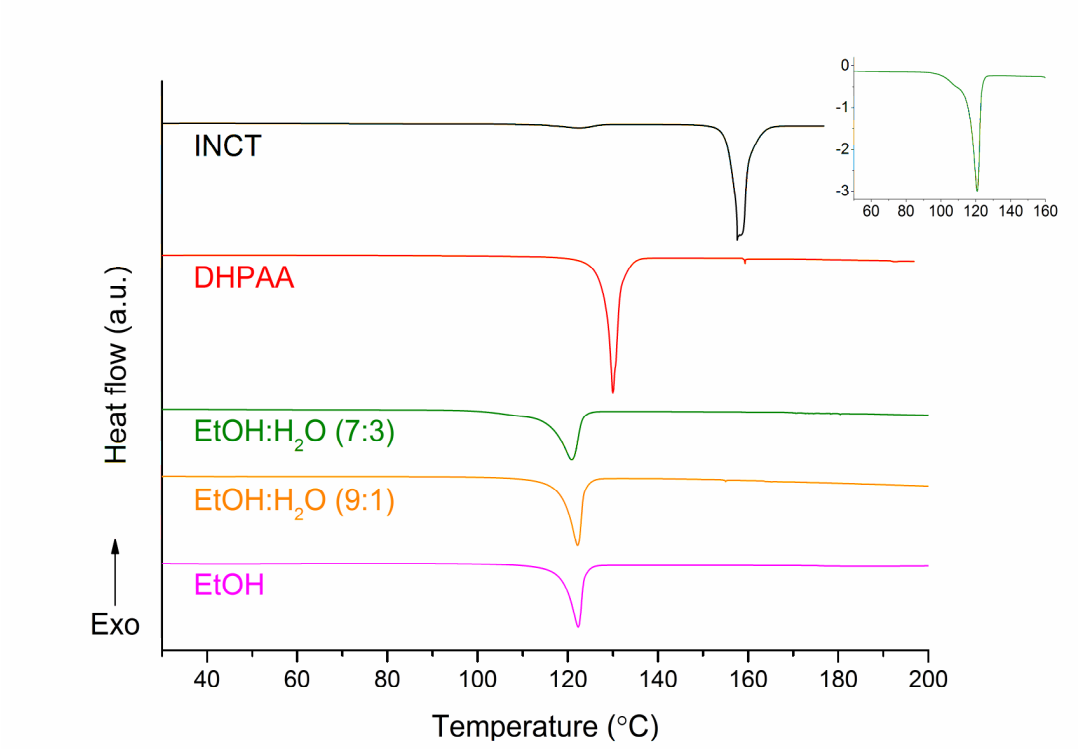

Figure 4-28. DSC thermograms for crystals formed by inkjet printing ethanolic solutions of INCT and DHPAA, and the two raw materials; INCT and DHPAA. The inset plot shows a magnified view of the endothermic events in the trace for the sample printed from EtOH:H_2O (7:3) solution.

It is likely that the large endotherms in all three of the traces for the printed crystals are a result of the melting of co-crystals formed by printing. As was observed for INCT-HPAA, the melting endotherms of the two raw materials occur at higher temperatures and with

much higher associated enthalpies of fusion (INCT: 157 °C, 184 J g^{-1}; DHPAA: 128 °C, 200.6 J g^{-1}) than those of the printed crystals.

TGA analysis (Figure 4-29) shows that the printed crystals decompose at a temperature higher than INCT but lower than DHPAA or a physical mixture of the two components. This different behaviour, particularly in relation to the mixture, lends support to the theory that a co-crystal has formed in the printing process.

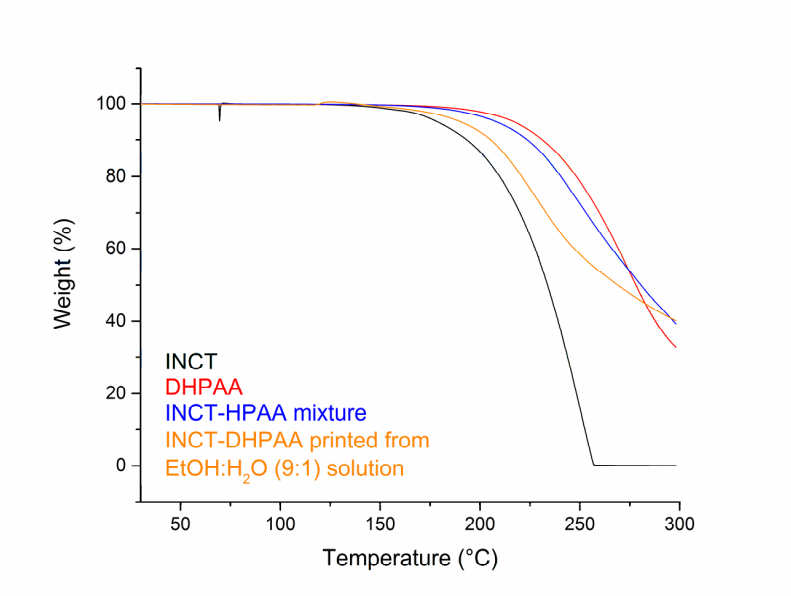

Figure 4-29. TGA data for INCT, DHPAA, a physical mixture of the two and crystals printed from an ethanolic solution of the two.

4.3.2.3.3. FTIR spectroscopy

Comparison of the FTIR spectra for printed crystals and a physical mixture of INCT-DHPAA (Figure 4-30) reveals differences in the materials. The broad band between 3150 cm^{-1} and 3400 cm^{-1} is narrower for the printed sample and the band at 3450 cm^{-1} in the spectrum for the mixture is missing from the crystals' data. There is a band at 1730 cm^{-1} for the printed sample that is absent from the mixture, and there is a band missing from the printed spectrum at 995 cm^{-1} (Figure 4-30, inset). Therefore it can be assumed that the printed crystals are not simply a physical mixture and that there are new interactions occurring.

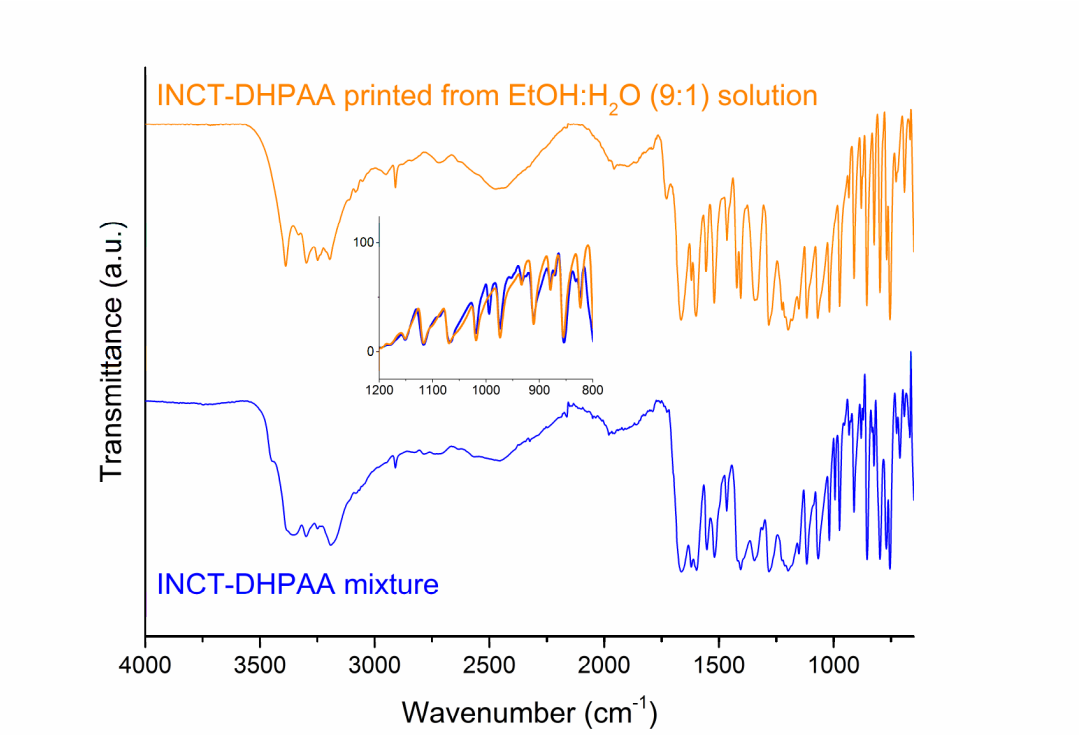

Figure 4-30. FTIR spectra for a physical mixture of INCT and DHPAA and crystals printed from an equimolar solution of INCT and DHPAA in ethanol and water (7:3 v/v). Inset: data from 900 to 1200 cm^{-1}.

Spectra for the printed crystals and the two raw materials can be seen in Figure 4-31. At the higher wavenumbers similar behaviour can be seen to that of INCT-HPAA. The two INCT N—H bands at 3360 cm^{-1} and 3180 cm^{-1} appear to experience a small shift to lower and higher wavenumbers respectively, when printed with DHPAA. The sharp strong O—H bands, associated with the hydroxyl groups on the benzene ring of DHPAA, both shift to lower wavenumbers following printing. This is also the case for the broad medium intensity band at 3000 cm^{-1} representing the acidic O—H, which undergoes a large shift to 2500 cm^{-1}. This suggests that changes in interactions involving the OH groups of the DHPAA, of which there are three, are more significant than those involving the amide of the INCT. Changes in the fingerprint region are far more complex and difficult to assign. All of the IR shifts outlined can be accounted for by the changes in intermolecular interactions described in Section 4.3.2.3.1.

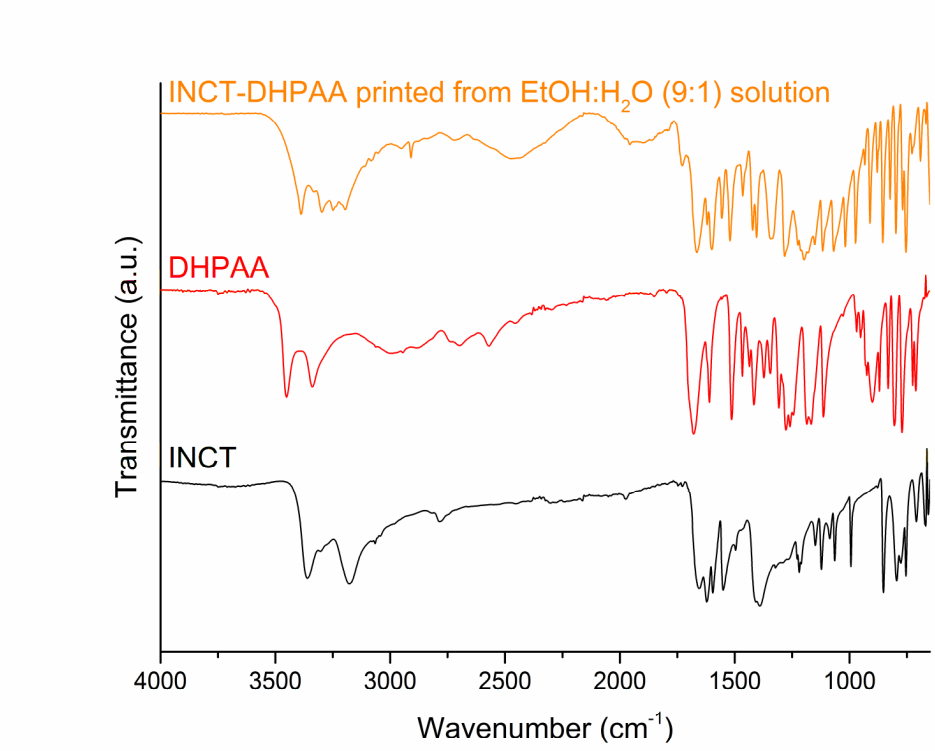

Figure 4-31. FTIR spectra for INCT, DHPAA and crystals printed from an equimolar solution of the two in ethanol and water (9:1).

4.3.2.4. INCT-LABA

4.3.2.4.1. PXRD

Crystals produced by printing equimolar solutions of INCT and LABA in EtOH and EtOH with either 10 % or 30 % v/v water all produced patterns with reflections occurring at the same angles (Figure 4-32). The intensity to noise ratio is higher and the peak resolution of the patterns collected for crystals printed from the solutions in EtOH and EtOH with 10 % v/v water is far higher than those of the crystals printed from EtOH with 30 % v/v water. This may be a product of the longer evaporation time due to the higher water to ethanol ratio of the solvent, resulting in more disruption of the crystal growth as the acetate sheet remained wet for longer than the other two samples. This opposes the behaviour observed for the INCT-DHPAA system. However, it appears that the products from all three printing processes are the same, as all of the Bragg reflections occur at the same angles in each of the three patterns and the intensity ratios are similar.

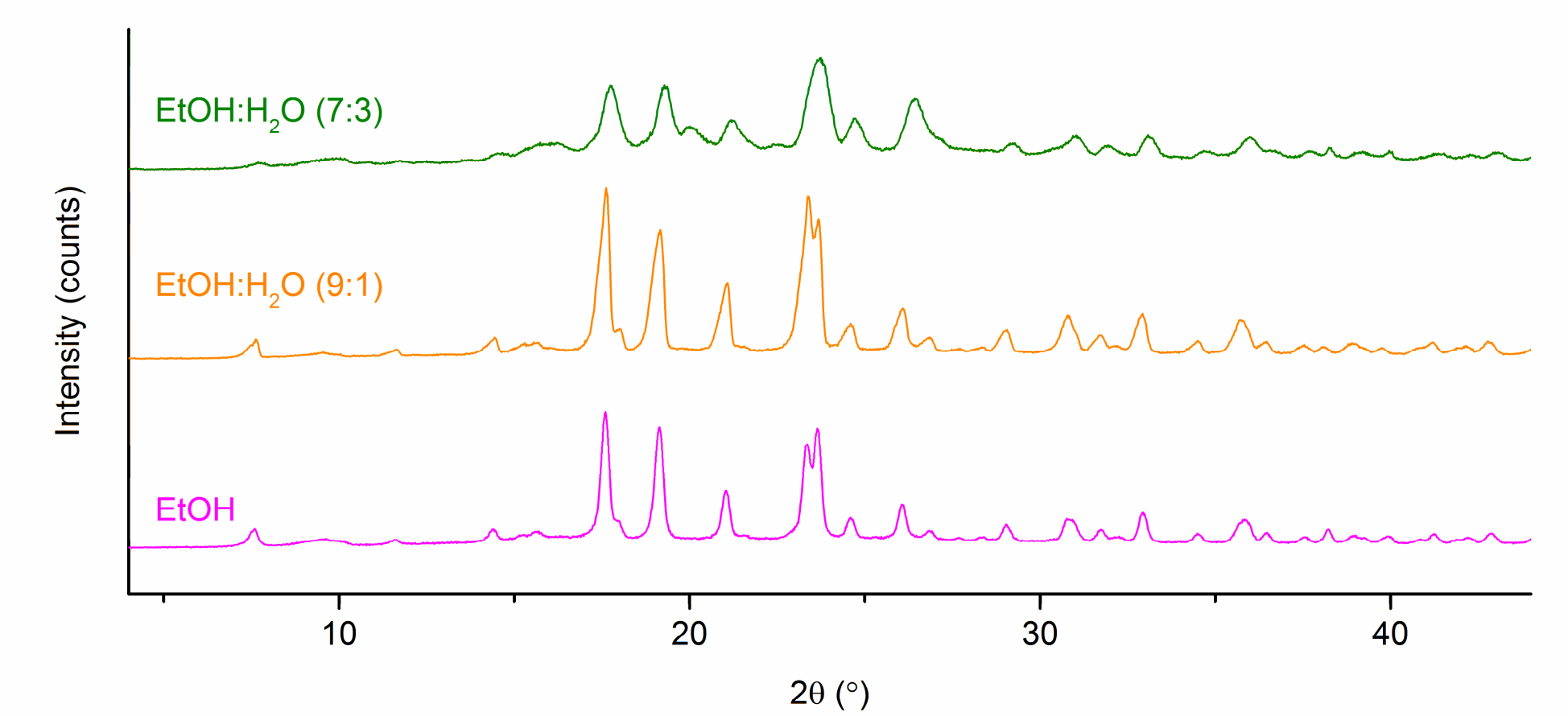

Figure 4-32. Diffraction patterns for crystals printed from equimolar solutions of INCT and LABA in EtOH, EtOH with 10 % v/v water and EtOH with 30 % v/v water.

As with the three previous samples it was necessary to compare the patterns of the printed crystals to those of the raw materials and a mixture of the raw materials to confirm that the printed crystals were not just a physical mixture of the two components. Crystals printed from solution in ethanol produced diffraction patterns with the narrowest peak shape and highest resolution and so these were used for all further analysis. Data are presented in Figure 4-33. There are major differences between the diffraction patterns of the printed crystals and the raw materials. The most obvious being the absence in the printed crystal data of the main reflection of LABA at 10.5°. This is a very high intensity reflection in both the patterns for LABA and the physical mixture and so its absence suggests a change in the structure of LABA. It should be noted that although the reflection in the pattern for LABA at 15.7° is absent in that of the printed crystals it is also absent from the pattern for the physical mixture, and cannot therefore definitely be ascribed to a change in structure; more likely its disappearance is caused by preferred orientation. The remaining three high intensity reflections from the LABA pattern, between 27.5° and 30.5°, are also absent from the pattern of the printed crystals and so it appears that its structure must have changed in the printing process.

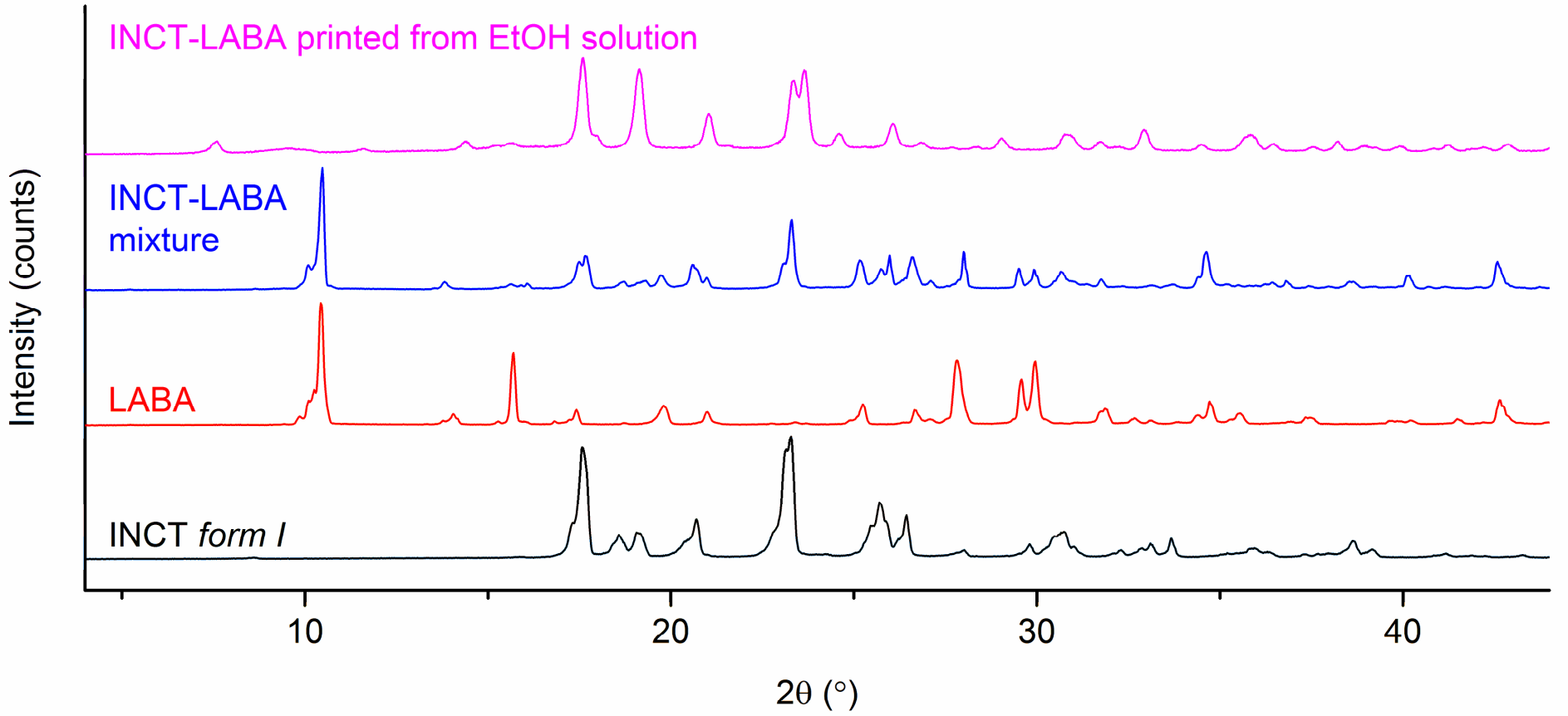

Figure 4-33. Diffraction patterns for INCT, LABA, a physical mixture of the two and crystals printed from an equimolar solution of the two in ethanol.

Differences from INCT I are more subtle. The two main reflections at 17.6° and 23.3° cannot be distinguished from reflections at the same angles in the pattern of the printed crystals, and neither can any of the lower intensity reflections. There are however new reflections present in the pattern for the printed crystals at 7.6°, 19.1°, 23.6°, and 24.6°. These differences indicate the formation of a co-crystal has occurred between the two materials, although it may be that INCT has recrystallised to the same form as the initial material and LABA has crystallised to a new form. However, there is currently only one LABA structure reported in the literature. More likely, it seems that there may have been excess INCT in the initial mixture and that this has recrystallised to INCT I while the rest of the material has co-crystallised.

Comparison of the diffraction data for the printed crystals with that predicted from the single crystal reaction product grown by solvent evaporation can be seen in Figure 4-34. The two patterns are clearly different, even if the presence of INCT I is taken into account. The PXRD data therefore indicate that inkjet printing has resulted in a structural change to LABA, but not the chemical reaction that took place in the solvent evaporation experiments. However it cannot be definitively concluded that a co-crystal has formed between the two materials due to the similarities in the pattern of the printed crystals and that of INCT prior to printing, and the differences between the printed crystal data and the single crystal data.

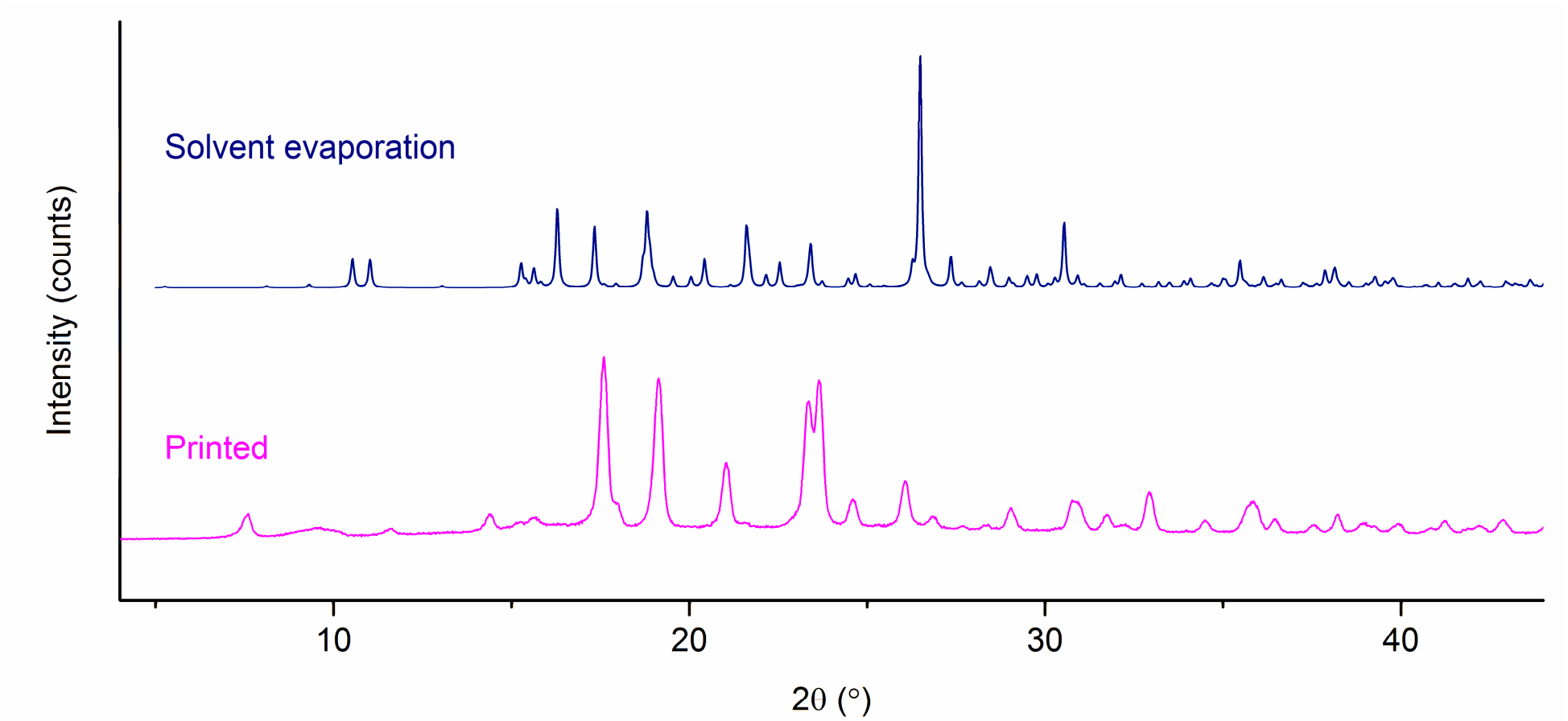

Figure 4-34. Powder diffraction pattern for crystals printed from an equimolar solution of INCT:LABA in EtOH and a predicted powder pattern for crystals grown by solvent evaporation from an equimolar ethanolic solution.

4.3.2.4.2. DSC and TGA

DSC data for crystals printed from INCT and LABA are presented in Figure 4-35. The crystals printed from ethanol have what appears to be a small endotherm with an onset at *ca.* 42 °C. On closer inspection (Figure 4-35 (b)) it was concluded that there is a concurrent step change in the baseline at this point, which results from a change in heat capacity of the solvent and is characteristic of a glass transition in an amorphous material. The endotherm at the same position is a result of enthalpic relaxation of the amorphous portion of the sample. This event is visible in the traces from the other printed samples, but it is so small it can barely be seen. This indicates that the printing process results in the vitrification of some of the material, however it is not clear whether it is one or both of the components.

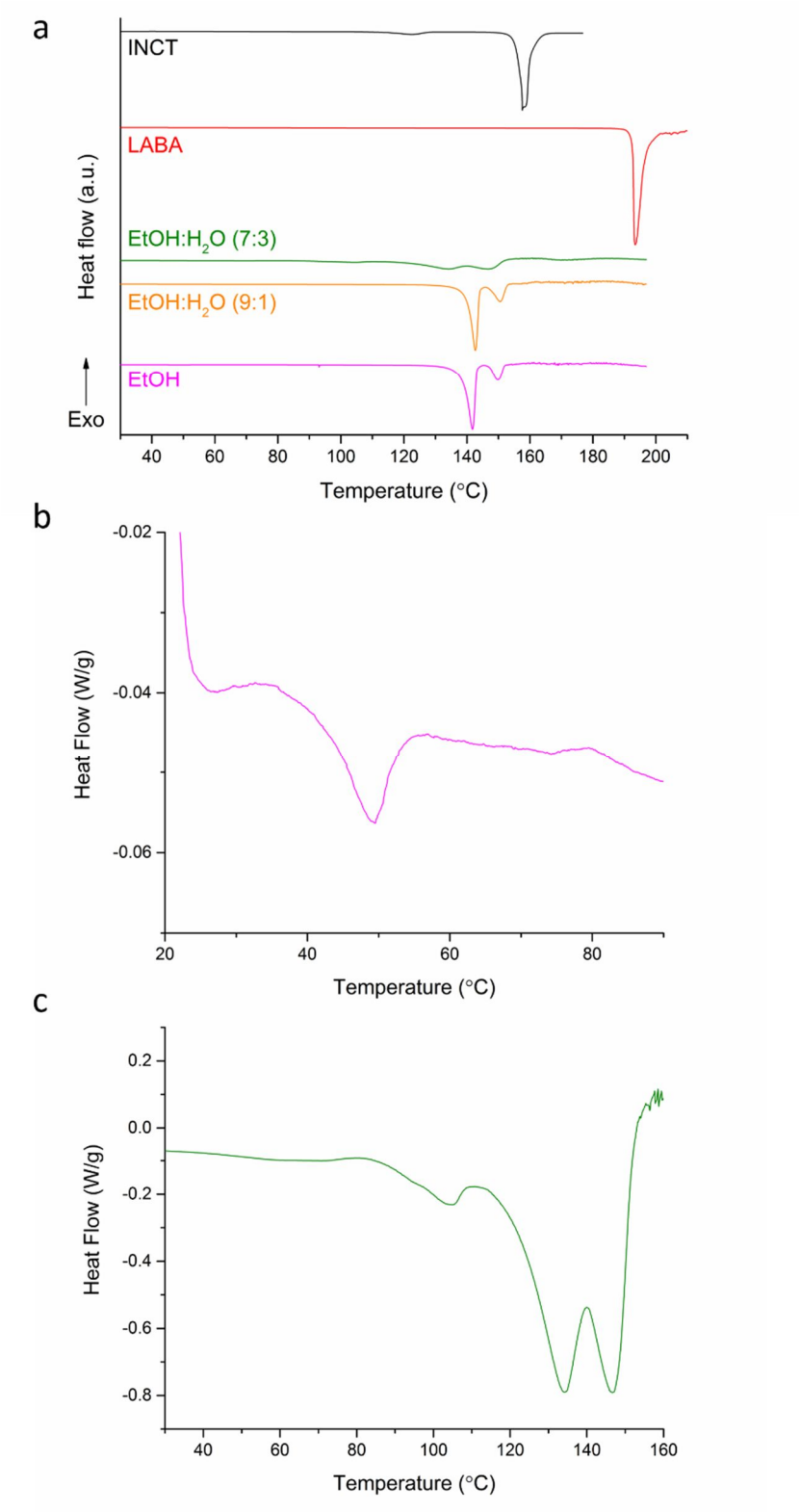

Figure 4-35. DSC thermograms for (a) crystals formed by inkjet printing solutions of INCT and LABA and the two raw materials; INCT and LABA, (b) an enlarged plot of the T_g region of the crystals printed from solution in ethanol, and (c) an enlargement of the trace for crystals printed from solution in water and ethanol (7:3 v/v).

At *ca.* 80 °C, in all three traces, there is a small exotherm. It is so small that it is not possible to measure the onset temperature or associated enthalpy. It is likely that this is caused by the crystallisation of the amorphous material that caused the T_g.

Immediately following this crystallisation in the data for the crystals printed from ethanol with 30 % water (Figure 4-35 (c)) is an endotherm, which peaks at *ca.* 105 °C. This is not present in either of the other two traces and occurs at too low a temperature to be either of the two raw materials melting.[246,249] It may however represent melting of a metastable polymorph of a co-crystal that has formed.

Above 110 °C events in all three traces are similar and consist of two endotherms, although these occur *ca.* 20 °C lower for the crystals printed from the 7:3 v/v solution. For the other two samples the first of these endotherms (onset 139-140 °C) has a higher enthalpy (125-129 J g^{-1}) than the second and occurs at a temperature lower than either of the two raw materials, and so must be the result of a new structure forming. The highest temperature endotherm has an onset of 147 °C with an enthalpy of 24-28 J g^{-1}. This second endotherm has an onset 10 °C lower than that of INCT and 46 °C lower than LABA. It is possible that there may have been residual INCT present following printing and that the presence of the co-crystal has supressed its melting point resulting in the second endotherm. It is also possible that first endotherm corresponds to the melting of a metastable form, which then crystallised to the most stable form, and finally the latter melted, with the exotherm of crystallisation being hidden by the two large endotherms relating to fusion. The similarity of the two data sets of the crystals printed from solutions of higher proportions of ethanol is such that the materials produced must be the same. The differences and poor quality of the other sample is a consequence of slower solvent evaporation resulting from excess water.

4.3.2.4.3. FTIR spectroscopy

Figure 4-36 shows FTIR spectra for crystals printed from an INCT-LABA solution in ethanol and a physical mixture of the two components. There are a few very obvious differences. There is a small sharp band at 3525 cm^{-1} in the spectrum of the mixture that is absent from the printed crystal data. There is also a strong sharp band at 3180 cm^{-1} in the mixture spectrum, whereas the same region in the printed crystal spectrum has a strong but much broader band. There are also subtle differences in the data between 650 cm^{-1} and 1800 cm^{-1} that suggest shifts in band positions, possibly due to changes in H-bonding. It is clear from the comparison of these two spectra that the printed crystals are not simply a physical mixture of the two materials.

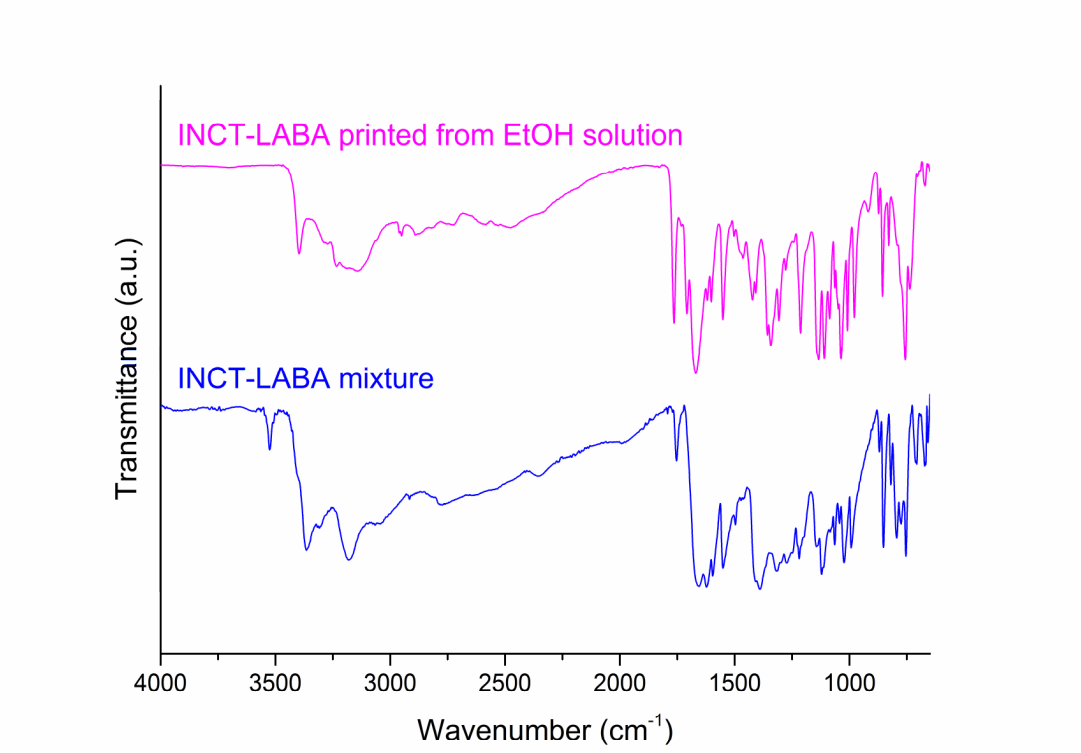

Figure 4-36. FTIR spectra for a physical mixture of INCT and LABA and crystals printed from an equimolar solution of INCT and LABA in ethanol.

In the high wavenumber region the differences between the spectra of the raw materials and the printed crystals are obvious. LABA has four strong sharp bands at 3525 cm^{-1}, 3405 cm^{-1}, 3310 cm^{-1}, and 3205 cm^{-1} representing OH stretching of the four hydroxyl groups. In the same region the data for INCT display two strong sharp bands associated with the NH stretching of its amide group. This region of the printed crystal spectrum has just one sharp strong band at 3395 cm^{-1} followed by a broad strong band with a number of minima superimposed upon it at 3290 cm^{-1}, 3270 cm^{-1}, 3235 cm^{-1}, 3190 cm^{-1}, and 3140 cm^{-1}. These changes are all related to the functional groups in each of the raw materials that are likely to be involved in hydrogen bonding in a crystal. Changes below 1800 cm^{-1} are again much more subtle and consist of slight shifts in many of the bands but both materials appear to be represented in the spectrum of the printed crystals. The subtlety of these changes suggests the formation of a new crystal structure, possibly a co-crystal rather than the occurrence of a reaction between the two materials. However, without single crystal data to support this summation it is not possible to comment on the changes in intermolecular interactions. Hence, it is not possible to link the FTIR data with changes around specific bonds.

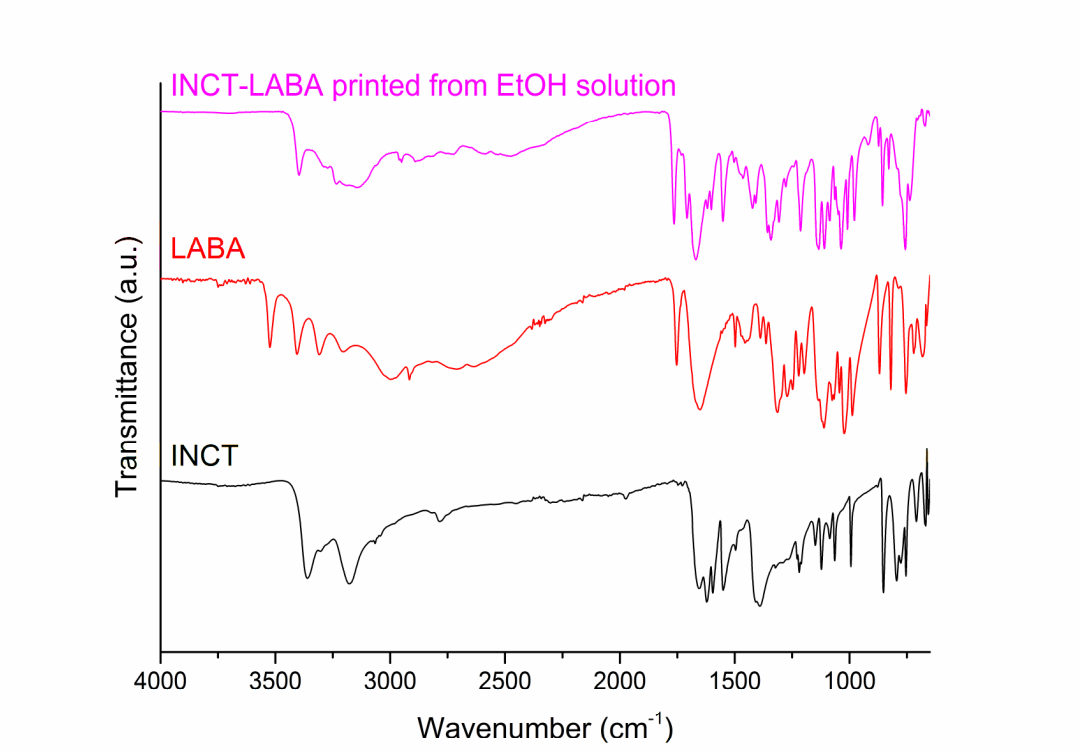

Figure 4-37. FTIR spectra for INCT, LABA and crystals printed from an equimolar solution of the two in ethanol.

4.3.3. Heat induced co-crystallisation

Heat induced co-crystallisation is a very simple and environmentally friendly method for screening for co-crystals.[86] Its green credentials stem from the fact that it requires no solvent and its simplicity is due to the method involving no more than heating a mixture of two or more components. It has even been shown in at least one case that simply making contact between two single crystals of materials that are amenable to co-crystallisation, at ambient temperatures, can result in the spontaneous melting of the components and their recrystallisation as a co-crystal.[87]

4.3.3.1. INCT-HBA

DSC thermograms were recorded for two different mixtures of INCT and HBA in a 1:1 molar ratio. The first was made up by simply weighing and mixing the two materials in the condition in which they were received from the supplier. The second was made up by first grinding each of the two materials separately in a pestle and mortar and then mixing them. The traces can be compared in Figure 4-38. Both mixtures produced similar profiles with a number of events. The non-ground mixture has an almost imperceptible endotherm that peaks at 129.2 °C (onset: 122.9 °C; enthalpy: 3.127 J g^{-1}), followed by another larger endotherm (onset: 143.2 °C, enthalpy: 50.72 J g^{-1}) peaking at 145.6 °C.

The ground mixture has a similar set of events with a small endotherm at 132.6 °C (peak: 135.6 °C), immediately followed by a small overlapping exotherm (peak: *ca.* 137 °C), which itself is followed by an overlapping endotherm (peak: 144.0 °C). Due to the overlapping of these events accurate onset temperatures and enthalpies cannot be calculated. However, estimates show the enthalpies of the two endotherms to be 4.8 J g^{-1} and 63.7 J g^{-1} respectively.

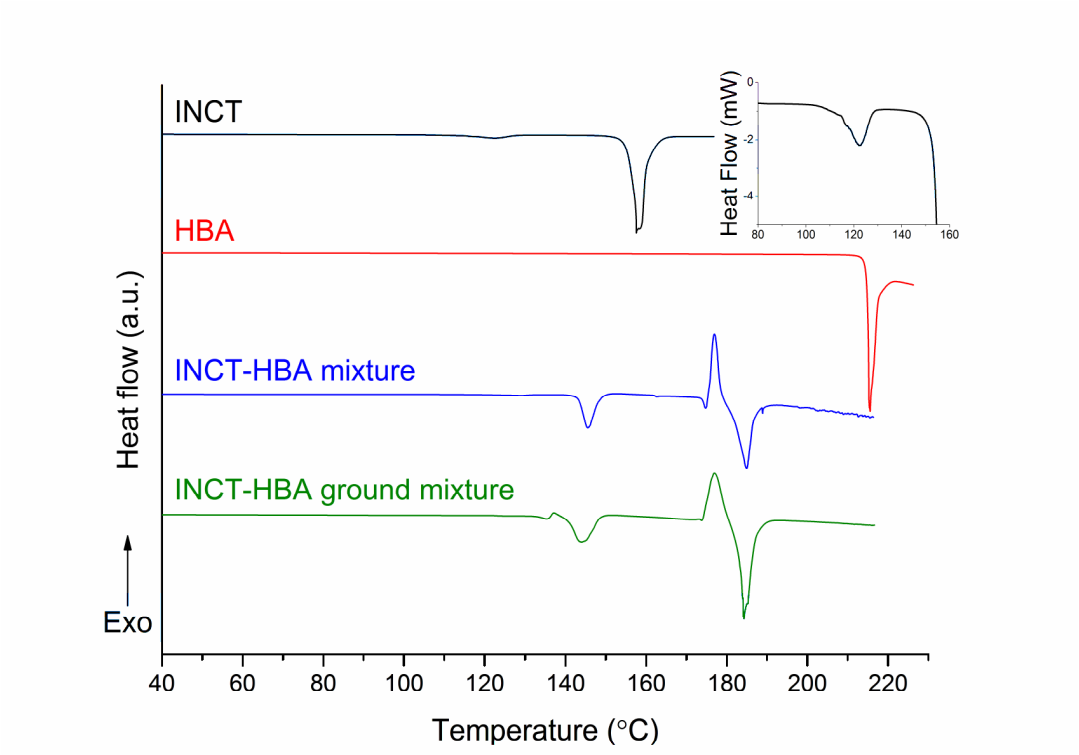

Figure 4-38. DSC thermograms recorded for INCT, HBA, a mixture of the two raw materials as received, and a mixture of the two materials after grinding them separately in a pestle and mortar. Inset: an enlargement of the INCT II→I endotherm.

Both mixtures then go on to experience an endo-exo-endo event beginning at 173.9 °C (non-ground) and 173.4 °C (ground). Again, the onsets and enthalpies of the succeeding exotherm and endotherm in both datasets cannot be accurately analysed due to the overlap of the events. However, a visual comparison indicates the enthalpies are similar and the peaks of the two events occur at 177.0 °C and 185.0 °C for the mixture and at 176.9 °C and 184.3 °C for the ground mixture. The similarity between all of the events observed must be a result of the same phase transitions occurring in each of the two mixtures.

The events observed in the data for the mixtures all occur at temperatures at which there are no events observed in the thermograms for the raw materials. However, the final endotherm in both datasets occurs at the same temperature as the endotherm observed for the printed samples of the same materials (peak: 184.1 °C). The higher temperature

events in both DSC traces must be caused by the co-crystallisation of the materials followed immediately by their melting. Furthermore, it appears that the initial co-crystallisation begins with a melt, characterised by the small endotherm immediately prior to the exotherm. It should be noted that some effects of decomposition are observed immediately following the endotherm at 145 °C. However, TGA data recorded for samples of the same two mixtures (Figure 4-39) show that, although decomposition definitely begins prior to the second set of events, at 193 °C 92.5 % of the material remains. It may be coincidental that the endotherm at 185 °C occurs at the same temperature as that of the printed sample but the data strongly suggest the formation and subsequent melting of the same co-crystals, despite this decomposition.

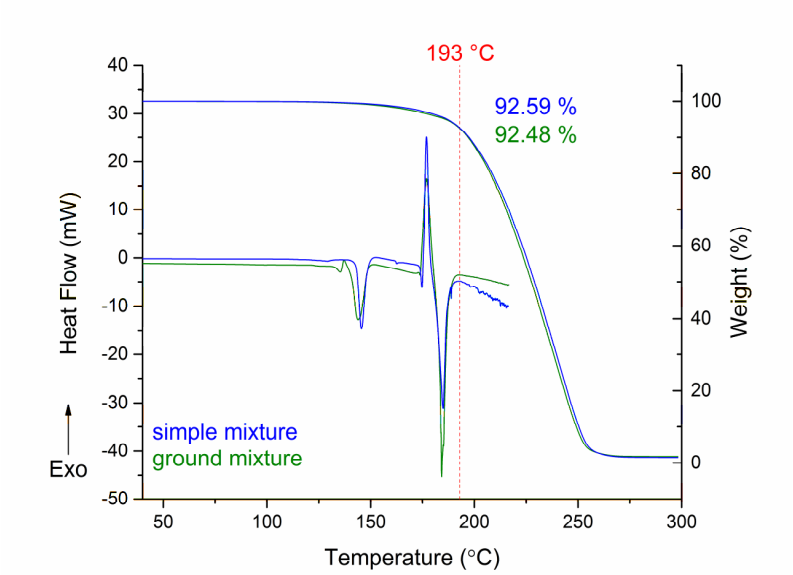

Figure 4-39. DSC and TGA thermograms recorded for a simple equimolar mixture of INCT and HBA and a mixture in which the two constituents had been ground separately in a pestle and mortar prior to mixing.

The explanation for the lower temperature group of events is less clear. Data for the raw materials and the printed crystals do not display such an event. To understand this in more detail, a sample of the physical mixture of the two materials as received was subjected to combined DSC-XRD analysis. The experiment was stopped at 170 °C to prevent decomposition of the sample in the DSC cell. The diffraction data and DSC thermogram (Figure 4-40) display two very obvious phase changes beginning at 123.4 °C (3.72 J g^{-1}) and 141.9 °C (59.02 J g^{-1}). Both transformations involve structural changes and are endothermic. The events observed are clearly the same events observed in the two samples previously discussed as they occur at similar temperatures and have similar associated enthalpies. There is also a third, transient phase that gradually grows in at around 67 °C and disappears with the phase transition at 123.4 °C.

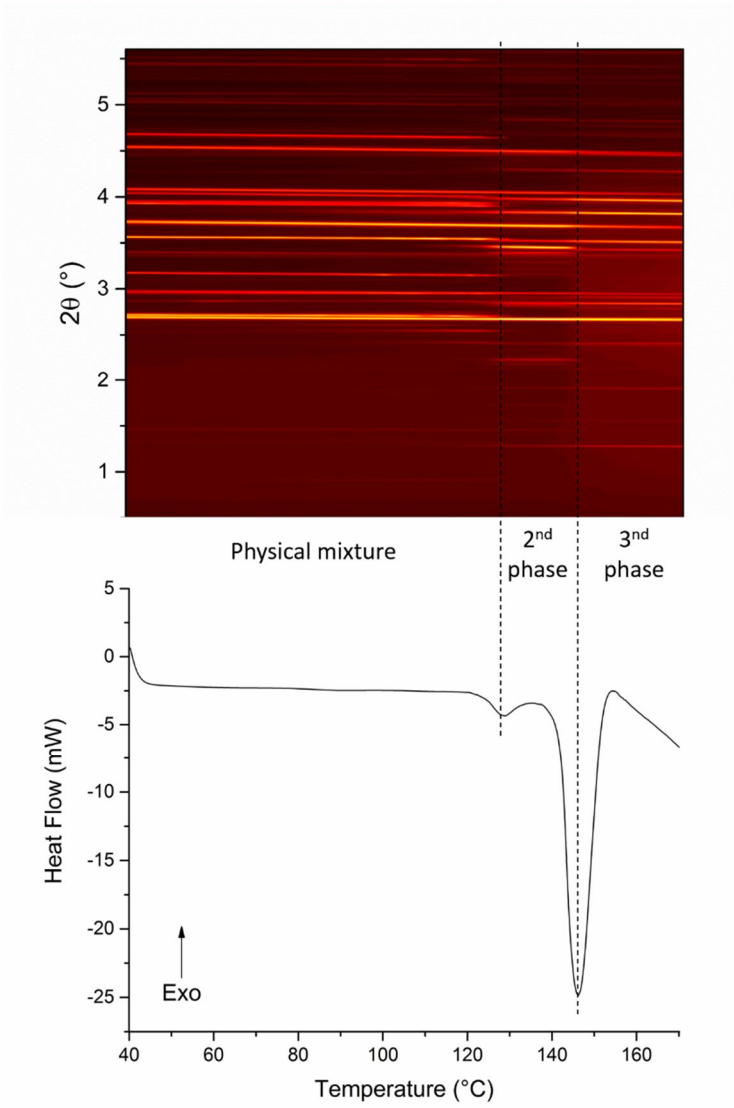

Figure 4-40. Simultaneous DSC-XRD data for an equimolar physical mixture of INCT and HBA.

Rietveld refinement against the pattern for the physical mixture recorded at 40 °C in the DSC can be seen in Figure 4-41. Starting models used for all refinements on this system are presented in Table 4-3. Refined unit cell data can be seen inTable 4-4. The initial sample was a physical mixture of INCT I and HBA and so the pattern recorded was expected to be a combination of the two and initial refinements were carried out using these materials. However, there was a small unidentified reflection at 2.61° and so other possible structures were introduced, including all known polymorphs of INCT, VAKTOR,[232] and the co-crystal grown by solvent evaporation (discussed in section 4.3.1). Surprisingly, the best fit was achieved when refining the structure for the new co-crystal grown in this work. It seems that simply mixing the two materials resulted in growth of a small amount of the co-crystal. However, at this temperature, only 5.3 % of the sample was converted and visual inspection of the pattern suggests this may result

from the poor powder character of the sample and resultant unrepresentative intensity ratios.

Table 4-3. Starting models used for Rietveld refinement against diffraction patterns collected for an equimolar mixture of INCT and HBA.

Species	Model
INCT *form I*	EHOWIH01*
INCT *form II*	EHOWIH02*
HBA	JOZZIH*
Co-crystal *Literature*	VAKTOR*
Co-crystal *This work*	Collected data (section 4.3.1)

*taken from the CSD.

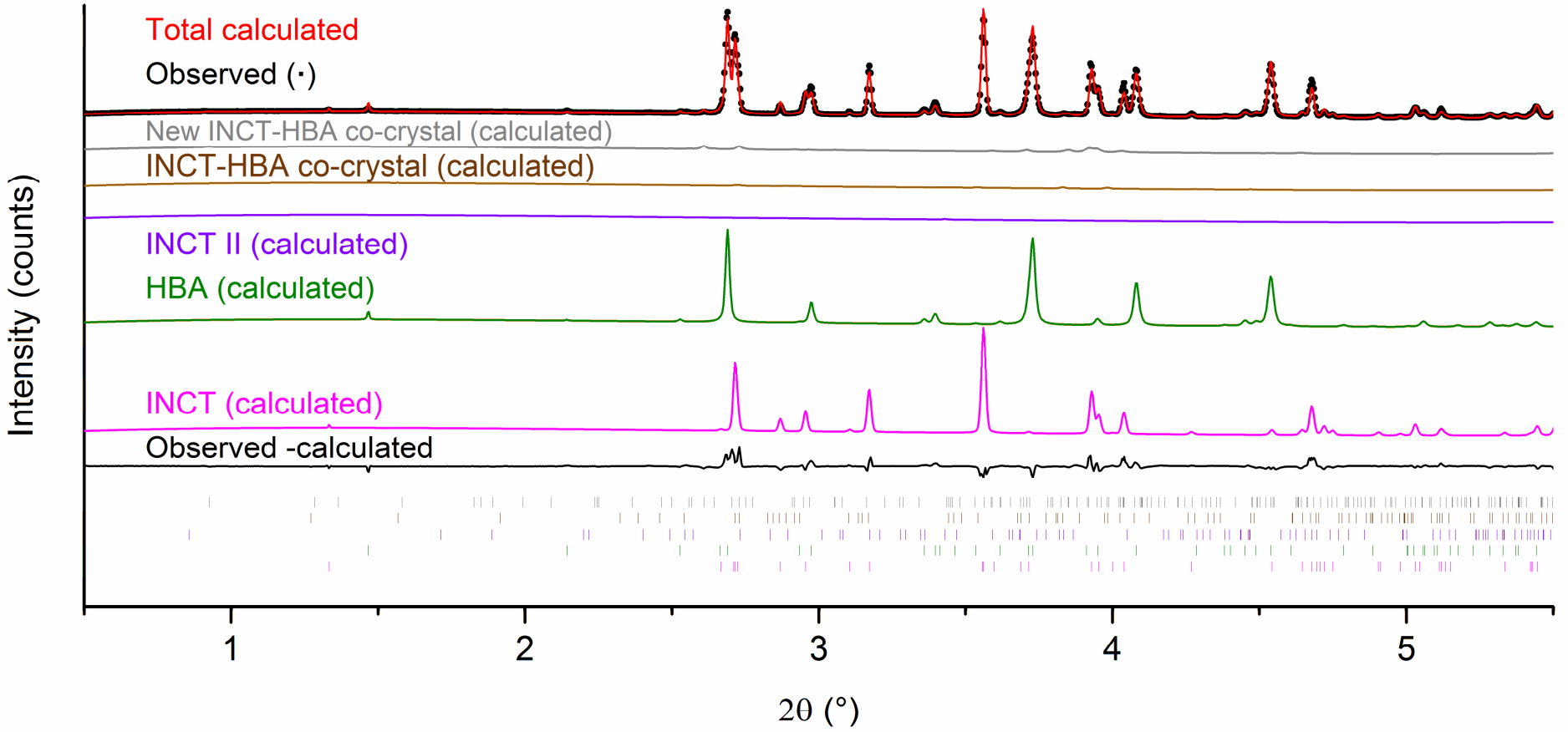

Figure 4-41. Rietveld refinement data for a physical mixture of INCT and HBA at 40 °C. Tick marks show the positions of allowed reflections of each phase.

Table 4-4. Refinement parameters for a physical mixture of INCT and HBA at 40 °C. The starting models were taken from the CSD (INCT: EHOWIH01; HBA: JOZZIH).

Property	INCT	HBA	Co-crystal *This work*
T / °C		40	
Space group	$P2_1/c$	$P2_1/a$	$P2_1/c$
a / Å	10.2442(8)	18.504(4)	10.656(9)
b / Å	5.7426(5)	5.2373(3)	29.31(12)
c / Å	10.0650(7)	6.3345(13)	7.743(7)
α / °	90	90	90
β / °	97.259(7)	93.205(12)	97.82(10)
γ / °	90	90	90
Cell volume / Å^3	587.36(8)	612.95(16)	2396(10)
R_{wp}		0.0757	
$R_{wp\text{-}bkd}$		0.1843	
Phase Fraction*	43.1 %	50.5 %	5.3 %

*Due to the graininess of the sample, representative errors cannot be calculated. However, the author conservatively estimates the error to be in the region of 5 %. As a result the sum does not equal 100 % as a small portion of the material was assigned to the other structures included in the refinement.

At 97 °C characteristic reflections of the new co-crystal are much more intense, and reflections from a fourth structure are present. The results of Rietveld refinements carried out on the pattern recorded at this temperature can be seen in Figure 4-42 and Table 4-5. The new entity has been identified as the co-crystal already reported by Vishweshwar *et* al.[232] The relative intensities of the reflections of the two co-crystals compared to those of the two raw materials are low, as are the relative quantities. As with samples discussed in Chapters 2 and 3 this sample was relatively grainy and not a perfect powder, and so the pattern recorded consisted of rings of spots rather than smooth Debye-Scherrer rings. As a result the intensity ratios of the reflections were not a true representation of the structure of the material and so, the identity of the new phase/phases cannot be confirmed with complete certainty at this temperature. That being said, none of the other refined structures were a good fit, so the most likely explanation for the new reflections is the co-crystallisation of the materials into these two structures.

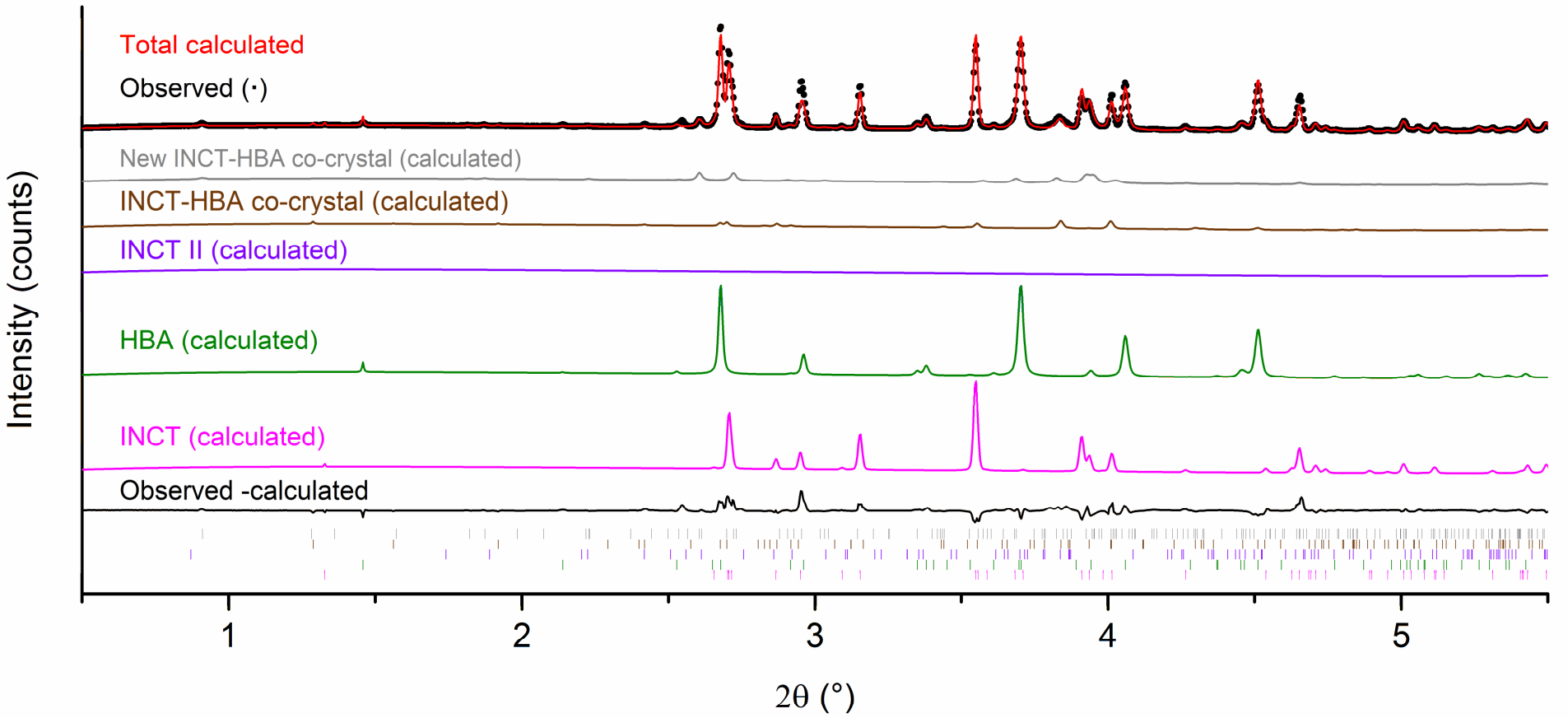

Figure 4-42. Rietveld refinement data for a physical mixture of INCT and HBA at 97 °C. Tick marks show the positions of allowed reflections of each phase.

Table 4-5. Refinement parameters for a physical mixture of INCT and HBA at 97 °C. The starting models for the raw materials were taken from the CSD (INCT: EHOWIH01; HBA: JOZZIH; Co-crystal: VAKTOR) and single crystal data reported in Section 4.3.1 was used for the new co-crystal.

Property	INCT	HBA	Co-crystal *VAKTOR*	Co-crystal *This work*
T / °C		97		
Space group	$P2_1/c$	$P2_1/a$	$P2_1/n$	$P2_1/c$
a / Å	10.2815(12)	18.601(4)	5.964(7)	10.722(4)
b / Å	5.7575(6)	5.2598(4)	9.536(10)	29.75(4)
c / Å	10.0893(9)	6.3409(16)	21.253(19)	7.725(4)
α / °	90	90	90	90
β / °	96.909(9)	92.837(1)	98.78(9)	98.90(6)
γ / °	90	90	90	90
Cell volume / Å^3	592.91(11)	619.6(2)	1194(2)	2427(3)
R_{wp}		0.0924		
$R_{wp\text{-}bkd}$		0.2227		
Phase Fraction*	37.6 %	50.37 %	5.85 %	6.10 %

*Due to the graininess of the sample, representative errors cannot be calculated. However, the author conservatively estimates the error to be in the region of 5 %.

At 122 °C the mixture has become extremely complex and refinement (Figure 4-43) reveals the presence of five species: INCT forms I and II, HBA, and both co-crystals. Examination of the contour plot (Figure 4-40) at this temperature shows that the pattern was recorded during the first significant phase transition of the experiment and rather than a simple conversion from the two initial materials to the known co-crystal there appear to be numerous transformations occurring. INCT I and II are enantiotropically related with the I→II conversion reported by Li *et al.*[246] to occur at 131.7 °C at a heating rate of 70 °C min^{-1}. At lower heating rates this can be expected to occur at a lower temperature and samples from the same study by Li were shown to convert to form II at *ca.*120 °C. Thus the presence of form II at 122 °C is not unexpected. At this temperature both forms of the co-crystal are still present. From this pattern alone it is not possible to deduce whether VAKTOR results from the transformation of the first co-crystal or from the transformation of HBA with either one or both of the forms of INCT.

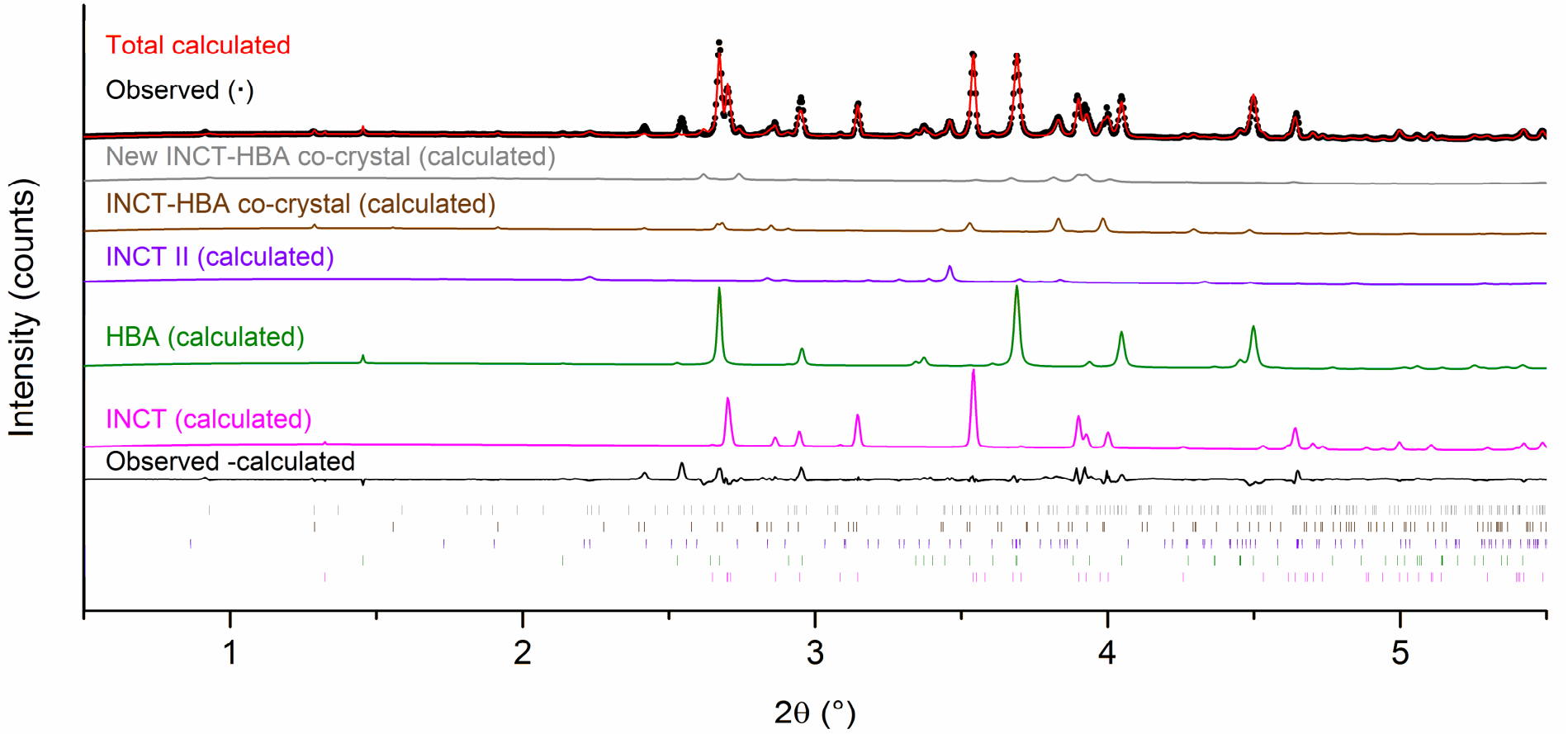

Figure 4-43. Rietveld refinement data for a physical mixture of INCT and HBA at 122 °C. Tick marks show the positions of allowed reflections of each phase.

Table 4-6. Refinement parameters for a physical mixture of INCT and HBA at 122 °C. The starting models for the raw materials were taken from the CSD (INCT I: EHOWIH01; INCT II: EHOWIH02; HBA: JOZZIH; reported co-crystal: VAKTOR), and the single crystal data reported in Section 4.3.1 was used for the new co-crystal structure.

Property	INCT *Form I*	HBA	INCT *Form II*	Co-crystal *VAKTOR*	Co-crystal *This work*
T / °C			122		
Space group	$P2_1/c$	$P2_1/a$	$P2_1/c$	$P2_1$/n	$P2_1/c$
a / Å	10.306(1)	18.653(5)	16.267(6)	6.040(4)	10.628(6)
b / Å	5.7654(7)	5.2696(4)	7.996(7)	9.560(6)	29.18(7)
c / Å	10.107(1)	6.346(2)	9.922(8)	21.16(1)	7.826(5)
α / °	90	90	90	90	90
β / °	96.82(1)	92.69(2)	105.66(6)	96.39(6)	98.26(8)
γ / °	90	90	90	90	90
Cell volume / Å^3	596.29(12)	623.1(3)	1242(1)	1214(1)	2402(6)
R_{wp}			0.0923		
$R_{wp\text{-}bkd}$			0.2191		
Phase Fraction*	31.4 %	41.5 %	7.3 %	10.7 %	9.1 %

*Due to the graininess of the sample, representative errors cannot be calculated. However, the author conservatively estimates the error to be in the region of 5 %.

At 139 °C, the midpoint of the second clear phase in the contour plot and between the two endotherms in the DSC trace, reflections of INCT I and the low temperature co-crystal have completely disappeared. Only INCT II, HBA and VAKTOR remain and they are present in significant quantities. It should be noted that the two single component crystal species are again present in a 1:1 ratio.

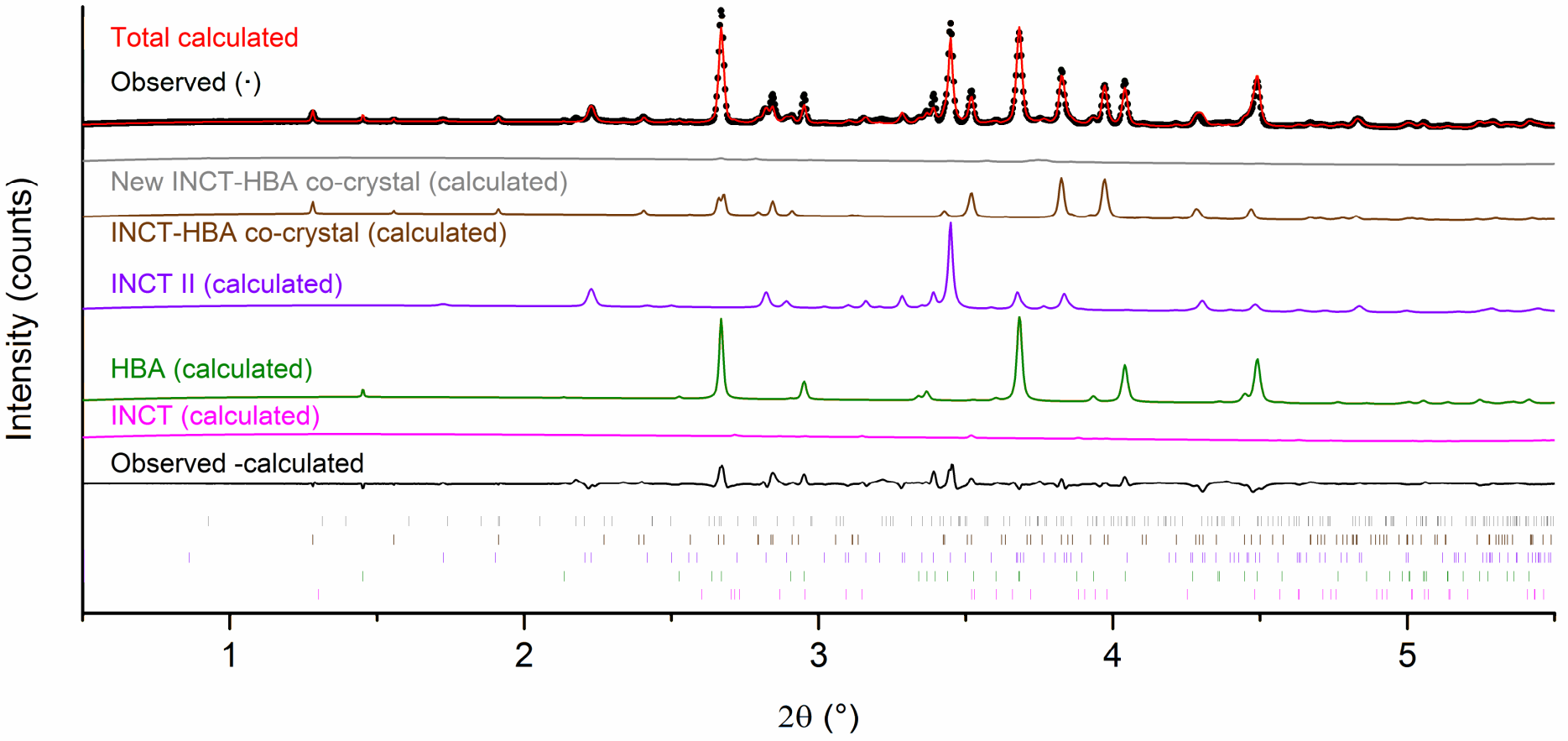

Figure 4-44. Rietveld refinement data for a physical mixture of INCT and HBA at 139 °C. Tick marks show the positions of allowed reflections of each phase.

Table 4-7. Refinement parameters for a physical mixture of INCT and HBA at 139 °C. The starting models for the raw materials were taken from the CSD (INCT II: EHOWIH02; HBA: JOZZIH; reported co-crystal: VAKTOR).

Property	HBA	INCT *Form II*	Co-crystal *VAKTOR*
T / °C		139	
Space group	$P2_1/a$	$P2_1/c$	$P2_1/n$
a / Å	18.667(5)	16.298(1)	6.060(1)
b / Å	5.2744(4)	7.993(1)	9.547(2)
c / Å	6.354(2)	9.964(2)	21.279(4)
α / °	90	90	90
β / °	92.59(2)	105.29(1)	96.26(2)
γ / °	90	90	90
Cell volume / Å^3	625.0(3)	1252.0(3)	1223.8(4)
R_{wp}		0.0930	
$R_{wp\text{-}bkd}$		0.2280	
Phase Fraction*	38.1 %	35.3 %	26.6 %

*Due to the graininess of the sample, representative errors cannot be calculated. However, the author conservatively estimates the error to be in the region of 5 %.

Refinement of the final pattern recorded at 170 °C (Figure 4-45 and Table 4-8) reveals that there is very little INCT II left in the sample. Inspection of the plots suggests that the value of 4.8 % that has been attributed to this form is probably incorrect and that there is in fact no pure INCT character remaining in the sample. The largest reflection in the calculated pattern for this species (3.4°) is probably a result of the software compensating for the disproportionately high intensity reflection present at the same angle in the pattern of VAKTOR. The vast majority of the remaining crystalline material can be attributed to the structure of the known co-crystal. However, there remains some residual HBA that has not co-crystallised. It seems odd that there is pure HBA left but no INCT as the initial mixture has been shown to be a 1:1 molar ratio and the unit cell of the co-crystal formed contains one molecule of each. Furthermore, the pattern recorded at 138 °C showed the same ratio of raw materials.

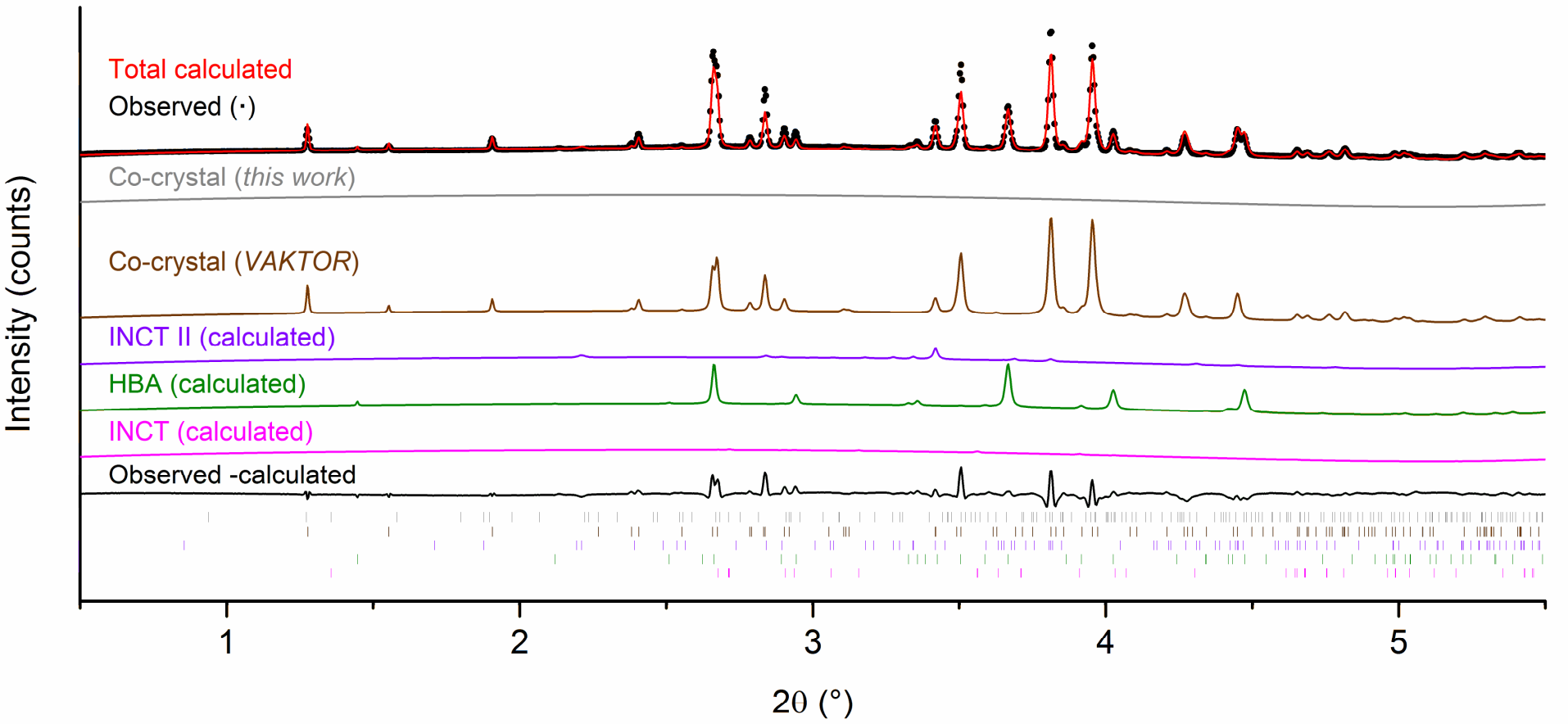

Figure 4-45. Rietveld refinement data for a physical mixture of INCT and HBA at 170 °C. Tick marks show the positions of allowed reflections of each phase.

Table 4-8. Refinement parameters for a physical mixture of INCT and HBA. The starting models were taken from the CSD (HBA: JOZZIH; Co-crystal: VAKTOR).

Property	HBA	INCT *Form II*	Co-crystal *VAKTOR*
T / °C		170	
Space group	$P2_1/a$	$P2_1/c$	$P2_1/n$
a / Å	18.780(11)	16.450(9)	6.064(1)
b / Å	5.2887(9)	8.070(9)	9.571(1)
c / Å	6.381(5)	9.905(11)	21.377(2)
α / °	90	90	90
β / °	92.61(4)	105.43(9)	96.442(11)
γ / °	90	90	90
Cell volume / Å^3	633.0(6)	1268(2)	1232.805(11)
R_{wp}		0.0855	
$R_{wp\text{-}bkd}$		0.2821	
Phase Fraction*	9.6 %	4.8 %	73.8 %

*Due to the graininess of the sample, representative errors cannot be calculated. However, the author conservatively estimates the error to be in the region of 5 %. As a result the sum does not equal 100 % as a small portion of the material was assigned to the other structures included in the refinement.

Simultaneous DSC and diffraction data can be seen in Figure 4-40. Plotting the total integrated intensity of each phase present as a function of time (Figure 4-46) it can be seen that there is little change in the overall content of HBA throughout the experiment until *ca.* 145 °C. There is some initial growth, presumably due to heat expansion causing more material to be lifted into the beam, followed by a gradual decline as the two co-crystals grow. INCT I experiences a concomitant decline. At *ca.* 120 °C there is a sharp drop in the content of INCT I and the new co-crystal, accompanied by equally sharp increases in the content of INCT II and VAKTOR. It seems that residual INCT I is converting to INCT II and the new co-crystal is converting to VAKTOR. At 132 °C INCT I and the new co-crystal have disappeared and the growth of VAKTOR slows before, soon after, INCT II and HBA undergo conversion to VAKTOR. However, the INCT disappears at a much higher rate than HBA. Examination of the DSC-XRD data (Figure 4-40) reveals that, coincident with the peak of the second endotherm in the DSC trace (146.2°), there is an obvious structural change occurring, characterised by the disappearance of many reflections and a broad increase in background intensity of the diffraction data (indicated by a subtle change in colour). These changes are caused by the melting of the remaining INCT II, albeit at a lower temperature than reported,[242,246,247,249] but that is expected behaviour for materials in mixtures.

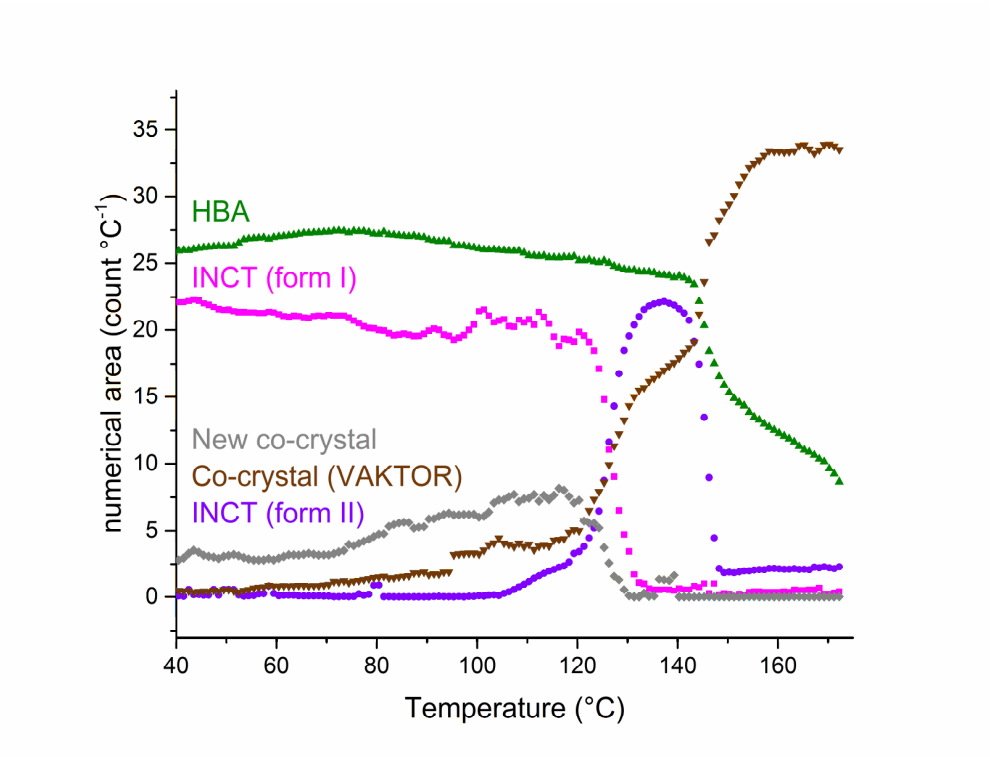

Figure 4-46. Plot of relative quantity as a function of time for each of the phases present in a mixture of INCT and HBA.

4.3.3.2. INCT-HPAA

As crystal growth experiments have shown INCT and HPAA to form a co-crystal in the molar ratio 2:1 (4.3.1), these were the proportions in which a physical mixture was made up for co-crystallisation by heating. Initial DSC analysis can be seen in Figure 4-47. The thermogram recorded for the mixture has three endothermic events, all of which are absent from the thermograms of the two raw materials. The first is very broad and has an onset at 94.4 °C and peaks at 97.9 °C. The enthalpy associated with this event can be approximated as 54.9 J g^{-1} but there is a visible difference in the baseline before and after the peak due to the extended lead in to the following endotherm, thus accurate measurement is impossible. The following events are overlapping, meaning analysis is significantly impaired. However, the onset of the first occurs at *ca.* 123.6 °C, with a peak at 125.2 °C and the second has an onset of *ca.* 126.3 °C and peaks at 127.7 °C. The associated enthalpies cannot be assessed. The broad nature of the first endotherm may conceal a number of events, whereas the second and third are much sharper and may indicate melting. This cannot be attributed to the melting of either of the raw materials in their most stable forms, as the temperature is too low. TGA of the mixture and the raw materials shows that mixing the two has a stabilising effect, with the raw materials experiencing 10 % mass loss at 193 °C (INCT) and 195 °C (HPAA), and the mixture at 205 °C. This suggests that intermolecular interactions may have taken place. However,

the TGA trace for the printed co-crystals (Section 4.3.2.2.1) contradicts this, showing 10 % mass loss at 175 °C. Again, sample mass may be a factor as the printed sample was much smaller than the prepared mixture.

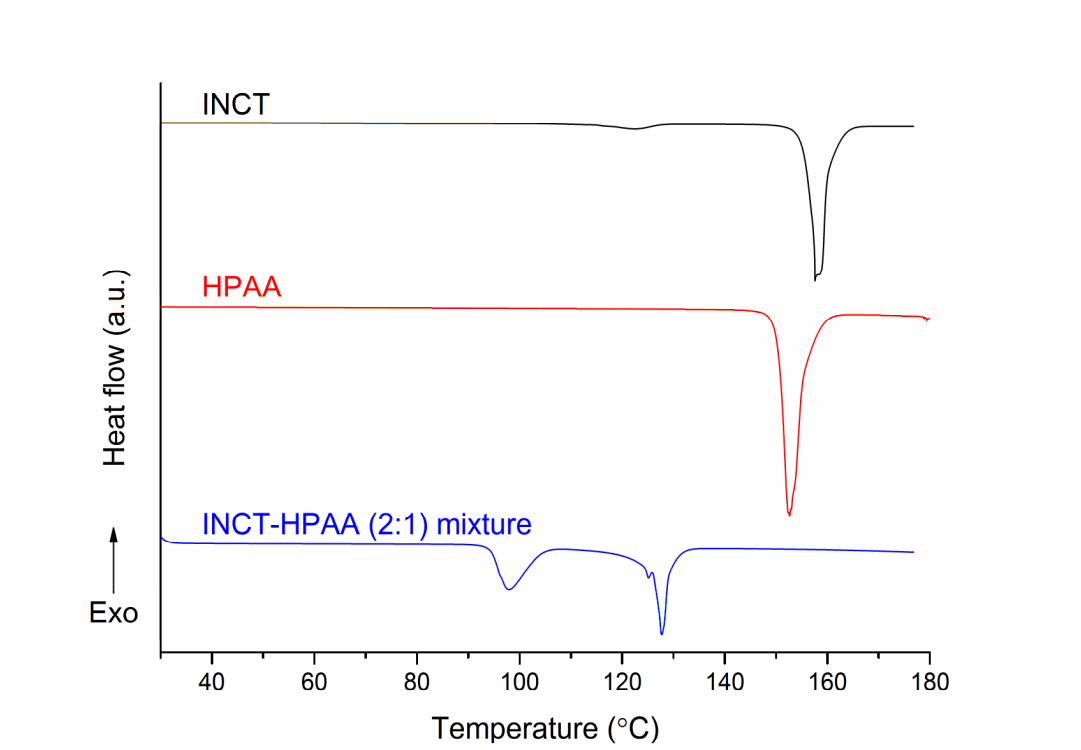

Figure 4-47. DSC thermograms recorded for INCT (black), HPAA (red), and a mixture of the two raw materials (2:1 molar ratio) as received (blue).

The same physical mixture was subjected to combined DSC-XRD (Figure 4-48). The diffraction data show two major phase transitions, occurring at *ca.* 95 °C and *ca.* 125 °C. Each of these has a corresponding endotherm in the DSC trace with onsets at 94.6 °C and 127.0 °C respectively. The thermogram has a very similar form to those discussed above. The first endotherm is smaller than the second but, rather than being broad, has a small shoulder on either side, indicating that the event occurring at this temperature either occurs in multiple stages or is in fact multiple events. The second, larger, endotherm has the same small event occurring just before it, as is seen in the previous thermogram, appearing as a shoulder. Again, this suggests a two stage process or multiple events. The total loss of Bragg reflections following the endotherm at 127.0 °C confirms the event as a melt.

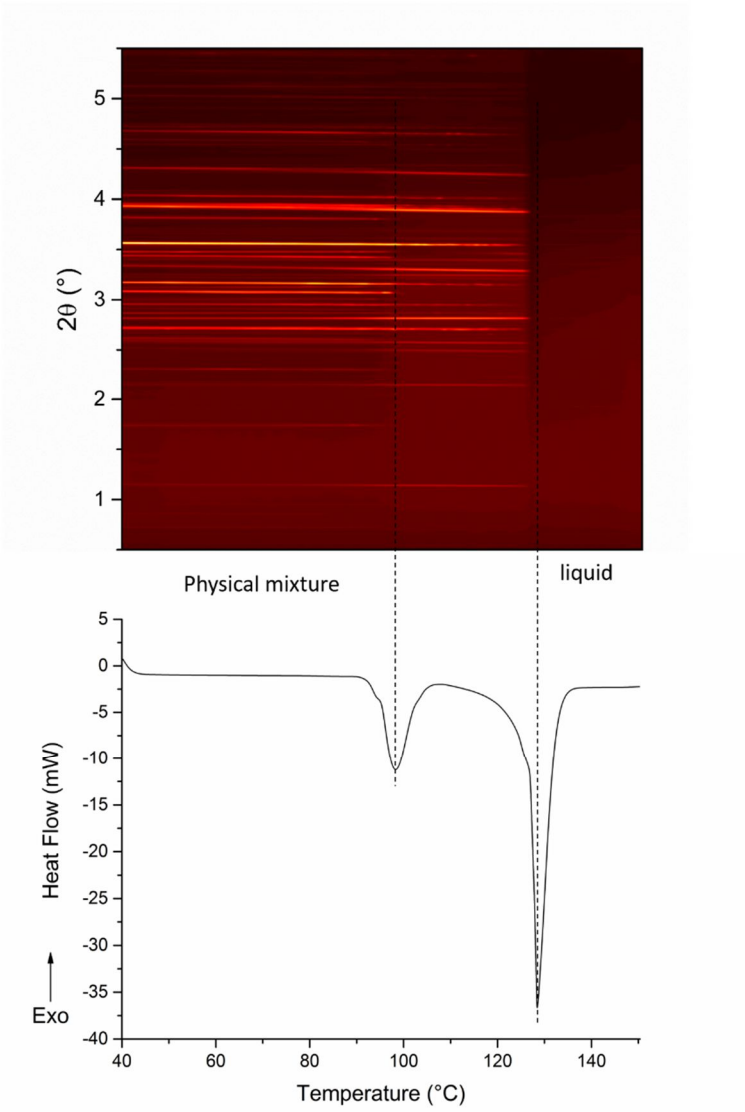

Figure 4-48. Simultaneous DSC-XRD data for a 2:1 molar ratio physical mixture of INCT and HPAA.

Results of Rietveld refinement of the initial pattern recorded for the mixture can be seen in Figure 4-49 andTable 4-9. The calculated patterns show the initial sample to be made up of mostly INCT I and HPAA as expected, but surprisingly there was also another species present. Structures of each of the known polymorphs of INCT were included in the refinement but none improved the fit. There are no other known polymorphs of HPAA, but inclusion of the co-crystal grown by solvent evaporation into the refinement showed it to be a close match to the unknown species. The fit of the calculated pattern to the data is not as good as for previous systems, with a R_{wp} of 0.1431. This can be partially explained by the significant difference in intensity between the data and the refinements of the reflections at 2.71° and 3.17°, characteristic of INCT. As with previous samples, this can be attributed to the presence of large grains of material, which resulted in effects similar to preferred orientation. There are also three low intensity observed reflections at

0.73°, 2.62°, and 2.92° that are absent from the calculated pattern. The cause of these reflections is unclear. It is unlikely to be another consequence of the grainy sample as this would not cause the appearance of new reflections, just differences in observed and calculated intensities. All three reflections are present from the first recorded pattern and fade from the data at the same temperature as the HPAA reflections, suggesting they are related. In contrast, the INCT reflections fade at a higher temperature and the co-crystal reflections are present throughout the experiment. The three unexplained reflections may be the result of some impurity in the sample.

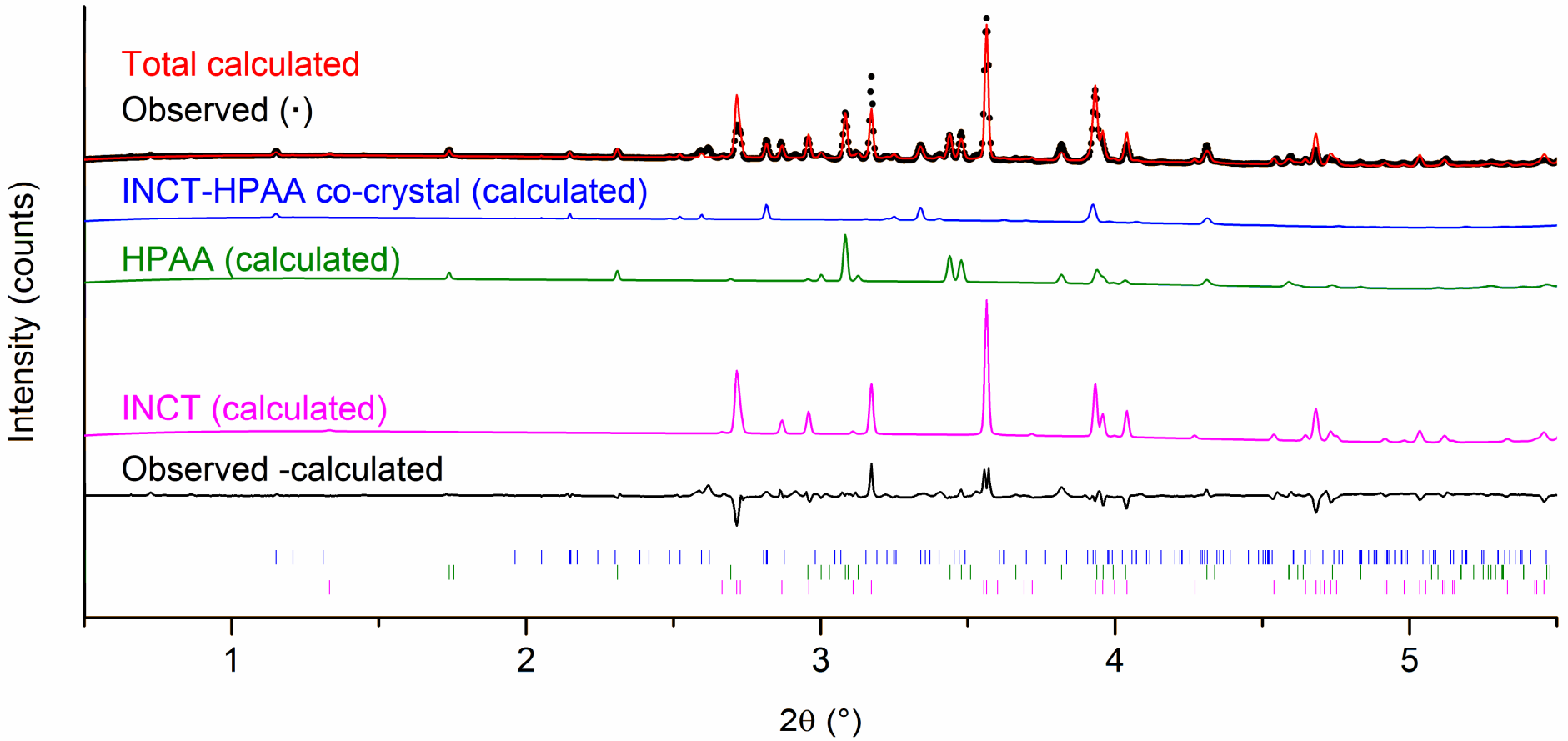

Figure 4-49. Rietveld refinement data for a mixture of INCT and HPAA at 40 °C. Tick marks show the positions of allowed reflections of each phase.

Table 4-9. Refinement parameters for a physical mixture of INCT and HPAA at 40 °C. The starting models for the raw materials were taken from the CSD (INCT: EHOWIH01; HPAA: QAPBAL) and single crystal data reported in section 4.3.1 was used for the co-crystal.

Property	INCT	HPAA	INCT-HPAA *Co-crystal*
T / °C		40	
Space group	$P2_1/c$	$P2_12_12_1$	P-1
a / Å	10.251(2)	5.3187(9)	6.792(6)
b / Å	5.729(1)	9.027(3)	12.31(2)
c / Å	10.065(1)	15.443(7)	12.81(2)
α / °	90	90	111.08(9)
β / °	97.30(1)	90	95.80(9)
γ / °	90	90	99.36(7)
Cell volume / Å^3	586.24(15)	741.4(4)	971(2)
R_{wp}		0.1431	
$R_{wp\text{-}bkd}$		0.2893	
Phase Fraction*	61.8 %	25.0 %	13.2 %

*Due to the graininess of the sample, representative errors cannot be calculated. However, the author conservatively estimates the error to be in the region of 5 %.

Refinement of the pattern recorded at 113 °C (Figure 4-50), between the two endotherms, has shown the sample to consist of just INCT and the co-crystal following the first phase transition, with the majority of the material being the co-crystal. The overall R_{wp} and the standard uncertainties (Table 4-10) for the co-crystal are much lower than those calculated for the same species in the 40 °C pattern. The major reflections in the co-crystal pattern occur at similar angles to those in the lower temperature pattern, and the three unidentified reflections are no longer present. This strengthens the argument that the third species in the initial mixture was the co-crystal. The three unidentified reflections may be the result of a contaminant or possibly an unknown polymorph of one of the components. It appears that, like the INCT-HBA mixture, just mixing INCT and HPAA caused some co-crystallisation to occur.

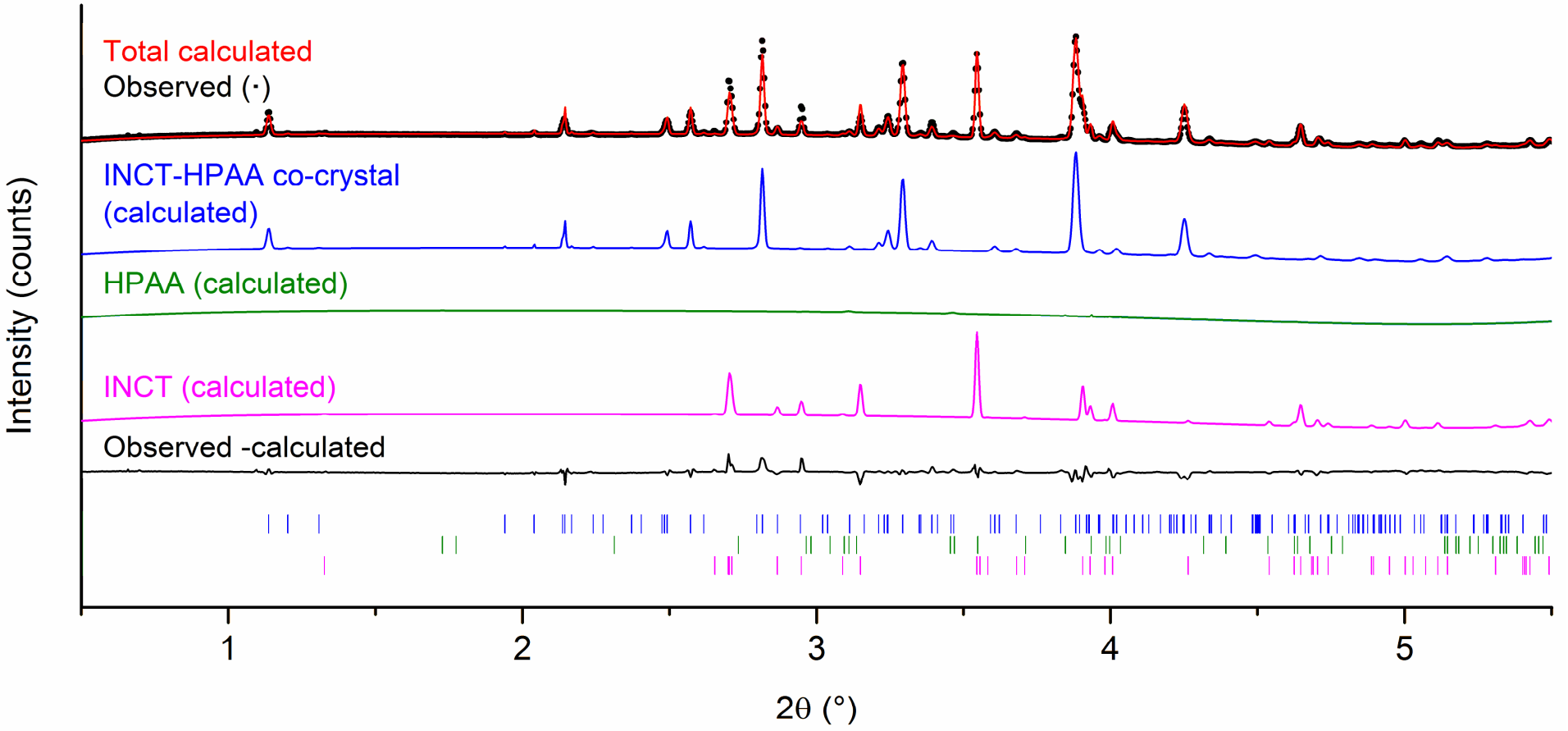

Figure 4-50. Rietveld refinement data for a mixture of INCT and HPAA at 113 °C. Tick marks show the positions of allowed reflections of each phase.

Table 4-10. Refinement parameters for a mixture of INCT and HPAA at 113 °C. The starting models for the raw materials were taken from the CSD (INCT: EHOWIH01; HPAA: QAPBAL) and single crystal data reported in Section 4.3.1 used for the co-crystal.

Property	INCT	HPAA	INCT-HPAA *Co-crystal*
T / °C		113	
Space group	$P2_1/c$	$P2_12_12_1$	P-1
a / Å	10.284(2)	5.24(4)	6.8176(8)
b / Å	5.762(10)	9.14(6)	12.3148(19)
c / Å	10.0956(10)	15.27(9)	12.9137(19)
α / °	90	90	110.754(10)
β / °	96.815(11)	90	95.425(11)
γ / °	90	90	99.067(8)
Cell volume / Å^3	594.0(3)	731(8)	987.8(3)
R_{wp}		0.0678	
$R_{wp\text{-}bkd}$		0.1810	
Phase Fraction*	34.0 %	0.8 %	65.2 %

*Due to the graininess of the sample, representative errors cannot be calculated. However, the author conservatively estimates the error to be in the region of 5 %.

The original stock mixture was made up at an INCT:HPAA molar ratio of 2:1, so it seems odd that at 113 °C, following the exhaustion of the HPAA, there is still a significant amount of INCT left in the sample. The integrated area under the curve for the pattern of each of the reactants at 40 °C was used to calculate the relative amounts of each material in the beam, it seems there was an excess of INCT of around 22 % of the total sample in the beam. The remaining 12 % can be accounted for by the melting of some of the HPAA. This is visible in the diffraction patterns above *ca.* 100 °C as an increase in the background intensity (Figure 4-48), characteristic of a liquid or amorphous material.

The evolution of the structures in the sample can be visualised in Figure 4-51. Initially the material consisted of mostly INCT, with less HPAA and a little of the co-crystal. The content of all three remained relatively stable until around 80-90 °C when both INCT and HPAA began to decrease rapidly, whilst the co-crystal content increases. This is the result of co-crystallisation and coincides with the first endotherm in the DSC trace. This endotherm arises from multiple events, with both co-crystallisation and melting occurring simultaneously. As there are three peaks it is probable that both INCT and HPAA undergo a local melt, and then recrystallise as the co-crystal. The combination of these two endothermic events presumably masks the exothermic crystallisation peak. Above *ca.* 100 °C the HPAA has been exhausted and the remaining INCT continues to melt while the co-crystal formation slows and eventually stops. Finally the co-crystal melts. The melting of INCT and the co-crystal coincide with the second endotherm in the DSC trace, and the occurrence of these two melts explains the presence of the small shoulder on this event. As with INCT-HPAA the presence of the co-crystal appears to destabilise INCT so that it melts at a much lower temperature than the pure crystalline powder.

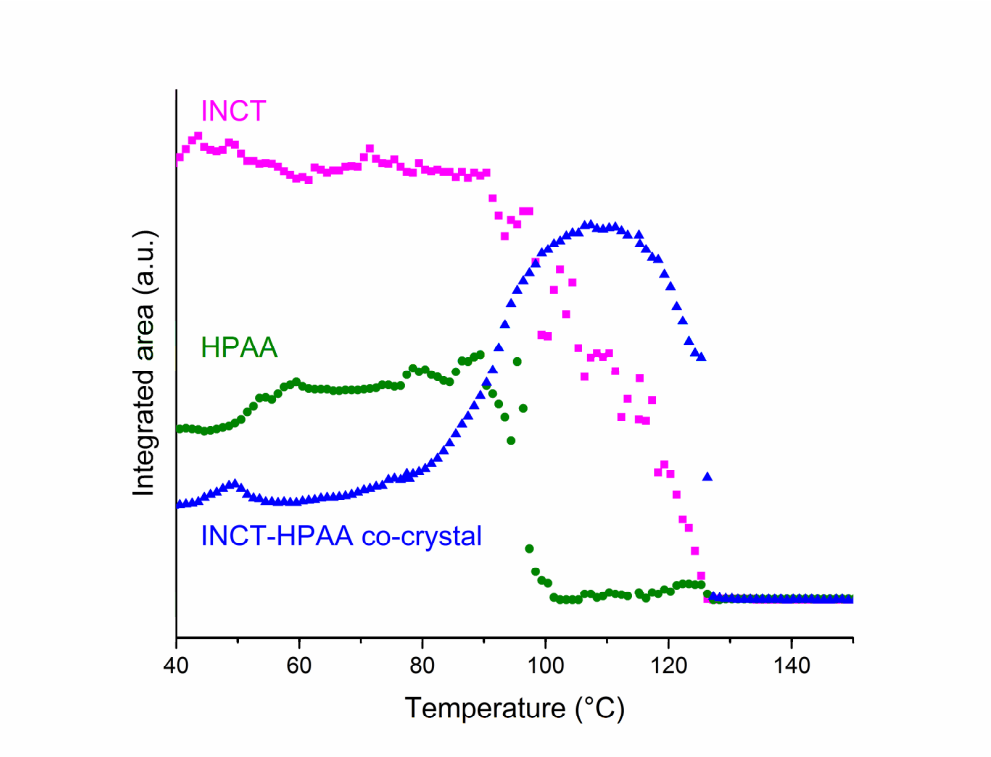

Figure 4-51. Plot of relative quantity as a function of time for each of the phases present in a mixture of INCT and HPAA.

4.3.3.3. INCT-DHPAA

Diffraction patterns collected during simultaneous DSC-XRD experiments on a binary mixture of INCT and DHPAA (Figure 4-52) appear to show the occurrence of two phase transitions. Reflections of the phases present before and after the first transition overlap in a broad range of temperatures (*ca.* 95–115 °C). From these data alone it would appear that a single event is occurring. However, the DSC thermogram shows that there are in fact at least three endothermic events taking place between 90 °C and 120 °C. The final transition is much clearer and is represented by the complete loss of Bragg reflections and a sharp endotherm, and is the final melting of the sample.

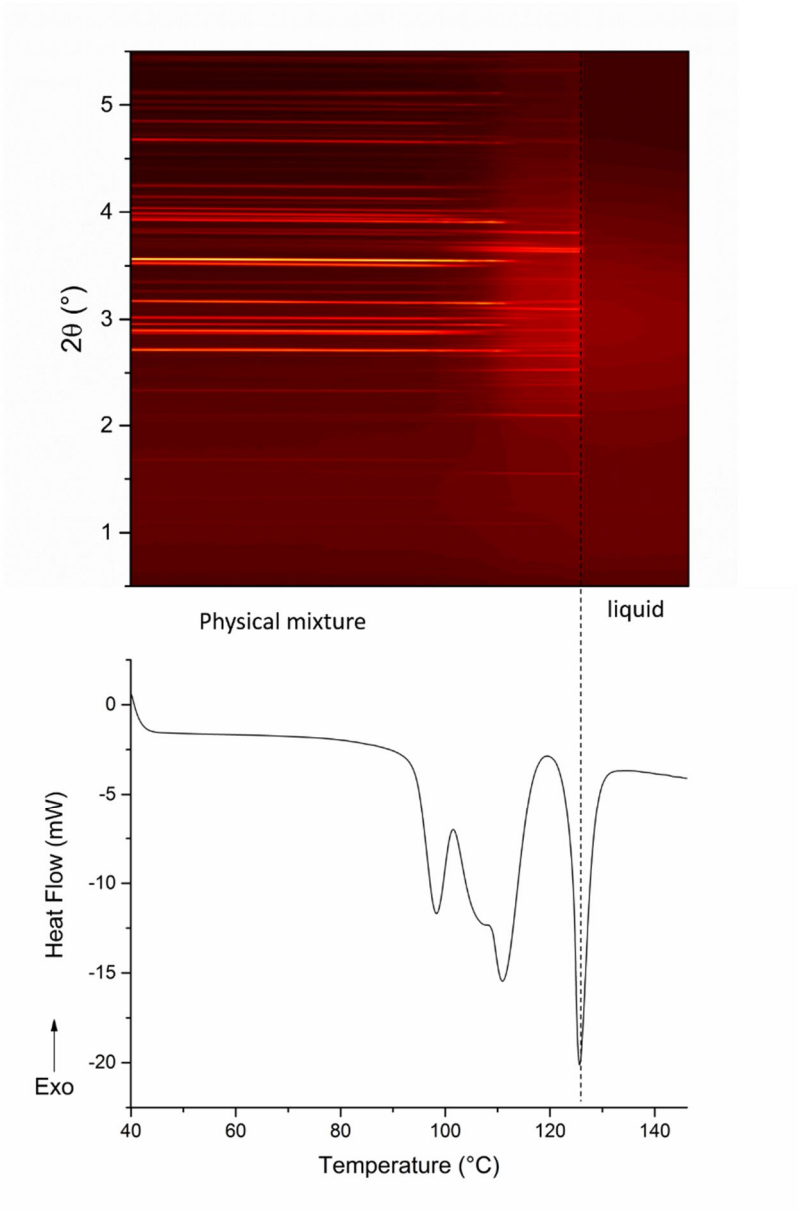

Figure 4-52. Simultaneous DSC-XRD data for an equimolar mixture of INCT and DHPAA.

Closer examination of the diffraction data between 80 °C and 120 °C does not offer any explanation of the multiple thermal events in the thermogram. The Bragg reflections present at the beginning of the experiment are continuous until their disappearance at *ca.* 120 °C and the same is true of the reflections representing the second crystalline phase from their appearance at *ca.* 90 °C until their disappearance at 126 °C. This then suggests that the multiple endotherms are probably caused by different stages of the same process as the crystal lattices of the two materials are first disrupted before realigning into the lattice of the co-crystal. Figure 4-53 and Table 4-11 show refinement data for the initial pattern recorded for the sample at 40 °C. Structures of both of the raw materials achieved a very good fit with an overall weighted profile R-factor of 0.0556.

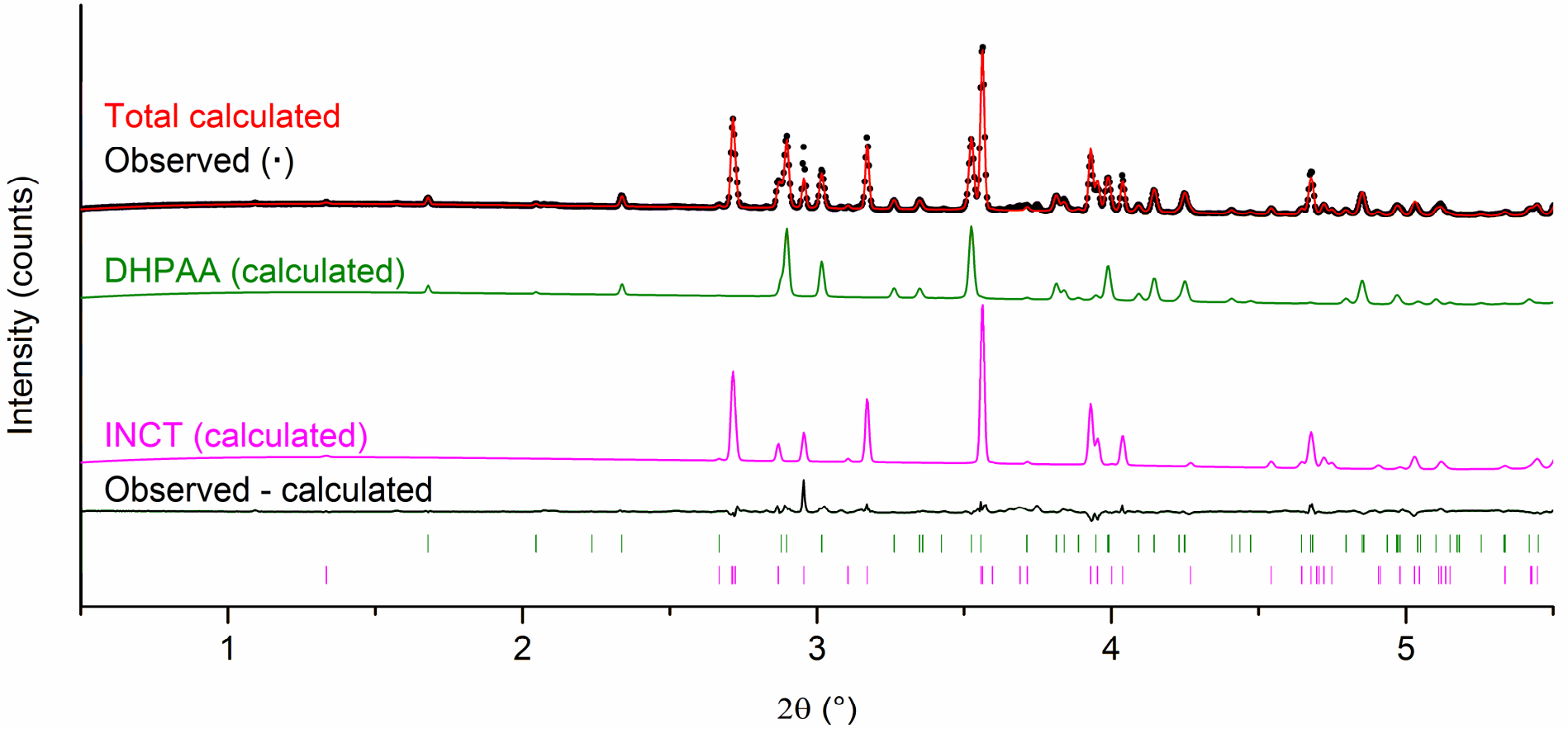

Figure 4-53. Rietveld refinement data for a mixture of INCT and DHPAA at 40 °C. Tick marks show the positions of allowed reflections of each phase.

Table 4-11. Refinement parameters for a mixture of INCT and DHPAA at 40 °C. The starting models for the raw materials were taken from the CSD (INCT: EHOWIH01; DHPAA: NELTON).

Property	INCT	DHPAA
T / °C	40	
Space group	$P2_1/c$	*Pbca*
a / Å	10.2414(7)	16.1356(19)
b / Å	5.7407(4)	11.5933(8)
c / Å	10.0693(5)	7.9176(3)
α / °	90	90
β / °	97.253(5)	90
γ / °	90	90
Cell volume / Å^3	587.27(6)	1481.1(2)
R_{wp}	0.0556	
$R_{wp\text{-}bkd}$	0.1693	
Phase Fraction*	54.5 %	45.5 %

*Due to the graininess of the sample, representative errors cannot be calculated. However, the author conservatively estimates the error to be in the region of 5 %.

The pattern recorded at 122 °C (Figure 4-54), after the first phase transition, could not be fitted by the structures of any of the known polymorphs of the two raw materials or that of the INCT-DHPAA co-crystal grown by solvent evaporation and described in Section 4.3.1. Many of the reflections in the pattern collected by DSC-XRD occur at similar angles to reflections in the predicted pattern (Figure 4-54), but there are significant absences (in particular the two main reflections at 3.02° and 3.76°). The new structure must be either the result of co-crystal formation or the crystallisation of a new polymorph of one of the two raw materials. There is also a high background that is not present in the lower temperature patterns, indicating the presence of some amorphous or melted material. This is visible as an increase of the background of the diffraction data (Figure 4-52) and coincides with the third endotherm.

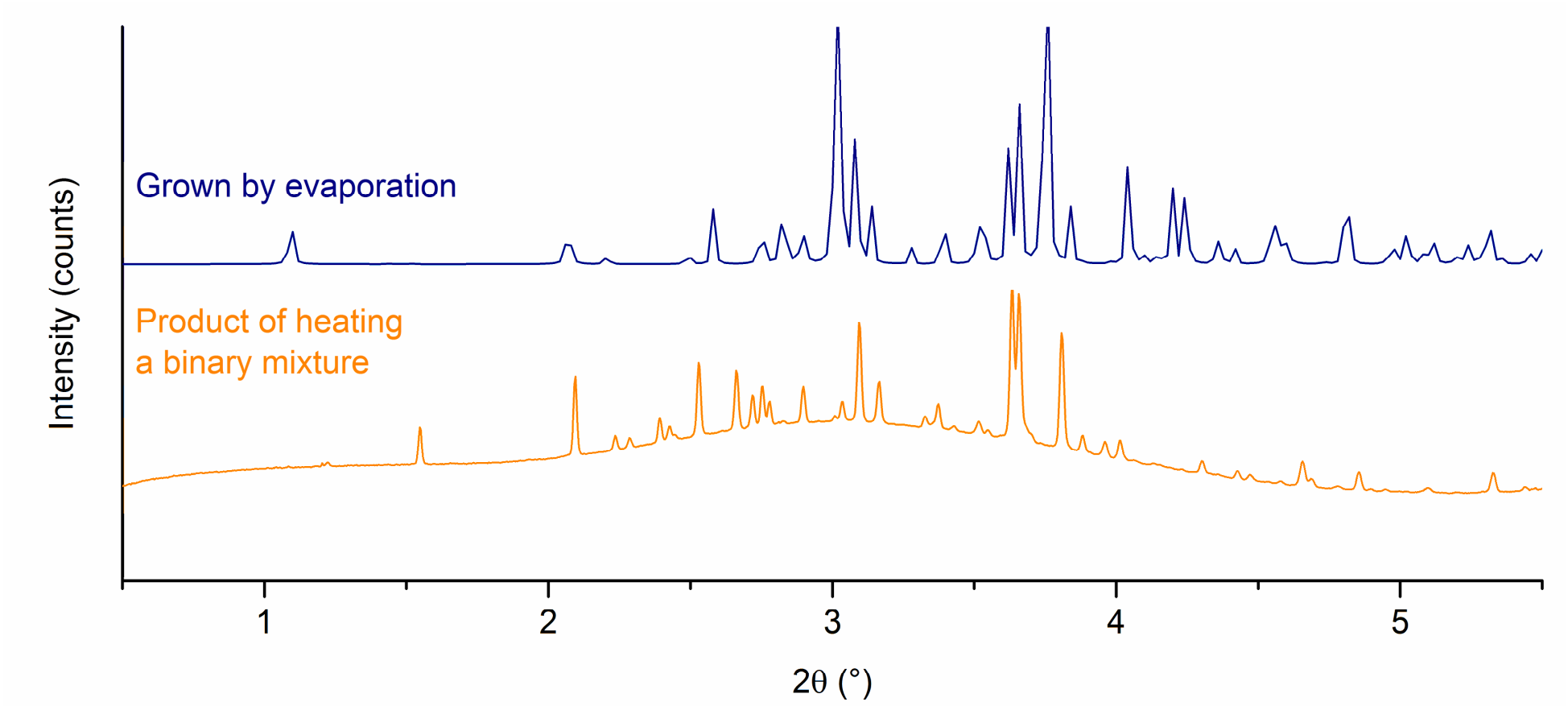

Figure 4-54. Powder diffraction pattern for crystals produced by heating an equimolar binary mixture of INCT and DHPAA and a predicted powder pattern for crystals grown by solvent evaporation from an equimolar ethanolic solution.[248]

Plotting the integrated area under the calculated pattern of each species as a function of temperature (Figure 4-55) it can be seen that the content of both of the raw materials remains relatively constant until *ca.* 95 °C, at which point both begin to decline. This coincides with the onset of the first endotherm in the thermogram (94.2 °C). However, the total disappearance of DHPAA and INCT does not occur until 108.8 °C and 113.9 °C respectively. These endpoints match closely the minima of the second (*ca.* 108 °C) and third (111.05 °C) endotherms. The overlapping nature of these events and the likelihood of an invisible exothermic event relating to crystallisation means that a confident assignment is not possible. That said, it can be deduced that the disappearance of both structures from the sample is not due simply to melting, as the raw materials have melting points at temperatures in excess of 120 °C. It is therefore likely to be the result of a conversion from one solid form to another. It cannot be ascertained from these data whether that form is a co-crystal or a new polymorph of one of the two individual components.

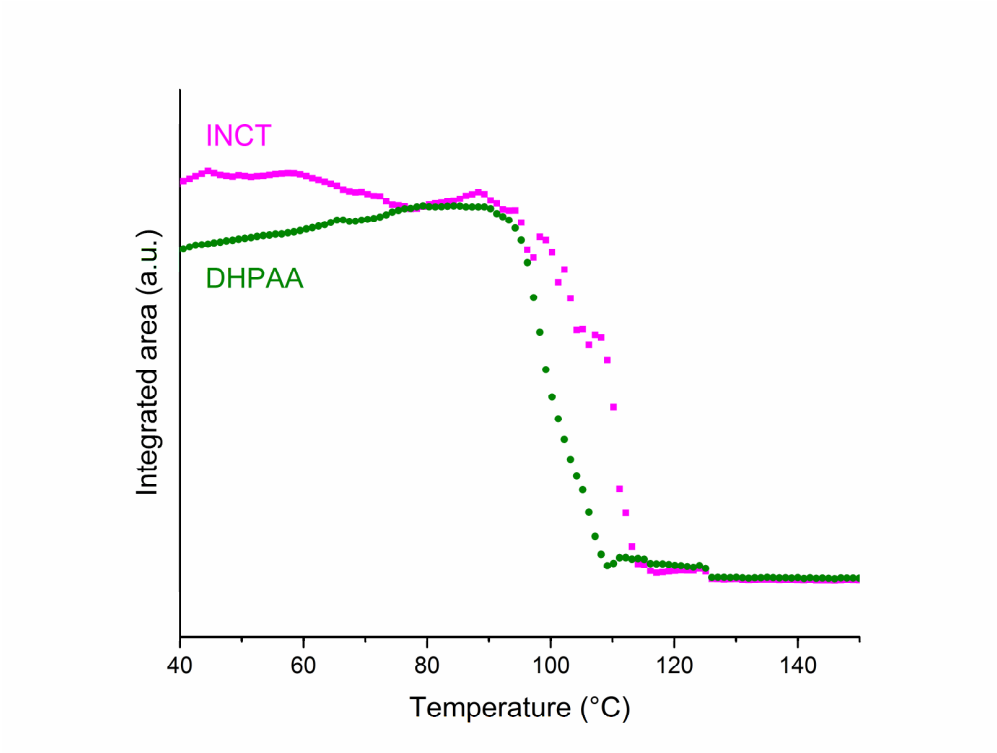

Figure 4-55. Plot of integrated area as a function of time for each of the raw materials present in a mixture of INCT and DHPAA.

4.3.3.4. INCT-LABA

The DSC-XRD data for a binary mixture of INCT and LABA (Figure 4-56) in a 1:2 molar ratio are more complex than the four systems discussed previously. As before, structural refinement was carried out on the initial pattern recorded for the physical mixture (Figure

4-57 and Table 4-12). The fit was poorer than has been seen previously with some of the other systems and a R_{wp} value of 0.1098 was the best that could be achieved. The reason for this can be seen when comparing the observed pattern to the total calculated pattern. There are obvious differences between the intensities of reflections at 2.67°, 2.71°, 3.03°, 3.22° and 3.85°, resulting from the grainy texture of the powder.

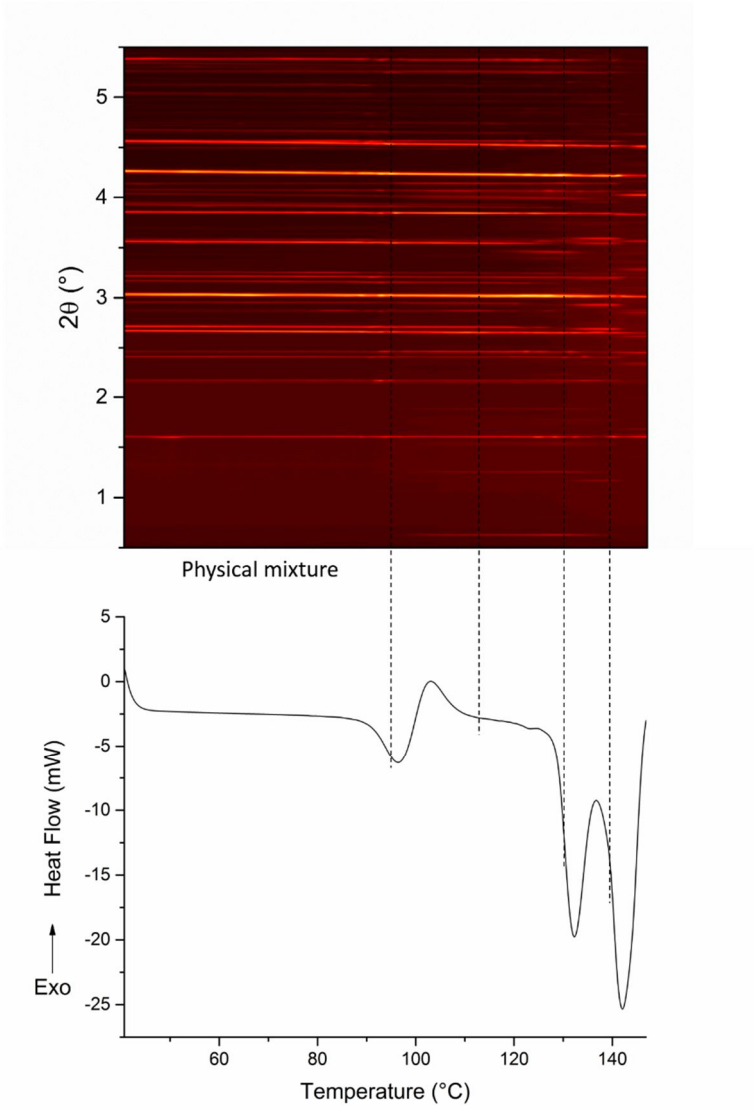

Figure 4-56. DSC-XRD plot for a binary mixture of INCT and LABA in a 1:2 molar ratio. Dotted lines indicate the first appearance of new Bragg reflections in the diffraction data.

Phase quantification analysis shows that the initial mixture consisted of INCT (22.7 %), LABA (73.9 %), and the reaction product crystal observed in the single crystal experiments (3.4 %, Section 4.3.1.4). Closer examination of the calculated pattern for the reaction crystal reveals that, unlike the previous samples, where clear reflections corresponding to the co-crystal were visible at the start of the experiment, there are no obvious reflections assigned to this phase and that the fraction of material apportioned to this structure is probably a consequence of compensation by the software for a

combination of the imperfect fit of the background to the data and discrepancies in the intensities of some of the reflections.

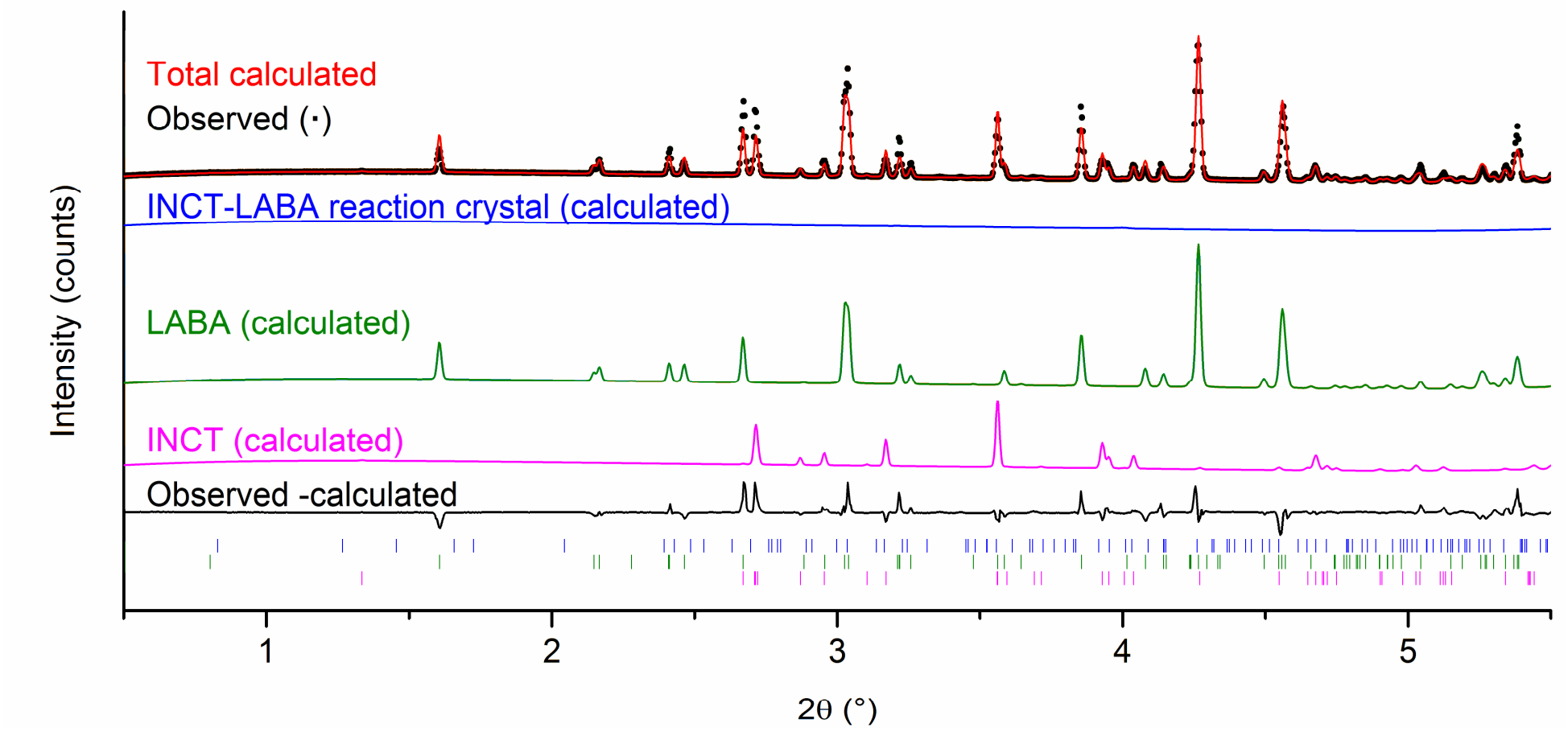

Figure 4-57. Rietveld refinement data for a 1:2 molar ratio mixture of INCT and LABA at 41 °C. Tick marks show the positions of allowed reflections of each phase.

Table 4-12. Refinement parameters for a 1:2 molar ratio mixture of INCT and LABA. The starting models for the raw materials were taken from the CSD (INCT: EHOWIH01; LABA: LASCAC12) and single crystal data reported in section 4.3.1 was used for the co-crystal.

Property	INCT *Form I*	LABA	Reaction crystal
T / °C		40.7	
Space group	$P2_1/c$	$P2_1$	$P2_12_12_1$
a / Å	10.232(2)	6.3969(5)	5.4(1)
b / Å	5.748(2)	6.3546(2)	11.3(4)
c / Å	10.068(2)	17.103(1)	32.7(6)
α / °	90	90	90
β / °	97.20(2)	99.341(7)	90
γ / °	90	90	90
Cell volume / Å^3	587.4(2)	686.04(9)	2009(86)
R_{wp}		0.1098	
$R_{wp\text{-}bkd}$		0.2930	
Phase Fraction*	22.7 %	73.9 %	0 %

*Due to the graininess of the sample, representative errors cannot be calculated. However, the author conservatively estimates the error to be in the region of 5 %. It should also be noted that there are no reflections present that can be assigned to the co-crystal and its presence is attributed to the imperfect fit of the background curve.

Upon heating the sample underwent a number of phase transitions; the first appearance of reflections ascribed to each of the new phases is represented by dotted lines in Figure 4-56. The first change can be seen as an endo-exo event in the DSC trace beginning at 90.5 °C. At this point a number of new reflections (phase 1) appear in the diffraction plot, which remain until 141.8 °C. The next new species appears at 114.9 °C and reflections remain until 136.6 °C. Calorimetrically this is represented by a low enthalpy broad endotherm. Reflections of a third species (phase 2) appear at 127.8 °C, the same temperature at which a number of reflections from the initial pattern disappear, and are accompanied by the first of two very large energy endotherms. These reflections are also present until 141.8 °C. Finally, at 136.6 °C a large group of new reflections appear and remain until the end of the experiment. This growth is coincident with the second of the large endotherms and also the decay of phase 1 and phase 2.

Rietveld refinement against the pattern recorded at 131.2 °C can be seen in Figure 4-58. At this temperature there are reflections present from all but the last phase to appear. Structures of all five known polymorphs of INCT, the only known polymorph of LABA, and that of the reaction crystal reported in Section 4.3.1 were all refined against the data. Of the four phases present only two could be identified, INCT form II and LABA (Table 4-13). The original form of INCT (polymorph I) is no longer present and none of the other structures achieved a good fit to species 1 or 2. Refinements were carried out on selected patterns in which only one of the unidentified phases was present as well as identifiable patterns for INCT, LABA and the reaction crystal (or a combination of the three). Neither

of the structures were a good fit to the data. However, comparison of the pattern collected at 131.2 °C with the pattern of the printed crystals shows that reflections for one of the two unidentified species (phase 2) occur at similar angles to the major reflections of the printed crystals.

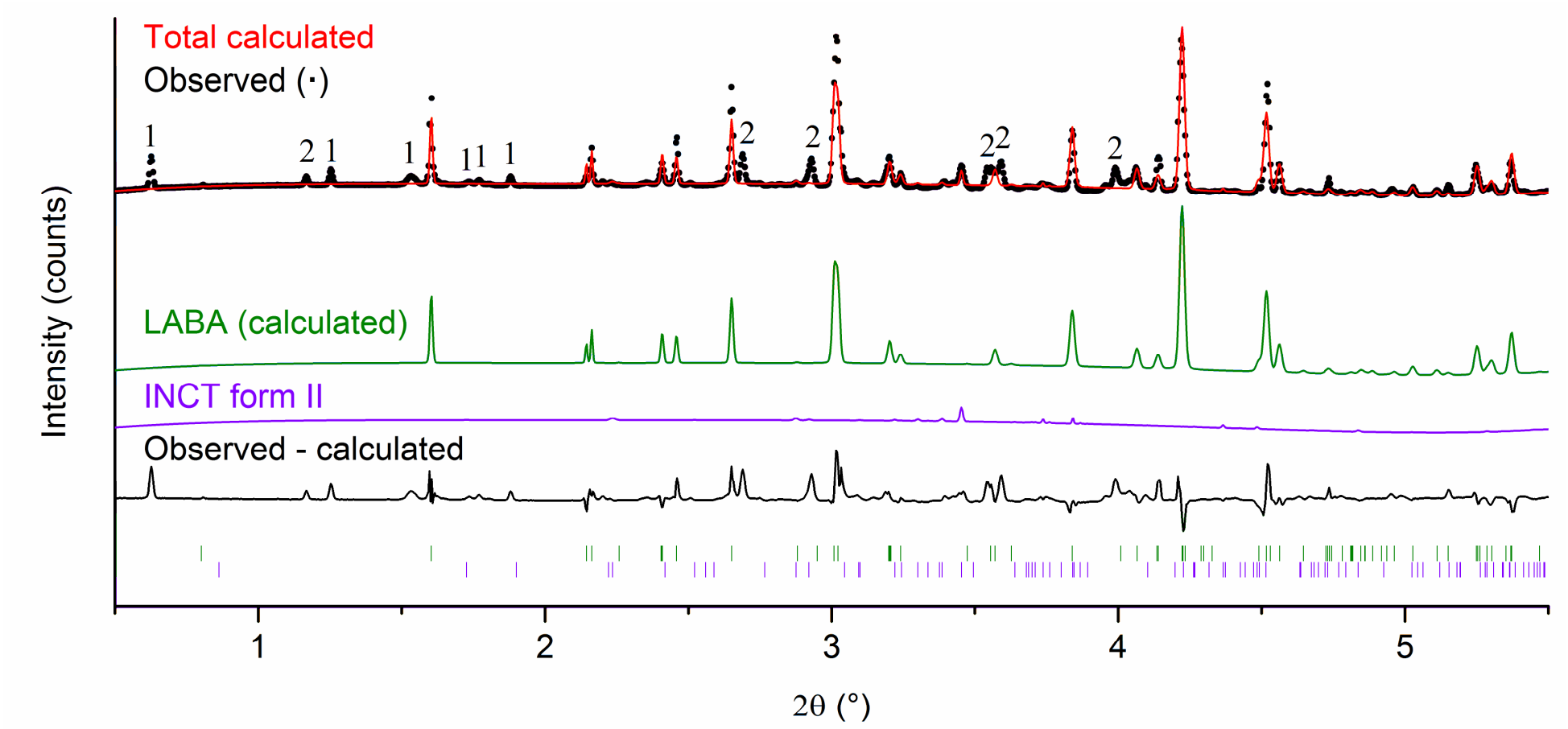

Figure 4-58. Rietveld refinement data for a 1:2 molar ratio mixture of INCT and LABA at 131 °C. Observed reflections from two unidentified phases are denoted by either a 1 or 2 directly above. Tick marks show the positions of allowed reflections of INCT form II and LABA.

Table 4-13. Refinement parameters for a 1:2 molar ratio mixture of INCT and LABA. Starting models were taken from the CSD (INCT: EHOWIH02; LABA: LASCAC12).

Property	INCT *Form II*	LABA
T / °C	131.2	
Space group	$P2_1/c$	$P2_1$
a / Å	16.322(8)	6.4060(7)
b / Å	8.005(14)	6.4196(3)
c / Å	9.801(11)	17.135(2)
α / °	90	90
β / °	105.89(7)	99.401(10)
γ / °	90	90
Cell volume / Å^3	1231(7)	695.20(13)
R_{wp}	0.1354	
$R_{wp\text{-}bkd}$	0.4542	
Phase Fraction*	3.4 %	96.6 %

*fraction of the identifiable material, not the whole sample.

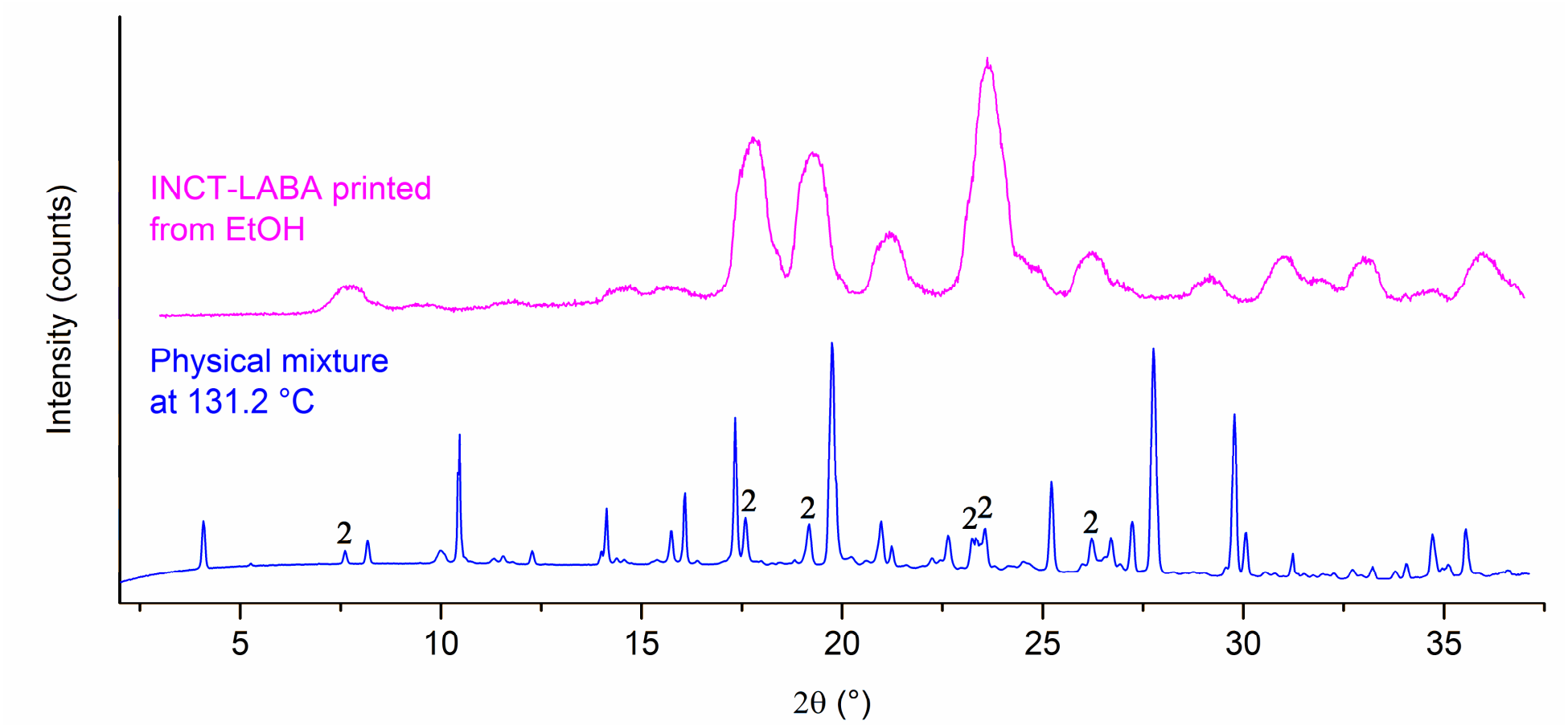

Figure 4-59. PXRD patterns collected for crystals printed from an equimolar ethanolic solution of INCT and LABA and for an equimolar physical mixture of the two at 131.2 °C.

Refinement of the pattern collected at 147 °C, (Figure 4-60 andTable 4-14) shows the sample to consist of INCT, LABA and the reaction crystal. The presence of INCT I indicated by the refinements is an error caused by compensation for the imperfect intensity ratios of the other species present. There is in fact none left as this species disappears from the diffraction data at 127.8 °C, as previously mentioned. It seems some of the INCT has reacted with the LABA but not all of it; almost half of the remaining material at 147 °C is LABA, and they were initially mixed in the appropriate ratio to form the reaction crystal. Patterns recorded above this temperature were observed to have a higher background than those below it suggesting some melting of INCT, hence the remaining LABA.

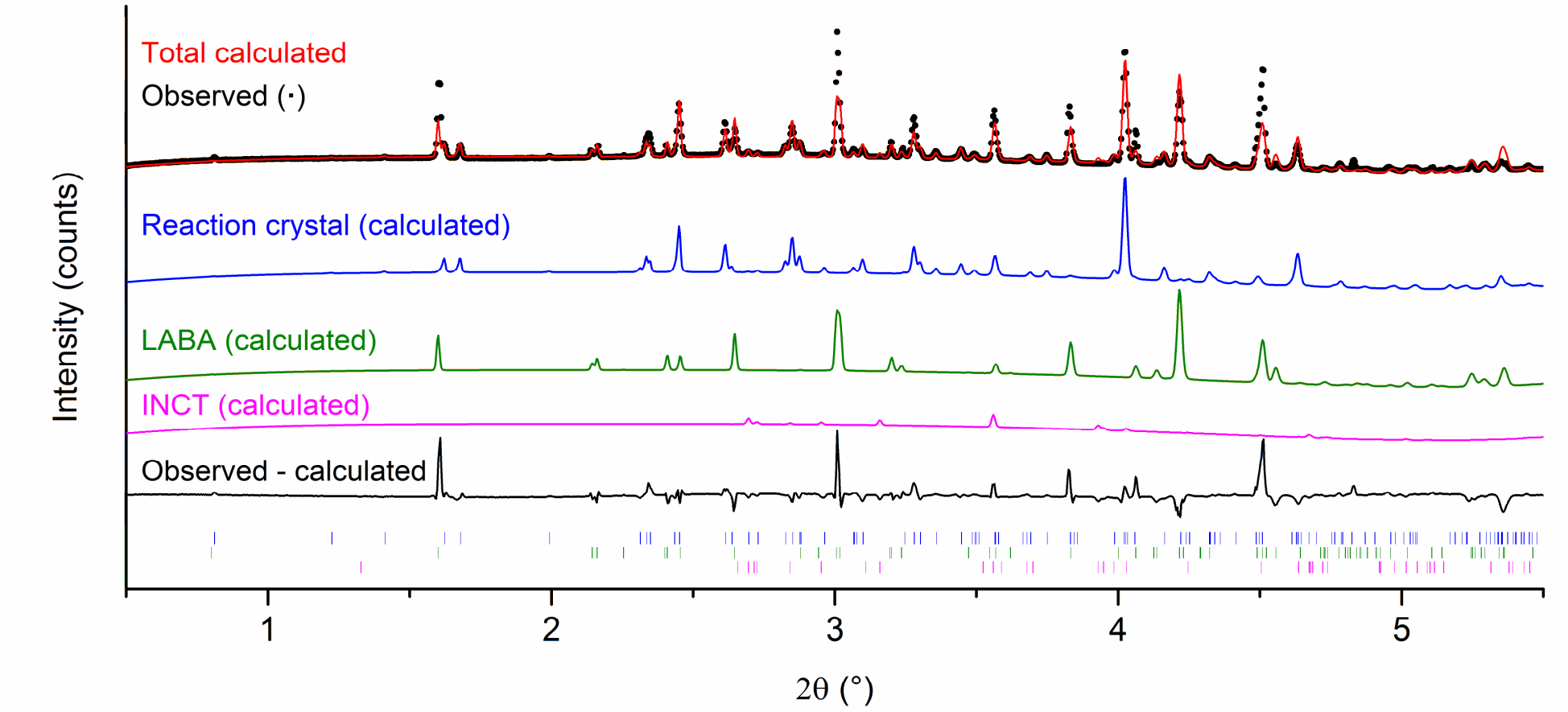

Figure 4-60. Rietveld refinement data for a 1:2 molar ratio mixture of INCT and LABA at 147 °C. Tick marks show the positions of allowed reflections of each phase.

Table 4-14. Refinement parameters for a 1:2 molar ratio mixture of INCT and LABA. The starting models for the raw materials were taken from the CSD (INCT: EHOWIH01; LABA: LASCAC12) and single crystal data reported in section 4.3.1 was used for the co-crystal.

Property	INCT *Form I*	LABA	Reaction crystal
T / °C		146.9	
Space group	$P2_1/c$	$P2_1$	$P2_12_12_1$
a / Å	10.29(2)	6.4079(11)	5.1995(10)
b / Å	5.721(13)	6.4282(4)	11.711(2)
c / Å	10.145(13)	17.171(3)	33.382(6)
α / °	90	90	90
β / °	97.64(16)	99.4971(18)	90
γ / °	90	90	90
Cell volume / Å^3	592(2)	697.59(19)	2032.7(7)
R_{wp}		0.0987	
$R_{wp\text{-}bkd}$		0.4149	
Phase Fraction*	3.9 %	44.8 %	51.3 %

*Due to the graininess of the sample, representative errors cannot be calculated. However, the author conservatively estimates the error to be in the region of 5 %. It should be noted that the standard uncertainties for INCT are very high and its presence in the refinements is due to the poor fit of the intensities of the other species.

The evolution of the four identifiable species in the sample can be seen in Figure 4-61. There is no change in the content of any of the four until 86 °C when the amount of INCT present begins to decrease before levelling off at 101 °C. The rate of decay initially is fairly slow, and it appears that the reaction crystal begins to grow here, but this is an artefact of the refinements and the powder quality. In the same temperature range there is a step in the content of LABA in the sample. At 117 °C the decay of INCT I increases and by 128 °C there is no longer any remaining. At 113.7 °C INCT II appears and grows steadily until reaching its maximum content at 126.6 °C, at which point it immediately begins to decrease. At the same temperature LABA begins to decrease dramatically and continues to do so until the end of the heating programme. At 138 °C the reaction crystal emerges and grows rapidly until 145 °C when it plateaus.

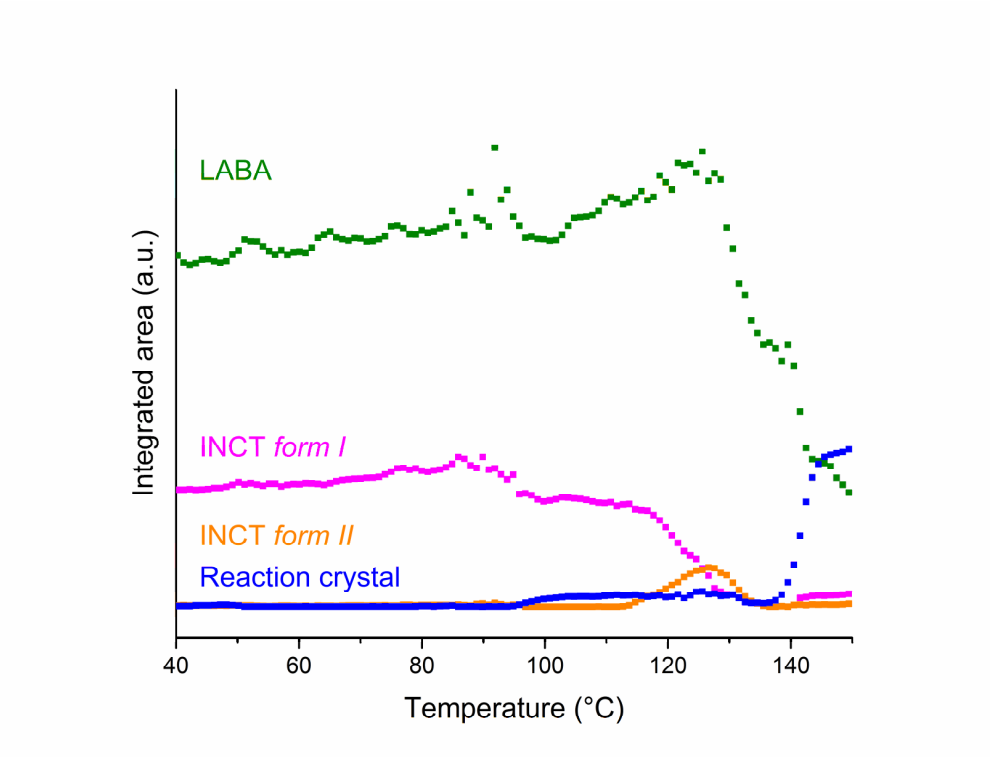

Figure 4-61. Plot of relative quantity as a function of time for each of the identified species present in a mixture of INCT and LABA [Data points for INCT *form I* between 130 °C and 140 °C have been removed as refinements were incorrect in this range].

The first period of decline of INCT I is a result of either a conversion to a currently unreported polymorph, co-crystallisation or reaction with LABA. The appearance of the first new species (phase 1) at 90.5 °C corresponds closely to this decline. However, as phase 1 remains unidentified and the data for LABA at the same temperature is ambiguous, exactly which event is occurring remains uncertain. The steeper gradient of the second period of decline of INCT I is a direct result of the further conversion of some of the material to INCT II, and the maximum intensities of reflections for phase 1 and INCT II occur at 128.7 °C and 126.6 °C respectively. Both then begin to decline. The decrease in LABA begins at the same temperature at which the second unidentified species (phase 2) appears, suggesting phase 1 is a new polymorph of LABA. Emergence of the reaction crystal does not occur until all of the known forms of INCT have disappeared and at the same temperature there is an increase in the rate of decline of LABA.

The complex nature of the data make it very difficult to ascertain exactly which forms of the two raw materials directly preclude the reaction crystal. However, it is clear that both forms of INCT melt prior to its first appearance. It appears that INCT in the reaction crystal results from either a solid state reaction from phase 1 or growth from the melt. LABA is simpler, and appears to undergo a solid state reaction from phase 2, since the

disappearance of this structure occurs over the same temperature range as the appearance of the reaction crystal.

The rapid decline of LABA following completion of reaction crystallisation may be attributed to melting, albeit at a lower temperature than expected due to destabilisation by the other species present. A more likely explanation, however, is that decomposition occurs: in all DSC traces of this system significant degradation was observed above 150 °C.

4.3.4. Co-crystallisation by milling

4.3.4.1. INCT-HBA

DSC analysis of the powder produced by ball milling an equimolar mixture of INCT and HBA at 20 Hz for 15 minutes can be seen in Figure 4-62. There is one clear endothermic event with an onset at 183.3 °C, after which the material begins to degrade. This endotherm occurs at the same temperature as the endotherm in the DSC trace for the printed crystals (181.6 °C), and so the same conclusions can be drawn as those in Section 4.3.2.1.1: it appears that a co-crystal has formed.

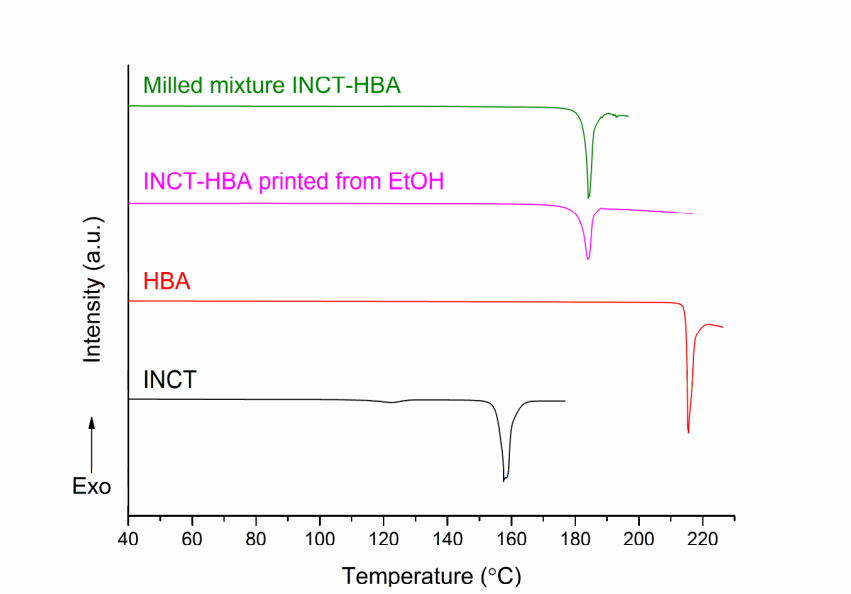

Figure 4-62. DSC data for INCT, HBA, crystals printed from an equimolar ethanolic solution of both and a mixture of the two following ball milling.

PXRD analysis (Figure 4-63) resulted in a pattern very similar to that of the previously reported co-crystal,[232] albeit with an overall shift in reflection positions to lower angles. The intensity ratios are very similar, as are the relative peak positions. The similarity of the two patterns suggests that the structures of the two samples are the same. The shift

in angles of diffraction can be attributed to the difference in temperature of the two samples. Data for the milled sample were collected at room temperature whereas data for VAKTOR were collected at −120 °C.

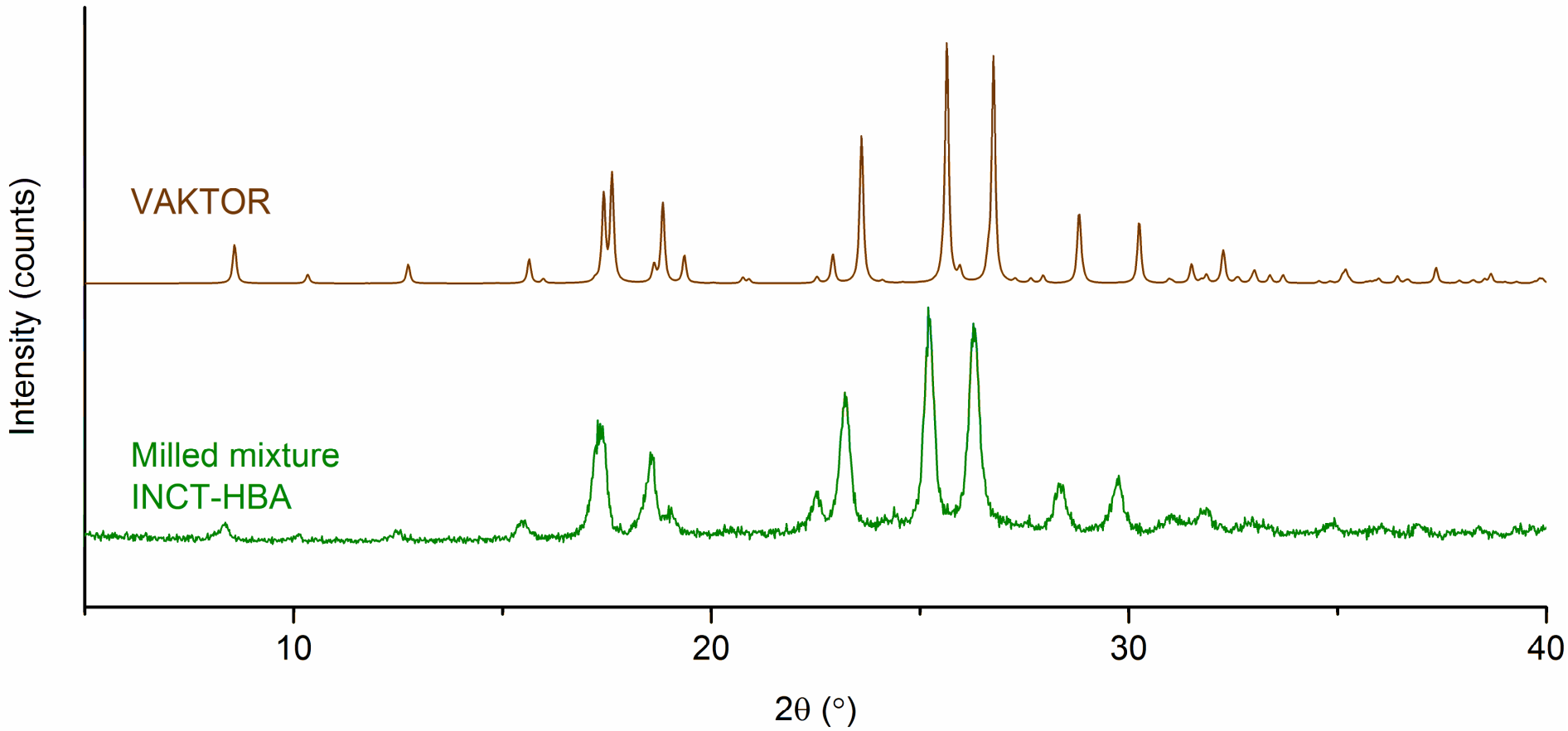

Figure 4-63. PXRD patterns collected for a ball milled mixture of INCT and HBA and predicted from single crystal data obtained from the CSD (VAKTOR).

The FTIR spectrum recorded for the milled sample (Figure 4-64) is almost identical to the spectrum recorded for the printed crystals, which again supports the conclusion that a co-crystal has formed upon milling.

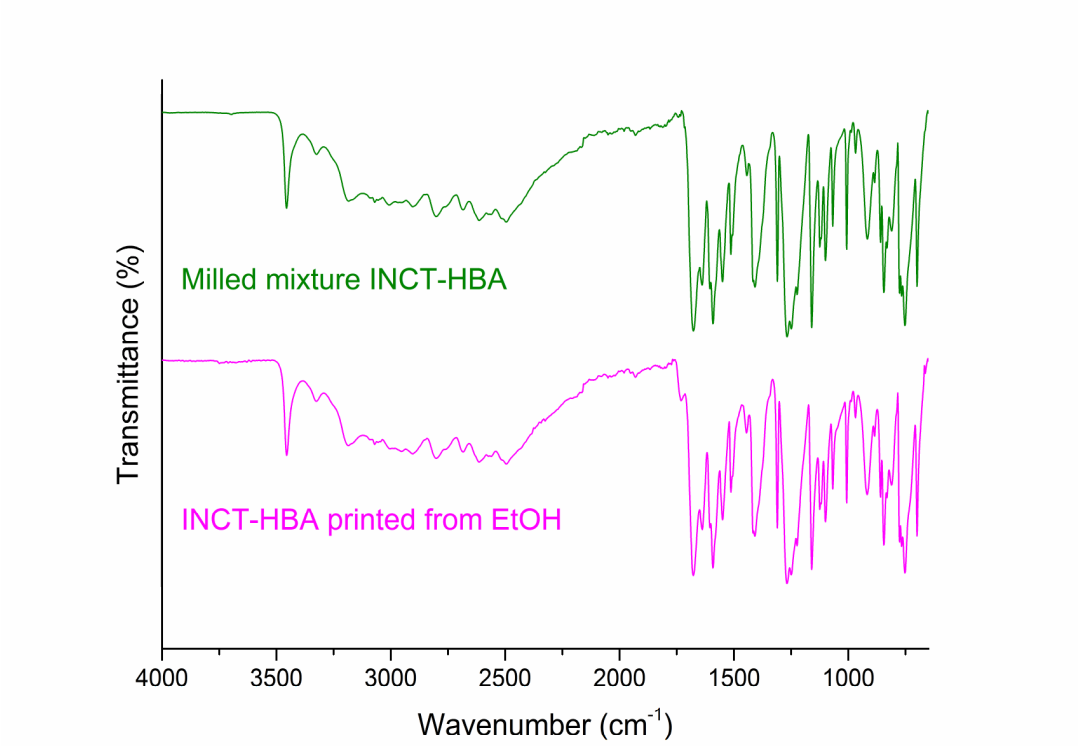

Figure 4-64. FTIR spectra for a ball milled mixture of INCT and HBA and for crystals printed from an equimolar ethanolic solution of the two.

4.3.4.2. INCT-HPAA

The results obtained after milling mixtures of INCT and HPAA in a 2:1 molar ratio are similar to those of INCT and HBA, in as much as they strongly resemble the findings with crystals grown by solvent evaporation and those printed and discussed in Sections 4.3.1 and 4.3.2.2 respectively. The DSC data (Figure 4-65) exhibit a single endotherm with onset at 126.3 °C, the same temperature as the printed crystals (125.9 °C). The implications of this are discussed in Section 4.3.2.2.1. The formation of a co-crystal is strongly suggested by this observation.

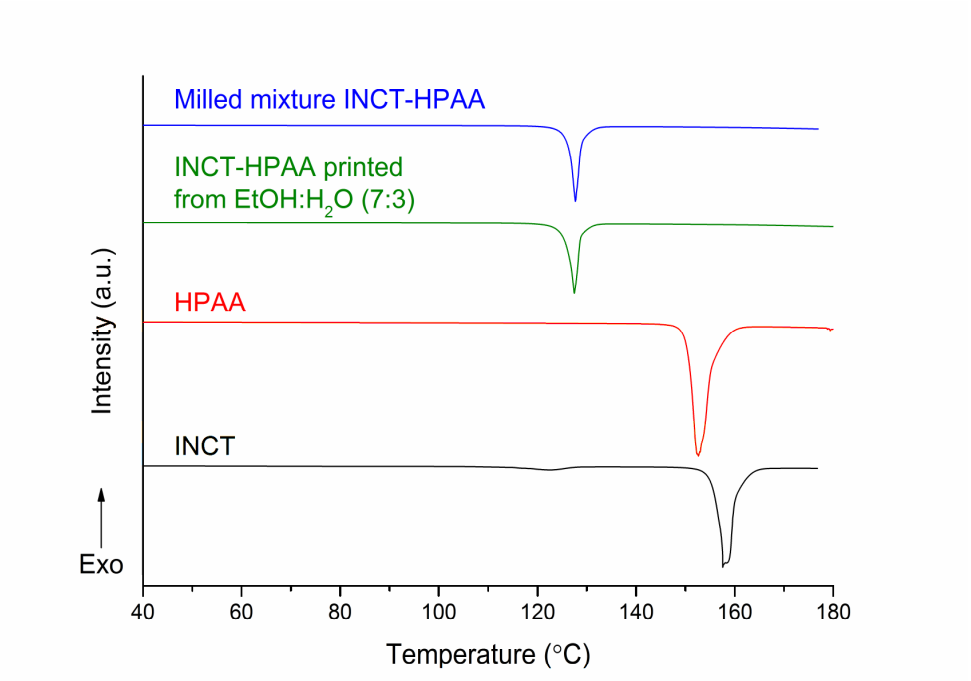

Figure 4-65. DSC data for INCT, HPAA, and crystals printed from a 2:1 molar ratio solution of the two in EtOH:H_2O (7:3 v/v), and a 2:1 molar ratio mixture of the two following ball milling.

Comparison of the powder diffraction data with the pattern simulated from the single crystal data shows the two to be very similar. Like the INCT-HBA milled sample the intensity ratios of the two are very similar as are the angles of diffraction, with the milled reflections all appearing at slightly lower angles as a consequence of thermal expansion of the unit cell.

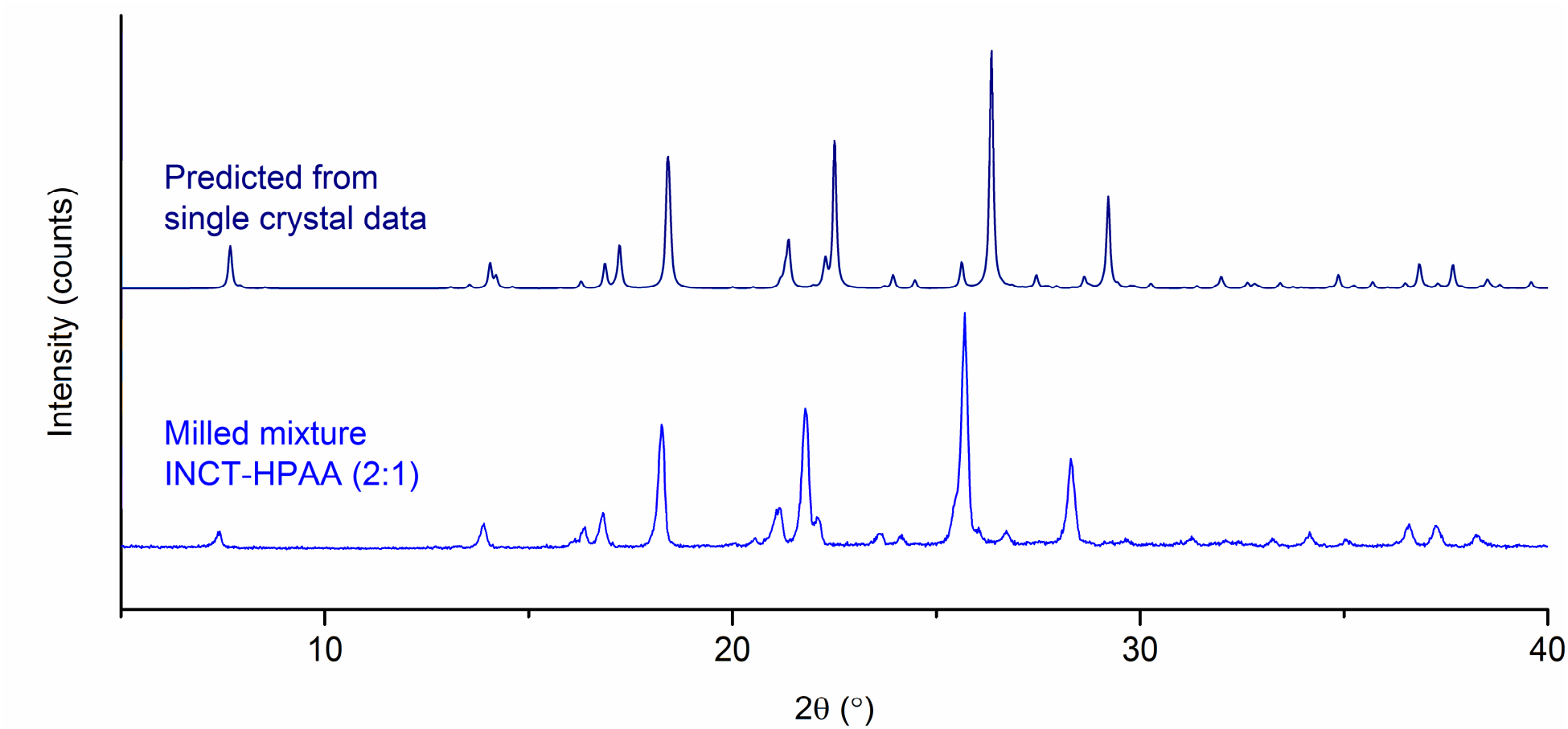

Figure 4-66. PXRD patterns collected for a ball milled mixture of INCT and HPAA and that predicted from single crystal data collected for a crystal grown from solution (see Section 4.3.1).

FTIR spectra for both the printed crystals and the milled sample (Figure 4-67) are almost identical, suggesting that the same co-crystal is grown *via* both methods.

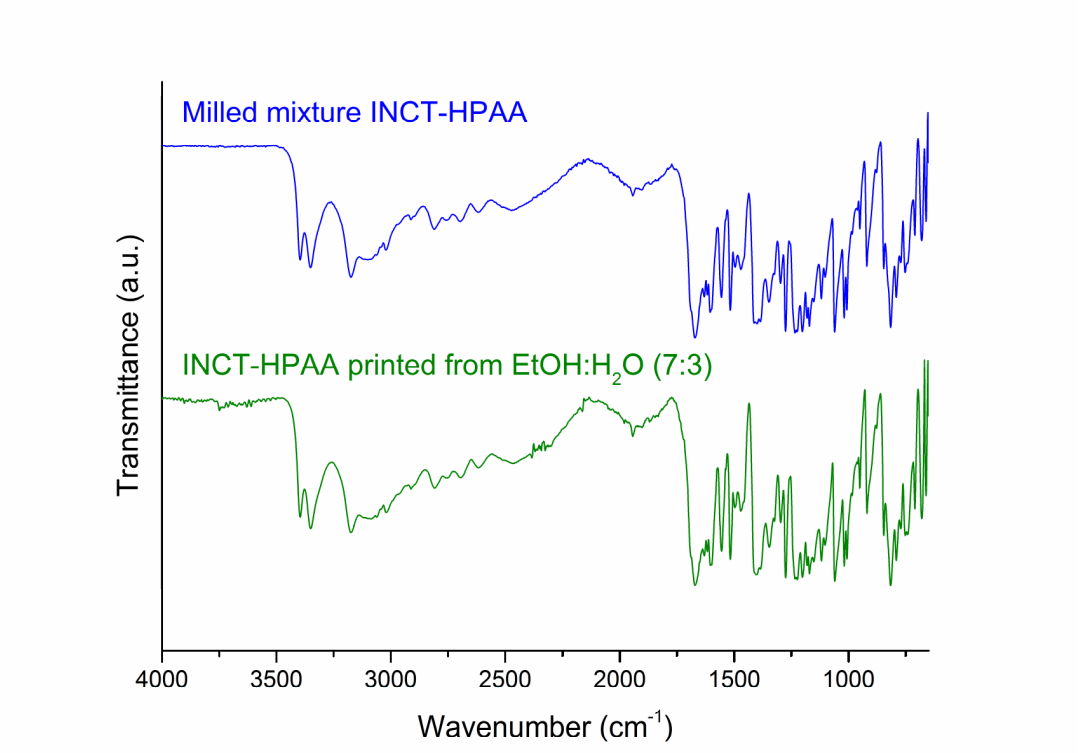

Figure 4-67. FTIR spectra for a ball milled 2:1 molar mixture of INCT and HBA and for crystals printed from a 2:1 molar solution of the two in EtOH:H_2O (7:3).

The combination of DSC, PXRD, and FTIR data for the milled sample of INCT and HPAA and their comparison to similar data for a single crystal grown by evaporation and crystals formed by thermal inkjet printing strongly suggest the three methods all result in the formation of the same co-crystal, described in detail in Section 4.3.1.

4.3.4.3. INCT-DHPAA

As with the two ball milled samples discussed in the previous paragraphs the DSC data (Figure 4-68) for a milled sample of INCT and DHPAA displayed one endotherm at a similar temperature to the one observed for the crystals formed by inkjet printing (122.6 °C and 118.6 °C respectively), although a little too high to be confident that the two are a result of the same event. In fact, the enthalpy associated with melt of the printed crystals is 111.7 J g^{-1} and that of the milled sample is 163.0 J g^{-1}, suggesting that the two events are different. The onset of the endotherm for the milled sample is more than 8 °C higher than the observed I→II transition in INCT (114.3 °C) and its magnitude is much larger than that of the I→II transition which occurs with an associated enthalpy of 19.1 J g^{-1}. The melt of DHPAA occurs at 128.3 °C and has an enthalpy of 198.3 J g^{-1}.

The difference in onset temperatures between this and the milled sample is not so large that they can be affirmed as different events, but the difference in enthalpies confirms that they are. The DSC data suggest milling may have formed a different co-crystal to those formed by thermal and printing methods.

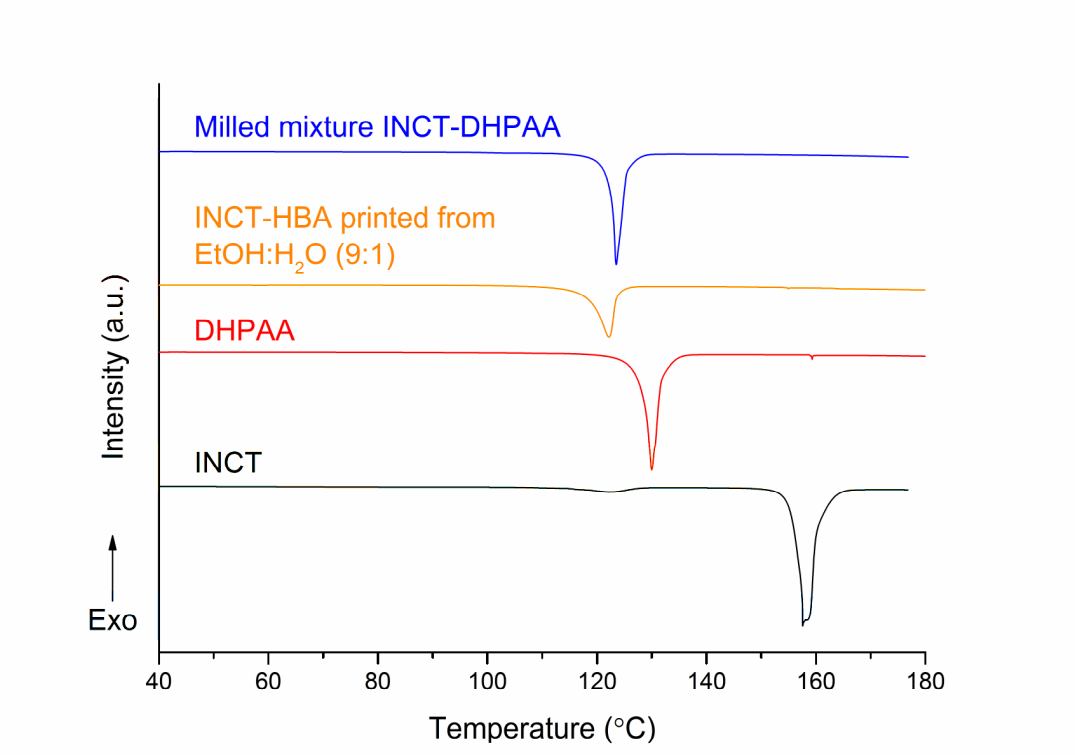

Figure 4-68. DSC data for INCT, DHPAA, crystals printed from an equimolar solution of both in EtOH:H2O (9:1) and a mixture of the two following ball milling.

The PXRD data (Figure 4-69) are less clear. The pattern collected for the milled sample has many reflections at similar angles to the co-crystal grown by solvent evaporation, as well as the two raw materials. However, the intensity ratio of the reflections suggests that the milled material has a different structure to all three. The Bragg angles of the two main reflections (20.5°, 24.2°) do not correspond to those of any of the other materials, and the reflection at 16.2° is only present in the milled material, not in any of the other substances. From these data it appears that ball milling has caused co-crystallisation of INCT and DHPAA to a second structure. The higher onset of the endotherm in the DSC trace suggests this is a more stable form of the co-crystal than those formed by inkjet printing and solvent evaporation. However, the separate formation of new polymorphs of the raw materials cannot be ruled out.

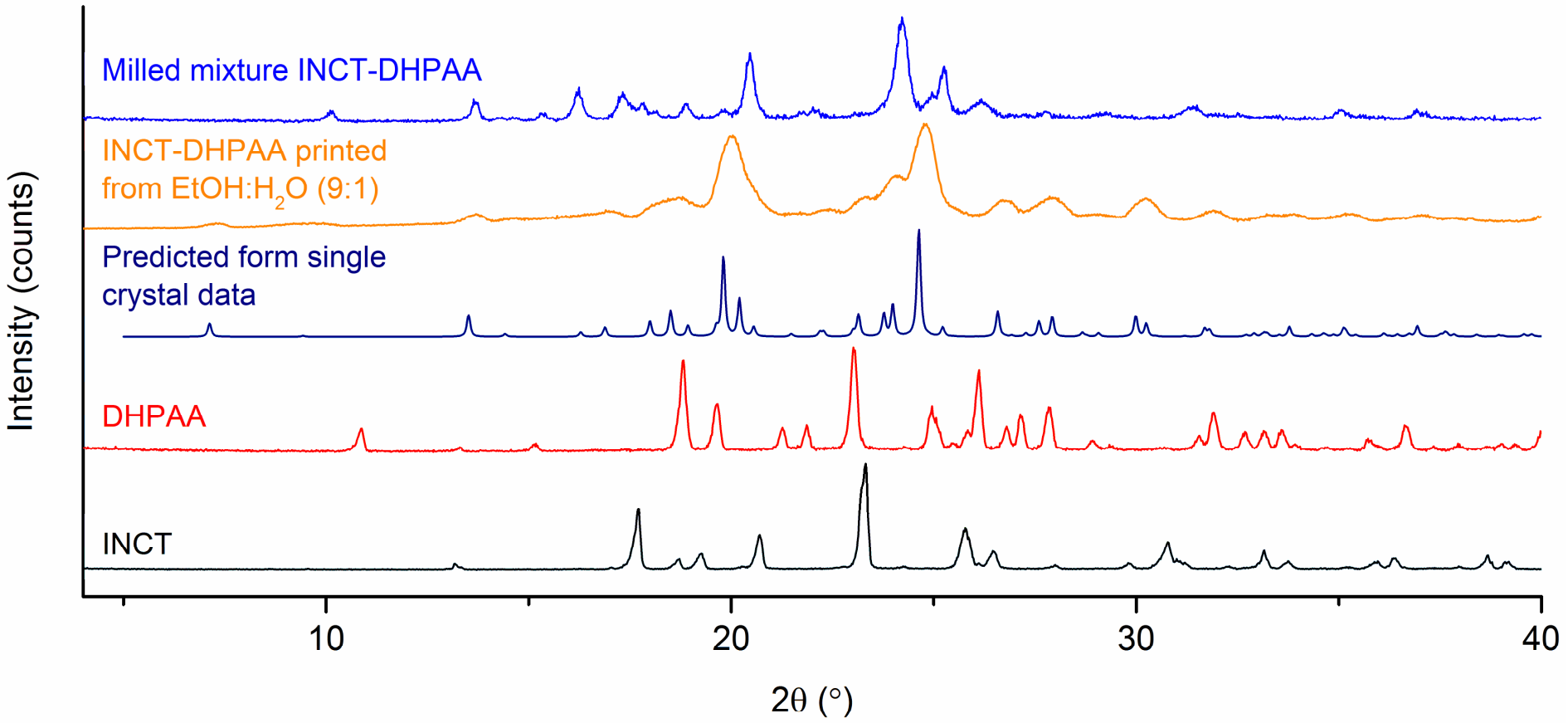

Figure 4-69. PXRD patterns collected for INCT and DHPAA.

FTIR spectra can be seen in Figure 4-70. Aside from the disappearance of the weak band at 1728 cm^{-1}, probably relating to a carbonyl stretch, the spectra are identical. This confirms the materials present have not undergone any chemical changes but does not provide any additional data to confirm whether a co-crystal has formed.

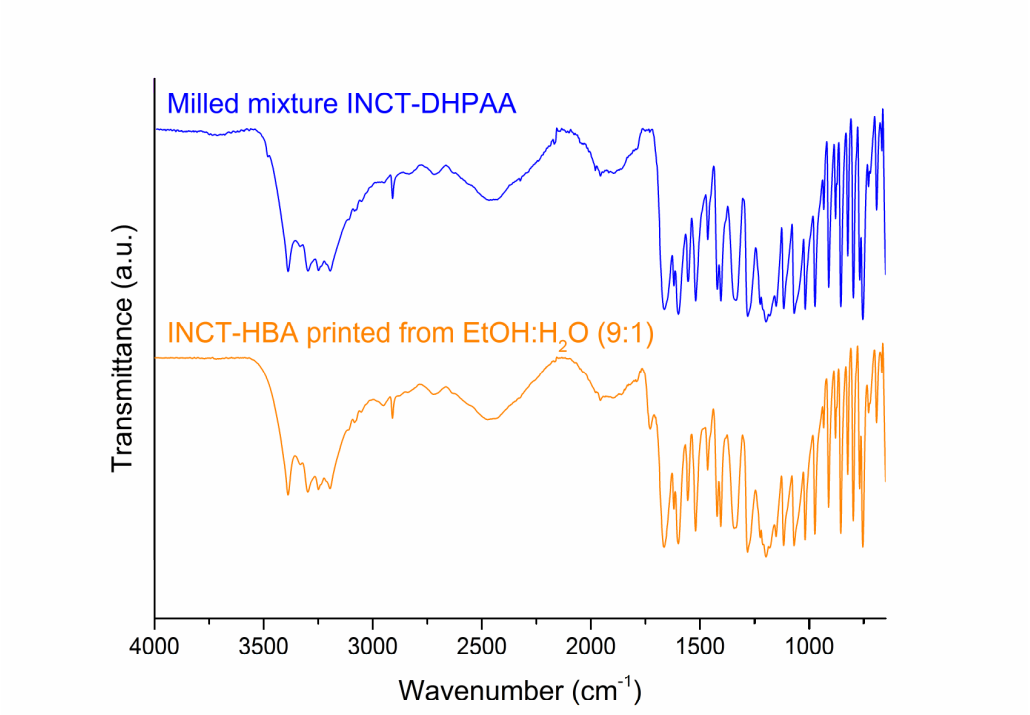

Figure 4-70. FTIR spectra for a ball milled mixture of INCT and DHPAA and for crystals printed from an equimolar solution of the two in EtOH:H_2O (9:1).

4.3.4.4. INCT-LABA

The DSC trace for a milled mixture of INCT and LABA (Figure 4-71) has multiple events of both endothermic and exothermic enthalpies. The trace most closely resembles that of a mixture of the two materials after they have been ground separately. The calorimetric data appear to follow the same pattern as the sample analysed by DSC-XRD, only with higher peak resolution. Had all of the material reacted during milling then it is likely that the thermogram would contain only one endotherm at *ca.* 140 °C, as the reaction crystal melted. As was observed in Section 4.3.3.4, DSC suggests the milling of the two results in few or no new intermolecular interactions.

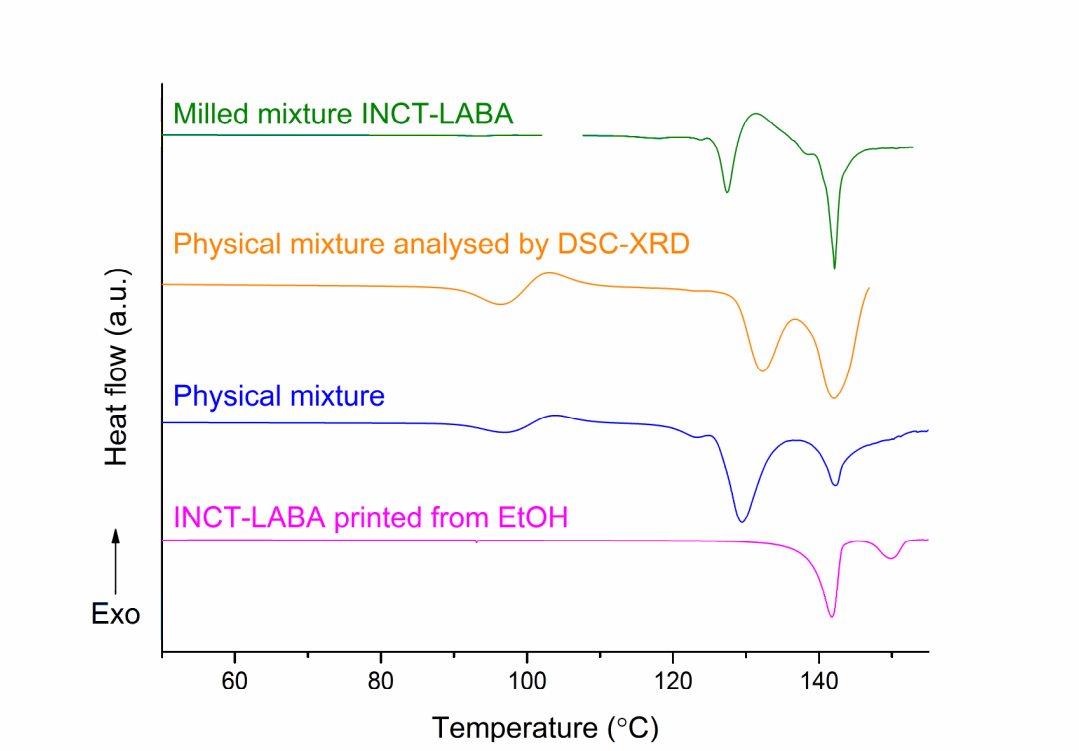

Figure 4-71. DSC data for crystals printed from an equimolar ethanolic solution of INCT and LABA, and from mixtures of the two after being ground separately or ball milling [Data points for the milled mixture between 102 °C and 108 °C have been removed as the data contained an artefact in this range].

The diffraction pattern for the milled sample of INCT and LABA (Figure 4-72) further clarifies the identity of the material. The pattern contains reflections which correspond to both of the raw materials and the crystals formed by printing, but it is unclear whether there are any from the other crystal formed by reaction and subsequent solvent evaporation. Although the intensities are different the peak positions of the milled mixture are all the same as those of the physical mixture and so it seems the most likely outcome is no co-crystallisation.

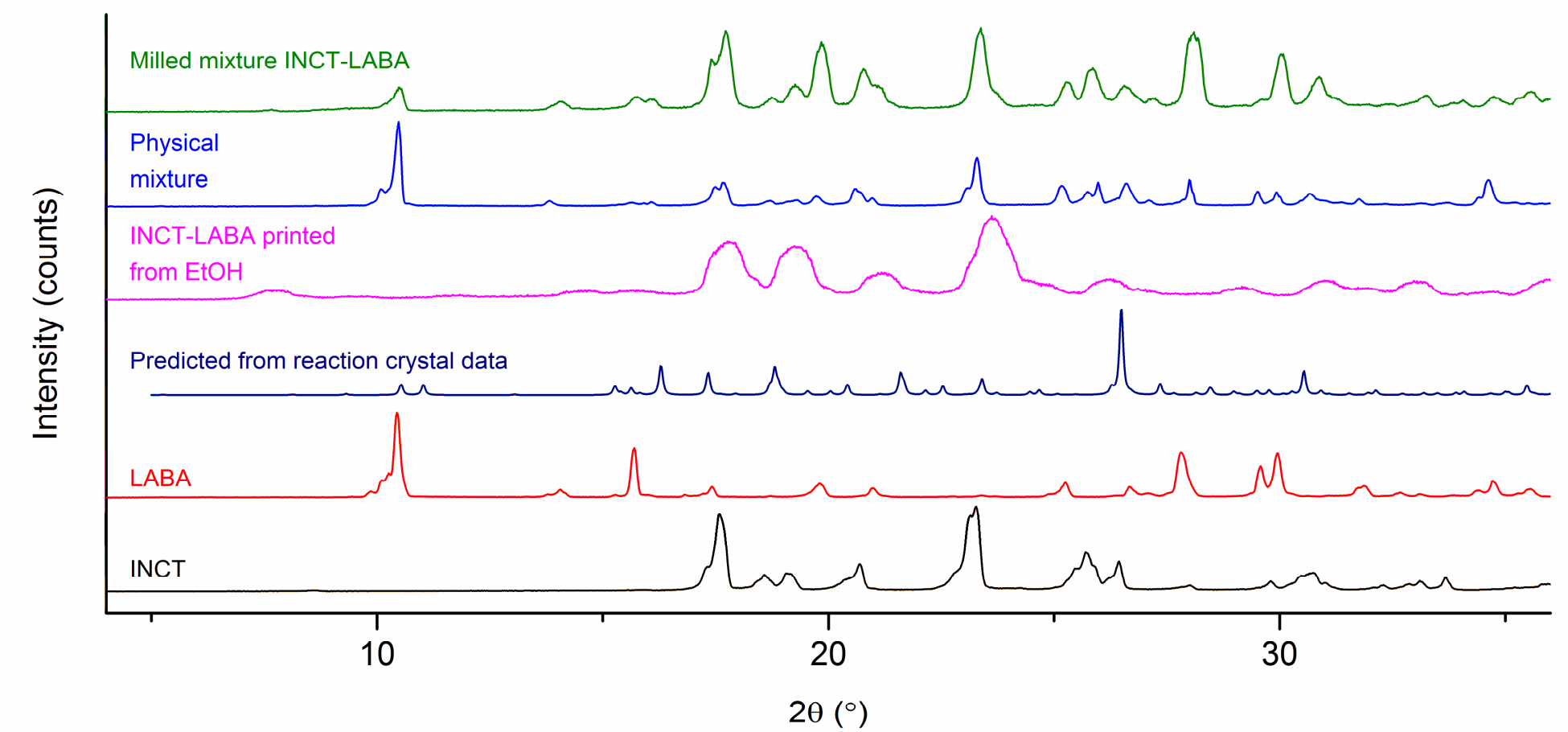

Figure 4-72. PXRD patterns collected for the INCT and LABA system products of each method.

Finally, FTIR spectra recorded for the milled sample and the physical mixture that underwent no grinding (Figure 4-73) are almost identical. Again this suggests that no changes in structure have occurred and confirms that no chemical changes have occurred. As with the spectra for the INCT-DHPAA system, the only noticeable difference is the appearance of a weak band at 1707 cm^{-1}, relating to C=O stretching.

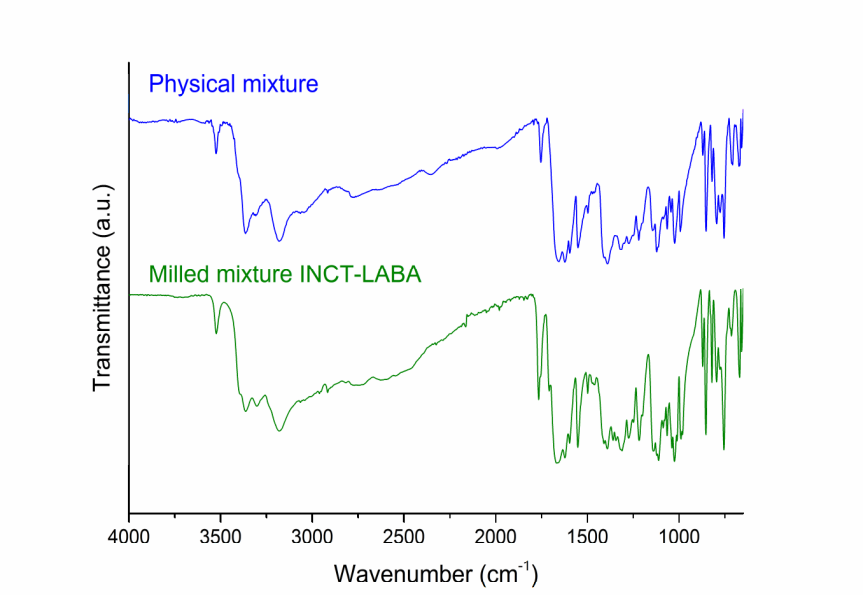

Figure 4-73. FTIR spectra for a ball milled mixture of INCT and LABA and for an equimolar physical mixture of the two.

4.4. Discussion

Four co-formers (HBA, HPAA, DHPAA and LABA) were selected and their ability to form co-crystals with INCT investigated using four synthesis methods (solvent evaporation, thermal inkjet printing, heat co-crystallisation and ball milling). It is possible to synthesize co-crystals of INCT and three of the four chosen co-formers, not only by the traditional method of solvent evaporation, but for HBA, HPAA and DHPAA, by the three much faster methods. In each case a co-crystal was grown by solvent evaporation and analysed by single crystal XRD. These analyses defined crystal structures that were then used to generate predicted powder patterns for comparison with data collected for samples produced by the other three methods. The single crystal data were also used to carry out Rietveld refinements on PXRD patterns collected for samples produced by heat induced co-crystallisation using the combined DSC-XRD method described in Chapter 2.

Table 4-15. Results of co-crystallisation of the four co-formers with INCT by the four methods studied.

	Solvent evaporation	Thermal Inkjet Printing	Heat induced	Milling
HBA	✓	✓	✓	✓
HPAA	✓	✓	✓	✓
DHPAA	✓	✓	Unknown	✓
LABA	×	×	×	×

INCT-HBA was the only system studied that had previously been reported to form a co-crystal (VAKTOR). In this work a second, as yet unreported, co-crystal structure with the monoclinic space group $P2_1/c$ was grown by solution evaporation. DSC and PXRD analyses confirmed that thermal inkjet printing resulted in crystals with the structure of the previously reported co-crystal, rather than the new form produced in this work. Rietveld refinement of DSC-XRD diffraction data has shown in great detail the process by which heating a mixture of INCT and HBA results in their transition to VAKTOR. Initially, INCT I and HBA form the newly discovered co-crystal before the evolution of INCT becomes dominated by its conversion to INCT II. Following this, the new co-crystal converts to VAKTOR, and INCT II and HBA combine to form the known co-crystal. This system was also successfully co-crystallised *via* ball milling, as shown by DSC and PXRD, and supported by FTIR.

Solvent evaporation has been employed to grow single co-crystals of INCT-HPAA in a 2:1 molar ratio with the triclinic space group *P*-1. All other methods employed were successful in their attempts to grow the same co-crystals. Diffraction patterns collected for samples produced by thermal inkjet printing and ball milling very closely matched that predicted from single crystal diffraction data. Rietveld refinements of DSC-XRD data have shown heat induced co-crystallisation to occur by what appears to be a localised melt re-crystallisation mechanism for both materials with no other phases present. The melt of the co-crystal in this experiment was shown to be the same as that of the printed and ball milled samples, adding support to the conclusion that each method resulted in the same co-crystals.

Solvent evaporation experiments on INCT and DHPAA were unsuccessful, however co-crystals have previously been grown from a solution of these materials by other researchers, although the results are yet to be reported. These crystals were formed in a 1:1 molar ratio in the triclinic space group *P*-1. Thermal inkjet printing has produced co-crystals with the same structure as those formed by solvent evaporation as demonstrated by the similarity of the PXRD patterns of both. Applying heat to a mixture of the two materials does appear to have resulted in co-crystallisation, but to a different crystal structure to that of the solvent-grown and printed crystals. The same can be said for the ball milled material. DSC traces for these two events exhibit a similar endothermic

event at a slightly higher temperature than that of the printed crystals but their diffraction patterns are distinct. Suggesting the occurrence of at least three polymorphs of this co-crystal.

INCT and LABA reacted when in solution and results of the other methods are inconclusive but appear to have been unsuccessful. It seems that the two materials are incapable of co-crystallisation.

The results of the inkjet printing experiments were in line with those seen by Buanz and co-workers[81] who highlighted the necessity for multiple print passes to prepare sufficient quantity for analysis, whilst also commenting on the low intensity to noise ratio resulting from the small crystallite size, an effect observed here. Thermally driven co-crystallisation has been shown to occur in all systems in which co-crystallisation was possible, whilst in agreement with Yamashita's[86] work no crystallisation exotherms were observed although it is expected that their suggestion of altering the heating rate would reveal one in the two cases of confirmed co-crystallisation.

4.5. Conclusion

For all but one of the systems thermal inkjet printing produced co-crystals of the same structure as those grown by solvent evaporation, which is unsurprising as the process is very similar but on a much smaller scale. This method was very quick but resulted in very small crystals and small sample sizes and so the quality of the diffraction data was not as good as the other methods. Ball milling was by far the fastest and easiest method employed and also produced co-crystals for all three systems in which it is deemed possible.

Full characterisation of a co-crystal can most easily be carried out by single crystal analysis and so solvent evaporation remains best method for this. However, initial screening for the co-crystallisation potential of a system need not take so long. Thermal inkjet printing is a cheaper and quicker alternative and ball milling provides an extremely fast, cheap and environmentally friendly alternative but DSC-XRD analysis stands out as the best method for fast screening and detailed analysis of the mechanism by which two materials co-crystallise. Although the requirement of a synchrotron does mean it is more expensive than all of the other methods, this would be an easy service for synchrotron facilities to offer researchers, reducing the cost and in many cases resulting in higher quality data.

5. Physical Vapour Deposition of APIs

5.1. Introduction

As described in Chapter 1, amorphous materials have the structure of a liquid but the physical properties of a solid. Upon cooling, at the T_m, a liquid will either crystallise (if possible) or, if cooled sufficiently quickly to avoid crystallisation, become a metastable supercooled liquid. In this state the response of the specific volume or enthalpy to further cooling is the same as would be expected from a liquid above T_m[2] and the system will remain in equilibrium. If the supercooled liquid is cooled further the molecular movements will continue to slow until eventually equilibrium cannot be maintained and the rate of volume/enthalpy change becomes slower than the predicted liquid behaviour. This is the T_g, and is the point at which the supercooled liquid becomes a glass.[112,118]

There are a number of methods currently employed in the vitrification of pharmaceuticals, some of the most common being spray-drying, freeze drying, quench cooling, melt extrusion, milling, and compaction.[2,250] Glasses prepared by different methods exhibit different stabilities,[251] and quench cooling has been shown to produce some of the most stable amorphous materials.[4]

Quench cooling applies the theory of rapid cooling very simply. The API in question is heated to just above its melting point and held there until any crystalline character has dissipated, whilst taking care not to let the sample degrade, before then quenching the melt at a temperature below the T_g. Liquid nitrogen (LN_2) is commonly used as the quenching medium, although this is compound dependent (some are easier to vitrify than others). So long as the rate of cooling is rapid enough that crystallisation does not occur, the quenched sample will pass from the liquid phase through the supercooled liquid phase and transition to a glass at the T_g.[252] The benefits of quench cooling lie in its simplicity: all that is required is a heat source and a quenching source. However, some materials decompose upon melting or cannot be cooled quickly enough to avoid crystallisation.[2]

PVD is an atomistic or molecular deposition process. This term refers to the mechanism by which the deposition occurs, i.e. as individual atoms or molecules. Deposition in this report refers solely to molecular deposition. The amorphous drug is produced by placing a solid sample in a vacuum. The solid is then vaporised via either melting and boiling or sublimation. Following vaporisation, the material is deposited onto a substrate. As molecules arrive at the substrate from the vapour phase they join a fluid layer that is

several molecules thick.[118] At low deposition rates, molecular mobility in the surface layer is sufficiently high that molecules will orientate themselves so that they are close to equilibrium. They will then lose the ability for translational motion when subsequent layers are deposited. There is a direct relationship between the temperature of the substrate, the rate at which material is deposited, and the stability of the resulting film.[119] The role of the substrate is to remove the thermal energy of the molecules as they are deposited, fixing them with reference to their position in space and their orientation on the substrate or previous layer of molecules. The rate at which a vaporised molecule travels towards the substrate will affect the time allowed to remove the thermal energy before it is locked into place by the next layer.

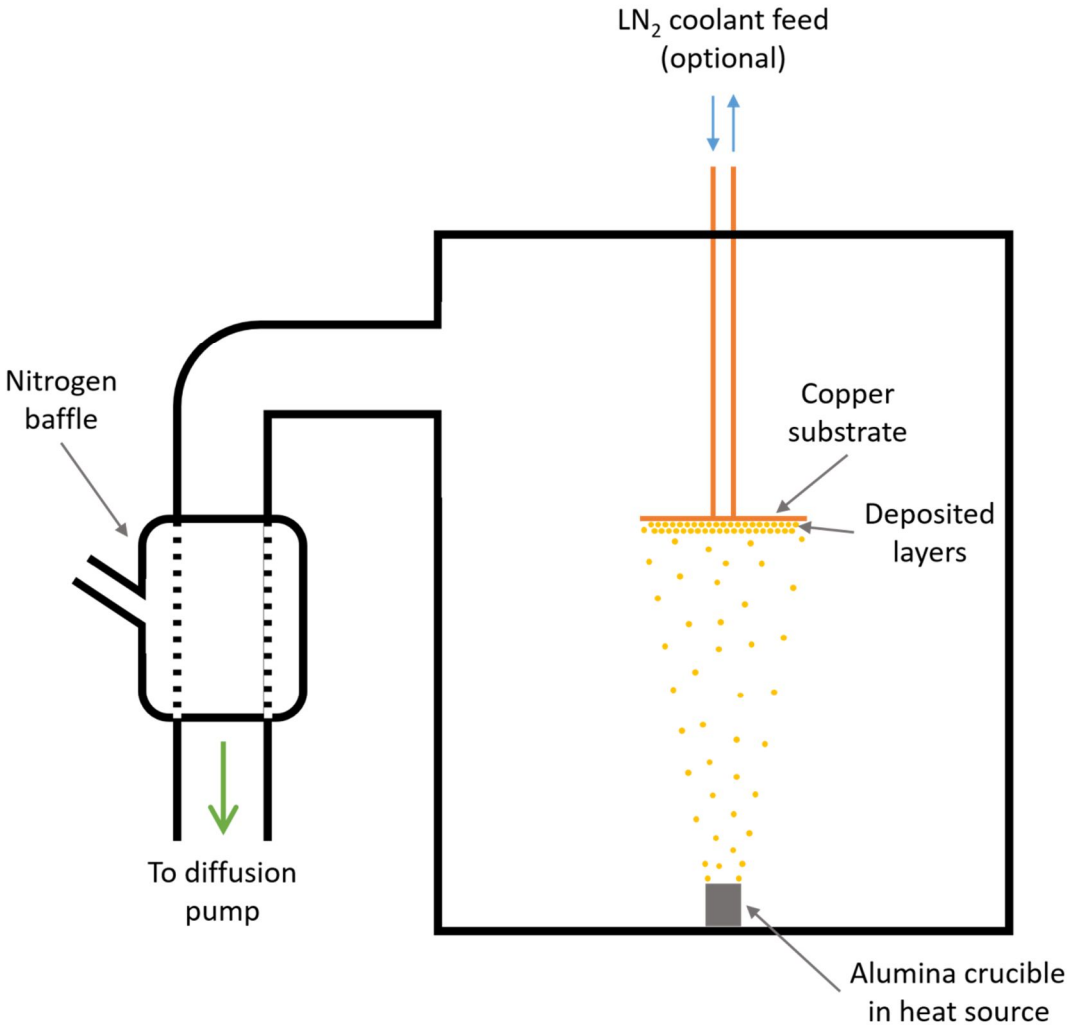

Figure 5-1. A schematic of the PVD apparatus.

Physical vapour deposition (PVD) has long been recognised as a feasible technique for producing amorphous materials.[121] However, until recently, these glasses were considered to be high energy unstable materials that, as a result of this instability, would relax and become crystalline far more rapidly than amorphous forms of the same species

prepared *via* other, more conventional, methods.[121–124] The reason for this perceived instability stems from early studies into the properties of PVD samples, which were deposited at low temperatures (in the region of −233 °C and above)[124] without considering the rate of molecular deposition. As a result of the findings of these studies there has been little research into PVD for pharmaceuticals. If amorphous forms of a drug are to be used clinically, they need to be stable at room temperature but highly soluble, with a rapid rate of dissolution. Early reports suggested samples prepared *via* PVD would dissolve quickly but also revert to crystallinity very quickly, therefore losing the advantageous properties of an amorphous material.[121–124,253]

Considering the nature of amorphous materials it makes sense that if low temperature deposition occurs at a fast rate the molecules will not have time to reorient themselves into a more stable, lower energy, position relative to their surroundings before they are trapped by subsequent molecules. This will lead to a bulk material with a few small regions of short range order that is very unstable and relaxes quickly. Conversely, deposition at the same rate onto a higher temperature substrate means that the molecules in the mobile surface layer have more thermal energy and so will be able to adjust their position more rapidly and settle into a more stable position before being trapped by the next layer of material deposited. This should result in a bulk with larger regions of short range order. Both methods will deliver amorphous products but with different relaxation and dissolution characteristics. The former will both relax and dissolve more rapidly than the latter, but both will dissolve more rapidly than the crystalline form of the same substance; hence, the second option is more favourable when considering drugs, as the resultant material is more stable and will retain its amorphous character for longer upon storage.

It seems that the rate of deposition has a greater effect on the stability of the resulting material[127] than the substrate temperature. For any substance it is hypothesised that there must be a combination of deposition rate and temperature at which the most stable amorphous configuration will form, and from this point any decrease in temperature will require a decrease in deposition rate to hold that equilibrium. If the rate is too low the material will crystallise and if it is too high the product will have a higher energy and lower stability.

Recently, it has been reported that vapour deposition can be utilised to prepare glasses that are of lower energy and higher stability than those prepared via quenching of the melt.[119,129] This has been achieved by depositing on to low temperature substrates at a low rate, and it is predicted that glasses prepared this way will be more stable than those

aged for a period of more than 1000 years. These have been termed “ultrastable glasses”.[118,120,127]

Swallen *et al.*[129] have shown that deposition of a material onto a substrate 50 °C below its glass transition temperature (T_g−50) results in glasses with higher kinetic and thermodynamic stabilities than those of the same substance vitrified via melt quenching. The criterion for determining greater kinetic stability was a higher onset temperature for the T_g, since this demonstrated that the molecules require more energy to alter their glassy configurations. The thermodynamic stability was assessed by calculating the fictive temperature (T_f) and comparing that of the two methods of vitrification. The T_f is the temperature at which the supercooled liquid would have last been in structural equilibrium (i.e. structural rearrangements occur at a high enough rate that the enthalpy/volume reduces linearly with temperature) when the physical temperature dropped below it. Therefore, the lower the T_f of a material the higher its stability. Swallen also made the observation that a slower deposition rate results in a more stable glass.[129]

Kearns et al.[119] looked at the influence of substrate temperature on stability and found that the most stable indomethacin (IMC) glasses were obtained when deposited at 0.85 T_g and at a rate of 15 ± 3 nm s^{-1}. No other compounds were studied, however, meaning no general trends could be established.[119] In 2010 another study led by Kearns used nanocalorimetry to analyse the heat capacities of IMC glass formed at 0.84 T_g by PVD, and showed that they are lower than those deposited at T_g, and therefore the former are more stable.[126] Kearns further investigated the effect of deposition rate on the stability of the glass produced at constant substrate temperature, and found that the slower the rate the higher the stability was.[127]

It has been reported that tris(naphthylbenzene) vapour deposited at 0.85 T_g shows translational movements at least 100 times slower than those of the supercooled liquid.[254] This is supported by the work of Dawson *et al.*[118] who have also shown, *via* wide angle X-ray scattering, that in samples deposited at 0.2 nm s^{-1} and 0.84 T_g there is a different local molecular packing arrangement to those of the melt quenched glass and the supercooled liquid. These authors also reported that, when annealed slightly above or slightly below the T_g, there is a phase transition resulting in the local packing reverting to that of the supercooled liquid.[118]

This chapter will describe in detail studies to use PVD to prepare amorphous forms of a range of active ingredients. The PVD vacuum chamber and its component parts will be described, together with the extensive modifications required to render it suitable for working with pharmaceutical materials. Following this, data will be presented for a

number of pharmaceuticals that have been deposited using this apparatus with the aim of metastable polymorph discovery according to Ostwald's rule of stages (see Chapter 1).

5.2. The Physical Vapour Deposition Apparatus

5.2.1. Vacuum Chamber

Prior to the work reported here the apparatus described was developed by Jacob Shephard for the preparation of amorphous solid water (ASW).[125] The vacuum chamber used (Figure 5-2) is a bespoke, stainless steel cabinet, with an aluminium door housing a small glass window. It is manufactured by Kurt J. Lesker, and is the largest single part of the apparatus. The internal dimensions of the chamber are 24 x 12 x 12 inches and it has nine recesses, each leading to either a KF40 or an LF100 flange. These are standard sizes and were used so that standard market components could easily be added to the chamber. The volume of the chamber, including the attached components, is estimated to be ~0.080 m^3 with an internal surface area of ~1 m^2.

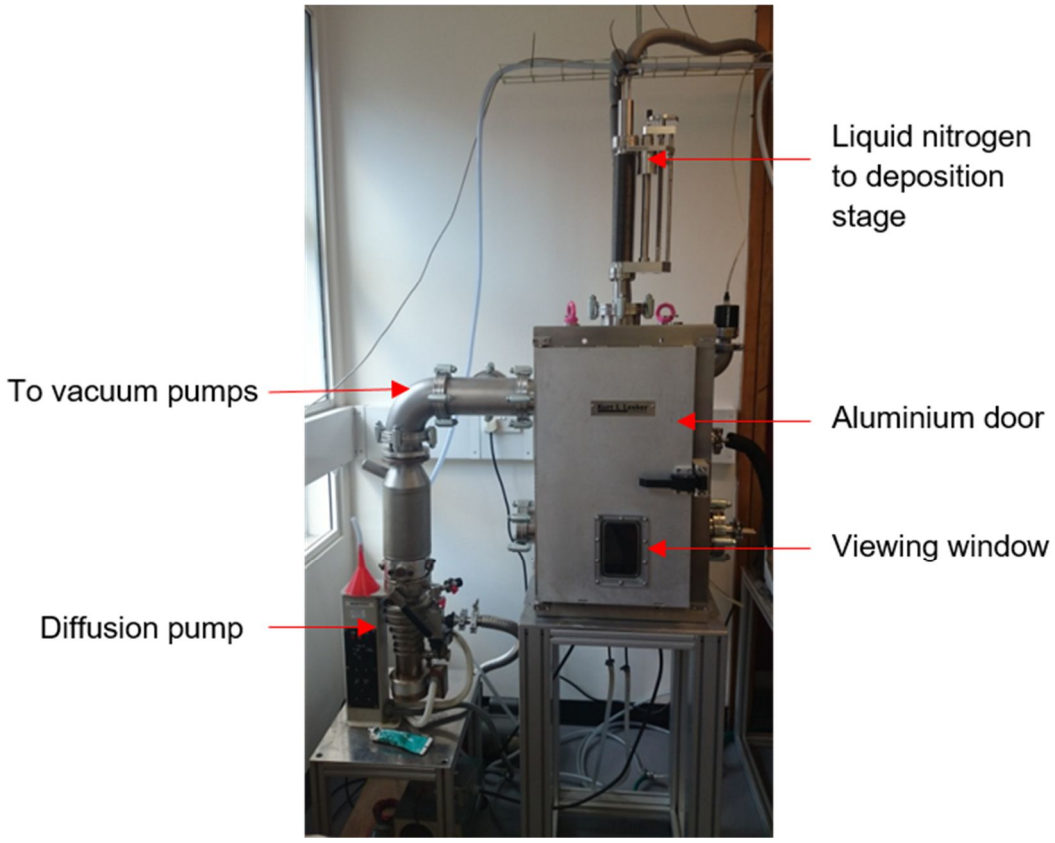

Figure 5-2. The deposition apparatus.

5.2.2. Diffusion Pump

The chamber is evacuated using a Diffstak 63 diffusion pump (BOC Edwards, Crawley) (**Error! Reference source not found.**) with a water cooled body. Additionally, the pump i s equipped with a liquid nitrogen (LN_2) cooling baffle to reduce backstreaming (the process of the oil vapour not condensing quickly enough and travelling backwards through the system, thus contaminating the internal surface of the chamber). The diffusion pump is a high vacuum pump and was used to consistently achieve chamber pressures of 1.5 x 10^{-5} mbar and lower.

5.2.3. Deposition Stage and Plate

As the chamber was originally intended for the preparation of ASW at −193 °C, the deposition stage was designed to operate at this temperature. It consists of a 6 mm thick, 203 mm diameter copper plate. Embedded within the upper side of the stage is a coil of ¼ inch diameter copper tubing through which nitrogen vapour, at −193 °C, can flow via the bespoke stainless steel feedthrough (Kurt J. Lesker) from which it is also suspended. Attached to the underside of the deposition stage, by six bolts, is a copper deposition plate of the same dimensions as the stage (Figure 5-3). This allows for removal of the plate following deposition and easy retrieval of the deposited material (Figure 5-4). The upper face of the plate has seven protruding cylindrical copper contacts to allow for visual inspection of the connection between it and the stage.

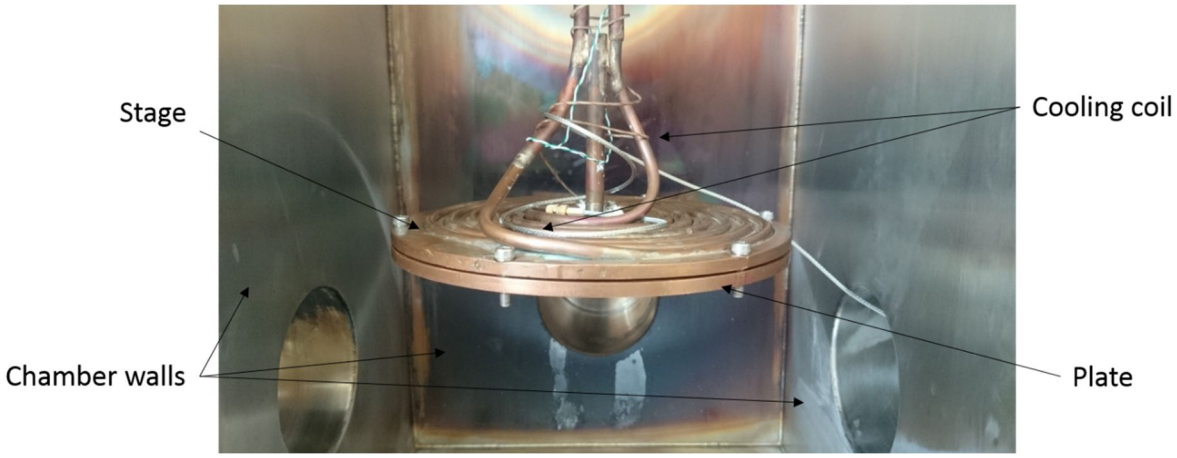

Figure 5-3. The deposition stage and plate within the vacuum chamber.

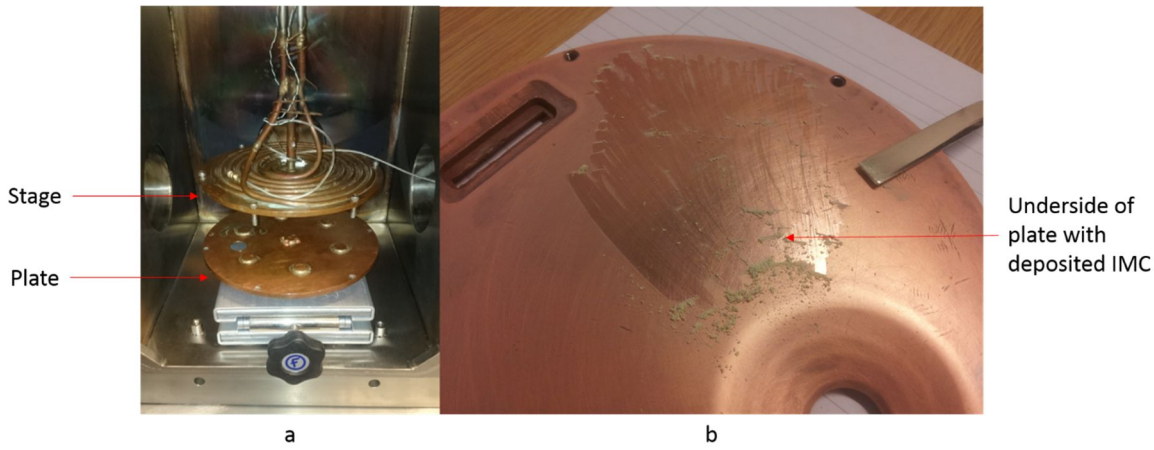

Figure 5-4. (a) The deposition plate being removed from the deposition stage and (b) deposited IMC being removed from the lower face of the deposition plate with a spatula.

The temperature of the deposition stage can be monitored by a K-type thermocouple fixed to the upper side of the stage with a bolt and thermal paste, a temperature controller (331, Lakeshore Cryotronics) and the Labview computer software (National Instruments). Nitrogen flow was achieved by connecting one side of the feedthrough to a 5 L Dewar with ~2 m of insulated rubber tubing and the other side to a rotary vane pump (Sogevac SV16, Oerlikon Leybold Vacuum) by ~5 m of rubber tubing. A copper coil submerged in a water bath was placed between the feedthrough and the rotary vane pump to increase the temperature of the nitrogen vapour and so protect the pump (Figure 5-5). It is possible to control the flow of the nitrogen vapour through the system, and thus the temperature of the stage, by adjusting a valve positioned between the water bath and the pump.

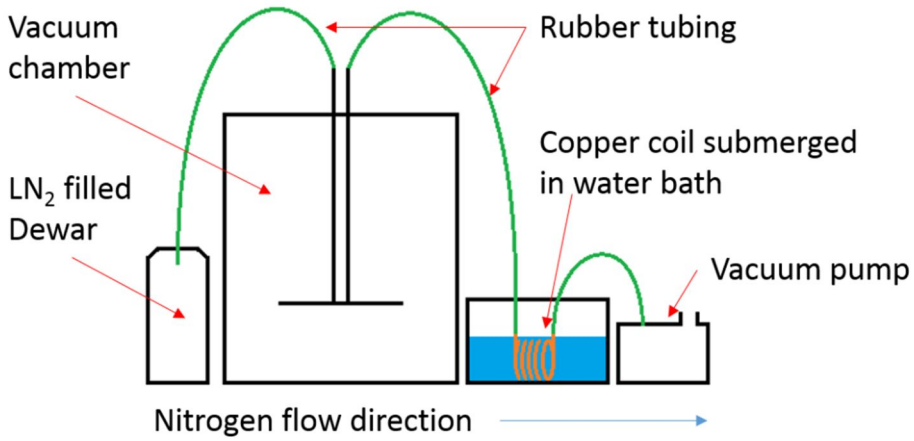

Figure 5-5. A schematic illustrating the apparatus used for cooling the deposition stage with liquid nitrogen.

5.2.4. Sample Dosing Apparatus

The original sample heating set up (Figure 5-6) was designed to vaporise both water and a solid, separately, within the evacuated chamber. It was originally used by Jacob Shephard in the study of two-component liquids, namely water and fullerene, as it allowed the deposition of a layer of fullerene between two layers of amorphous solid water. A flange was fitted with a stainless steel tube, offset from the centre of the plate, to which a bespoke water feeding set up could be attached outside the chamber. Next to this, offset from the centre by an equal distance, is an electrical feedthrough to which a tungsten basket filament (6.3 V, 43 A, 271 W, 1800 °C) (EVB8B3025W+, Kurt J. Lesker) can be fitted within the chamber. Initial experiments involved placing powdered solid IMC (ca. 0.3 g when filled) in an alumina crucible (13 mm diameter) designed to fit within the coil of the filament whilst maintaining as much thermal contact as possible. The water dosing apparatus connects to the stainless steel tube outside the chamber via a clamp and O-ring, and consists of a needle valve and bespoke 3 chambered ground glass flask. The feedthrough plate is located within a recess in the centre of the bottom face of the chamber, directly beneath the centre of the deposition stage. The seal is created by a gasket and O-ring (not pictured).

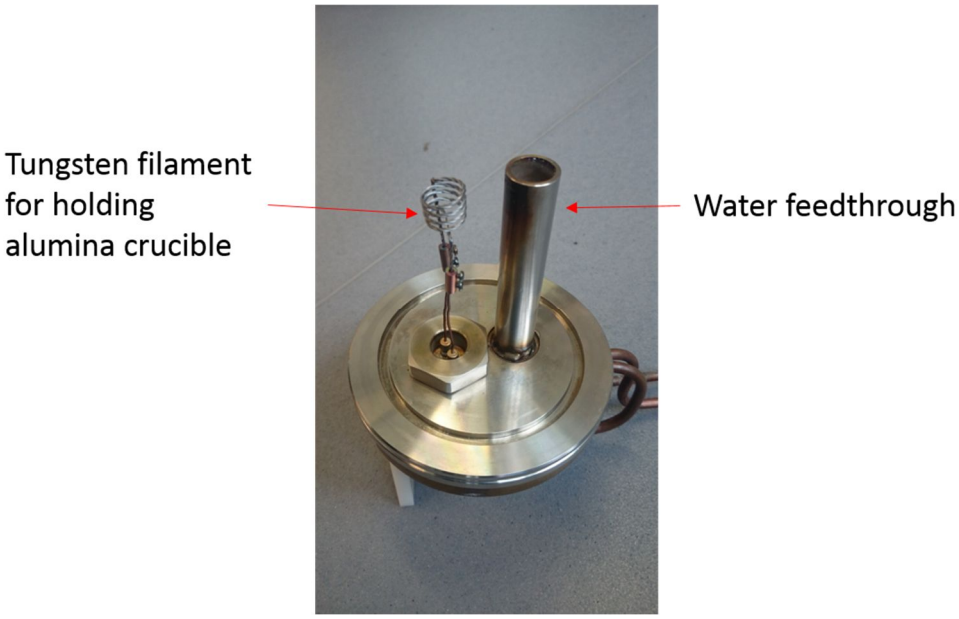

Figure 5-6. Photograph of the water/electrical feedthrough baseplate.

5.3. Alterations and Additions to the Vacuum Chamber

5.3.1. Quartz Crystal Microbalance

When carrying out physical vapour deposition it is advantageous to employ a system for monitoring the rate at which the material is being deposited onto the substrate. This rate will affect the physical form and properties of the final product, as it dictates the time each molecule will have to realign itself into a more stable position before being locked into position by the next layer.[118] Kearns *et al.*[127] have shown that lowering the deposition rate by two orders of magnitude, in two substances, lowered their respective fictive temperatures by at least 10 K.

A quartz crystal microbalance (QCM, 710-SH Sensor Head, Allectra) was installed to permit the deposition rate to be monitored. The QCM consists of a thin quartz disc with gold plated electrodes and a sensor head (Figure 5-7) which is used to apply an alternating electrical potential across the crystal. Quartz is a piezoelectric material and therefore the application of an electrical potential will cause mechanical stress within it. An oscillating electrical field applied across the crystal will result in an oscillating mechanical response (a wave). The impedance experienced by the propagating acoustic wave is measured using an impedance analyser (N2PK Vector Network Analyser (VNA), makarov.ca) in conjunction with a graphical user interface (GUI) (myVNA, makarov.ca). This information is interrogated using another piece of software (QTZ, Institute of Physical Chemistry, Clausthal University of Technology) allowing determination of a number of parameters, including the frequency shift experienced by the crystal when material is deposited onto its surface. The amplitude of the oscillation will reach a maximum when the thickness of the crystal is a multiple of a half wavelength of the acoustic wave, at this point the conductance also reaches a peak.[255] The frequency of the oscillation is directly influenced by any material in contact with it, be that gas, liquid or solid. A change in the mass, Δm, of the material accumulated on the crystal will result in a change in the frequency, Δf, at which the crystal oscillates (Figure 5-8).[256] This change in frequency can then be used to calculate the mass of the material adsorbed using the Sauerbrey equation:[256–258]

$$\Delta f = -\frac{2f_0^2}{\sqrt{\mu_q \rho_q}} \Delta m \qquad (1)$$

Where f_0 is the resonant frequency of the crystal, μ_q is the shear modulus of the quartz crystal, and ρ_q is the density of the quartz. Subsequently, the rate at which the material is being deposited can be calculated by plotting the mass adsorbed against time and taking the differential of the curve. The QTZ software has the option of plotting the Sauerbrey thickness (thickness of the adsorbed layer) against time and, as is the convention for deposition rate recording in the literature, has been used to calculate a rate in nm s^{-1}.

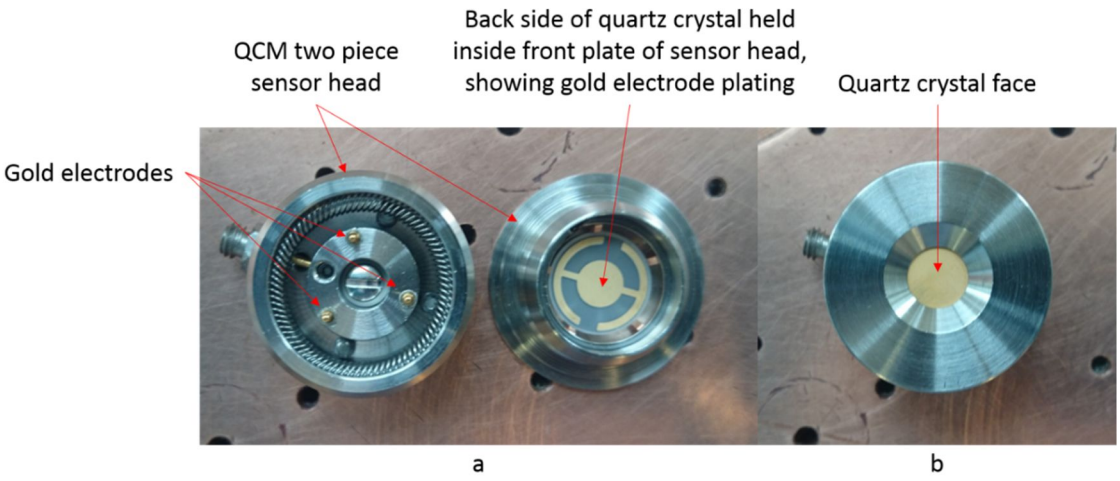

Figure 5-7. (a) Internal view of the two parts of the QCM sensor head showing the back of the quartz crystal and the gold plated electrodes, and (b) the assembled QCM sensor head with a quartz crystal *in situ*.

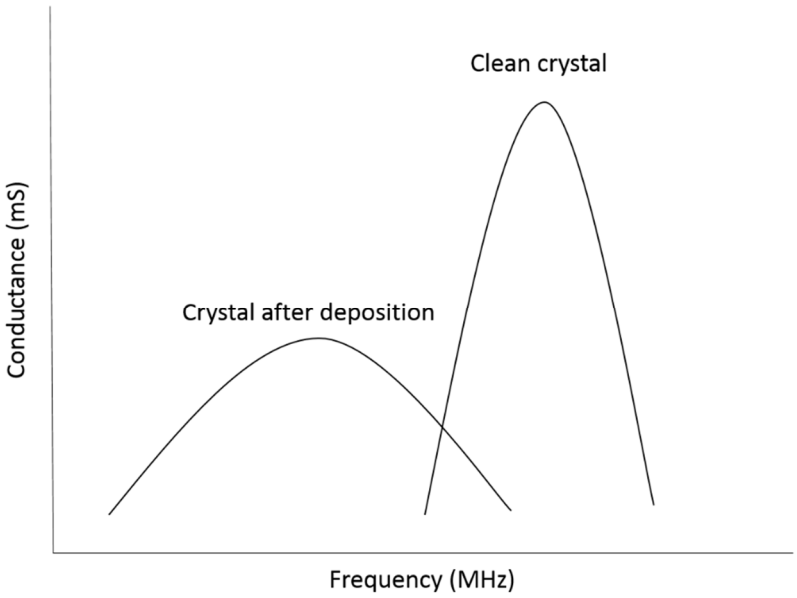

Figure 5-8. A schematic showing the frequency shift experienced by the quartz crystal when material is deposited onto it.

The QCM has been positioned in the centre of the deposition plate, directly above the centre of the base plate feedthrough (Figure 5-9), because this is where the rate of deposition will be highest and where the bulk of the material will be deposited.

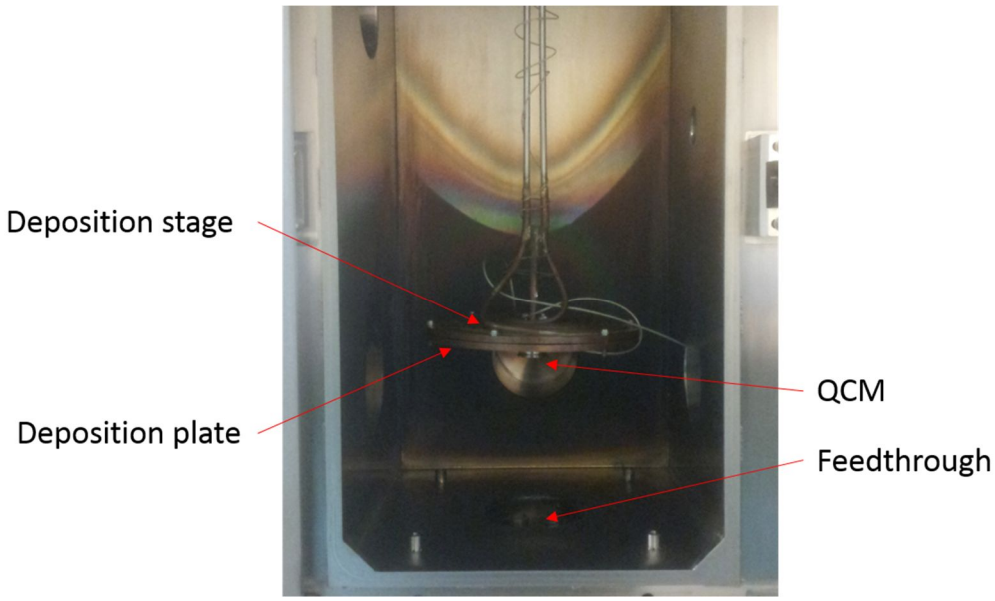

Figure 5-9. The PVD assembly in experimental configuration, including the QCM.

5.3.2. Sample Dosing Apparatus

5.3.2.1. Alumina coated tungsten filament/crucible

Early experiments with indomethacin (IMC, Molekula) were carried out using the feedthrough with the water dosing configuration previously developed and described in

Section 5.2.4. However, a number of problems were encountered. A significant drawback was the lack of reproducibility of the rate at which material could be deposited onto the substrate, as can be seen from the three examples in Figure 5-10. Two of the depositions were carried out by filling the crucible with IMC and applying an initial voltage of 70.0 mV at the transformer (which translates to 7.0 A at the filament), which was later increased to achieve a higher rate of deposition, yet despite the use of identical initial conditions the increase in the thickness of the layer deposited onto the quartz crystal was very different. The third (black squares) was carried out by applying 75.0 mV to the transformer and increasing this incrementally to 113.0 mV, at which point deposition was observed. This demonstrates a clear problem with poor reproducibility of deposition rate. This is directly related to the temperature within the crucible.

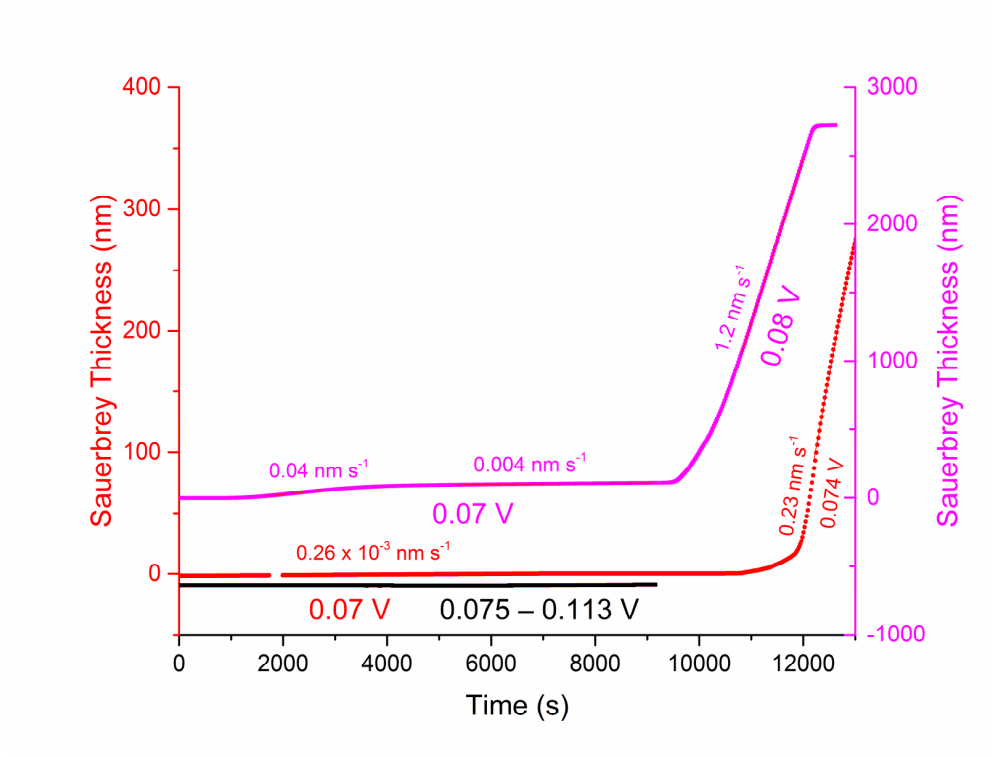

Figure 5-10. Plots of Sauerbrey thickness versus time for three different depositions of IMC using the original dosing configuration.

The chamber pressure in all of the initial depositions was relatively uniform, as can be seen from the examples in Figure 5-11, which shows the pressure dropping to between 1.8 x 10^{-6} mbar and 2.6 x 10^{-6} mbar on all three occasions. This is representative of all of the depositions carried out. This consistency of the base pressure of the chamber indicates the temperature of the crucible is the cause of the poor reproducibility of the deposition rate.

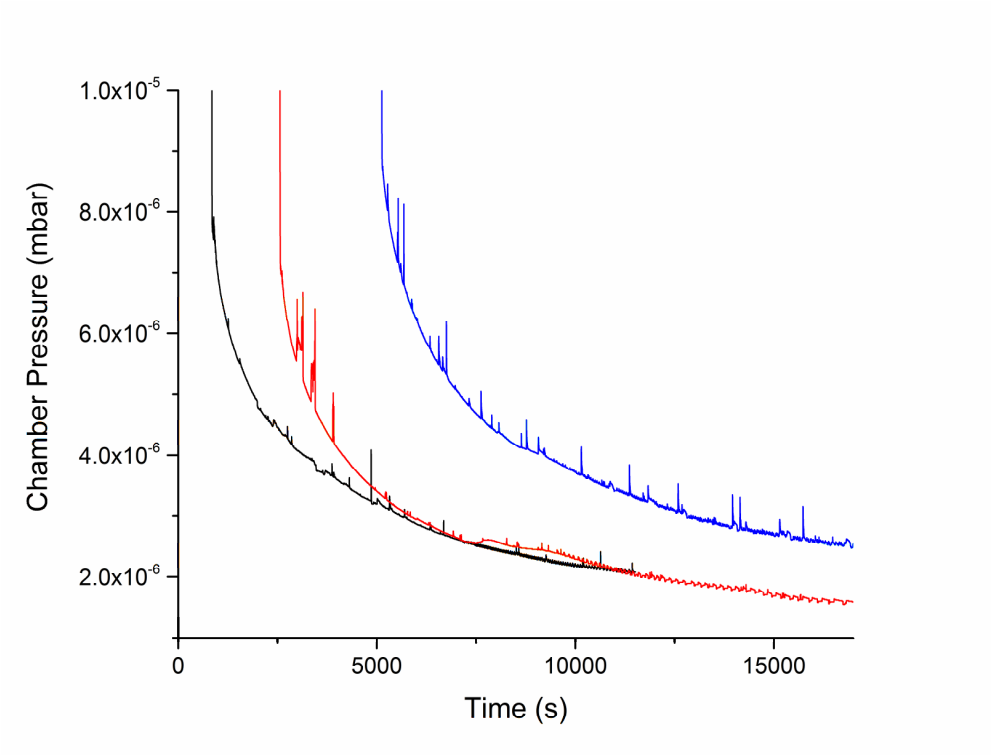

Figure 5-11. Plots of chamber pressure versus time for three depositions of IMC, using the original dosing configuration.

As the crucible and basket filament are separate items it is possible that the physical contact between the two may not have been the same for each experiment. Between each deposition the crucible was removed from the chamber and cleaned before refilling it with sample and again placing it in the filament. The orientation of the crucible in relation to the filament may not have been exactly the same each time, or the crucible may not have been placed within the filament with the same amount of pressure. The decision was made to replace the dosing apparatus with an alumina coated tungsten filament/crucible (NC-11, Megatech) (Figure 5-12).

Figure 5-12. A photograph of the alumina coated tungsten filament.

In addition to this alteration, it was necessary to replace the entire electrical feedthrough assembly responsible for applying current to the filament. The original configuration was unable to accommodate the new coated filament and, as stated previously, was capable of depositing both water and a solid sample simultaneously. The water dosing apparatus was not necessary for this study and therefore a new baseplate was built without this feature. Figure 5-13 shows the new baseplate and copper feedthroughs (261-1000WC-BP, Allectra). Whereas the original baseplate required a bespoke water cooled brass plate to be manufactured and fitted, the new feedthroughs were designed, by the manufacturer, with an integrated water cooling feature. This should reduce any effects caused by radiated heat. Another advantage of the new arrangement is that the coated filament sits more centrally between the two copper feedthroughs and therefore deposits more centrally on the deposition plate. This is more important with the addition of the QCM to the centre of the face of the deposition plate.

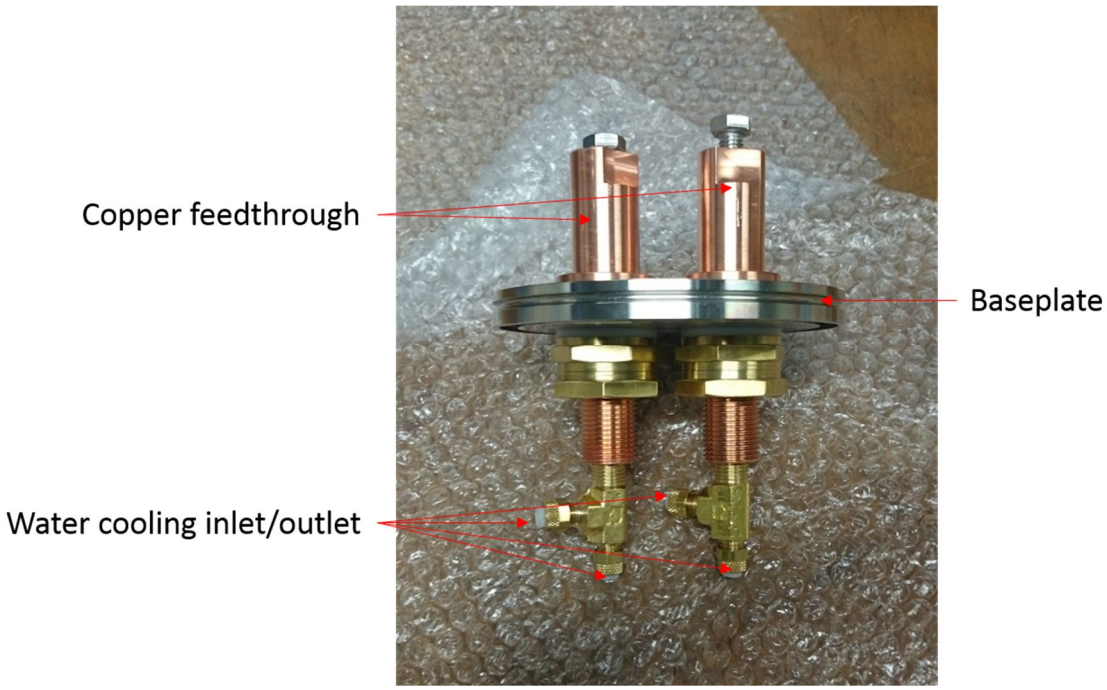

Figure 5-13. A photograph of the new baseplate and water-cooled copper feedthrough assembly.

Deposition rates of IMC from the coated tungsten filament were more reproducible than with the original sample dosing configuration, as can be seen in Figure 5-14. However, the reproducibility was still unacceptable. The major drawback of this and the previous set up was that the temperature of the crucible could not be monitored directly. Initially the heating apparatus was designed to sublime fullerene, which requires much higher temperatures at the crucible than any pharmaceutical material would. Consequently, a much lower current was required across the filament to achieve sublimation of IMC and

so a relatively small change in the voltage applied had a large effect on the behaviour of the sample. As a current was applied to the filament, its temperature increased, causing a rise in its resistance and thus the current, and so the voltage, to drop. Over time this caused a decrease in temperature at the sample. This change in voltage was observed at the transformer for all deposition experiments carried out with both sample dosing configurations. Therefore, apparatus allowing more precise control of voltage was required to implement a reproducible process.

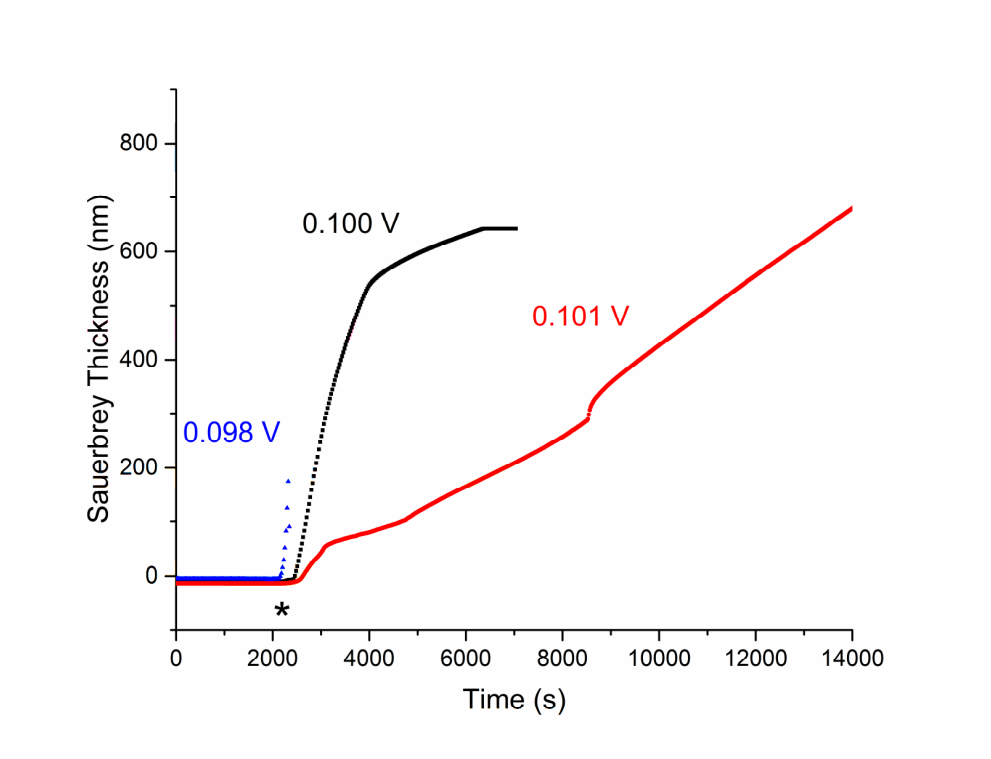

Figure 5-14. Sauerbrey thickness as a function of time when supplying 0.100 ± 0.005 V to an alumina coated tungsten filament containing IMC [* denotes time at which voltage was supplied to the filament].

A further problem observed for the coated filament was that following each experiment very little material was present on the deposition plate. This is a consequence of two factors: the small size of the crucible, and its conical shape, resulting in a much broader cone of sublimation than the cylindrical crucible used with the initial heat source. As a result, less material was directed towards the deposition plate, and much of it collected on the chamber walls. This was observed when cleaning the chamber following each experiment. For these reasons a third heat source was installed.

5.3.2.2. Low Temperature Evaporator (LTE)

To solve the problems outlined above the filament/crucible was replaced by a proportional integral differential (PID) controlled (2208e, Eurotherm) low temperature

evaporator (LTE10, Kurt J. Lesker) (Figure 5-15). This allows direct control of the crucible temperature between 50 and 600 °C, to a tolerance of ± 0.1 °C. Samples were loaded into an aluminium oxide crucible (EVCEF-10AO, Kurt J. Lesker) which was then placed within the heating coil. The temperature at the base of the crucible was monitored by external contact with a K-type thermocouple connected to the PID controller. The crucible used with this heat source was cylindrical and much larger than either of the two previous sample vessels, and so had the advantage of a more directed cone of deposition. Thus, less material was lost to the vacuum pumps. This addition was the final alteration made to the sample heat source.

Figure 5-15. The LTE heat source showing full assembly (left) and heating coil with stainless steel housing removed (right).

The initial objective of the work in this chapter was to produce high stability amorphous APIs *via* physical vapour deposition and to assess the stability of these materials upon storage using a number of different techniques. However, development of the vacuum chamber took significantly longer than anticipated and so, rather than attempt to produce high stability amorphous materials the work herein demonstrates the utility of the technique for preparing novel amorphous pharmaceuticals.

5.4. Materials and Methods

IMC and griseofulvin (GF) were purchased from Molekula and used as received. Benzoic acid (BA) was purchased from Sigma-Aldrich, while famotidine (FMT) and finasteride (FST) were purchased from Alfa Aesar and used as received. Urea was purchased from Fluka. Due to their large particle size BA and urea were gently ground in a pestle and mortar before loading into the PVD crucible.

5.4.1. Physical vapour deposition

Vapour-deposited samples of all APIs were prepared in a Kurt J. Lesker vacuum chamber, the components of which have been described in Sections 5.2.1 and 5.3. The crystalline powder sample was placed in the crucible in the LTE within the vacuum chamber (Figure 5-2), which was then evacuated to a base pressure of no more than 5 x 10^{-6} mbar. The sample was then heated and vaporised and the vapour deposited onto a copper substrate held at either 20 °C or −189 °C. The deposition plate was removed from the stage and the deposited material scraped from it using a spatula. Material deposited at −189 °C was removed from the chamber and deposition plate under LN_2 to avoid any phase transitions resulting from a rise in temperature, and to avoid the adsorption of atmospheric water. Cold-deposited materials were also stored under LN_2.

5.4.2. PXRD

Room temperature powder X-ray diffraction patterns were recorded using a Rigaku Miniflex 600 instrument operating at 40 kV and 15 mA (Cu Kα radiation, λ = 1.5418 Å) with powder samples mounted onto aluminium plates. Diffracted intensity from the sample holder did not interfere with characterisation.

Cold (−186 °C) powder X-ray diffraction was conducted on a Stoe Stadi-P diffractometer (Ge 111 monochromated Cu K_α, 40 kV, 30 mA). Samples were transferred under LN_2 to bespoke brass sample holders with Kapton windows before mounting on the goniometer. Data were collected using a Mythen 1K linear detector, and the temperature of the sample was controlled by an Oxford Instruments CryojetHT.

5.4.3. DSC

Conventional DSC measurements were carried out on a TA Instruments Q2000 calorimeter. Calibrations for cell constant and enthalpy were performed with indium (T_m = 156.6 °C, ΔH_f = 28.71 J g^{-1}) according to the manufacturer's instructions. The cell was purged with dry nitrogen at a flow rate of 50 mL min^{-1} throughout experiments. TA Instruments Tzero aluminium pans and lids and a heating rate of 10 °C min^{-1} were used for all experiments unless stated otherwise. Data were analysed using the TA Instruments Universal Analysis software, and transformation temperatures are reported as extrapolated onsets unless stated otherwise.

Low-temperature DSC measurements were conducted on a Perkin Elmer DSC 8000. Samples were transferred into stainless steel pans with threaded lids under LN_2 before

transferring to the precooled (−180 °C) furnace. A heating rate of 10 °C min^{-1} and a helium flow rate of 40 mL min^{-1} was used for all samples.

5.5. Results and Discussion

PVD was attempted on a number of materials with varying success. Some relevant data are presented in Table 5-1. Due to the relatively high vapour pressure of BA it sublimed while lowering the chamber pressure and, as there was no way to cool the sample, deposition was impossible. In contrast, IMC, GF and FMT all appeared to melt and boil in the chamber rather than sublime. Whilst this led to some sputtering effects for all three, in the case of IMC it was still possible to collect sample from the deposition stage. GF was abandoned in preference of a subliming sample, and upon removing the crucible from the chamber following deposition of FMT the remaining material was observed to have browned and degraded, and so this compound too was abandoned. Urea is reported to have a vapour pressure higher than the base pressure reached when evacuating the chamber (*ca.* 3.5 x 10^{-6} mbar), but nevertheless deposition was successful and no evidence of sublimation prior to heating of the sample was observed. This suggests that the literature vapour pressure might be incorrect. No data could be found relating to the vapour pressure of FST, however deposition was successful onto the substrate at ambient temperature.

Table 5-1. APIs submitted to PVD, with some relevant physical properties.

Property	IMC	GF	BA	FMT	FST	Urea
$T_{melting}$ / °C	158.95[259]	220[260]	122.38[259]	163.38[259]	258.7[261]	133.85[259]
$T_{boiling}$* / °C	499.4 ± 45.0[262]	570.4 ± 50.0[262]	249.3 ± 9.0[262]	662.4 ± 65.0[263]	576.6 ± 50.0[262]	196.6 ± 23.0[262]
Vapour pressure at 25 °C / mbar	1.15 x 10^{-10} [263]*	4.15 x 10^{-11} [263]*	1.09 x 10^{-3} [264]	-	-	2.33 x 10^{-5} [265]
Deposition success	Y	N	N	N	Y	Y

*values are predicted due to lack of experimental data. No vapour pressure data could be found for FMT or FST.

5.5.1. Indomethacin

IMC was deposited at ambient temperature. Figure 5-16 (a) shows a DSC trace typical of the IMC samples prepared *via* PVD.

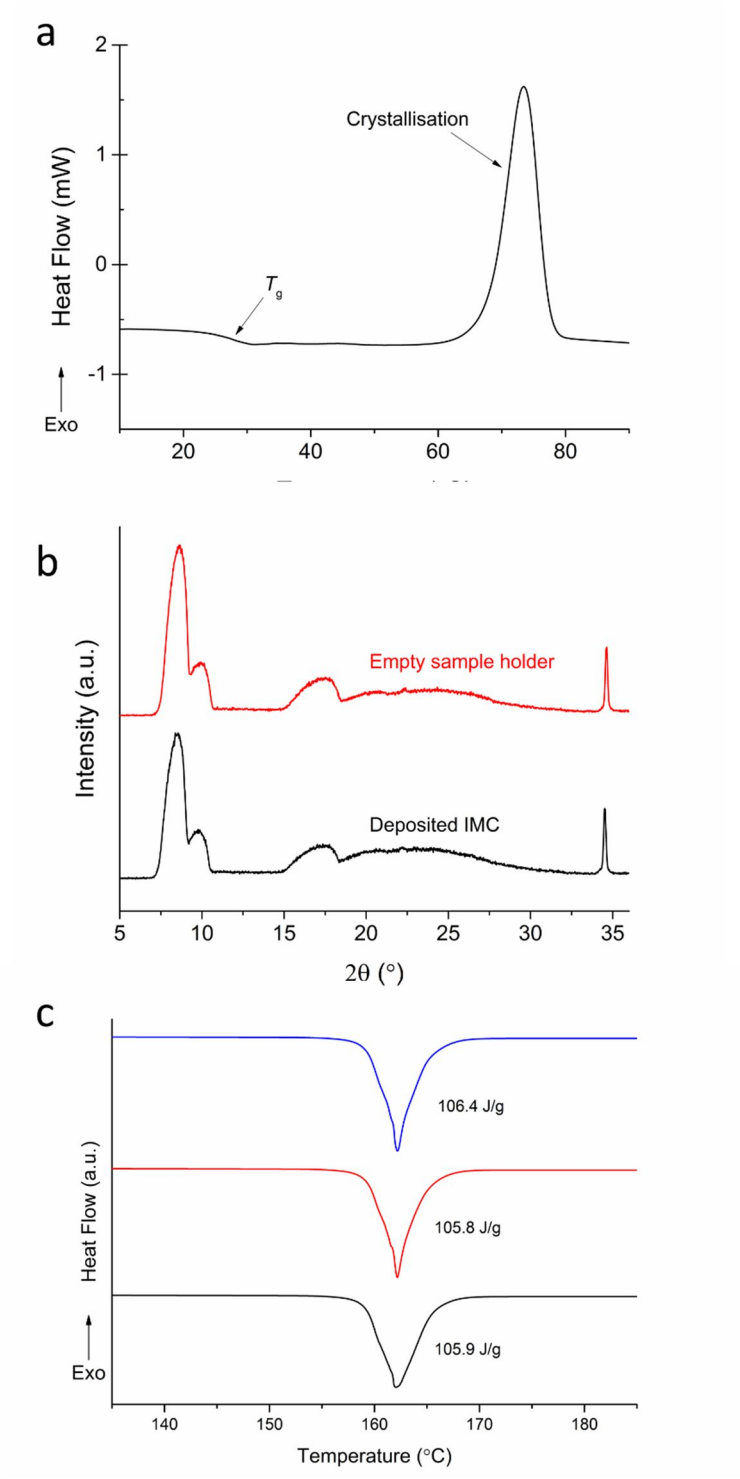

Figure 5-16. (a) A DSC thermogram of amorphous IMC prepared by PVD. Both the T_g and endotherm of crystallisation are present. (b) PXRD patterns of an empty sample holder (red) and IMC prepared by PVD in the same sample holder (black). (c) DSC thermograms of the melting endotherms for three samples of *γ*-IMC. The enthalpy of fusion is shown for each.

There is an obvious T_g at 23.8 °C confirming the presence of amorphous material. The temperature at which this transition occurs is much lower than the value of *ca.* 42-50 °C generally reported in the literature for the T_g of IMC.[110,266–268] This indicates that the glass

formed by PVD is less kinetically stable than glasses formed *via* other techniques, as it requires much less energy to enable the molecules to find equilibrium.[129]

The X-ray pattern of the deposited material (Figure 5-16 (b)) contains no Bragg reflections and so confirms the presence of amorphous material. These data prove the utility of the apparatus for the preparation of amorphous pharmaceutical materials.

5.5.2. Finasteride

FST was submitted to ambient PVD using the LTE heat source described in Section 5.3.2.2. The chamber pressure was maintained between 1.5 x 10^{-5} mbar and 6.2 x 10^{-6} mbar (Figure 5-17). Initial experiments were conducted to establish the temperature required to induce deposition, as monitored by the QCM. For all experiments, irrespective of the dosing configuration, there was a spike in chamber pressure observed when first supplying power to the heat source. It is unclear what caused this but there is a similar event in the QCM data, which indicates that it may be the sample outgassing (releasing trapped/adsorbed gas) or an artefact resulting from the chamber not being earthed. Following this there is a steady increase in Sauerbrey thickness of the material adsorbed to the quartz crystal, resulting from vaporisation and deposition of the sample. Initially, the temperature was set to 70 °C. The deposition rate was monitored and as the heat source reached the target temperature it was increased by 5 °C. This was repeated up to 175 °C and is visible as steps in the deposition data in Figure 5-17. The range of temperatures applied to the sample resulted in deposition rates up to *ca.* 10 nm s^{-1}.

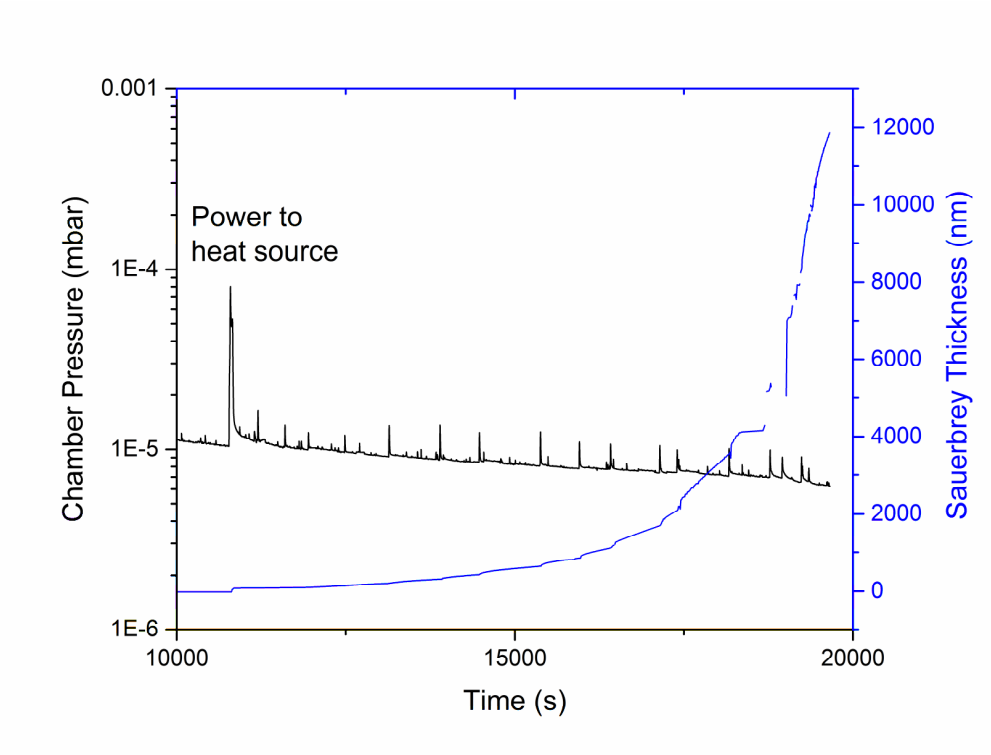

Figure 5-17. Chamber pressure and deposition rate for a sample of finasteride deposited onto a substrate at ambient temperature.

Following deposition the sample was removed from the copper plate at ambient temperature and pressure and characterised by PXRD. Insufficient material was retrieved from the substrate for additional DSC analysis. The resulting diffraction pattern (Figure 5-18) is absent of Bragg reflections, and displays no evidence of any crystal structure. Thus PVD is a useful technique for vitrifying FST. A literature search revealed only one other instance of amorphous FST, a patent application which refers to recovery of the material from solution.[269] This work appears to be the first instance of dry vitrification of FST.

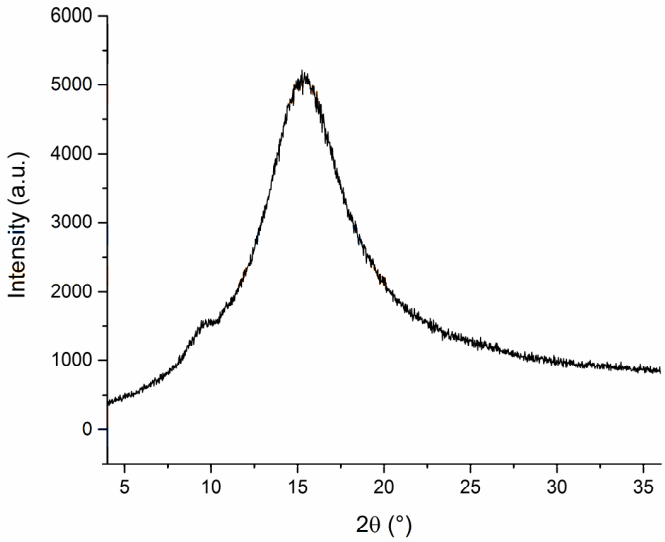

Figure 5-18. The PXRD pattern for a sample of FST deposited onto a substrate at room temperature.

A second sample of FST was prepared by PVD. The crucible was heated to 170 °C as quickly as possible, which resulted in a deposition rate of 55 nm s^{-s} (Figure 5-19), a fivefold increase in the maximum rate observed for the previous deposition at 175 °C. It was noticed in subsequent experiments that the heat source thermocouple was intermittently outputting an error message. The temperature controller was programmed to cut power in this instance, which may be the explanation for the difference in deposition rates. Eventually the thermocouple was replaced.

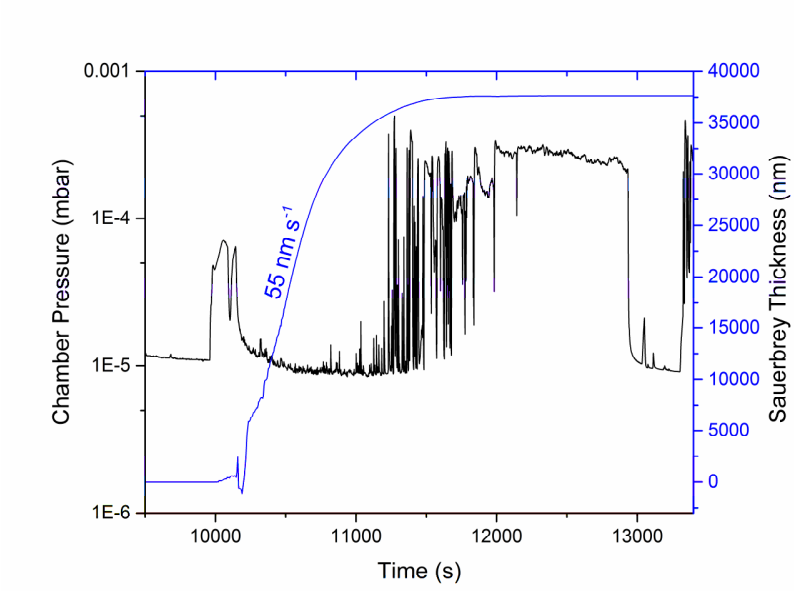

Figure 5-19. Chamber pressure and deposition rate data for a sample of FST submitted to PVD onto a substrate at ambient temperature. The sample was heated at 170 °C, achieving a deposition rate of 55 nm s^{-1}.

Towards the end of the deposition, at around 11200 s, the chamber pressure began to fluctuate and increased to *ca.* 2.8 x 10^{-4} mbar. It is unclear whether this was caused by a leak in the system or a problem with the diffusion pump. It does not appear to have been caused by the sample as deposition had almost completely stopped by 12000 s and the pressure remained high until 12930 s, at which point it rapidly dropped back down to 1.0 x 10^{-5} mbar. This does not appear to have affected the material properties.

The sample was removed from the chamber as was the previous sample and submitted to simultaneous DSC-XRD (Figure 5-20 (a and b)). Again the deposition process resulted in the vitrification of the drug, as can be observed by the complete absence of reflections in the contour plot. The pattern collected at 39.9 °C (Figure 5-20 (c)) shows only those reflections resulting from the experimental set up that were observed in all datasets. Upon heating there is a broad endotherm visible in the thermogram, which continues until *ca.* 120 °C, just prior to the onset of the subsequent exotherm. This is a result of water loss, which is commonly observed around 100 °C. This is confirmed by the lack of changes in the diffraction data. Amorphous materials are known to be much more hygroscopic than crystals[2] and so it is unsurprising that water loss was observed in the DSC trace for FST glass. The presence of water in an amorphous material is also known to be a plasticiser leading to the eventual crystallisation of the substance.[2] It is interesting that the sample did not crystallise prior to analysis, suggesting that even in the presence of a plasticiser such as water PVD FST is a relatively stable glass.

Immediately following the water loss the sample begins to crystallise as can be seen by the appearance of a number of reflections in the diffraction data, which are accompanied by an exotherm with a small shoulder on the low temperature side. The onsets of the two peaks occur at 127.6 °C and 135.2 °C respectively, and it appears they are both a result of the same process, as the diffraction data show the appearance of only one set of Bragg reflections.

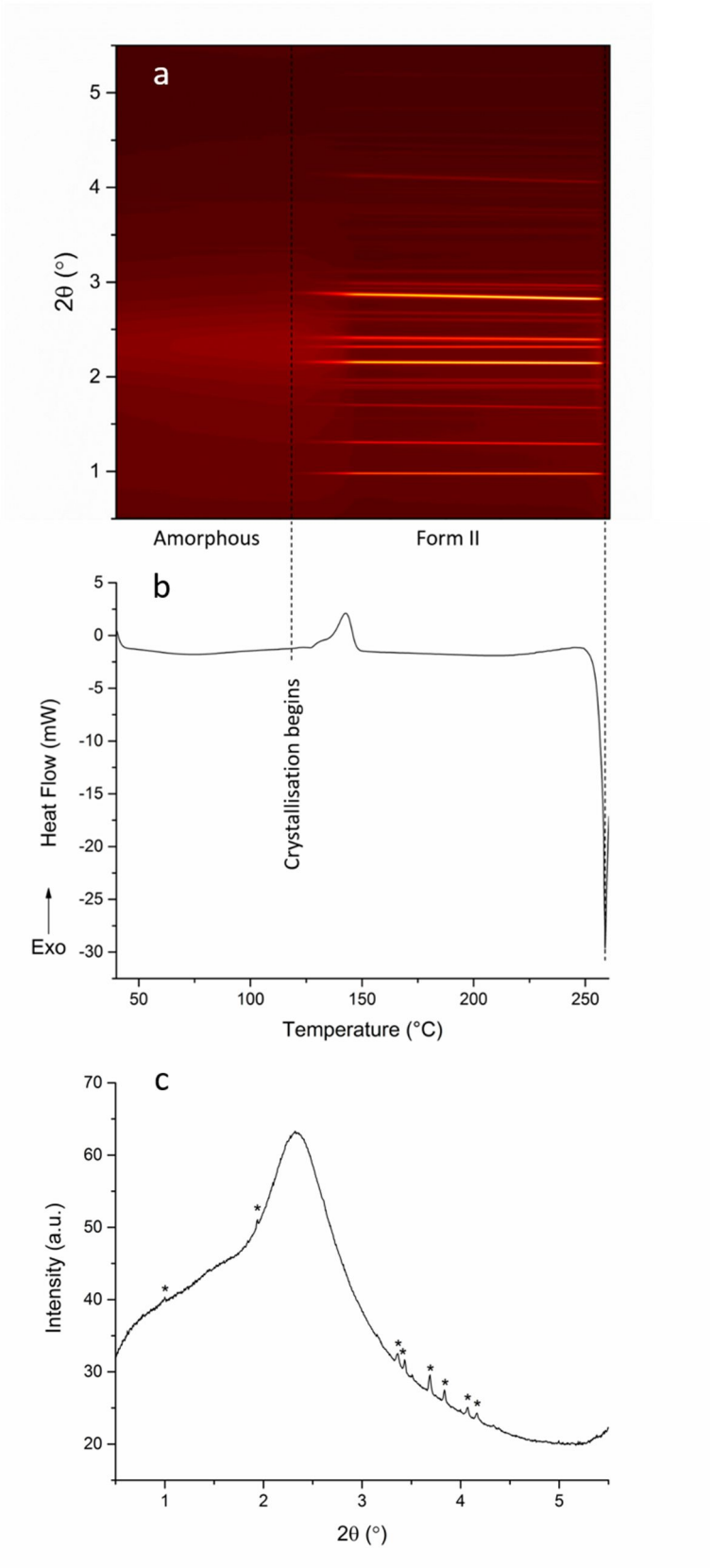

Figure 5-20. (a and b) DSC-XRD data for a sample of FST after physical vapour deposition onto a copper substrate at *ca.* 25 °C. (c) the PXRD pattern collected at 39.9 ºC for the same sample [reflections marked * are a result of the experimental set up].

Rietveld refinement of the pattern recorded at 237.2 °C (Figure 5-21 and Table 5-2) shows that the glass has crystallised to FST polymorph II, with no other species present, confirming the exotherm to be a result of crystallisation to a single species. The multiplicity of the exotherm suggests the crystallisation occurs in two steps.

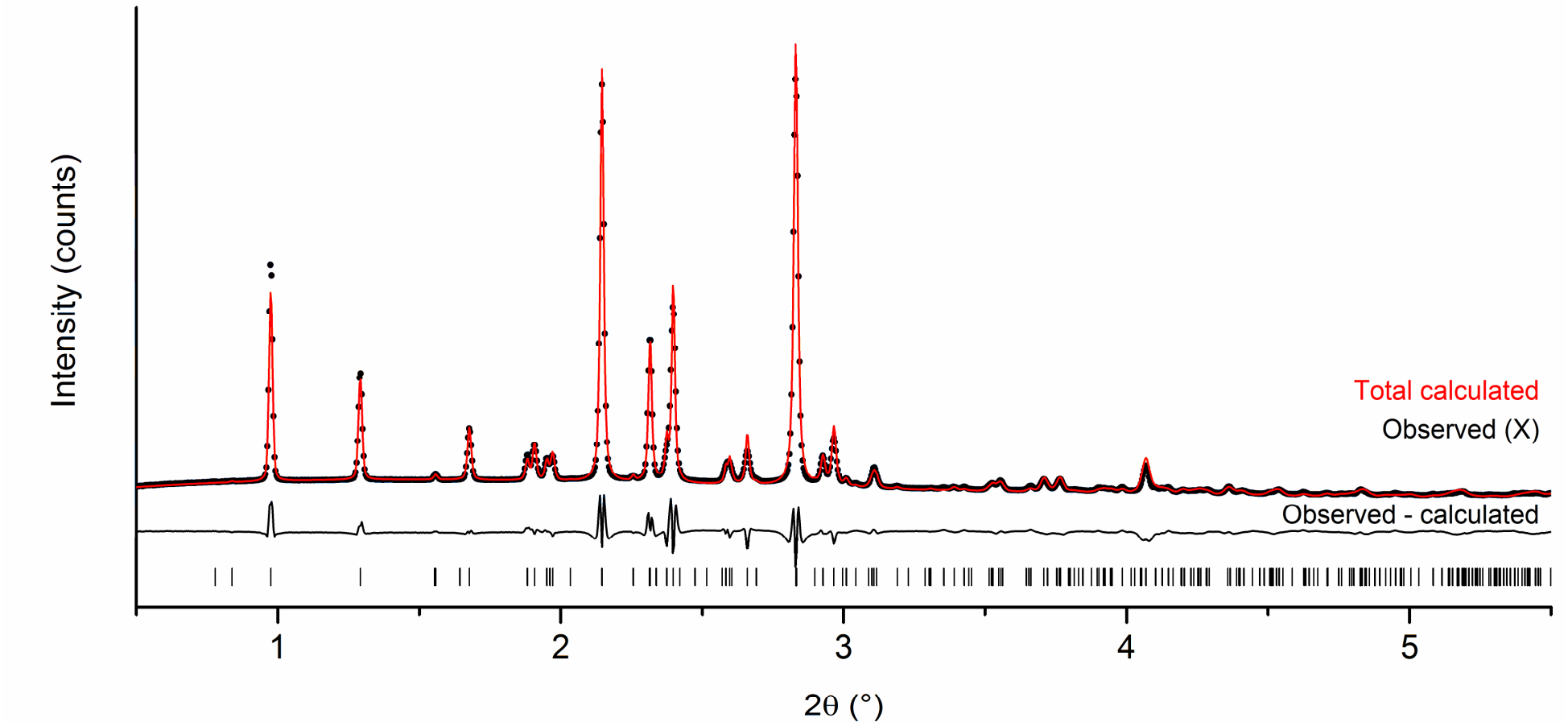

Figure 5-21. Rietveld refinement data for FST at 237.2 °C following preparation *via* PVD. The tick marks show the positions of allowed reflections.

Table 5-2. Refinement parameters for a vapour-deposited sample of FST following heat induced crystallisation. The starting model was taken from the CSD (WOLXOK03).

Property	Finasteride *Form II*
T / °C	237.2
Space group	$P2_1$
a / Å	16.8042(11)
b / Å	7.9090(4)
c / Å	18.086(2)
α / °	90
β / °	105.926(6)
γ / °	90
Cell volume / Å^3	2311.5(3)
R_{wp}	0.0727
$R_{wp\text{-}bkd}$	0.1625

Material from the same deposition experiment was subjected to a number of further DSC analyses under different conditions (Figure 5-22). The aim of initial experiments was to establish whether the broad endotherm was water loss and if this had an effect on the subsequent crystallisation. Annealing at 80 °C and 100 °C before cooling the sample and reheating successfully removed the endotherm, confirming the event was caused by evaporation of water.

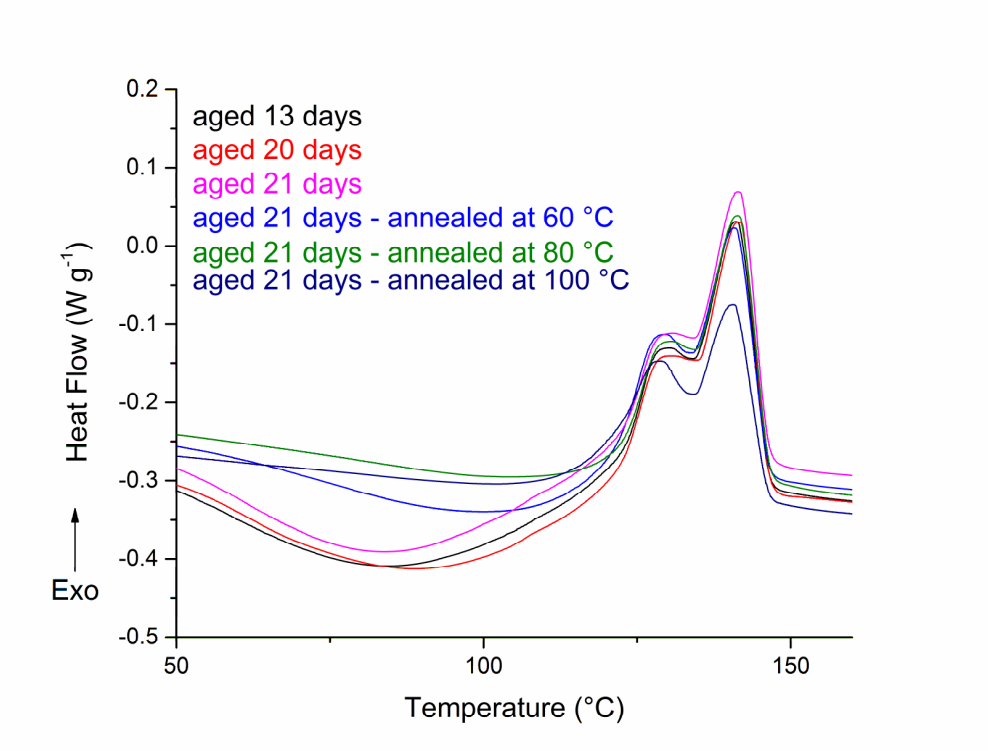

Figure 5-22. DSC thermograms showing crystallisation of a sample of vapour deposited FST after aging and annealing. For all samples the annealing time was 5 minutes and the heating rate 10 °C min^{-1}.

Due to the proximity of the endotherm to the crystallisation exotherms it was not possible to accurately measure the enthalpy of crystallisation (ΔH_c). However, the data in Figure 5-22 are all normalised to units of W g^{-1} and so the peak shapes, sizes and positions are directly comparable. The ΔH_c for all samples except that annealed at 100 °C are very similar and all crystallisation occurs at the same temperature. It appears that the crystallisation from amorphous to form II occurs *via* a two-step process, although it is unclear what these two steps may be.

Dawson *et al*[118] used WAXS to probe the structure of amorphous IMC prepared by PVD and compared it to that of the supercooled liquid of the same compound. Diffraction patterns collected for the supercooled liquid and the glass prepared by quenching the melt (Figure 5-23 (a)) show very subtle differences in intensity, indicating the average local packing changes only slightly with temperature. The initial pattern recorded for the PVD IMC (Figure 5-23 (b)) displays a broad, high intensity reflection at low angles that is not present in the other disordered phases. These data suggest the existence of two glass structures. One is essentially the same as that of the melt and is accessed by supercooling it, the other is accessible by PVD. Annealing of the deposited sample for relatively long periods (in excess of 13 hours) above T_g resulted in its reversion to the packing of the quench cooled glass, whereas little change was observed in the structure of the supercooled liquid as a function of temperature. It was initially thought that this may be the reason for the doublet nature of the exotherm of crystallisation for FST. However closer inspection of the diffraction data shows no change in the profile of the amorphous pattern as a function of temperature, only the appearance of Bragg reflections as the material crystallises. In fact, the profile of the pattern recorded at 39.9 °C for the deposited material closely matches the pattern recorded for the melt. The two-step nature of the crystallisation is not observable in the diffraction data and it appears in this instance that DSC is more sensitive to the changes occurring.

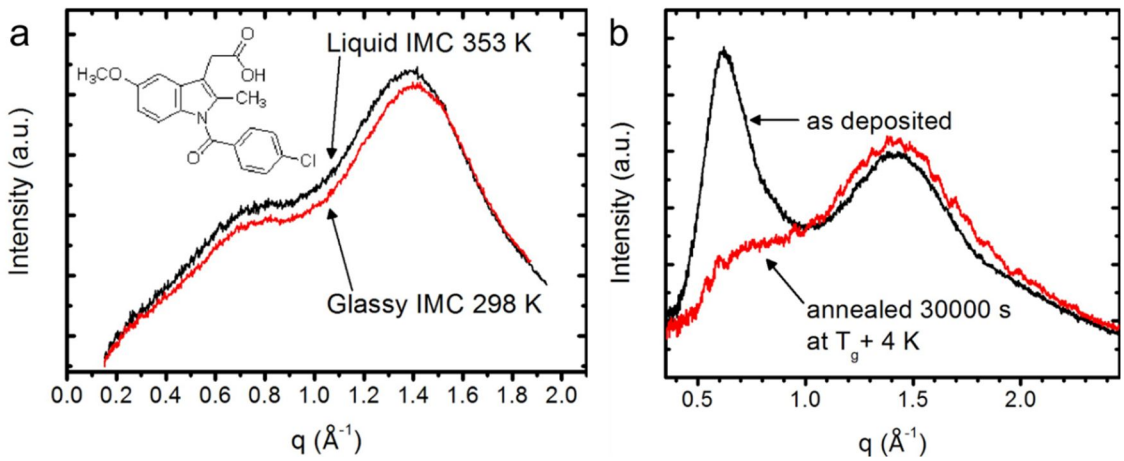

Figure 5-23. WAXS patterns for IMC (a) in the supercooled liquid state, and the melt quenched glass state, and (b) vapour deposited onto a substrate at −8 °C and annealed at 46 °C (4 °C above T_g) for 500 min. Permission to reproduce these images has been granted by Dawson *et al.*[118]

The evolution of FST from amorphous to polymorph II is depicted in Figure 5-24. The initial crystallisation occurs very rapidly and is complete by 148 °C, which shows good agreement with the exothermic peak in the DSC data at 142.7 °C. Following crystallisation the amount of crystalline material in the beam continues to grow but at a much slower rate; this is probably due to more material being lifted into the beam from the bottom of the sample pan as it expands. It is unlikely that there would be additional crystallisation occurring with further heating, since nucleation from the crystalline material already present would result in rapid crystallisation of any amorphous material in contact with it in the first stage of crystallisation. Finally the sample melted, and by 259 °C there was no crystalline material left; this coincides with the peak of the large endotherm in the DSC trace (258.9 °C).

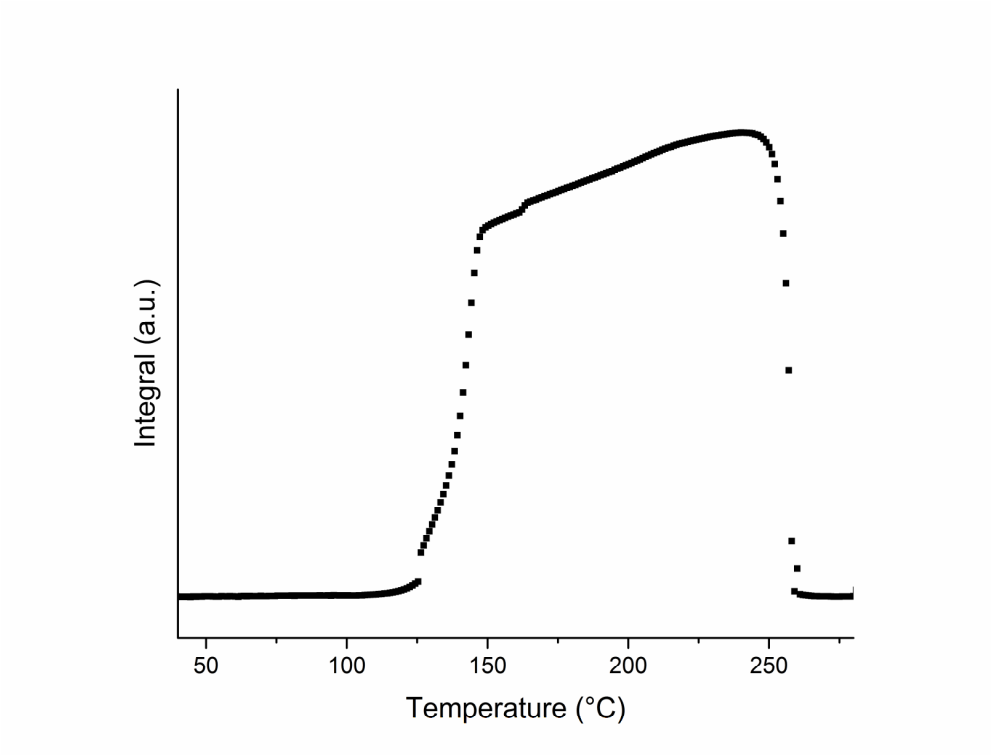

Figure 5-24. A plot of integrated area under the diffraction pattern of FST form II as a function of temperature for a sample prepared by PVD.

5.5.3. Urea

5.5.3.1. Determination of temperature required for deposition

Urea was deposited onto a substrate held at −189 °C. As with FST, initial experiments were run to establish the temperature range in which an acceptable rate of deposition would occur. The chamber pressure (Figure 5-25) remained relatively constant at 4 x 10^{-6} mbar throughout the experiment except for three large spikes at 7880 s, 8560 s and 11140 s. This behaviour was observed in all experiments and coincides with the application of more power to the heat source. These spikes are an artefact and probably a result of the chamber not being earthed properly. Initially the heat source was set to 50 °C, but overshot this and settled at 67 °C. At this temperature the rate of deposition was around 2.4 nm s^{-1} and the QCM was still responsive so the set point was increased. The final temperature was 80 °C, which resulted in a deposition rate of over 15 nm s^{-1}. Following this the QCM became saturated with adsorbed material and no more useful readings could be obtained. This was deemed an acceptable deposition rate to produce a large enough sample for analysis and so further experiments were carried out heating at 80 °C.

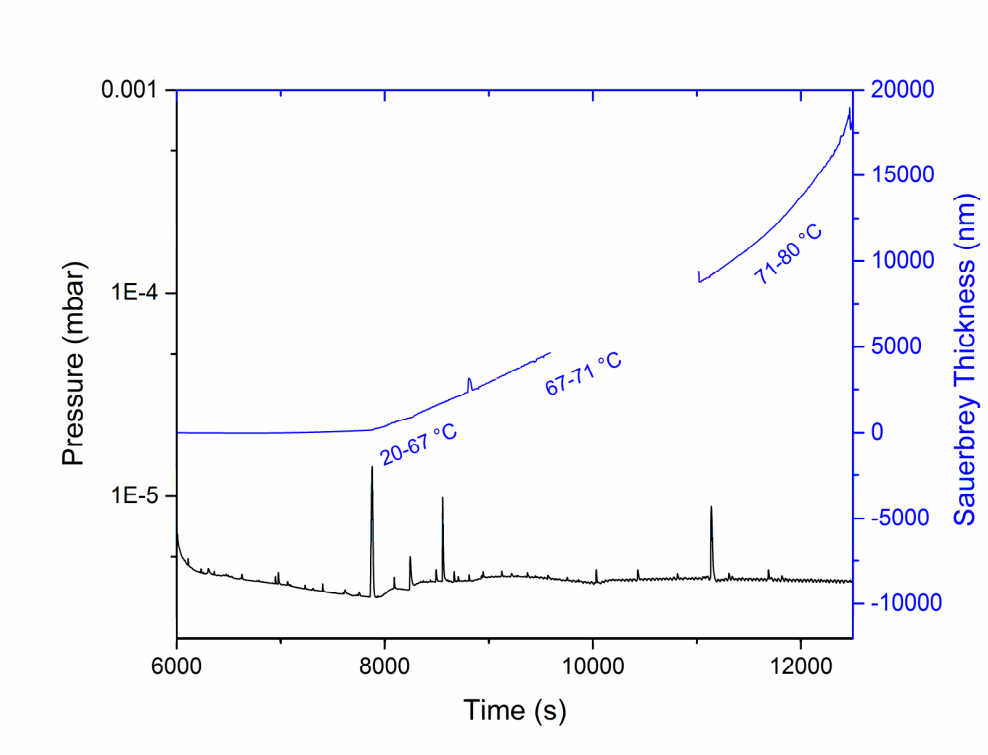

Figure 5-25 Chamber pressure and deposition rate data for a sample of urea deposited at −189 °C. The sample was heated gradually from ambient to 80 °C [Sauerbrey thickness data between 9600 s and 11000 s have been removed as the QCM timed out in this range].

Following deposition the sample was analysed by PXRD (Figure 5-26). The procedure for carrying out this analysis involved working under LN_2 and using a bespoke sample holder with Kapton windows. For this reason all diffraction patterns of samples deposited at −189 °C display a broad high intensity reflection at 5.6° 2θ. The first pattern was collected at −185 °C. Due to the complex nature of the sample transfer under LN_2 it was very difficult to ensure the material was not allowed contact with atmospheric air. Consequently there are a number of reflections in the pattern that have been assigned to hexagonal ice. It is apparent from the nature of the broad high intensity background that most of the urea in the sample was amorphous, however there are three unassigned reflections (*). This suggests the presence of some crystalline urea.

A second pattern was recorded after heating the sample to −123 °C (Figure 5-26). The Kapton and hexagonal ice reflections remain unchanged, as does the background. However, the three unidentified reflections from the first pattern are absent. This indicates that the crystalline entity present in the lower temperature pattern is no longer present. It seems unlikely that the species was less stable than the amorphous form but it is unclear why it has disappeared.

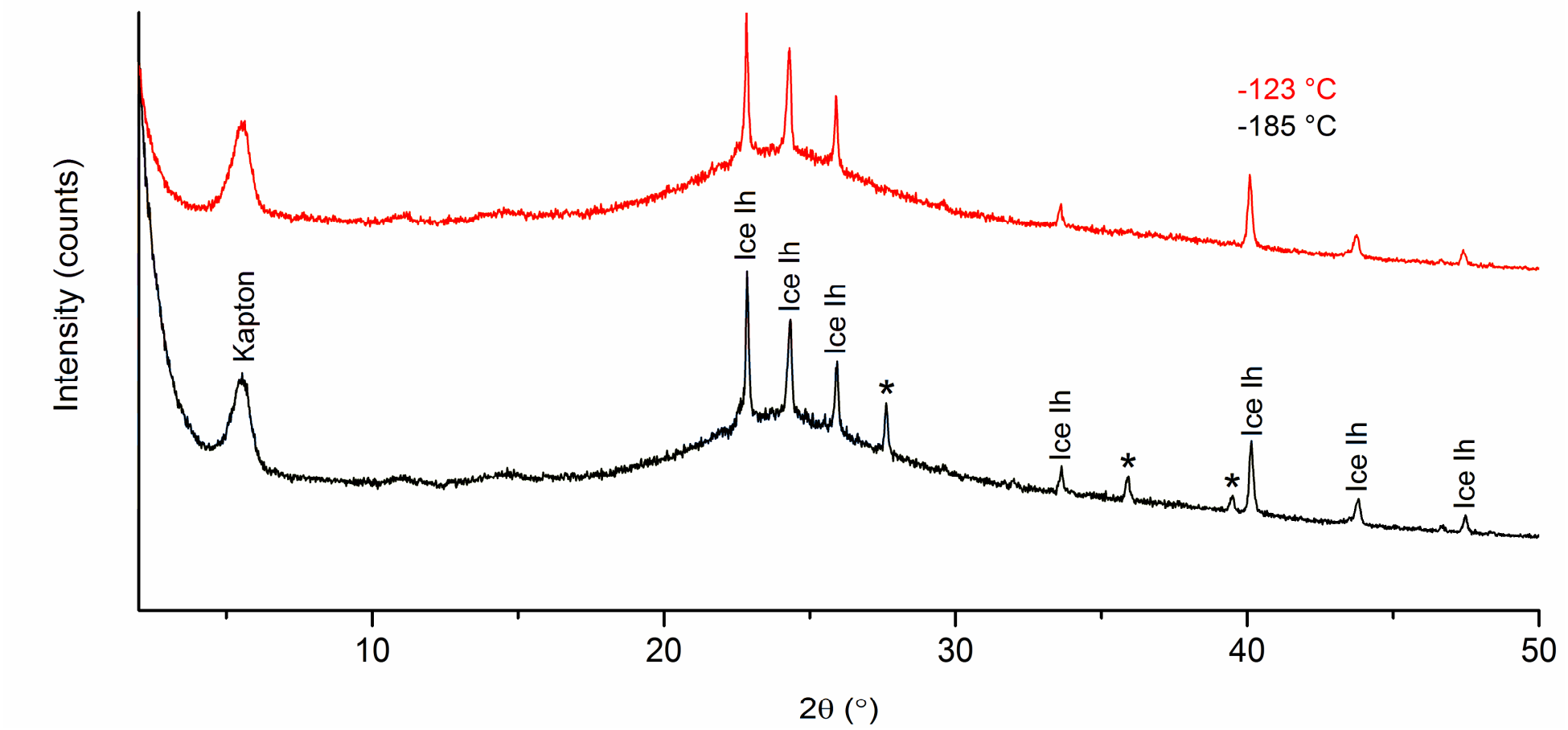

Figure 5-26. Diffraction patterns for a sample of deposited urea at −185 °C and following heating to −123 °C.

A final pattern was recorded for this sample of urea at −83 °C (Figure 5-27), at which temperature the material has fully crystallised to polymorph I. Some hexagonal ice remains in the sample and the reflection for Kapton is also still present, but there are no unassignable reflections. Other than the disappearance of the three unidentified reflections it should be noted that there is a range of high intensity diffraction at low 2θ values that gradually decreases in intensity as the sample is heated.

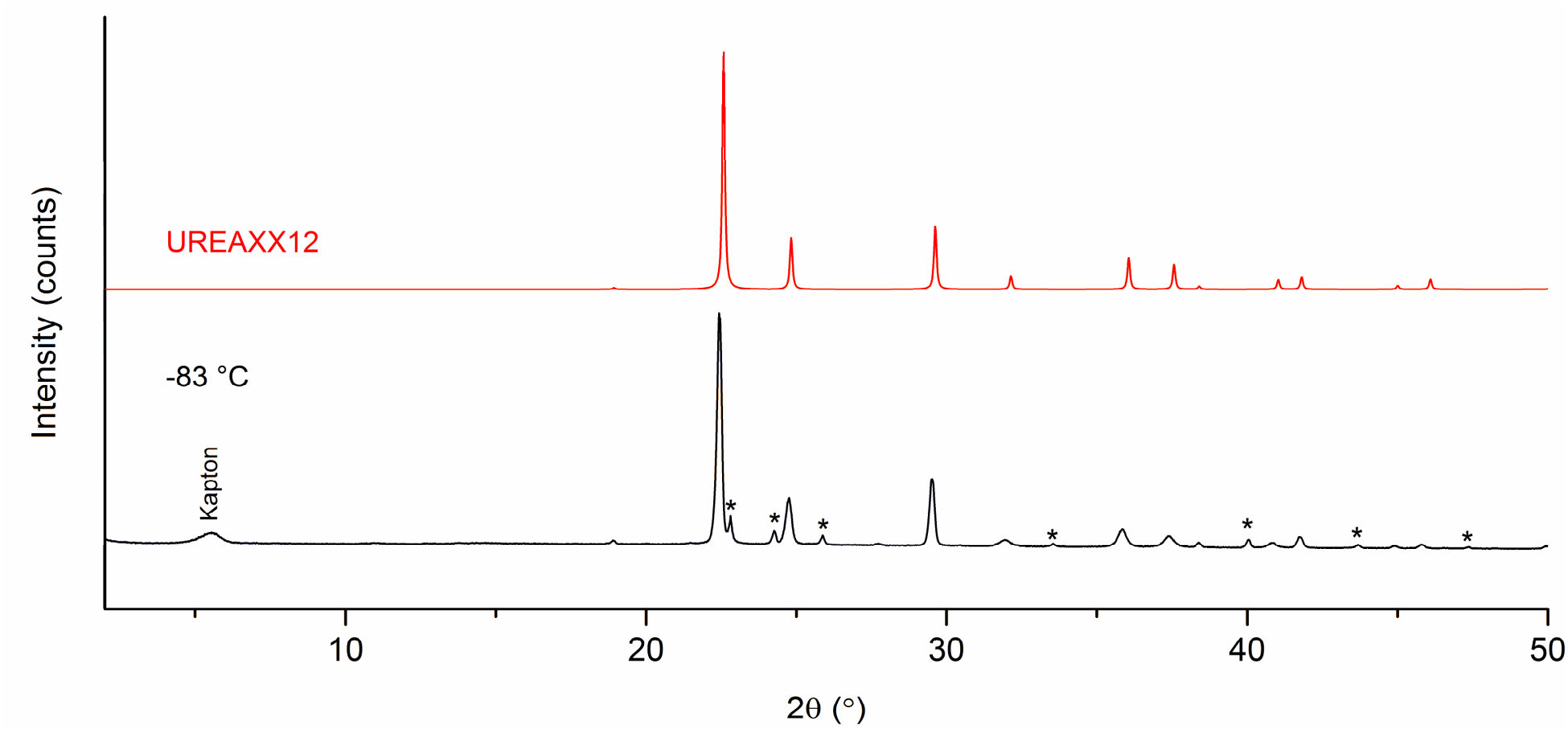

Figure 5-27. Diffraction pattern collected for a deposited sample of urea after heating to -83 °C and predicted from single crystal data obtained from the CSD (UREAXX12).[270] Reflections marked * are attributed to hexagonal ice.

These data show amorphous urea without additives can be prepared by PVD onto a substrate at −189 °C and crystallises to form I between −123 °C and −83 °C. This appears to be the first time this has been achieved. The data also suggest the existence of another polymorph at low temperatures, although there are not enough reproducible data to confirm this. There are two other polymorphs of urea reported in the literature[271] but they have only been shown to exist at high pressures.

5.5.3.2. DSC

A second urea formulation was prepared by PVD onto a cold substrate by heating the sample to 80 °C under vacuum. Following collection from the substrate three samples of the material were subjected to DSC analysis (Figure 5-28). All three traces have a relatively small exotherm at −90 °C, a result of crystallisation of form I from the glass. Two of the three traces display a large exotherm at *ca*. −154 °C that is absent from the third. This absence is a consequence of the difficulty of the sample transfer under liquid nitrogen. It seems that the temperature of the third sample increased during loading of the DSC pan, allowing the exothermic event to occur before analysis. It is interesting that the large exotherm is of a different magnitude in each of the two traces in which it is present. This may also be a result of some increase in temperature during loading of the pan. The temperature at which the exotherm occurs coincides with the range of temperatures at which the unidentified reflections disappear from PXRD patterns of the first sample, suggesting the two responses are caused by the same event. It is also possible that whatever caused the decrease in intensity at low 2θ is responsible for the exothermic events in the thermograms. This is discussed in section 5.5.3.3.

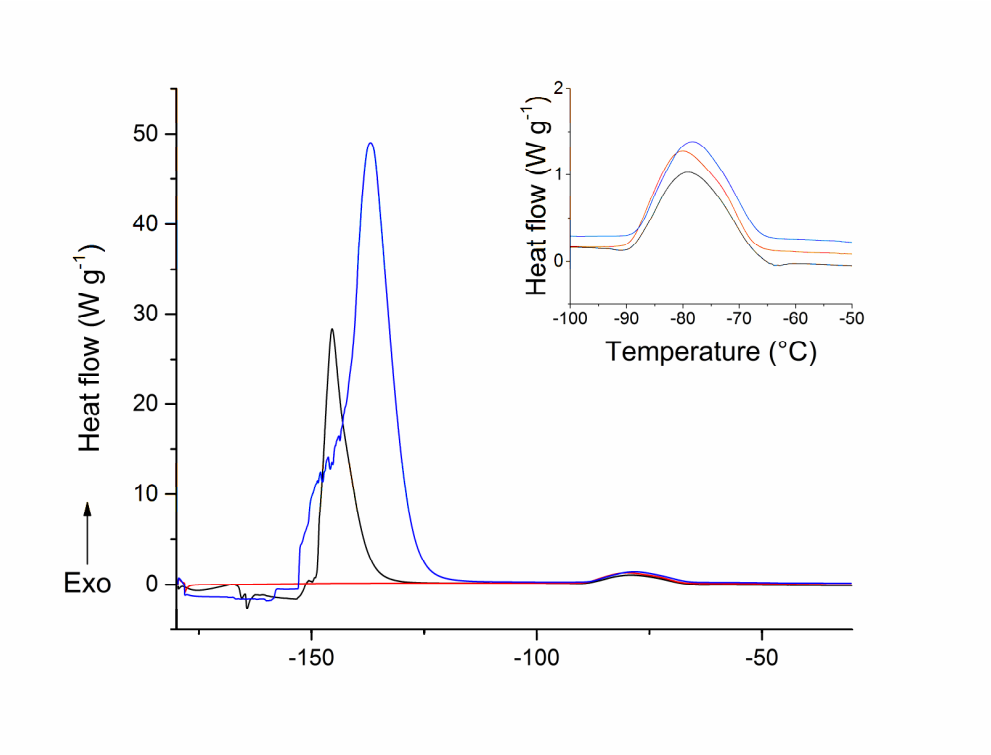

Figure 5-28. DSC traces recorded for urea deposited onto a substrate at -189 °C. All samples were deposited during the same experiment.

5.5.3.3. Low Temperature PXRD

Following the two initial experiments described in the previous paragraphs attempts were made to deposit sufficient sample for both DSC and XRD analysis of material from the same experiment. Data were collected for four depositions; the results were the same in all cases, and thus data for one representative sample are given. Figure 5-29 shows PXRD patterns recorded for the deposited urea as a function of temperature. As was described in Section 5.5.3.1, the pattern collected at −185 °C displays reflections indicating the presence of hexagonal ice and a medium intensity broad reflection caused by the Kapton window of the sample holder, but the urea is amorphous. However, there are no unidentifiable reflections in this case. Again there is a region of high intensity at low angles. From −183 °C to −103 °C the only observable change in the data is a reduction in the low angle intensity, and between −103 °C and −93 °C the glass crystallises to urea form I.

The DSC trace recorded for material from the same deposition (Figure 5-30) shows crystallisation at −88 °C, but the large exotherm at −154 °C observed previously for deposited urea (Section 5.5.3.2) has been replaced by a much smaller (relative to the exotherm of crystallisation) broad exothermic event that appears to also have an accompanying change in heat capacity. A change in heat capacity would usually be

associated with the glass transition of a sample, which may be the case here. However, the intensity of the low angle reflection in the XRD data undergoes a gradual decrease over the temperature range of the experiment and may be caused by the same event. Recent work probing the formation of metal organic frameworks (MOFs) using *in situ* synchrotron PXRD has ascribed an increase in low angle diffraction at the beginning of the process to the formation of non-crystalline aggregates.[272] These clusters of molecules go on to form crystal nuclei. The result of this is a decrease and eventual disappearance of the low angle scattering. This may be the explanation for the presence and behaviour of the diffracted intensity at low angles in this work.

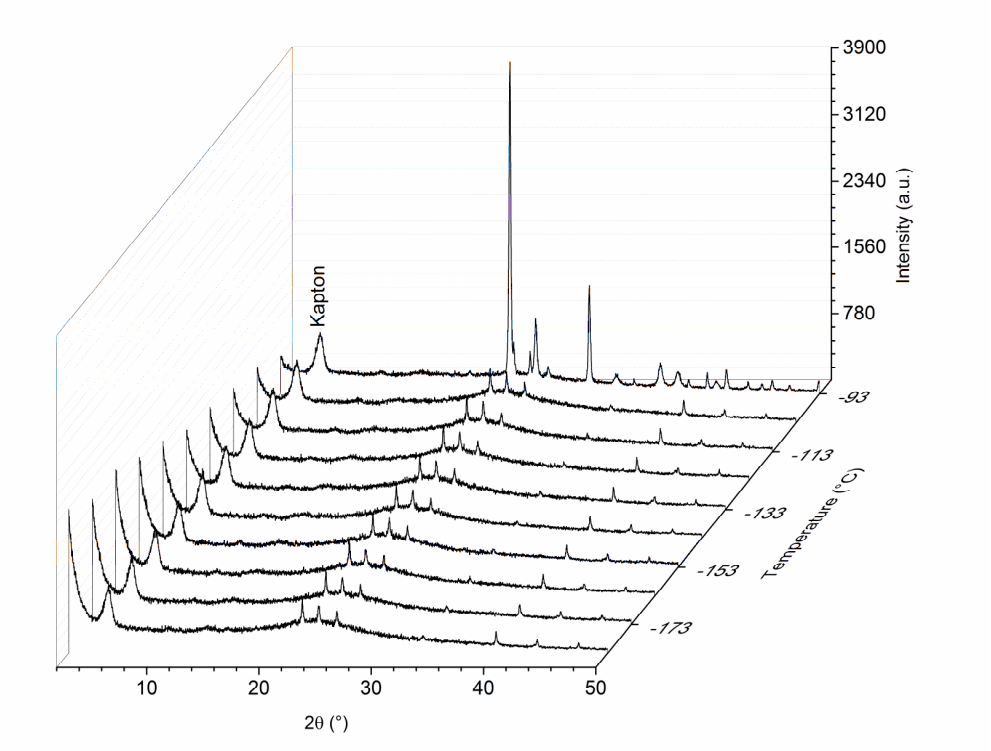

Figure 5-29. PXRD patterns recorded as a function of temperature for a sample of urea deposited onto a copper substrate at −189 °C.

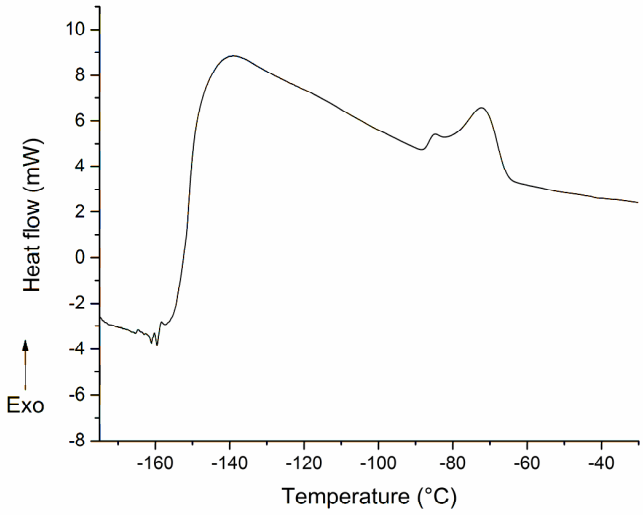

Figure 5-30. A DSC thermogram for a sample of urea deposited onto a copper substrate at −189 °C.

Despite numerous attempts, DSC and PXRD data from the first two samples deposited could not be replicated. The identity of the crystalline species present between −185 °C and −123 °C remains unknown. However, it has been shown that PVD is an effective method for the vitrification of urea, and that the transition from this glass to polymorph I occurs at −90 °C.

5.6. Discussion

The aim of this study was to vitrify a number of pharmaceutical materials that could either not be made glassy by other methods or that could be made into transient, unstable amorphous materials by other methods. Following which it was hoped that, upon heating, these glasses may recrystallise to new metastable polymorphs according to Ostwald's rule of stages. Initial experiments with IMC were promising and produced amorphous material but the mechanism by which the drug was vaporised (*i.e.* boiling rather than sublimation) resulted in spluttering of the material onto the substrate and so the deposited film was not uniform. Successful depositions of IMC in the literature were carried out at pressures in the region of 10^{-8} mbar,[127,128] around two orders of magnitude lower than reported here. No mention of this sputtering was found in the literature and although its effect on the properties of the prepared drug was not known it was decided to deposit other materials, having proven the ability of the experimental set up to vitrify a model glass former.

Studies of FST were successful in vitrification without sputtering, indicating the vaporisation process occurred *via* sublimation rather than boiling. Samples were

submitted to detailed analysis *via* simultaneous DSC-XRD, and the glass was shown to be reproducibly stable, upon heating, to 120 °C, at which point it crystallised to form II. There is no literature with which to compare these results.

Urea was also successfully vitrified but onto a substrate cooled with a flow of liquid nitrogen. These data are particularly promising as only one mention of amorphous urea has been found in the literature. Lu attempted to prepare amorphous matrices from physical mixtures of urea and tolbutamide by quench cooling the melt. Urea crystallised immediately following quenching when present with tolbutamide in an equal mass ratio, but mixtures with less than 40 % w/w urea remained amorphous. Furthermore, attempts at vitrifying pure urea by quench cooling were unsuccessful, even when quenching with LN_2 (−196 °C).[273]

A Scopus search using the terms *amorphous* and *pharmaceuticals* on 22 August 2017 returned 27871 results, whereas a search for *amorphous*, *physical vapour deposition* and *pharmaceuticals* returned 107, 25 of which had a common author. In the past 5 years the average number of publications per year is less than 13. It is clear that the topic is little known to the pharmaceutical scientific community. Furthermore, much of the work was carried out on indomethacin (adding *indomethacin* to the vapour deposition search returned 58 documents), widely used as a model pharmaceutical glass former, suggestive of a difficulty in vitrifying other materials by this method. Although a number of others have been shown to form stable glasses by PVD.[132]

The literature undoubtedly shows PVD to be a technique capable of producing extremely stable glasses.[118,120,127–129,132,274–276] However, work in this thesis has proven it to be a very technically challenging process that requires a very delicate balance of parameters to achieve the best results. Furthermore, it seems unlikely to be easily scaled up for the purpose of the production of large quantities of material without considerable expense.

5.7. Conclusions

Physical vapour deposition has been shown to be an effective method for the vitrification of pharmaceutical materials. Indomethacin, a material known to form a glass *via* PVD,[118,119,127,129] was used as a model material to demonstrate the ability of the technique to produce glasses. Subsequently, FST (a drug with just one instance of glass formation in the literature) and urea (with no history of glass formation) were vitrified by the same method. Simultaneous DSC-XRD has shown vapour deposited FST to crystallise to form II at 120.1 °C. Examination of the crystallisation exotherm reveals that the glass is stable at ambient temperature over a period of three weeks. Deposition of urea at −189 °C

resulted in its glass formation for, to the best of my knowledge, the first time. Upon heating, crystallisation to form I occurs at −90 °C. PXRD suggests there may be another polymorph of urea to be found at temperatures below −150 °C, however this finding was unfortunately not reproducible.

6. Conclusions

Solubility and dissolution are major barriers to the successful development of new solid state medicines and can considerably affect the bioavailability of an active pharmaceutical ingredient (API). The vitrification of drugs or formulation as metastable polymorphs and co-crystals are all approaches which have the potential to overcome this problem. However, for many APIs methods of vitrification are frequently incapable of producing glasses of adequate stability, and methods of screening possible co-crystals are slow, expensive, and often many must be employed to be confident that any polymorphs likely to appear in future manufacturing processes have been discovered.

A major aim of this work was to develop a novel method for the analysis of phase transitions in pharmaceutical materials by combining high energy synchrotron X-ray diffraction with differential scanning calorimetry (DSC-XRD) and thus collect *in situ* structural and calorimetric data on temperature driven phase transitions. Initial work was designed to prove the utility of the hyphenated technique by examining two enantiotropically polymorphic systems (Chapter 2), and subsequently it was used to examine phase transitions in materials exhibiting multiple polymorphs (Chapter 3). Building on this, Chapter 3 moved on to examine the effect of the addition of sugar based excipients on the crystallisation behaviour of paracetamol glass upon heating, with particular emphasis on the stabilisation of metastable polymorphs II and III.

The aims of the experiments discussed in Chapter 4 were to create new co-crystals between isonicotinamide, a common pharmaceutically acceptable co-former, and four antioxidant compounds, whilst also assessing the ability of four different techniques (solvent evaporation, thermal inkjet printing, heating, and milling) to prepare co-crystals. Again DSC-XRD was employed for the study of the processes by which temperature driven co-crystallisation progresses.

Finally, physical vapour deposition, a novel technique in the field of pharmaceuticals, was investigated for the preparation of amorphous materials, with particular emphasis on drugs considered to be poor glass formers, such as griseofulvin, or that had not been vitrified without excipients before, such as finasteride, and urea. Additionally it was hoped that preparation of these glasses may lead to the discovery of new polymorphs of the materials according to Ostwald’s rule of stages.

6.1. Chapter 2

The data presented in Chapter 2 have evidenced the simplicity of the set-up required to modify a DSC for use in conjunction with synchrotron X-ray diffraction techniques. With the application of high intensity synchrotron radiation it is possible to collect diffraction patterns on a sample mounted in a conventional DSC pan in seconds simply by drilling two holes in the DSC cell. This allows the simultaneous probing of both energetic and structural changes occurring in the sample as it is heated. Rietveld refinement of the pattern collected for a sample of sulfathiazole procured as phase pure form III identified two phases, form III and unexpectedly the metastable form IV. As expected, increasing the temperature of the sample caused expansion of the unit cell in all three dimensions for both polymorphs. At 154 °C forms III and IV simultaneously underwent an endothermic solid-solid conversion to polymorph I, which is stable at high temperatures. A sample of glutaric acid (GA) explored by DSC-XRD was shown to be the ambient temperature stable *β* polymorph at room temperature. When heated, *β*-GA transformed to the high temperature stable *α* polymorph at 72 °C *via* a solid-solid pathway. Of particular importance is the potential of the technique to provide information on otherwise hidden phases, as exhibited in the data recorded for sulfathiazole. Direct solid-solid phase transitions were observed and batch Rietveld refinements were carried out on the hundreds of patterns collected for each sample, allowing the assessment of changes in the unit cell parameters and phase quantification as a function of temperature.

6.2. Chapter 3

The use of DSC-XRD to study phase transitions has revealed that many are more complex than previously thought. The mechanism of many solid-solid phase transitions has been shown to progress *via* a rapid transitional melt phase within small regions of the sample, with some melting and recrystallising before others melt, resulting in the continuous presence of crystalline material in the sample.

Dihydrocarbamazepine form II was shown to convert to form I on heating, by a solid-solid phase transition. Carbamazepine (CBZ) form IV transformed to form I at 182 °C by the same mechanism, and from a third sample of CBZ, consisting of forms II and III, form II underwent a solid-solid conversion to form I at 119 °C and form III appeared to simultaneously melt-recrystallise and sublime, presumably recrystallising[207] out of the path of the incident beam due to the pan being open.

Monitoring the lattice constants as a function of temperature and comparing these data with the hydrogen bonding patterns throughout has allowed establishment of a

directional order of stability in three dimensions. Dimensions dominated by stronger intermolecular bonding patterns (*e.g.* H-bonds) show smaller expansion per unit temperature rise than those with weaker interactions (*e.g.* π interactions). Expansion rates were shown to be similar in polymorphs of different materials.

Pure paracetamol glass, prepared *via* quench-cooling the melt at ambient temperature in a DSC pan, crystallises to a mixture of forms II and III upon heating. Form III crystallisation occurs much more rapidly than form II and goes on to transform to form II at *ca.* 125 °C, whilst form II melts at 158 °C. Adding 10 % w/w HPMC to the material prior to the melting and subsequent vitrification process had the effect of either stabilising form II or destabilising form III so that only form III crystallised from the glass. This remained until *ca.* 135 °C, at which point it converted to form II which then melted just below 160 °C. Vitrification of PCM with 10 % w/w lactose was incomplete and some form II crystallised during cooling. However, even in the presence of form II crystals, lactose was successful in stabilising form III, which crystallised from the glass and remained stable until 130 °C, when it transformed to form II before melting at the expected temperature. As with lactose, vitrification of trehalose was incomplete and some form II crystallised from the melt. Upon heating form II grew from the amorphous material and converted to form I at 116 °C; the form I produced then melted at 170 °C. No form III was observed, and it seems trehalose has the effect of destabilising polymorph III and promoting the II$\rightarrow$I conversion.

6.3. Chapter 4

Three of the co-formers examined in Chapter 4: 4-hydroxybenzoic (HBA) acid, 4-hydroxyphenylacetic acid (HPAA) and 3,4-dihydroxyphenylacetic acid (DHPAA), were found to form co-crystals with isonicotinamide (ICNT), and all four methods explored (solvent evaporation, thermal inkjet printing, heating, and milling) were found capable of producing co-crystals. L-ascorbic acid reacted with INCT in solution and data from inkjet printing, heating and milling were inconclusive. For the other three co-formers, co-crystals were formed by solvent evaporation and analysed by single crystal XRD. These data were used to solve the structures of the new co-crystals.

The INCT-HBA co-crystal was found to crystallise in the $P2_1/c$ space group when grown from solution, and is different to the previously reported structure (CSD reference: VAKTOR).[232] Separate DSC and PXRD analyses showed the crystals grown by thermal inkjet printing to be the same as the known co-crystal, rather than that reported here. The rapid evaporation of solvent during printing, being much faster than the slow evaporation from the single crystal growth experiments, may have been the reason for

the growth of two different polymorphs of the same co-crystal. Rietveld refinement of DSC-XRD diffraction data showed that on heating a mixture of INCT I and HBA in a 1:1 molar ratio, some material converts to the new form of the co-crystal and some INCT converts to the enantiotropically related INCT polymorph II *via* a solid-solid transition. Subsequently, the new metastable polymorph of the co-crystal converts to VAKTOR by a solid-solid pathway. At the same time, some of the remaining INCT II and HBA co-crystallise to VAKTOR, whilst some of the INCT II melts. Crystals produced by ball milling were also of the same structure as VAKTOR.

For INCT mixed with HPAA in a 2:1 molar ratio all four co-crystallisation techniques produced crystals in the prepared ratio with the triclinic space group *P*-1. This is demonstrated with room temperature PXRD data, and in the case of thermal co-crystallisation, Rietveld refinements from DSC-XRD. The refinements revealed that 13.2 % of the physical mixture of the two materials had in fact co-crystallised prior to heating in the DSC. Combined DSC-XRD also demonstrated that the co-crystallisation of the remaining INCT and HPAA occurred by a localised melt-recrystallisation pathway of both materials until the HPAA is exhausted, after which the remaining INCT melts, followed closely by the co-crystal at *ca.* 120 °C, more than 30 °C below the melting point of ICNT form II, the stable polymorph above this temperature.

A co-crystal of INCT and DHPAA was grown by solvent evaporation prior to this work,[248] with a 1:1 molar ratio and crystallising in the triclinic space group *P*-1. Thermal inkjet printing produced crystals of the same structure, as evidenced by PXRD. Heating a mixture of the two raw materials appears to have formed a second co-crystal however, again confirmed by comparison of diffraction data. Unfortunately structural determination of this product could not be carried out due to the lack of single crystal diffraction data for this species. A ball milled sample of the two materials in the same ratio produced crystals that, when analysed by DSC, exhibited a similar endothermic event as the crystals produced by heating, but their diffraction patterns proved them to be different structures.

Thermal inkjet printing produced co-crystals of the same structure as those grown by solvent evaporation for two of the three systems that were successfully co-crystallised. This method proved to be very rapid, but produced very small crystals and sample sizes, meaning that the diffraction data suffered from a low intensity to noise ratio and low peak resolution. Ball milling was the quickest, easiest and cheapest method and also successfully produced co-crystals in the three systems. Since these methods do not generally allow the formation of single crystals, solvent evaporation experiments are

required to solve the structure of new polymorphic forms. However, for scale up purposes the ball milling approach in particular has great potential. A wealth of information on the mechanism and energetics of the co-crystallisation process could be obtained by DSC-XRD, making it too an incredibly valuable tool for the screening of co-crystals.

6.4. Chapter 5

In Chapter 5 the development of a vacuum chamber for the physical vapour deposition of amorphous pharmaceutical materials was explored, and a number of materials were successfully vitrified. Initially indomethacin, a good glass former, was used as a model drug to prove the utility of the method for the task and was successfully converted to a stable glass. Following this, deposition was attempted unsuccessfully with a number of other materials (benzoic acid, griseofulvin and famotidine). Problems stemmed from the materials' vapour pressure being too high, such that sublimation occurred whilst reducing the pressure, or the process caused the APIs to melt and boil (rather than sublime) and sputtering of the sample resulted in non-uniform films on the deposition plate.

Finally finasteride and urea glasses were successfully deposited, at ambient temperature and −189 °C respectively. Amorphous finasteride remained stable up to 120 °C, at which point it crystallised to form II. This marks the first time that crystallisation from amorphous finasteride has been studied/observed. This is also the first report of the vitrification of pure urea, to the best of the authors' knowledge. The urea glass remained stable up to −90 °C, at which point it crystallised to form I. Tantalisingly, PXRD data hints at the existence of an additional polymorph to be found below −150 °C, but owing to time constraints and equipment malfunction it was not possible to explore this in detail.

6.5. Future Work

DSC-XRD is a powerful too that may be used to carry out detailed examination of solid-state phase transitions at different heating rates. Many of the transitions reported here involved multiple overlapping events in both the DSC and XRD data. Reducing the heating rate may allow the separation of these events and interpretation of the underlying processes in these transitions. Isothermal measurements may also be used to collect additional information on the mechanisms by which these conversions occur. These experiments would be informative both for the materials discussed in this work, but also for many polymorphic pharmaceutical materials.

The DSC-XRD technique may also be used to further interrogate co-crystallising systems in conjunction with single crystal techniques. Once structures have been solved from

single crystal XRD, they may be used to monitor the evolution of different phases during heat induced co-crystallisation processes.

The work carried out in Chapter 5 on physical vapour deposition proceeded slowly due to large amount of time it took to develop the vacuum chamber and the associated equipment to allow the collection of pharmaceutical glasses. Now the system is optimised, it would be interesting to carry out more work on the vitrification of materials such as felbinac, lidocaine, naproxen and tolbutamide, all of which are known to be poor glass formers. It can also be further explored to make ultrastable glasses from them.

The potential for the chamber as a polymorph discovery tool, by applying Ostwald's rule of stages and vitrifying materials at low temperatures then analysing phase changes as they are heated should also be further explored. In this work, there was the glimpse of a possible new phase of urea below −150 °C, but owing to time constraints this could not be thoroughly investigated. This field of work seems to be an avenue of research with potentially far reaching benefits for the pharmaceutical industry. Preparing more samples of amorphous urea and analysing them by low temperature PXRD would be a good starting point. Further work may be conducted on any number of materials, starting with a survey of the Cambridge Structural Database to identify those pharmaceutical materials that have not been found to exhibit polymorphism to date. It has long been believed that all compounds are capable of polymorphism, and all that is required to discover polymorphs is time and effort.[277]

7. References

(1) Aulton, M. E. Dissolution and Solubility. In *Aulton's Pharmaceutics: The Design and Manufacture of Medicines*; Aulton, M. E., Taylor, K., Eds.; Elsevier: London, 2013; pp 20–37.

(2) Gaisford, S.; Saunders, M. Physical Form II – Amorphous Materials. In *Essentials of Pharmaceutical Preformulation*; John Wiley & Sons, Ltd: Chichester, UK, 2012; pp 156–180.

(3) Gaisford, S.; Saunders, M. Dissolution. In *Essentials of Pharmaceutical Preformulation*; John Wiley & Sons, Ltd: Chichester, UK, 2012; pp 86–97.

(4) Laitinen, R.; Lo̊mann, K.; Strachan, C. J.; Grohganz, H.; Rades, T. Emerging Trends in the Stabilization of Amorphous Drugs. *International Journal of Pharmaceutics*. Elsevier B.V. August 30, 2013, pp 65–79.

(5) Engers, D.; Teng, J.; Jimenez-Novoa, J.; Gent, P.; Hossack, S.; Campbell, C.; Thomson, J.; Ivanisevic, I.; Templeton, A.; Byrn, S.; Newman, A. A Solid-State Approach to Enable Early Development Compounds: Selection and Animal Bioavailability Studies of an Itraconazole Amorphous Solid Dispersion. *J. Pharm. Sci.* **2010**, *99* (9), 3901–3922.

(6) Kawabata, Y.; Wada, K.; Nakatani, M.; Yamada, S.; Onoue, S. Formulation Design for Poorly Water-Soluble Drugs Based on Biopharmaceutics Classification System: Basic Approaches and Practical Applications. *Int. J. Pharm.* **2011**, *420* (1), 1–10.

(7) Hammond, C. *The Basics of Crystallography and Diffraction*, 2nd ed.; Oxford University Press: New York, 2001.

(8) Atkins, P.; de Paula, J. Solids. In *Atkins' Physical Chemistry*; Oxford University Press: Oxford, 2014; pp 639–688.

(9) Gaisford, S.; Saunders, M. Physical Form I – Crystalline Materials. In *Essentials of Pharmaceutical Preformulation*; John Wiley & Sons, Ltd: Chichester, UK, 2012; pp 127–155.

(10) Aitipamula, S.; Banerjee, R.; Bansal, A. K.; Biradha, K.; Cheney, M. L.; Choudhury, A. R.; Desiraju, G. R.; Dikundwar, A. G.; Dubey, R.; Duggirala, N.;

Ghogale, P. P.; Ghosh, S.; Goswami, P. K.; Goud, N. R.; Jetti, R. R. K. R.; Karpinski, P.; Kaushik, P.; Kumar, D.; Kumar, V.; Moulton, B.; Mukherjee, A.; Mukherjee, G.; Myerson, A. S.; Puri, V.; Ramanan, A.; Rajamannar, T.; Reddy, C. M.; Rodriguez-Hornedo, N.; Rogers, R. D.; Row, T. N. G.; Sanphui, P.; Shan, N.; Shete, G.; Singh, A.; Sun, C. C.; Swift, J. A.; Thaimattam, R.; Thakur, T. S.; Kumar Thaper, R.; Thomas, S. P.; Tothadi, S.; Vangala, V. R.; Variankaval, N.; Vishweshwar, P.; Weyna, D. R.; Zaworotko, M. J. Polymorphs, Salts, and Cocrystals: What's in a Name? *Cryst. Growth Des.* **2012**, *12* (5), 2147–2152.

(11) Buckton, G. Solid-State Properties. In *Aulton's Pharmaceutics: The Design and Manufacture of Medicines*; Aulton, M. E., Taylor, K., Eds.; Elsevier: London, 2013; pp 126–137.

(12) Savjani, K. T.; Gajjar, A. K.; Savjani, J. K. Drug Solubility: Importance and Enhancement Techniques. *ISRN Pharm.* **2012**, *2012* (100), 1–10.

(13) Anjana, M. N.; Joseph, J.; Nair, S. C. Solubility Enhancement Methods - A Promising Technology for Poorly Water Soluble Drugs. *Int. J. Pharm. Sci. Rev. Res.* **2013**, *20* (2), 127–134.

(14) Alam, M.; Mallik, S.; Ahmad, S.; Ibrahim, M.; Raza, A. K.; Hasan, A. Bioavailability Enhancement by Increasing the Solubility of the Drug: A Recent Review. *Pharmagene* **2013**, *1* (3), 66–72.

(15) Gaisford, S. Pharmaceutical Preformulation. In *Aulton's Pharmaceutics: The Design and Manufacture of Medicines*; Aulton, M. E., Taylor, K. M. G., Eds.; Elsevier: London, 2013; pp 367–394.

(16) Cockcroft, J. K.; Barnes, P. Reflection Multiplicity http://pd.chem.ucl.ac.uk/pdnn/symm2/multj.htm (accessed Feb 7, 2018).

(17) Gabbot, P.; Mann, T. Diffrerential Scanning Calorimetry. In *Principles of Thermal Analysis and Calorimetry*; Gaisford, S., Kett, V., Haines, P., Eds.; The Royal Society of Chemistry: Cambridge, 2016; pp 67–103.

(18) Aulton, M. E. Drying. In *Aulton's Pharmaceutics: The Design and Manufacture of Medicines*; Aulton, M. E., Taylor, K. M. G., Eds.; Elsevier: London, 2013; pp 487–503.

(19) Cruz-Cabeza, A. J.; Reutzel-Edens, S. M.; Bernstein, J. Facts and Fictions about

Polymorphism. *Chem. Soc. Rev.* **2015**, *44* (23), 8619–8635.

(20) Brittain, H. Polymorphism and Solvatomorphism 2010. *J. Pharm. Sci.* **2012**, *101* (2), 464–484.

(21) Ward, M. D. Perils of Polymorphism: Size Matters. *Isr. J. Chem.* **2017**, *57* (1), 82–92.

(22) Llinàs, A.; Goodman, J. M. Polymorph Control: Past, Present and Future. *Drug Discov. Today* **2008**, *13* (5–6), 198–210.

(23) Yu, L. Survival of the Fittest Polymorph: How Fast Nucleater Can Lose to Fast Grower. *CrystEngComm* **2007**, *9* (10), 847.

(24) Beckmann, W. Seeding the Desired Polymorph: Background, Possibilities, Limitations, and Case Studies. *Org. Process Res. Dev.* **2000**, *4* (5), 372–383.

(25) Lee, A. Y.; Erdemir, D.; Myerson, A. S. Crystal Polymorphism in Chemical Process Development. *Annu. Rev. Chem. Biomol. Eng* **2011**, *2*, 259–280.

(26) Burley, J. C.; Duer, M. J.; Stein, R. S.; Vrcelj, R. M. Enforcing Ostwald's Rule of Stages: Isolation of Paracetamol Forms III and II. *Eur. J. Pharm. Sci.* **2007**, *31* (0), 271–276.

(27) Bernstein, J. *Polymorphism in Molecular Crystals*, 1st ed.; Oxford University Press: Oxford, 2002.

(28) Al-Zoubi, N.; Malamataris, S. Effects of Initial Concentration and Seeding Procedure on Crystallisation of Orthorhombic Paracetamol from Ethanolic Solution. *Int. J. Pharm.* **2003**, *260* (1), 123–135.

(29) Davey, R. J.; Allen, K.; Blagden, N.; Cross, W. I.; Lieberman, H. F.; Quayle, M. J.; Righini, S.; Seton, L.; Tiddy, G. J. T. Crystal Engineering – Nucleation, the Key Step. *CrystEngComm* **2002**, *4* (47), 257–264.

(30) Staab, E.; Addadi, L.; Leiserowitz, L.; Lahav, M. Control of Polymorphism by "Tailor-Made" Polymeric Crystallization Auxiliaries. Preferential Precipitation of a Metastable Polar Form for Second Harmonic Generation. *Adv. Mater.* **1990**, *2* (1), 40–43.

(31) Davey, R. J.; Blagden, N.; Potts, G. D.; Docherty, R. Polymorphism in Molecular Crystals: Stabilization of a Metastable Form by Conformational Mimicry. *J. Am.*

Chem. Soc. **1997**, *119* (7), 1767–1772.

(32) Chadwick, K.; Myerson, A.; Trout, B. Polymorphic Control by Heterogeneous Nucleation - A New Method for Selecting Crystalline Substrates. *CrystEngComm* **2011**, *13* (22), 6625.

(33) Ward, M. D. Bulk Crystals to Surfaces: Combining X-Ray Diffraction and Atomic Force Microscopy to Probe the Structure and Formation of Crystal Interfaces. *Chem. Rev.* **2001**, *101* (6), 1697–1725.

(34) Bonafede, S. J.; Ward, M. D. Selective Nucleation and Growth of an Organic Polymorph by Ledge-Directed Epitaxy on a Molecular Crystal Substrate. *J. Am. Chem. Soc.* **1995**, *117* (30), 7853–7861.

(35) Hiremath, R.; Basile, J. A.; Varney, S. W.; Swift, J. A. Controlling Molecular Crystal Polymorphism with Self-Assembled Monolayer Templates. *J. Am. Chem. Soc.* **2005**, *127* (51), 18321–18327.

(36) Mitchell, C. A.; Yu, L.; Ward, M. D. Selective Nucleation and Discovery of Organic Polymorphs through Epitaxy with Single Crystal Substrates. *J. Am. Chem. Soc.* **2001**, *123* (44), 10830–10839.

(37) Parambil, J. V; Poornachary, S. K.; Tan, R. B. H.; Heng, J. Y. Y. Template-Induced Polymorphic Selectivity: The Effects of Surface Chemistry and Solute Concentration on Carbamazepine Crystallisation. *CrystEngComm* **2014**, *16* (23), 4927–4930.

(38) Lang, M.; Grzesiak, A. L.; Matzger, A. J. The Use of Polymer Heteronuclei for Crystalline Polymorph Selection. *J. Am. Chem. Soc.* **2002**, *124* (50), 14834–14835.

(39) Arlin, J.-B.; Price, L. S.; Price, S. L.; Florence, A. J. A Strategy for Producing Predicted Polymorphs: Catemeric Carbamazepine Form V. *Chem. Commun.* **2011**, *47* (25), 7074.

(40) Srirambhatla, V. K.; Guo, R.; Price, S. L.; Florence, A. J. Isomorphous Template Induced Crystallisation: A Robust Method for the Targeted Crystallisation of Computationally Predicted Metastable Polymorphs. *Chem. Commun.* **2016**, *52* (46), 7384–7386.

(41) Wokal, A. K.; Nguyen, T. T. H.; Roberts, K. J. Polymorph-Directing Seeding of

Entacapone Crystallization in Aqueous/ Acetone Solution Using a Self-Assembled Molecular Layer on Au (100). *Cryst. Growth Des.* **2009**, *9* (10), 4324–4334.

(42) Dressler, D. H.; Hod, I.; Mastai, Y. Stabilization of α-L-Glutamic Acid on Chiral Thin Films-A Theoretical and Experimental Study. *J. Cryst. Growth* **2008**, *310* (7–9), 1718–1724.

(43) Weissbuch, I.; Frolow, F.; Addadi, L.; Lahav, M.; Leiserowitz, L. Oriented Crystallization as a Tool for Detecting Ordered Aggregates of Water-Soluble Hydrophobic a-Amino Acids at the Air-Solution Interface. *J. Am. Chem. Soc.* **1990**, *112* (21), 7718–7724.

(44) McKellar, S. C.; Urquhart, A. J.; Lamprou, D. A.; Florence, A. J. Polymer Templating of Supercooled Indomethacin for Polymorph Selection. *ACS Comb. Sci.* **2012**, *14* (3), 155–159.

(45) Pfund, L. Y.; Price, C. P.; Frick, J. J.; Matzger, A. J. Controlling Pharmaceutical Crystallization with Designed Polymeric Heteronuclei. *J. Am. Chem. Soc.* **2015**, *137* (2), 871–875.

(46) Zhang, J.; Liu, A.; Han, Y.; Ren, Y.; Gong, J.; Li, W.; Wang, J. Effects of Self-Assembled Monolayers on Selective Crystallization of Tolbutamide. *Cryst. Growth Des.* **2011**, *11* (12), 5498–5506.

(47) Haisa, M.; Kashino, S.; Kawai, R.; Maeda, H. The Monoclinic Form of P-Hydroxyacetanilide. *Acta Crystallogr. Sect. B Struct. Crystallogr. Cryst. Chem.* **1976**, *32* (4), 1283–1285.

(48) Haisa, M.; Kashino, S.; Maeda, H. The Orthorhombic Form of P-Hydroxyacetanilide. *Acta Crystallogr. Sect. B Struct. Crystallogr. Cryst. Chem.* **1974**, *30* (10), 2510–2512.

(49) Perrin, M.-A.; Neumann, M. a; Elmaleh, H.; Zaske, L. Crystal Structure Determination of the Elusive Paracetamol Form III. *Chem. Commun.* **2009**, No. 22, 3181.

(50) Di Martino, P.; Guyot-Hermann, A. M.; Conflant, P.; Drache, M.; Guyot, J. C. A New Pure Paracetamol for Direct Compression: The Orthorhombic Form. *Int. J.*

Pharm. **1996**, *128* (1–2), 1–8.

(51) Rossi, A.; Savioli, A.; Bini, M.; Capsoni, D.; Massarotti, V.; Bettini, R.; Gazzaniga, A.; Sangalli, M. E.; Giordano, F. Solid-State Characterization of Paracetamol Metastable Polymorphs Formed in Binary Mixtures with Hydroxypropylmethylcellulose. *Thermochim. Acta* **2003**, *406* (1–2), 55–67.

(52) Giordano, F.; Rossi, A.; Bettini, R.; Savioli, A.; Gazzaniga, A.; Novák, C. Thermal Behavior of Paracetamol-Polymeric Excipients Mixtures. *J. Therm. Anal. Calorim.* **2002**, *68* (2), 575–590.

(53) Di Martino, P.; Conflant, P.; Drache, M.; Huvenne, J.-P.; Guyot-Hermann, A.-M. Preparation and Physical Characterization of Forms II and III of Paracetamol. *J. Therm. Anal.* **1997**, *48* (3), 447–458.

(54) Femi-Oyewo, M. N.; Spring, M. S. Studies on Paracetamol Crystals Produced by Growth in Aqueous Solutions. *Int. J. Pharm.* **1994**, *112* (1), 17–28.

(55) Kachrimanis, K.; Malamataris, S. Crystallization of Paracetamol from Ethanol-Water Solutions in the Presence of Polymers. *J. Pharm. Pharmacol.* **1999**, *51* (11), 1219–1227.

(56) Garekani, H. A.; Ford, J. L.; Rubinstein, M. H.; Rajabi-Siahboomi, A. R. Highly Compressible Paracetamol: I: Crystallization and Characterization. *Int. J. Pharm.* **2000**, *208* (1–2), 87–99.

(57) Gaisford, S.; Buanz, A. B. M.; Jethwa, N. Characterisation of Paracetamol Form III with Rapid-Heating DSC. *J. Pharm. Biomed. Anal.* **2010**, *53* (3), 366–370.

(58) Shan, N.; Zaworotko, M. J. The Role of Cocrystals in Pharmaceutical Science. *Drug Discov. Today* **2008**, *13* (9–10), 440–446.

(59) Duggirala, N. K.; Perry, M. L.; Almarsson, Ö.; Zaworotko, M. J. Pharmaceutical Cocrystals: Along the Path to Improved Medicines. *Chem. Commun.* **2016**, *52*, 640–655.

(60) Miroshnyk, I.; Mirza, S.; Sandler, N. Pharmaceutical Co-Crystals-an Opportunity for Drug Product Enhancement. *Expert Opin. Drug Deliv.* **2009**, *6* (4), 333–341.

(61) Hickey, M. B.; Peterson, M. L.; Scoppettuolo, L. a.; Morrisette, S. L.; Vetter, A.; Guzmán, H.; Remenar, J. F.; Zhang, Z.; Tawa, M. D.; Haley, S.; Zaworotko, M.

J.; Almarsson, Ö. Performance Comparison of a Co-Crystal of Carbamazepine with Marketed Product. *Eur. J. Pharm. Biopharm.* **2007**, *67* (1), 112–119.

(62) Basavoju, S.; Boström, D.; Velaga, S. P. Indomethacin-Saccharin Cocrystal: Design, Synthesis and Preliminary Pharmaceutical Characterization. *Pharm. Res.* **2008**, *25* (3), 530–541.

(63) Almarsson, Ö.; Zaworotko, M. J. Crystal Engineering of the Composition of Pharmaceutical Phases. Do Pharmaceutical Co-Crystals Represent a New Path to Improved Medicines? *Chem. Commun. (Camb).* **2004**, No. 17, 1889–1896.

(64) Schultheiss, N.; Newman, A. Pharmaceutical Cocrystals and Their Physicochemical Properties. *Cryst. Growth Des.* **2009**, *9* (6), 2950–2967.

(65) Seefeldt, K.; Miller, J.; Alvarez-Núñez, F.; Rodríguez-Hornedo, N. Crystallization Pathways and Kinetics of Carbamazepine-Nicotinamide Cocrystals from the Amorphous State by in Situ Thermomicroscopy, Spectroscopy, and Calorimetry Studies. *J. Pharm. Sci.* **2007**, *96* (5), 1147–1158.

(66) Desiraju, G. Supramolecular Synthons in Crystal Engineering—a New Organic Synthesis. *Angew. Chemie Int. Ed.* **1995**, *34* (21), 2311–2327.

(67) Vishweshwar, P.; McMahon, J. A.; Bis, J. A.; Zaworotko, M. J. Pharmaceutical Co-Crystals. *J. Pharm. Sci.* **2006**, *95* (3), 499–516.

(68) Blagden, N.; de Matas, M.; Gavan, P. T.; York, P. Crystal Engineering of Active Pharmaceutical Ingredients to Improve Solubility and Dissolution Rates. *Adv. Drug Deliv. Rev.* **2007**, *59* (7), 617–630.

(69) Qiao, N.; Li, M.; Schlindwein, W.; Malek, N.; Davies, A.; Trappitt, G. Pharmaceutical Cocrystals: An Overview. *Int. J. Pharm.* **2011**, *419* (1–2), 1–11.

(70) Berry, D. J.; Seaton, C. C.; Clegg, W.; Harrington, R. W.; Coles, S. J.; Horton, P. N.; Hursthouse, M. B.; Storey, R.; Jones, W.; Friščić, T.; Blagden, N. Applying Hot-Stage Microscopy to Co-Crystal Screening: A Study of Nicotinamide with Seven Active Pharmaceutical Ingredients. *Cryst. Growth Des.* **2008**, *8* (5), 1697–1712.

(71) Eddleston, M. D.; Sivachelvam, S.; Jones, W. Screening for Polymorphs of

Cocrystals: A Case Study. *CrystEngComm* **2013**, *15* (1), 175–181.

(72) Thakuria, R.; Delori, A.; Jones, W.; Lipert, M. P.; Roy, L.; Rodríguez-Hornedo, N. Pharmaceutical Cocrystals and Poorly Soluble Drugs. *Int. J. Pharm.* **2013**, *453* (1), 101–125.

(73) Caira, M. R. Molecular Complexes of Sulfonamides. Part 1. 1?1 Complexes between Sulfadimidine [4-Amino-N-(4,6-Dimethyl-2-Pyrimidinyl)benzenesulfonamide] and 2- and 4-Aminobenzoic Acids. *J. Crystallogr. Spectrosc. Res.* **1991**, *21* (5), 641–648.

(74) Caira, M. R. Molecular Complexes of Sulfonamides. 2.1:1 Complexes between Drug Molecules: Sulfadimidine-Acetylsalicylic Acid and Sulfadimidine-4-Aminosalicylic Acid. *J. Crystallogr. Spectrosc. Res.* **1992**, *22* (2), 193–200.

(75) Ghosh, M.; Basak, a. K.; Mazumdar, S. K.; Sheldrick, B. Structure and Conformation of the 1:1 Molecular Complex Sulfaproxyline–caffeine. *Acta Crystallogr. Sect. C Cryst. Struct. Commun.* **1991**, *47* (3), 577–580.

(76) Etter, M. C.; Reutzel, S. M. Hydrogen Bond Directed Cocrystallization and Molecular Recognition Properties of Acyclic Imides. *J. Am. Chem. Soc.* **1991**, *113* (7), 2586–2598.

(77) Walsh, R. D. B.; Bradner, M. W.; Fleischman, S.; Morales, L. a.; Moulton, B.; Rodríguez-Hornedo, N.; Zaworotko, M. J. Crystal Engineering of the Composition of Pharmaceutical Phases. *Chem. Commun.* **2003**, No. 2, 186–187.

(78) Childs, S. L.; Chyall, L. J.; Dunlap, J. T.; Smolenskaya, V. N.; Stahly, B. C.; Stahly, G. P. Crystal Engineering Approach to Forming Cocrystals of Amine Hydrochlorides with Organic Acids. Molecular Complexes of Fluoxetine Hydrochloride with Benzoic, Succinic, and Fumaric Acids. *J. Am. Chem. Soc.* **2004**, *126* (41), 13335–13342.

(79) Chiarella, R. A.; Davey, R. J.; Peterson, M. L. Making Co-Crystals — The Utility of Ternary Phase Diagrams. *Cryst. Growth Des.* **2007**, *7* (7), 1223–1226.

(80) Buanz, A. B. M.; Gaisford, S. Formation of Highly Metastable β Glycine by Confinement in Inkjet Printed Droplets. *Cryst. Growth Des.* **2017**, *17* (3), 1245–1250.

(81) Buanz, A. B. M.; Telford, R.; Scowen, I. J.; Gaisford, S. Rapid Preparation of

Pharmaceutical Co-Crystals with Thermal Ink-Jet Printing. *CrystEngComm* **2013**, *15* (6), 1031–1035.

(82) Childs, S. L.; Rodríguez-Hornedo, N.; Reddy, L. S.; Jayasankar, A.; Maheshwari, C.; McCausland, L.; Shipplett, R.; Stahly, B. C. Screening Strategies Based on Solubility and Solution Composition Generate Pharmaceutically Acceptable Cocrystals of Carbamazepine. *CrystEngComm* **2008**, *10* (7), 856.

(83) Grant, D. J. W. Theory and Origin of Polymorphism. In *Polymorphism in Pharmaceutical Solids*; Brittain, H. G., Ed.; Marcel Dekker, Inc: New York, 1999; pp 1–34.

(84) Aher, S.; Dhumal, R.; Mahadik, K.; Paradkar, A.; York, P. Ultrasound Assisted Cocrystallization from Solution (USSC) Containing a Non-Congruently Soluble Cocrystal Component Pair: Caffeine/maleic Acid. *Eur. J. Pharm. Sci.* **2010**, *41* (5), 597–602.

(85) Blagden, N.; Berry, D. J.; Parkin, A.; Javed, H.; Ibrahim, A.; Gavan, P. T.; De Matos, L. L.; Seaton, C. C. Current Directions in Co-Crystal Growth. *New J. Chem.* **2008**, *32* (10), 1659–1672.

(86) Yamashita, H.; Hirakura, Y.; Yuda, M.; Teramura, T.; Terada, K. Detection of Cocrystal Formation Based on Binary Phase Diagrams Using Thermal Analysis. *Pharm. Res.* **2013**, *30* (1), 70–80.

(87) Chadwick, K.; Davey, R.; Cross, W. How Does Grinding Produce Co-Crystals? Insights from the Case of Benzophenone and Diphenylamine. *CrystEngComm* **2007**, *9* (9), 732.

(88) Fucke, K.; Myz, S. a.; Shakhtshneider, T. P.; Boldyreva, E. V.; Griesser, U. J. How Good Are the Crystallisation Methods for Co-Crystals? A Comparative Study of Piroxicam. *New J. Chem.* **2012**, *36* (10), 1969.

(89) Lu, E.; Rodríguez-Hornedo, N.; Suryanarayanan, R. A Rapid Thermal Method for Cocrystal Screening. *CrystEngComm* **2008**, *10* (6), 665.

(90) Sládková, V.; Cibulková, J.; Eigner, V.; Šturc, A.; Kratochvíl, B.; Rohlíček, J. Application and Comparison of Cocrystallization Techniques on Trospium Chloride Cocrystals. *Cryst. Growth Des.* **2014**, *14* (6), 2931–2936.

(91) Yan, Y.; Chen, J.-M.; Lu, T.-B. Thermodynamics and Preliminary Pharmaceutical

Characterization of a Melatonin–pimelic Acid Cocrystal Prepared by a Melt Crystallization Method. *CrystEngComm* **2015**, *17*, 612–620.

(92) Manin, A. N.; Voronin, A. P.; Drozd, K. V.; Manin, N. G.; Bauer-Brandl, A.; Perlovich, G. L. Cocrystal Screening of Hydroxybenzamides with Benzoic Acid Derivatives: A Comparative Study of Thermal and Solution-Based Methods. *Eur. J. Pharm. Sci.* **2014**, *65*, 56–64.

(93) Hasa, D.; Schneider Rauber, G.; Voinovich, D.; Jones, W. Cocrystal Formation through Mechanochemistry: From Neat and Liquid-Assisted Grinding to Polymer-Assisted Grinding. *Angew. Chemie Int. Ed.* **2015**, *54* (25), 7371–7375.

(94) Hasa, D.; Carlino, E.; Jones, W. Polymer-Assisted Grinding, a Versatile Method for Polymorph Control of Cocrystallization. *Cryst. Growth Des.* **2016**, *16* (3), 1772–1779.

(95) Majumder, M.; Buckton, G.; Rawlinson-Malone, C.; Williams, A. C.; Spillman, M. J.; Shankland, N.; Shankland, K. A Carbamazepine-Indomethacin (1 : 1) Cocrystal Produced by Milling. *CrystEngComm* **2011**, *13* (21), 6327.

(96) Shan, N.; Toda, F.; Jones, W. Mechanochemistry and Co-Crystal Formation: Effect of Solvent on Reaction Kinetics. *Chem. Commun. (Camb).* **2002**, No. 20, 2372–2373.

(97) Friščić, T.; Childs, S. L.; Rizvi, S. A. A.; Jones, W. The Role of Solvent in Mechanochemical and Sonochemical Cocrystal Formation: A Solubility-Based Approach for Predicting Cocrystallisation Outcome. *CrystEngComm* **2009**, *11* (3), 418–426.

(98) Braga, D.; Maini, L.; Grepioni, F. Mechanochemical Preparation of Co-Crystals. *Chem. Soc. Rev.* **2013**, *42* (18), 7638–7648.

(99) Cheetham, A. K.; Wilkinson, A. P. Structure Determination and Refinement with Synchrotron X-Ray Powder Diffraction Data. *J. Phys. Chem. Solids* **1991**, *52* (10), 1199–1208.

(100) Harris, K. D. M.; Tremayne, M. Crystal Structure Determination from Powder Diffraction Data. *Chem. Mater.* **1996**, *8* (11), 2554–2570.

(101) Braga, D.; Giaffreda, S. L.; Grepioni, F.; Pettersen, A.; Maini, L.; Curzi, M.; Polito, M. Mechanochemical Preparation of Molecular and Supramolecular

Organometallic Materials and Coordination Networks. *Dalt. Trans.* **2006**, No. 10, 1249.

(102) James, S. L.; Adams, C. J.; Bolm, C.; Braga, D.; Collier, P.; Friščić, T.; Grepioni, F.; Harris, K. D. M.; Hyett, G.; Jones, W.; Krebs, A.; Mack, J.; Maini, L.; Orpen, a G.; Parkin, I. P.; Shearouse, W. C.; Steed, J. W.; Waddell, D. C. Mechanochemistry: Opportunities for New and Cleaner Synthesis. *Chem. Soc. Rev.* **2012**, *41* (1), 413–447.

(103) Ross, S. A.; Lamprou, D. A.; Douroumis, D. Engineering and Manufacturing of Pharmaceutical Co-Crystals: A Review of Solvent-Free Manufacturing Technologies. *Chem. Commun.* **2016**, *52* (57), 8772–8786.

(104) Friščić, T.; Jones, W. Recent Advances in Understanding the Mechanism of Cocrystal Formation via Grinding. *Cryst. Growth Des.* **2009**, *9* (3), 1621–1637.

(105) Etter, M. C.; Reutzel, S. M.; Choo, C. G. Self-Organization of Adenine and Thymine in the Solid State. *J. Am. Chem. Soc.* **1993**, *115* (10), 4411–4412.

(106) Caira, M. R.; Nassimbeni, L. R.; Wildervanck, A. F. Selective Formation of Hydrogen Bonded Cocrystals between a Sulfonamide and Aromatic Carboxylic Acids in the Solid State. *J. Chem. Soc. Perkin Trans. 2* **1995**, No. 12, 2213.

(107) Jayasankar, A.; Somwangthanaroj, A.; Shao, Z. J.; Rodríguez-Hornedo, N. Cocrystal Formation during Cogrinding and Storage Is Mediated by Amorphous Phase. *Pharm. Res.* **2006**, *23* (10), 2381–2392.

(108) Tan, D.; Loots, L.; Friščić, T. Towards Medicinal Mechanochemistry: Evolution of Milling from Pharmaceutical Solid Form Screening to the Synthesis of Active Pharmaceutical Ingredients (APIs). *Chem. Commun.* **2016**, *7760* (52), 7760–7781.

(109) Trask, A. V.; Motherwell, W. D. S.; Jones, W. Solvent-Drop Grinding: Green Polymorph Control of Cocrystallisation. *Chem. Commun.* **2004**, No. 7, 890.

(110) Hancock, B. C.; Shamblin, S. L.; Zografi, G. Molecular Mobility of Amorphous Pharmaceutical Solids below Their Glass Transition Temperatures. *Pharmaceutical research*. June 1995, pp 799–806.

(111) Nagapudi, K.; Jona, J. Amorphous Active Pharmaceutical Ingredients in Preclinical Studies: Preparation, Characterization, and Formulation. *Curr. Bioact.*

Compd. **2008**, *4* (4), 213–224.

(112) Ediger, M. D.; Angell, C. A.; Nagel, S. R. Supercooled Liquids and Glasses. *J. Phys. Chem.* **1996**, *100*, 13200–13212.

(113) Einfalt, T.; Planinšek, O.; Hrovat, K. Methods of Amorphization and Investigation of the Amorphous State. *Acta Pharm.* **2013**, *63* (3), 305–334.

(114) Bhugra, C.; Shmeis, R.; Pikal, M. J. Role of Mechanical Stress in Crystallization and Relaxation Behavior of Amorphous Indomethacin. *J. Pharm. Sci.* **2008**, *97* (10), 4446–4458.

(115) Van den Mooter, G. The Use of Amorphous Solid Dispersions: A Formulation Strategy to Overcome Poor Solubility and Dissolution Rate. *Drug Discov. Today Technol.* **2012**, *9* (2), e79–e85.

(116) Lu, J.; Rohani, S. Polymorphism and Crystallization of Active Pharmaceutical Ingredients (APIs). *Curr. Med. Chem.* **2009**, *16* (7), 884–905.

(117) Descamps, M.; Willart, J. F. Perspectives on the Amorphisation/milling Relationship in Pharmaceutical Materials. *Adv. Drug Deliv. Rev.* **2016**, *100*, 51–66.

(118) Dawson, K. J.; Kearns, K. L.; Yu, L.; Steffen, W.; Ediger, M. D. Physical Vapor Deposition as a Route to Hidden Amorphous States. *Proc. Natl. Acad. Sci. U. S. A.* **2009**, *106* (36), 15165–15170.

(119) Kearns, K. L.; Swallen, S. F.; Ediger, M. D.; Wu, T.; Yu, L. Influence of Substrate Temperature on the Stability of Glasses Prepared by Vapor Deposition. *J. Chem. Phys.* **2007**, *127* (15), 154702.

(120) Singh, S.; Ediger, M. D.; de Pablo, J. J. Ultrastable Glasses from in Silico Vapour Deposition. *Nat. Mater.* **2013**, *12* (2), 139–144.

(121) Oguni, M.; Hikawa, H.; Suga, H. Enthalpy Relaxation in Vapor-Deposited Butyronitrile. *Thermochim. Acta* **1990**, *158* (1), 143–156.

(122) Takeda, K.; Yamamuro, O.; Suga, H. Calorimetric Study on Structural Relaxation of 1-Pentene in Vapor-Deposited and Liquid-Quenched Glassy States. *J. Phys. Chem.* **1995**, *99* (5), 1602–1607.

(123) Takeda, K.; Yamamuro, O.; Oguni, M.; Suga, H. Thermodynamic

Characterization of Vapor-Deposited Amorphous Solid. *Thermochim. Acta* **1995**, *253* (94), 201–211.

(124) Hikawa, H.; Oguni, M.; Suga, H. Construction of an Adiabatic Calorimeter for a Vapor-Deposited Sample and Thermal Characterization of Amorphous Butyronitrile. *J. Non. Cryst. Solids* **1988**, *101* (1), 90–100.

(125) Shephard, J. J.; Evans, J. S. O.; Salzmann, C. G. Structural Relaxation of Low-Density Amorphous Ice upon Thermal Annealing. *J. Phys. Chem. Lett.* **2013**, *4* (21), 3672–3676.

(126) Kearns, K. L.; Whitaker, K. R.; Ediger, M. D.; Huth, H.; Schick, C. Observation of Low Heat Capacities for Vapor-Deposited Glasses of Indomethacin as Determined by AC Nanocalorimetry. *J. Chem. Phys.* **2010**, *133* (1), 14702.

(127) Kearns, K. L.; Swallen, S. F.; Ediger, M. D.; Wu, T.; Sun, Y.; Yu, L. Hiking down the Energy Landscape: Progress toward the Kauzmann Temperature via Vapor Deposition. *J. Phys. Chem. B* **2008**, *112* (16), 4934–4942.

(128) Sepúlveda, A.; Swallen, S. F.; Kopff, L. a; McMahon, R. J.; Ediger, M. D. Stable Glasses of Indomethacin and A,α,β-Tris- Naphthylbenzene Transform into Ordinary Supercooled Liquids. *J. Chem. Phys.* **2012**, *137* (20), 204508.

(129) Swallen, S. F.; Kearns, K. L.; Mapes, M. K.; Kim, Y. S.; McMahon, R. J.; Ediger, M. D.; Wu, T.; Yu, L.; Satija, S. Organic Glasses with Exceptional Thermodynamic and Kinetic Stability. *Science* **2007**, *315* (5810), 353–356.

(130) Dawson, K. J.; Kearns, K. L.; Ediger, M. D.; Sacchetti, M. J.; Zografi, G. D. Highly Stable Indomethacin Glasses Resist Uptake of Water Vapor. *J. Phys. Chem. B* **2009**, *113* (8), 2422–2427.

(131) Sergio, S. L.; Chigira, A. K.; Oguni, M. Devitrification Properties of Vapor-Deposited Ethylcyclohexane Glasses and Interpretation of the Molecular Mechanism for Formation of Vapor-Deposited Glasses. *J. Phys. Chem. B* **2015**, *119* (10), 4076–4083.

(132) Chua, Y. Z.; Tylinski, M.; Tatsumi, S.; Ediger, M. D.; Schick, C. Glass Transition and Stable Glass Formation of Tetrachloromethane. *J. Chem. Phys.* **2016**, *144* (24).

(133) Laventure, A.; Gujral, A.; Lebel, O.; Pellerin, C.; Ediger, M. D. Influence of

Hydrogen Bonding on the Kinetic Stability of Vapor-Deposited Glasses of Triazine Derivatives. *J. Phys. Chem. B* **2017**, *121* (10), 2350–2358.

(134) Gaisford, S.; Saunders, M. Basic Principles of Preformulation Studies. In *Essentials of Pharmaceutical Preformulation*; John Wiley & Sons, Ltd: Chichester, UK, 2012; pp 1–35.

(135) Scowen, I. J.; Telford, R. Simultaneous Thermal Techniques. In *Principles of Thermal Analysis and Calorimetry*; Gaisford, S., Kett, V., Haines, P. J., Eds.; Royal Society of Chemistry: Cambridge, 2016; pp 214–231.

(136) Mirabella, F. M. Simultaneous Differential Scanning Calorimetry (DSC) and Infrared Spectroscopy Using an Infrared Microsampling Accessory (IRMA) and FT-IR. *Appl. Spectrosc.* **1986**, *40* (3), 417–420.

(137) de Bakker, C. J.; St. John, N. A.; George, G. A. Simultaneous DSC-FTIR-NIR Studies of the Cure Kinetics of Epoxy Resins. *Polym. Prepr. (American Chem. Soc. Div. Polym. Chem.* **1992**, *33* (1), 374–375.

(138) Sprunt, J. C.; Jayasooriya, A.; Wilson, R. H. A Simultaneous FT-Raman – DSC (SRD) Study of Polymorphism in Sn -1 , 3-Distearoyl-2-Oleoylglycerol (SOS). *Phys. Chem. Chem. Phys.* **2000**, *2* (19), 4299–4305.

(139) Huang, J.; Dali, M. Evaluation of Integrated Raman-DSC Technology in Early Pharmaceutical Development: Characterization of Polymorphic Systems. *J. Pharm. Biomed. Anal.* **2013**, *86*, 92–99.

(140) Ali, H. R. H.; Edwards, H. G. M.; Scowen, I. J. Insight into Thermally Induced Solid-State Polymorphic Transformation of Sulfathiazole Using Simultaneous in Situ Raman Spectroscopy and Differential Scanning Calorimetry. *J. Raman Spectrosc.* **2009**, *40* (8), 887–892.

(141) Hafsia, K. Ben; Ponçot, M.; Chapron, D.; Royaud, I.; Dahoun, A.; Bourson, P. A Novel Approach to Study the Isothermal and Non-Isothermal Crystallization Kinetics of Poly(Ethylene Terephthalate) by Raman Spectroscopy. *J. Polym. Res.* **2016**, *23* (5), 93.

(142) Kuo, P. C.; Lo, C. T.; Chen, C. Y. Crystallization and Microstructure of Poly(butylene Oxalate). *Polym. (United Kingdom)* **2013**, *54* (24), 6654–6662.

(143) de Villiers, M. M.; Terblanche, R. J.; Liebenberg, W.; Swanepoel, E.; Dekker, T.

G.; Song, M. Variable-Temperature X-Ray Powder Diffraction Analysis of the Crystal Transformation of the Pharmaceutically Preferred Polymorph C of Mebendazole. *J. Pharm. Biomed. Anal.* **2005**, *38* (3), 435–441.

(144) Karjalainen, M.; Airaksinen, S.; Rantanen, J.; Aaltonen, J.; Yliruusi, J. Characterization of Polymorphic Solid-State Changes Using Variable Temperature X-Ray Powder Diffraction. *J. Pharm. Biomed. Anal.* **2005**, *39* (1–2), 27–32.

(145) Walton, R. I.; O'Hare, D. Watching Solids Crystallise Using in Situ Powder Diffraction. *Chem. Commun.* **2000**, No. 23, 2283–2291.

(146) Buanz, A.; Prior, T. J.; Burley, J. C.; Raimi-abraham, B. T.; Telford, R.; Hart, M.; Seaton, C. C.; Davies, P. J.; Scowen, I. J.; Gaisford, S.; Williams, G. R. Thermal Behavior of Benzoic Acid/Isonicotinamide Binary Cocrystals. *Cryst. Growth Des.* **2015**, *15* (7), 3249–3256.

(147) Russell, T. P.; Koberstein, J. T. Simultaneous Differential Scanning Calorimetry and Small-Angle X-Ray Scattering. *J. Polym. Sci. Polym. Phys. Ed.* **1985**, *23*, 1109–1115.

(148) Ungar, G.; Feijoo, J. L. Simultaneous X-Ray Diffraction and Differential Scanning Calorimetry (XDDSC) in Studies of Molecular and Liquid Crystals. *Mol. Cryst. Liq. Cryst. Inc. Nonlinear Opt.* **1990**, *180* (2), 281–291.

(149) Koberstein, J. T.; Galambos, A. F. Multiple Melting in Segmented Polyurethane Block Copolymers. *Macromolecules* **1992**, *25* (21), 5618–5624.

(150) Wutz, C.; Bark, M.; Cronauer, J.; Diihrmann, R.; Zachmann, G. Simultaneous Measurements of Small Angle X-Ray Scattering, Wide Angle X-Ray Scattering, and Light Scattering during Phase Transitions in Polymers. *Rev. Sci. Instrum.* **1995**, *66* (2), 1303–1307.

(151) Hatta, I.; Takahashi, H.; Matuoka, S.; Amemiya, Y. Simultaneous X-Ray Diffraction and Differential Scanning Calorimetry in the Study of Phase Transitions. *Thermochim. Acta* **1995**, *253*, 149–154.

(152) Bayés-García, L.; Calvet, T.; Cuevas-Diarte, M. À.; Ueno, S.; Sato, K. In Situ Synchrotron Radiation X-Ray Diffraction Study of Crystallization Kinetics of Polymorphs of 1,3-Dioleoyl-2-Palmitoyl Glycerol (OPO). *CrystEngComm* **2011**,

13 (10), 3592.

(153) Bayés-García, L.; Calvet, T.; Àngel Cuevas-Diarte, M.; Ueno, S.; Sato, K. In Situ Observation of Transformation Pathways of Polymorphic Forms of 1,3-Dipalmitoyl-2-Oleoyl Glycerol (POP) Examined with Synchrotron Radiation X-Ray Diffraction and DSC. *CrystEngComm* **2013**, *15* (2), 302–314.

(154) Kellens, M.; Meeussen, W.; Hammersley, A.; Reynaers, H. Synchrotron Radiation Investigations of the Polymorphic Transitions in Saturated Monoacid Triglycerides. Part 1: Tripalmitin and Tristearin. *Chem. Phys. Lipids* **1991**, *58* (1–2), 131–144.

(155) Ryan, A. J.; Bras, W.; Mant, G. R.; Derbyshire, G. E. A Direct Method to Determine the Degree of Crystallinity and Lamellar Thickness of Polymers: Application to Polyethylene. *Polymer (Guildf).* **1994**, *35* (21), 4537–4544.

(156) Bras, W.; Derbyshire, G. E.; Devine, A.; Clark, S. M.; Cooke, J.; Komanschek, B. E.; Ryan, A. J. The Combination of Thermal-Analysis and Time-Resolved X-Ray Techniques - a Powerful Method for Materials Characterization. *J. Appl. Crystallogr.* **1994**, *28*, 26–32.

(157) Gilbert, E. P.; Nelson, A.; Sutton, D.; Terrill, N.; Martin, C.; Lal, J.; Lang, E. Phase Separation in the Organic Solid State: The Influence of Quenching Protocol in Unstable N -Alkane Blends. *Mol. Cryst. Liq. Cryst.* **2005**, *440* (1), 93–105.

(158) Yoshida, H.; Kinoshita, R.; Teramoto, Y. Development of the Simultaneous Thermal analysis/X-Ray Scattering Measurement System. *Thermochim. Acta* **1995**, *264* (C), 173–183.

(159) Keller, G.; Lavigne, F.; Forte, L.; Andrieux, K.; Dahim, M.; Loisel, C.; Ollivon, M.; Bourgaux, C.; Lesieur, P. DSC and X-Ray Diffraction Coupling: Specifications and Applications. *J. Therm. Anal. Calorim.* **1998**, *51*, 783–791.

(160) Brubach, J. B.; Jannin, V.; Mahler, B.; Bourgaux, C.; Lessieur, P.; Roy, P.; Ollivon, M. Structural and Thermal Characterization of Glyceryl Behenate by X-Ray Diffraction Coupled to Differential Calorimetry and Infrared Spectroscopy. *Int. J. Pharm.* **2007**, *336* (2), 248–256.

(161) Drakopoulos, M.; Connolley, T.; Reinhard, C.; Atwood, R.; Magdysyuk, O.; Vo, N.; Hart, M.; Connor, L.; Humphreys, B.; Howell, G.; Davies, S.; Hill, T.; Wilkin,

G.; Pedersen, U.; Foster, A.; De Maio, N.; Basham, M.; Yuan, F.; Wanelik, K. I12: The Joint Engineering, Environment and Processing (JEEP) Beamline at Diamond Light Source. *J. Synchrotron Radiat.* **2015**, *22* (3), 828–838.

(162) Basham, M.; Filik, J.; Wharmby, M. T.; Chang, P. C. Y.; El Kassaby, B.; Gerring, M.; Aishima, J.; Levik, K.; Pulford, B. C. A.; Sikharulidze, I.; Sneddon, D.; Webber, M.; Dhesi, S. S.; Maccherozzi, F.; Svensson, O.; Brockhauser, S.; Náray, G.; Ashton, A. W. Data Analysis WorkbeNch (DAWN). *J. Synchrotron Radiat.* **2015**, *22* (3), 853–858.

(163) Von Dreele, R. B.; Larson, A. C. *General Structure Analysis System (GSAS)*; 2004; Vol. 748.

(164) Coelho, A. A.; Evans, J.; Evans, I.; Kern, A.; Parsons, S. The TOPAS Symbolic Computation System. *Powder Diffr.* **2011**, *26* (S1), S22–S25.

(165) Grove, D. C.; Keenan, G. L. The Dimorphism of Sulfathiazole. *J. Am. Chem. Soc.* **1941**, *63* (1), 97–99.

(166) Hughes, D. S.; Hursthouse, M. B.; Threlfall, T.; Tavener, S. A New Polymorph of Sulfathiazole. *Acta Crystallogr. Sect. C - Cryst. Struct. Commun.* **1999**, *55* (Ii), 1831–1833.

(167) Chan, F. C.; Anwar, J.; Cernik, R.; Barnes, P.; Wilson, R. M. Ab Initio Structure Determination of Sulfathiazole Polymorph V from Synchrotron X-Ray Powder Diffraction Data. *J. Appl. Crystallogr.* **1999**, *32* (3), 436–441.

(168) Abu Bakar, M. R.; Nagy, Z. K.; Rielly, C. D.; Dann, S. E. Investigation of the Riddle of Sulfathiazole Polymorphism. *Int. J. Pharm.* **2011**, *414* (1–2), 86–103.

(169) Munroe, Á.; Rasmuson, Å. C.; Hodnett, B. K.; Croker, D. M. Relative Stabilities of the Five Polymorphs of Sulfathiazole. *Cryst. Growth Des.* **2012**, *12* (6), 2825–2835.

(170) Anwar, J.; Tarling, S. E.; Barnes, P. Polymorphism of Sulfathiazole. *J. Pharm. Sci.* **1989**, *78* (4), 337–342.

(171) Giron, D. Contribution of Thermal Methods and Related Techniques to the Rational Development of pharmaceuticals—Part 1. *Pharm. Sci. Technolo. Today*

1998, *1* (5), 191–199.

(172) Giron, D. Thermal Analysis, Microcalorimetry and Combined Techniques for the Study of Pharmaceuticals. *J. Therm. Anal. Calorim.* **1999**, *56* (3), 1285–1304.

(173) Zeitler, J. A.; Newnham, D. A.; Taday, P. F.; Threlfall, T. L.; Lancaster, R. W.; Berg, R. W.; Strachan, C. J.; Pepper, M.; Gordon, K. C.; Rades, T. Characterization of Temperature-Induced Phase Transitions in Five Polymorphic Forms of Sulfathiazole by Terahertz Pulsed Spectroscopy and Differential Scanning Calorimetry. *J. Pharm. Sci.* **2006**, *95* (11), 2486–2498.

(174) Mesley, R. J. The Polymorphism of Sulphathiazole. *J. Pharm. Pharmacol.* **1971**, *23* (9), 687–694.

(175) Blagden, N.; Davey, R. J.; Lieberman, H. F.; Williams, L.; Payne, R.; Roberts, R.; Rowe, R.; Docherty, R. Crystal Chemistry and Solvent Effects in Polymorphic Systems Sulfathiazole. *J. Chem. Soc. Faraday Trans.* **1998**, *94* (8), 1035–1044.

(176) Gelbrich, T.; Hughes, D. S.; Hursthouse, M. B.; Threlfall, T. L. Packing Similarity in Polymorphs of Sulfathiazole. *CrystEngComm* **2008**, *10* (10), 1328.

(177) Espeau, P.; Négrier, P.; Corvis, Y. Crystallographic and Pressure–Temperature State Diagram Approach for the Phase Behavior and Polymorphism Study of Glutaric Acid. *Cryst. Growth Des.* **2013**, *13* (2), 723–730.

(178) Bhattacharya, S.; Saraswatula, V. G.; Saha, B. K. Thermal Expansion in Alkane Diacids - Another Property Showing Alternation in an Odd-Even Series. *Cryst. Growth Des.* **2013**, *13* (8), 3651–3656.

(179) Grip, J.; Samuelsen, E. J. A Raman Study of Crystalline Glutaric Acid. *Phys. Scr.* **1984**, *29* (6), 556–560.

(180) Mangin, D.; Puel, F.; Veesler, S. Polymorphism in Processes of Crystallization in Solution: A Practical Review. *Org. Process Res. Dev.* **2009**, *13* (6), 1241–1253.

(181) Guyer, P. To-Day's Drugs: Carbamazepine. *BMJ* **1964**, *2* (5404), 295–295.

(182) Brewster, M. E.; Anderson, W. R.; Estes, K. S.; Bodor, N. Development of Aqueous Parenteral Formulations for Carbamazepine through the Use of Modified Cyclodextrins. *J. Pharm. Sci.* **1991**, *80* (4), 380–383.

(183) Reboul, J. P.; Cristau, B.; Soyfer, J. C.; Astier, J. P. 5H-

Dibenz[b,f]azépinecarboxamide-5 (Carbamazépine). *Acta Crystallogr. Sect. B Struct. Crystallogr. Cryst. Chem.* **1981**, *37* (10), 1844–1848.

(184) Lowes, M. M. J.; Caira, M. R.; Lötter, A. P.; Van Der Watt, J. G. Physicochemical Properties and X-Ray Structural Studies of the Trigonal Polymorph of Carbamazepine. *J. Pharm. Sci.* **1987**, *76* (9), 744–752.

(185) Grzesiak, A. L.; Lang, M.; Kim, K.; Matzger, A. J. Comparison of the Four Anhydrous Polymorphs of Carbamazepine and the Crystal Structure of Form I. *J. Pharm. Sci.* **2003**, *92* (11), 2260–2271.

(186) Lang, M.; Kampf, J. W.; Matzger, A. J. Form IV of Carbamazepine. *J. Pharm. Sci.* **2002**, *91* (4), 1186–1190.

(187) Cruz Cabeza, A. J.; Day, G. M.; Motherwell, W. D. S.; Jones, W. Importance of Molecular Shape for the Overall Stability of Hydrogen Bond Motifs in the Crystal Structures of Various Carbamazepine-Type Drug Molecules. *Cryst. Growth Des.* **2007**, *7* (1), 100–107.

(188) Bandoli, G.; Nicolini, M.; Ongaro, A.; Volpe, G.; Rubello, A. X-Ray Crystallographic Characterization of 10,11-Dihydro-5H-Dibenz[b, F]Azepine-5-Carboxamide. *J. Crystallogr. Spectrosc. Res.* **1992**, *22* (2), 177–183.

(189) Harrison, W. T. A.; Yathirajan, H. S.; Anilkumar, H. G. An Orthorhombic Polymorph of 10,11-Dihydrocarbamazepine. *Acta Crystallogr. Sect. C Cryst. Struct. Commun.* **2006**, *62* (5), o240–o242.

(190) Leech, C. K.; Florence, A. J.; Shankland, K.; Shankland, N.; Johnston, A. 10,11-Dihydrocarbamazepine (Form III). *Acta Crystallogr. Sect. E Struct. Reports Online* **2007**, *63* (2), o675–o677.

(191) Arlin, J.-B.; Johnston, A.; Miller, G. J.; Kennedy, A. R.; Price, S. L.; Florence, A. J. A Predicted Dimer-Based Polymorph of 10,11-Dihydrocarbamazepine (Form IV). *CrystEngComm* **2010**, *12* (1), 64–66.

(192) Nichols, G.; Frampton, C. S. Physicochemical Characterization of the Orthorhombic Polymorph of Paracetamol Crystallized from Solution. *J. Pharm. Sci.* **1998**, *87* (6), 684–693.

(193) Ehmann, H. M. A.; Werzer, O. Surface Mediated Structures: Stabilization of Metastable Polymorphs on the Example of Paracetamol. *Cryst. Growth Des.*

2014, *14* (8), 3680–3684.

(194) Nanubolu, J. B.; Burley, J. C. Investigating the Recrystallization Behavior of Amorphous Paracetamol by Variable Temperature Raman Studies and Surface Raman Mapping. *Mol. Pharm.* **2012**, *9* (6), 1544–1558.

(195) Hiremath, R.; Varney, S. W.; Swift, J. A. Selective Growth of a Less Stable Polymorph of 2-Iodo-4-Nitroaniline on a Self-Assembled Monolayer Template. *Chem. Commun.* **2004**, No. 23, 2676.

(196) Lee, E. H.; Byrn, S. R.; Carvajal, M. T. Additive-Induced Metastable Single Crystal of Mefenamic Acid. *Pharm. Res.* **2006**, *23* (10), 2375–2380.

(197) Gift, A. D.; Luner, P. E.; Luedeman, L.; Taylor, L. S. Influence of Polymeric Excipients on Crystal Hydrate Formation Kinetics in Aqueous Slurries. *J. Pharm. Sci.* **2008**, *97* (12), 5198–5211.

(198) Dowling, R.; Davey, R. J.; Curtis, R. a; Han, G.; Poornachary, S. K.; Chow, P. S.; Tan, R. B. H. Acceleration of Crystal Growth Rates: An Unexpected Effect of Tailor-Made Additives. *Chem. Commun. (Camb).* **2010**, *46* (32), 5924–5926.

(199) Jeffrey, G. A. Nature and Properties. In *An introduction to hydrogen bonding*; Oxford University Press, 1997.

(200) Bradley, J.-C.; Williams, A.; Lang, A. Jean-Claude Bradley Open Melting Point Dataset.

(201) Kang, M.; Zhang, P.; Cui, H.; Loverde, S. M. π-π Stacking Mediated Chirality in Functional Supramolecular Filaments. *Macromolecules* **2016**, *49* (3), 994–1001.

(202) Dunitz, J. D.; Gavezzotti, A. Supramolecular Synthons: Validation and Ranking of Intermolecular Interaction Energies. *Cryst. Growth Des.* **2012**, *12* (12), 5873–5877.

(203) Himes, V. L.; Mighell, A. D.; De Camp, W. H. Structure of Carbamazepine: 5H-Dibenz[b,f]azepine-5-Carboxamide. *Acta Crystallogr. Sect. B Struct. Crystallogr. Cryst. Chem.* **1981**, *37* (12), 2242–2245.

(204) Rustichelli, C.; Gamberini, G.; Ferioli, V.; Gamberini, M. C.; Ficarra, R.; Tommasini, S. Solid-State Study of Polymorphic Drugs: Carbamazepine. *J.*

Pharm. Biomed. Anal. **2000**, *23* (1), 41–54.

(205) McGregor, C.; Saunders, M. H.; Buckton, G.; Saklatvala, R. D. The Use of High-Speed Differential Scanning Calorimetry (Hyper-DSC™) to Study the Thermal Properties of Carbamazepine Polymorphs. *Thermochim. Acta* **2004**, *417* (2), 231–237.

(206) El Hassan, N.; Ikni, A.; Gillet, J.-M.; Spasojevic-de Biré, A.; Ghermani, N. E. Electron Properties of Carbamazepine Drug in Form III. *Cryst. Growth Des.* **2013**, *13* (7), 2887–2896.

(207) Behme, R. J.; Brooke, D. Heat of Fusion Measurement of a Low Melting Polymorph of Carbamazepine That Undergoes Multiple-Phase Changes During Differential Scanning Calorimetry Analysis. *J. Pharm. Sci.* **1991**, *80* (10), 986–990.

(208) Umeda, T.; Ohnishi, N.; Yokoyama, T.; Kuroda, K.; Kuroda, T.; Tatsumi, E.; Matsuda, Y. Kinetics of the Thermal Transition of Carbamazepine Polymorphic Forms in the Solid State. *Yakugaku Zasshi* **1984**, *104* (7), 786–792.

(209) Zeitler, J. A.; Taday, P. F.; Gordon, K. C.; Pepper, M.; Rades, T. Time-Resolved Terahertz Spectroscopy: Polymorphic Solid State Phase Transitions in Carbamazepine. In *2007 Joint 32nd International Conference on Infrared and Millimeter Waves and the 15th International Conference on Terahertz Electronics*; IEEE, 2007; pp 492–493.

(210) Telford, R.; Seaton, C. C.; Clout, A.; Buanz, A.; Gaisford, S.; Williams, G. R.; Prior, T. J.; Okoye, C. H.; Munshi, T.; Scowen, I. J. Stabilisation of Metastable Polymorphs: The Case of Paracetamol Form III. *Chem. Commun.* **2016**, *52* (81), 12028–12031.

(211) Boldyreva, E. V.; Drebushchak, V. A.; Paukov, I. E.; Kovalevskaya, Y. A.; Drebushchak, T. N. DSC and Adiabatic Calorimetry Study of the Polymorphs of Paracetamol: An Old Problem Revisited. *J. Therm. Anal. Calorim.* **2004**, *77* (2), 607–623.

(212) di Martino, P.; Palmieri, G. F.; Martelli, S. Molecular Mobility of the Paracetamol Amorphous Form. *Chem. Pharm. Bull. (Tokyo).* **2000**, *48* (8), 1105–1108.

(213) Sibik, J.; Sargent, M. J.; Franklin, M.; Zeitler, J. A. Crystallization and Phase Changes in Paracetamol from the Amorphous Solid to the Liquid Phase. *Mol.*

Pharm. **2014**, *11* (4), 1326–1334.

(214) Nunes, C.; Mahendrasingam, A.; Suryanarayanan, R. Quantification of Crystallinity in Substantially Amorphous Materials by Synchrotron X-Ray Powder Diffractometry. *Pharm. Res.* **2005**, *22* (11), 1942–1953.

(215) Qi, S.; Avalle, P.; Saklatvala, R.; Craig, D. Q. M. An Investigation into the Effects of Thermal History on the Crystallisation Behaviour of Amorphous Paracetamol. *Eur. J. Pharm. Biopharm.* **2008**, *69* (1), 364–371.

(216) Aakeröy, C. B. Crystal Engineering: Strategies and Architectures. *Acta Crystallogr. Sect. B Struct. Sci.* **1997**, *53* (4), 569–586.

(217) Godin, A. M.; Ferreira, W. C.; Rocha, L. T. S.; Seniuk, J. G. T.; Paiva, A. L. L.; Merlo, L. A.; Nascimento, E. B.; Bastos, L. F. S.; Coelho, M. M. Antinociceptive and Anti-Inflammatory Activities of Nicotinamide and Its Isomers in Different Experimental Models. *Pharmacol. Biochem. Behav.* **2011**, *99* (4), 782–788.

(218) Alba Sorolla, M.; Nierga, C.; José Rodríguez-Colman, M.; Reverter-Branchat, G.; Arenas, A.; Tamarit, J.; Ros, J.; Cabiscol, E. Sir2 Is Induced by Oxidative Stress in a Yeast Model of Huntington Disease and Its Activation Reduces Protein Aggregation. *Arch. Biochem. Biophys.* **2011**, *510* (1), 27–34.

(219) Wang, J.-R.; Yu, X.; Zhou, C.; Lin, Y.; Chen, C.; Pan, G.; Mei, X. Improving the Dissolution and Bioavailability of 6-Mercaptopurine via Co-Crystallization with Isonicotinamide. *Bioorg. Med. Chem. Lett.* **2015**, *25* (5), 1036–1039.

(220) Kang, Y.; Gu, J.; Hu, X. Syntheses, Structure Characterization and Dissolution of Two Novel Cocrystals of Febuxostat. *J. Mol. Struct.* **2017**, *1130*, 480–486.

(221) Drozd, K. V.; Manin, A. N.; Churakov, A. V.; Perlovich, G. L. Drug-Drug Cocrystals of Antituberculous 4-Aminosalicylic Acid: Screening, Crystal Structures, Thermochemical and Solubility Studies. *Eur. J. Pharm. Sci.* **2017**, *99*, 228–239.

(222) Li, J.; Wang, L.; Ye, Y. Q.; Fu, X.; Ren, Q.; Zhang, H.; Deng, Z. Improving the Solubility of Dexlansoprazole by Cocrystallization with Isonicotinamide. *Eur. J. Pharm. Sci.* **2016**, *85*, 47–52.

(223) Zeng, Q.-Z.; Ouyang, J.; Zhang, S.; Zhang, L. Structural Characterization and Dissolution Profile of Mycophenolic Acid Cocrystals. *Eur. J. Pharm. Sci.* **2017**,

102, 140–146.

(224) Sanphui, P.; Kumar, S. S.; Nangia, A. Pharmaceutical Cocrystals of Niclosamide. *Cryst. Growth Des.* **2012**, *12* (9), 4588–4599.

(225) Basavoju, S.; Bostrom, D.; Velaga, P. Pharmaceutical Cocrystals and Salts of Norfloxacin. *Cryst. Growth Des.* **2006**, *6* (12), 2699–2708.

(226) Rajesh Goud, N.; Khan, R. A.; Nangia, A. Modulating the Solubility of Sulfacetamide by Means of Cocrystals. *CrystEngComm* **2014**, *16* (26), 5859.

(227) Domingos, S.; Fernandes, A.; Duarte, M. T.; Piedade, M. F. M. New Multicomponent Sulfadimethoxine Crystal Forms: Sulfonamides as Participants in Supramolecular Interactions. *Cryst. Growth Des.* **2016**, *16* (4), 1879–1892.

(228) Sanphui, P.; Bolla, G.; Nangia, A. High Solubility Piperazine Salts of the Nonsteroidal Anti-Inflammatory Drug (NSAID) Meclofenamic Acid. *Cryst. Growth Des.* **2012**, *12* (4), 2023–2036.

(229) Báthori, N. B.; Lemmerer, A.; Venter, G. A.; Bourne, S. A.; Caira, M. R. Pharmaceutical Co-Crystals with Isonicotinamide—Vitamin B3, Clofibric Acid, and Diclofenac—and Two Isonicotinamide Hydrates. *Cryst. Growth Des.* **2011**, *11* (1), 75–87.

(230) Cysewski, P. Transferability of Cocrystallization Propensities between Aromatic and Heteroaromatic Amides. *Struct. Chem.* **2016**, *27* (5), 1403–1412.

(231) Aakeröy, C. B.; Beatty, A. M.; Helfrich, B. A. “Total Synthesis” Supramolecular Style: Design and Hydrogen-Bond-Directed Assembly of Ternary Supermolecules. *Angew. Chemie Int. Ed.* **2001**, *40* (17), 3240–3242.

(232) Vishweshwar, P.; Nangia, A.; Lynch, V. M. Supramolecular Synthons in Phenol–isonicotinamide Adducts. *CrystEngComm* **2003**, *5* (31), 164–168.

(233) CHO, J.-Y.; MOON, J.-H.; SEONG, K.-Y.; PARK, K.-H. Antimicrobial Activity of 4-Hydroxybenzoic Acid and Trans 4-Hydroxycinnamic Acid Isolated and Identified from Rice Hull. *Biosci. Biotechnol. Biochem.* **1998**, *62* (11), 2273–2276.

(234) Biskup, I.; Golonka, I.; Gamian, A.; Sroka, Z. Antioxidant Activity of Selected Phenols Estimated by ABTS and FRAP Methods. *Postepy Hig. Med. Dosw.*

2013, *67* (67), 958–963.

(235) Galley, H. Vitamin C and Pressure Sores. *J. Dermatolog. Treat.* **1995**, *6* (3), 195–198.

(236) Johnson, L. J.; Meacham, S. L. The Antioxidants-Vitamin C , Vitamin E , Selenium , and Carotenoids. *J. Agromedicine* **2003**, *9 (1)* (September 2013), 65–82.

(237) Aitipamula, S.; Chow, P. S.; Tan, R. B. H. Dimorphs of a 1 : 1 Cocrystal of Ethenzamide and Saccharin: Solid-State Grinding Methods Result in Metastable Polymorph. *CrystEngComm* **2009**, *11* (5), 889.

(238) Sheldrick, G. M. A Short History of SHELX. *Acta Crystallogr. Sect. A Found. Crystallogr.* **2007**, *64* (1), 112–122.

(239) Sheldrick, G. M. Crystal Structure Refinement with SHELXL. *Acta Crystallogr. Sect. C Struct. Chem.* **2015**, *71* (Md), 3–8.

(240) Buanz, A. B. M.; Saunders, M. H.; Basit, A. W.; Gaisford, S. Preparation of Personalized-Dose Salbutamol Sulphate Oral Films with Thermal Ink-Jet Printing. *Pharm. Res.* **2011**, *28* (10), 2386–2392.

(241) Allen, F. H.; Samuel Motherwell, W. D.; Raithby, P. R.; Shields, G. P.; Taylor, R. Systematic Analysis of the Probabilities of Formation of Bimolecular Hydrogen-Bonded Ring Motifs in Organic Crystal Structures. *New J. Chem.* **1999**, *23* (1), 25–34.

(242) Aakeröy, C. B.; Beatty, A. M.; Helfrich, B. A.; Nieuwenhuyzen, M. Do Polymorphic Compounds Make Good Cocrystallizing Agents? A Structural Case Study That Demonstrates the Importance of Synthon Flexibility. *Cryst. Growth Des.* **2003**, *3* (2), 159–165.

(243) Heath, E. a.; Singh, P.; Ebisuzaki, Y. Structure of P-Hydroxybenzoic Acid and P-Hydroxybenzoic Acid-Acetone Complex (2/1). *Acta Crystallogr. Sect. C Cryst. Struct. Commun.* **1992**, *48* (11), 1960–1965.

(244) Okabe, N.; Kyoyama, H. 3,4-Dihydroxyphenylacetic Acid. *Acta Crystallogr. Sect. E Struct. Reports Online* **2001**, *57* (8), o715–o716.

(245) Leis, D. G.; Curran, B. C. Electric Moments of Some γ-Substituted Pyridines. *J.*

Am. Chem. Soc. **1945**, *67* (1), 79–81.

(246) Li, J.; Bourne, S. a; Caira, M. R. New Polymorphs of Isonicotinamide and Nicotinamide. *Chem. Commun.* **2011**, *47* (5), 1530–1532.

(247) Li, B.; Wu, Y.; Zhu, J.; Chen, K.; Wu, B.; Ji, L. Determination and Correlation of Solubility and Mixing Properties of Isonicotinamide (Form II) in Some Pure Solvents. *Thermochim. Acta* **2016**, *627–629*, 55–60.

(248) Yan, D. *Unpublished Data*.

(249) Eccles, K. S.; Deasy, R. E.; Fábián, L.; Braun, D. E.; Maguire, A. R.; Lawrence, S. E. Expanding the Crystal Landscape of Isonicotinamide: Concomitant Polymorphism and Co-Crystallisation. *CrystEngComm* **2011**, *13* (23), 6923.

(250) Karmwar, P.; Graeser, K.; Gordon, K. C.; Strachan, C. J.; Rades, T. Effect of Different Preparation Methods on the Dissolution Behaviour of Amorphous Indomethacin. *Eur. J. Pharm. Biopharm.* **2012**, *80* (2), 459–464.

(251) Karmwar, P.; Graeser, K.; Gordon, K. C.; Strachan, C. J.; Rades, T. Investigation of Properties and Recrystallisation Behaviour of Amorphous Indomethacin Samples Prepared by Different Methods. *Int. J. Pharm.* **2011**, *417* (1–2), 94–100.

(252) Gaisford, S.; Saunders, M. Physical Form II - Amorphous Materials. In *Essentials of Pharmaceutical Preformulation*; John Wiley & Sons Ltd: Chichester, 2013.

(253) Ishii, K.; Nakayama, H.; Okamura, T.; Yamamoto, M.; Hosokawa, T. Excess Volume of Vapor-Deposited Molecular Glass and Its Change Due to Structural Relaxation: Studies of Light Interference in Film Samples. *J. Phys. Chem. B* **2003**, *107* (3), 876–881.

(254) Swallen, S. F.; Kearns, K. L.; Satija, S.; Traynor, K.; McMahon, R. J.; Ediger, M. D. Molecular View of the Isothermal Transformation of a Stable Glass to a Liquid. *J. Chem. Phys.* **2008**, *128* (21), 214514.

(255) O'Sullivan, C. K.; Guilbault, G. G. Commercial Quartz Crystal Microbalances – Theory and Applications. *Biosens. Bioelectron.* **1999**, *14* (8–9), 663–670.

(256) Sauerbrey, G. Verwendung von Schwingquarzen Zur Wägung Dünner Schichten

Und Zur Mikrowägung. *Zeitschrift für Phys.* **1959**, *155* (2), 206–222.

(257) Vashist, S. K.; Vashist, P. Recent Advances in Quartz Crystal Microbalance-Based Sensors. *J. Sensors* **2011**, *2011*, 1–13.

(258) Hillman, A. R.; Jackson, A.; Martin, S. J. The Problem of Uniqueness of Fit for Viscoelastic Films on Thickness-Shear Mode Resonator Surfaces. *Anal. Chem.* **2001**, *73* (3), 540–549.

(259) Bradley, J.-C.; Bradley, J.-C.; Lang, A.; Williams, A.; Curtin, E. ONS Open Melting Point Collection. *Nat. Preced.* **2011**, 1–699.

(260) Mahieu, A.; Willart, J.-F.; Dudognon, E.; Eddleston, M. D.; Jones, W.; Danède, F.; Descamps, M. On the Polymorphism of Griseofulvin: Identification of Two Additional Polymorphs. *J. Pharm. Sci.* **2013**, *102* (2), 462–468.

(261) Elder, J. P. Sublimation Measurements of Pharmaceutical Compounds by Isothermal Thermogravimetry. *J. Therm. Anal.* **1997**, *49* (2), 897–905.

(262) Chemspider http://www.chemspider.com/Chemical-Structure.3584.html?rid=d7d253ef-1bab-48e2-80e1-f8fcd63a3b90 (accessed Jul 26, 2017).

(263) Chemnet http://www.chemnet.com/cas/en/53-86-1/Indomethacin.html (accessed Jul 26, 2017).

(264) Colomina, M.; Jimenez, P.; Turrion, C. Vapour Pressures and Enthalpies of Sublimation of Naphthalene and Benzoic Acid. *J. Chem. Thermodyn.* **1982**, *14* (8), 779–784.

(265) Ferro, D.; Barone, G.; Dellagatta, G.; Piacente, V. Vapor-Pressures and Sublimation Enthalpies of Urea and Some of Its Derivatives. *J Chem Thermodyn* **1987**, *19* (9), 915–923.

(266) Vyazovkin, S.; Dranca, I. Physical Stability and Relaxation of Amorphous Indomethacin. *J. Phys. Chem. B* **2005**, *109* (39), 18637–18644.

(267) Kearns, K. L.; Swallen, S. F.; Ediger, M. D.; Sun, Y.; Yu, L. Calorimetric Evidence for Two Distinct Molecular Packing Arrangements in Stable Glasses of Indomethacin. *J. Phys. Chem. B* **2009**, *113* (6), 1579–1586.

(268) Yoshioka, M.; Hancock, B. C.; Zografi, G. Crystallization of Indomethacin from

the Amorphous State below and above Its Glass Transition Temperature. *J. Pharm. Sci.* **1994**, *83* (12), 1700–1705.

(269) Kumar, Y.; Kumar, S. M. D.; Singh, R.; Sathyanarayana, S. Amorphous Form of Finasteride and Processes for Its Preparation, 2005.

(270) Swaminathan, S.; Craven, B. M.; McMullan, R. K. The Crystal Structure and Molecular Thermal Motion of Urea at 12, 60 and 123 K from Neutron Diffraction. *Acta Crystallogr. Sect. B* **1984**, *40* (3), 300–306.

(271) Olejniczak, A.; Ostrowska, K.; Katrusiak, A. H-Bond Breaking in High-Pressure Urea. *J. Phys. Chem. C* **2009**, *113* (35), 15761–15767.

(272) Cliffe, M. J.; Castillo-Martínez, E.; Wu, Y.; Lee, J.; Forse, A. C.; Firth, F. C. N.; Moghadam, P. Z.; Fairen-Jimenez, D.; Gaultois, M. W.; Hill, J. A.; Magdysyuk, O. V.; Slater, B.; Goodwin, A. L.; Grey, C. P. Metal-Organic Nanosheets Formed via Defect-Mediated Transformation of a Hafnium Metal-Organic Framework. *J. Am. Chem. Soc.* **2017**, *139* (15), 5397–5404.

(273) Lu, E. Stabilization of Amorphous Pharmaceuticals by Excipients, 2008.

(274) Walters, D. M.; Richert, R.; Ediger, M. D. Thermal Stability of Vapor-Deposited Stable Glasses of an Organic Semiconductor. *J. Chem. Phys.* **2015**, *142* (13), 134504.

(275) Sepúlveda, A.; Tylinski, M.; Guiseppi-Elie, A.; Richert, R.; Ediger, M. D. Role of Fragility in the Formation of Highly Stable Organic Glasses. *Phys. Rev. Lett.* **2014**, *113* (4), 1–5.

(276) Swallen, S. F.; Windsor, K.; McMahon, R. J.; Ediger, M. D.; Mates, T. E. Transformation of Stable Glasses into Supercooled Liquids: Growth Fronts and Anomalously Fast Liquid Diffusion. *J. Phys. Chem. B* **2010**, *114* (8), 2635–2643.

(277) Guillory, J. K. Generation of Polymorphs, Hydrates, Solvates, and Amorphous Solids. In *Polymorphism in Pharmaceutical Solids*; Brittain, H. G., Ed.; Marcel Dekker, Inc: New York, 1999; pp 183–226.

8. Appendices

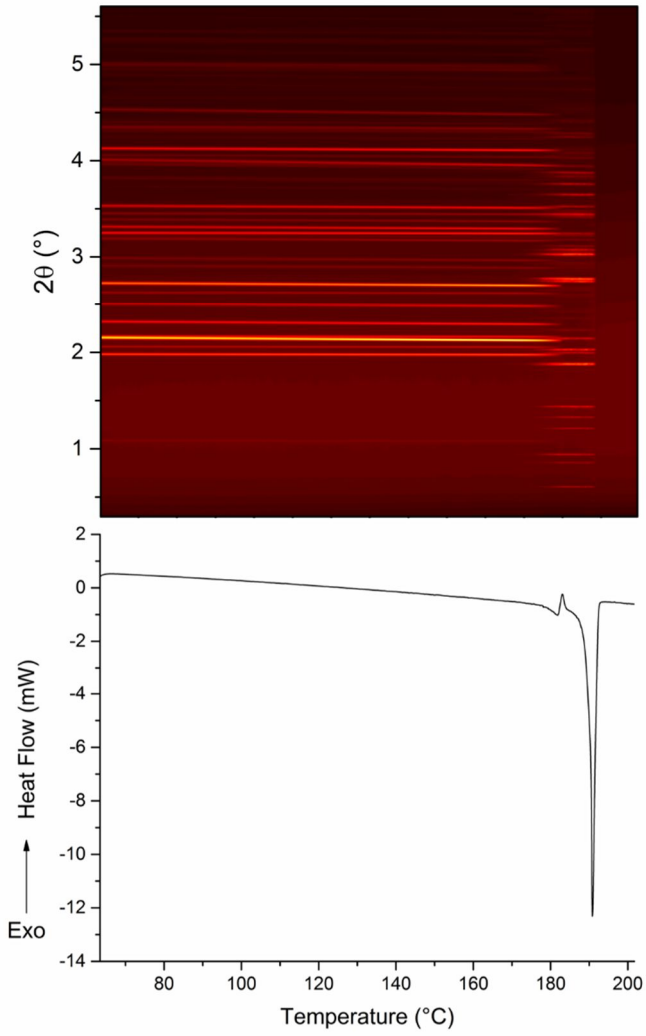

1. DSC-XRD data for a sample of carbamazepine form II heated at 2 °C min^{-1}.

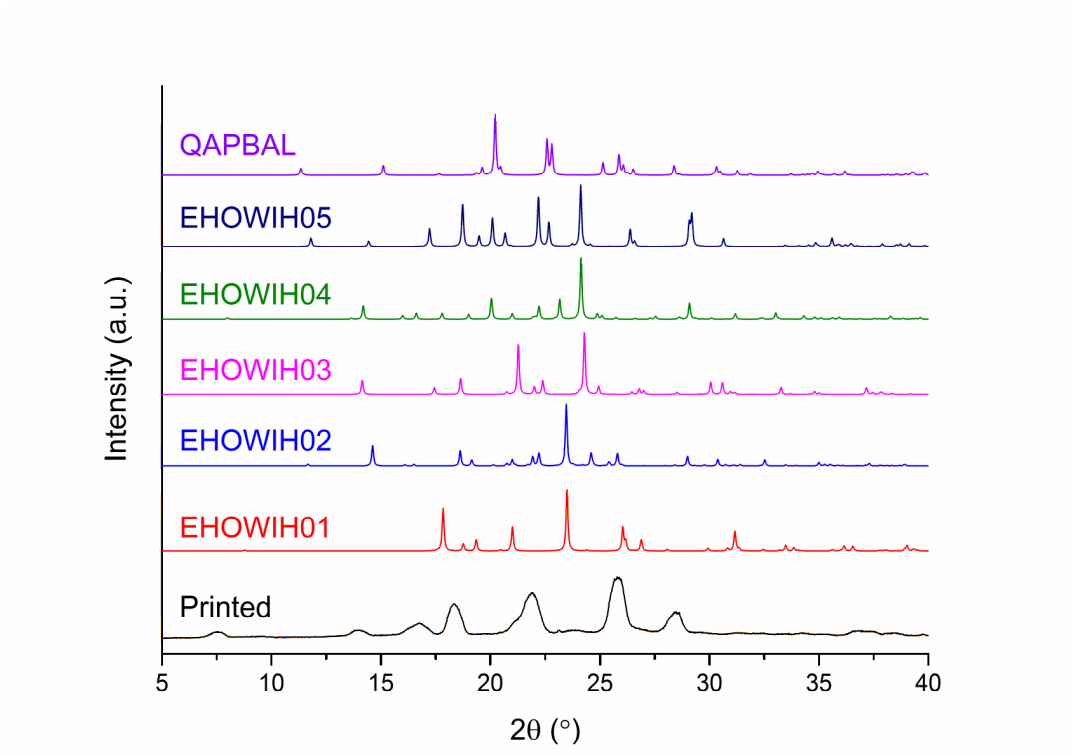

2. Comparison of the PXRD patterns for crystals printed from a 2:1 molar ratio mixture of INCT and HPAA and the known polymorphs of the two raw materials (INCT: EHOWIH, HPAA: QAPBAL).

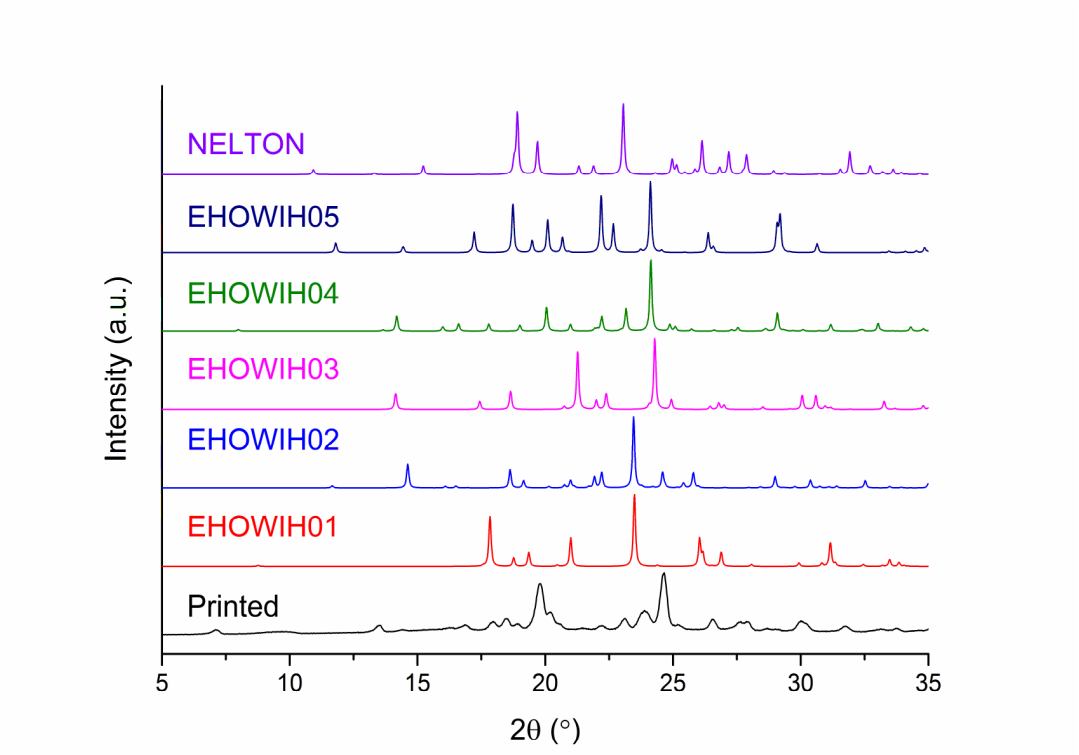

3. Comparison of the PXRD patterns for crystals printed from a 1:1 molar ratio mixture of INCT and DHPAA and the known polymorphs of the two raw materials (INCT: EHOWIH, DHPAA: NELTON).